NASA TECHNICAL MEMORANDUM

NASA TM X-3459

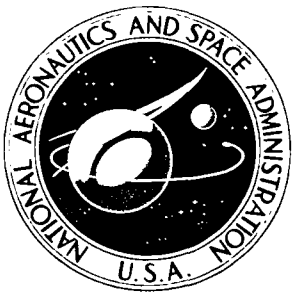

NASA TM X-3459

AILERON AND KRÜGER NOSE FLAP EFFECTIVENESS MEASURED ON AN OBLIQUE WING

Edward J. Hopkins and George H. Lovette

Ames Research Center

Moffett Field, Calif. 94035

NATIONAL AERONAUTICS AND SPACE ADMINISTRATION • WASHINGTON, D. C. • MARCH 1977

1. Report No.	2. Government Accession No.	3. Recipient's Catalog No.
NASA TM X-3459		

4. Title and Subtitle	5. Report Date
AILERON AND KRÜGER NOSE FLAP EFFECTIVENESS MEASURED ON AN OBLIQUE WING	March 1977
	6. Performing Organization Code

7. Author(s)	8. Performing Organization Report No.
Edward J. Hopkins and George H. Lovette*	A-6645
	10. Work Unit No.
9. Performing Organization Name and Address	505-06-31
NASA-Ames Research Center Moffett Field, Calif. 94035	11. Contract or Grant No.
	13. Type of Report and Period Covered
12. Sponsoring Agency Name and Address	Technical Memorandum
National Aeronautics and Space Administration Washington, D.C. 20546	14. Sponsoring Agency Code

15. Supplementary Notes

*Project Engineer, ARO, Inc., Moffett Field, Calif. 94035

16. Abstract

The effects that deflection of conventional ailerons have on the lateral/directional characteristics of an oblique wing mounted on top of a body of revolution were measured. The wing had an aspect ratio of 6 (based on the unswept wing span) and was tested at various sweep angles ranging from 0° to 60°. Krüger nose flaps mounted on drooped-nose flaps were investigated on the downstream wing panel (for sweep angles of 45° and 60°) in an attempt to create more symmetrical spanwise wing stalling at high lift coefficients. The tests were conducted over a Mach number range of 0.25 to 1.4 and an angle-of-attack range from −3° to 28°.

With the oblique wing in the swept position, considerable difference in the aileron effectiveness was measured for positive or negative differential aileron deflections. With the wing swept 45° at a Mach number of 0.8 and above, an extension of the span of the Krüger nose flaps on the downstream wing panel did not improve the linearity of the pitching-, rolling-, and yawing-moment curves.

17. Key Words (Suggested by Author(s))	18. Distribution Statement
Aileron effectiveness Krüger nose flaps	Unlimited STAR Category – 02

19. Security Classif. (of this report)	20. Security Classif. (of this page)	21. No. of Pages	22. Price*
Unclassified	Unclassified	275	$8.50

* For sale by the National Technical Information Service, Springfield, Virginia 22161

NOMENCLATURE

The axes systems and sign conventions are presented in figure 1. Lift, drag, and pitching moments are presented about the stability axes; side force, rolling moments, and yawing moments are presented about the body axes.

b	wing span
C_D	drag coefficient, $\frac{\text{drag}}{qS}$
C_l	rolling-moment coefficient about the body axes, $\frac{\text{rolling-moment}}{qSb}$
C_L	lift coefficient, $\frac{\text{lift}}{qS}$
C_m	pitching-moment coefficient (see fig. 2 for moment-center location), $\frac{\text{pitching moment}}{qS\bar{c}}$
C_n	yawing-moment coefficient about the body axes, $\frac{\text{yawing moment}}{qSb}$
C_Y	side-force coefficient about the body axes, $\frac{\text{side force}}{qS}$
c	wing chord
c_{aft}	portion of wing chord aft of the $0.25c$ line
c_{fwd}	portion of wing chord forward of the $0.25c$ line
c_{root}	wing root chord
$\bar{c}$	wing mean aerodynamic chord
H	vertical distance from wing reference plane to base line (see fig. 3(a))
$\frac{L}{D}$	lift-to-drag ratio
M	Mach number
q	free-stream dynamic pressure
RN/L	unit Reynolds number in millions per meter
r	body radius
S	wing area
$\left(\frac{t}{c}\right)_{\text{max}}$	maximum thickness-to-chord ratio
V	free-stream velocity

x	chordwise distance along airfoil
x_1	axial distance along body from the 57.45 cm longitudinal station
Y	distance along wing span (see fig. 3(a))
z	vertical distance above the airfoil chord line
α	angle of attack, deg
$\Delta\delta_a$	aileron deflection; for example, $\Delta\delta_a = 15°$ corresponds to the left aileron being deflected downward 15° and the right aileron being deflected upward 15°
Λ	sweep angle measured between a perpendicular to the body axis and the $0.25c$ line of the wing in a horizontal plane (the right wing tip is forward for positive Λ's), deg

AILERON AND KRÜGER NOSE FLAP EFFECTIVENESS MEASURED ON AN OBLIQUE WING

Edward J. Hopkins and George H. Lovette*

Ames Research Center

SUMMARY

The effects that deflection of conventional ailerons have on the lateral/directional characteristics of an oblique wing mounted on top of a body of revolution were measured. The wing had an aspect ratio of 6 (based on the unswept wing span) and was tested at various sweep angles ranging from 0° to 60°. Krüger nose flaps mounted on drooped-nose flaps were investigated on the downstream wing panel (for sweep angles of 45° and 60°) in an attempt to create more symmetrical spanwise wing stalling at high lift coefficients. The tests were conducted over a Mach number range of 0.25 to 1.4 and an angle-of-attack range from −3° to 28°.

With the oblique wing in the swept position, considerable difference in the aileron effectiveness was measured for positive or negative differential aileron deflections. With the wing swept 45° at a Mach number of 0.8 and above, an extension of the span of the Krüger nose flaps on the downstream wing panel did not improve the linearity of the pitching-, rolling-, and yawing-moment curves.

INTRODUCTION

It was shown in reference 1 that a wing-body combination employing a low aspect-ratio oblique wing (suitable for highly maneuverable vehicles) had greater aerodynamic efficiency than a conventional, fixed-sweep wing design over a Mach number range of 0.6 to 1.4. At a Mach number of 0.95, the maximum lift-to-drag ratio measured for the oblique-wing design was about twice that of the fixed-sweep design, both having 45° of sweep. At high lift coefficients, planar oblique wings suffer from an asymmetrical spanwise distribution of section lift coefficients and related asymmetrical stalling; this leads to nonlinear pitching-, rolling-, and yawing-moment curves.

Several possible means for overcoming this asymmetry of wing stalling have been investigated; namely, upward wing bending in references 2 and 3, Krüger nose flaps in reference 4, and drooped-nose flaps in reference 5. Krüger-nose flaps, mounted on drooped-nose flaps (deflected 5°) on the downstream wing panel, proved to be the only method investigated that considerably improved the linearity of the moment curves. In reference 4, the Krüger flaps covered only a portion of the downstream wing span of the oblique wing; therefore, in the present investigation the effect, on the spanwise stall progression, of having the Krüger nose flaps extend up to the wing-body juncture was explored.

*Project Engineer, ARO, Inc., Moffett Field, Calif. 94035.

The present investigation was undertaken mainly to measure the effectiveness of conventional ailerons on an oblique wing at various angles of sweep over a Mach number range of 0.25 to 1.4. The same intermediate bend, oblique wing that was used in reference 2 was selected for this study. It was necessary to test these ailerons with both positive and negative differential deflections because of the asymmetry of spanwise wing loading and stalling.

CONFIGURATION CODE

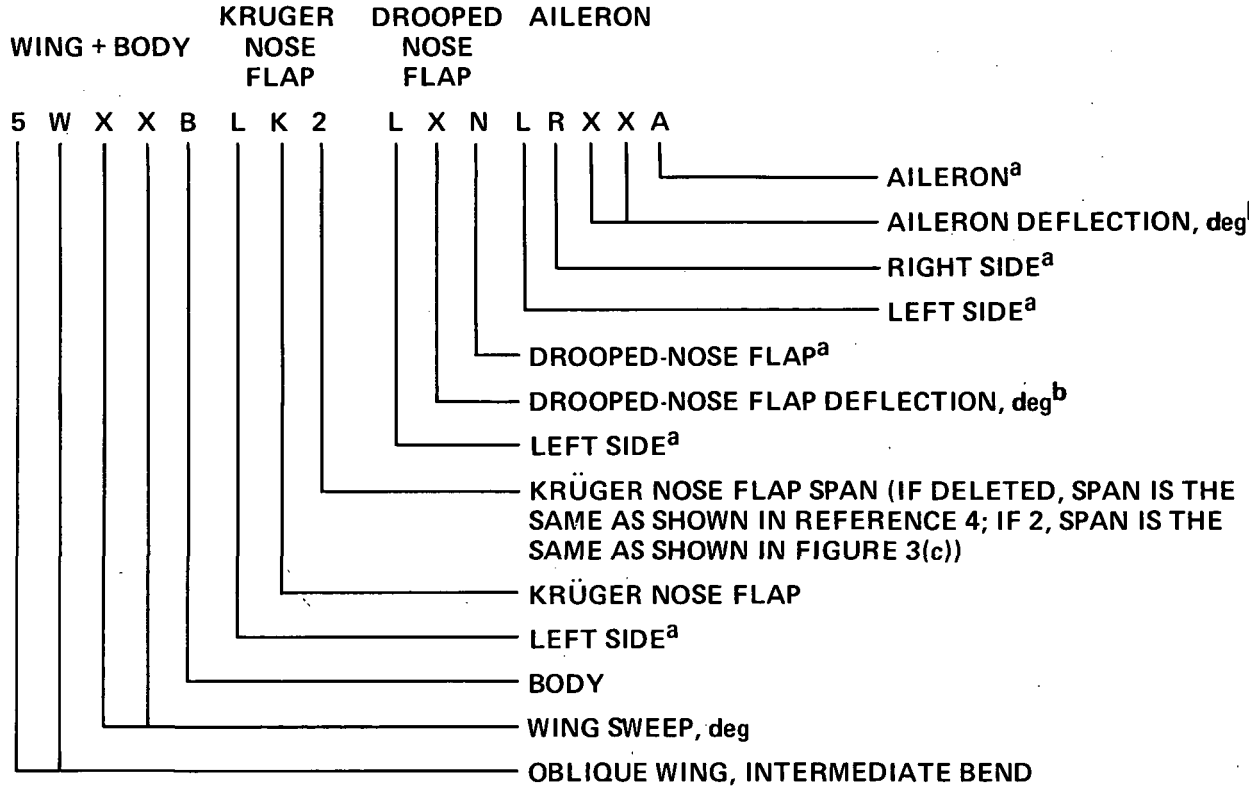

[a]When symbol is deleted, Krüger flaps are removed or ailerons and drooped-nose flaps are undeflected.

[b]When number is deleted, ailerons or drooped-nose flaps are undeflected. A positive number corresponds to the amount in degrees that the left aileron is deflected downward and the right aileron is deflected upward.

TEST FACILITY

The Ames 6- by 6-Foot Wind Tunnel is a variable pressure, continuous flow, closed return-type facility. The nozzle ahead of the test section consists of an asymmetric sliding block which permits a continuous variation of Mach number from 0.25 to 2.3. The test section has a perforated floor and ceiling for boundary-layer removal to permit transonic testing.

MODEL DESCRIPTION

The model consisted of an oblique wing mounted on top of a Sears-Haack body of revolution designed to have minimum wave drag for a given length and volume. With different fairing blocks installed under the wing (fig. 2) the wing could be swept 0°, 45°, 50°, 55°, and 60°. Details of the body and of the fairing blocks are given in table 3 of reference 3. Note in figure 2 that the wing pivot point and the moment center are located at $0.40c_{root}$ ($\Lambda = 0°$). The wing planform consisted of two semiellipses having the same major axis but different minor axes in the ratio of 3:1 so that the major axis is the quarter chord line. The aspect ratio of the wing ($\Lambda = 0°$) was 6.0. The wing panels were bent upward to form the so-called intermediate bend shown in figure 3(a). With the chord lines that are perpendicular to the quarter chord line remaining in horizontal planes, this type of bending is equivalent to wing twist when the wing is swept – that is, washout on the downstream panel and washin on the upstream panel. Additional geometric wing and body details are presented in table 1.

A subcritical Garabedian airfoil section with a maximum $t/c = 0.1016$ (designed for a lift coefficient of 1.3 at a Mach number of 0.6) was used perpendicular to the quarter chord line. This profile, shown in figure 3(b), was adjusted in maximum thickness from $0.11c$ at the wing root to $0.06c$ at the wing tip, according to the elliptical equation given in figure 3(a). Coordinates for the Garabedian profile are given in table 2.

The model was equipped with $0.25c$ ailerons that covered 45 percent of the wing semispan as shown in figure 3(c). For each aileron deflection, the gaps near the aileron nose were sealed and faired in smoothly with the wing contour.

The Krüger nose flaps were similar to those used on the same wing in reference 4; however, with the wing swept 45°, the flap span was increased up to the wing-body juncture. With the wing swept 60°, the Krüger nose flap span was the same as that for the wing swept 45°; therefore, a slight gap existed between the end of the flap and the body for this case. All gaps between Krüger nose flap segments shown in figure 3(c) were sealed. These flaps were only used on the downstream wing panel and were mounted on the nose flaps that were drooped 5°. The upper surface of the Krüger-nose flaps was faired into the nose flaps with putty.

DATA REDUCTION AND TEST PROCEDURE

The model was sting-supported through the base of the model on a 6-component electrical strain-gage balance as shown in figure 4. Measured drag forces were corrected to a condition corresponding to having the free-stream static pressure on the base of the fuselage. Moment data are presented about a center located on the body axis at $0.4c_{root}$ ($\Lambda = 0°$) (see fig. 2). Reference lengths and the wing area used in the reduction of the data are given in table 1.

Boundary-layer transition strips (0.1905 cm wide), consisting of a random distribution of glass spheres 0.01905 cm in diameter, were placed on the upper and lower surface of the wing 0.762 cm downstream of the wing and Krüger nose flap leading edges, and on the body 2.54 cm behind its tip. Sublimation studies made at wing sweep angles of 0° and 45° (flaps retracted) indicated that the boundary layer was tripped by the glass spheres near the roughness strips at $\alpha = 0°$ and 10° at Mach numbers of 0.6 and 0.9. Estimates of the required size of roughness to trip the boundary layer at other sweep angles and higher Mach numbers indicate that the chosen size should be adequate.

For most of the data, the unit Reynolds number was held constant at 8.2×10^6/m; however, at a Mach number of 0.25 the unit Reynolds number was sometimes reduced to 5.7×10^6/m, because of the dynamic overload restrictions of the balance. The model was mounted on a sting that was bent 10° to increase the maximum angle of attack; the resulting angle-of-attack range was from −3° to 28°. Angle of attack was indicated by an electrical dangleometer mounted in the support located downstream of the sting. Corrections were applied to the indicated angle of attack for balance and sting deflections.

For the aileron effectiveness measurements, the wing sweep was held successively at 0°, 45°, 50°, 55°, and 60°. With the wing in a swept position, the right and left ailerons were differentially deflected both plus and minus 5°, 10°, and 15°, because of the asymmetric spanwise loading associated with oblique wings.[1] For the Krüger nose flap measurements, the wing was swept either 45° or 60°.

RESULTS AND DISCUSSION

An indication of the effectiveness of the Krüger nose flaps in controlling the flow separation on the downstream wing panel of the oblique wing with intermediate bend, mounted with a sweep angle of 45°, is presented in figures 5 through 11. Similar results for the oblique wing mounted with a sweep angle of 60° are presented in figures 12 through 18. To assist in evaluating the Krüger nose flap results given in figures 5 through 18 for Mach numbers of 0.6 and above, results are also presented for the plain oblique wing. In figures 5 through 10, results from reference 4 for the oblique wing ($\Lambda = 45°$) equipped with the shortened Krüger nose flap, are also presented for comparison purposes. Similar data for the oblique wing swept 60° and with the shortened Krüger nose flap were not obtained. The aileron effectiveness on the oblique wing is presented in figures 19 through 22 for $\Lambda = 0°$; in figures 23 through 29 for $\Lambda = 45°$; in figures 30 through 36 for $\Lambda = 50°$;

[1] A positive aileron designation ($\Delta\delta_a$) on the figures corresponds to the extent, in degrees, that the left aileron is deflected downward and the right aileron deflected upward.

in figures 37 through 43 for $\Lambda = 55°$; and in figures 44 through 50 for $\Lambda = 60°$. In figures 19 through 50, the effects of aileron deflection on the static longitudinal stability characteristics are presented for a differential aileron deflection of ±15° only; the effectiveness of the aileron for producing rolling moments, yawing moments, and side force is presented for differential aileron deflections of ±5°, ±10°, and ±15°.

Krüger Nose Flaps

At Mach numbers of 0.25, 0.40, and 0.60, with a wing sweep of 45°, an extension of the span of the Krüger nose flap (mounted on only the downstream wing panel) up to the fuselage had the favorable effect of changing the "pitch-up" to a "pitch-down" tendency at C_L's between about 0.9 and 1.2. This extension also made the rolling-moment curves more linear, but had no beneficial effect on the yawing-moment curves (see figs. 5 through 7). At Mach numbers of 0.80 and above and a wing sweep of 45°, an extention of the span of the Krüger nose flaps did not improve the linearity of the pitching-, rolling-, and yawing-moment curves (see figs. 8 through 11).

At subsonic Mach numbers between 0.6 and 0.9, and for a wing sweep of 60°, the Krüger nose flaps (mounted on only the downstream wing panel) reduced the "pitch-up" tendency of the plain wing between lift coefficients of 0.7 and 1.0, and produced slightly more linear C_Y, C_n, and C_l curves (see figs. 14 through 16). At Mach numbers of 0.95 and 1.4 (figs. 17 and 18), there was little or no improvement in the linearity of either the C_m or C_l curves.

Aileron Effectiveness

For subsonic Mach numbers and all angles of wing sweep, somewhat larger rolling moments were produced by deflecting the aileron on the trailing wing panel upward and deflecting the aileron on the leading wing panel downward (negative $\Delta\delta_a$) than resulted from deflecting these ailerons in the opposite direction (e.g., see figs. 23(e) and 23(f) through figs. 26(e) and 26(f)). At low lift coefficients, it can be observed that more than 15° of aileron deflection on each wing panel is required to trim the rolling moment related to having the wing panels bent upward to the intermediate bend position. Since it was pointed out in reference 2 that bending the wing upward, to the form of the wing with intermediate bend, did not improve the asymmetrical spanwise wing stall; it only produced rolling moments to be trimmed at low lift coefficients. A better wing design might not have any upward bend and thus no associated rolling moments. At high lift coefficients, considerably more than 15° of aileron deflection on each panel would be required to trim the rolling moments resulting from the asymmetry of wing stalling. As shown in figures 23(c) through 50(c), the deflection of ailerons on swept oblique wings produces large pitching moments which would at least partly have to be trimmed by an auxiliary horizontal surface. However, for an oblique-winged airplane designed with positive static longitudinal stability and no builtin wing bend, the pitching moment produced by aileron deflection could be nearly "self trimming." At supersonic Mach numbers, slightly greater rolling moments were produced by deflecting the aileron on the trailing wing panel downward and deflecting the aileron on the leading wing panel upward (positive $\Delta\delta_a$), than by deflecting these ailerons in the opposite direction; for example, see figures 27(e) and 27(f) or 28(e) and 28(f).

CONCLUDING REMARKS

With the oblique wing in the swept position, considerable difference in the aileron effectiveness was measured for positive or negative differential aileron deflection. More than 15° of aileron deflection on each wing panel was required to trim the rolling moments produced at low lift coefficient when the wing panels were bent upward (in an attempt to alleviate the asymmetric spanwise wing stalling) and to trim the rolling moments at high lift coefficients due to wing stalling.

With the wing swept 45° at a Mach number of 0.8 and above, an extension of the span of the Krüger nose flaps on the downstream wing panel did not improve the linearity of the pitching-, rolling-, and yawing-moment curves. With the wing swept 60° at Mach numbers of 0.60 and 0.80, the Krüger nose flaps (mounted on only the downstream wing panel) reduced the pitch-up tendency of the plain wing and produced slightly more linear rolling- and yawing-moment curves, but had no beneficial effects at the higher Mach numbers.

Ames Research Center
National Aeronautics and Space Administration
Moffett Field, Calif. 94035, June 3, 1976

REFERENCES

1. Hopkins, Edward J.; and Levin, Alan D.: Study of Low-Aspect Ratio Swept and Oblique Wings. AIAA J. Aircraft, vol. 12, no. 8, 1975, pp. 648–652.

2. Hopkins, Edward J.: Effects of Wing Bend on the Aerodynamic Characteristics of a Low Aspect Ratio Oblique Wing. AIAA Preprint 75-995, AIAA Aircraft Systems and Technology Meeting, Los Angeles, Calif., Aug. 4–7, 1975.

3. Hopkins, Edward J.; Meriwether, Frank D.; and Pena, Douglas F.: Experimental Aerodynamic Characteristics of Low Aspect Ratio Swept and Oblique Wings at Mach Numbers Between 0.6 and 1.4. NASA TM X-62,317, 1973.

4. Hopkins, Edward J.; and Lovette, George H.: Effect of Krüger Nose Flaps on the Experimental Force and Moment Characteristics of an Oblique Wing. NASA TM X-3372, 1976.

5. Hopkins, Edward J.; and Lovette, George H.: Effect of Drooped-Nose Flaps on the Experimental Force and Moment Characteristics of an Oblique Wing. NASA TM X-3398, 1976.

TABLE 1.– MODEL GEOMETRY

Body	
Radius	$r = 3.856[1 - (1 - 2x_1/114.91)^2]^{3/4}$ cm
Length	
Closed	114.91 cm
Cutoff	91.44 cm
Maximum diameter	7.71 cm
Wing	
Planform ellipticity about 0.25 c line	4.7:1
Span	90.51 cm
Span (reference)	71.12 cm
Area (reference)	1365.09 cm^2
Mean aerodynamic chord (reference), $\bar{c}$	20.88 cm
Root chord	19.20 cm
Aspect ratio ($\Lambda = 0$)	6.0
Aspect ratio ($\Lambda = 45°$)	3.2
Incidence relative to body centerline	0
Profile perpendicular to 0.25 c line	Garabedian, subcritical (see table 2)

TABLE 2.– COORDINATES FOR GARABEDIAN PROFILE
[$(t/c)_{max}$ = 0.1016, design lift coefficient = 1.3 at M = 0.6]

x/c	z/c	x/c	z/c
0	0	0	0
−.00045	.00079	.00048	−.00058
−.00073	.00146	.00104	−.00120
−.00086	.00191	.00165	−.00176
−.00097	.00244	.00257	−.00249
−.00103	.00290	.00343	−.00308
−.00106	.00345	.00467	−.00382
−.00104	.00403	.00592	−.00445
−.00098	.00463	.00674	−.00481
−.00077	.00572	.00774	−.00519
−.00052	.00653	.00943	−.00570
−.00021	.00732	.01149	−.00620
.00026	.00830	.01539	−.00694
.00073	.00909	.02583	−.00837
.00163	.01033	.03967	−.00970
.00276	.01161	.06022	−.01116
.00464	.01340	.09339	−.01288
.00709	.01538	.13965	−.01462
.01197	.01878	.19880	−.01601
.02179	.02443	.25034	−.01684
.03187	.02928	.31761	−.01738
.04250	.03373	.38597	−.01735
.06373	.04113	.45495	−.01657
.09353	.04969	.50010	−.01568
.13389	.05882	.54359	−.01456
.17545	.06597	.57465	−.01363
.22415	.07249	.61351	−.01232
.28227	.07822	.65330	−.01090
.34741	.08236	.68122	−.00988
.41444	.08434	.71655	−.00865
.48168	.08406	.74682	−.00771
.55738	.08094	.77611	−.00702
.62052	.07591	.82243	−.00642
.68276	.06852	.87054	−.00698
.72012	.06288	.89717	−.00810
.75413	.05684	.91595	−.00941
.82318	.04227	.94348	−.01235
.85663	.03370	.96854	−.01674
.89115	.02388	.98615	−.02126
.92448	.01327	.99596	−.02434
.95410	.00145	1.00000	−.02600
.97175	−.00538		
.99163	−.01450		
1.00000	−.01900		

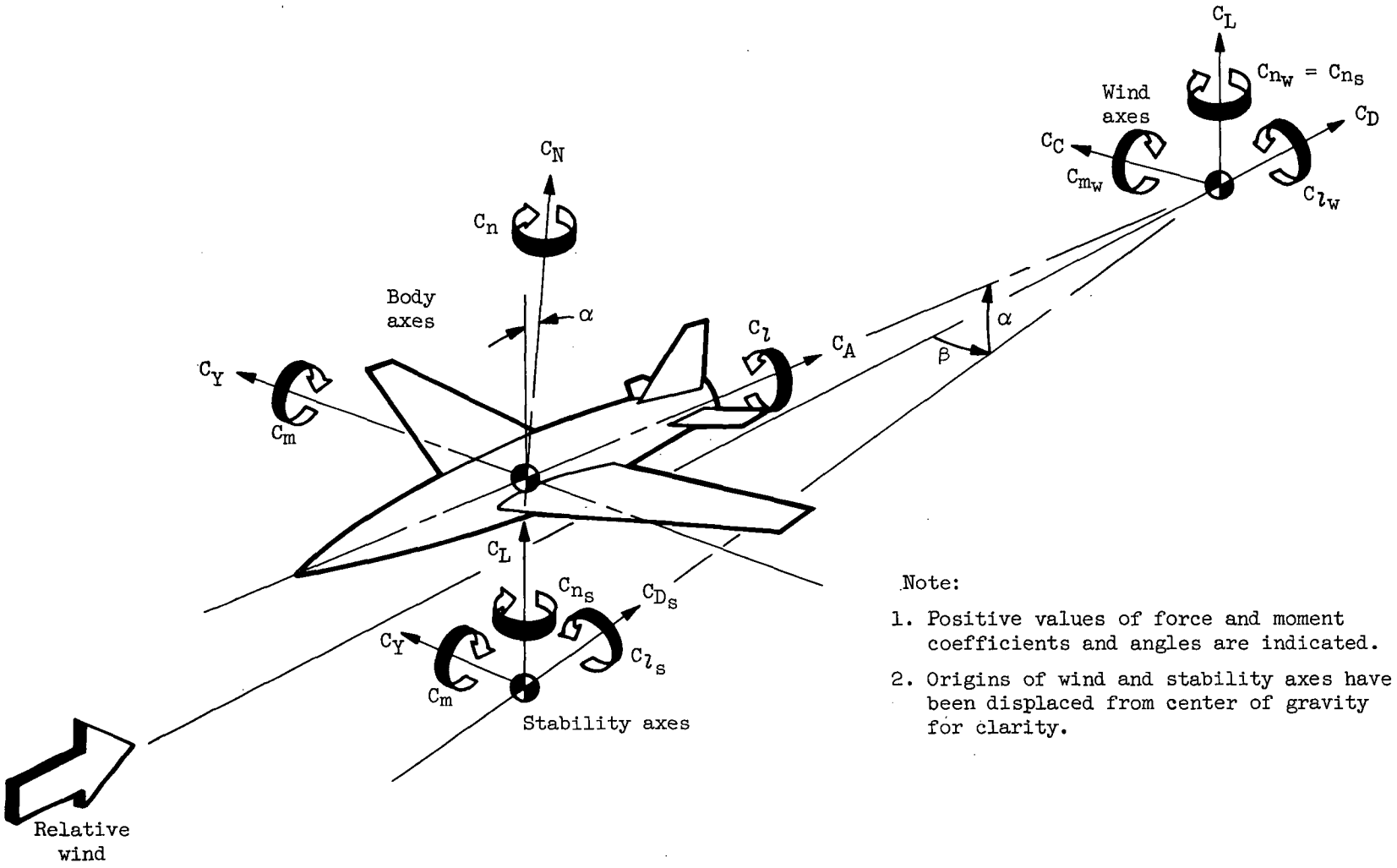

Note:

1. Positive values of force and moment coefficients and angles are indicated.
2. Origins of wind and stability axes have been displaced from center of gravity for clarity.

Figure 1.– Axes systems.

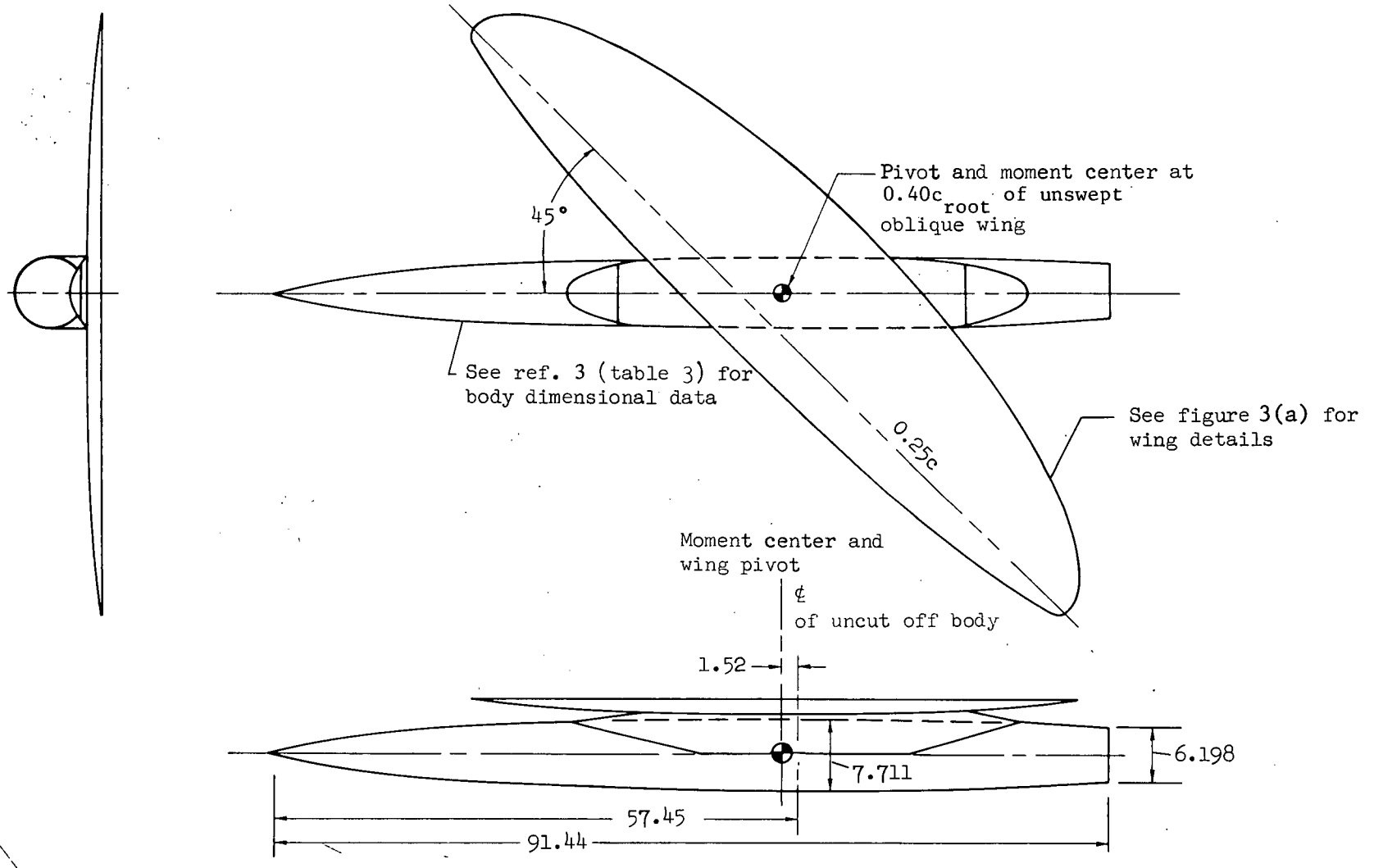

Figure 2.– Pivot and moment-center locations for the oblique wing mounted on top of the body of revolution.

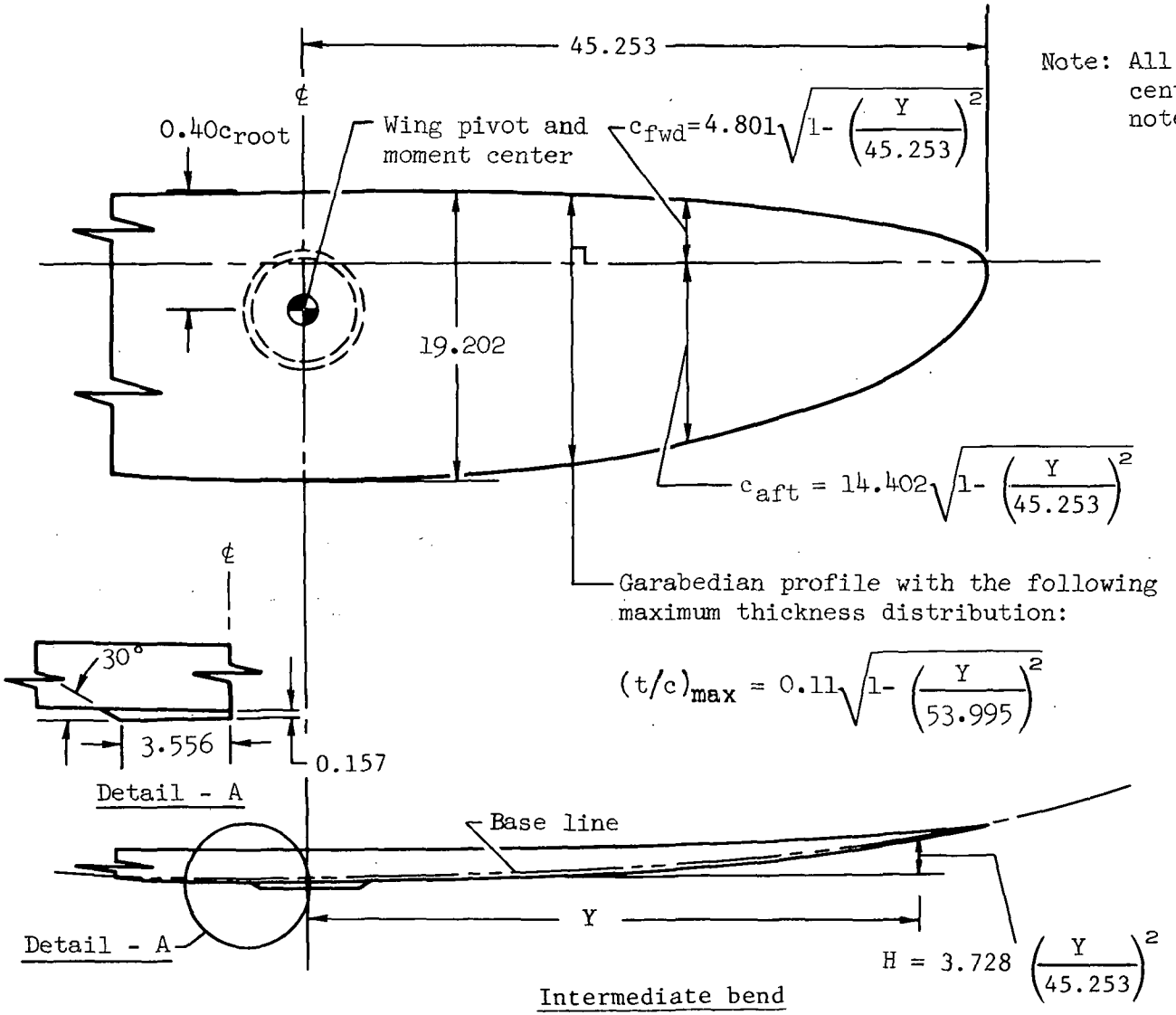

(a) Planform and bend lines.

Figure 3.– Geometry of the oblique wings.

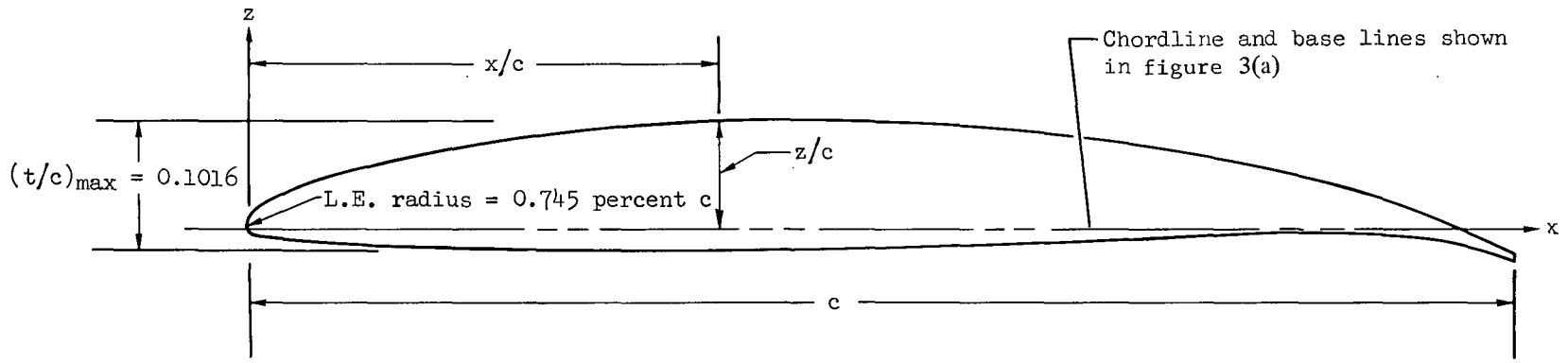

(b) Garabedian profile.

Figure 3.– Continued.

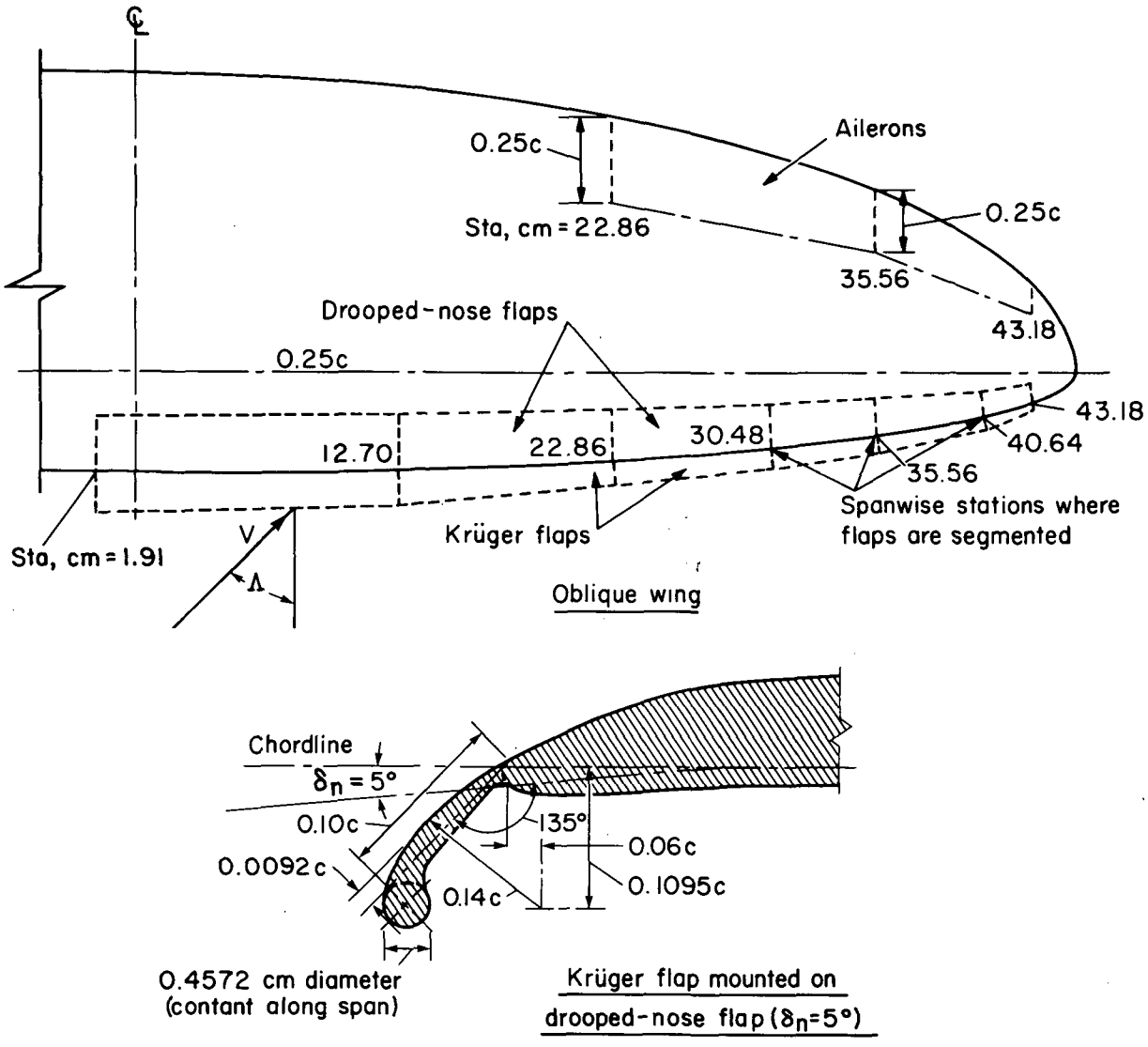

(c) Ailerons and Krüger flaps.

Figure 3.– Concluded.

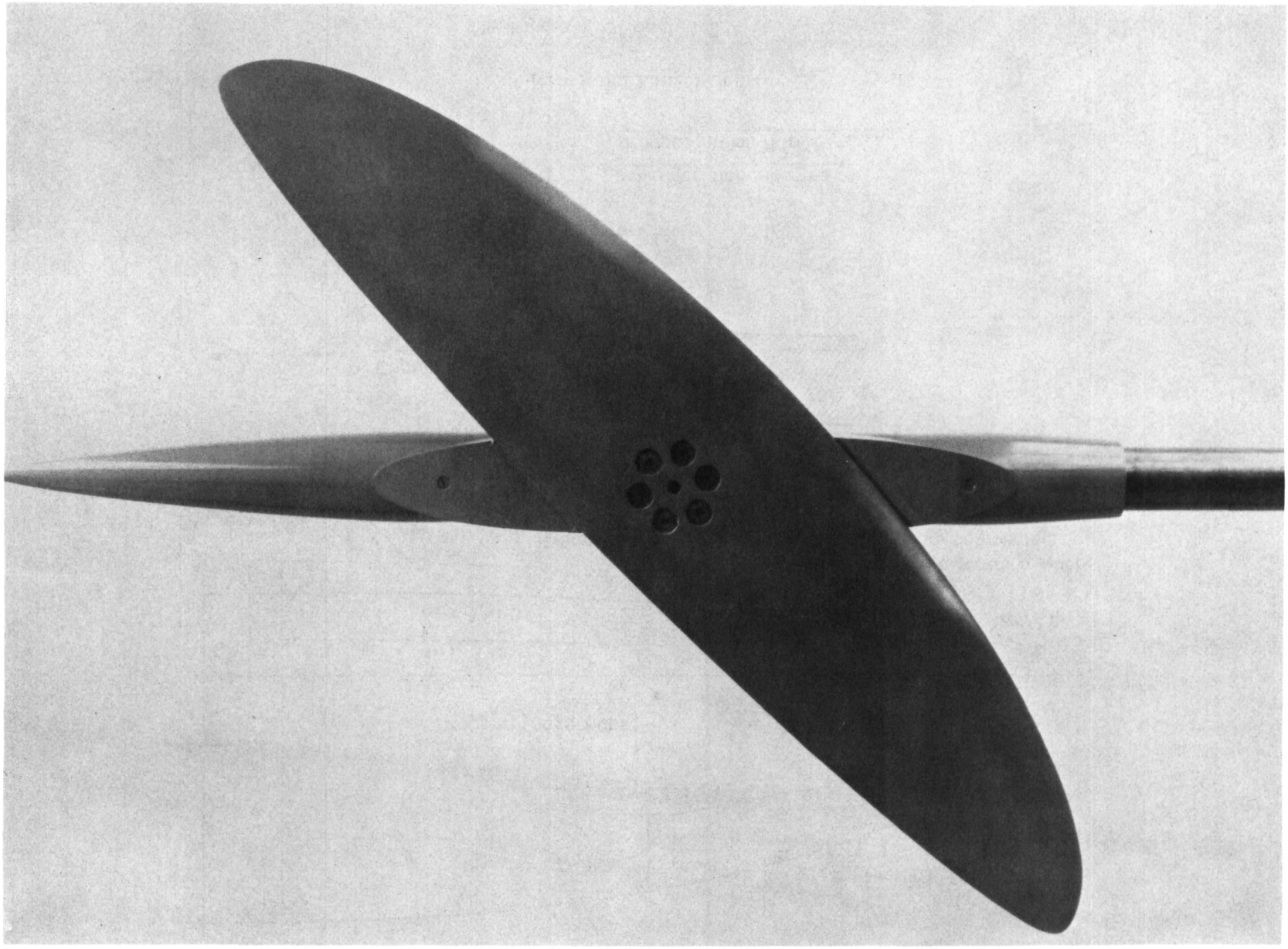

Figure 4.– Photograph of the oblique wing ($\Lambda = 45°$) mounted on top of the body of revolution.

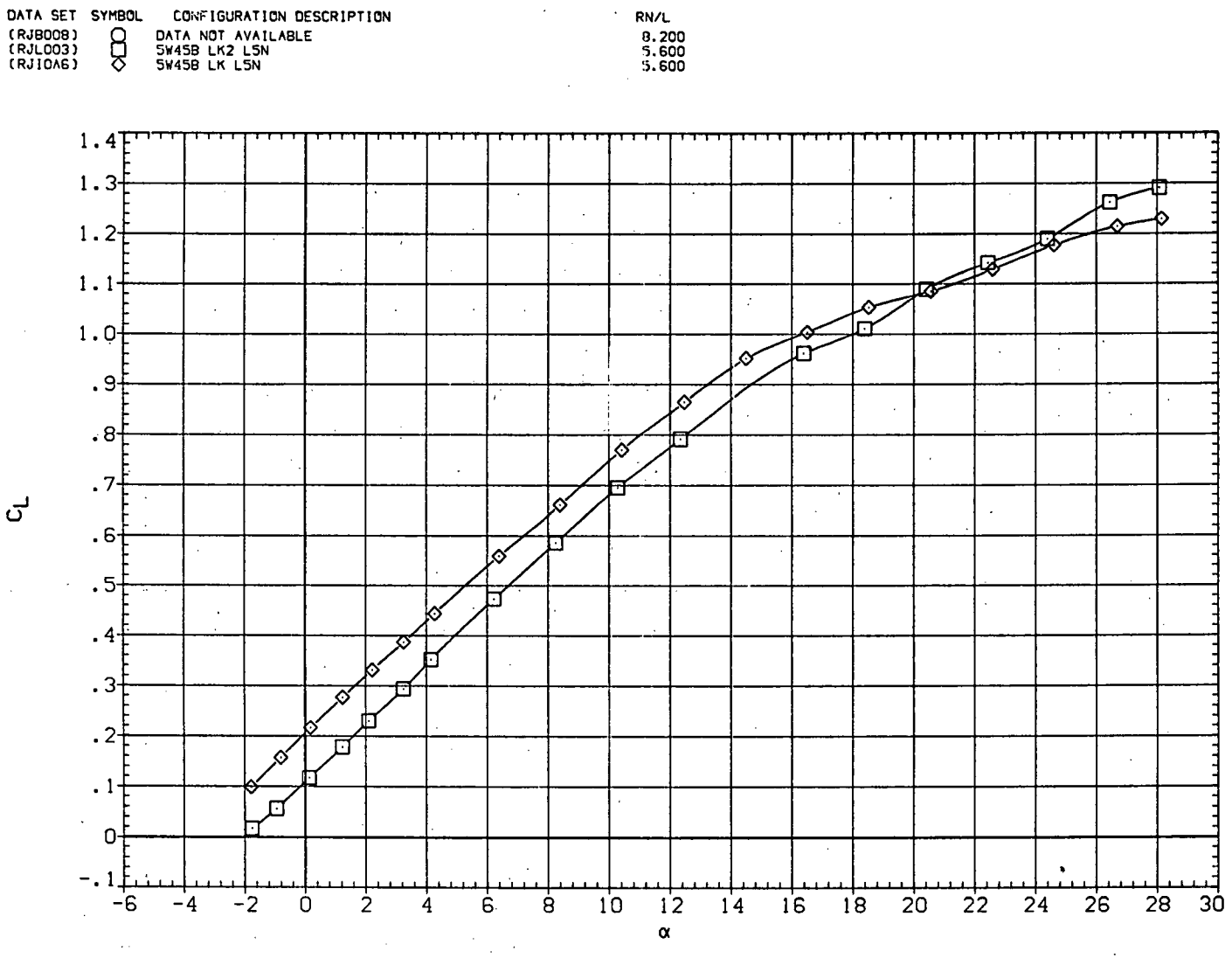

(a) C_L vs α

Figure 5.– Effect of Krüger flaps mounted on the drooped-nose flaps deflected 5°, downstream panel only: $\Lambda = 45°, M = 0.25$.

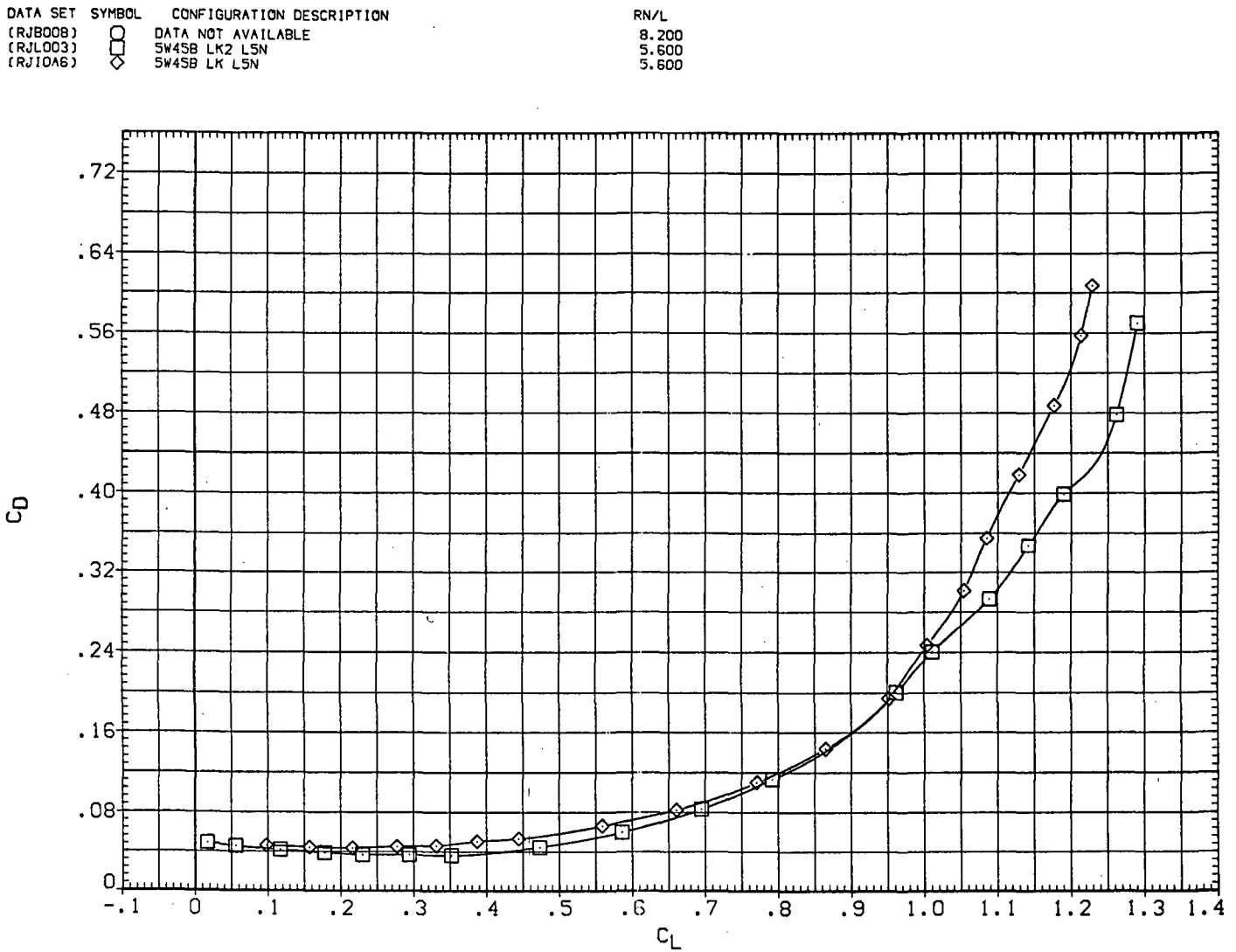

(b) C_D vs C_L

Figure 5.– Continued.

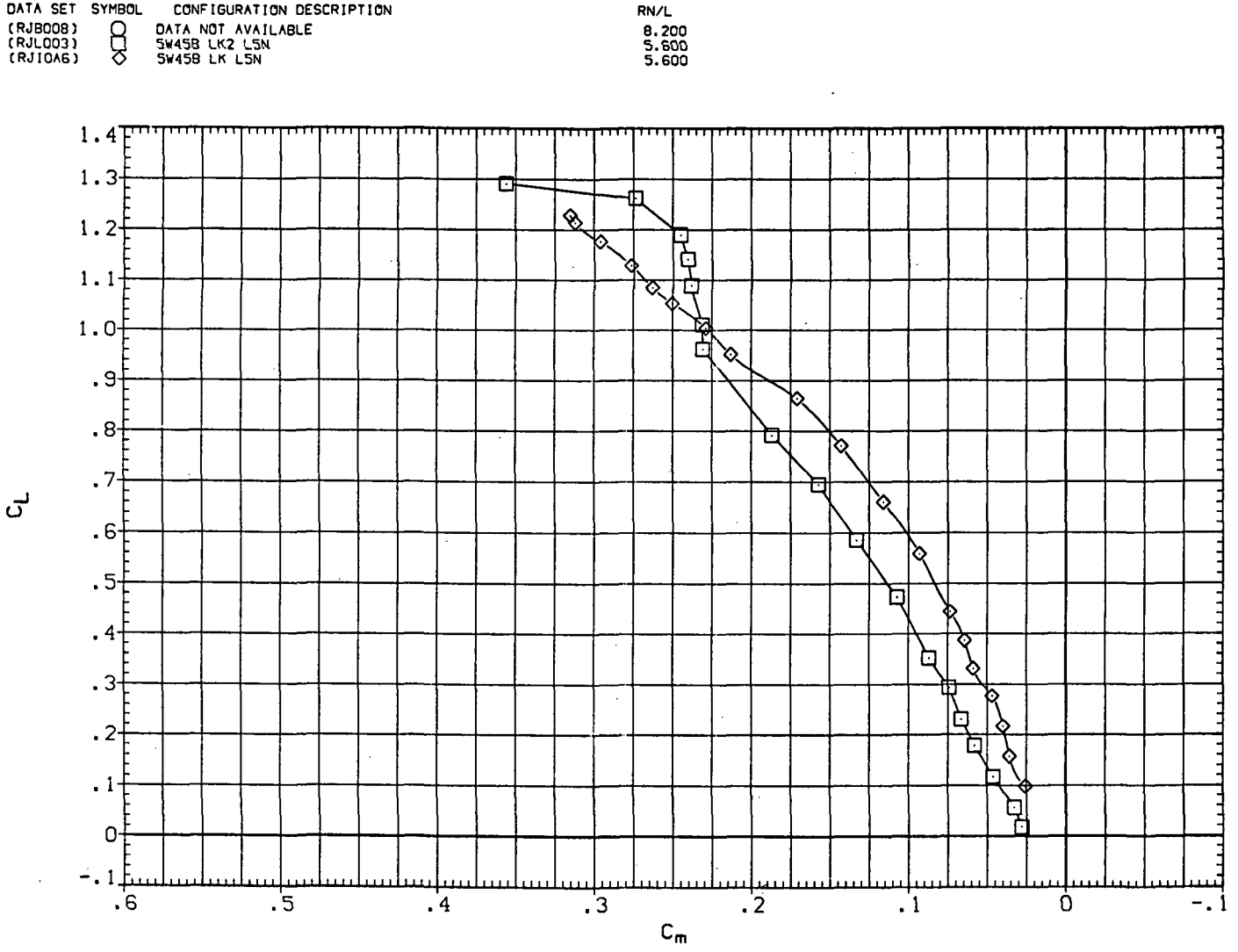

(c) C_L vs C_m

Figure 5.– Continued.

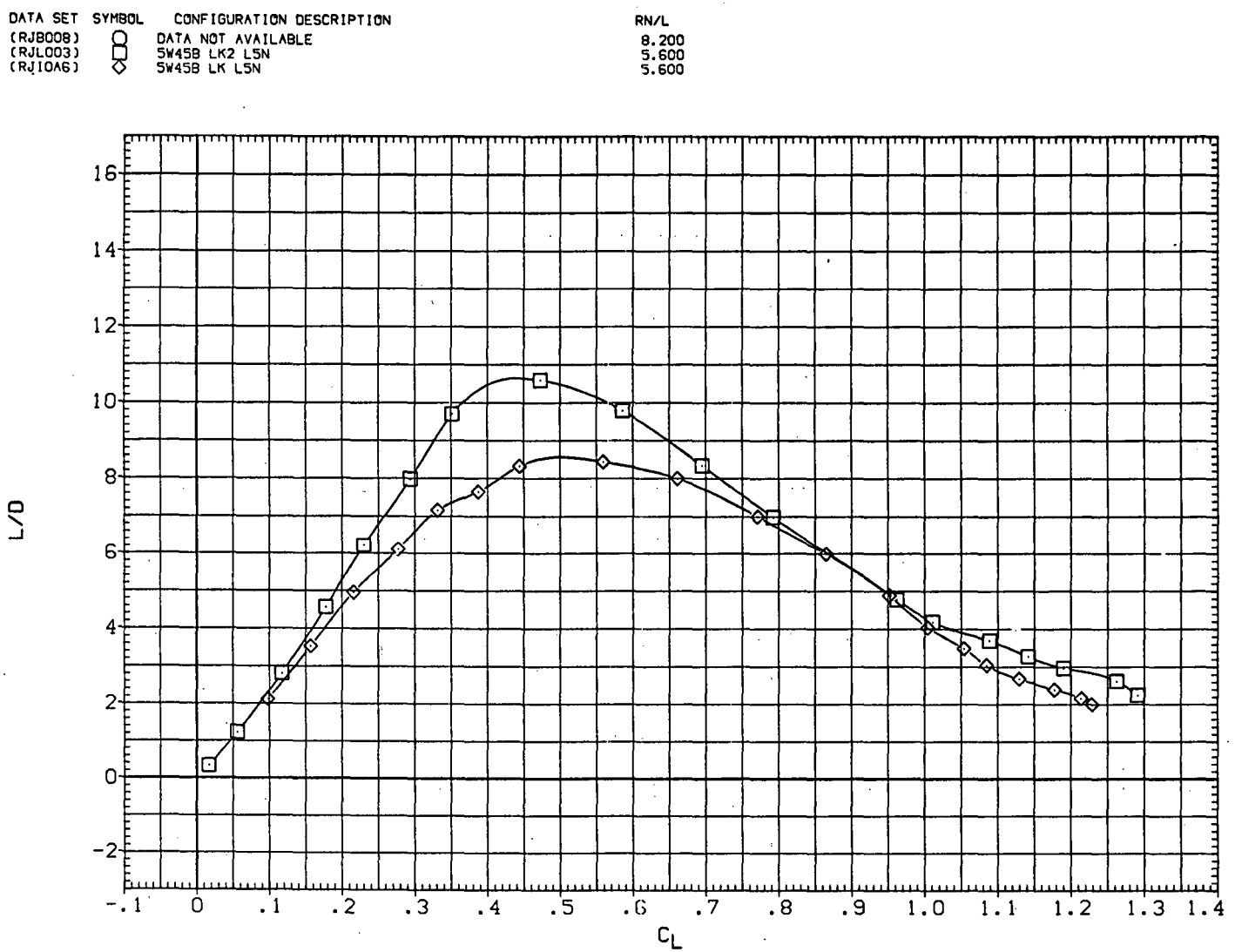

(d) L/D vs C_L

Figure 5.– Continued.

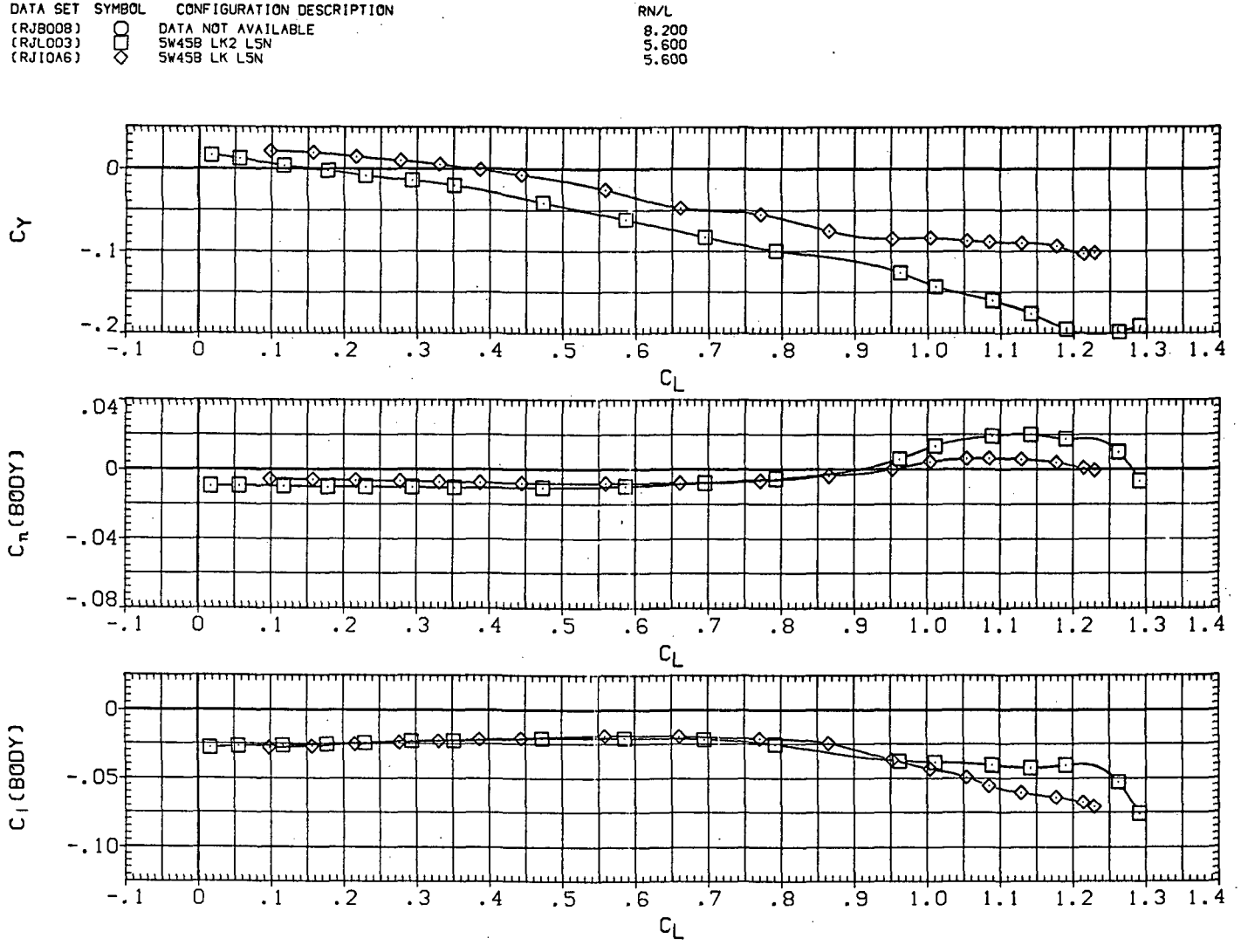

(e) C_Y, C_n, and C_l vs C_L

Figure 5.– Concluded.

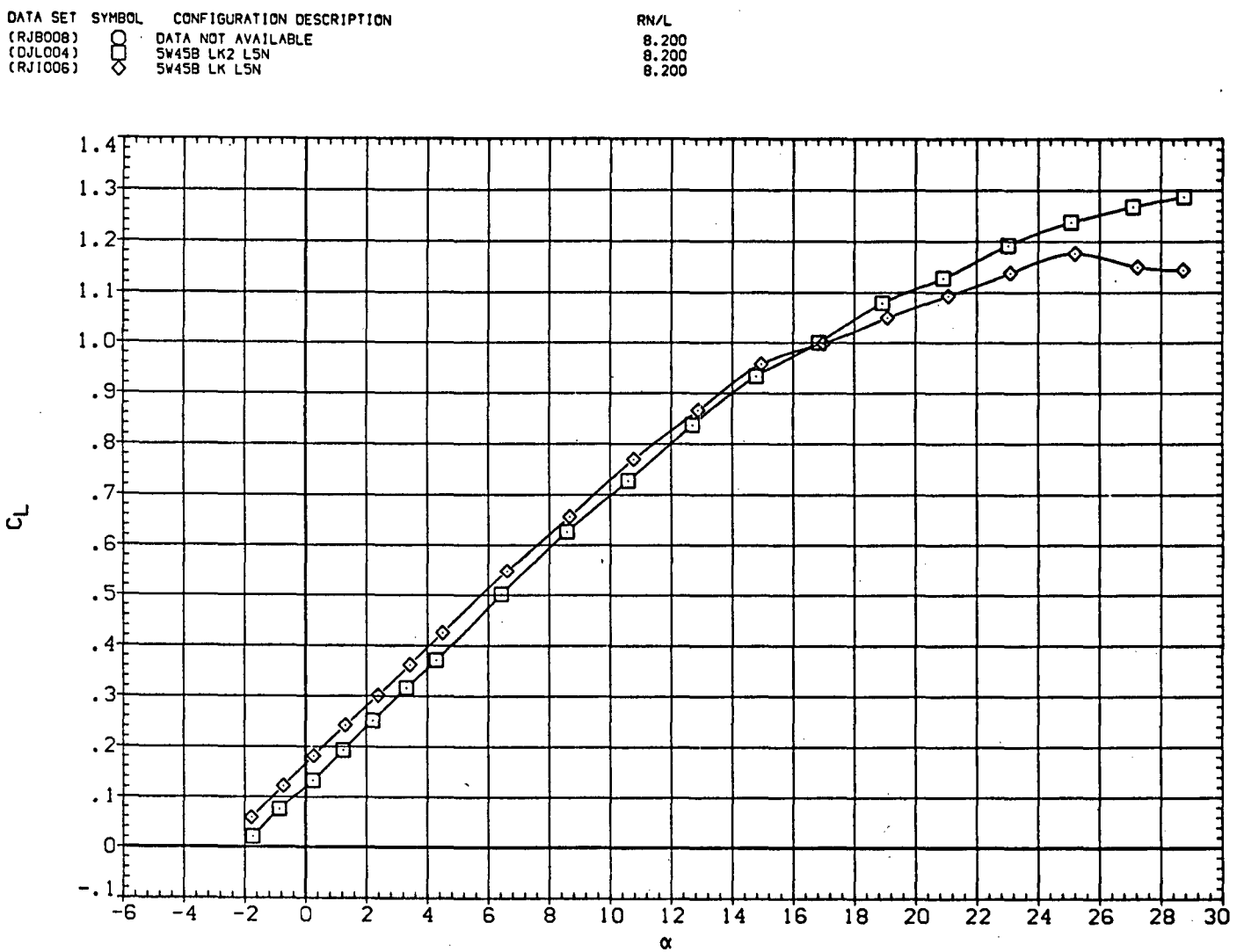

(a) C_L vs α

Figure 6.– Effect of Krüger nose flaps mounted on the drooped-nose flaps deflected 5°, downstream panel only: $\Lambda = 45°, M = 0.40$.

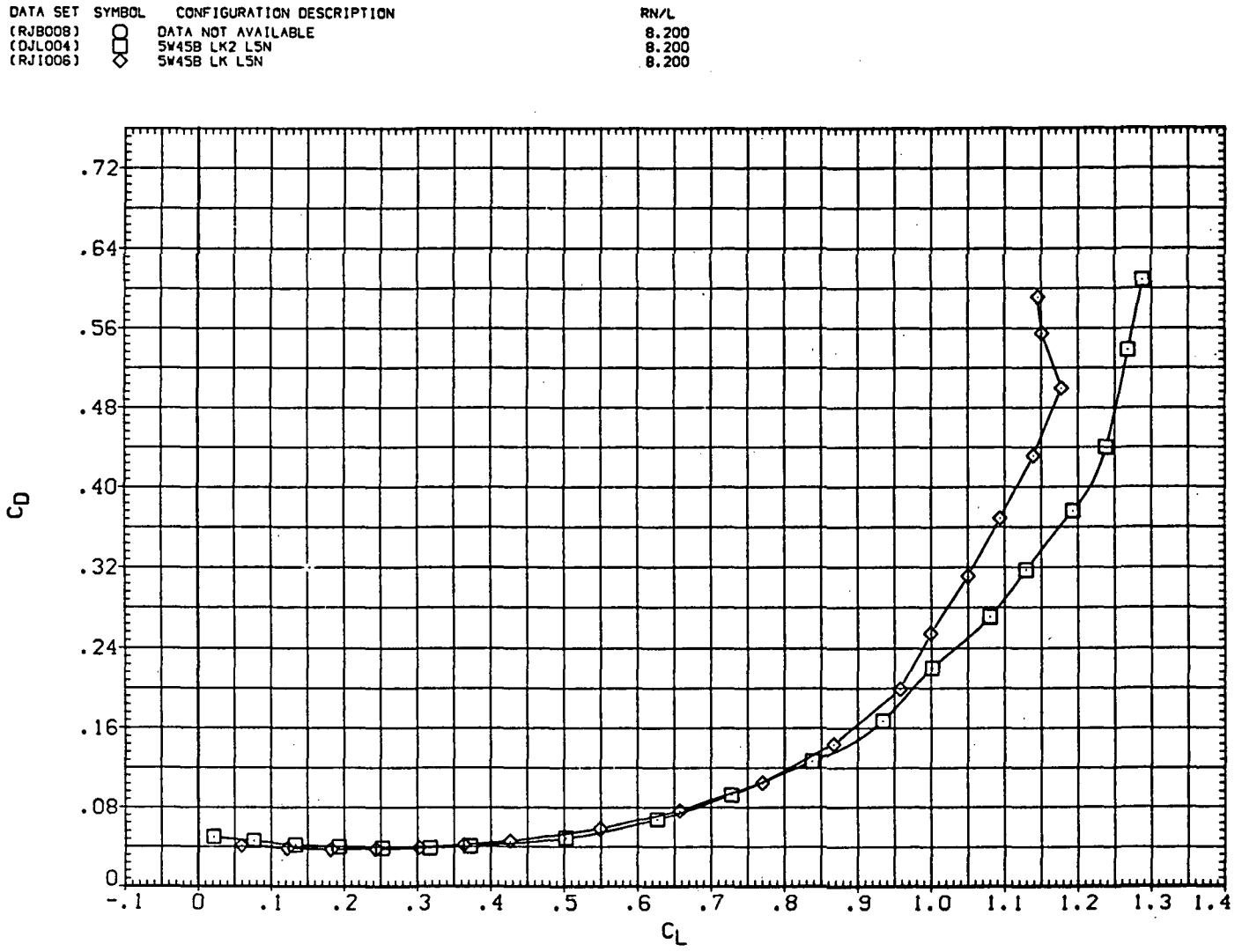

(b) C_D vs C_L

Figure 6.– Continued.

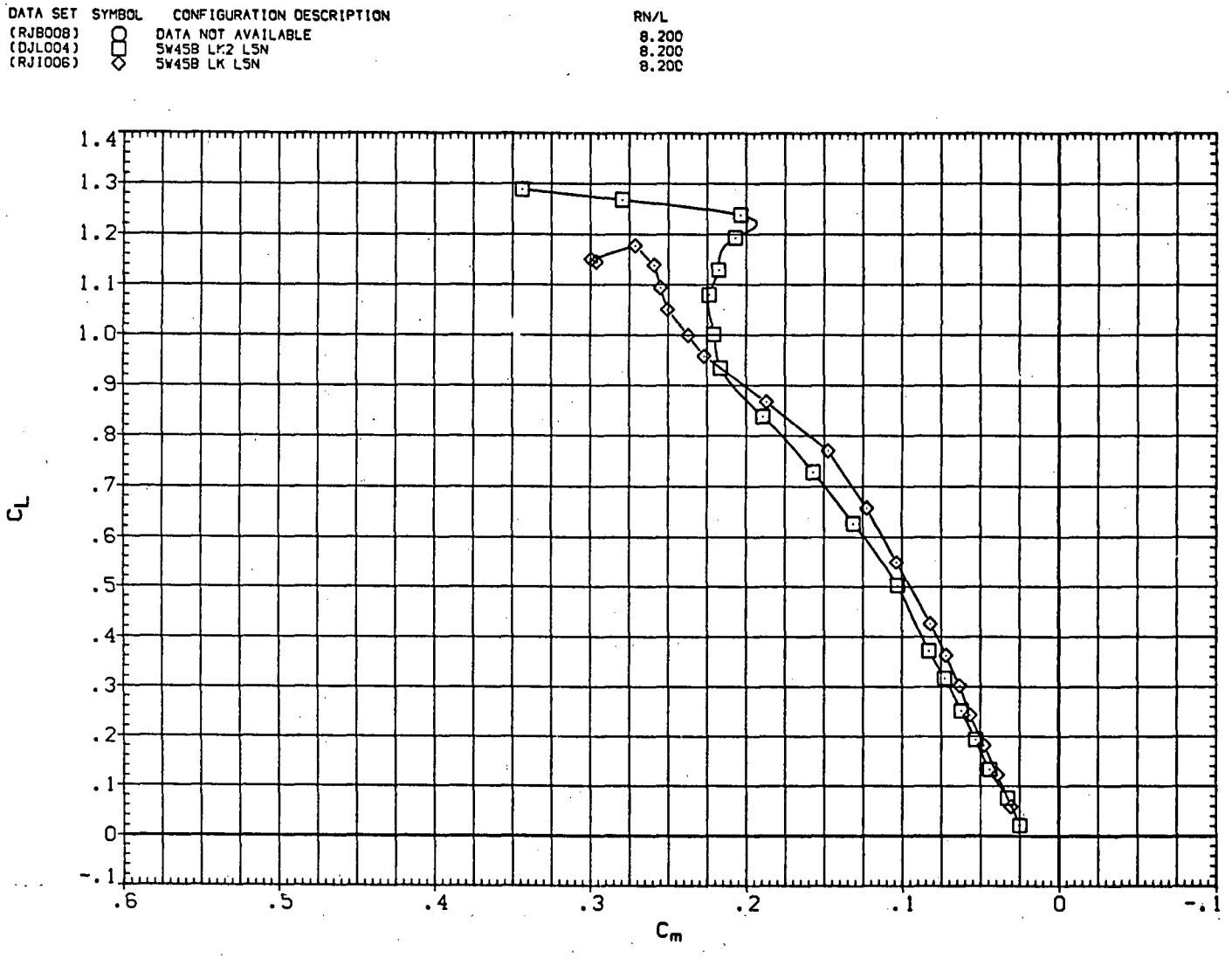

(c) C_L vs C_m

Figure 6.– Continued.

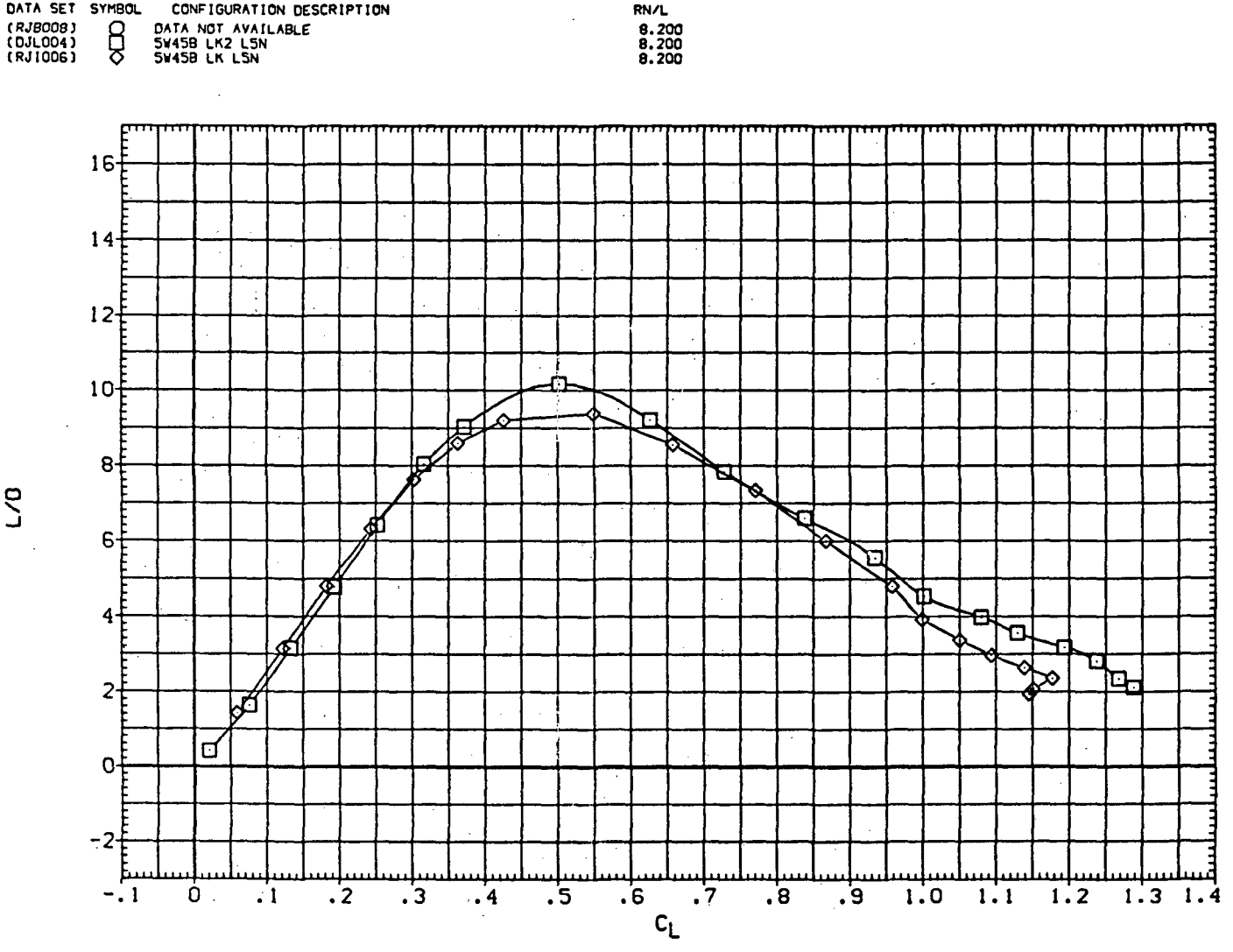

(d) L/D vs C_L

Figure 6.– Continued.

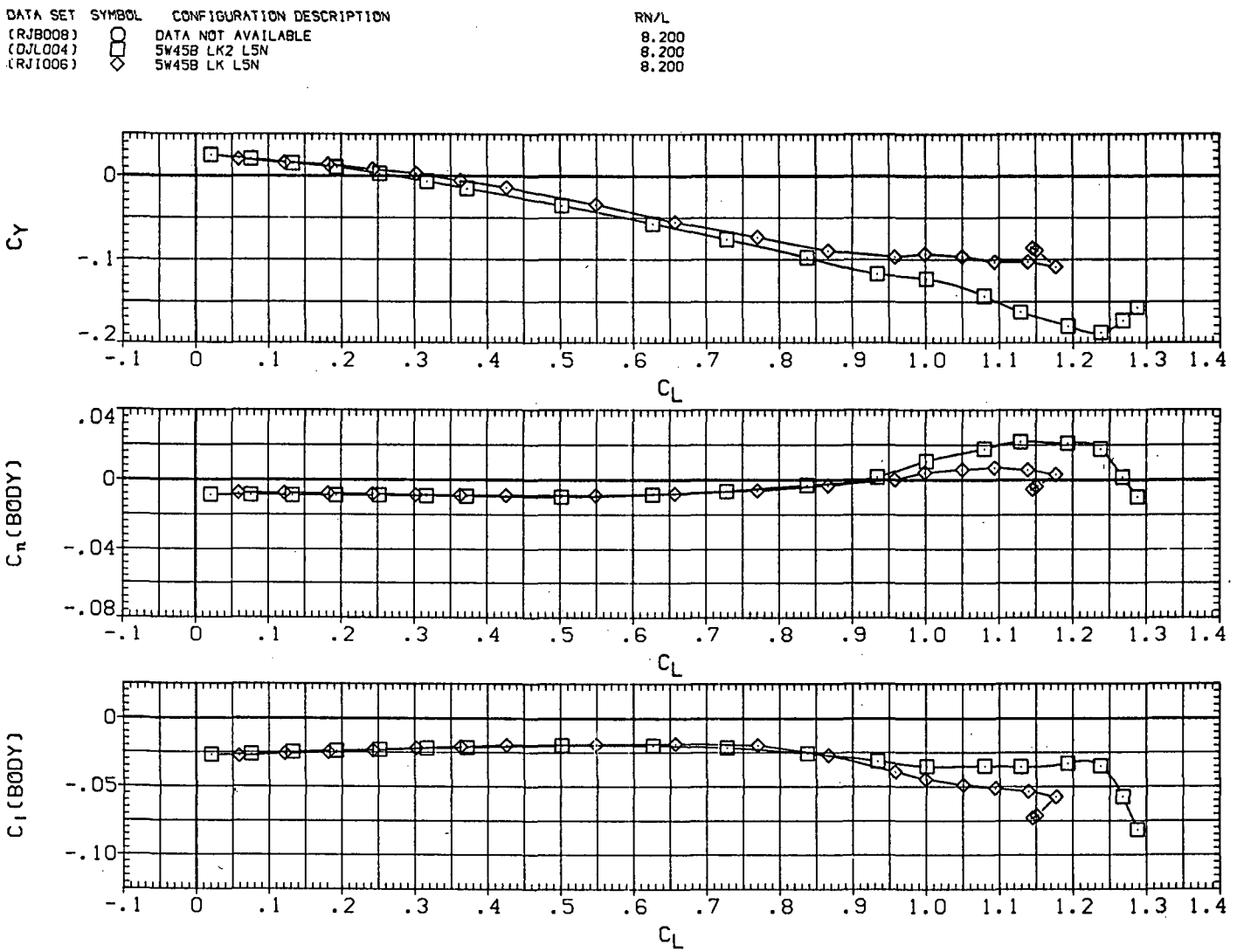

(e) C_Y, C_n, and C_l vs C_L

Figure 6.– Concluded.

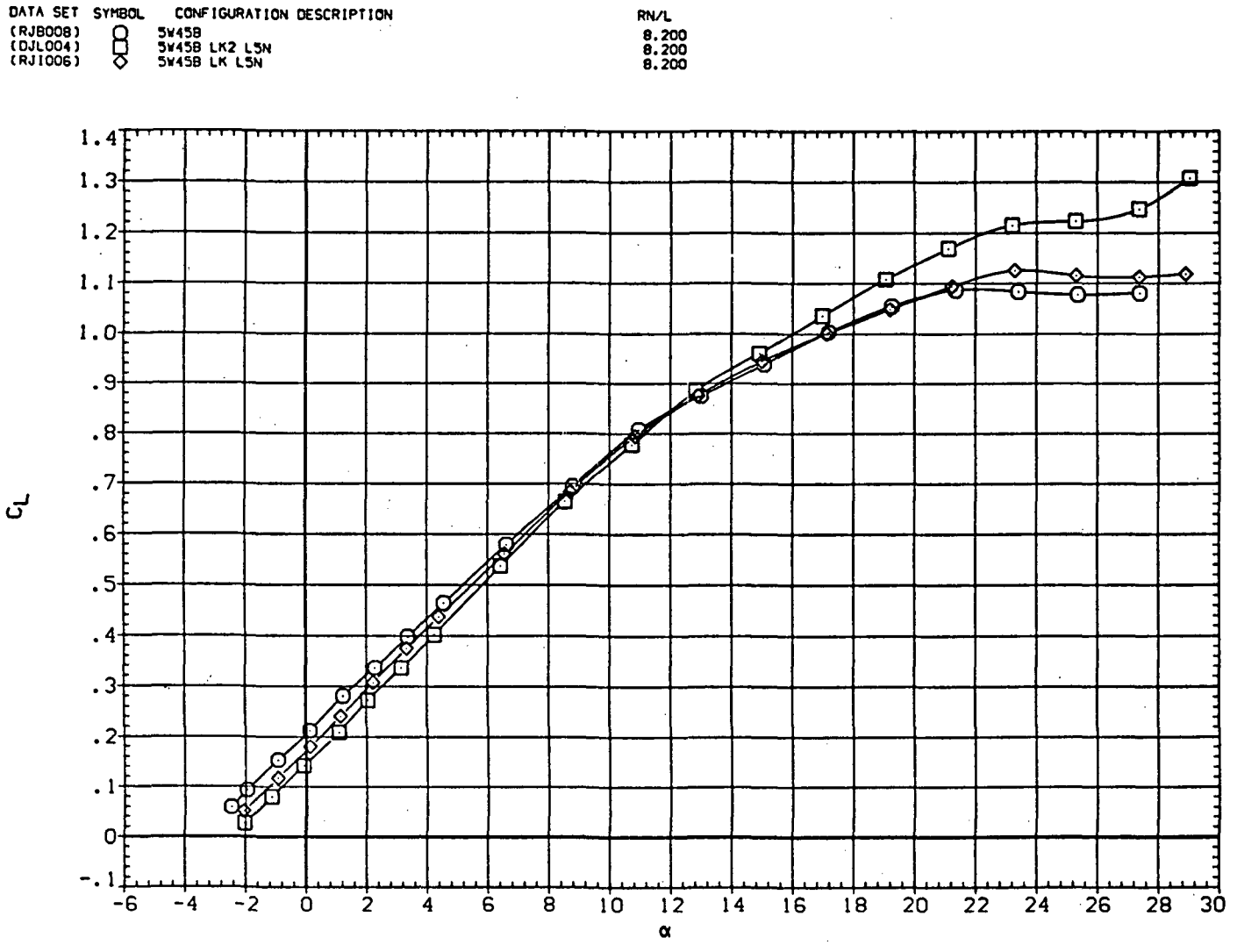

(a) C_L vs α

Figure 7.– Effect of Krüger nose flaps mounted on the drooped-nose flaps deflected 5°, downstream panel only: $\Lambda = 45°, M = 0.60$.

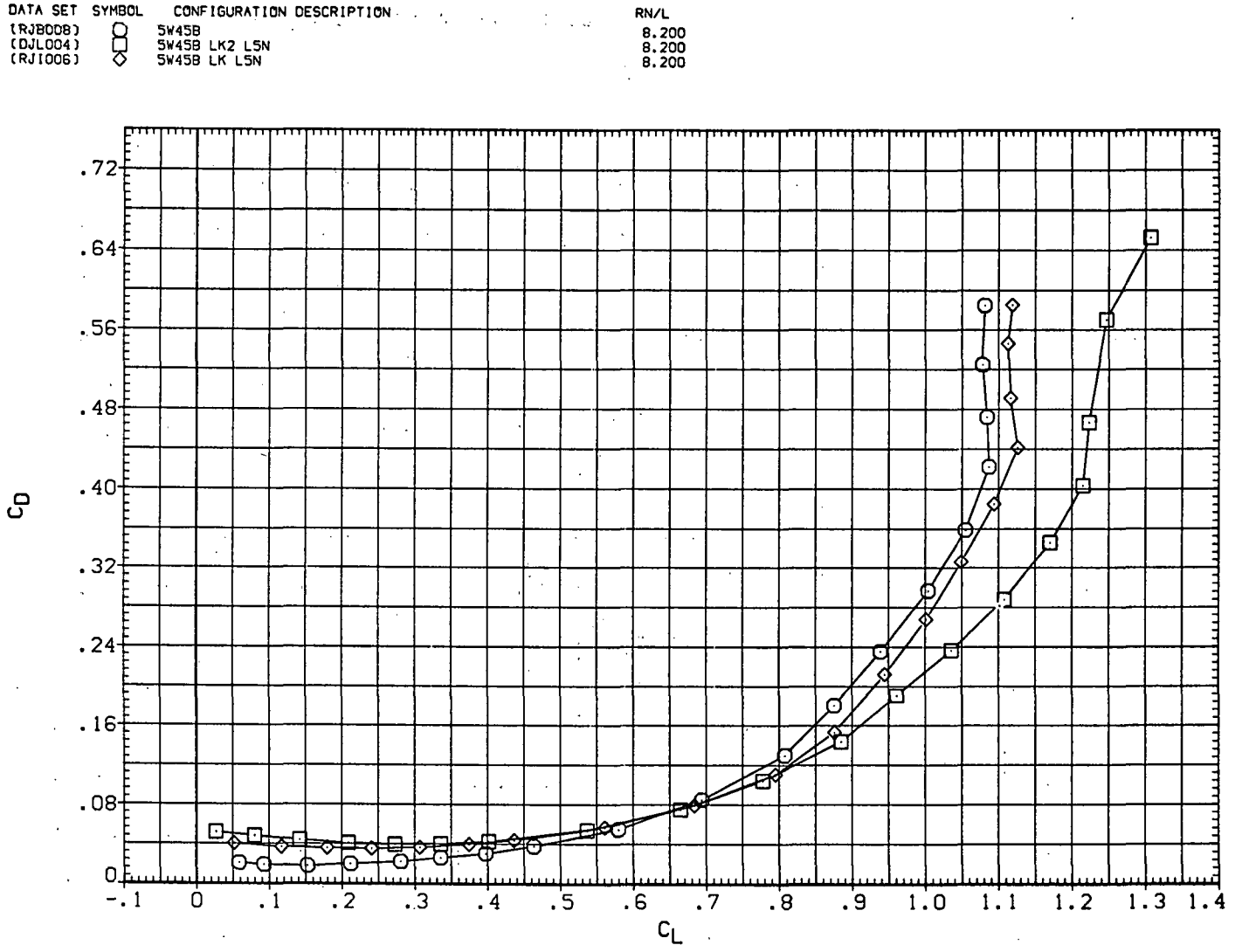

(b) C_D vs C_L

Figure 7.– Continued.

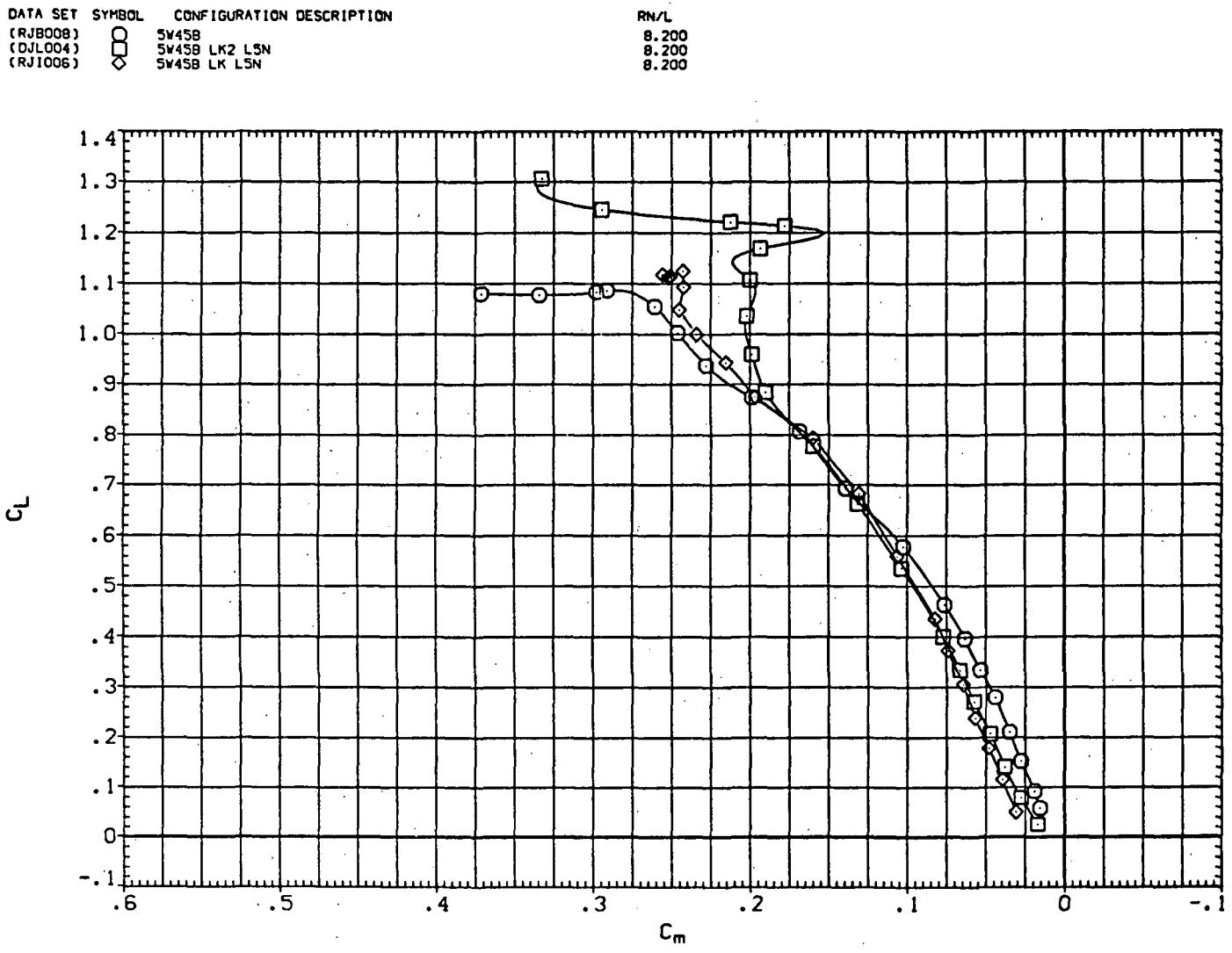

(c) C_L vs C_m

Figure 7.– Continued.

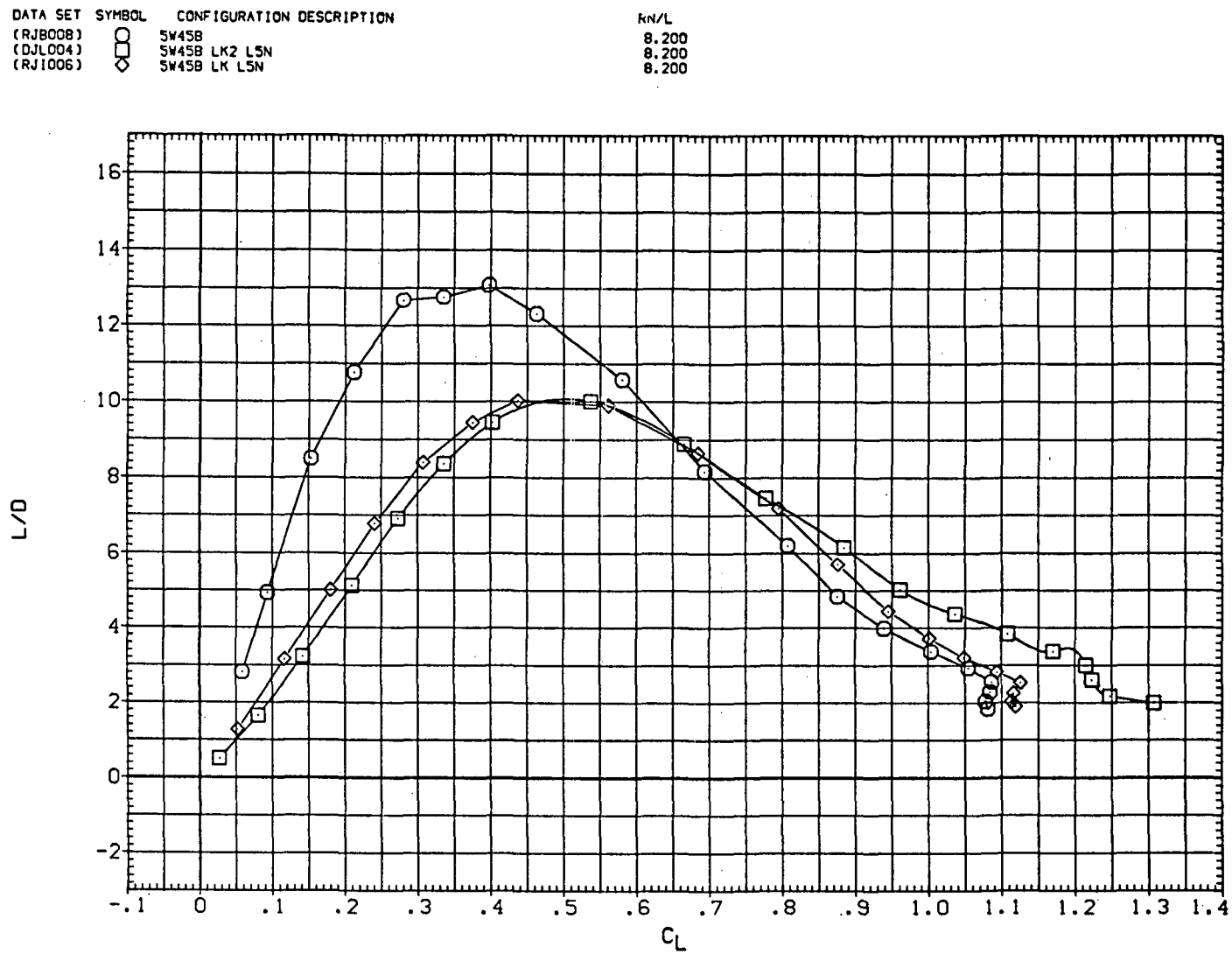

(d) L/D vs C_L

Figure 7.– Continued.

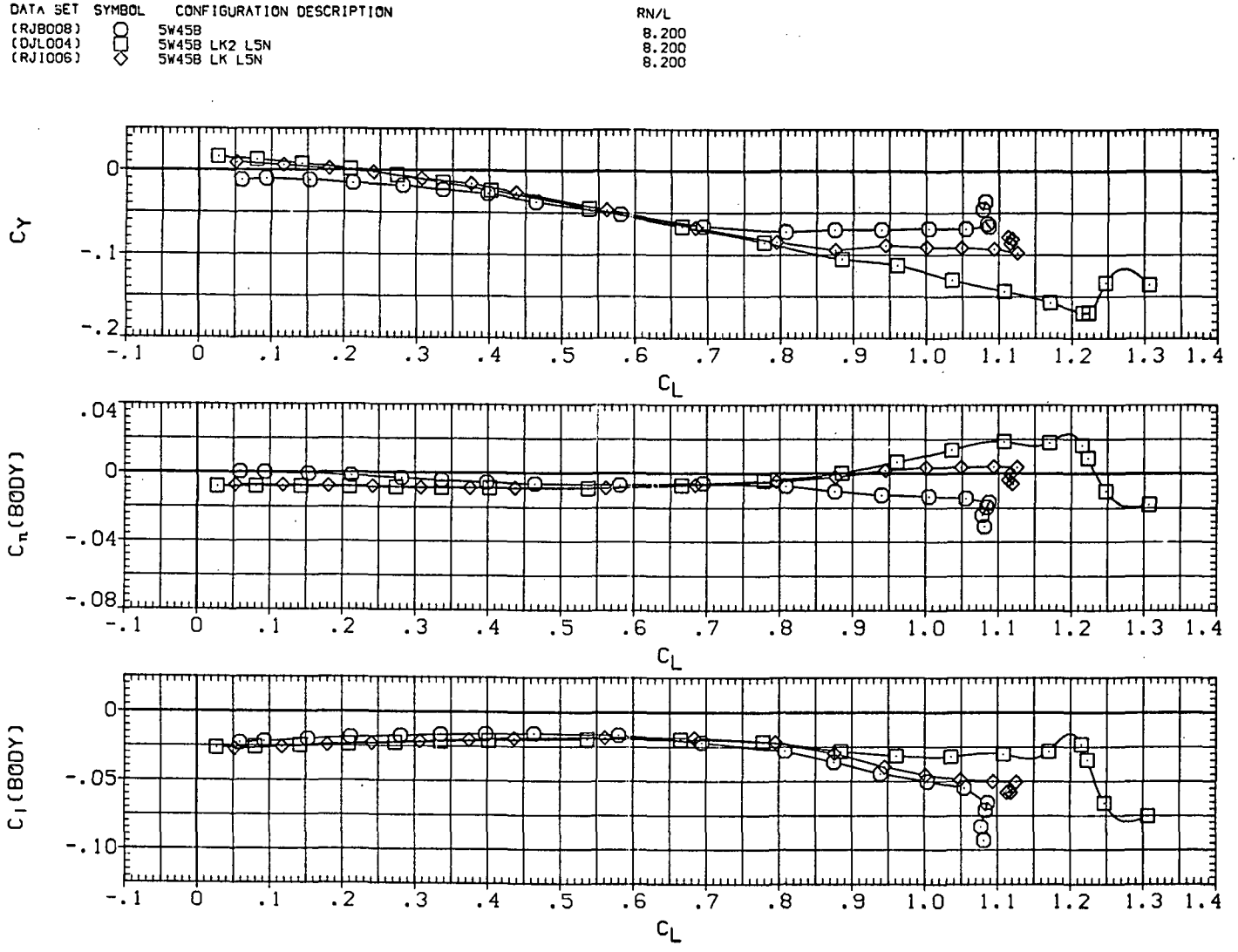

(e) C_Y, C_n, and C_l vs C_L

Figure 7.– Concluded.

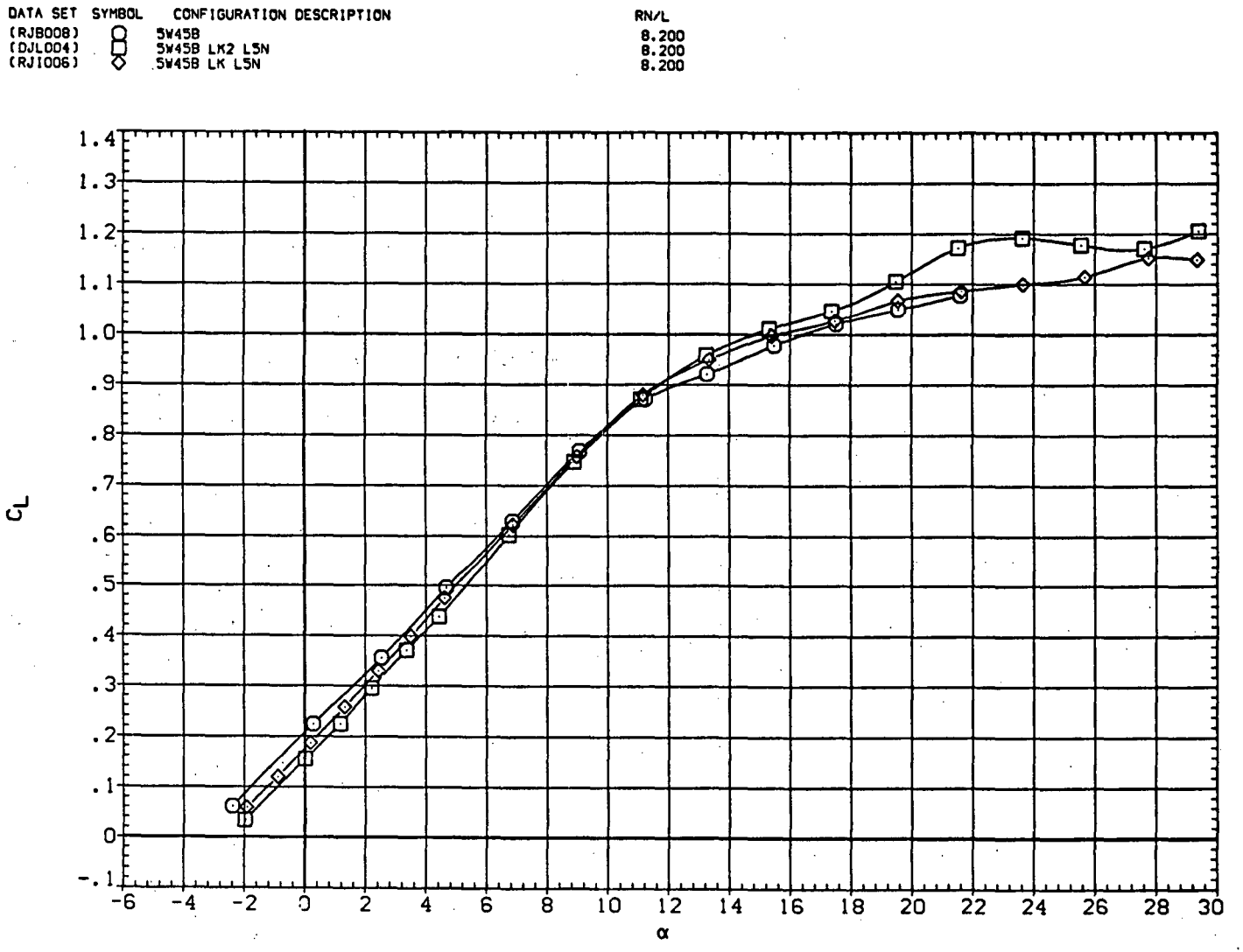

(a) C_L vs α

Figure 8.– Effect of Krüger nose flaps mounted on the drooped-nose flaps deflected 5°, downstream panel only: $\Lambda = 45°, M = 0.80$.

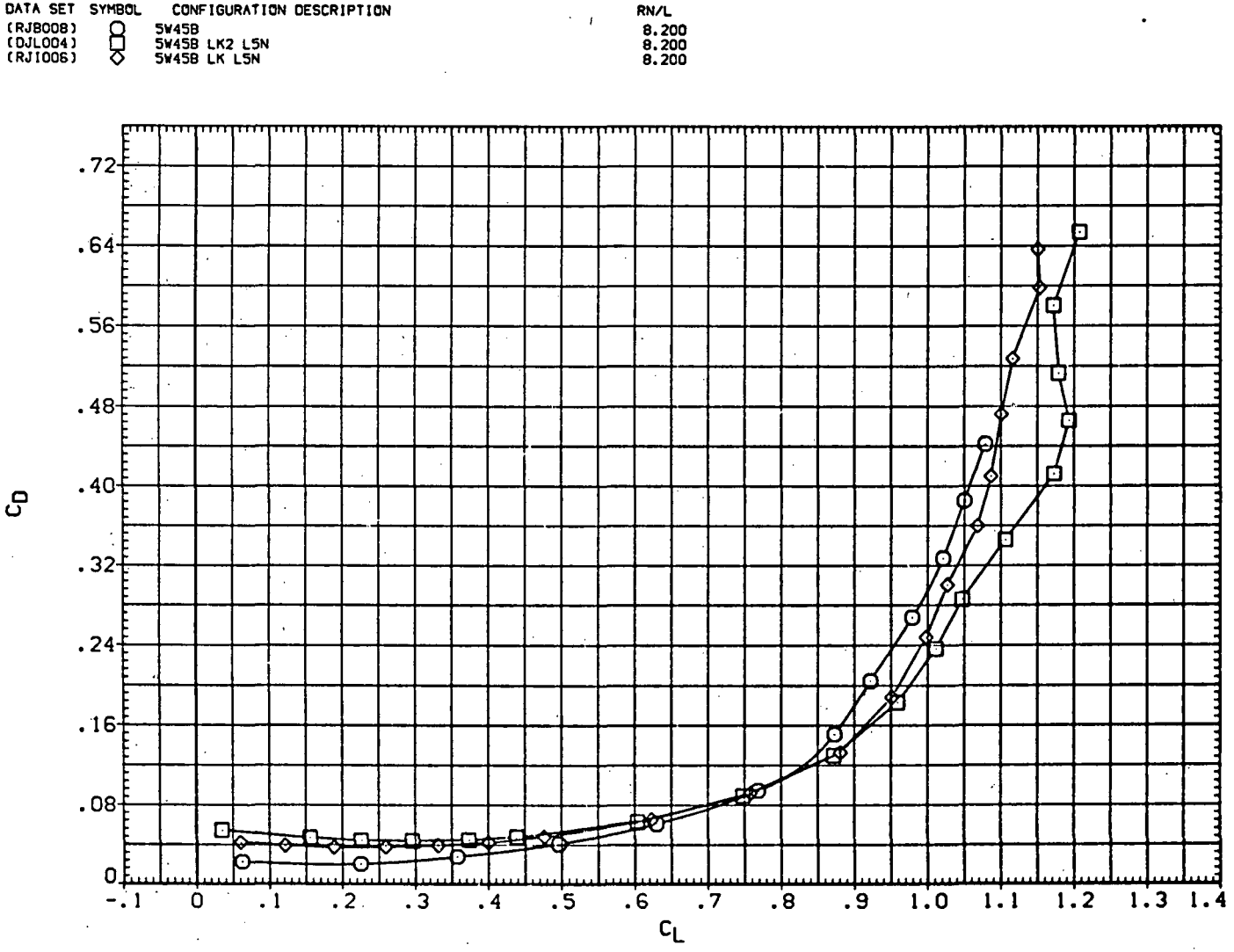

(b) C_D vs C_L

Figure 8.– Continued.

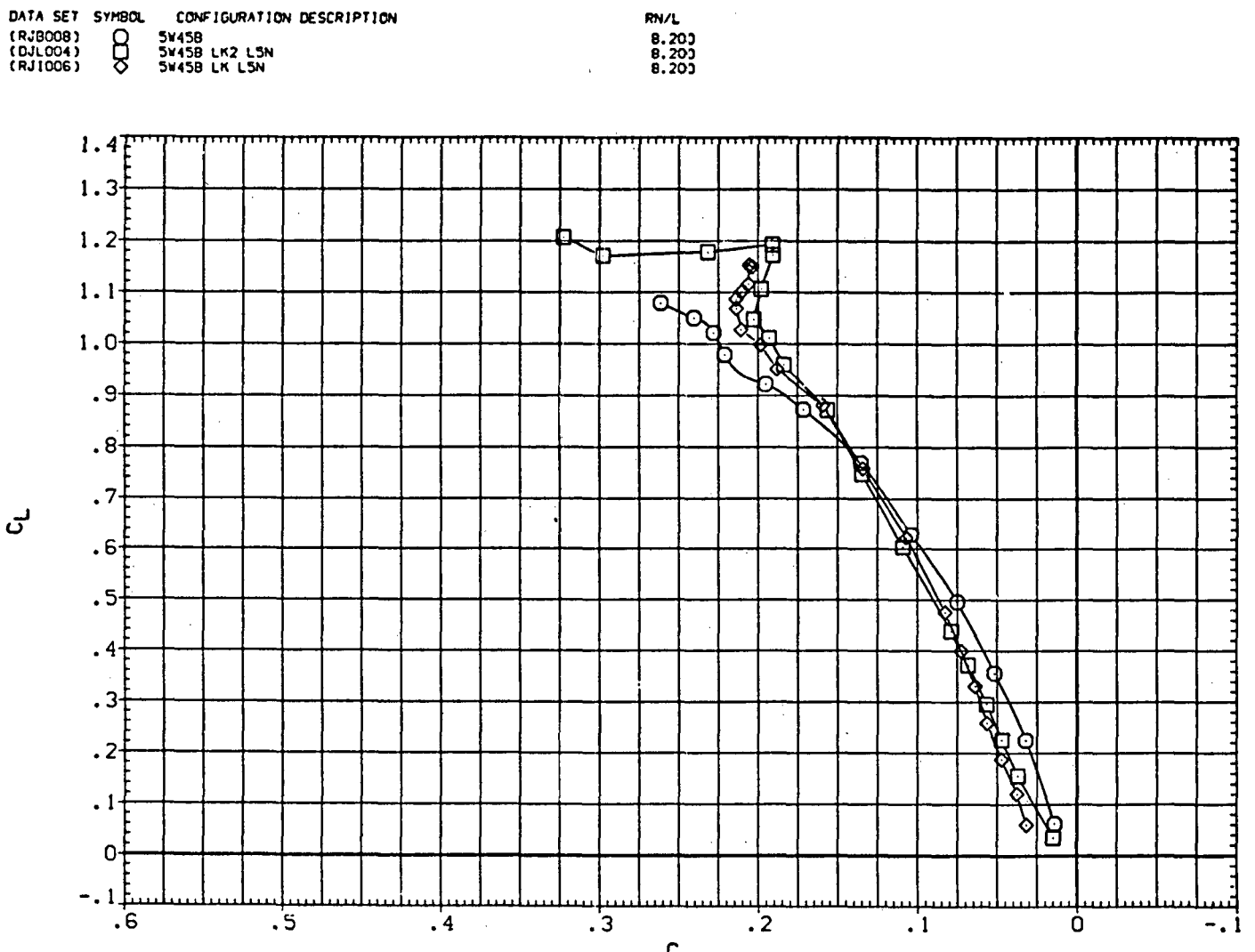

(c) C_L vs C_m

Figure 8.– Continued.

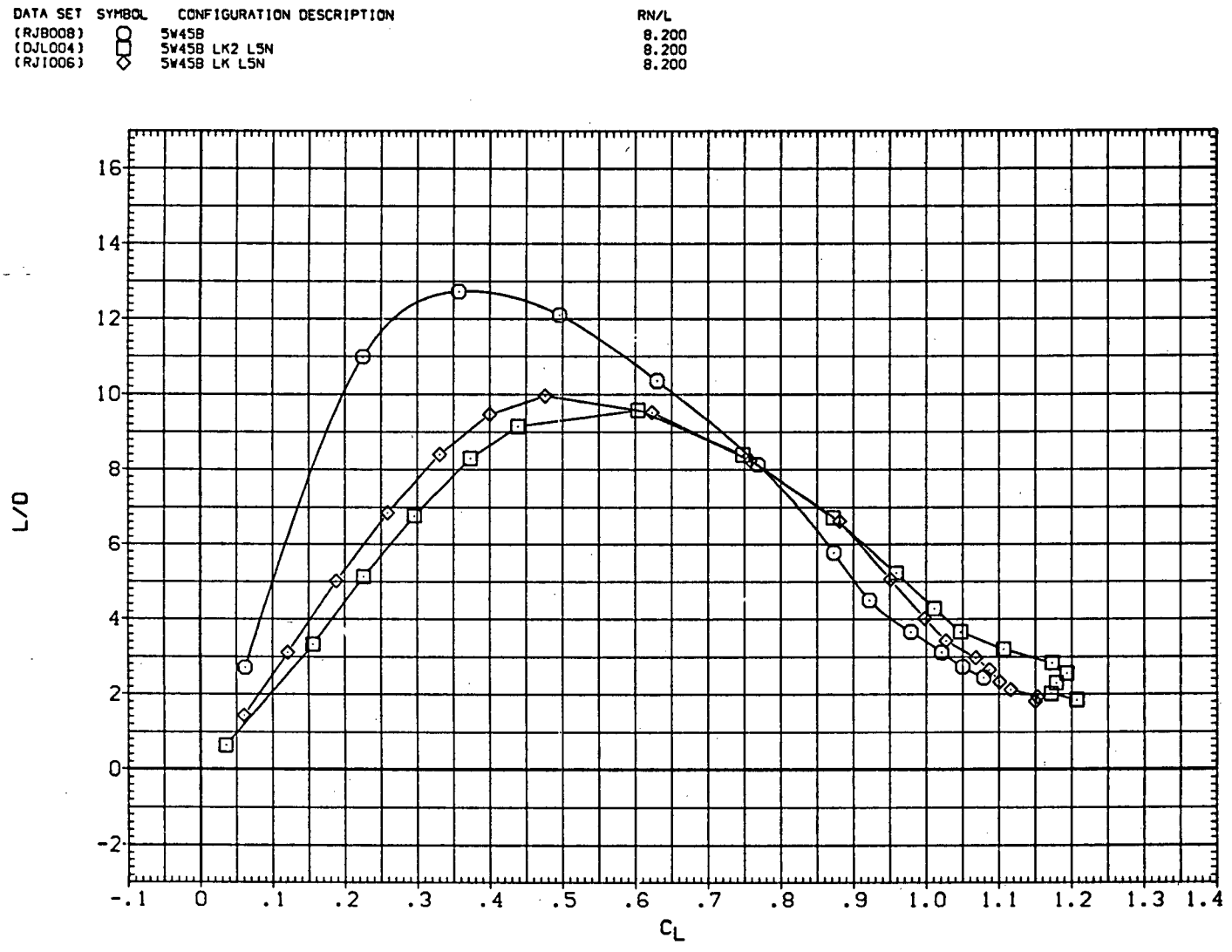

(d) L/D vs C_L

Figure 8.– Continued.

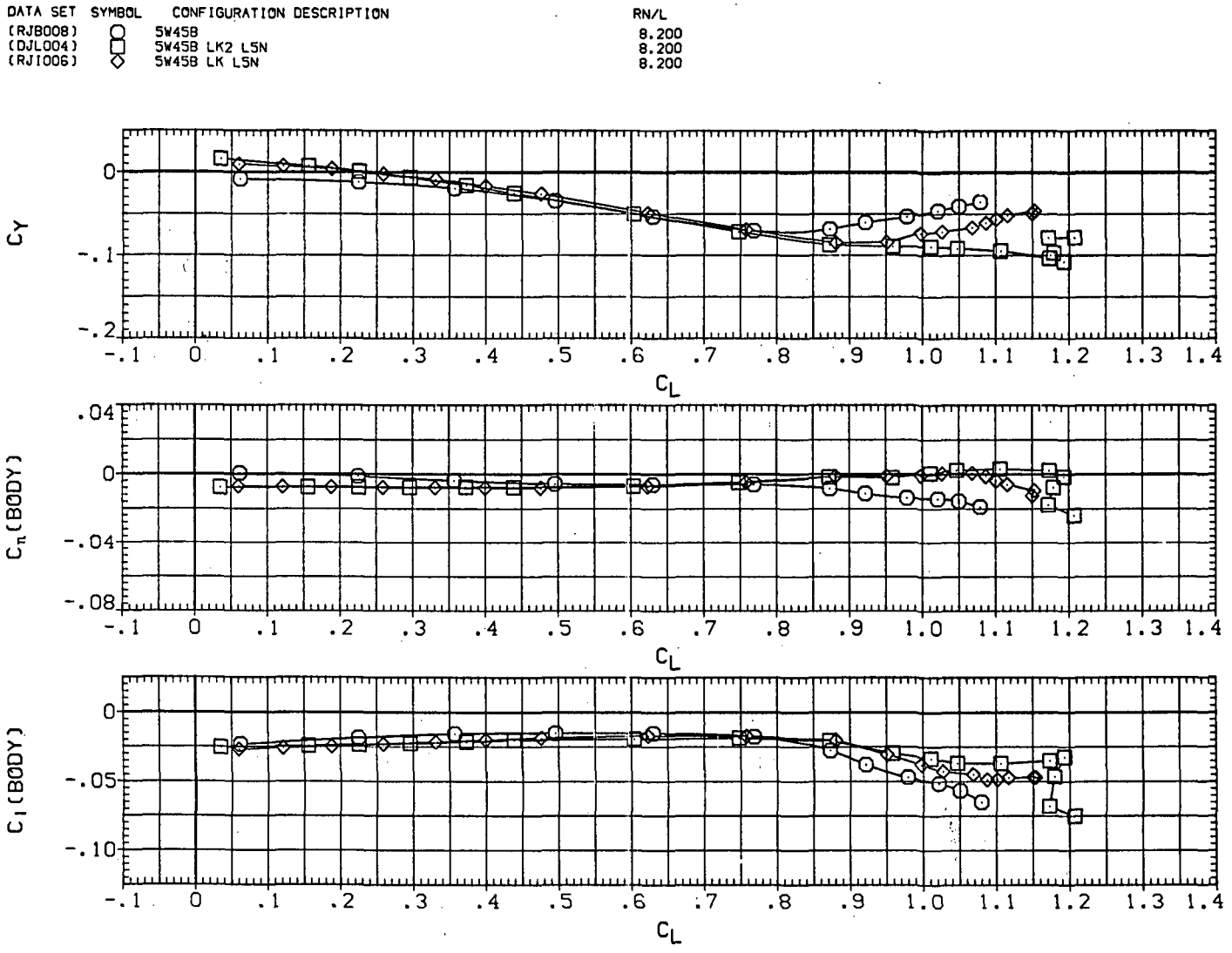

(e) C_Y, C_n, and C_l vs C_L

Figure 8.– Concluded.

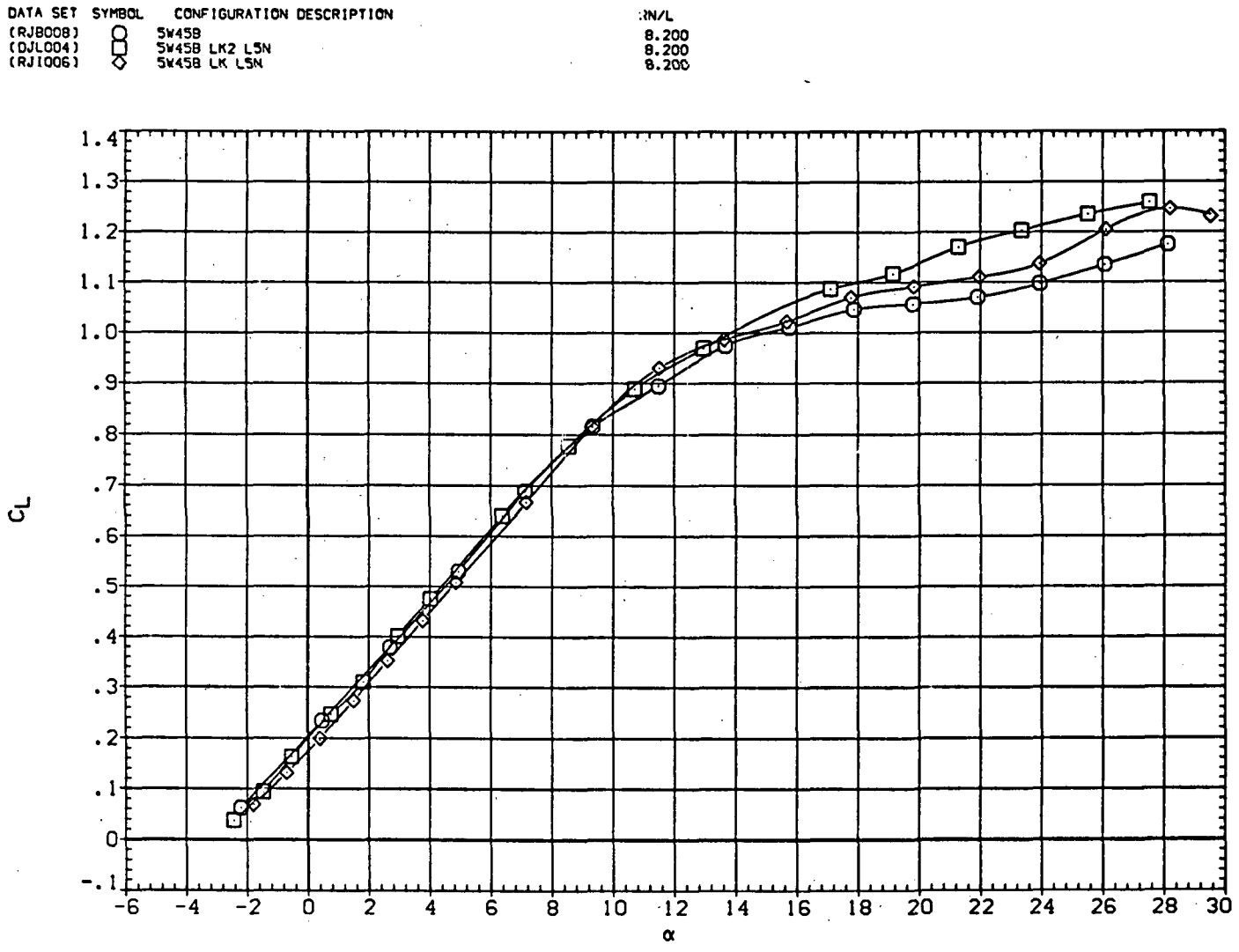

(a) C_L vs α

Figure 9.– Effect of Krüger nose flaps mounted on the drooped-nose flaps deflected 5°, downstream panel only: $\Lambda = 45°, M = 0.90$.

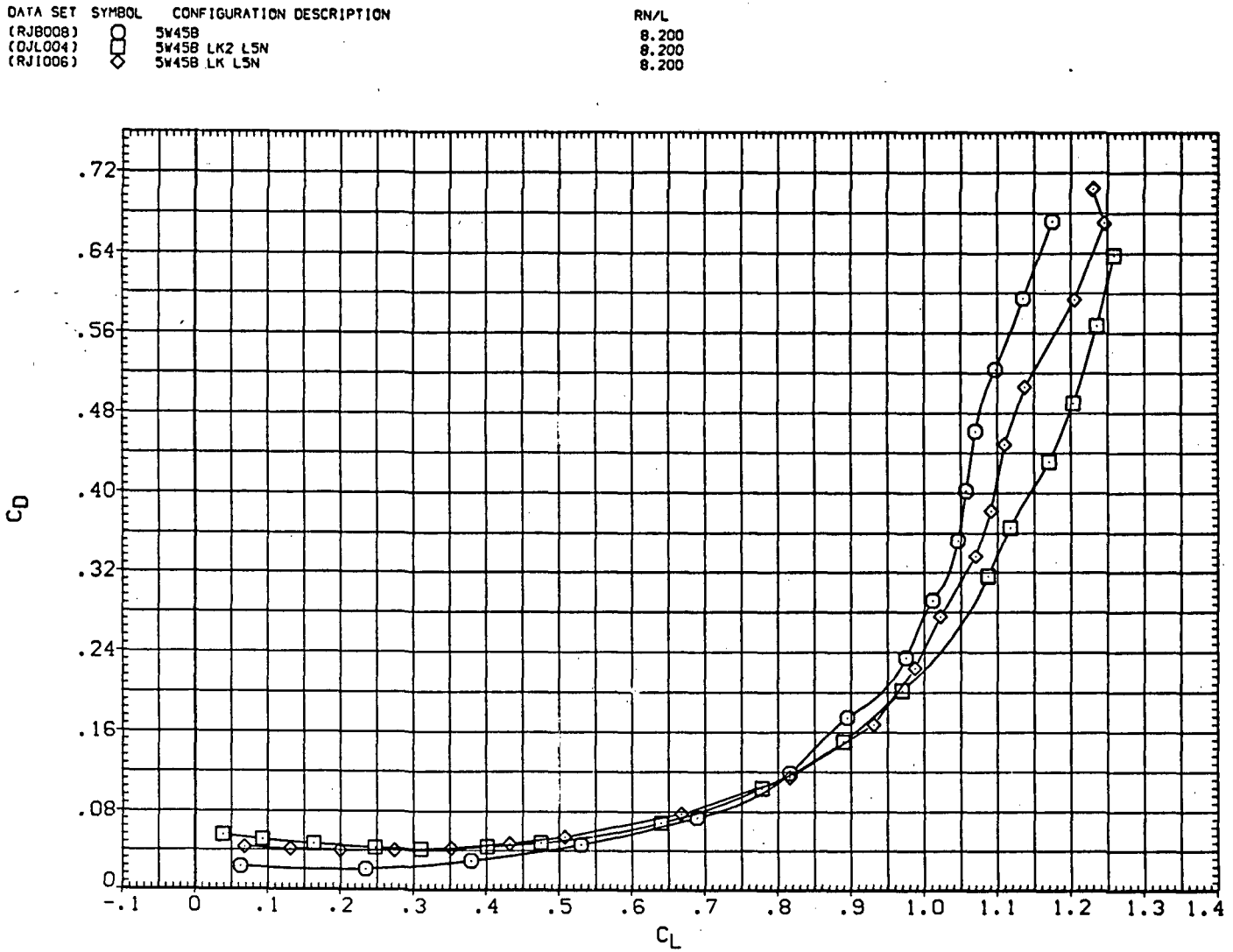

(b) C_D vs C_L

Figure 9.– Continued.

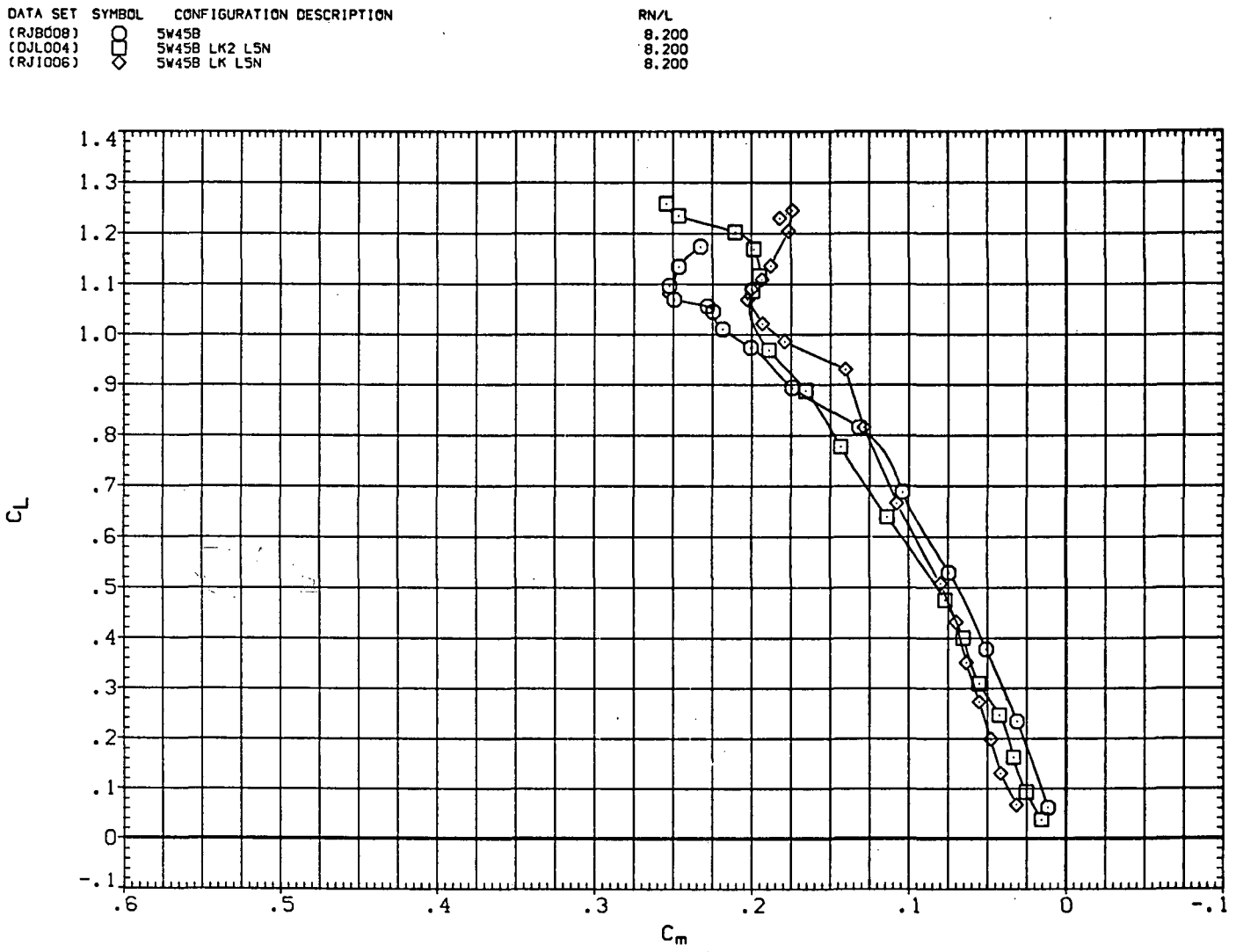

(c) C_L vs C_m

Figure 9.– Continued.

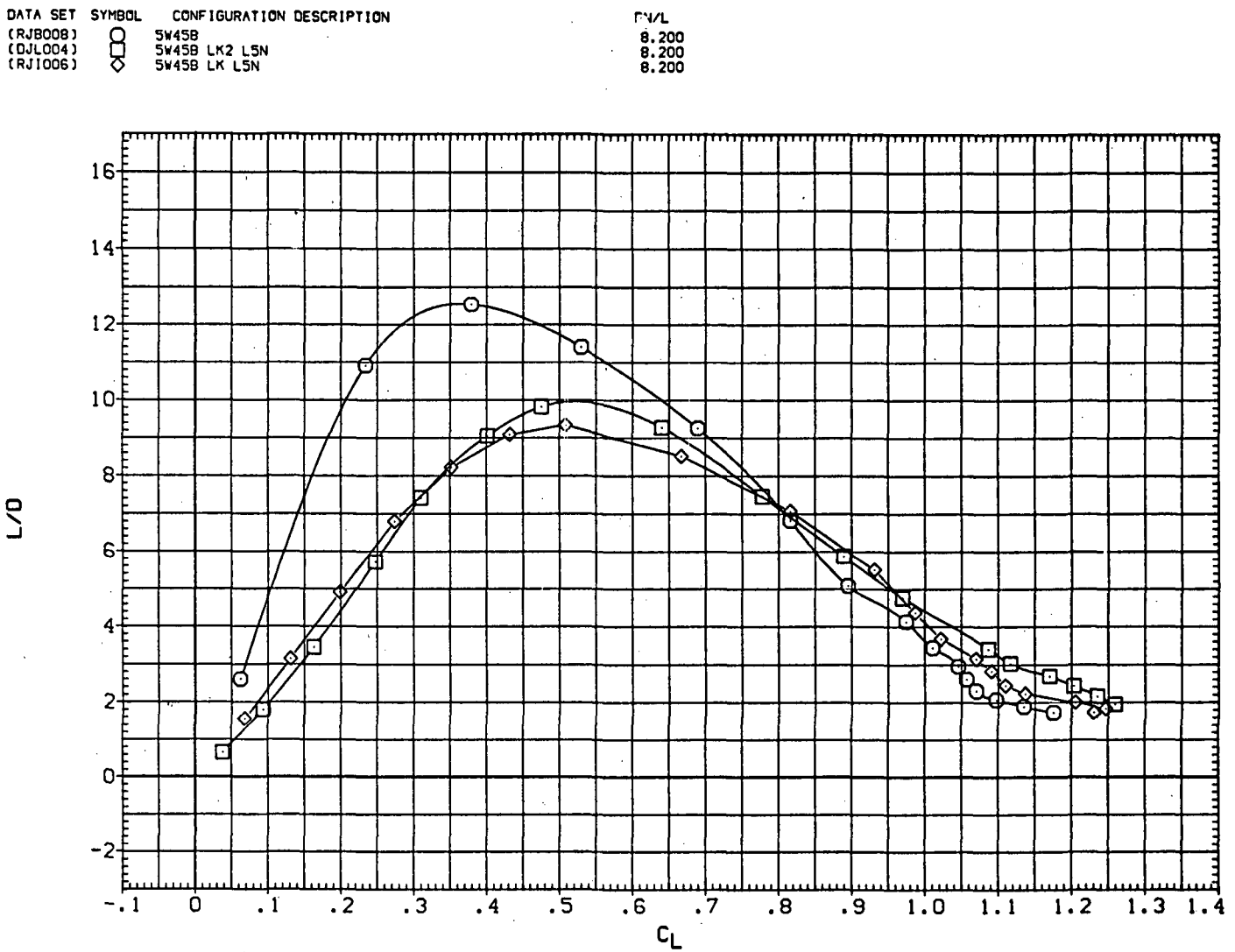

(d) L/D vs C_L

Figure 9.– Continued.

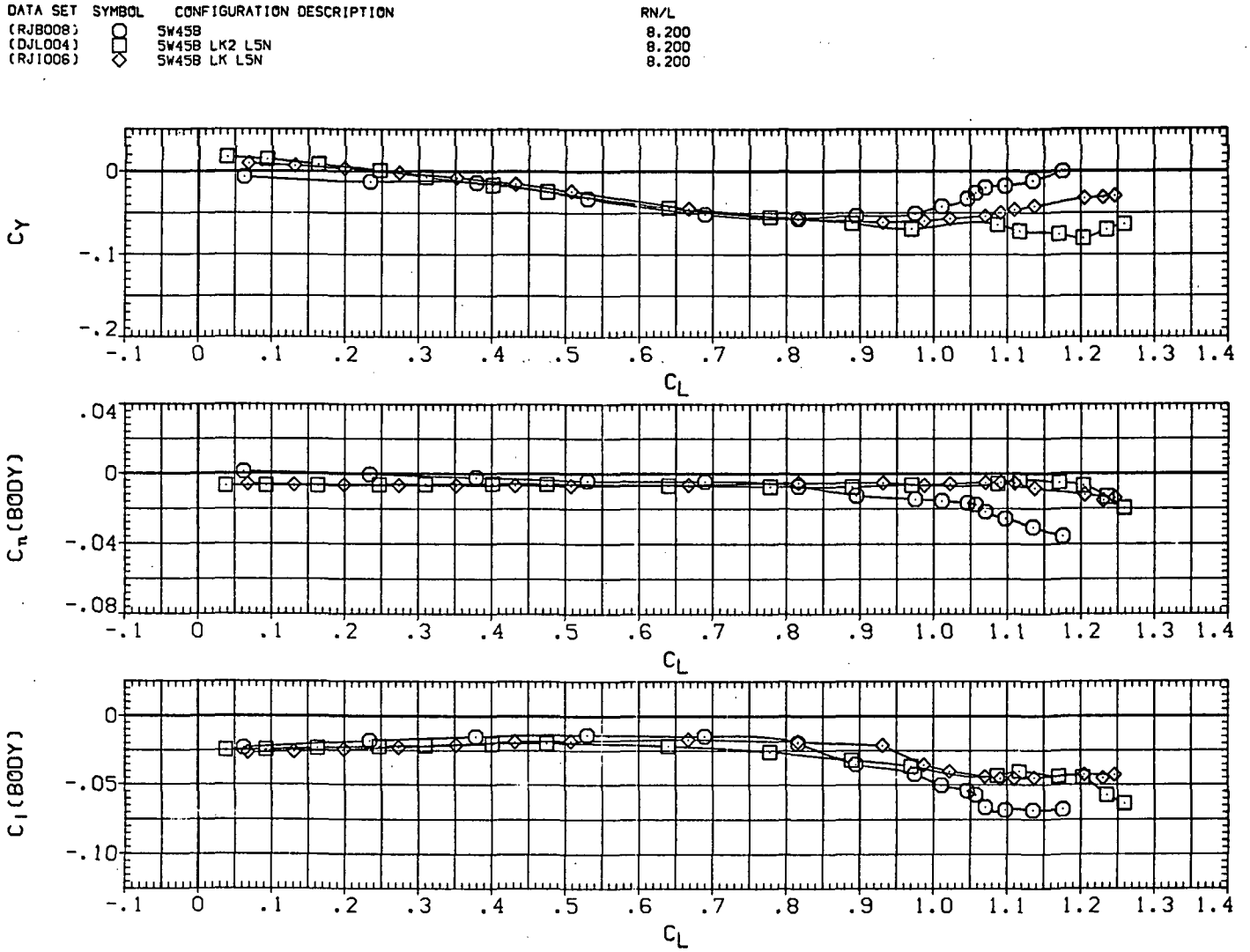

(e) C_Y, C_n, and C_l vs C_L

Figure 9.– Concluded.

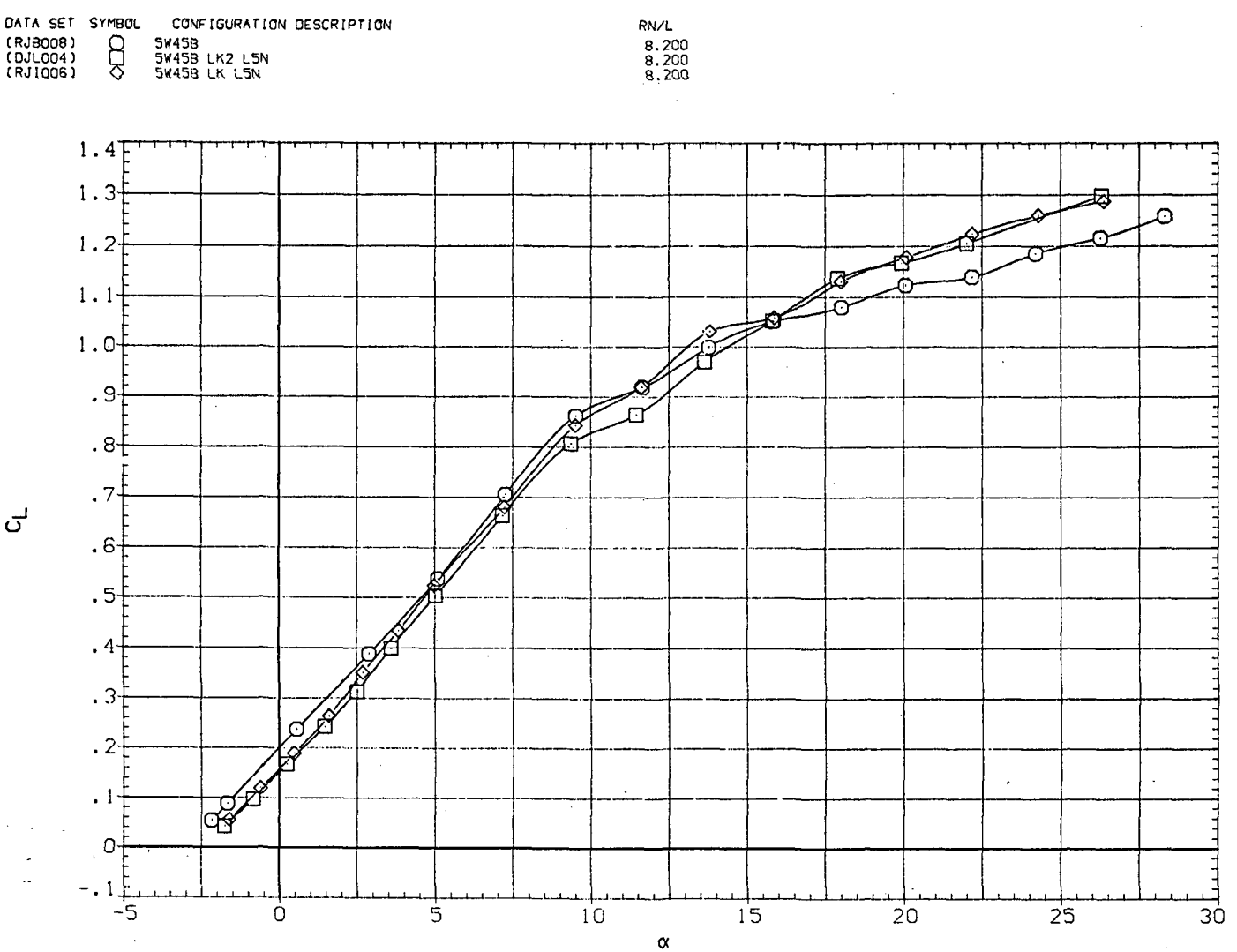

(a) C_L vs α

Figure 10.– Effect of Krüger nose flaps mounted on the drooped-nose flaps deflected 5°, downstream panel only: $\Lambda = 45°, M = 0.95$.

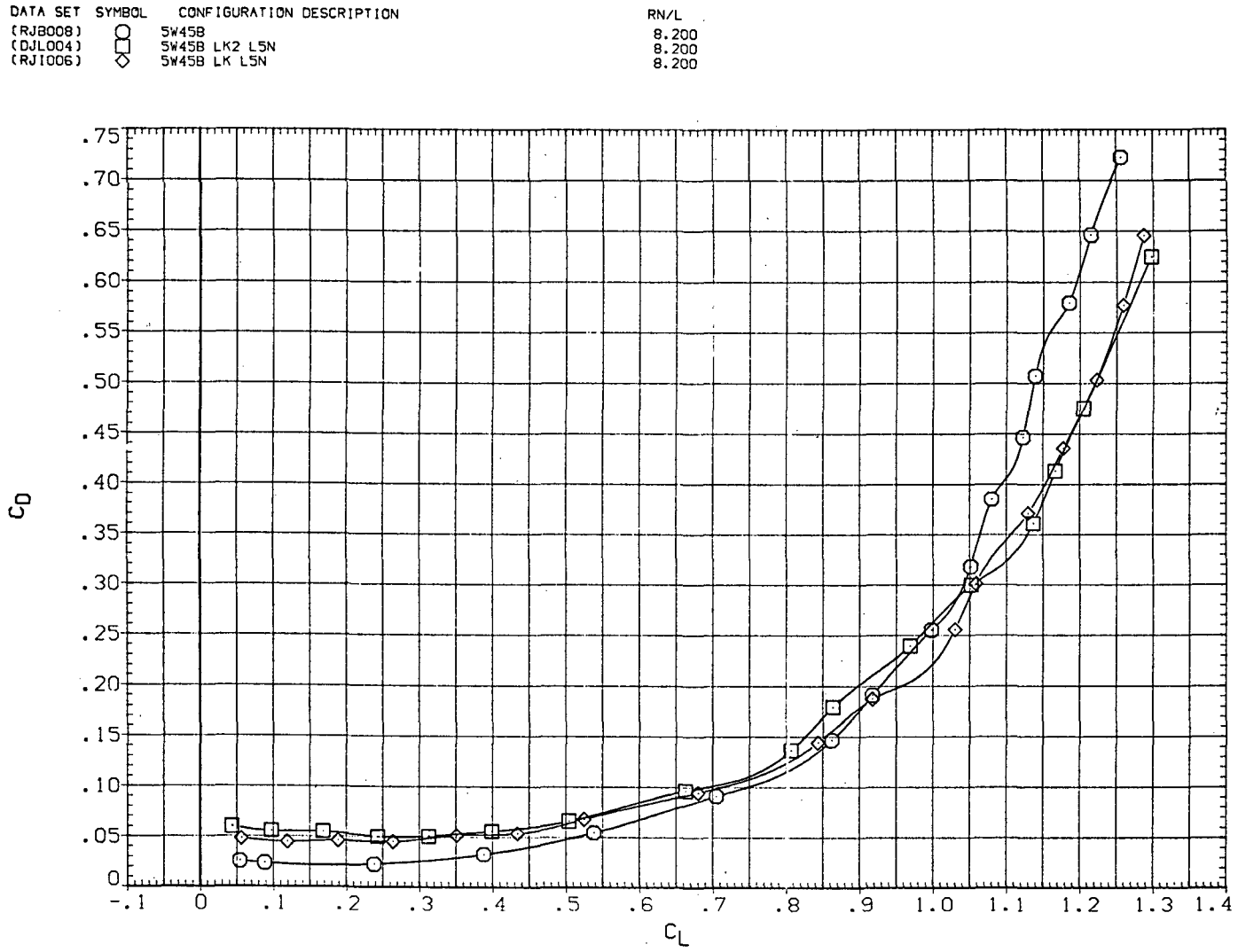

(b) C_D vs C_L

Figure 10.– Continued.

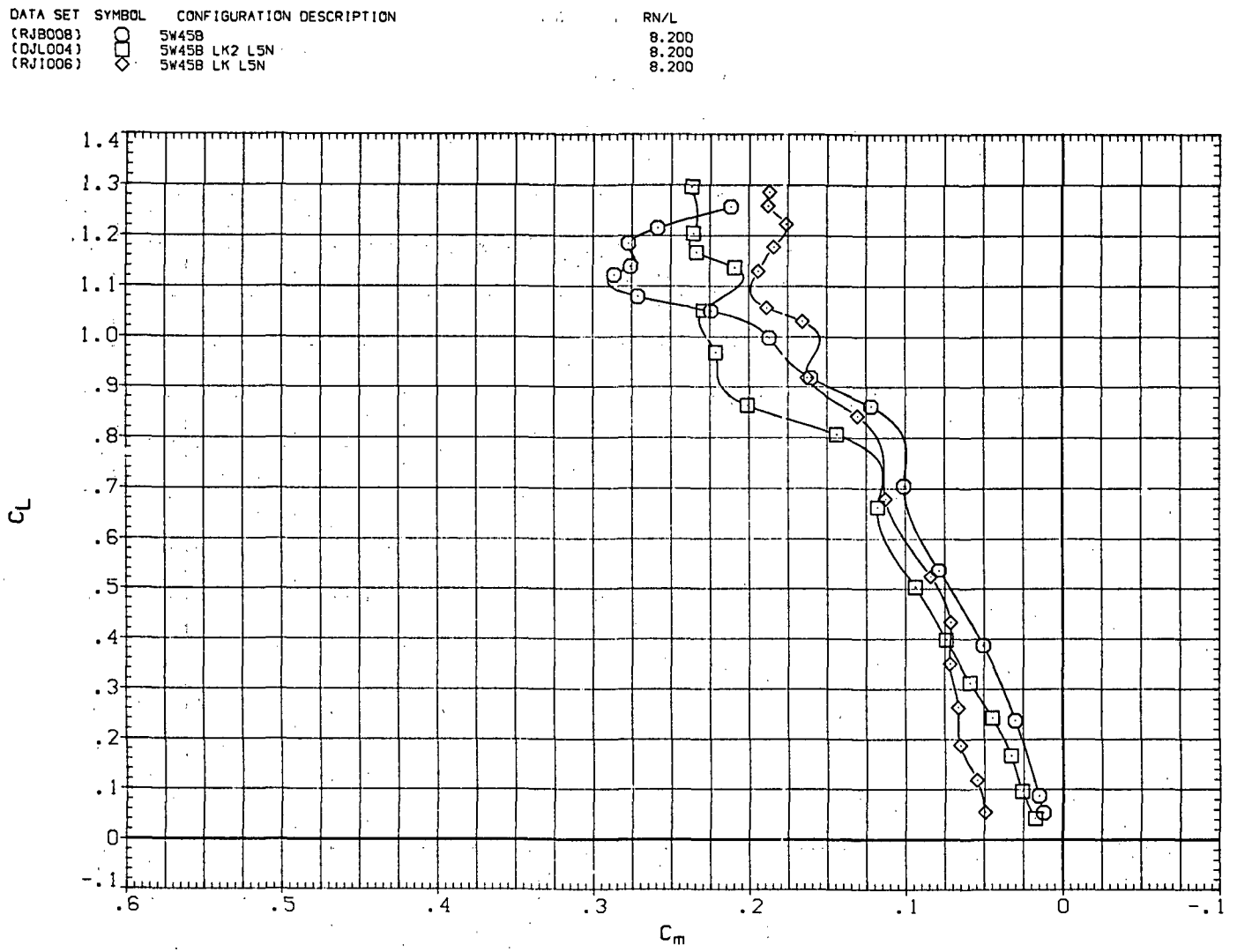

(c) C_L vs C_m

Figure 10.– Continued.

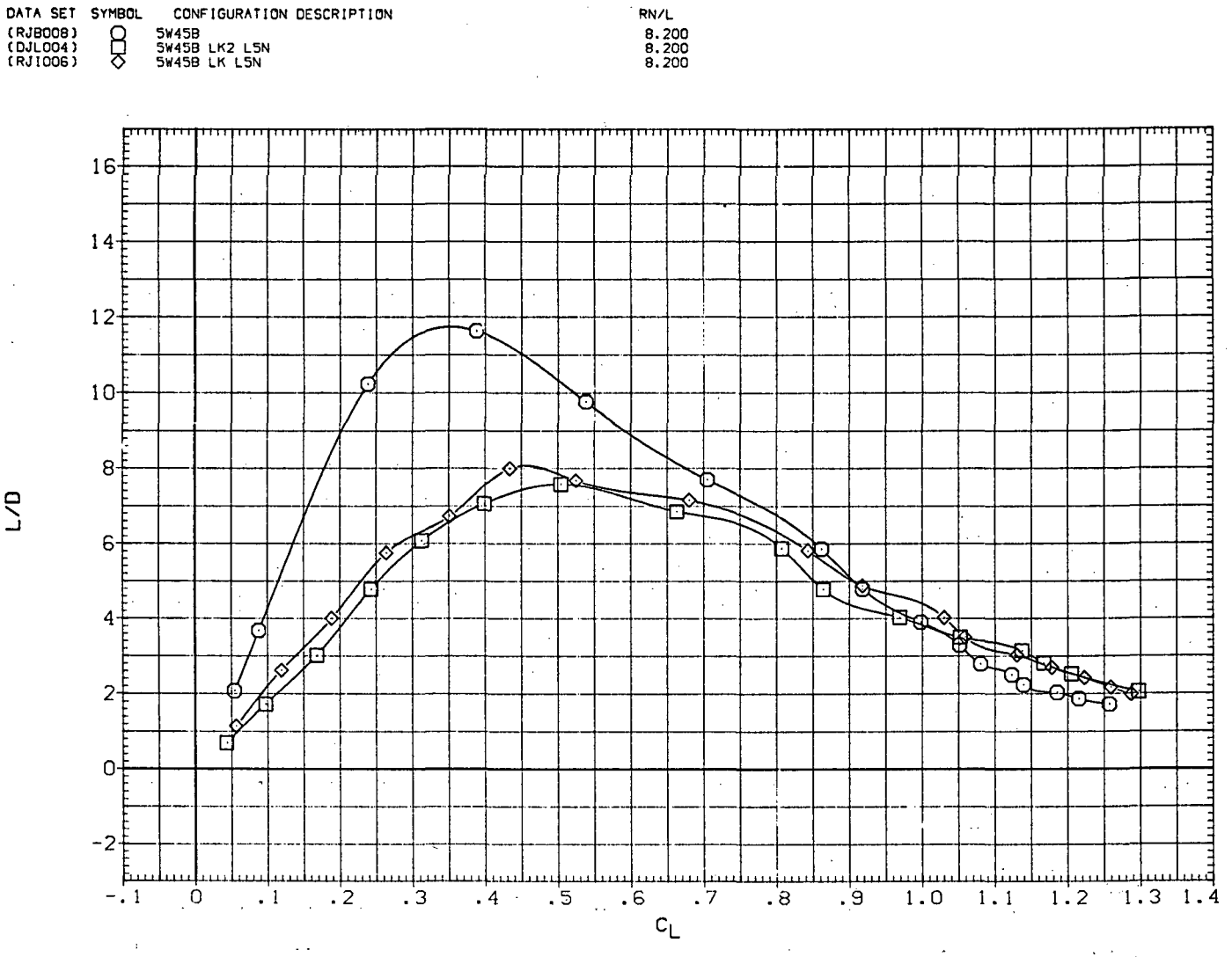

(d) L/D vs C_L

Figure 10.– Continued.

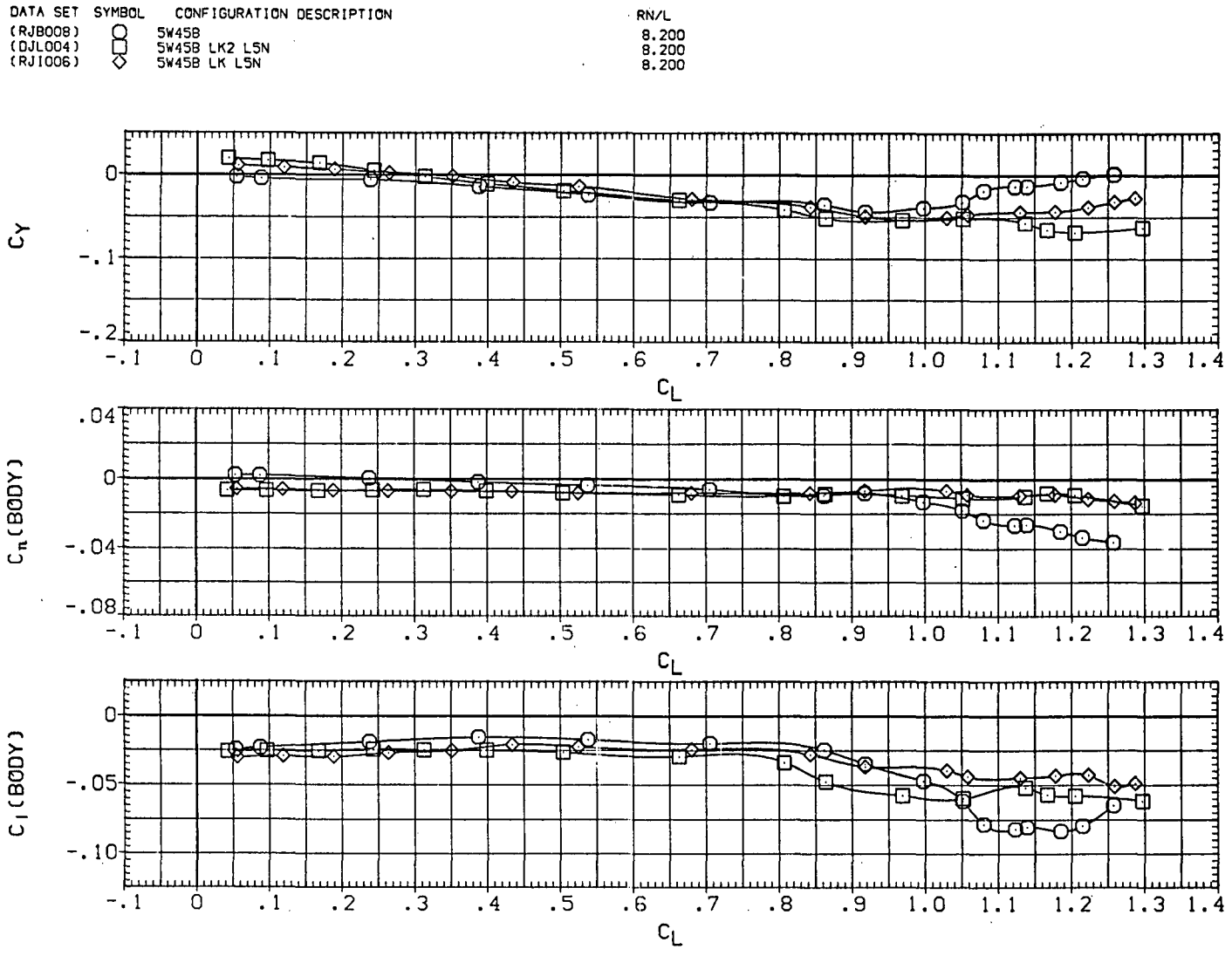

(e) C_Y, C_n, and C_l vs C_L

Figure 10.– Concluded.

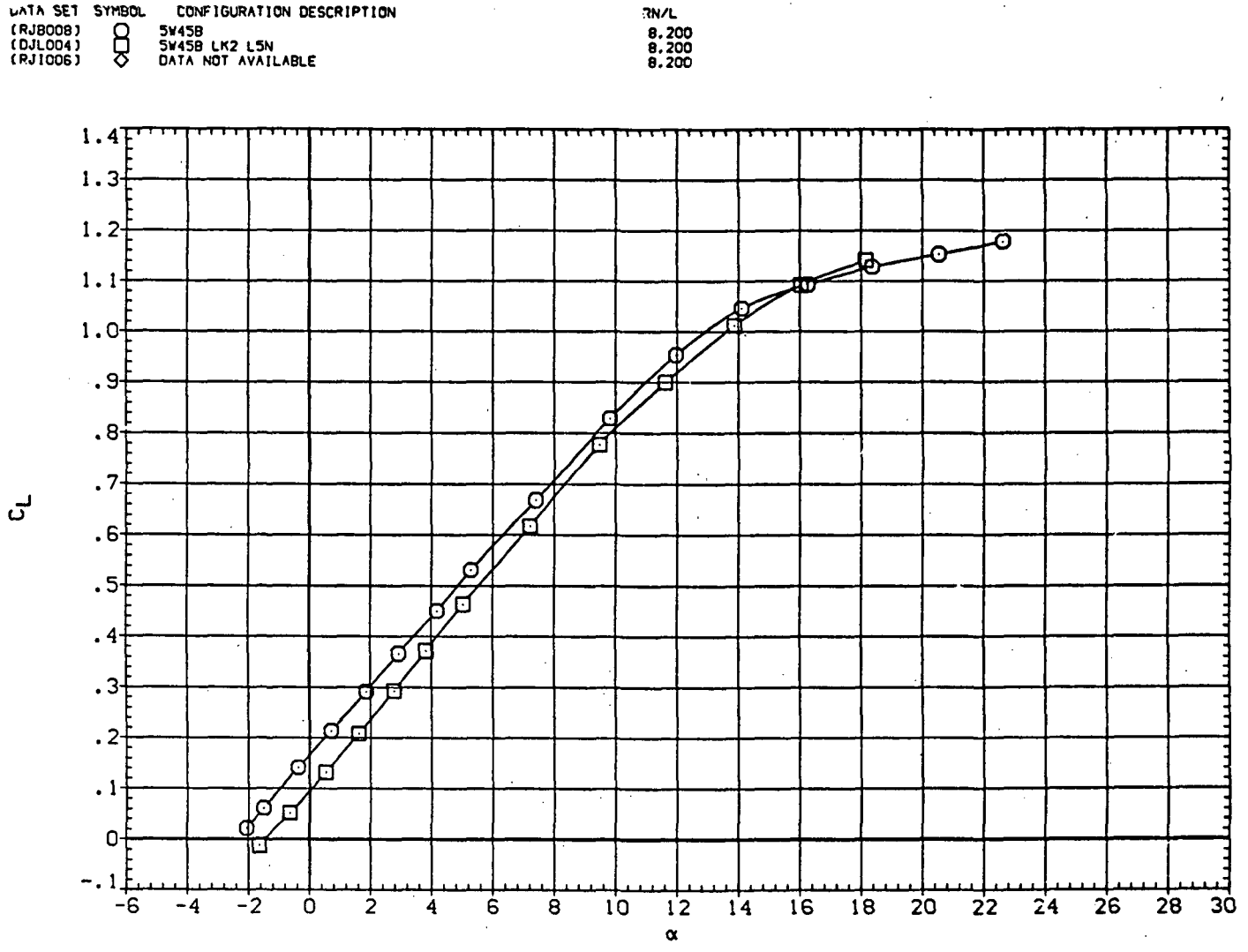

(a) C_L vs α

Figure 11.– Effect of Krüger nose flaps mounted on the drooped-nose flaps deflected 5°, downstream panel only: $\Lambda = 45°, M = 1.1$.

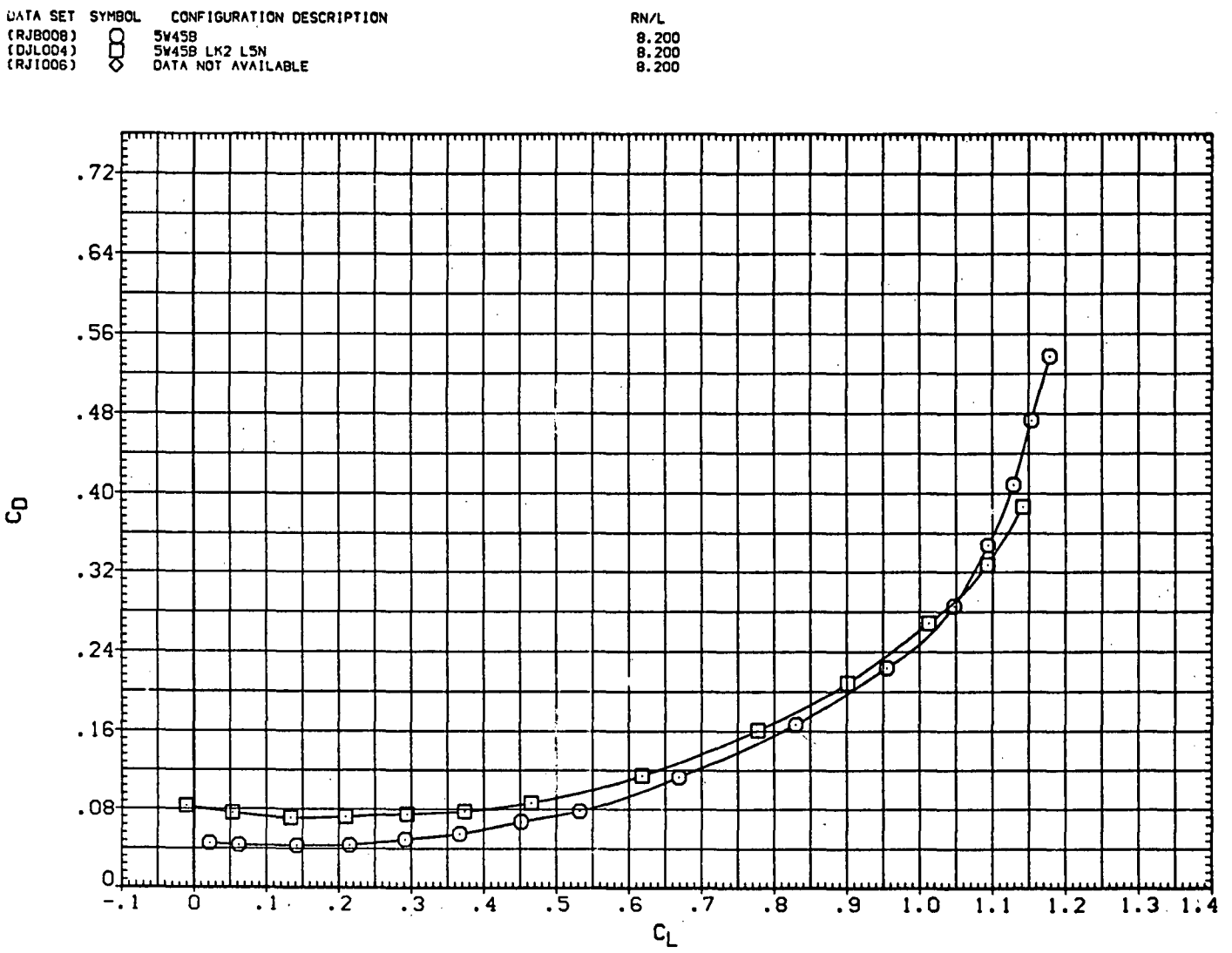

(b) C_D vs C_L

Figure 11.– Continued.

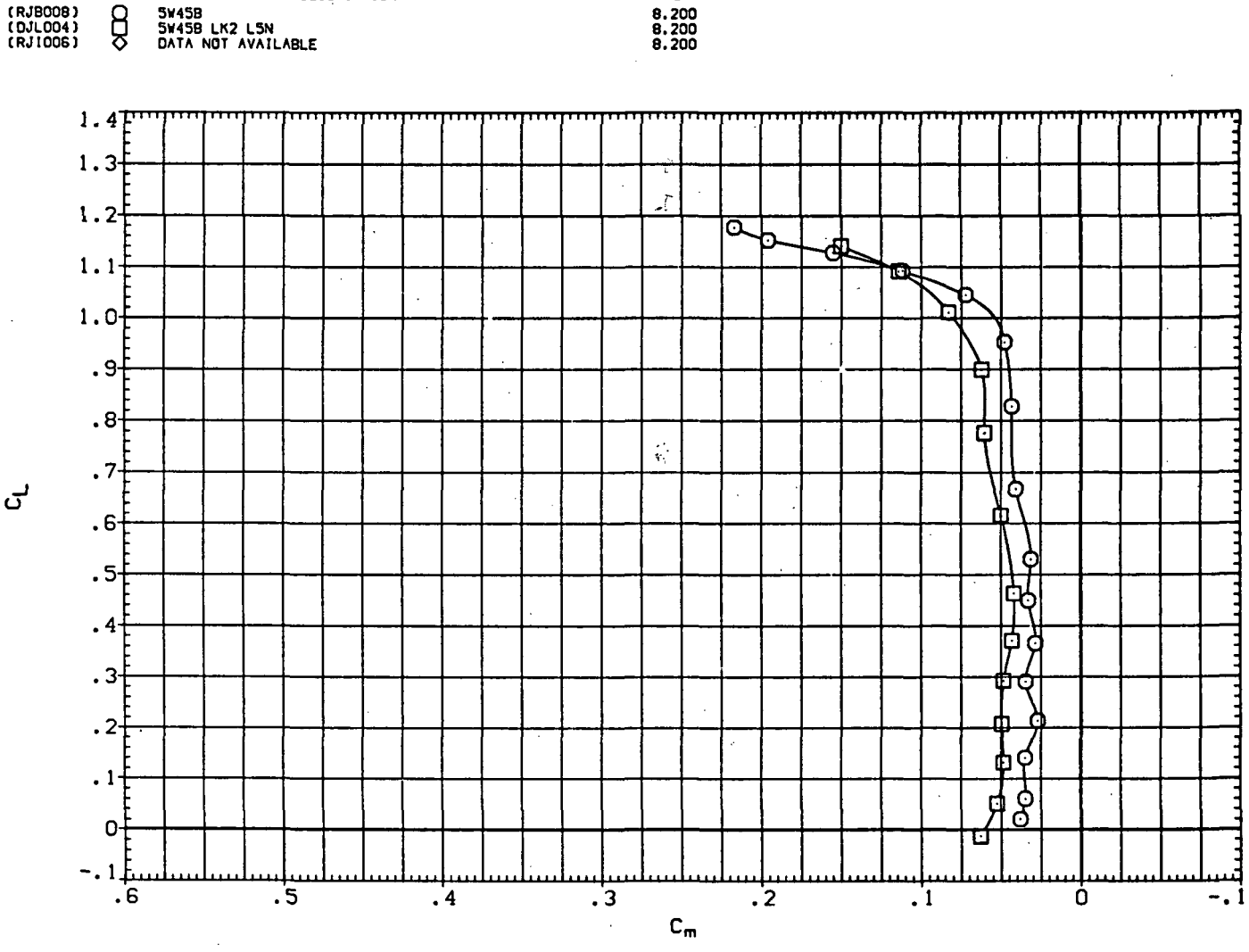

(c) C_L vs C_m

Figure 11.– Continued.

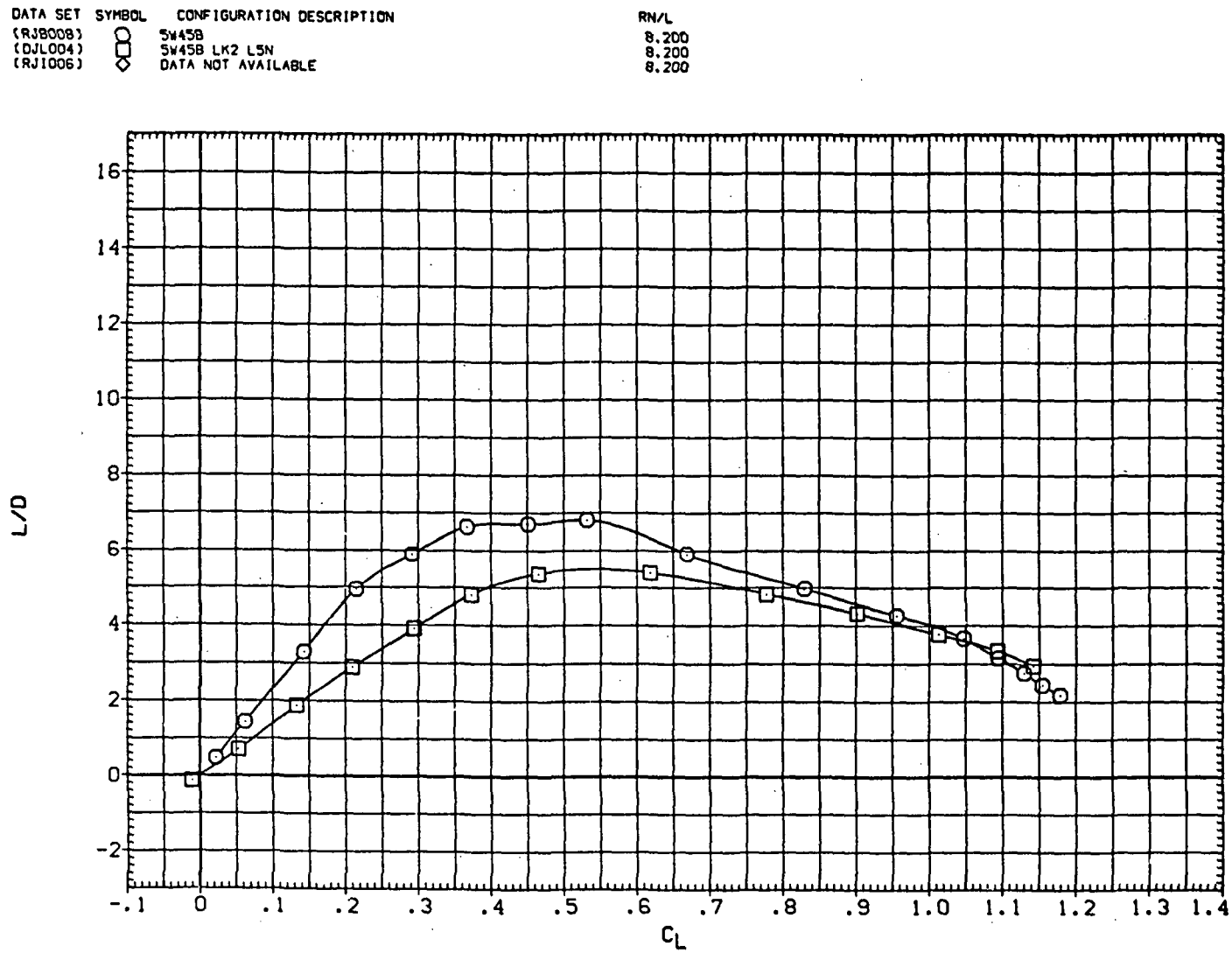

(d) L/D vs C_L

Figure 11.– Continued.

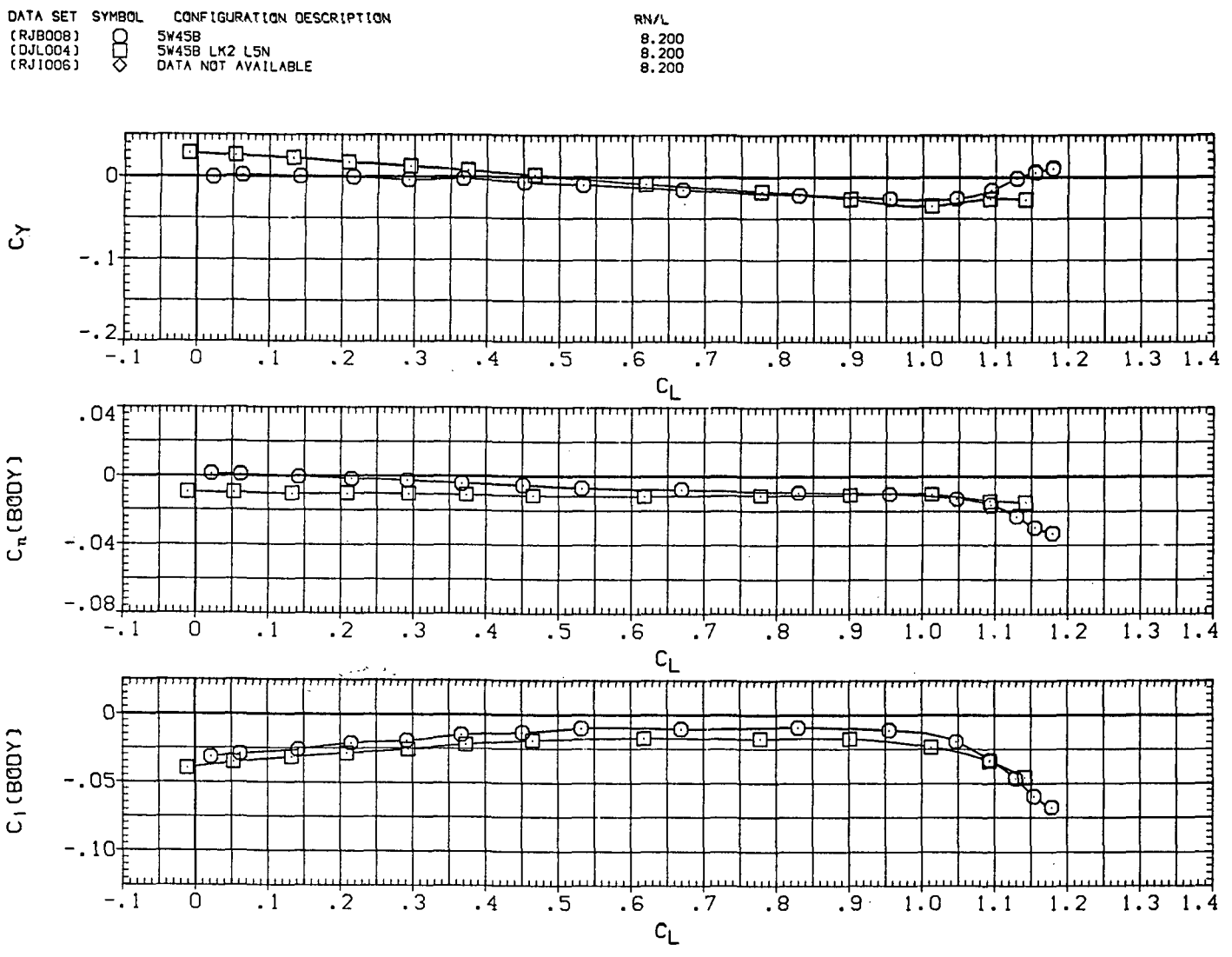

(e) C_n, C_Y, and C_l vs C_L

Figure 11.– Concluded.

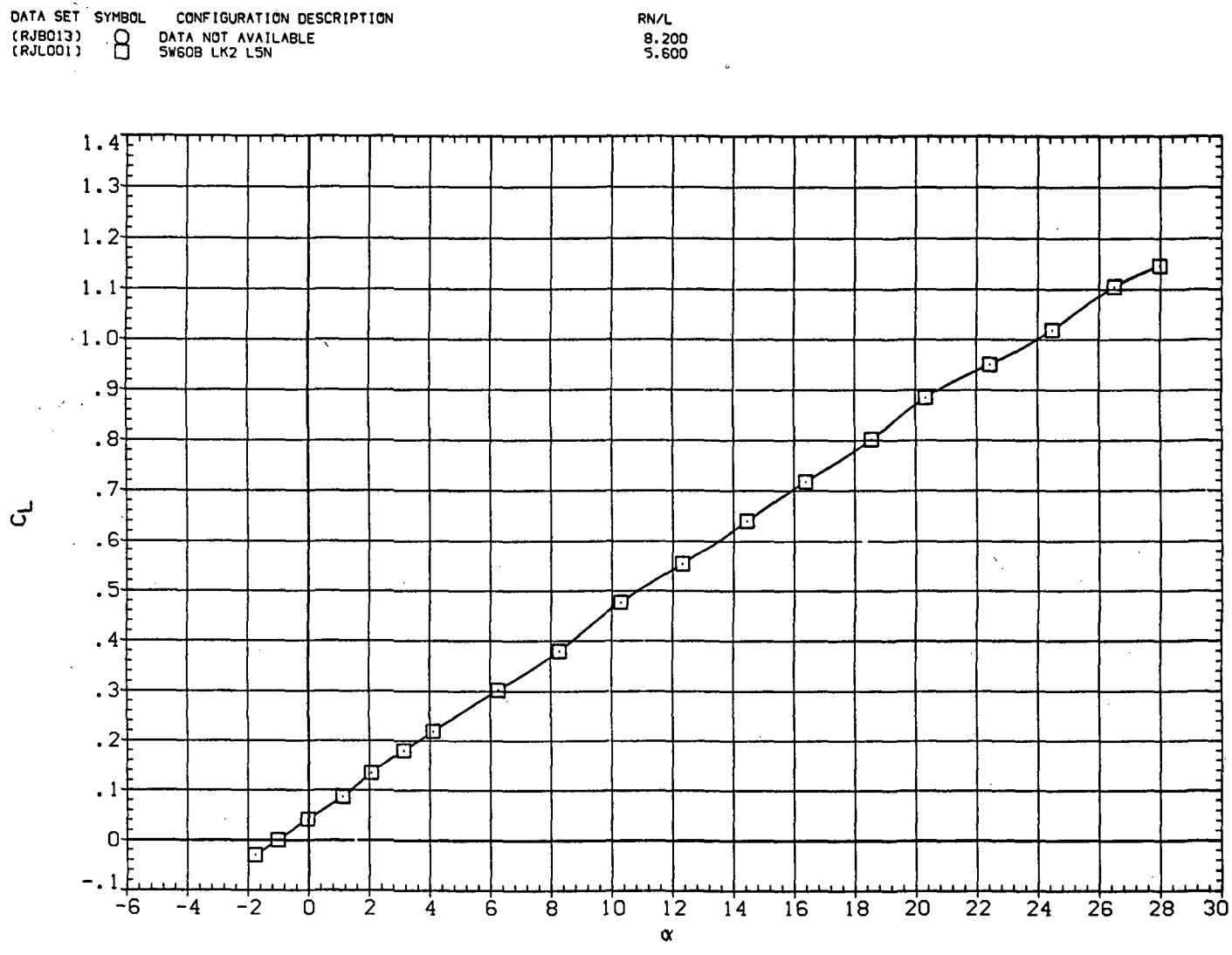

(a) C_L vs α

Figure 12.– Effect of Krüger nose flaps mounted on the drooped-nose flaps deflected 5°, downstream panel only: $\Lambda = 60°, M = 0.25$.

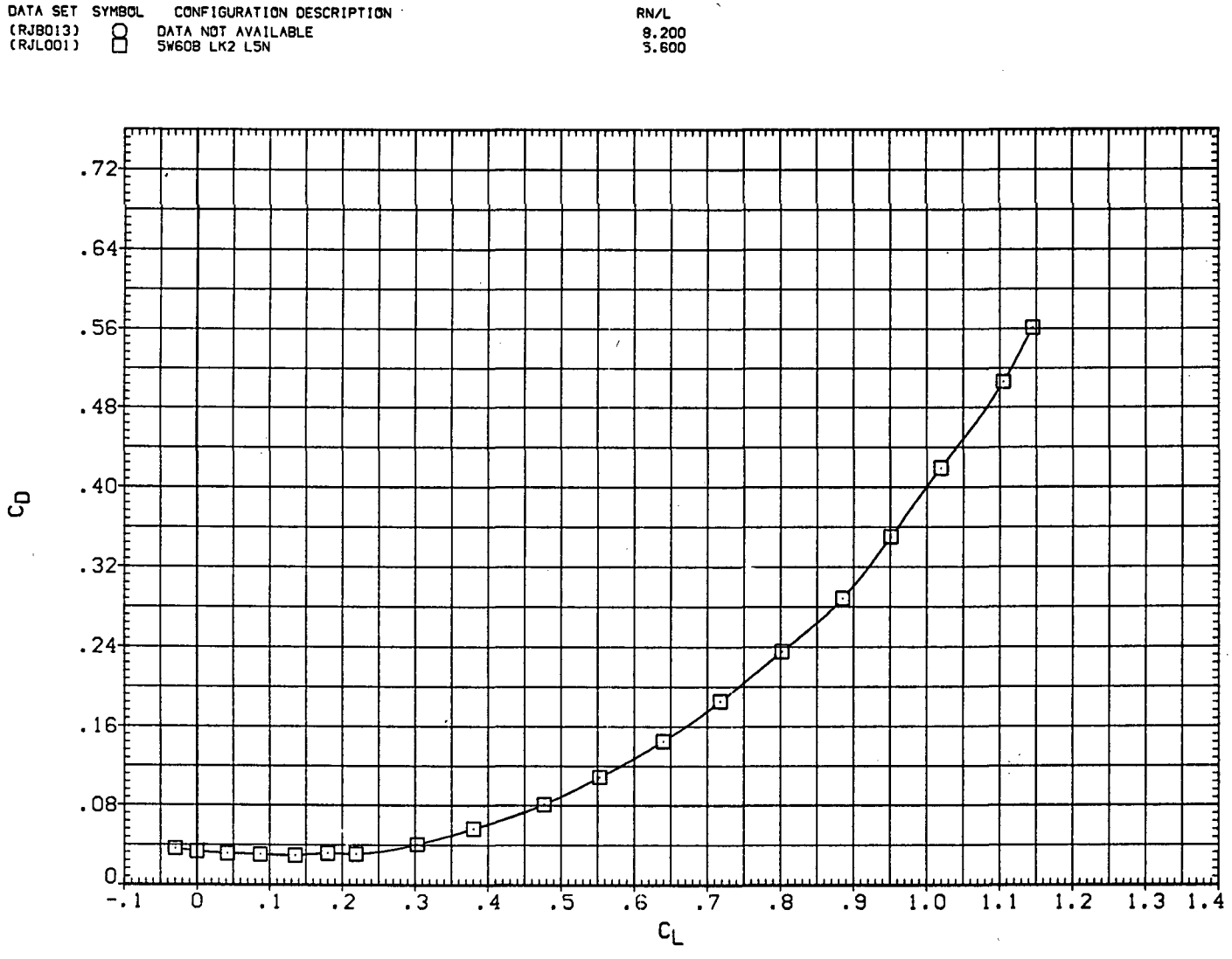

(b) C_D vs C_L

Figure 12.– Continued.

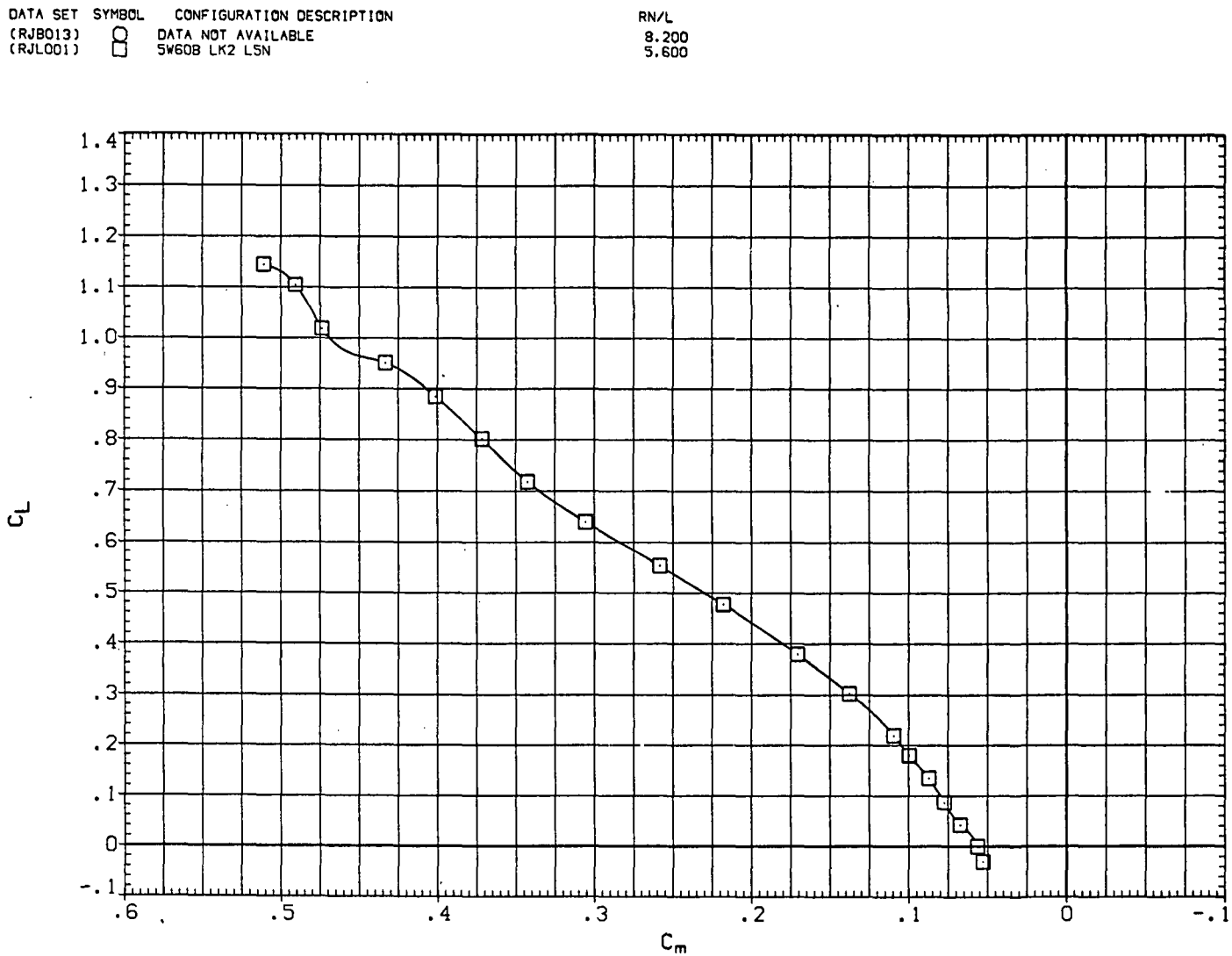

(c) C_L vs C_m

Figure 12.– Continued.

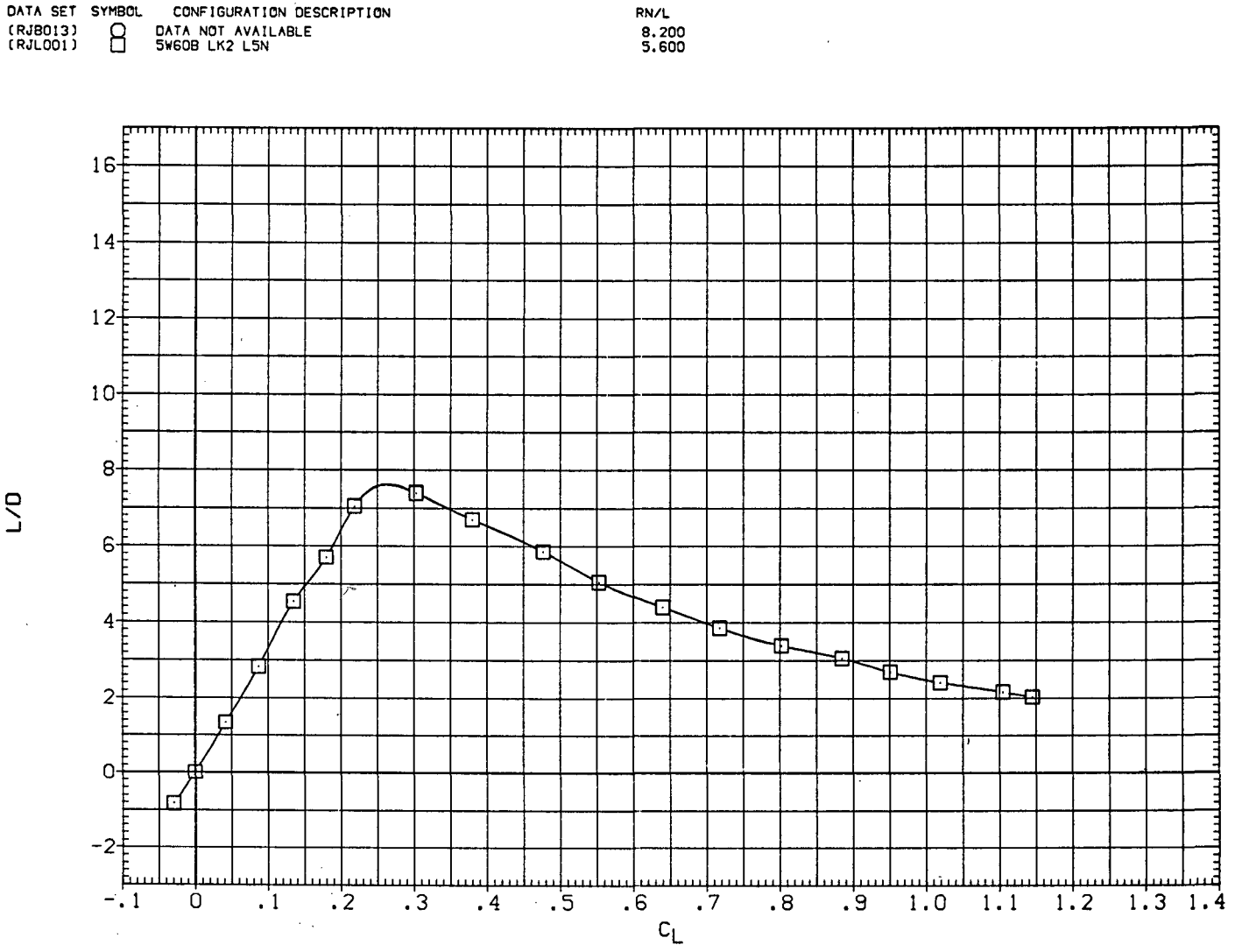

(d) L/D vs C_L

Figure 12.– Continued.

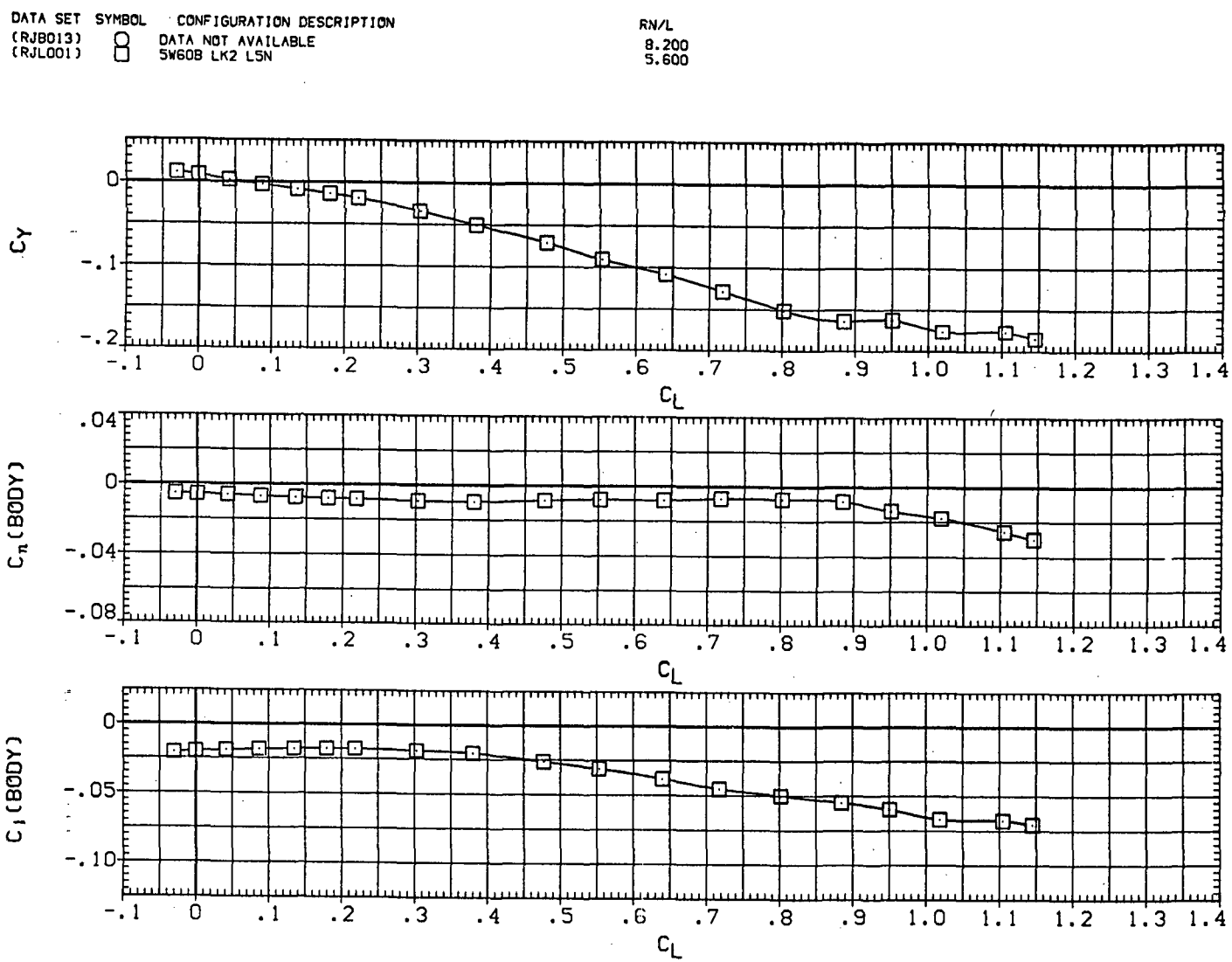

(e) C_Y, C_n, and C_l vs C_L

Figure 12.– Concluded.

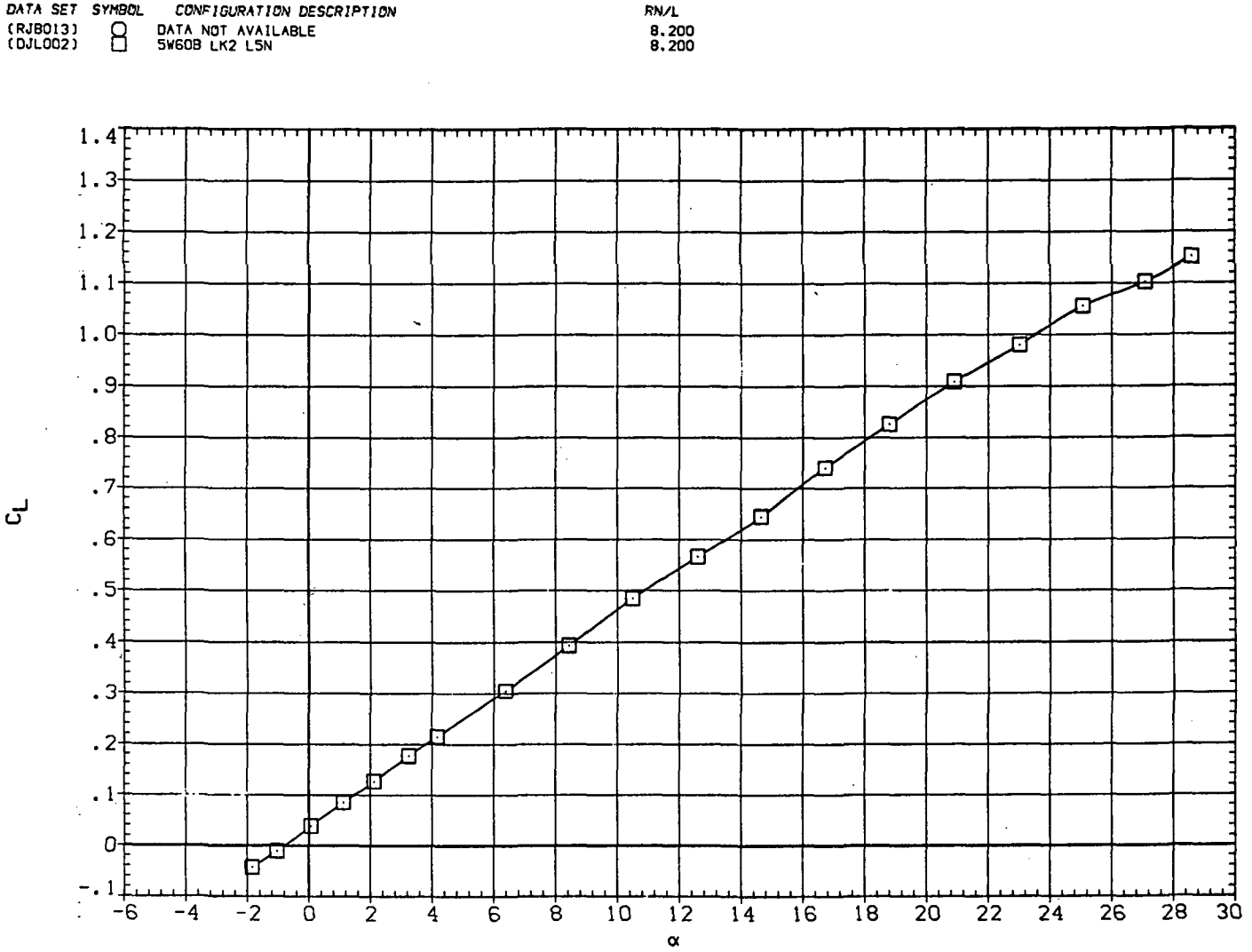

(a) C_L vs α

Figure 13.– Effect of Krüger nose flaps mounted on the drooped-nose flaps deflected 5°, downstream panel only: $\Lambda = 60°, M = 0.40$.

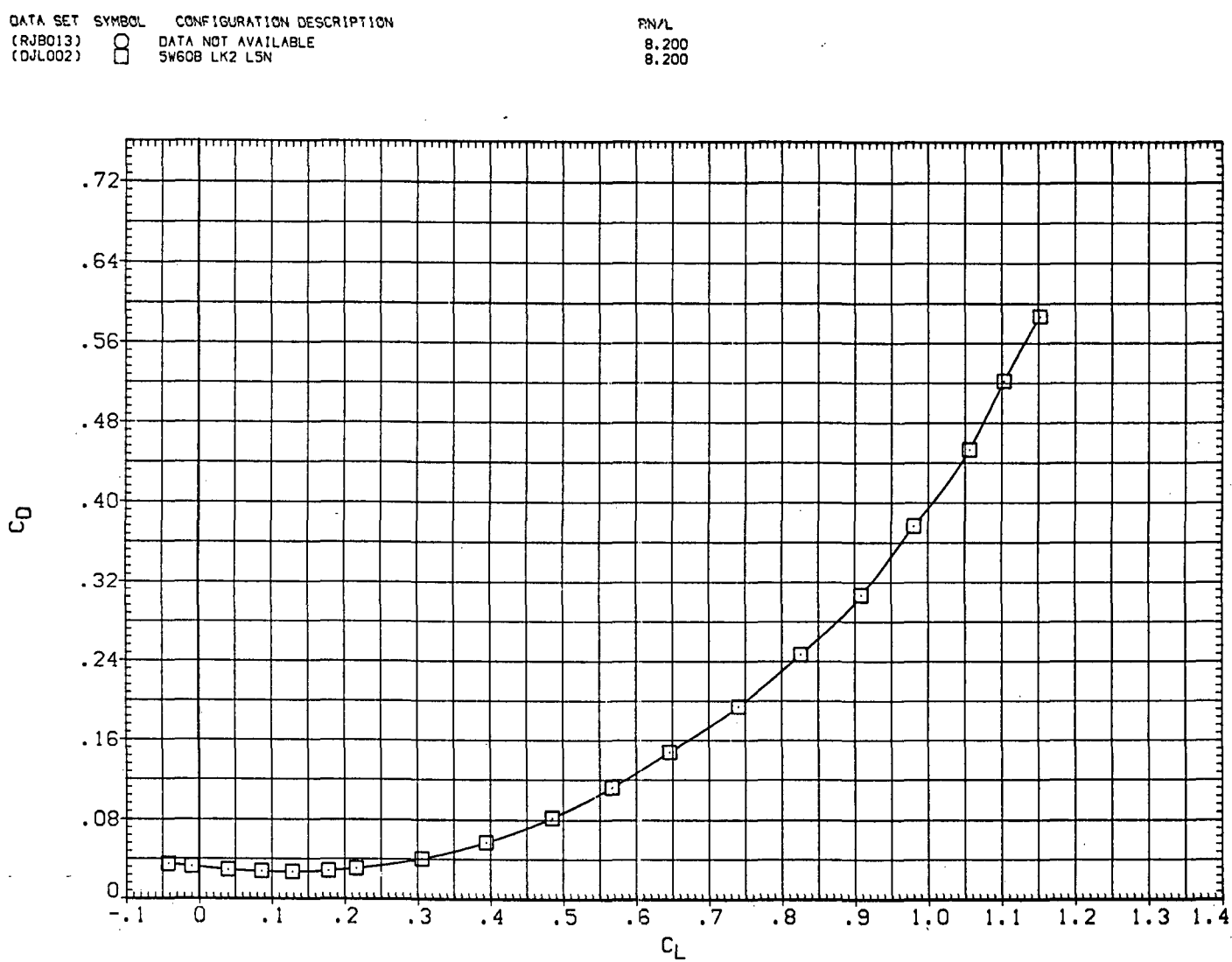

(b) C_D vs C_L

Figure 13.– Continued.

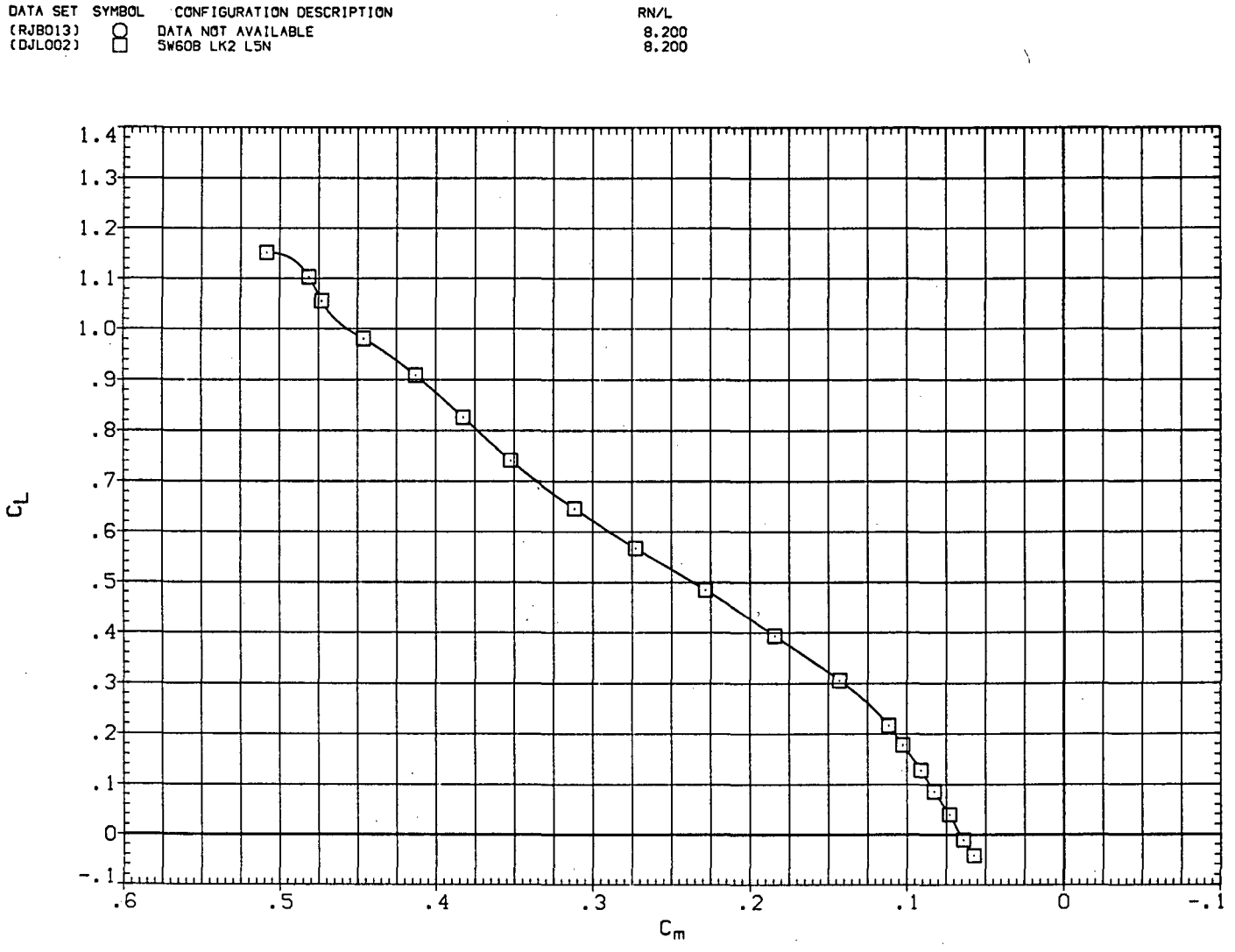

(c) C_L vs C_m

Figure 13.– Continued.

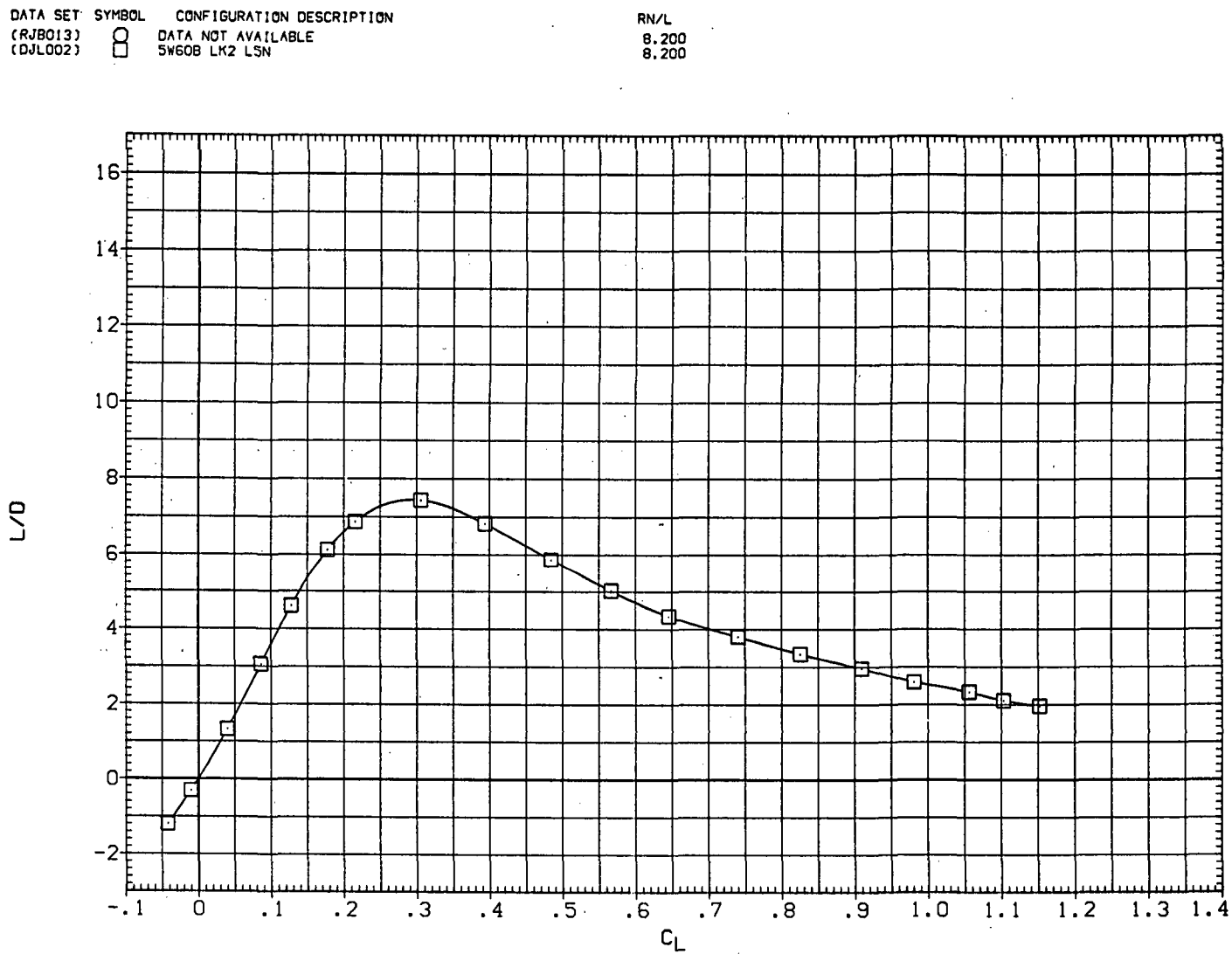

(d) L/D vs C_L

Figure 13.– Continued.

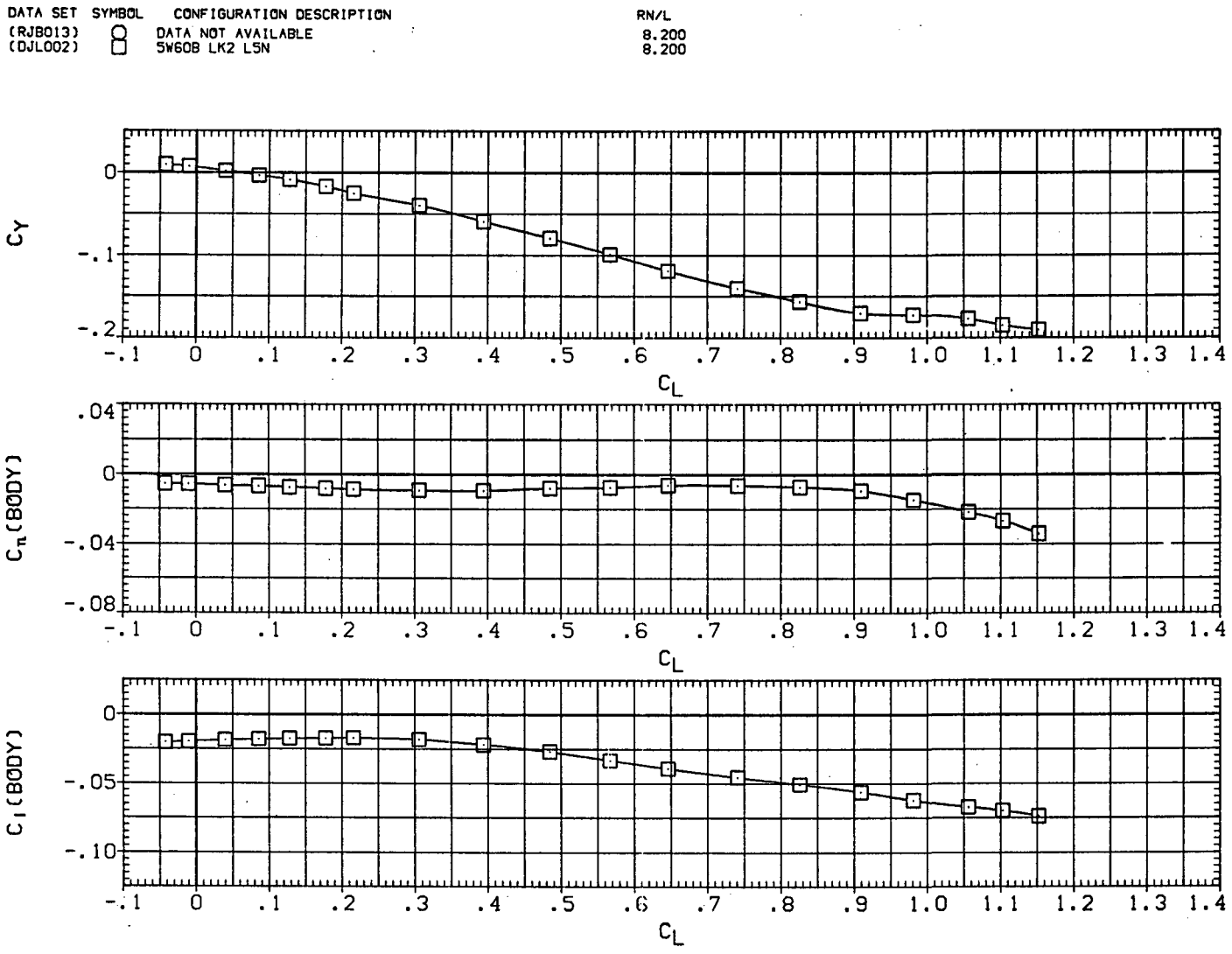

(e) C_Y, C_n and C_l vs C_L

Figure 13.– Concluded.

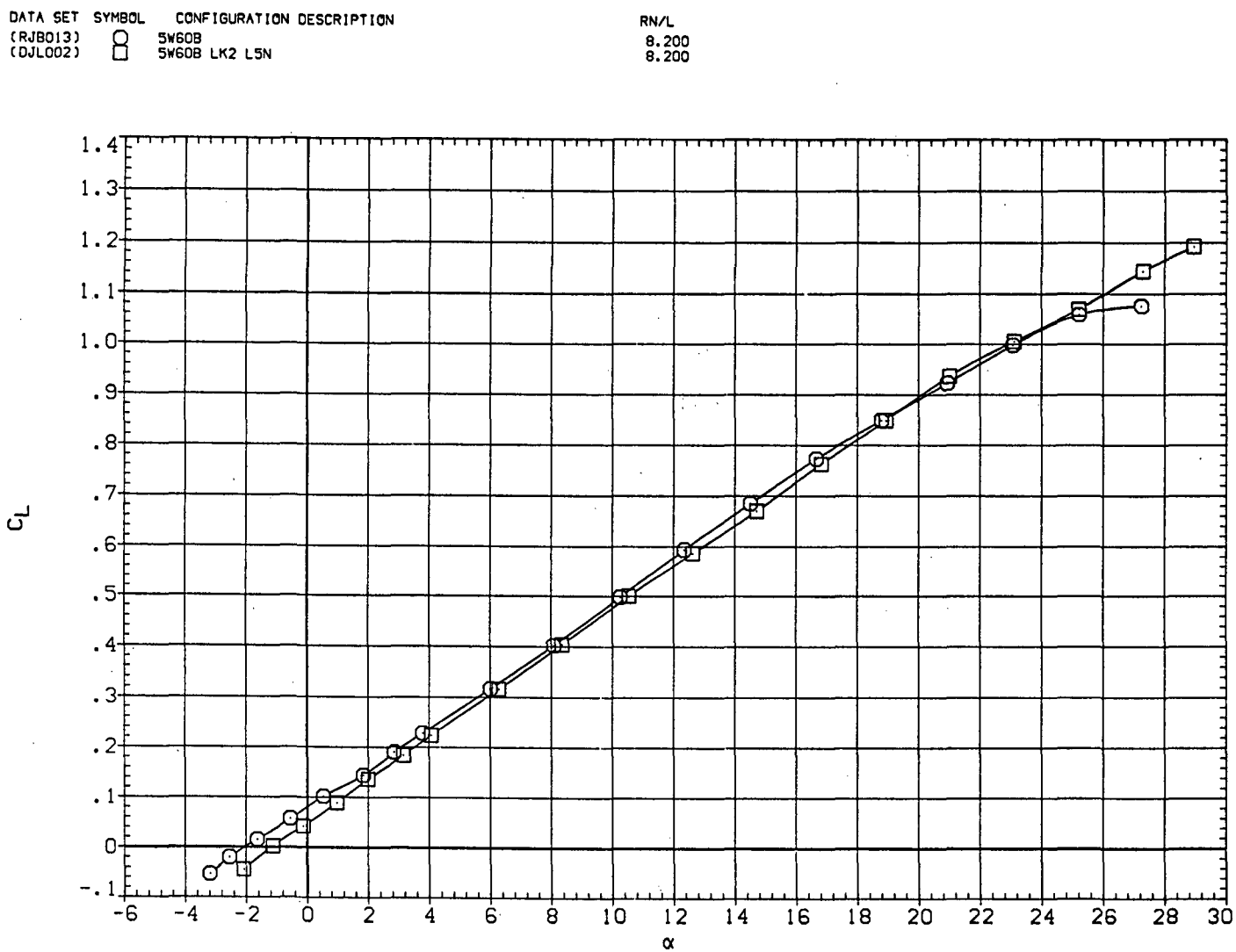

(a) C_L vs α

Figure 14.– Effect of Krüger nose flaps mounted on the drooped-nose flaps deflected 5°, downstream panel only: $\Lambda = 60°, M = 0.60$.

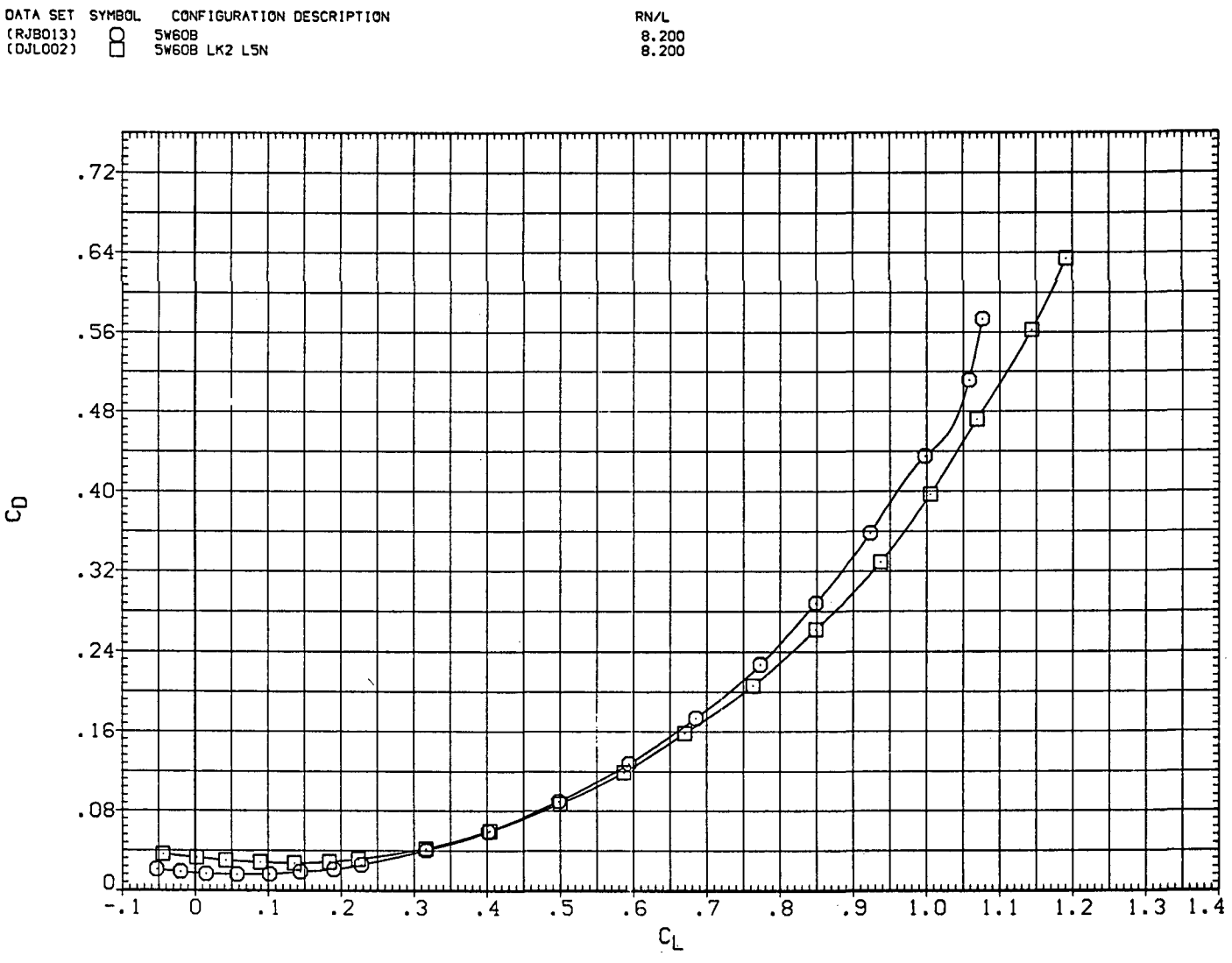

(b) C_D vs C_L

Figure 14.– Continued.

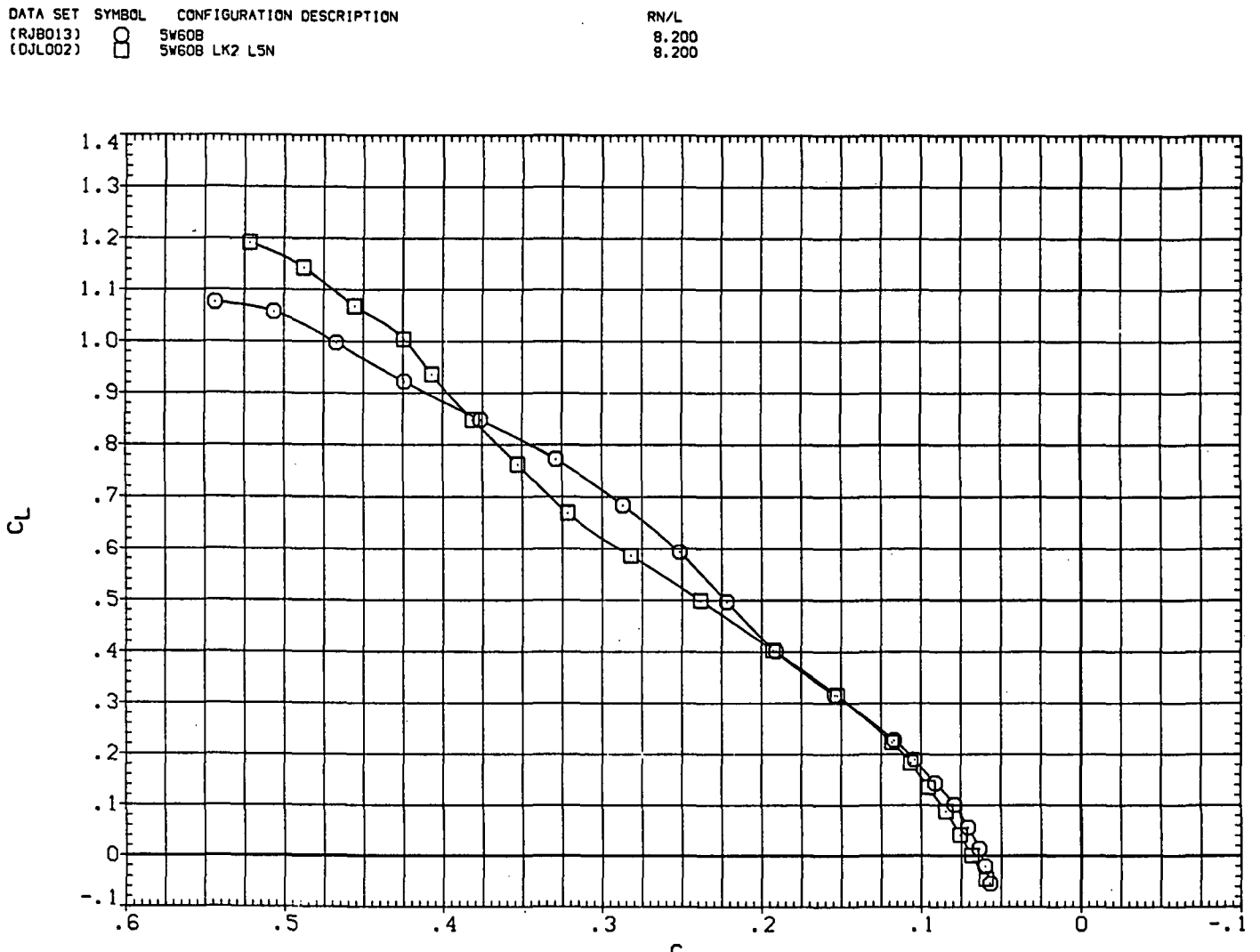

(c) C_L vs C_m

Figure 14.– Continued.

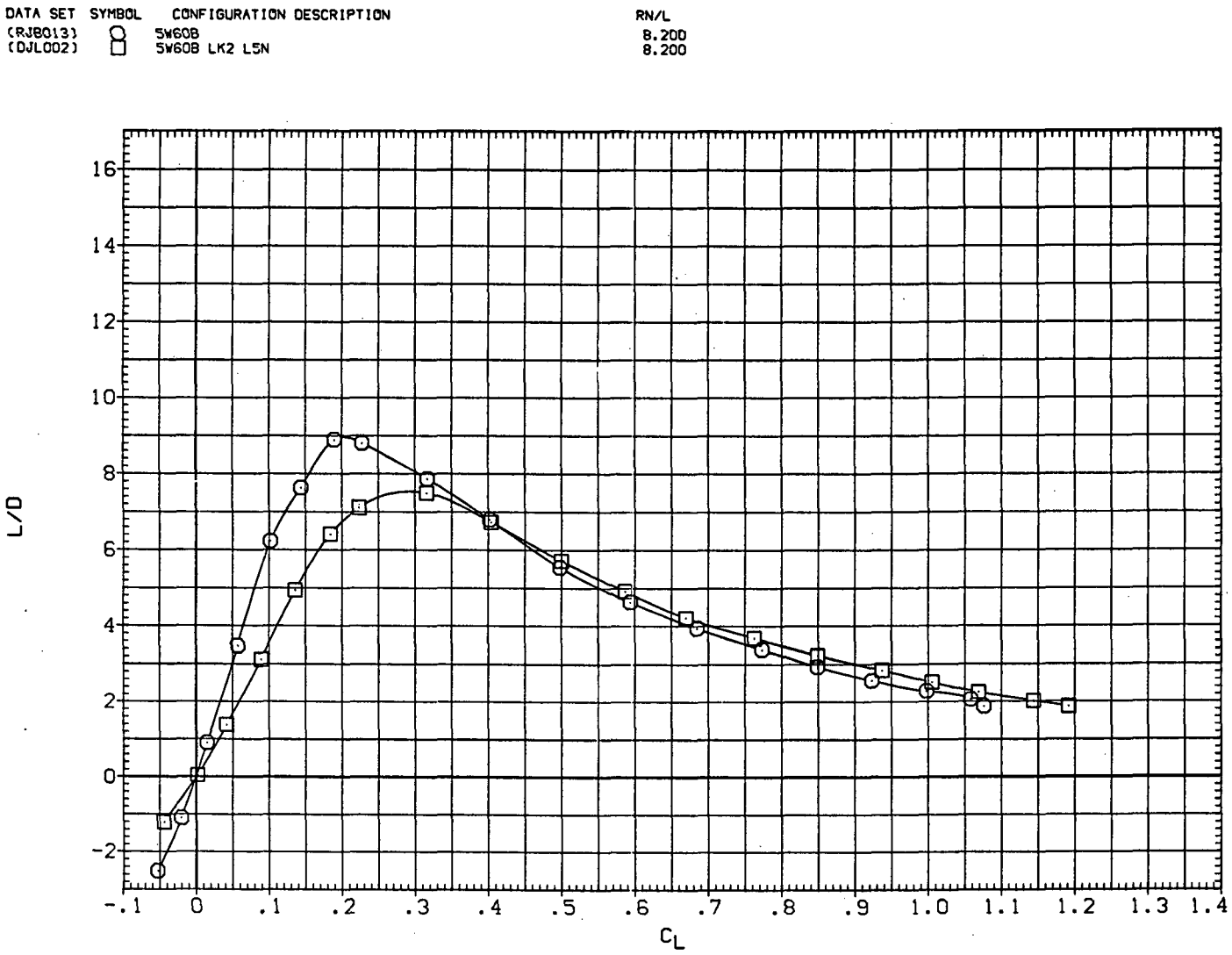

(d) L/D vs C_L

Figure 14.– Continued.

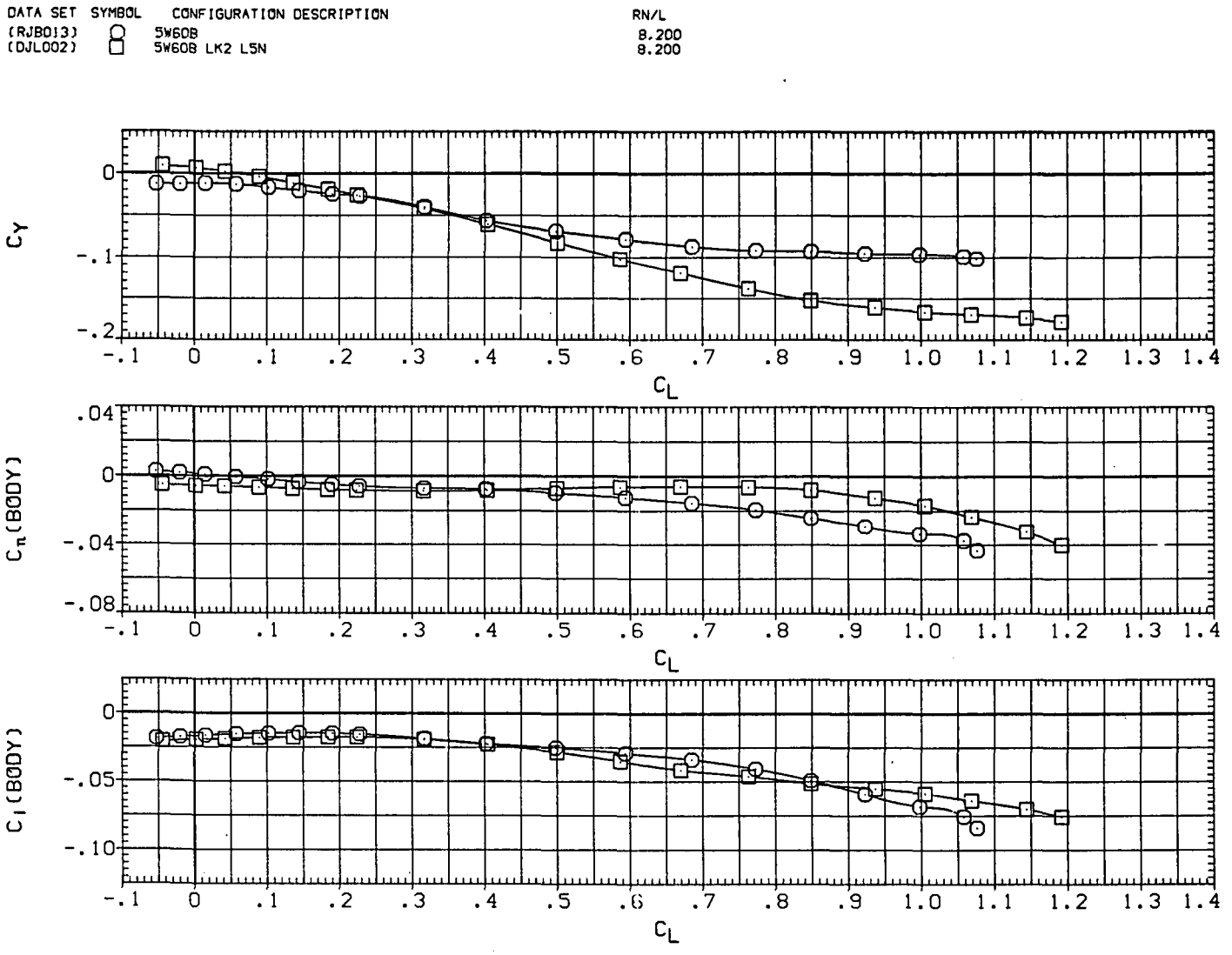

(e) C_Y, C_n, and C_l vs C_L

Figure 14.– Concluded.

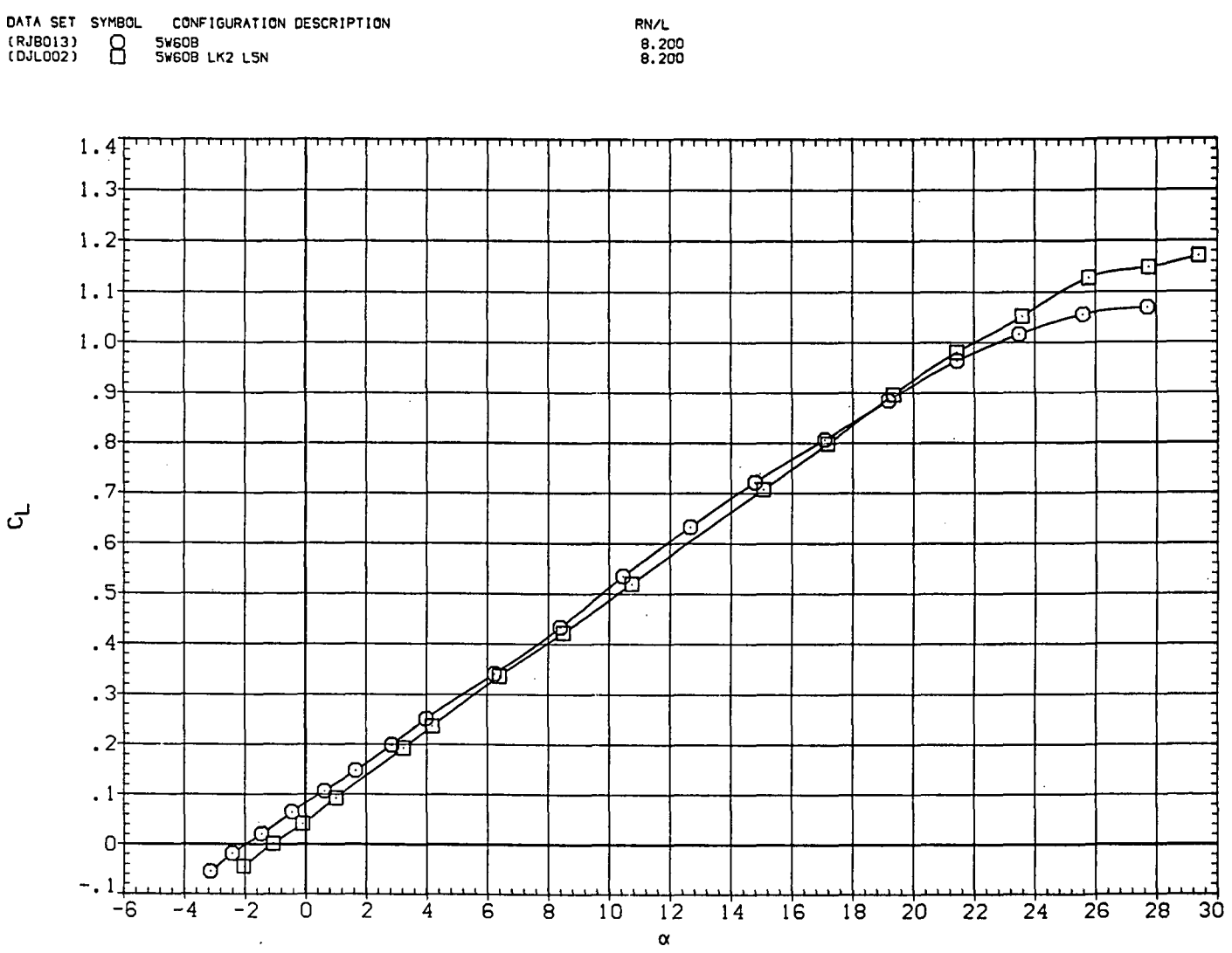

(a) C_L vs α

Figure 15.– Effect of Krüger nose flaps mounted on the drooped-nose flaps deflected 5°, downstream panel only: $\Lambda = 60°, M = 0.80$.

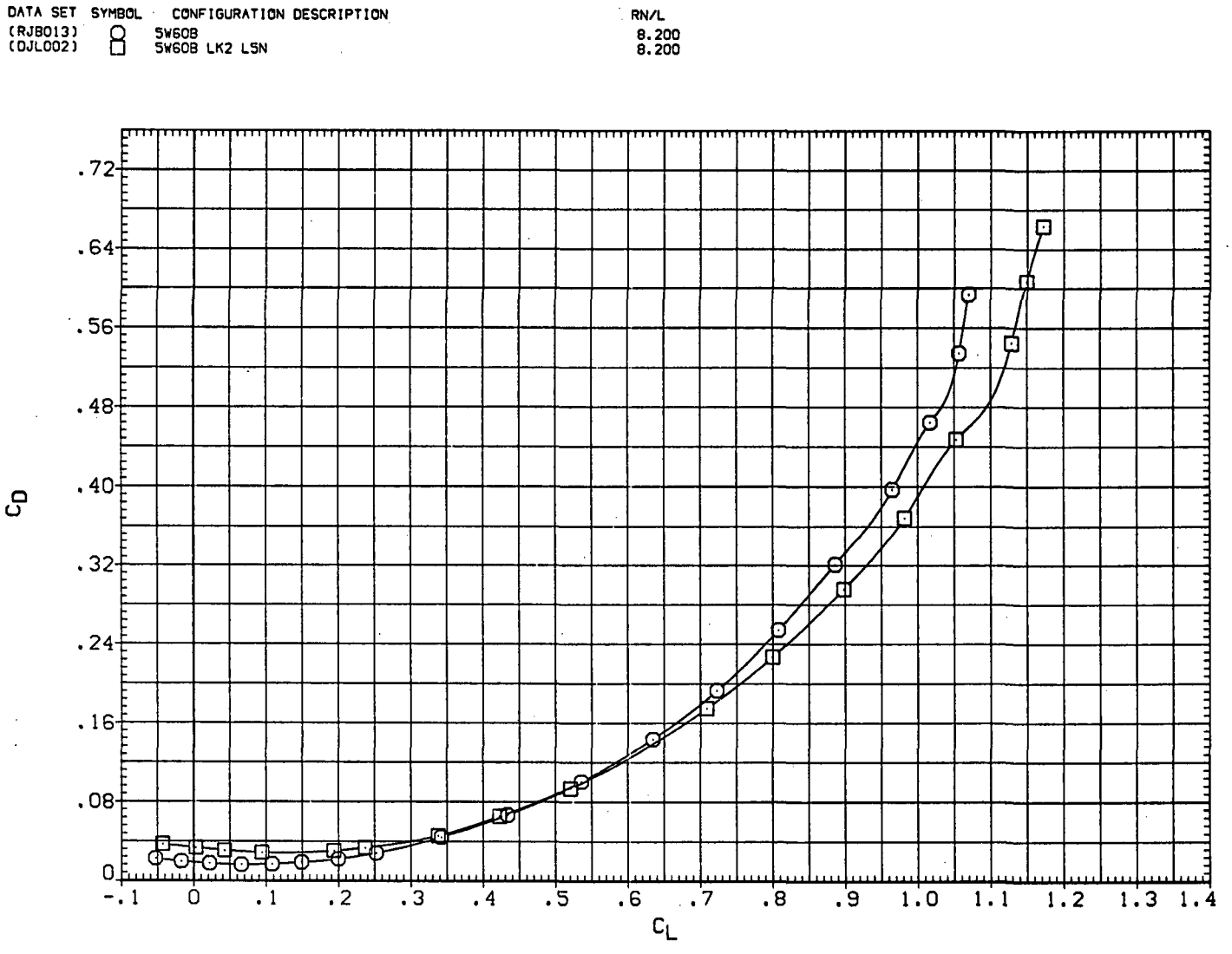

(b) C_D vs C_L

Figure 15.– Continued.

(c) C_L vs C_m

Figure 15.– Continued.

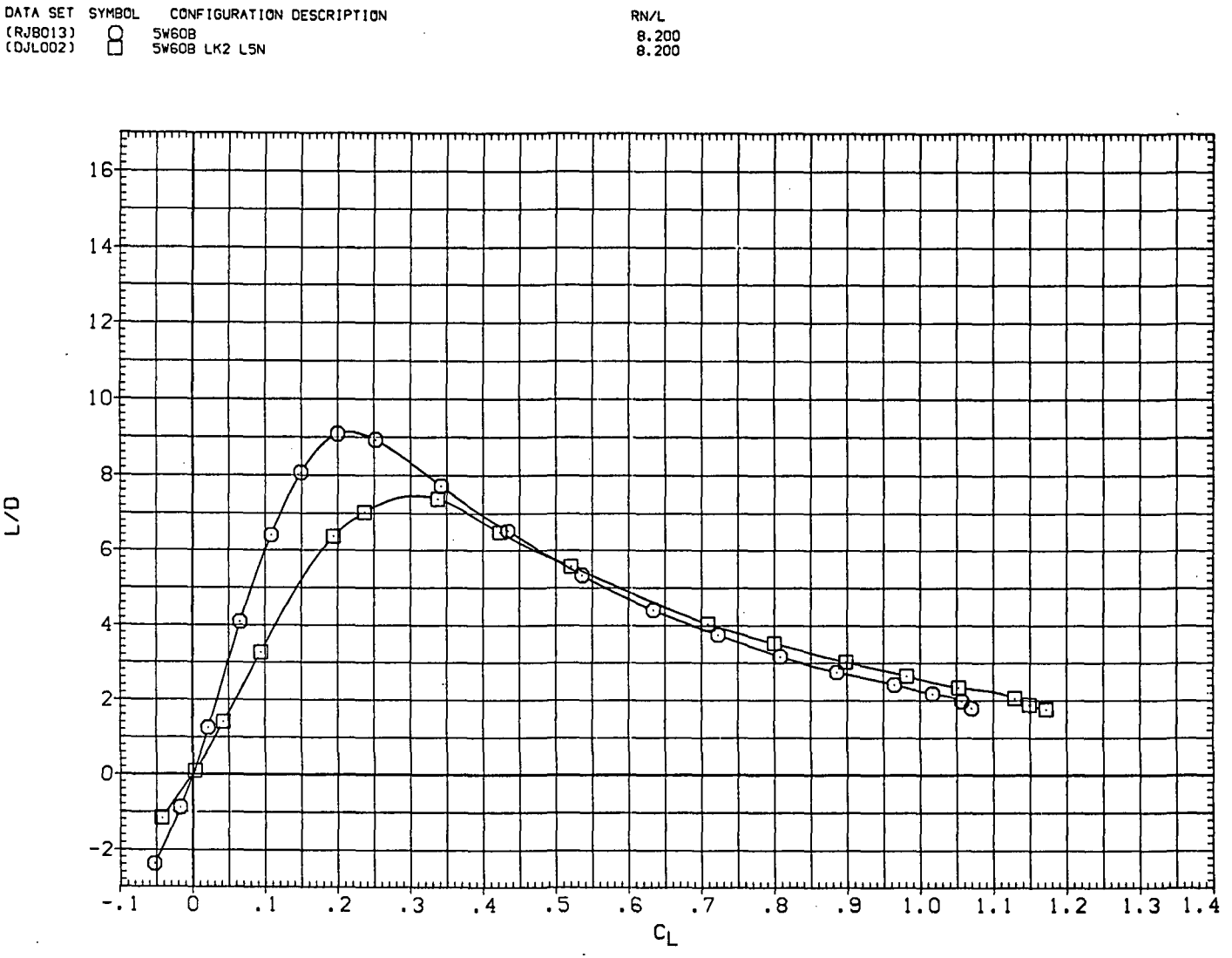

(d) L/D vs C_L

Figure 15.– Continued.

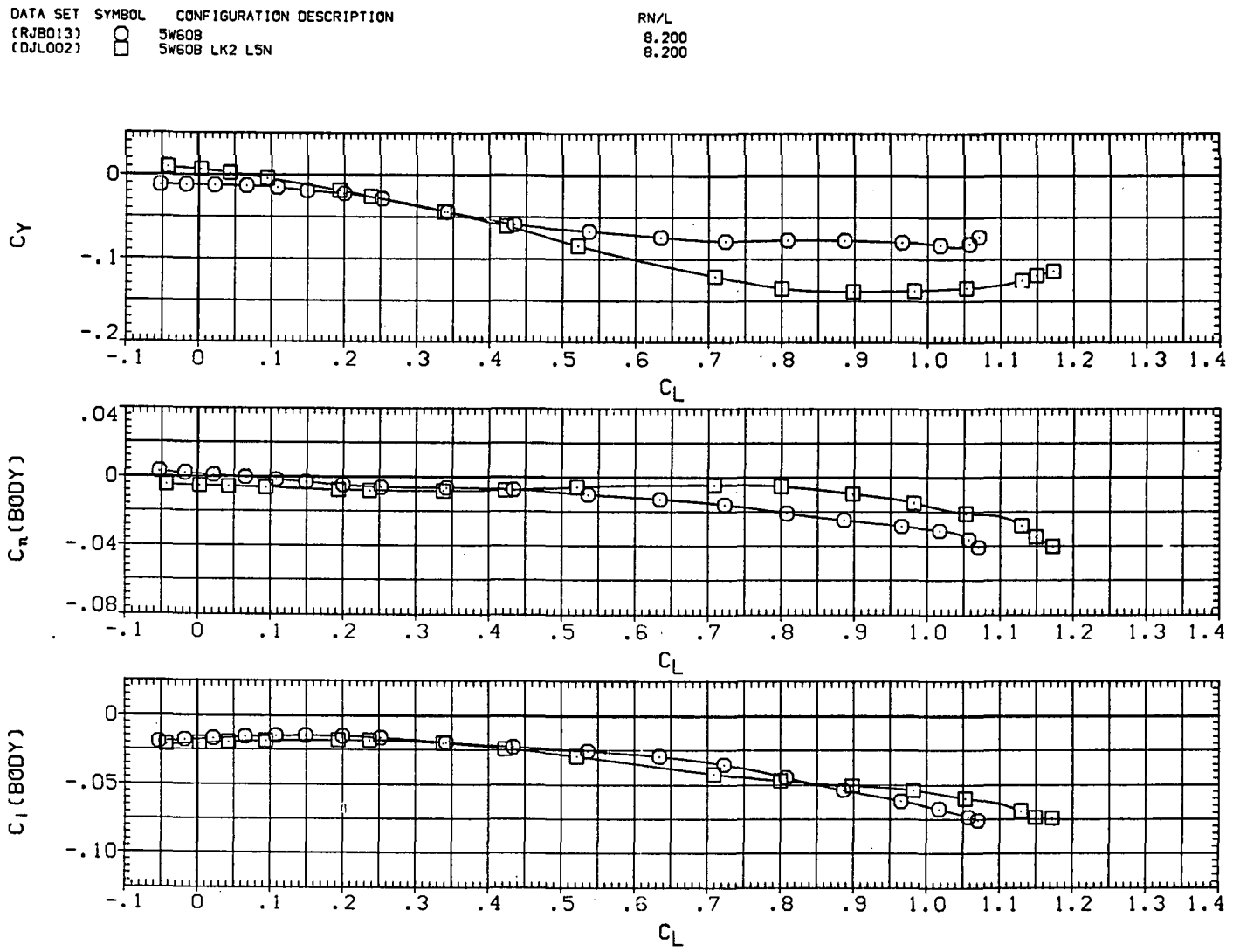

(e) C_Y, C_n, and C_l vs C_L

Figure 15.– Concluded.

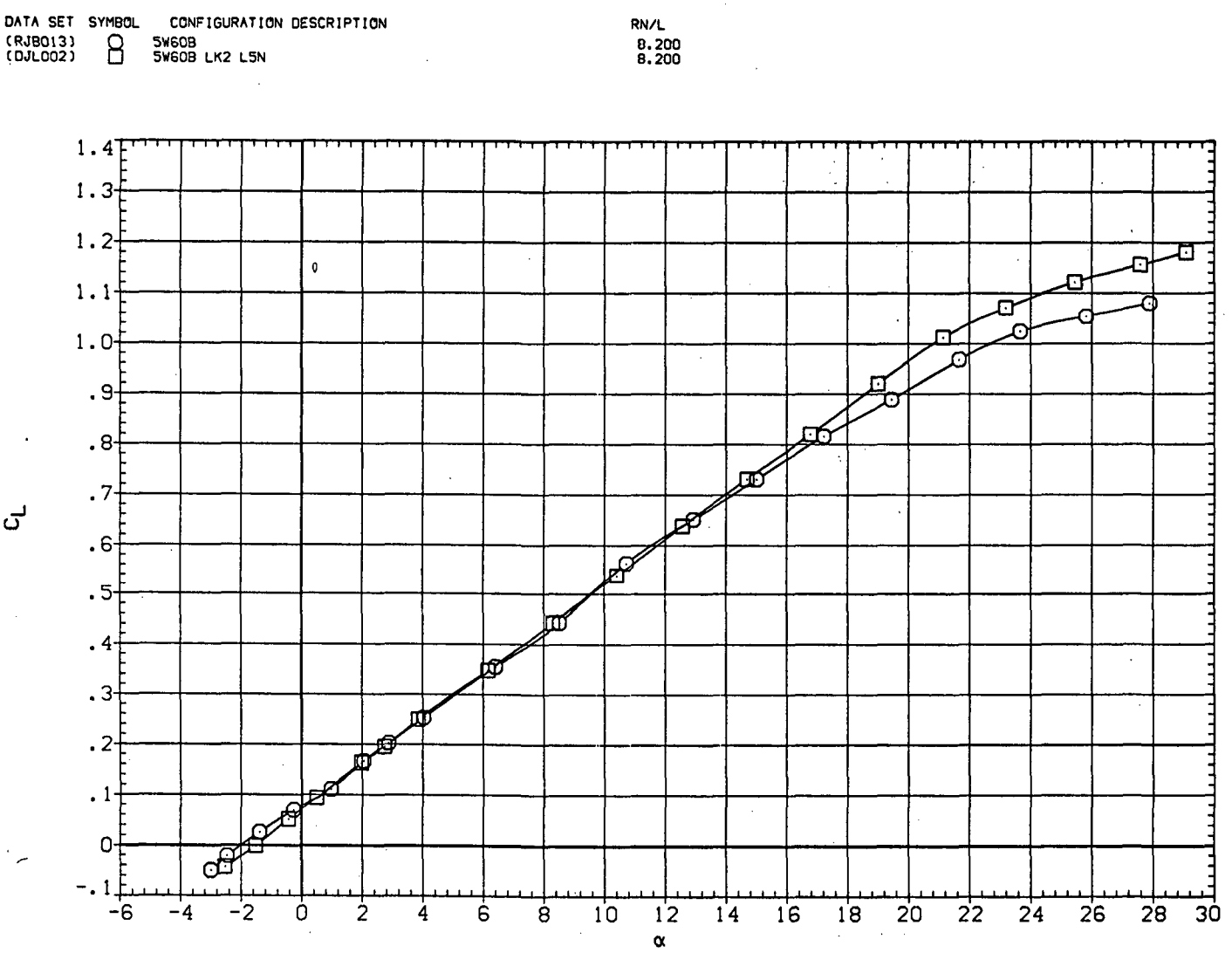

(a) C_L vs α

Figure 16.– Effect of Krüger nose flaps mounted on the drooped-nose flaps deflected 5°, downstream panel only: $\Lambda = 60°, M = 0.90$.

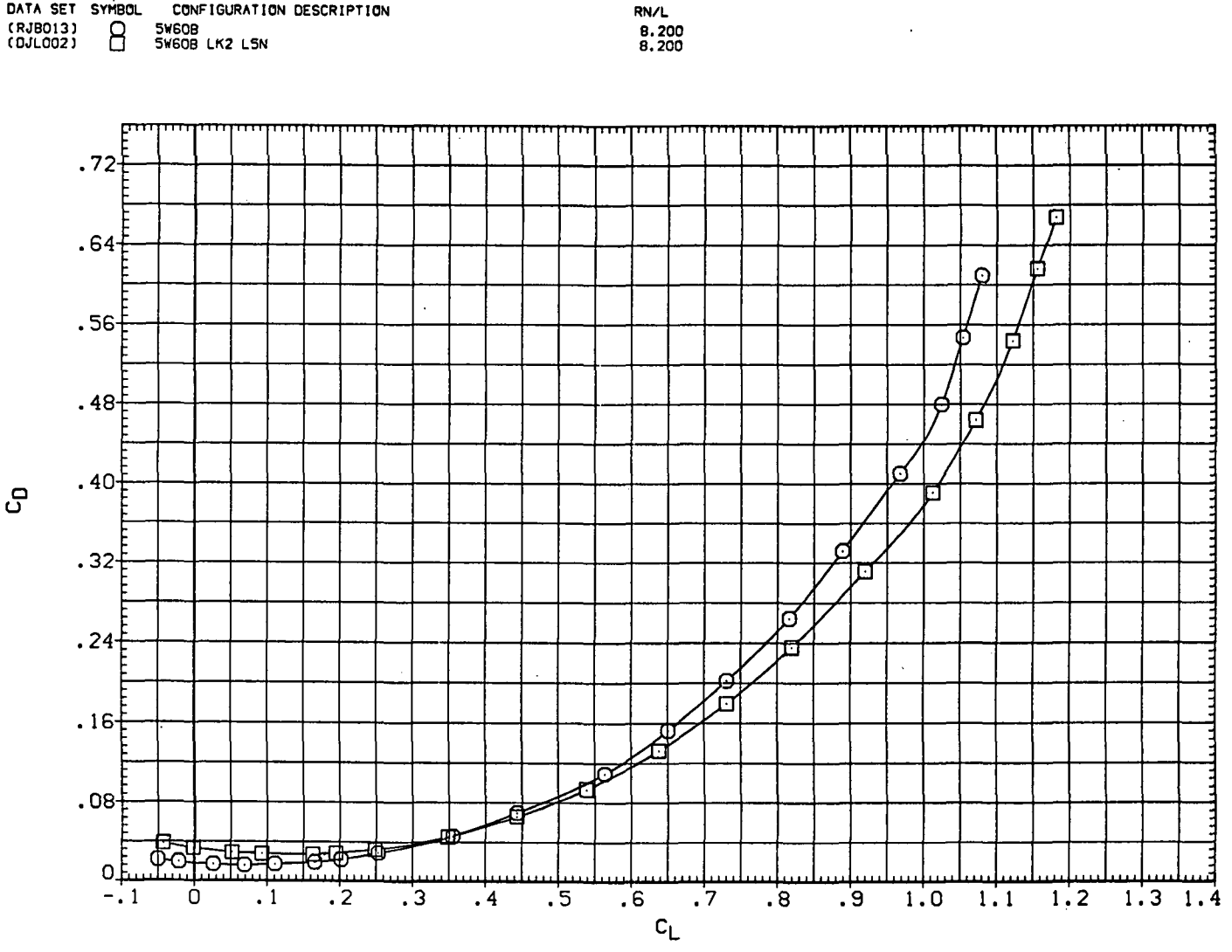

(b) C_D vs C_L

Figure 16.– Continued.

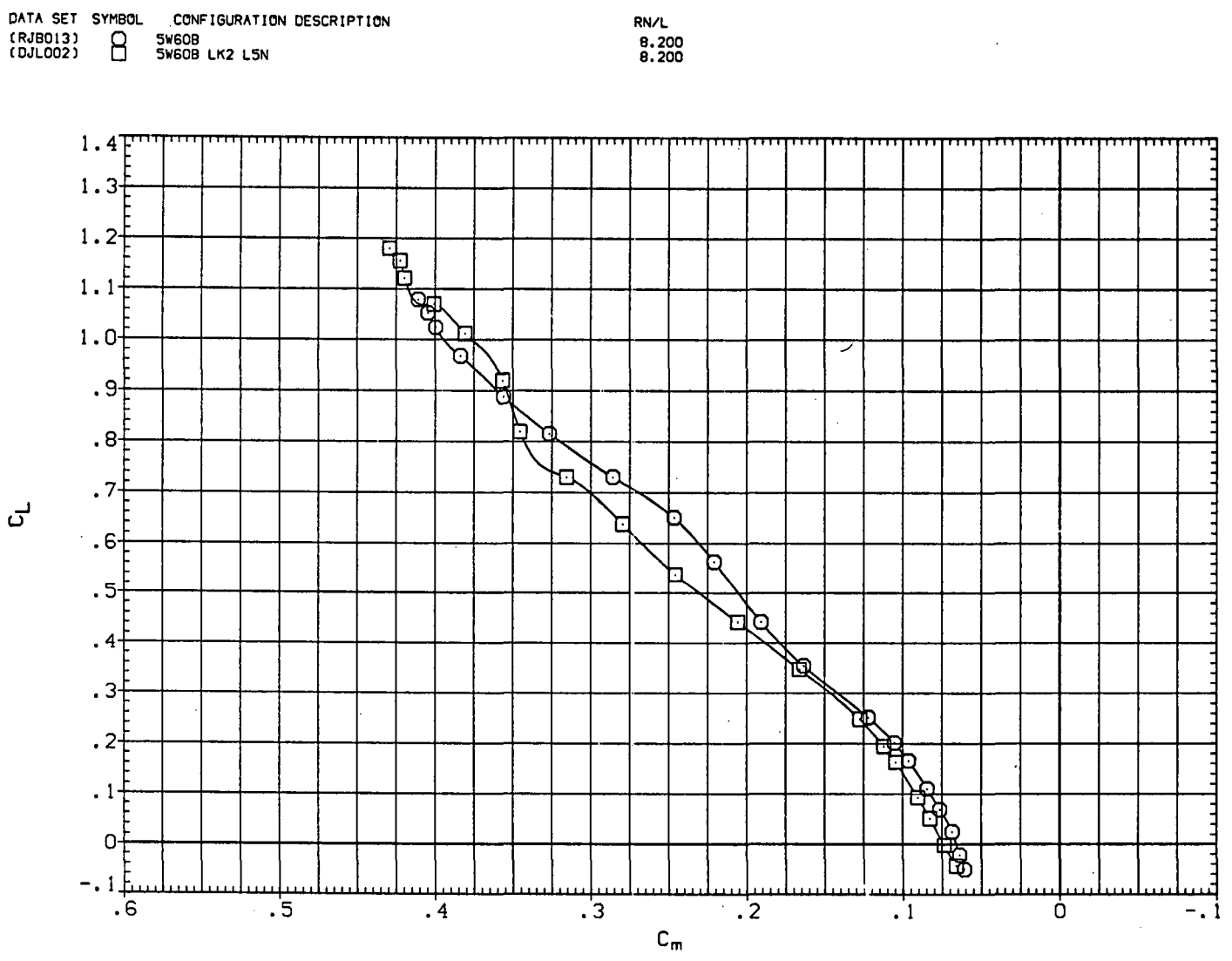

(c) C_L vs. C_m

Figure 16.– Continued.

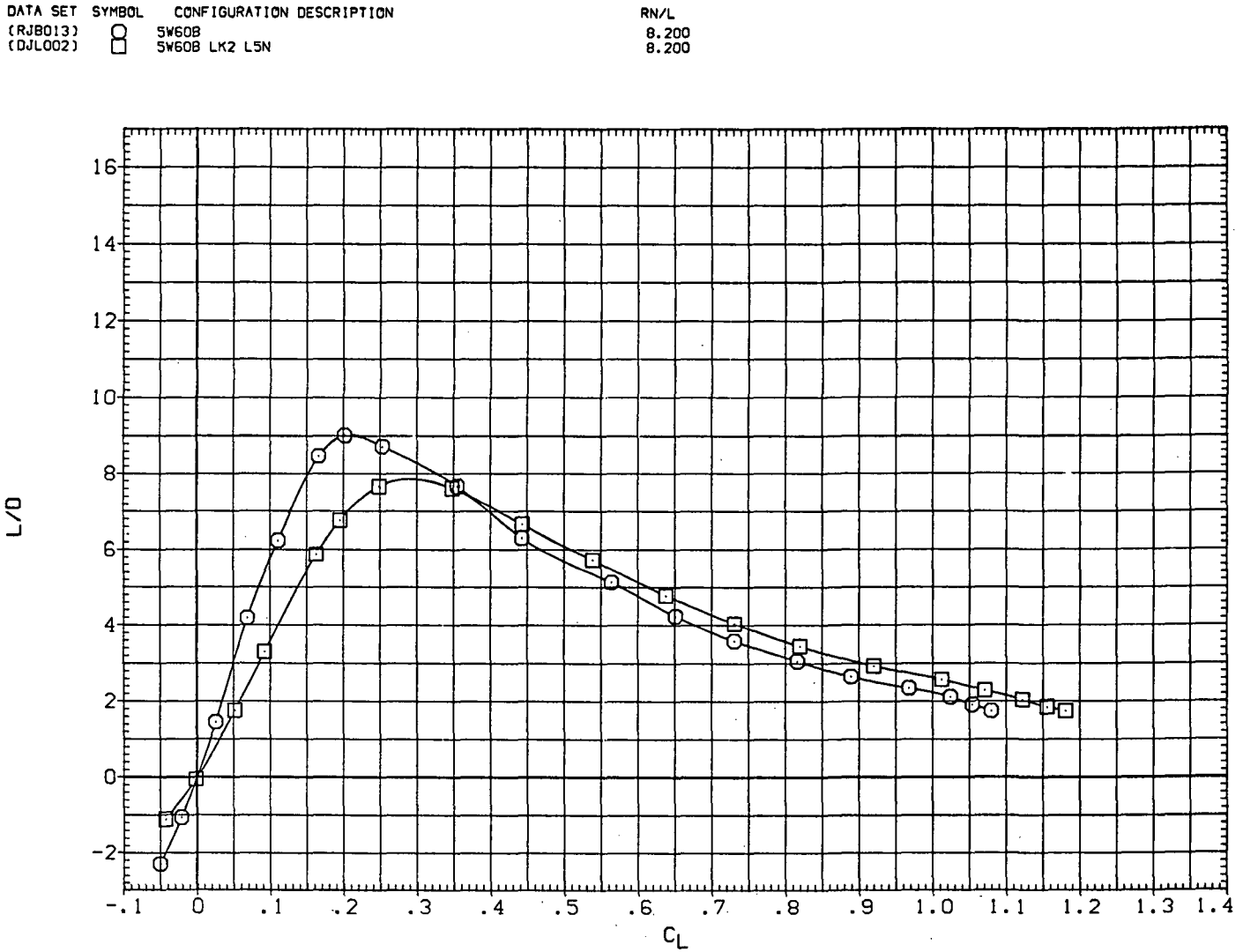

(d) L/D vs C_L

Figure 16.– Continued.

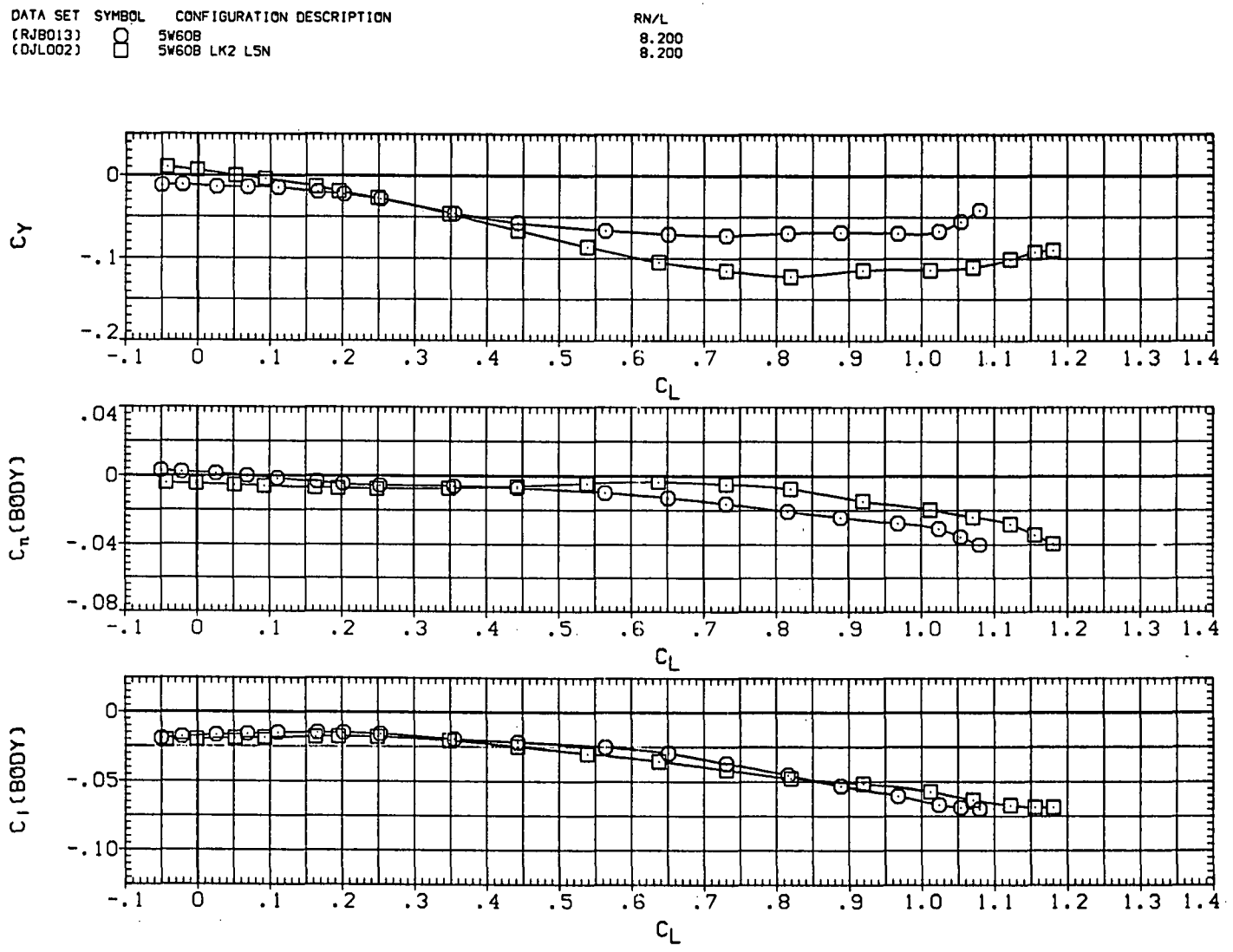

(e) C_Y, C_n, and C_l vs C_L

Figure 16.– Concluded.

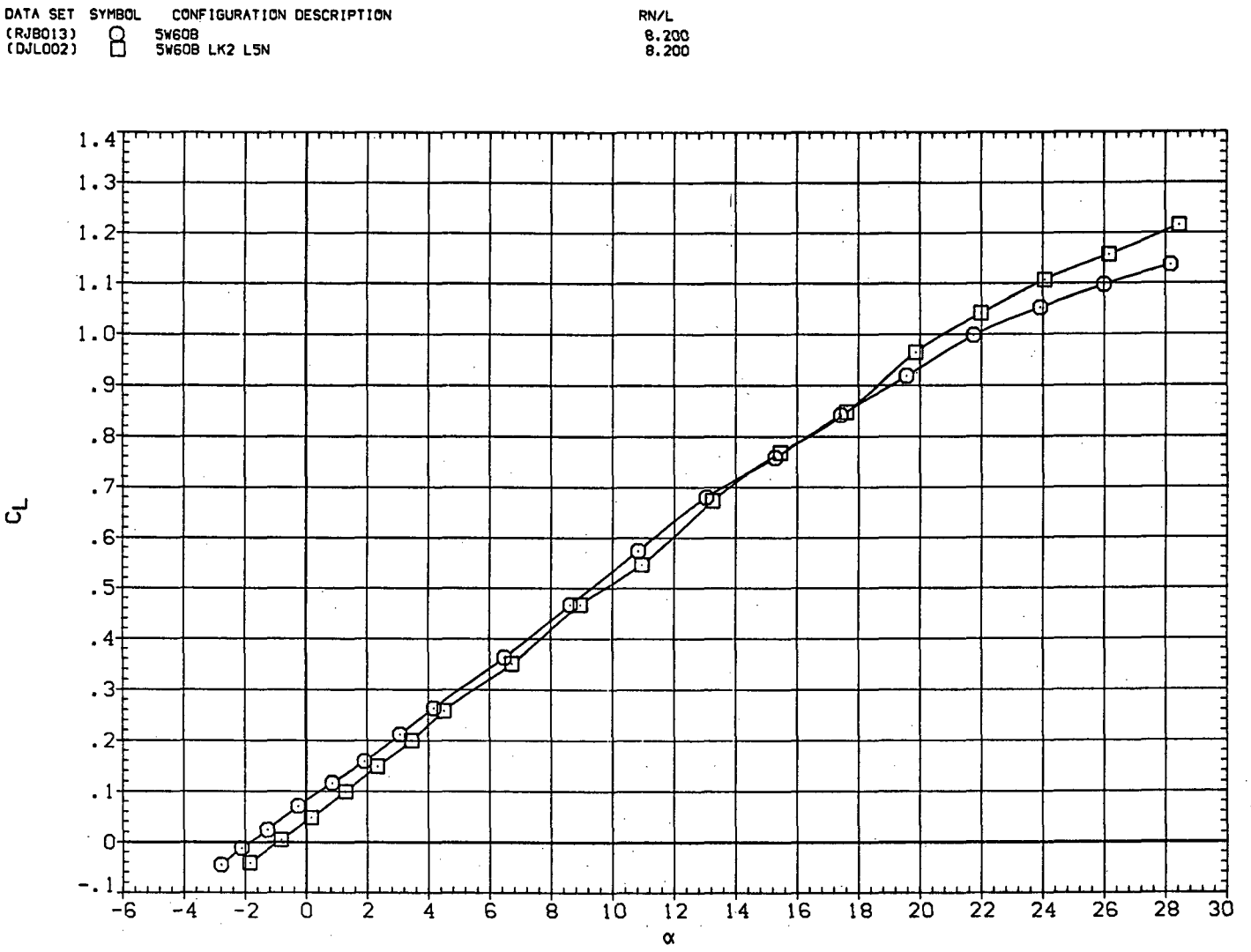

(a) C_L vs α

Figure 17.– Effect of Krüger nose flaps mounted on the drooped-nose flaps deflected 5°, downstream panel only: $\Lambda = 60°, M = 0.95$.

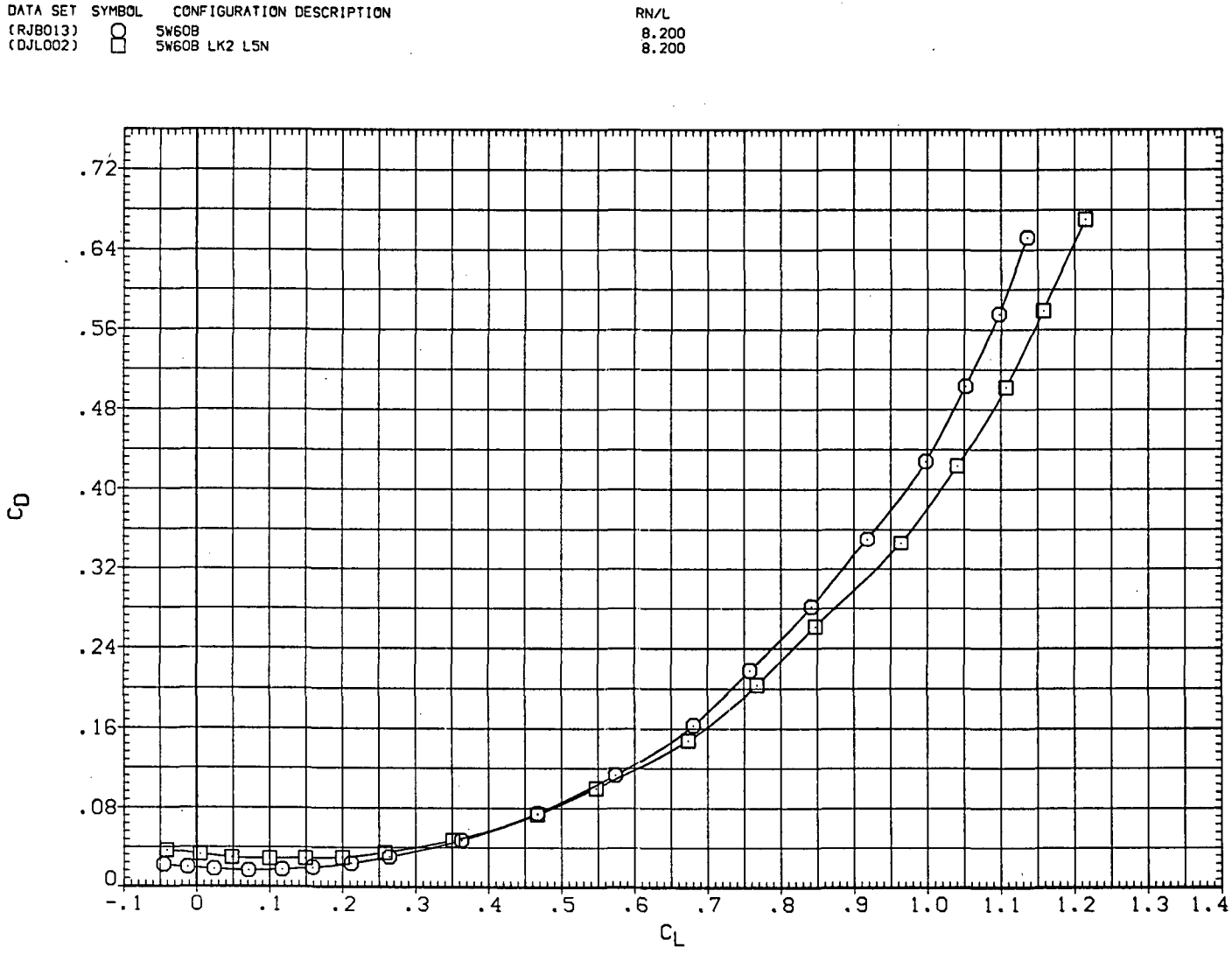

(b) C_D vs C_L

Figure 17.– Continued.

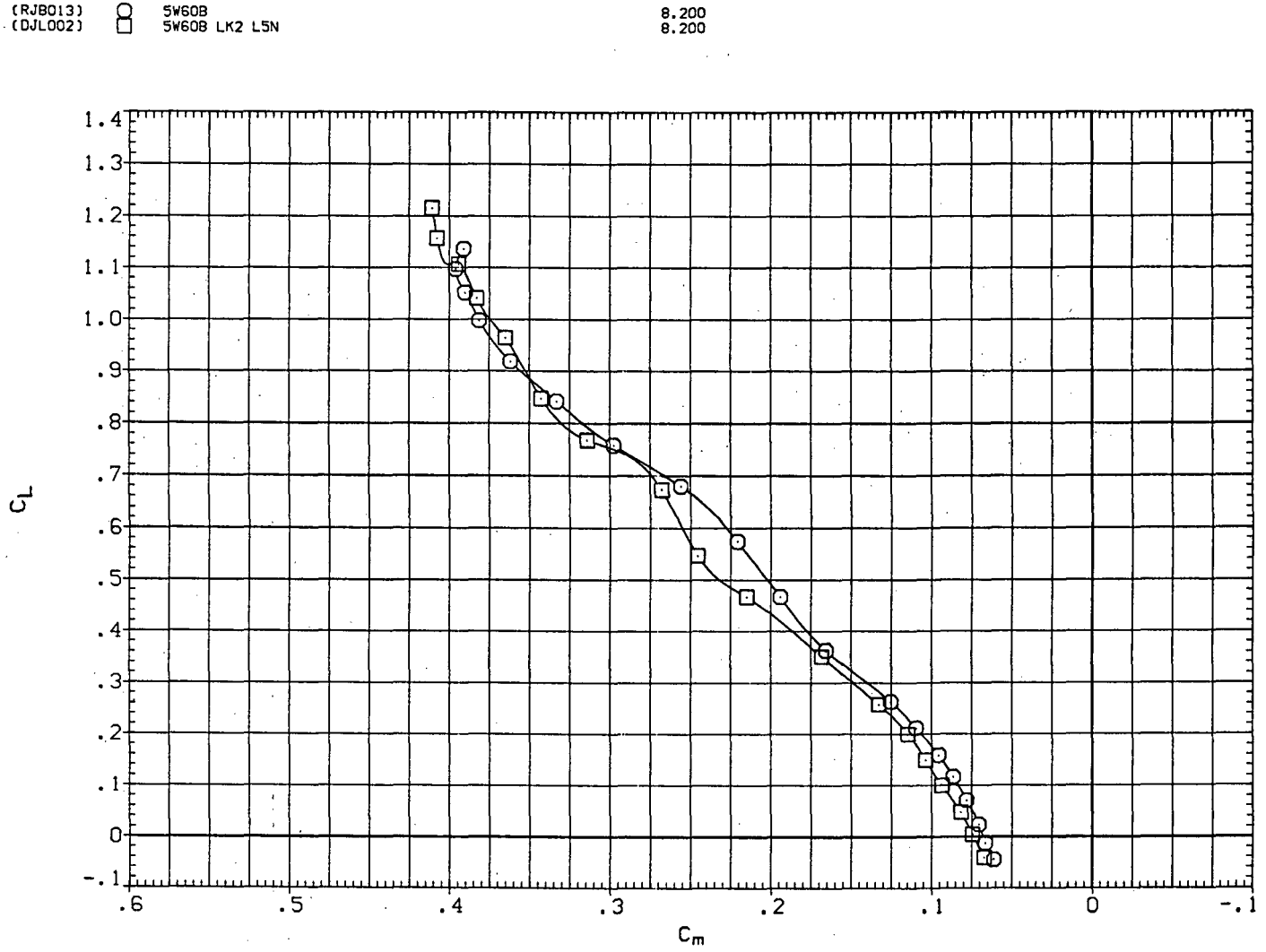

(c) C_L vs C_m

Figure 17.– Continued.

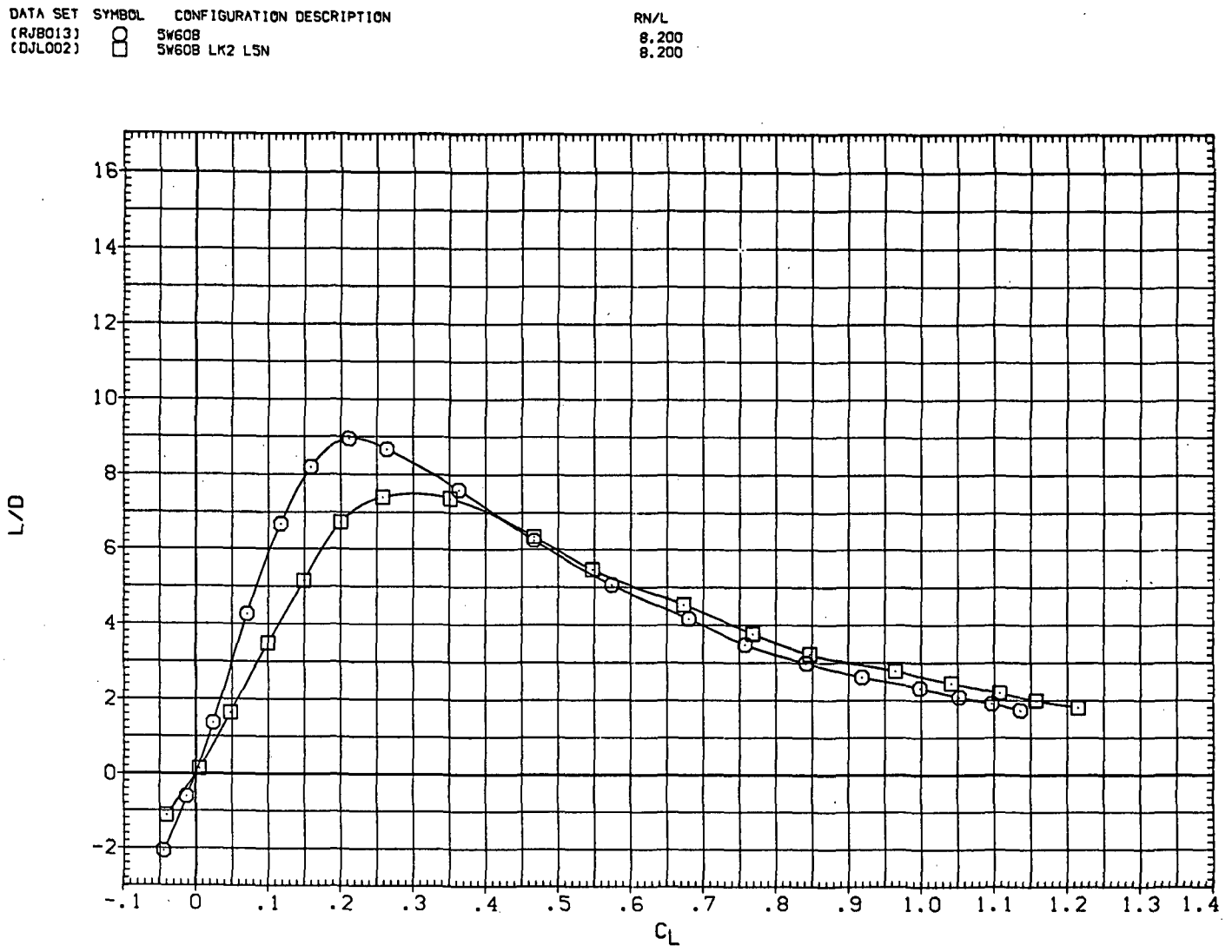

(d) L/D vs C_L

Figure 17.– Continued.

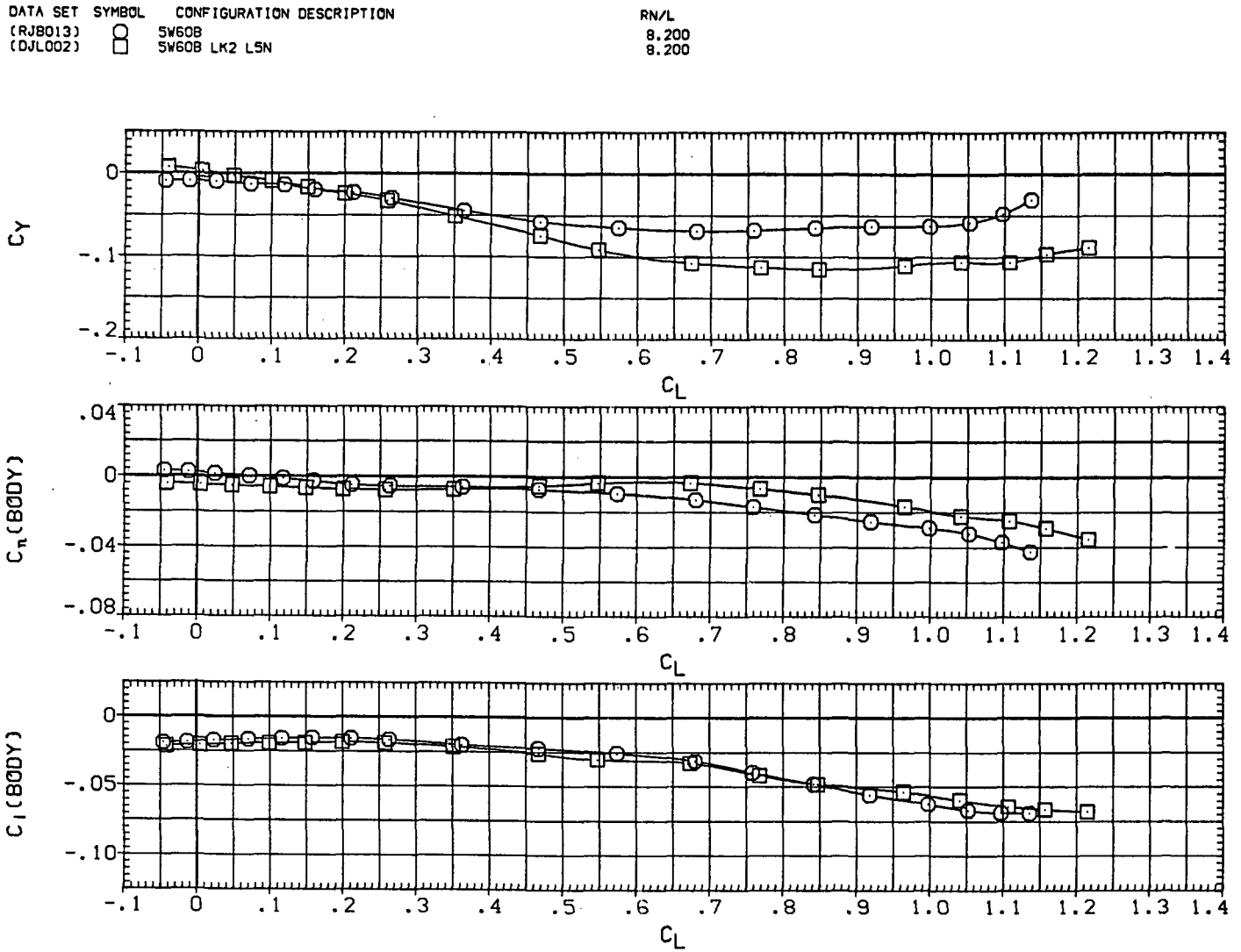

(e) C_Y, C_n, and C_l vs C_L

Figure 17.– Concluded.

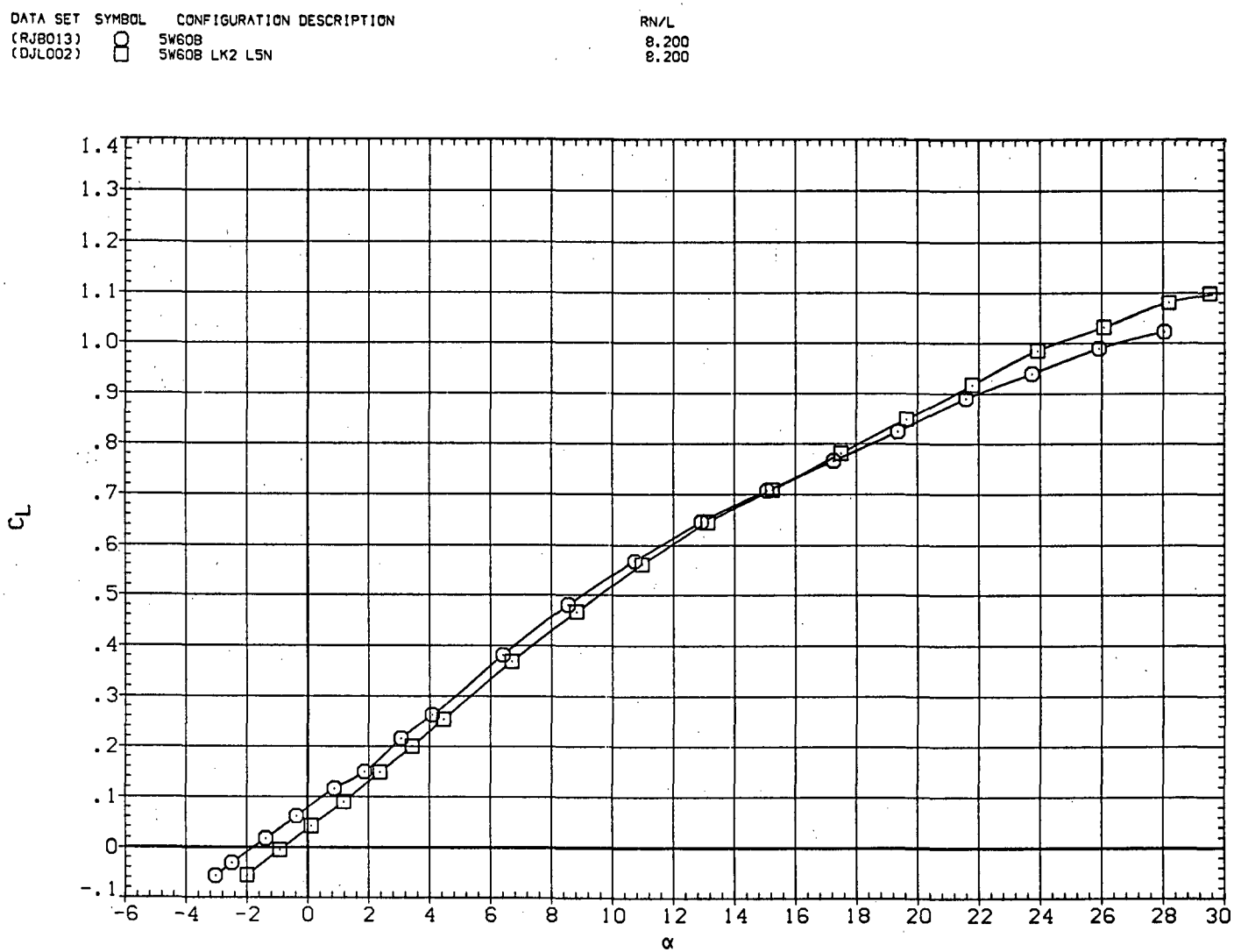

(a) C_L vs α

Figure 18.– Effect of Krüger nose flaps mounted on the drooped-nose flaps deflected 5°, downstream panel only: $\Lambda = 60°, M = 1.4$.

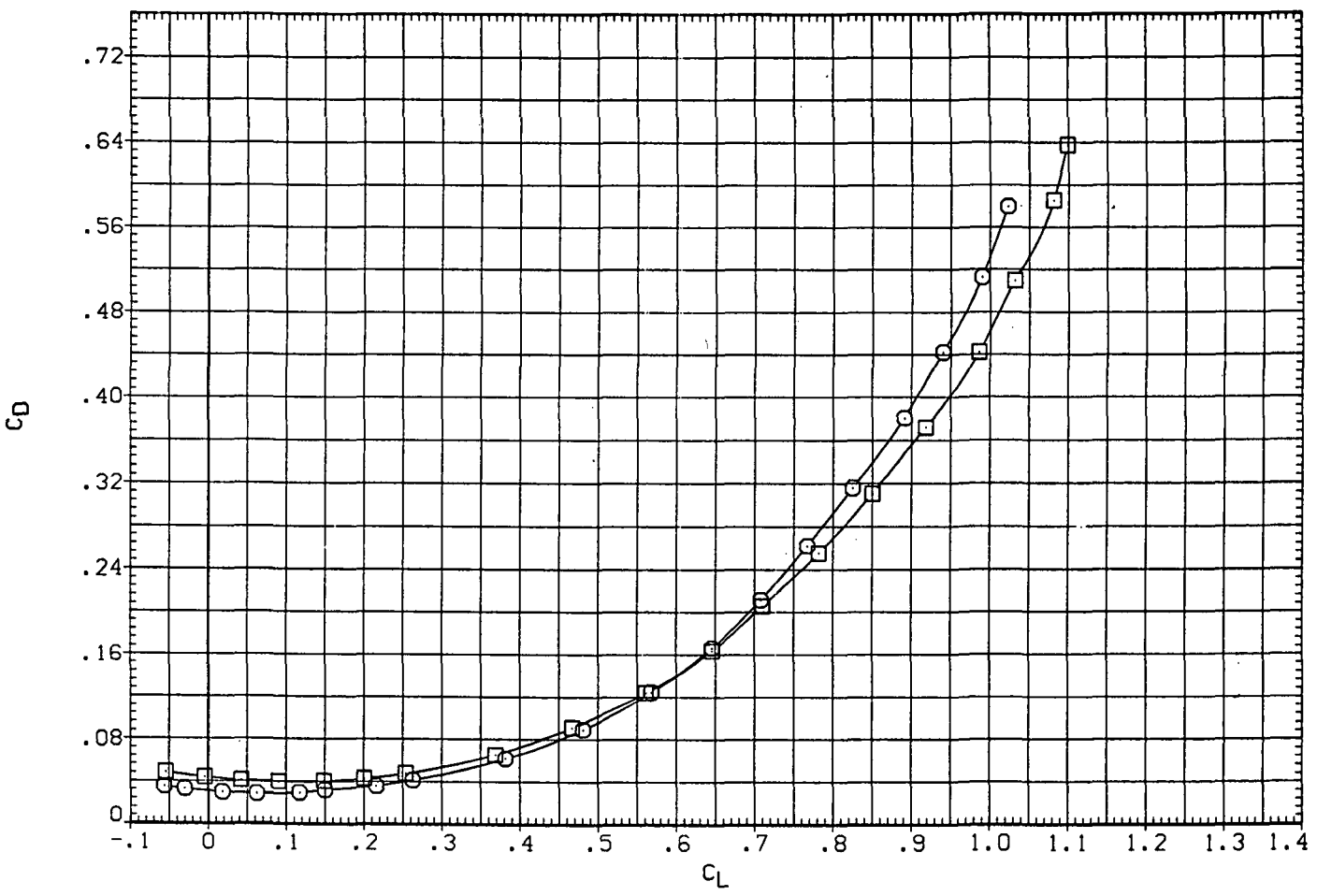

(b) C_D vs C_L

Figure 18.– Continued.

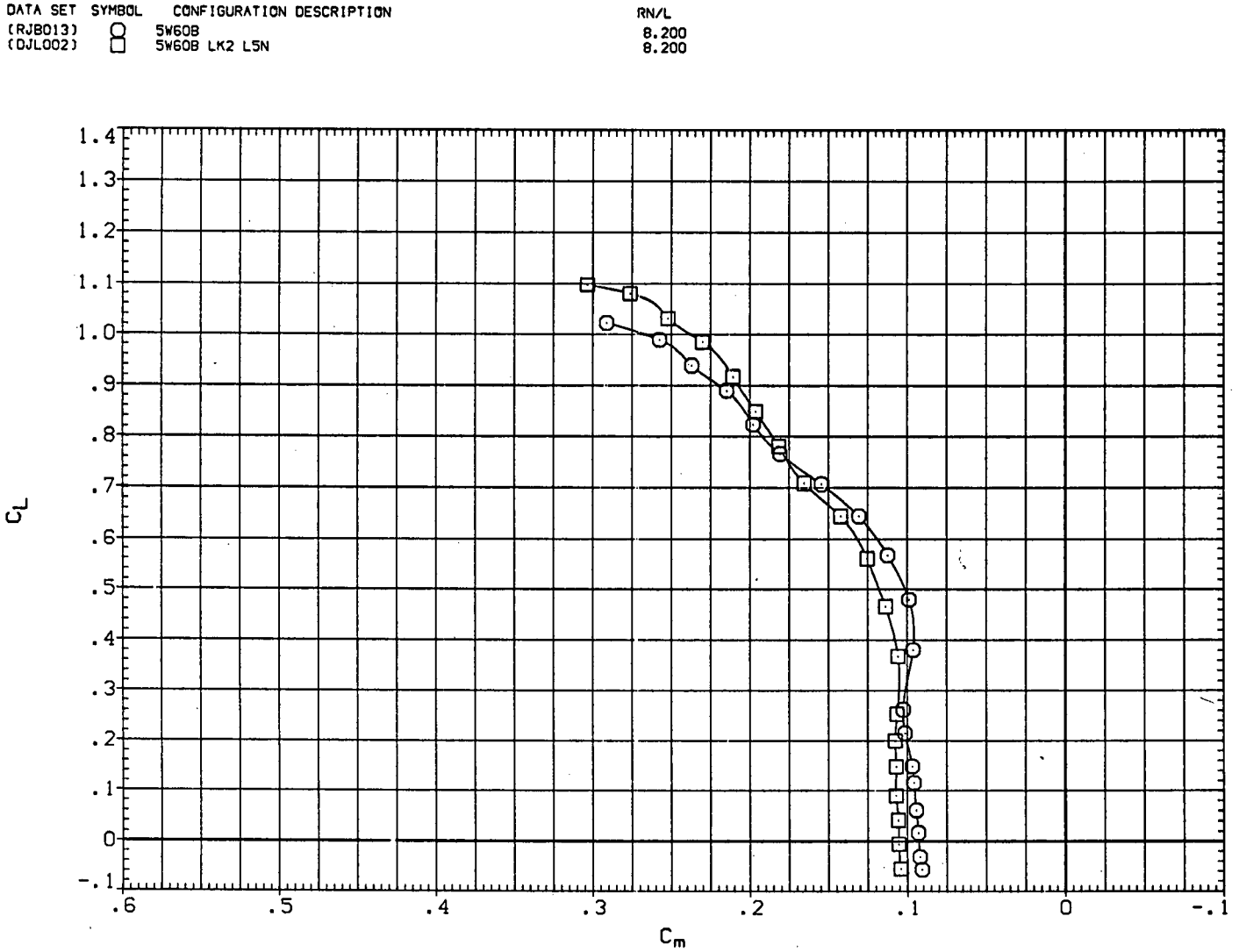

(c) C_L vs C_m

Figure 18.– Continued.

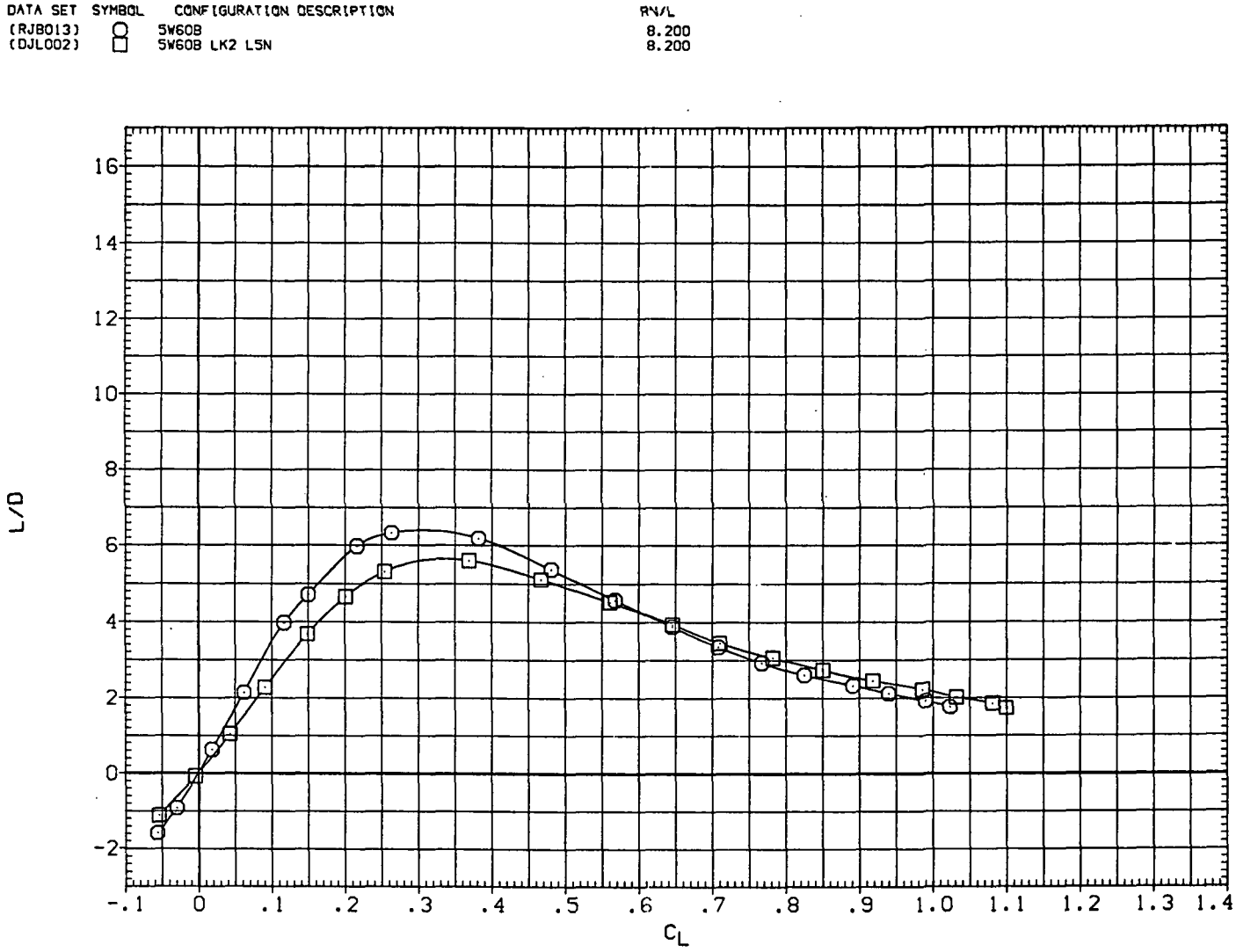

(d) L/D vs C_L

Figure 18.– Continued.

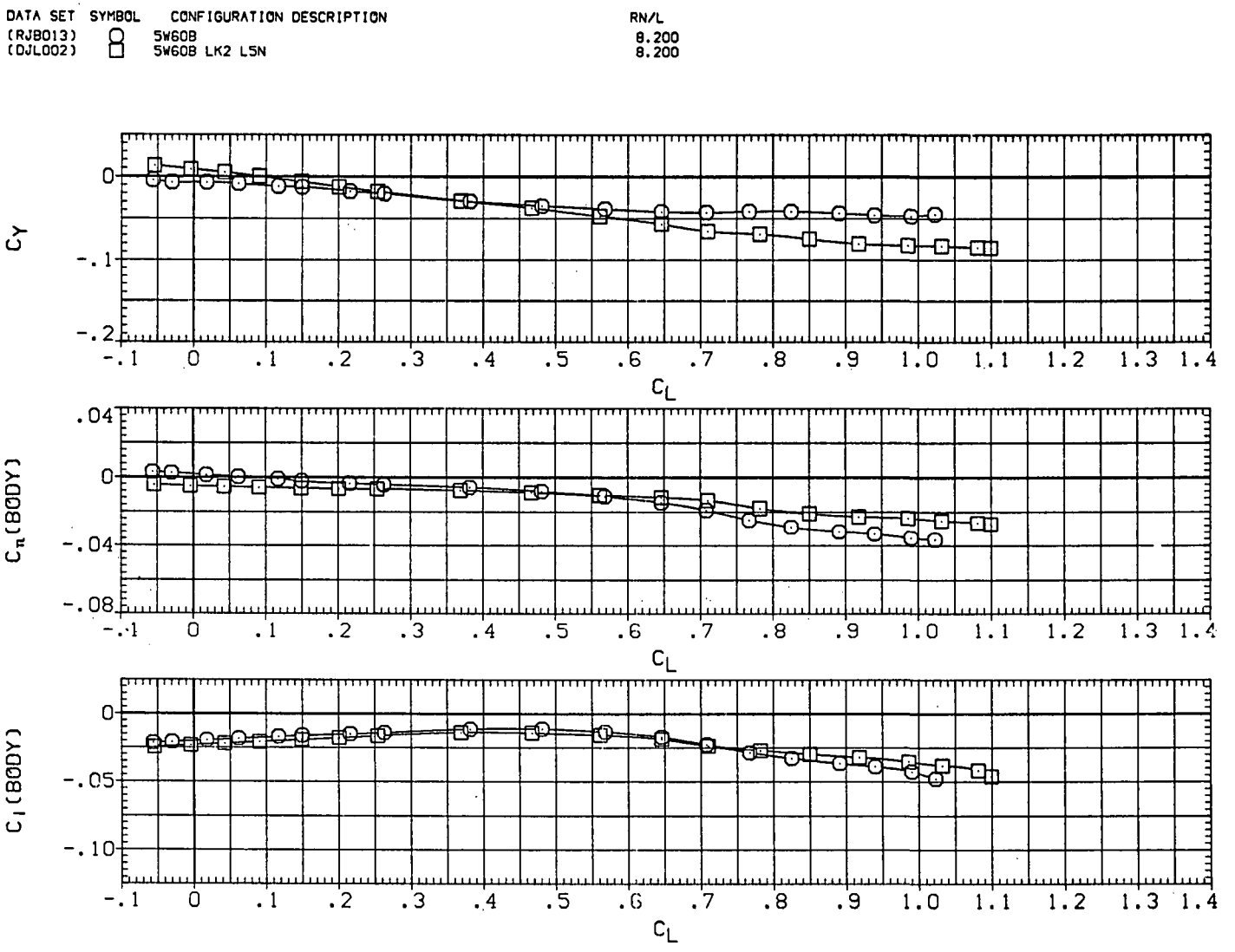

(e) C_Y, C_n, and C_l vs C_L

Figure 18.– Concluded.

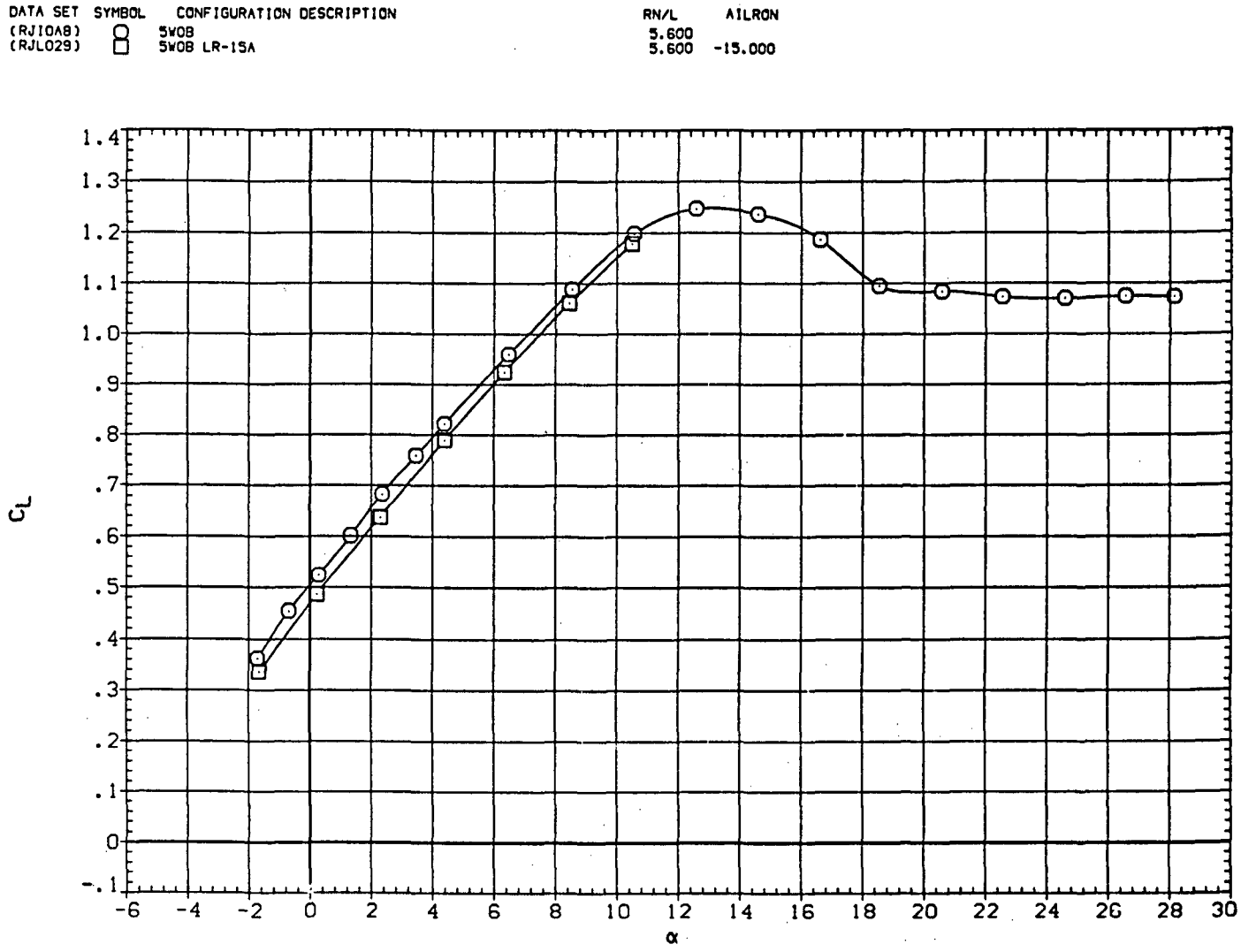

(a) C_L vs α

Figure 19.– Aileron effectiveness on the oblique wing with intermediate bend: $\Lambda = 0, M = 0.25$.

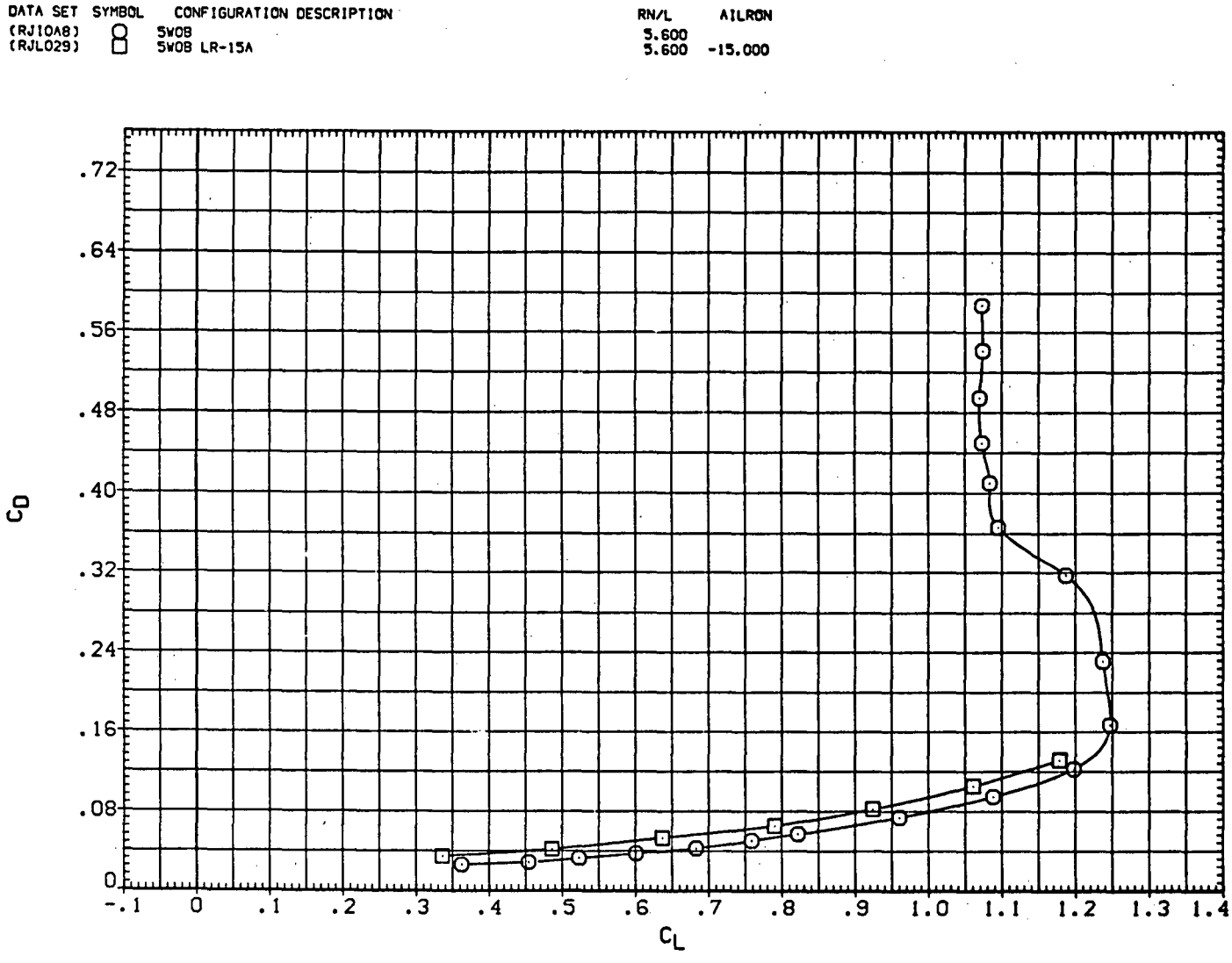

(b) C_D vs C_L

Figure 19.– Continued.

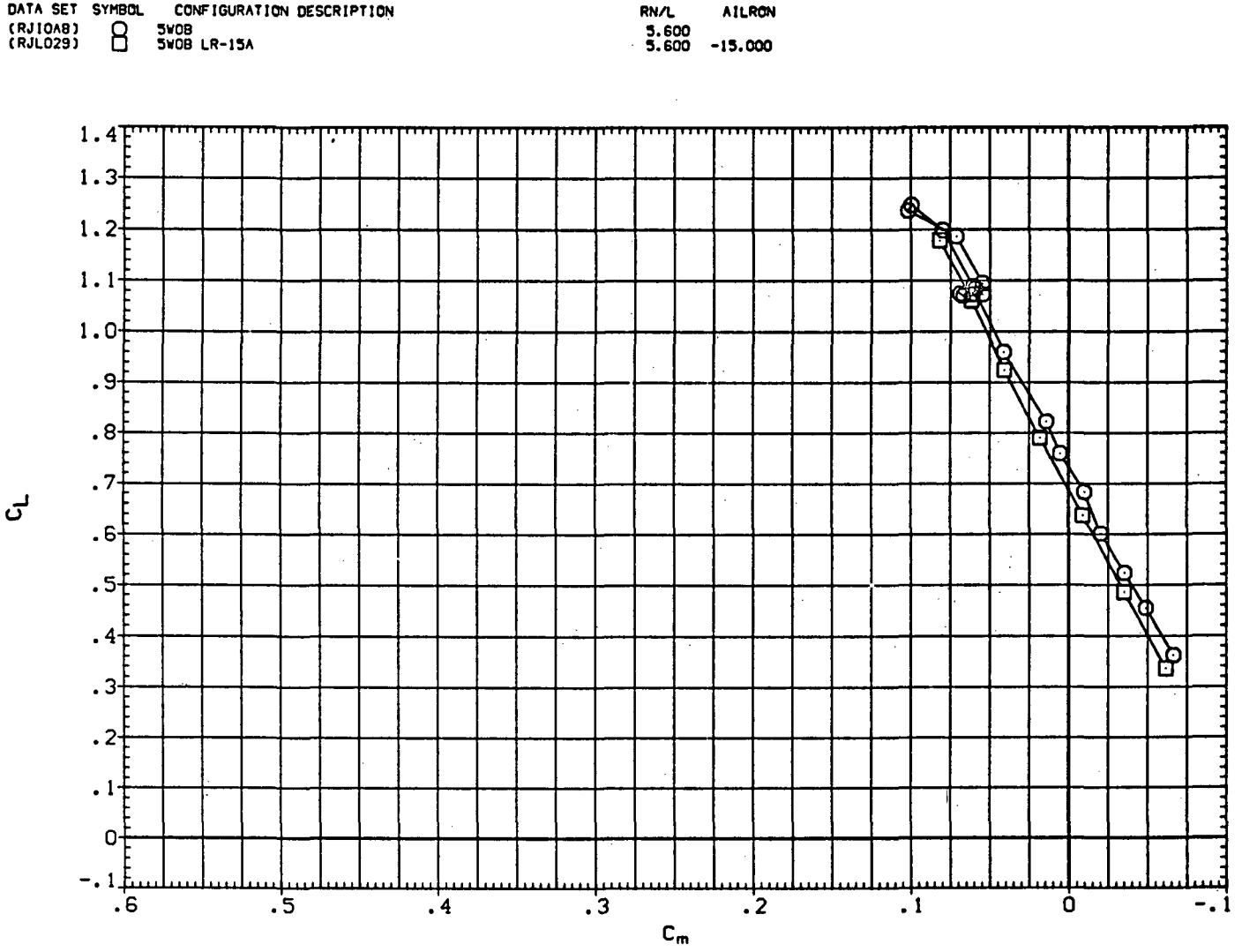

(c) C_L vs C_m

Figure 19.– Continued.

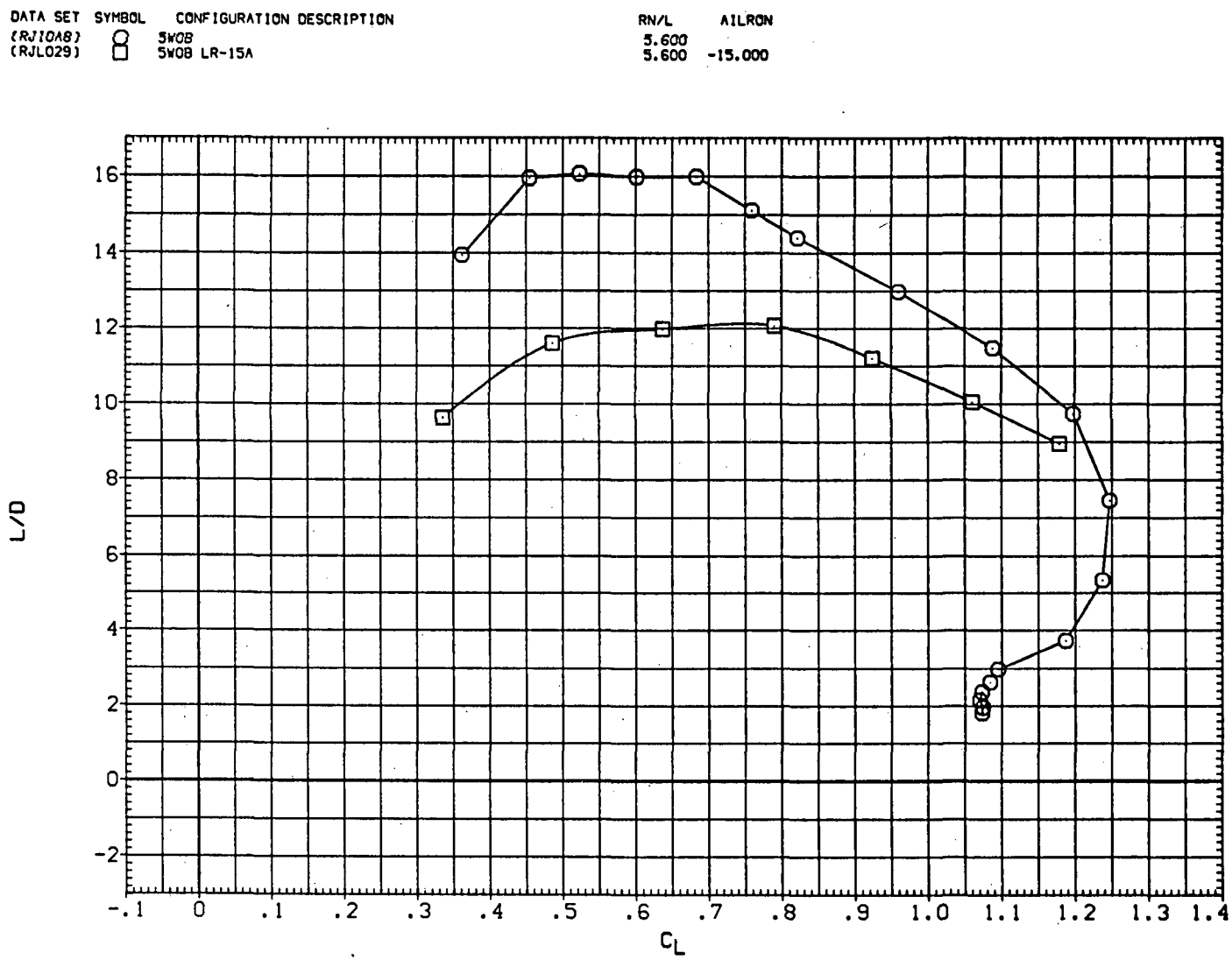

(d) L/D vs. C_L

Figure 19.– Continued.

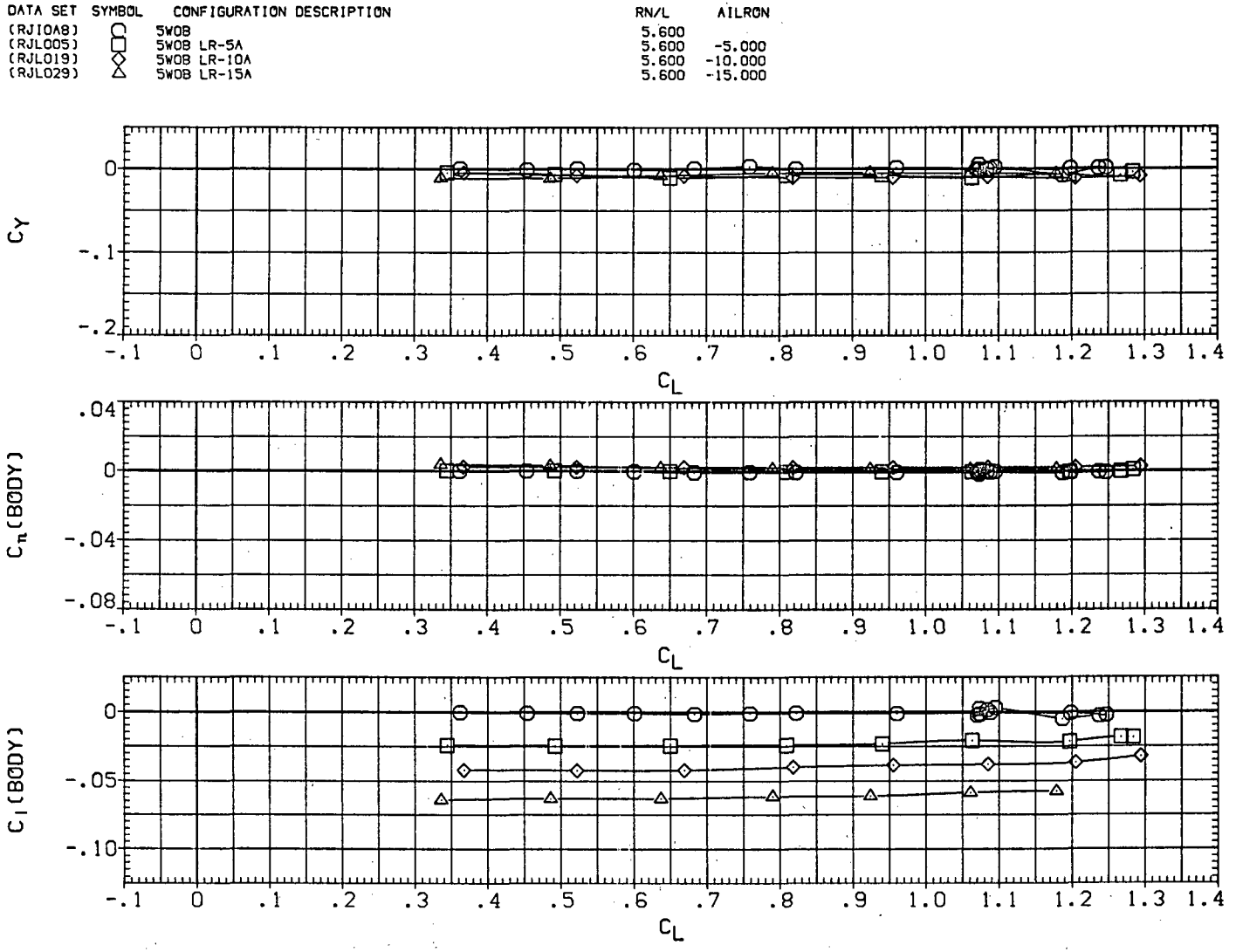

(e) C_Y, C_n, and C_l vs C_L

Figure 19.– Concluded.

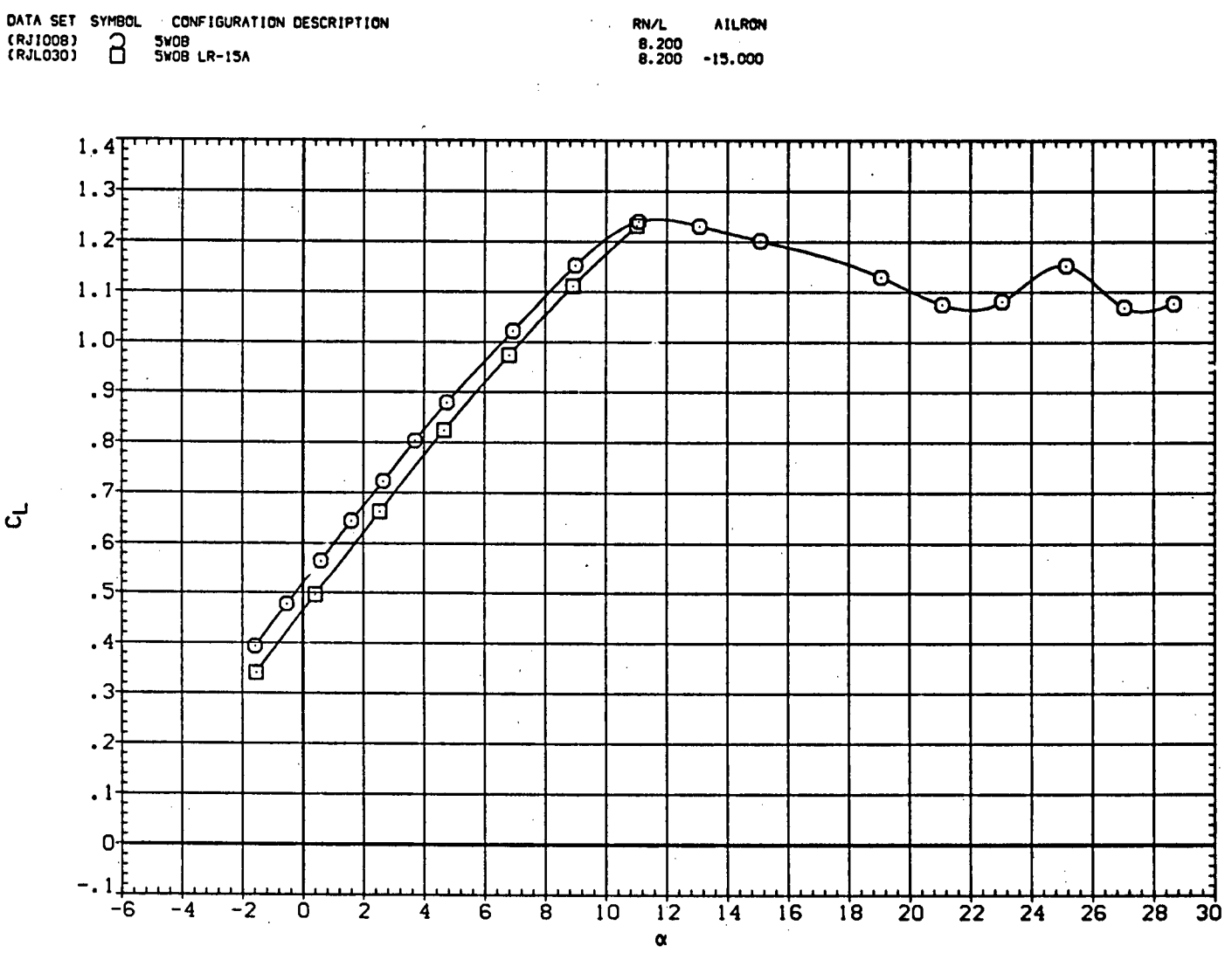

(a) C_L vs α

Figure 20.– Aileron effectiveness on the oblique wing with intermediate bend: $\Lambda = 0, M = 0.40$.

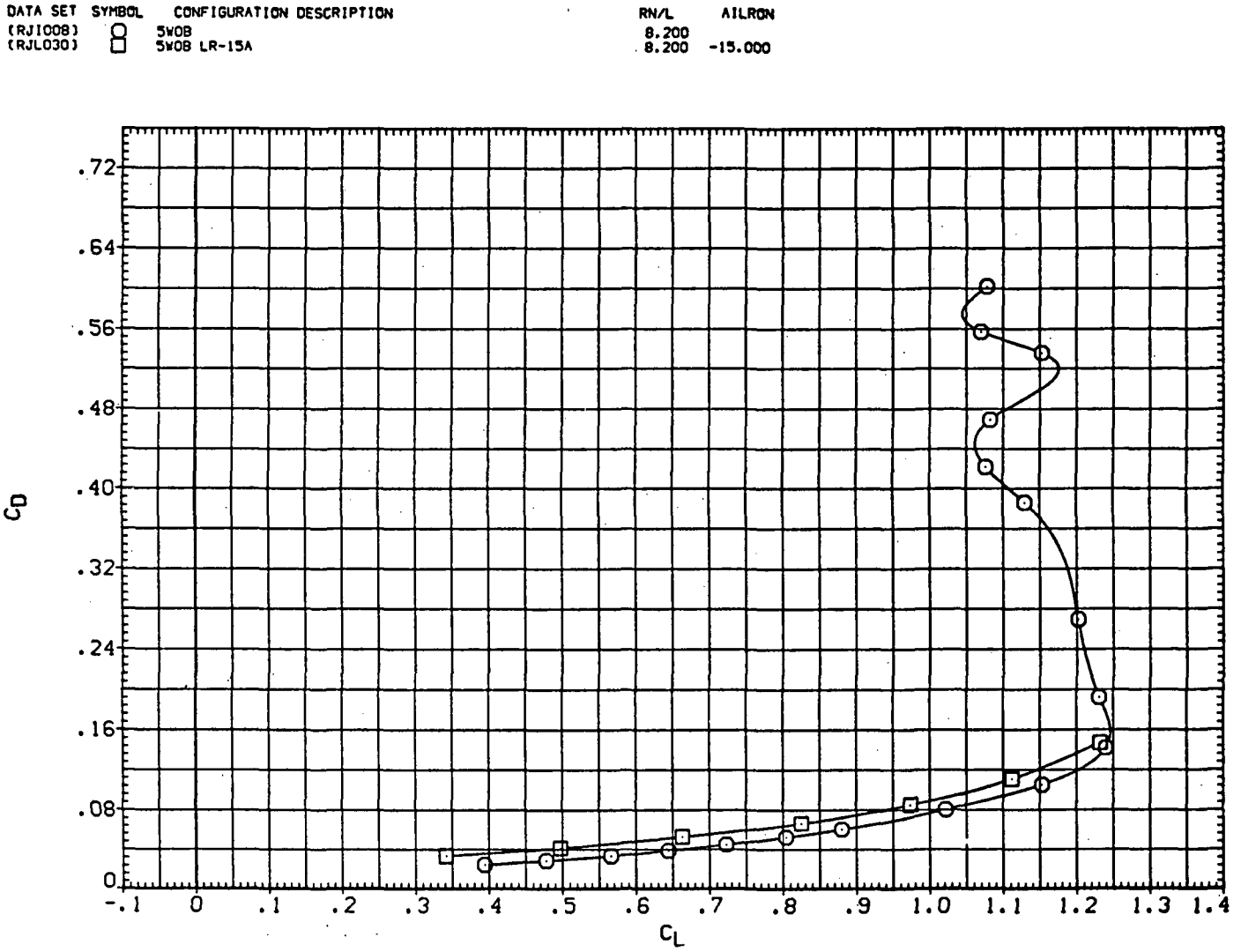

(b) C_D vs C_L

Figure 20.– Continued.

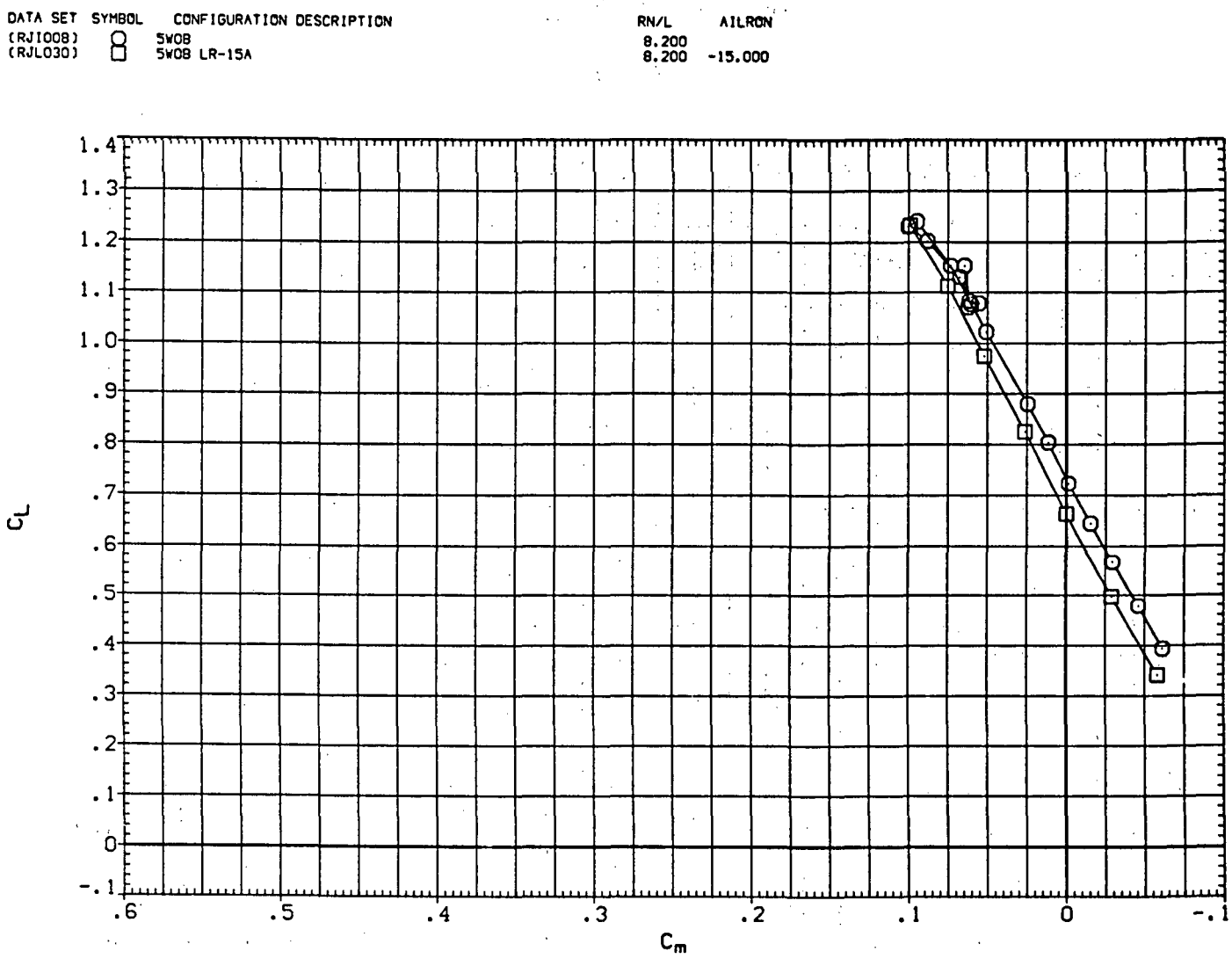

(c) C_L vs C_m

Figure 20.– Continued.

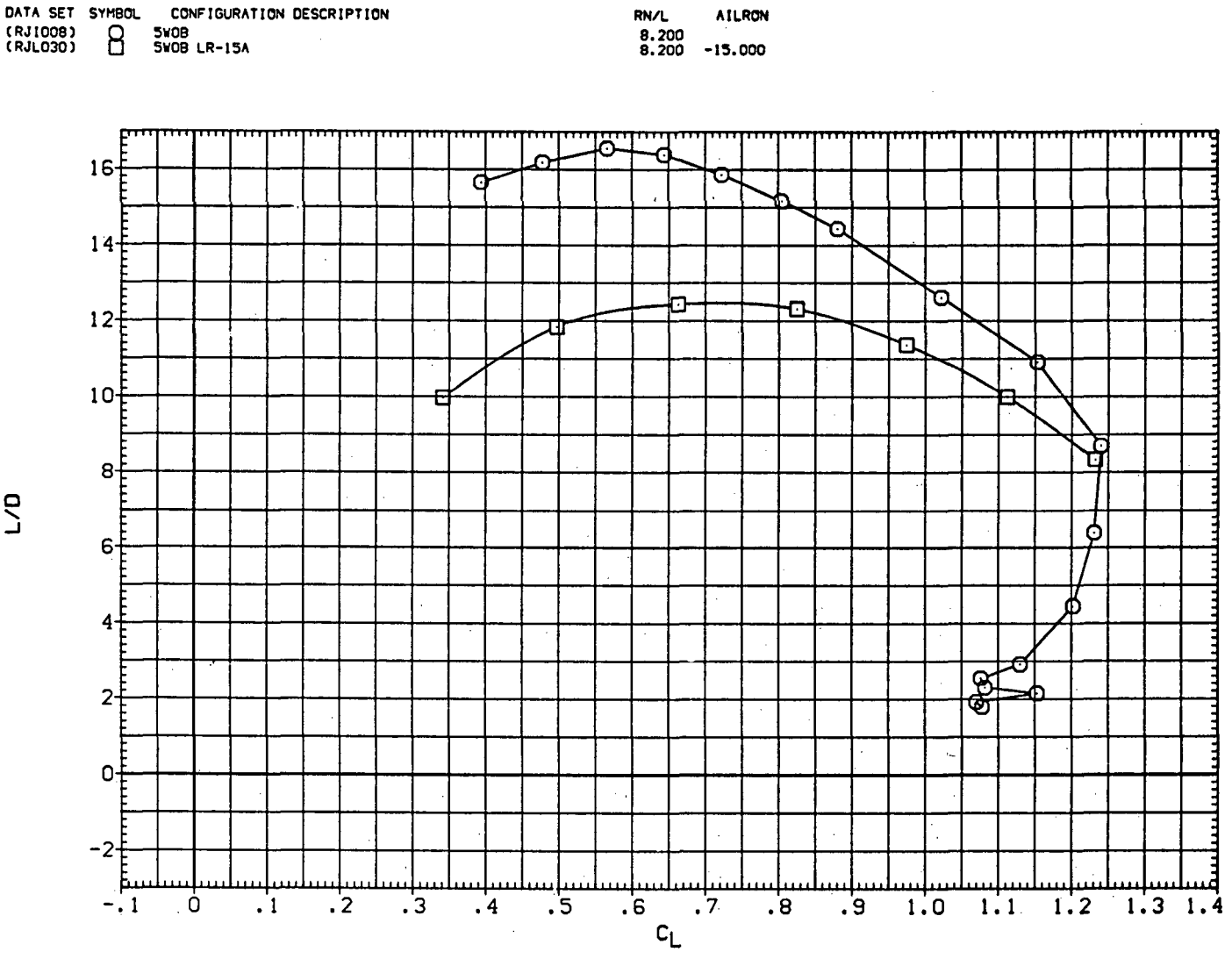

(d) L/D vs C_L

Figure 20.– Continued.

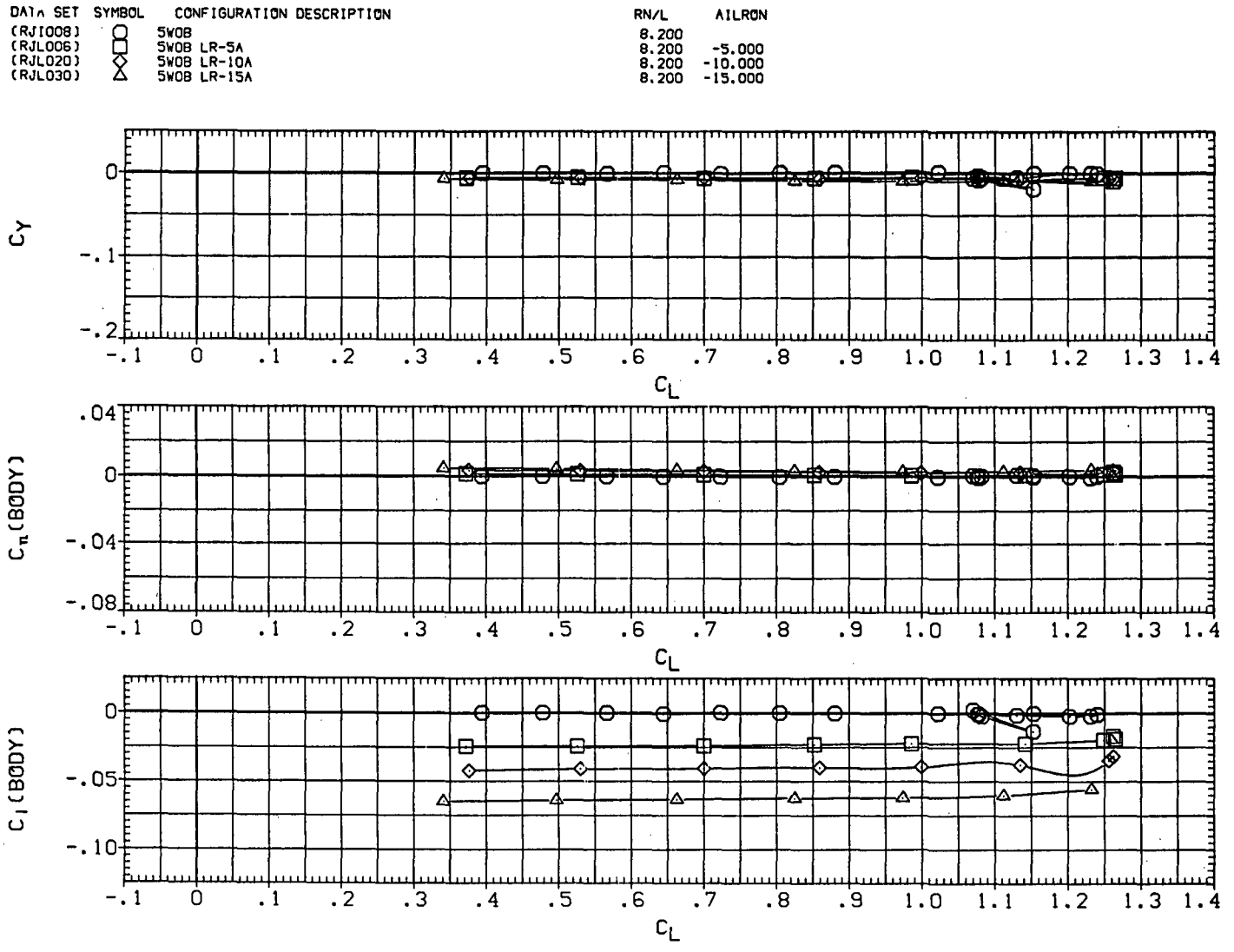

(e) C_Y, C_n, and C_l vs C_L

Figure 20.– Concluded.

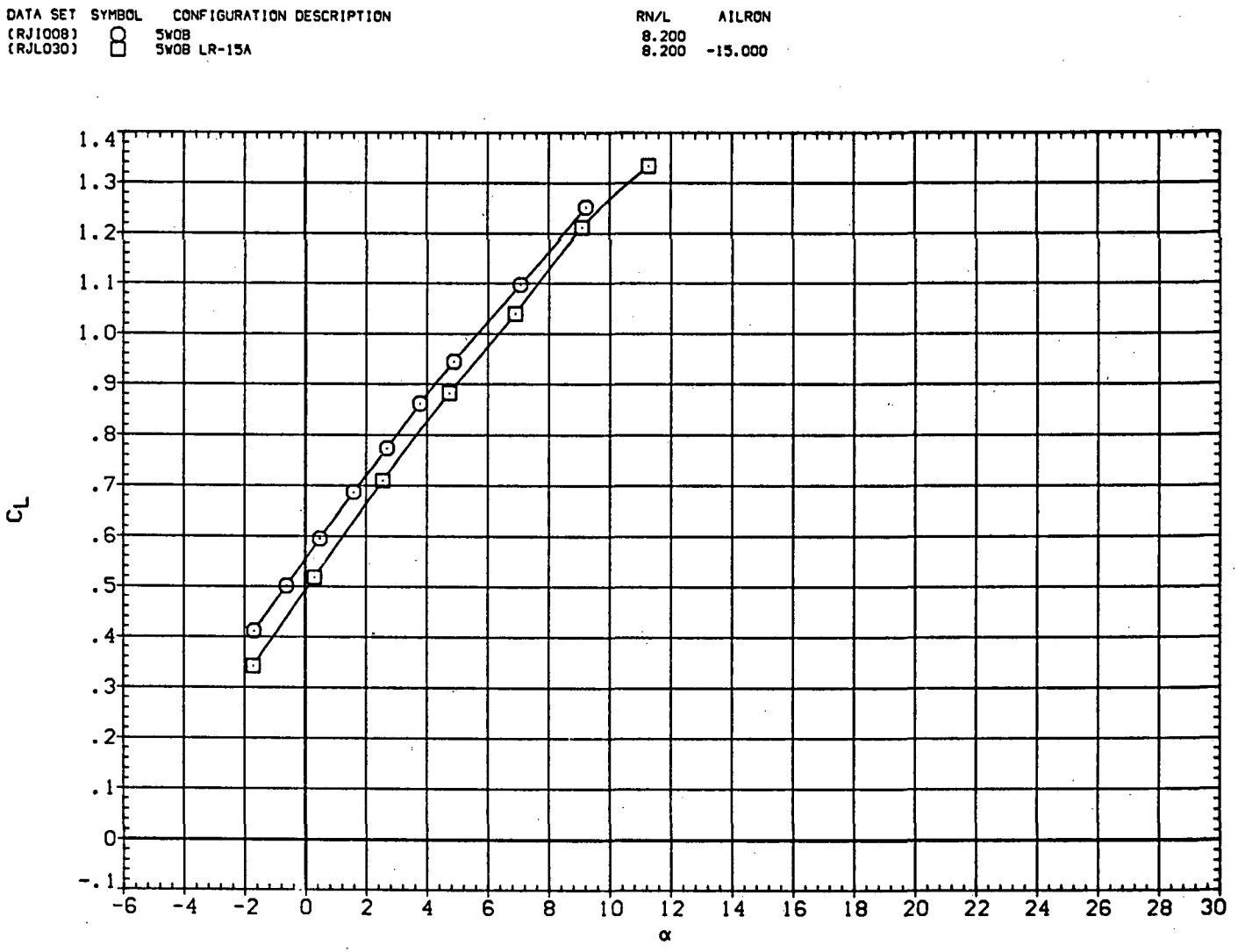

(a) C_L vs α

Figure 21.– Aileron effectiveness on the oblique wing with intermediate bend: $\Lambda = 0, M = 0.60$.

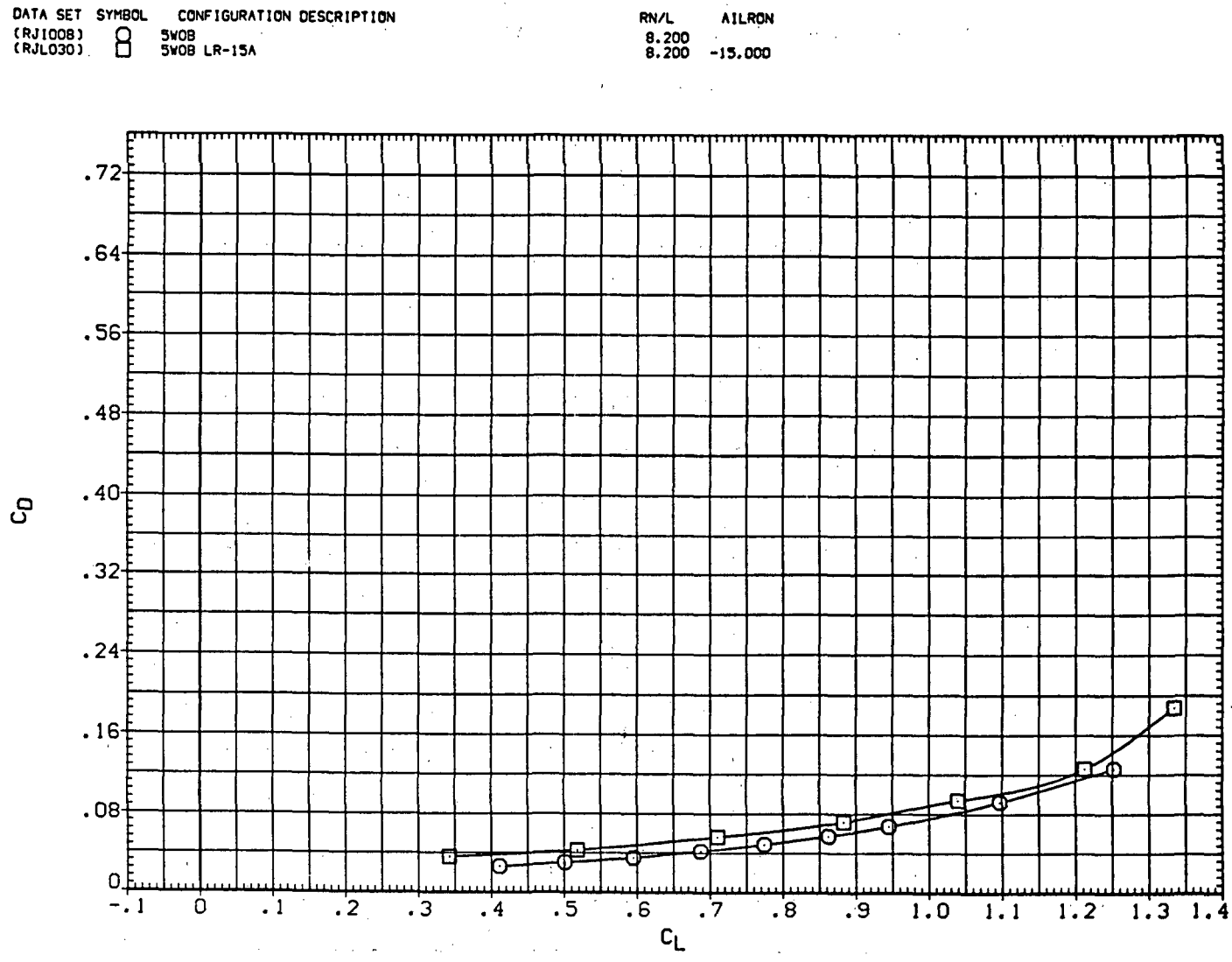

(b) C_D vs C_L

Figure 21.– Continued.

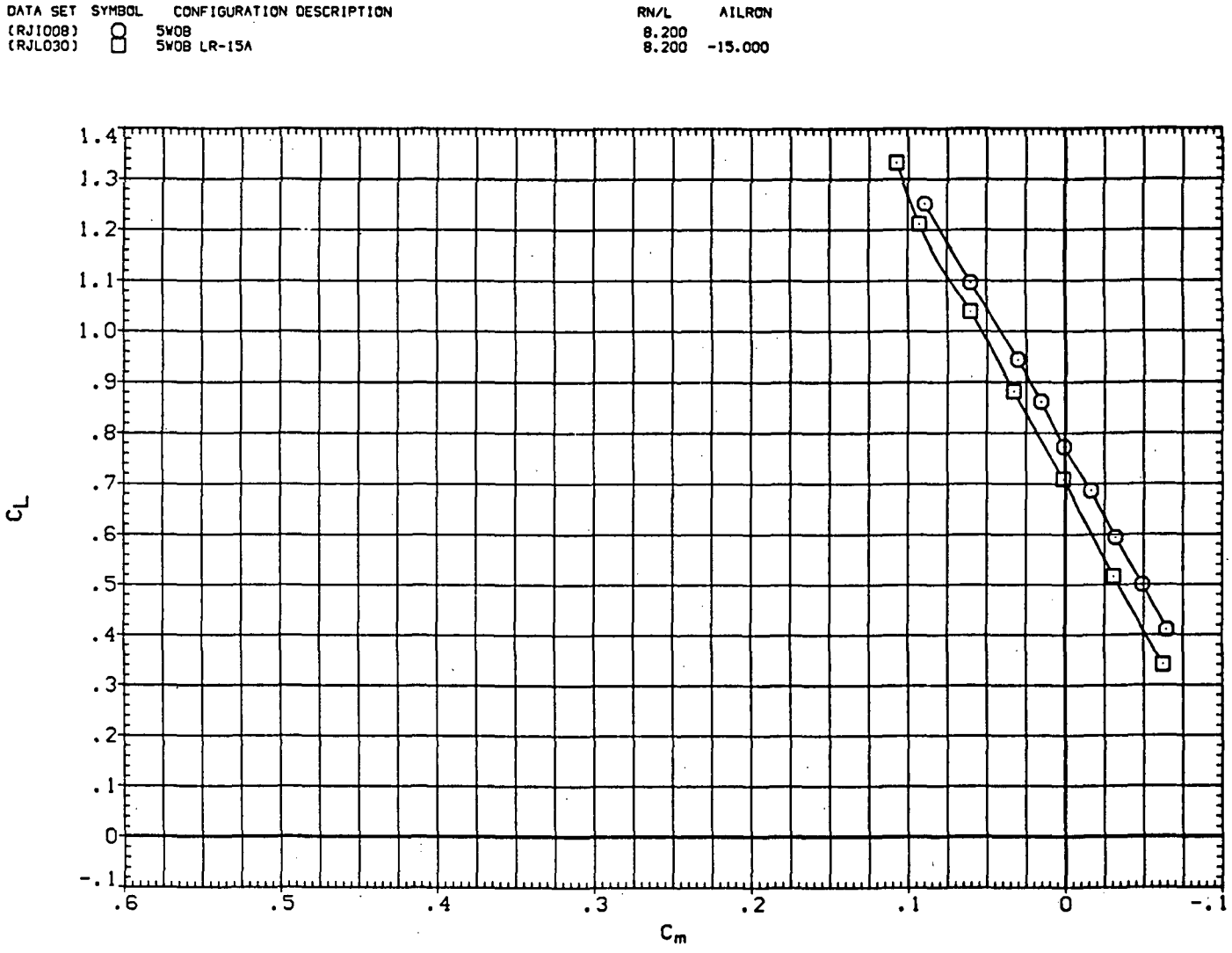

(c) C_L vs. C_m

Figure 21.– Continued.

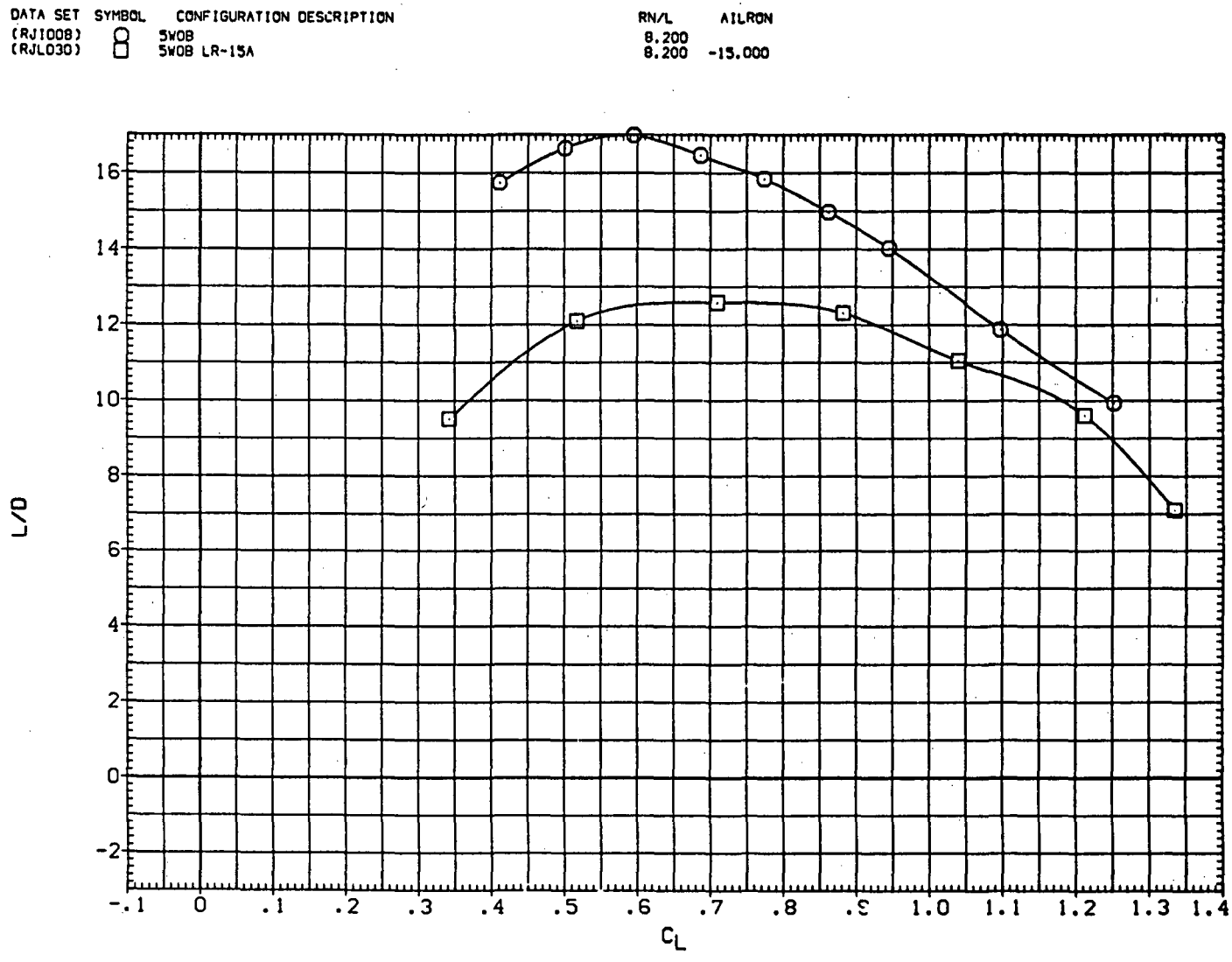

(d) L/D vs C_L

Figure 21.– Continued.

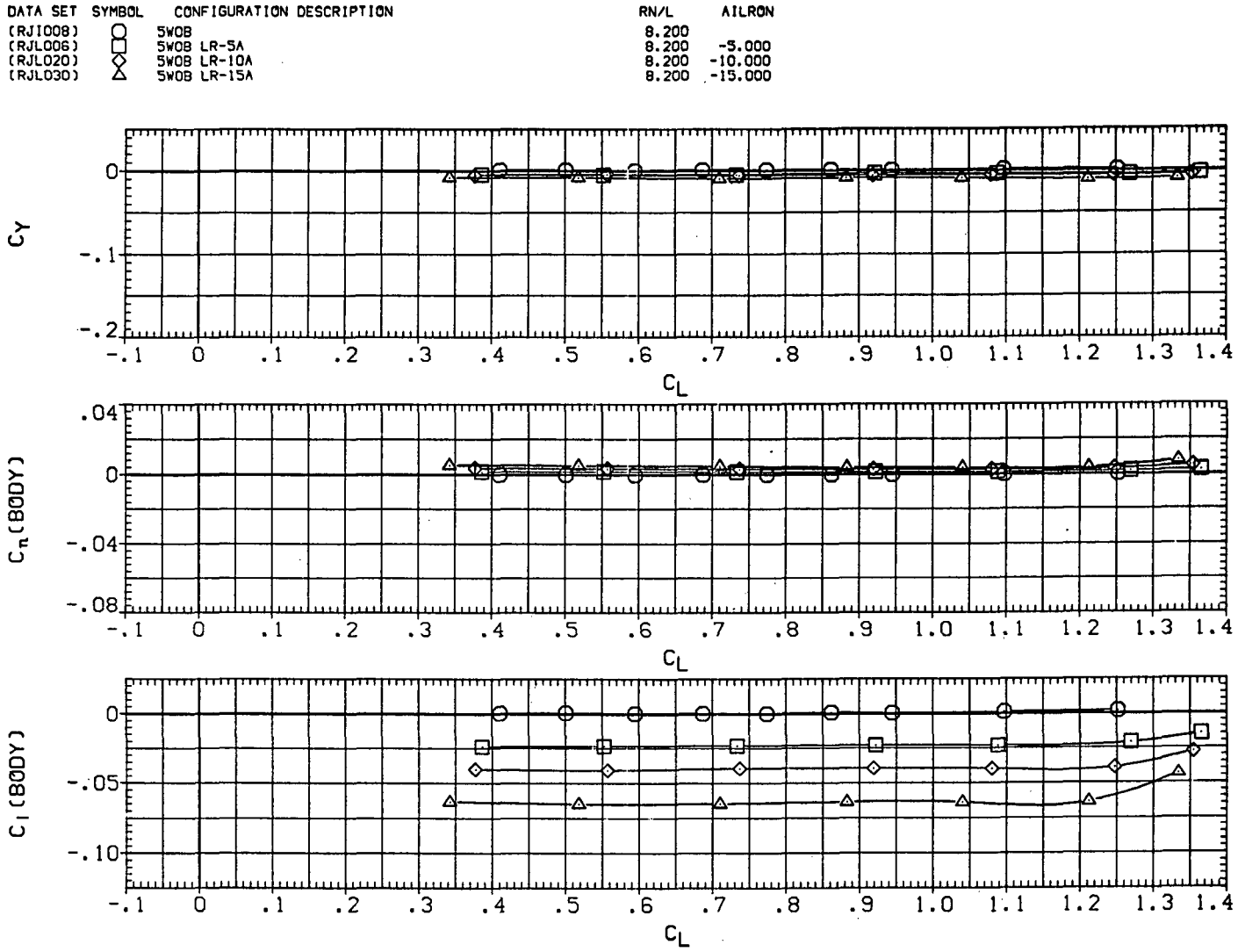

(e) C_Y, C_n, and C_l vs C_L

Figure 21.– Concluded.

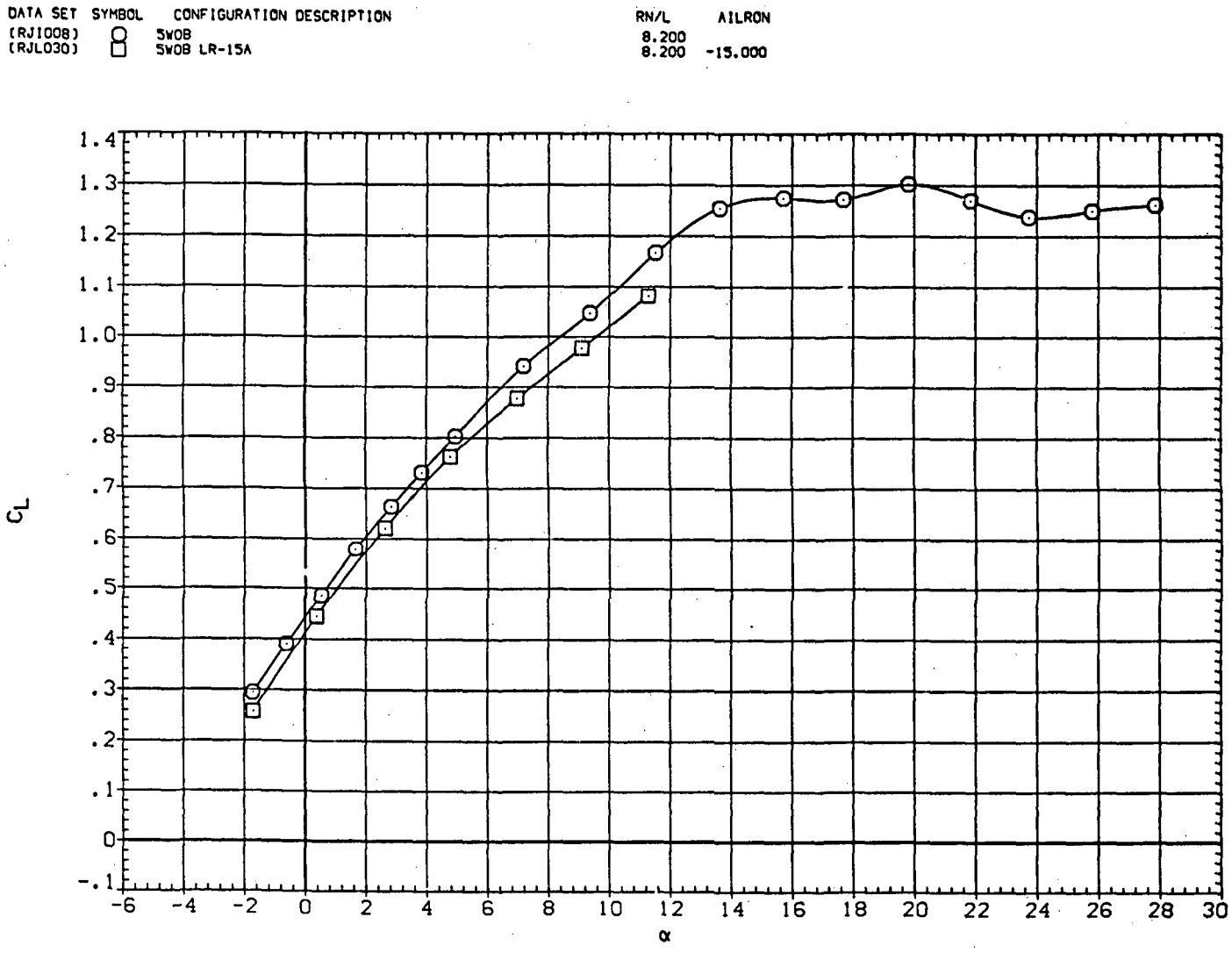

(a) C_L vs α

Figure 22.– Aileron effectiveness on the oblique wing with intermediate bend: $\Lambda = 0, M = 0.80$.

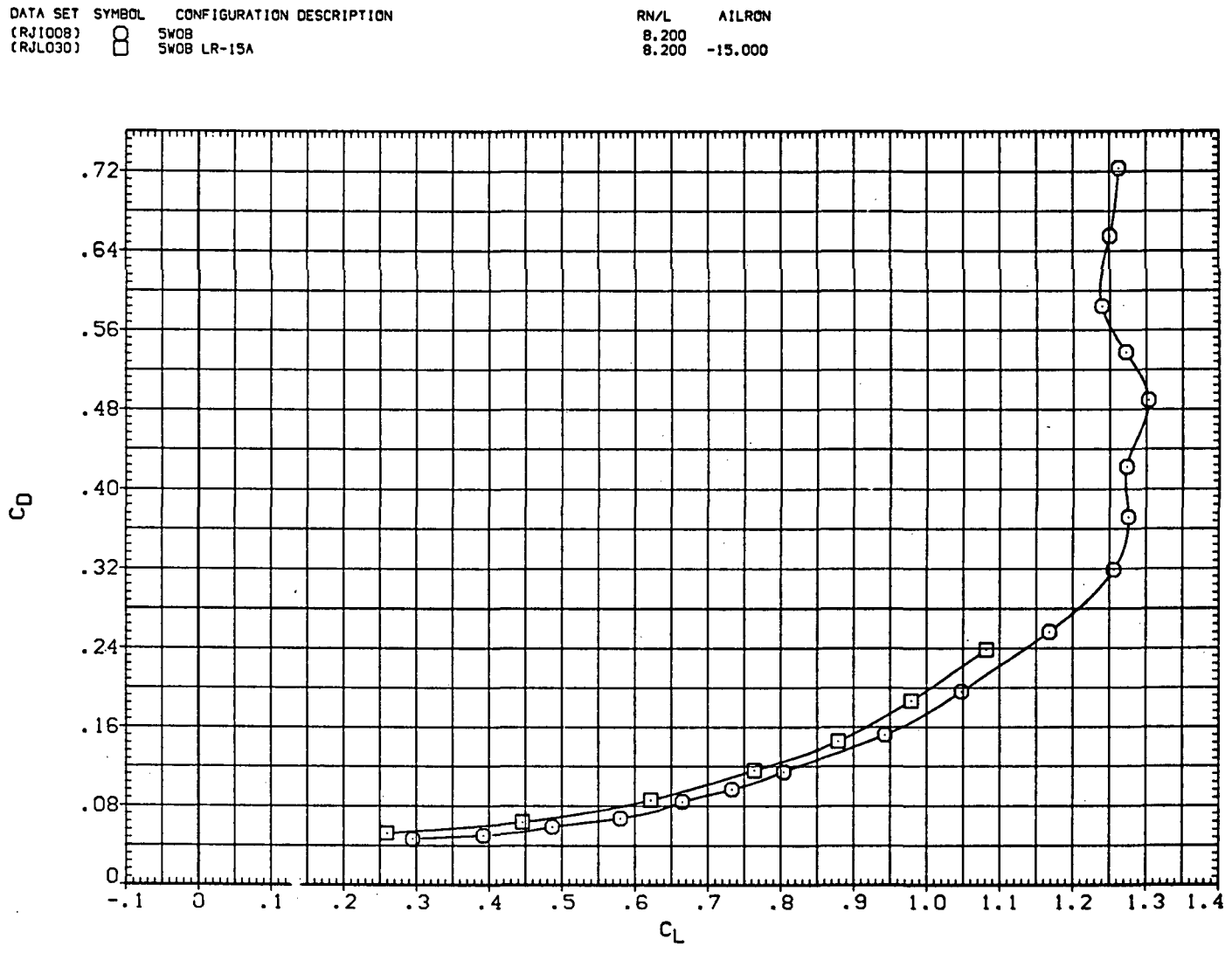

(b) C_D vs C_L

Figure 22.– Continued.

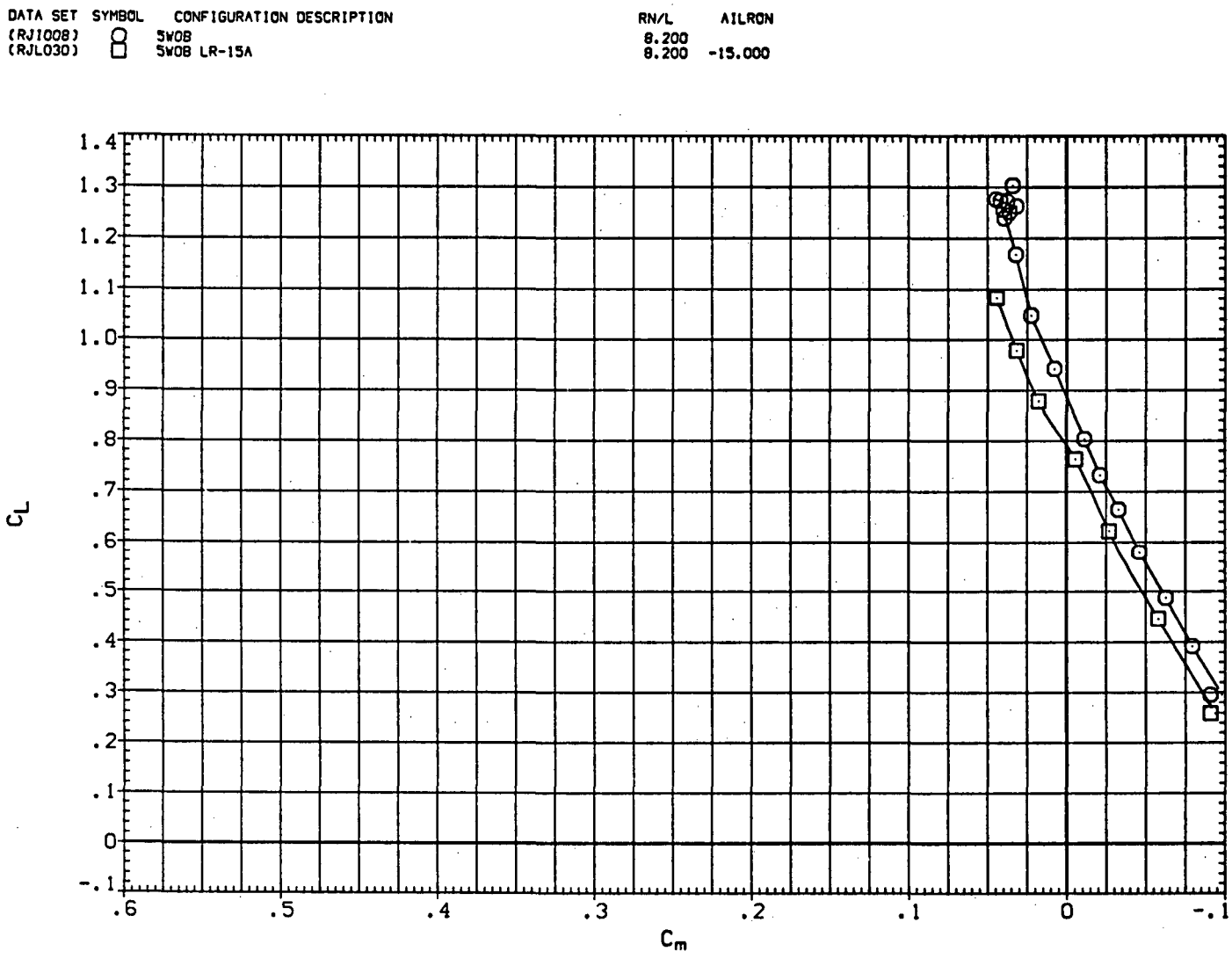

(c) C_L vs C_m

Figure 22.– Continued.

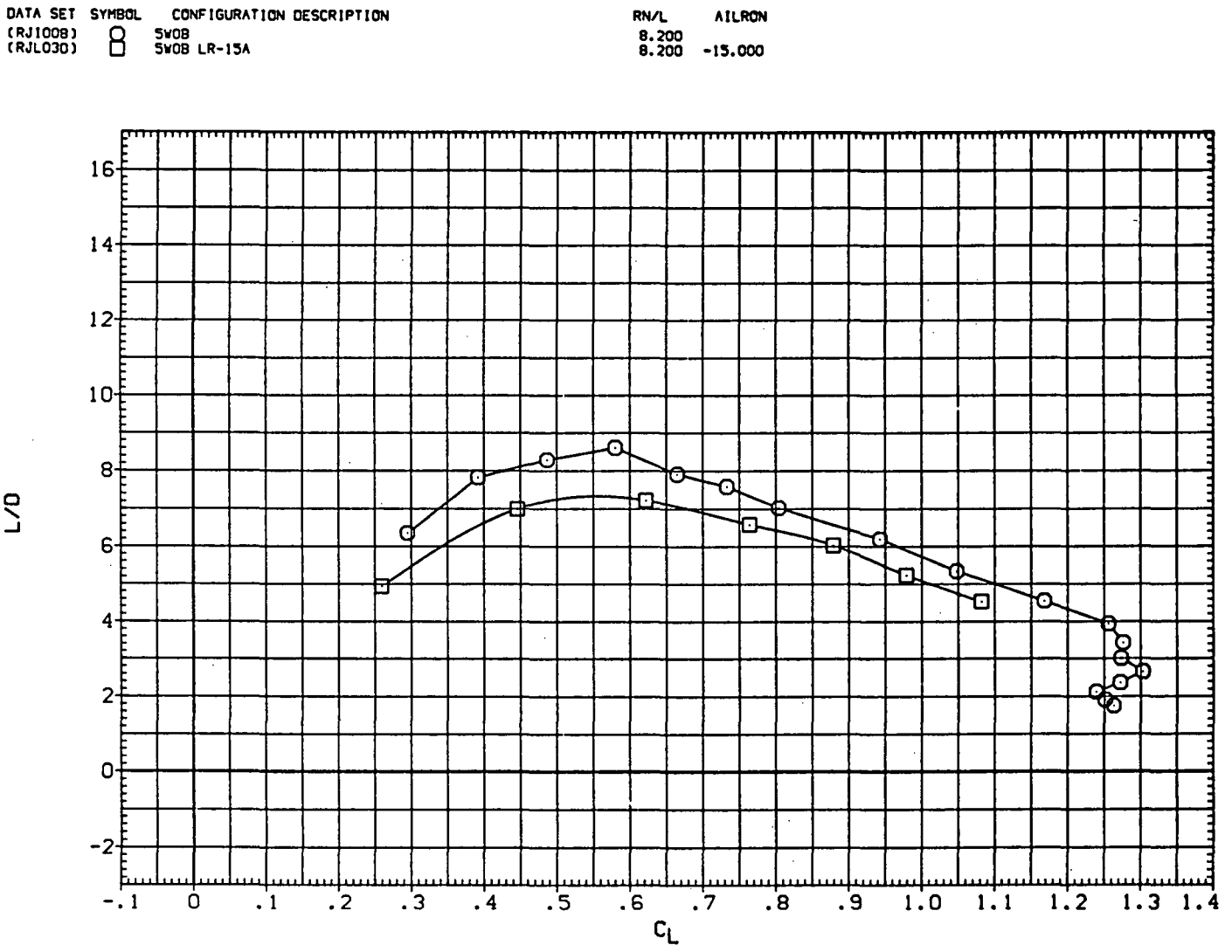

(d) L/D vs C_L

Figure 22.– Continued.

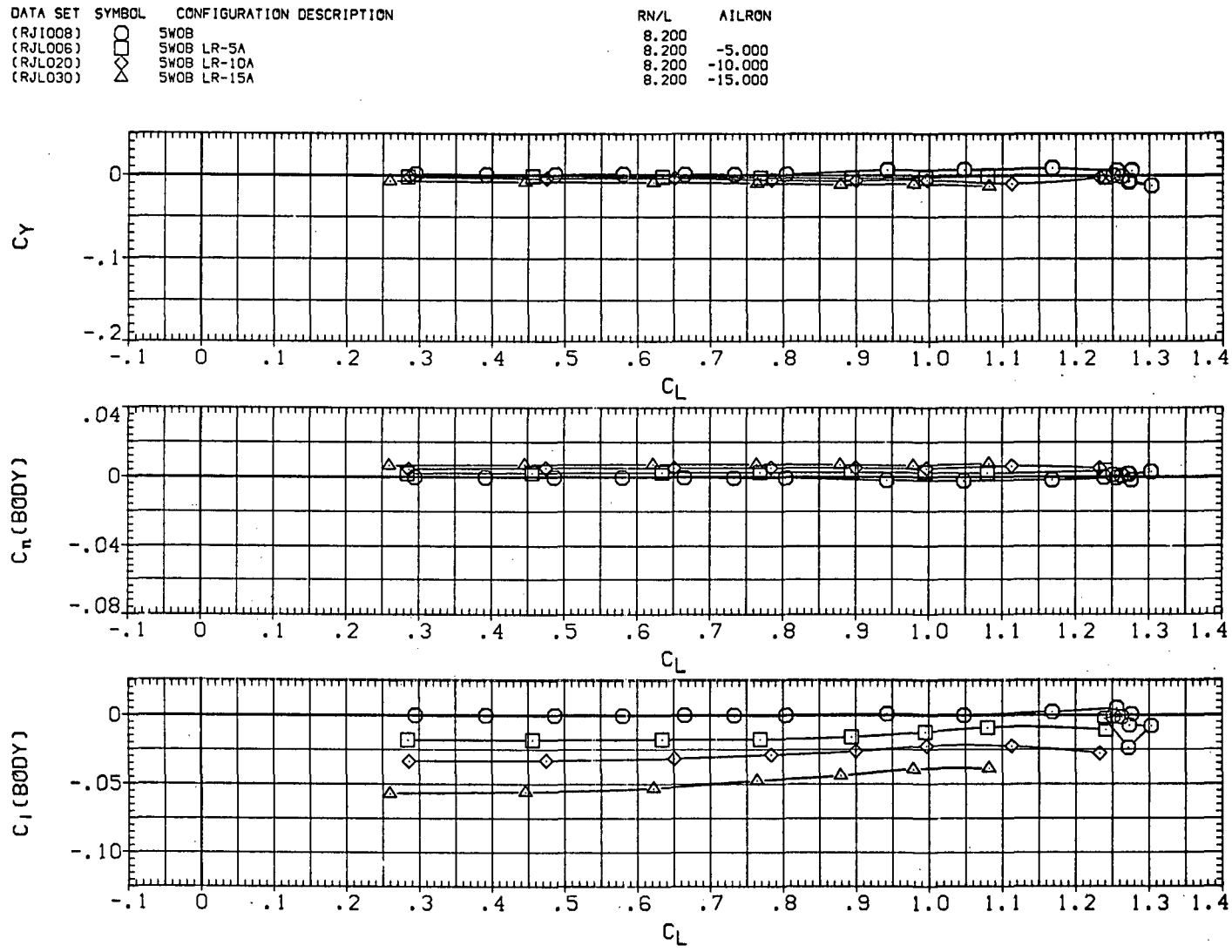

(e) C_Y, C_n, and C_l vs C_L

Figure 22.– Concluded.

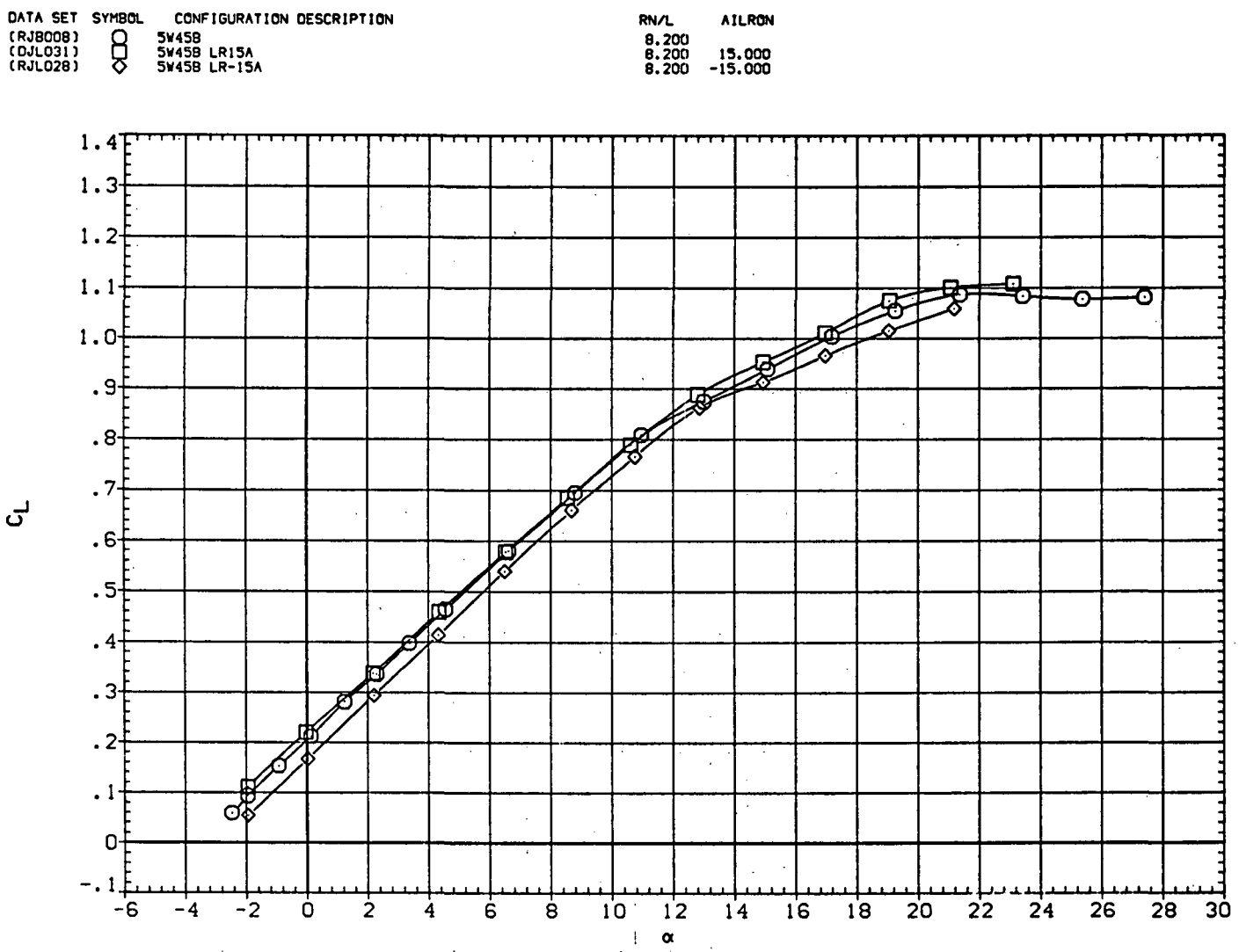

(a) C_L vs α

Figure 23.– Aileron effectiveness on the oblique wing with intermediate bend: $\Lambda = 45°, M = 0.60$.

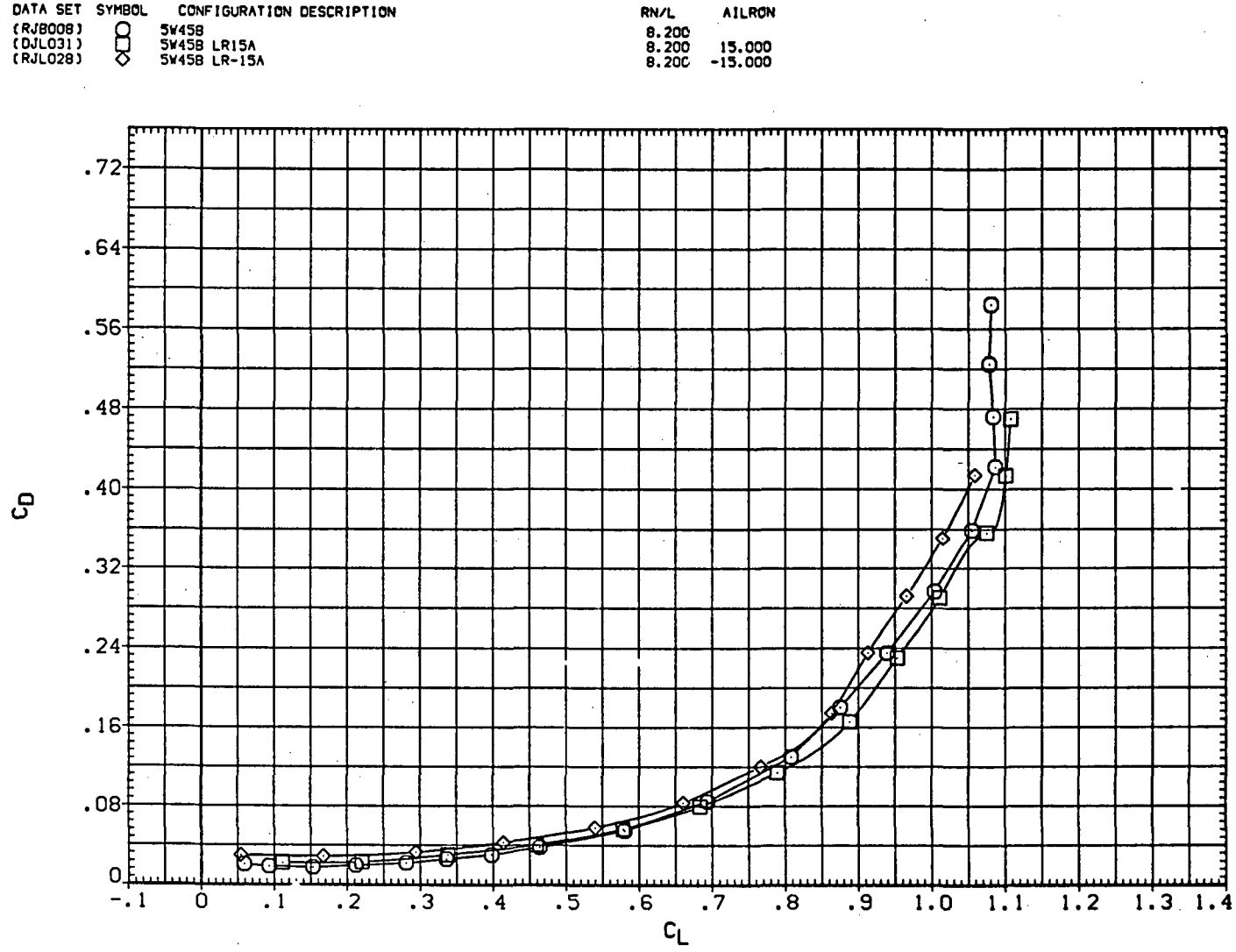

(b) C_D vs C_L

Figure 23.– Continued.

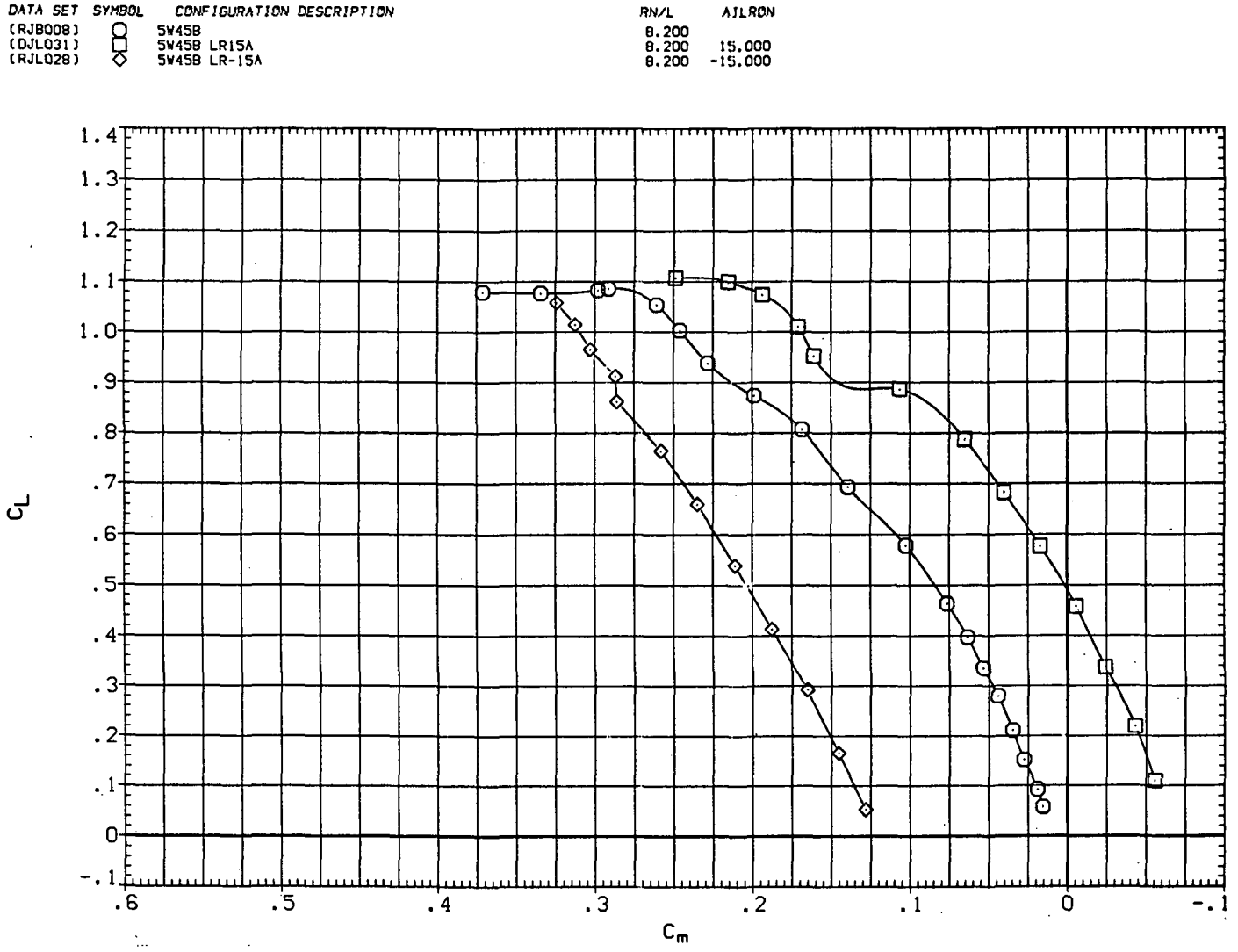

(c) C_L vs C_m

Figure 23.– Continued.

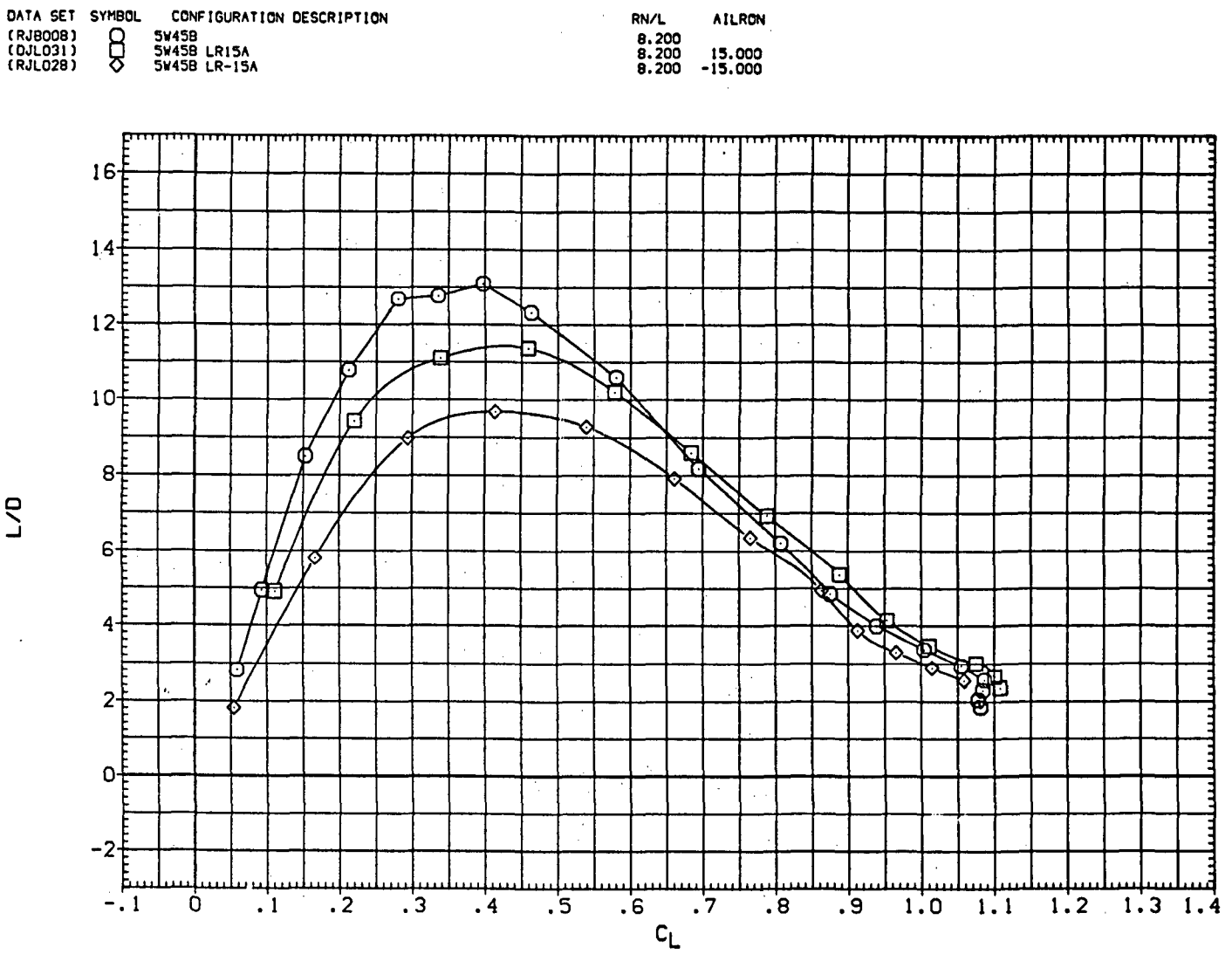

(d) L/D vs C_L

Figure 23.– Continued.

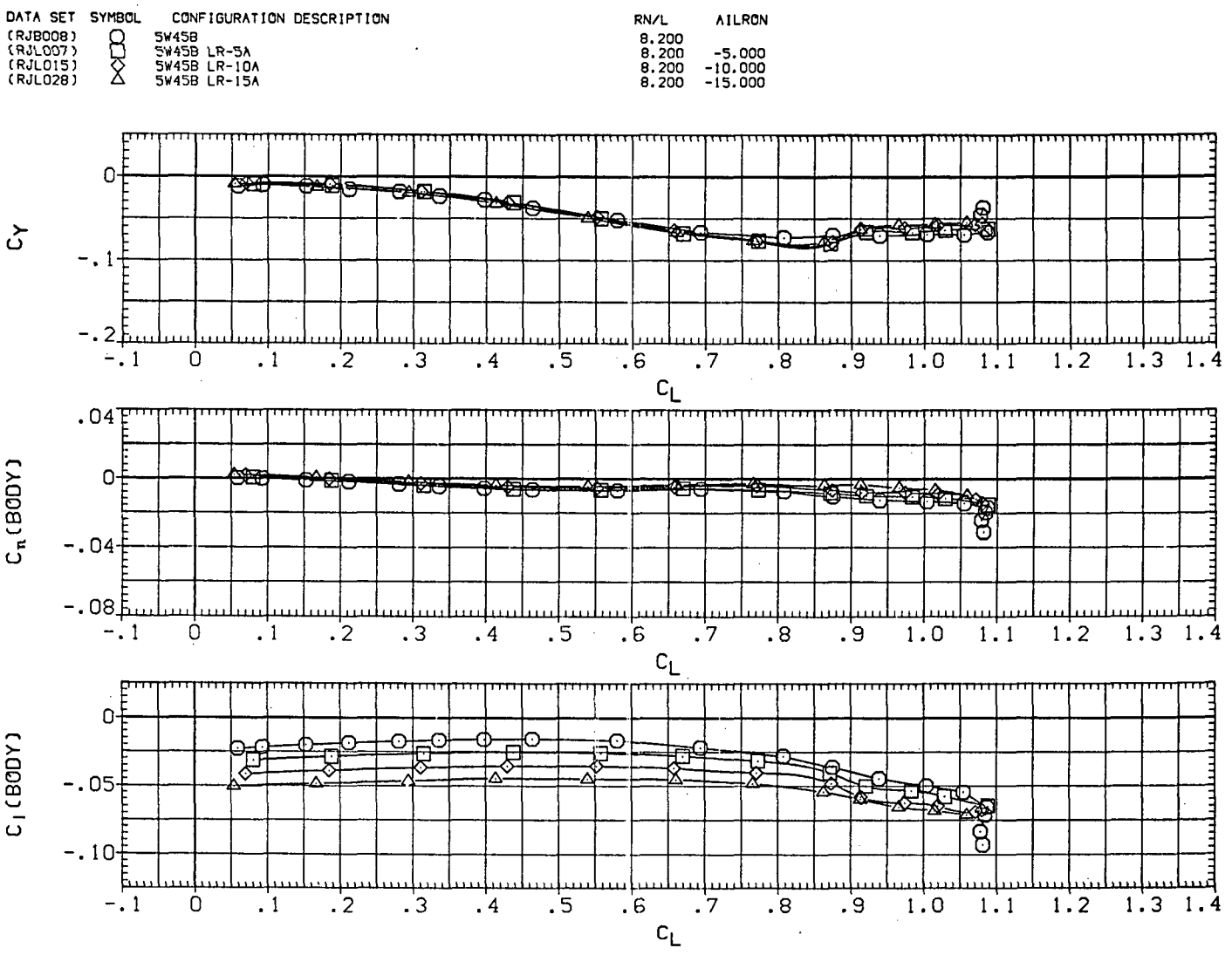

(e) C_Y, C_n, and C_l vs C_L (negative $\Delta\delta_a$'s).

Figure 23.– Continued.

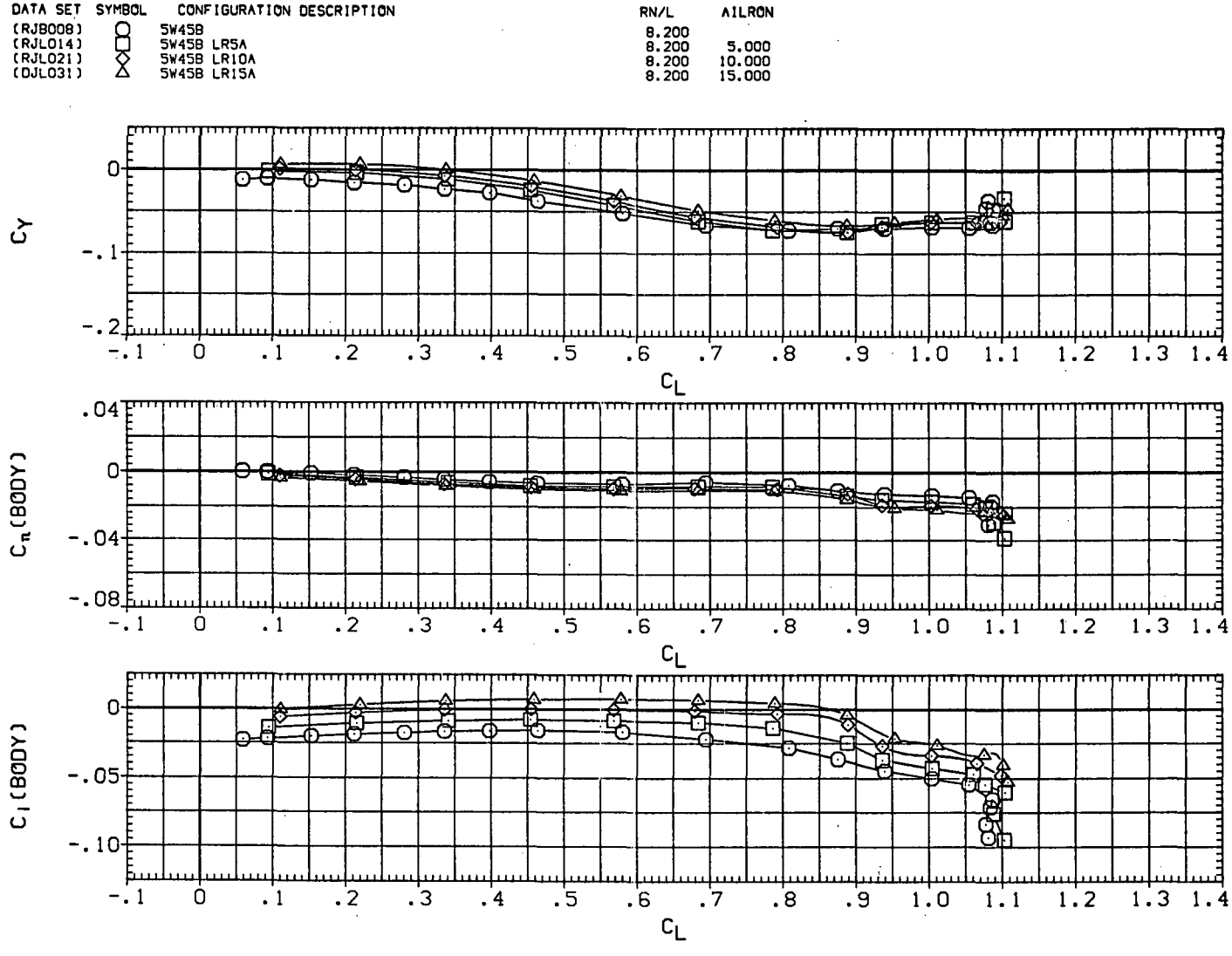

(f) C_Y, C_n, and C_l vs C_L (positive $\Delta\delta_a$'s).

Figure 23.– Concluded.

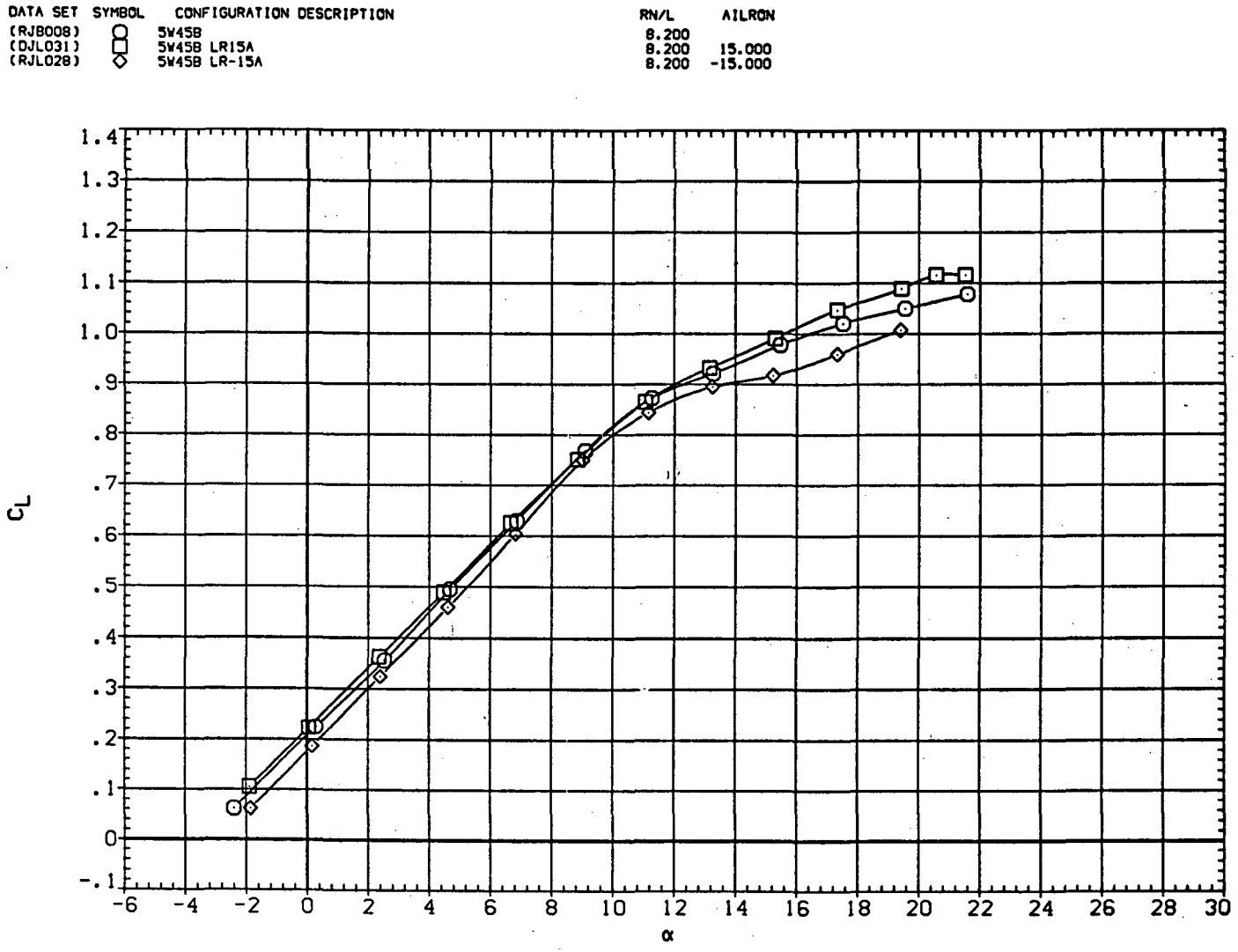

(a) C_L vs α

Figure 24.– Aileron effectiveness on the oblique wing with intermediate bend: $\Lambda = 45°, M = 0.80$.

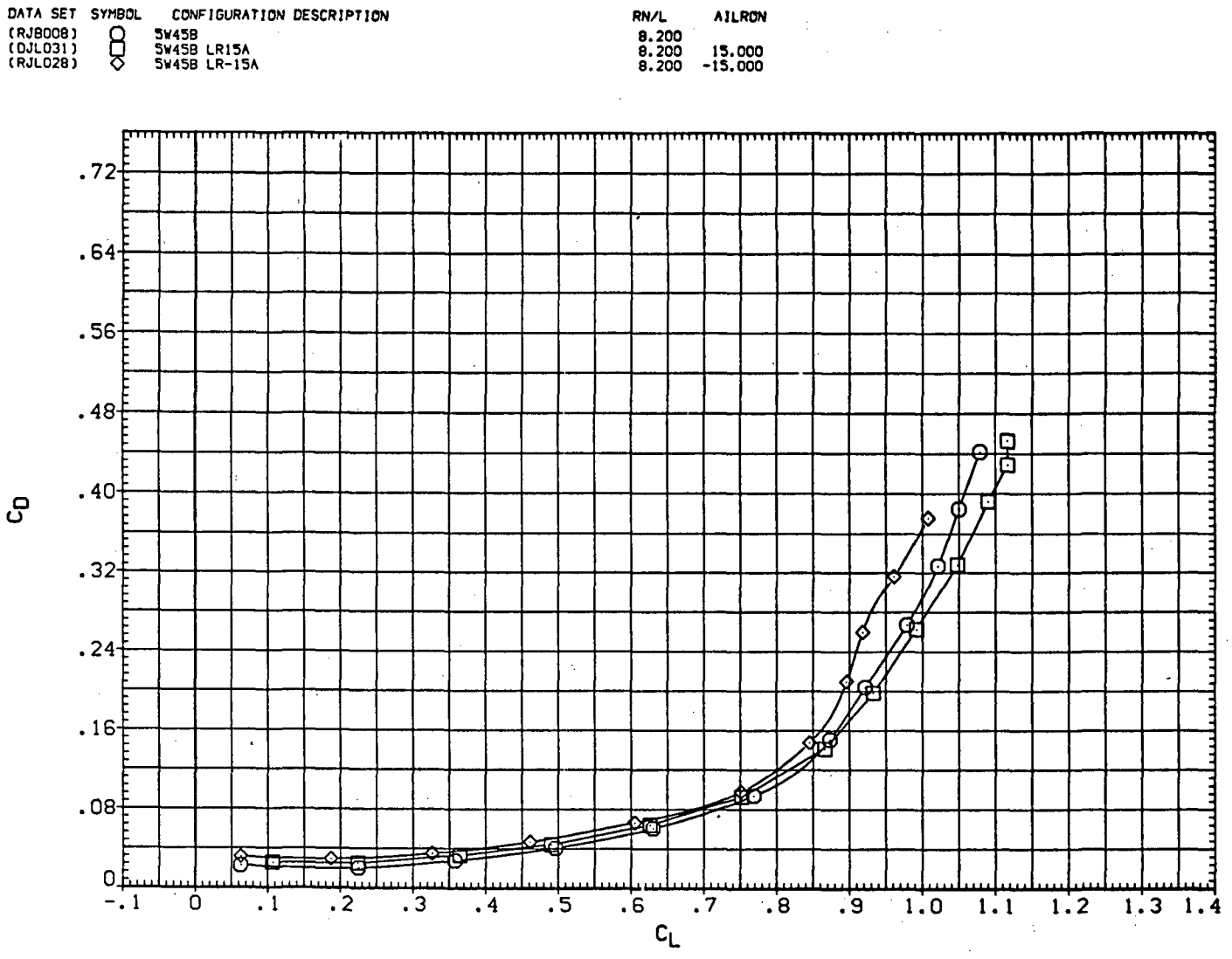

(b) C_D vs C_L

Figure 24.– Continued.

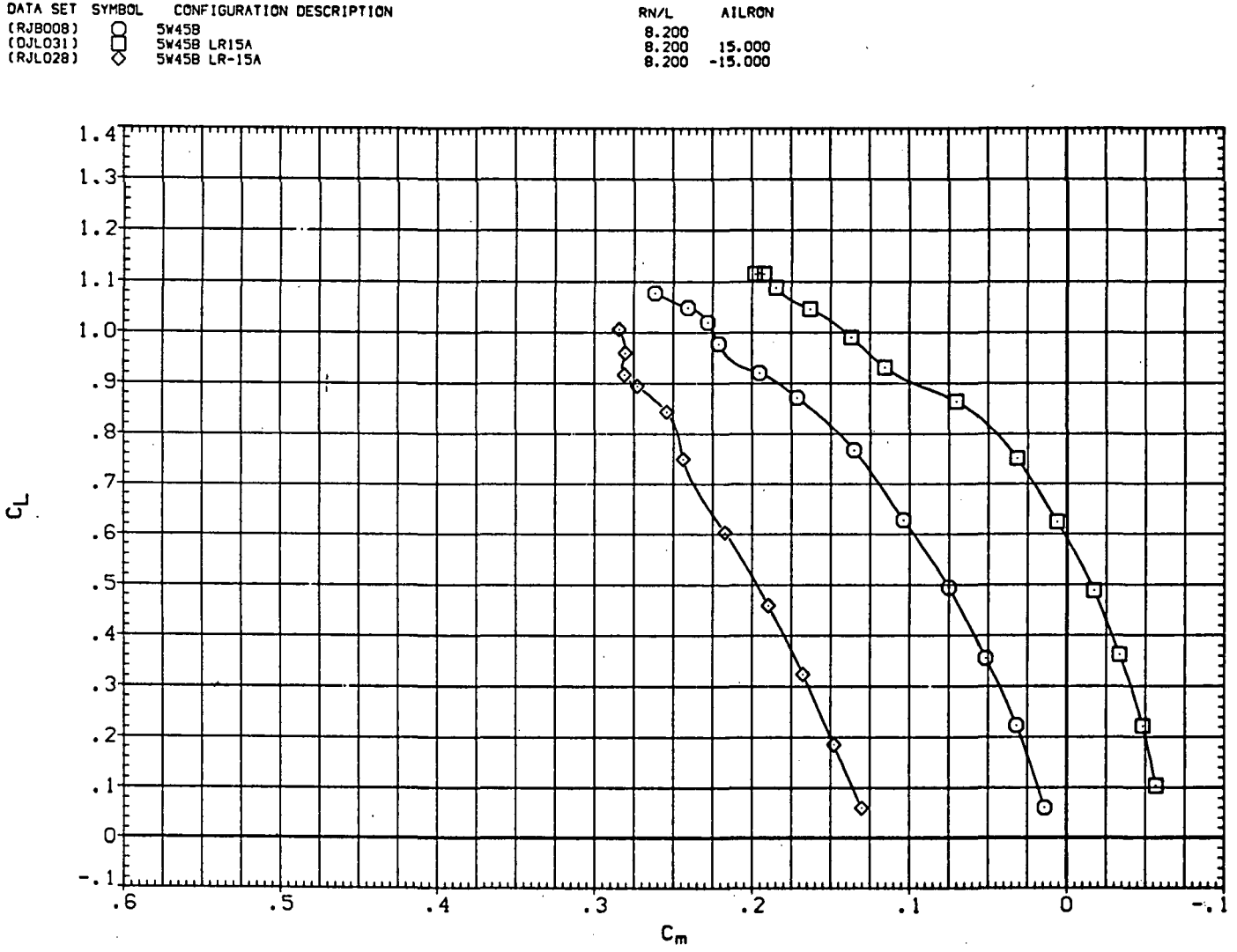

(c) C_L vs C_m

Figure 24.– Continued.

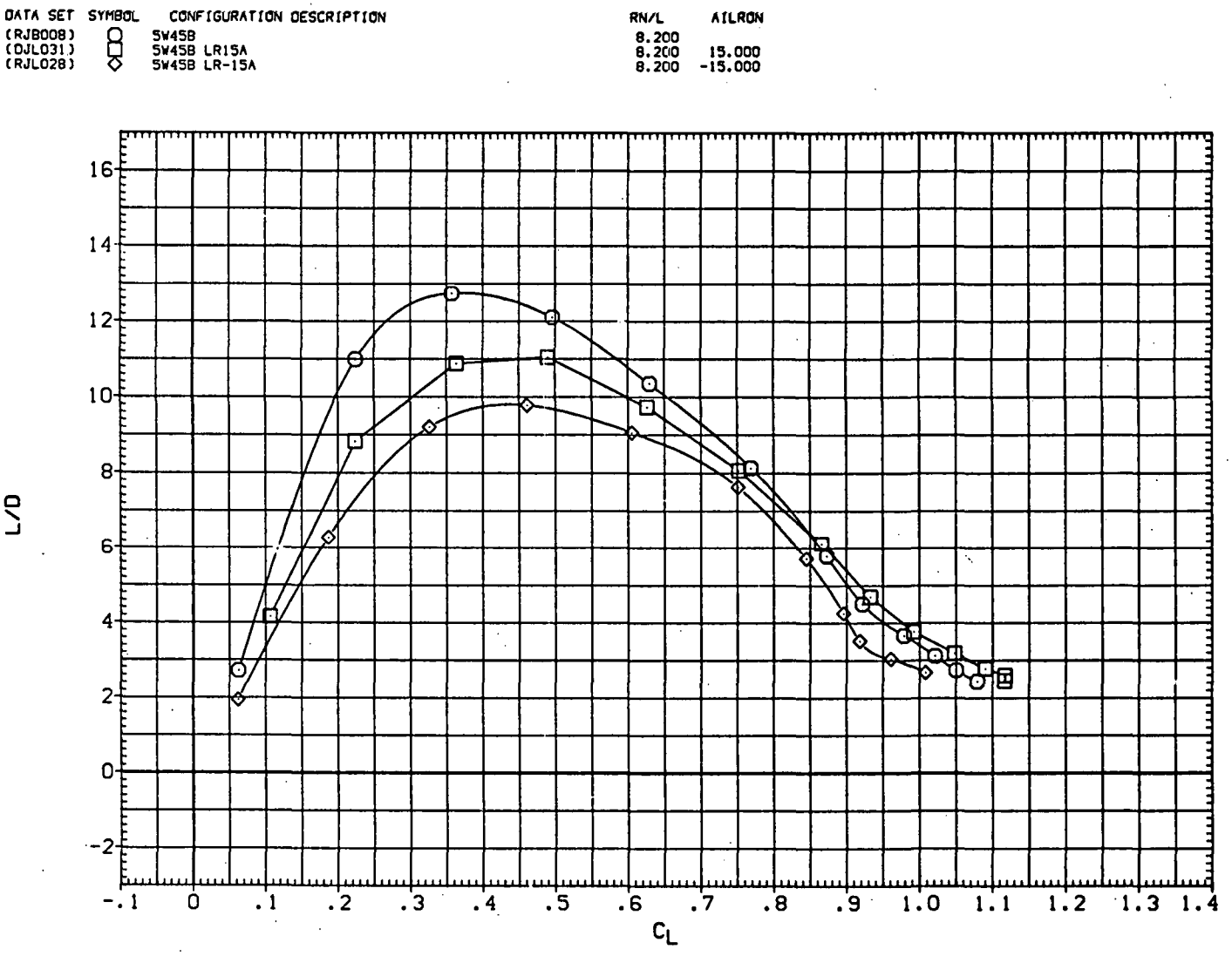

(d) L/D vs C_L

Figure 24.– Continued.

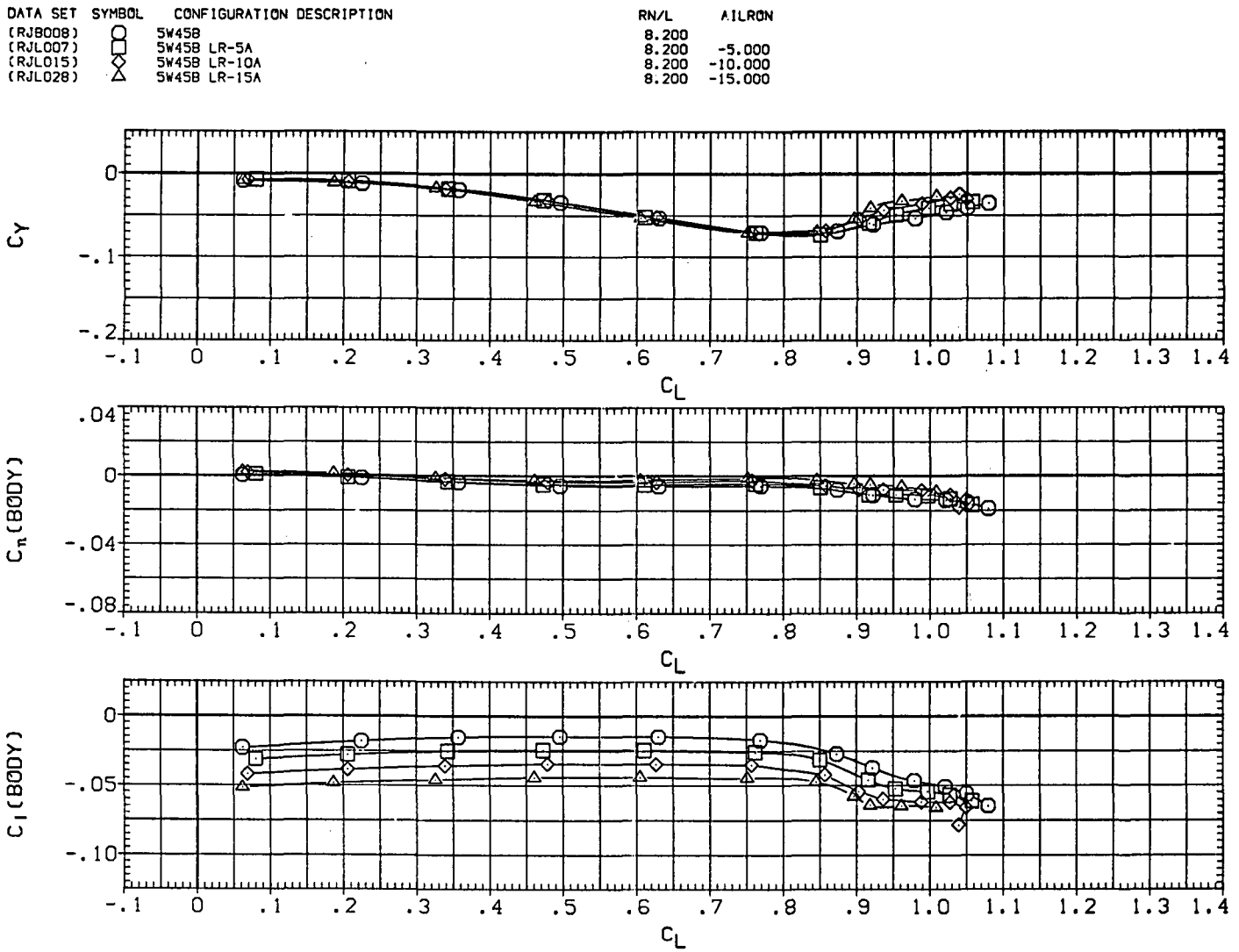

(e) C_Y, C_n, and C_l vs C_L (negative $\Delta\delta_a$'s).

Figure 24.– Continued.

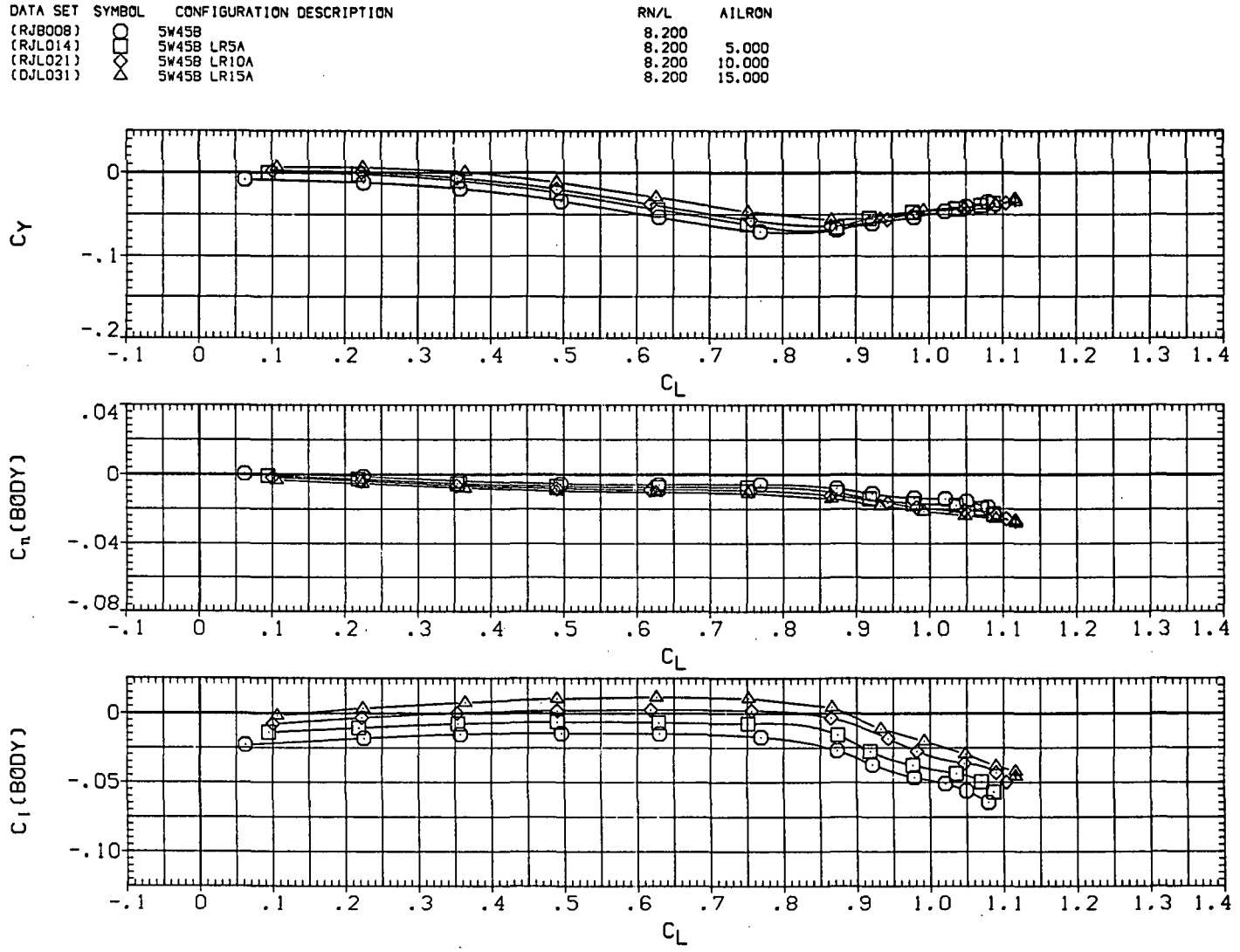

(f) C_Y, C_n, and C_l vs C_L (positive $\Delta\delta_a$'s).

Figure 24.– Concluded.

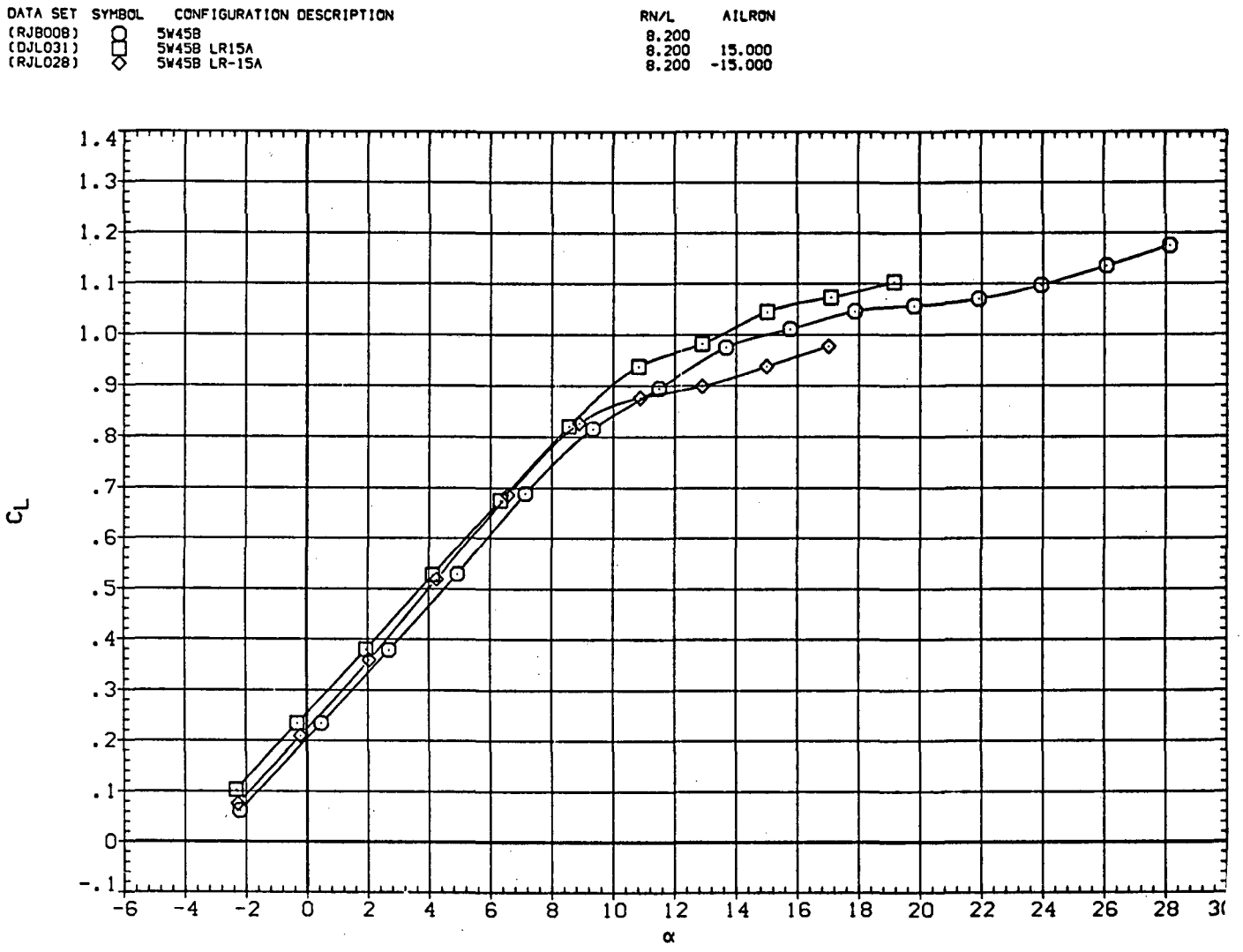

(a) C_L vs α

Figure 25.– Aileron effectiveness on the oblique wing with intermediate bend: $\Lambda = 45°, M = 0.90$.

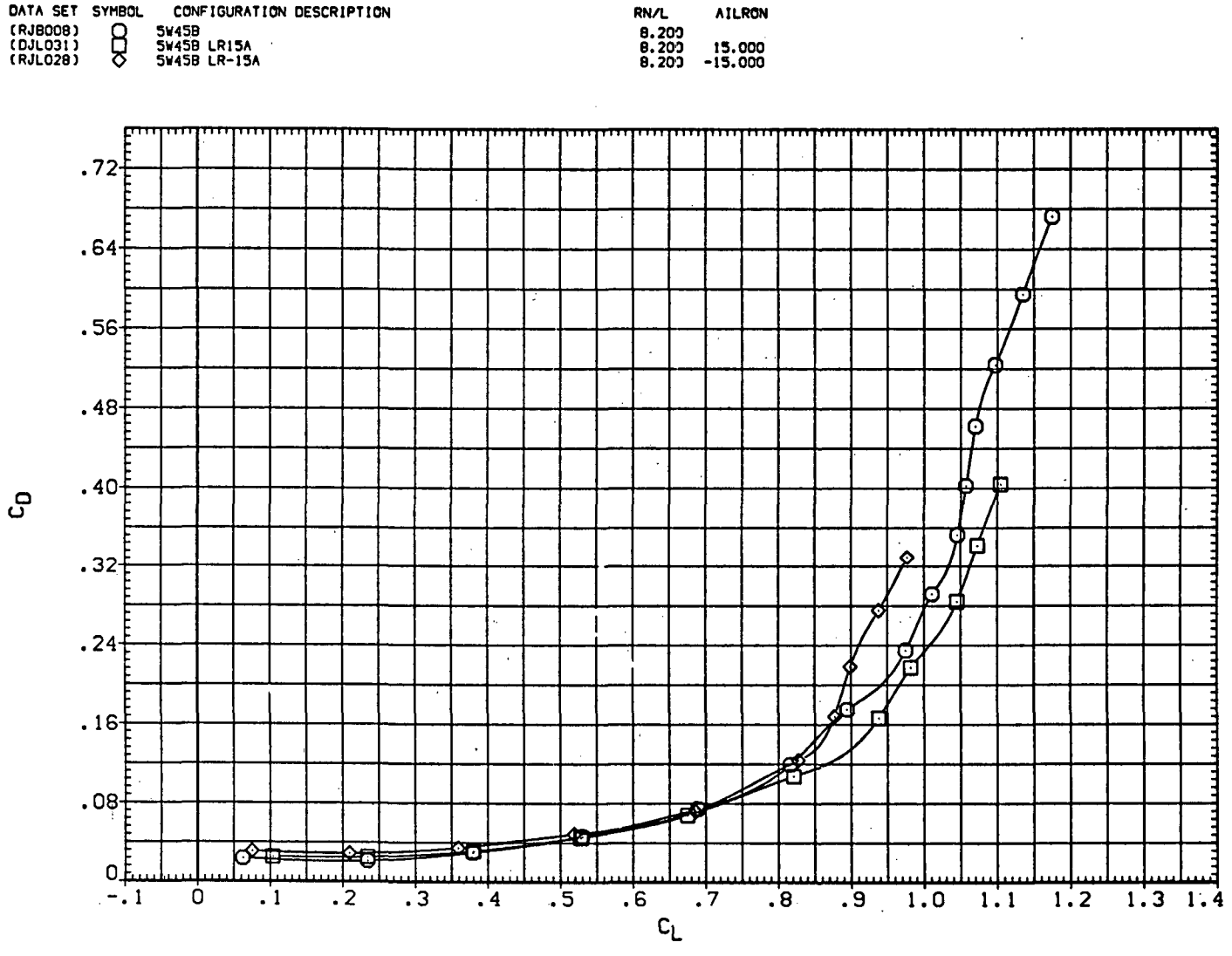

(b) C_D vs C_L

Figure 25.– Continued.

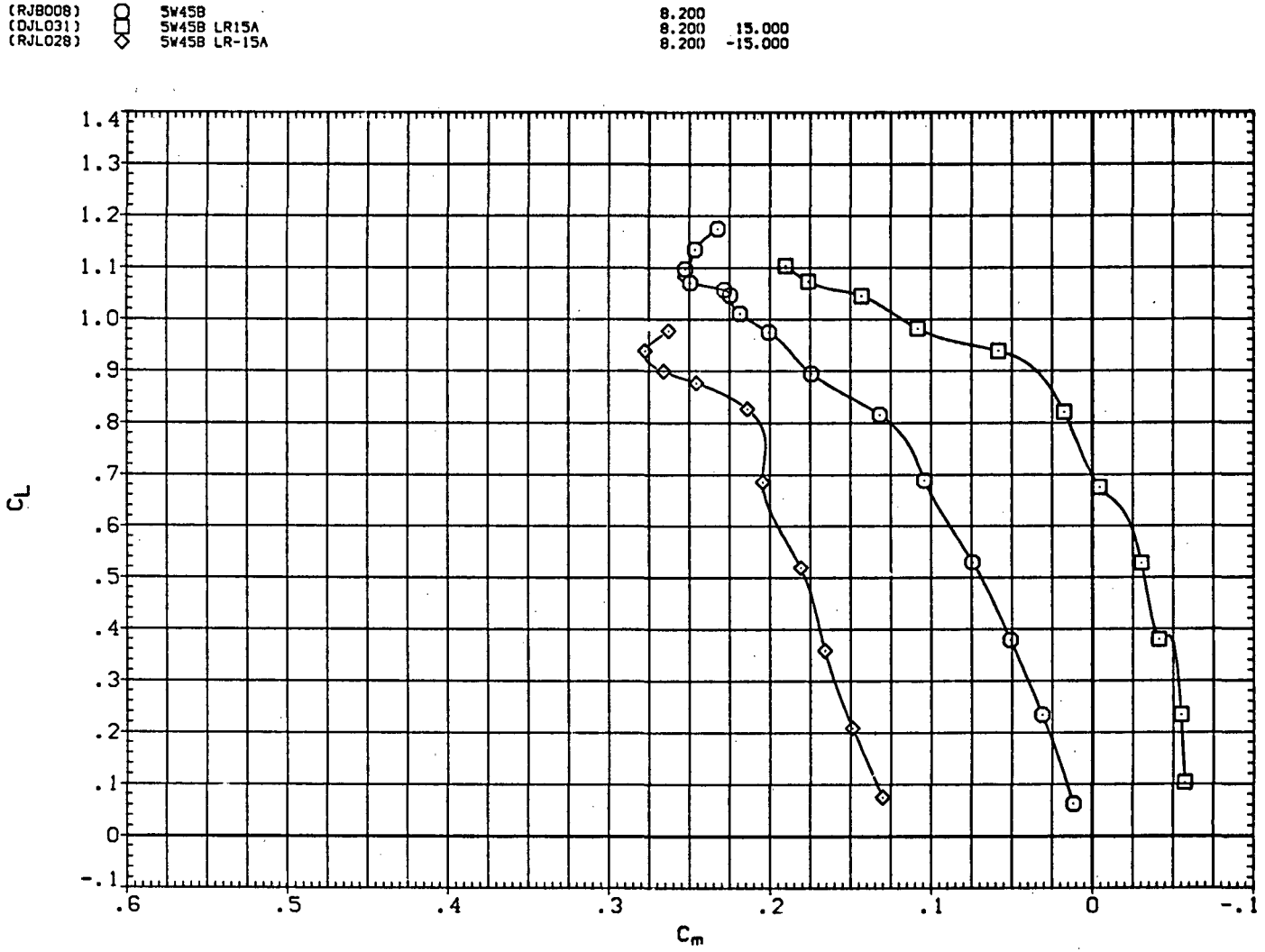

(c) C_L vs C_m

Figure 25.– Continued.

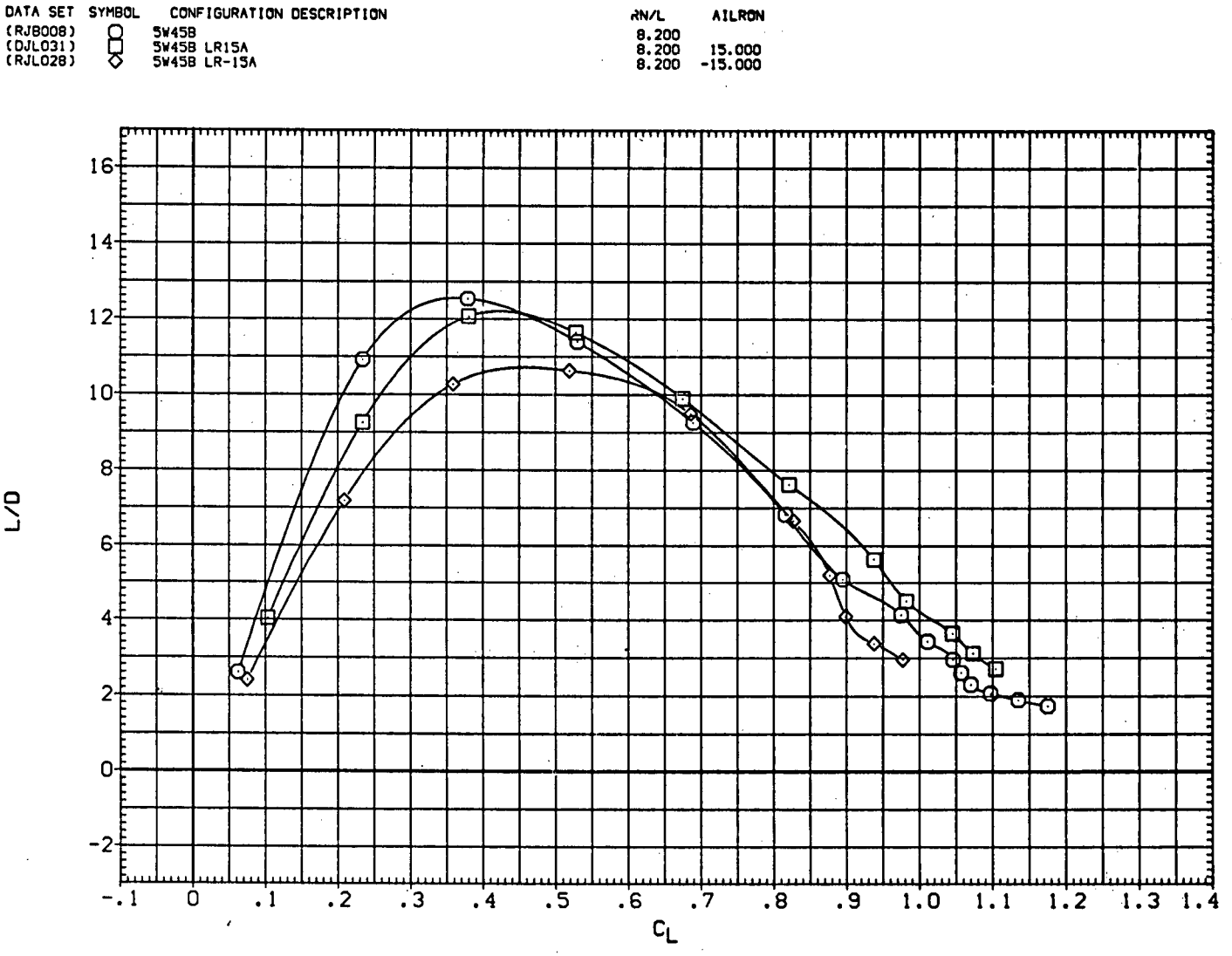

(d) L/D vs C_L

Figure 25.– Continued.

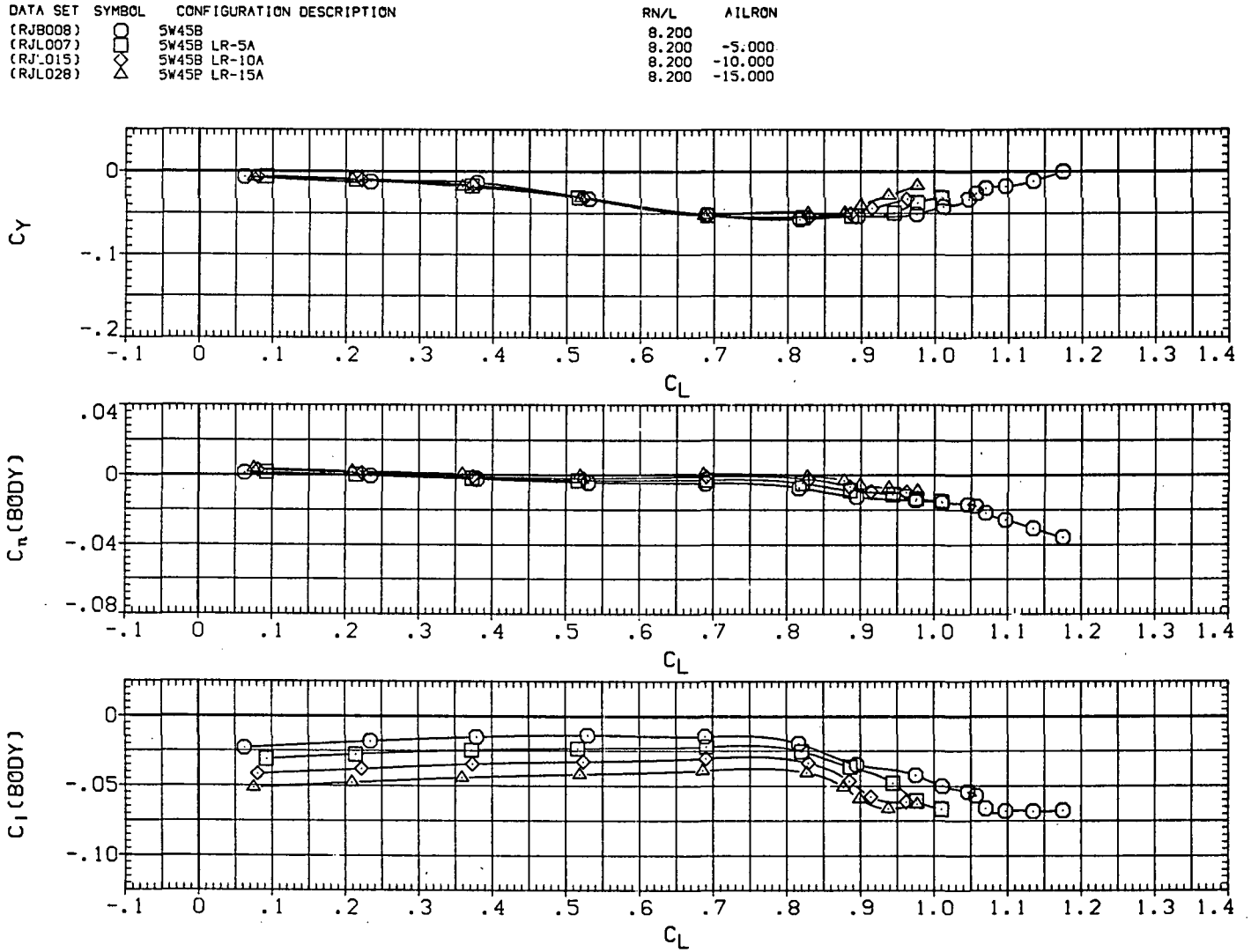

(e) C_Y, C_n, and C_l vs C_L (negative $\Delta\delta_a$'s).

Figure 25.– Continued.

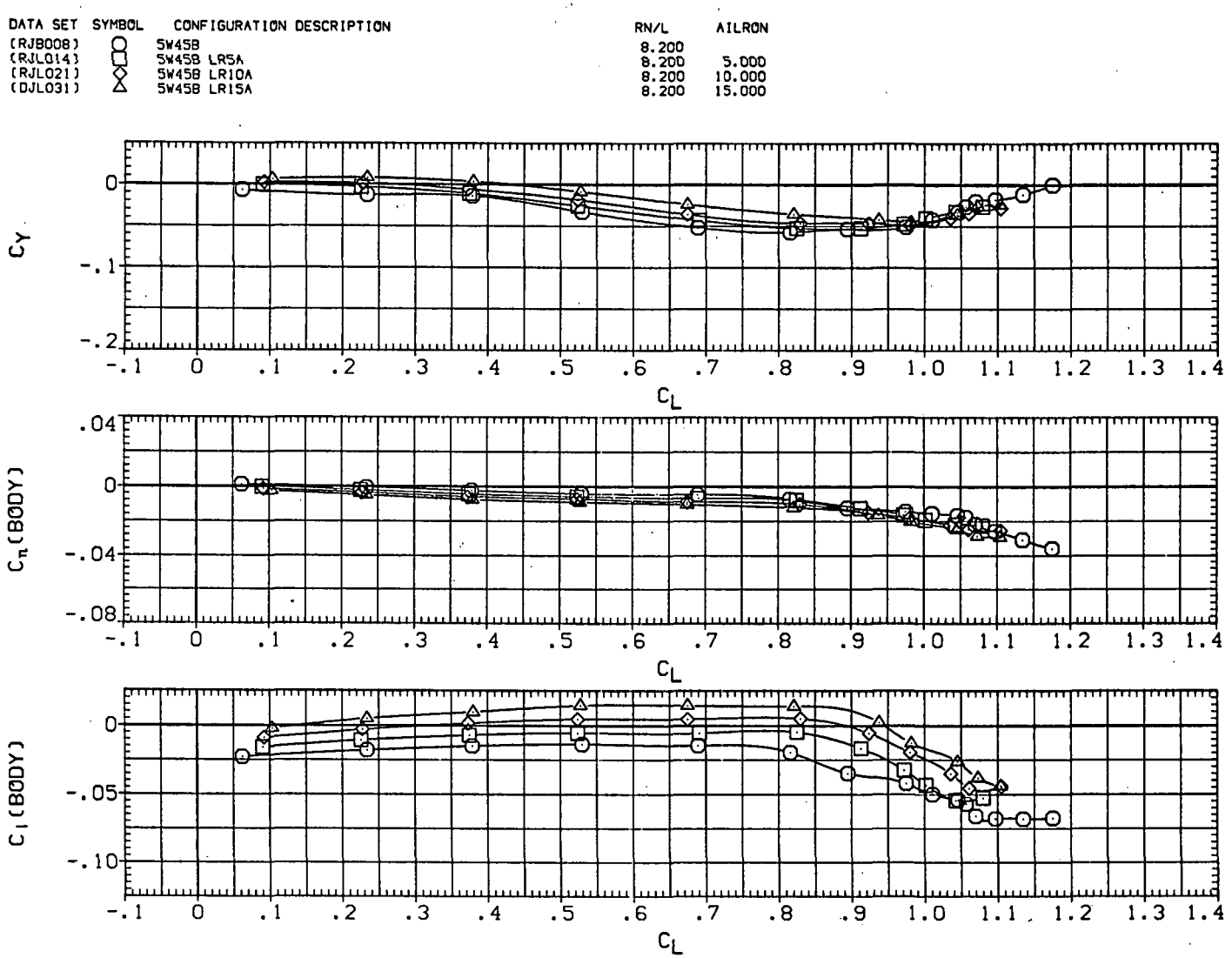

(f) C_Y, C_n, and C_l vs C_L (positive $\Delta\delta_a$'s).

Figure 25.– Concluded.

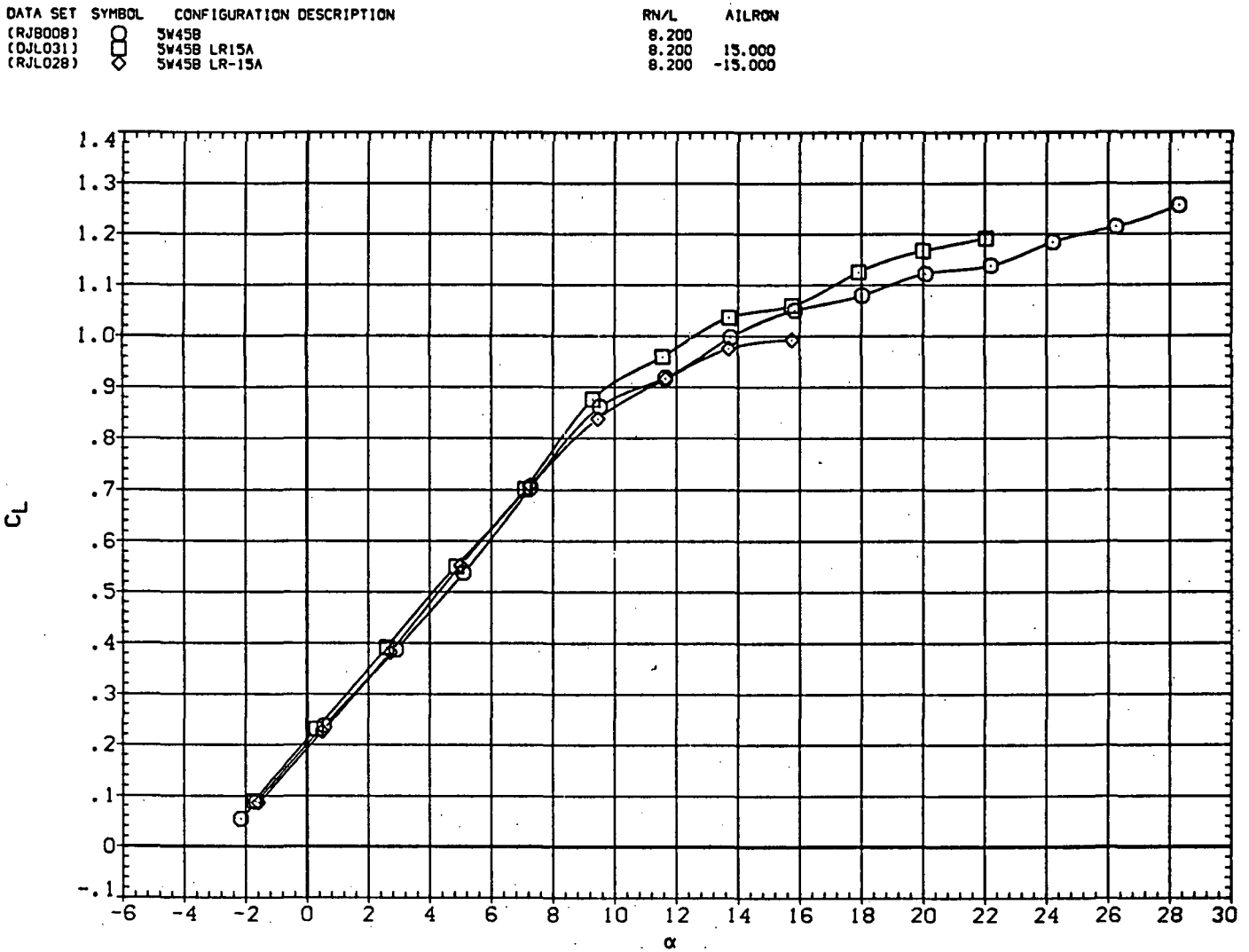

(a) C_L vs α

Figure 26.– Aileron effectiveness on the oblique wing with intermediate bend: $\Lambda = 45°, M = 0.95$.

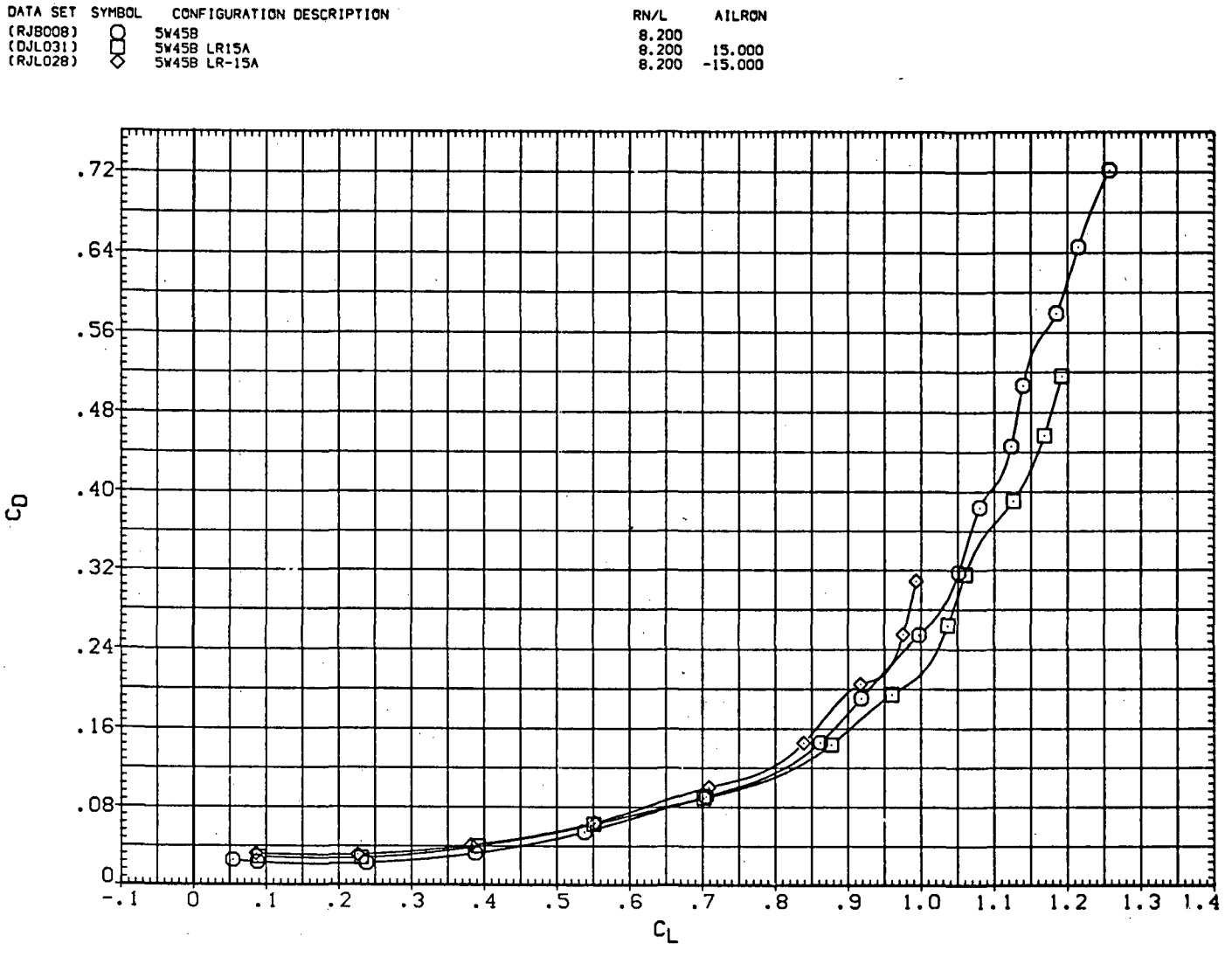

(b) C_D vs C_L

Figure 26.– Continued.

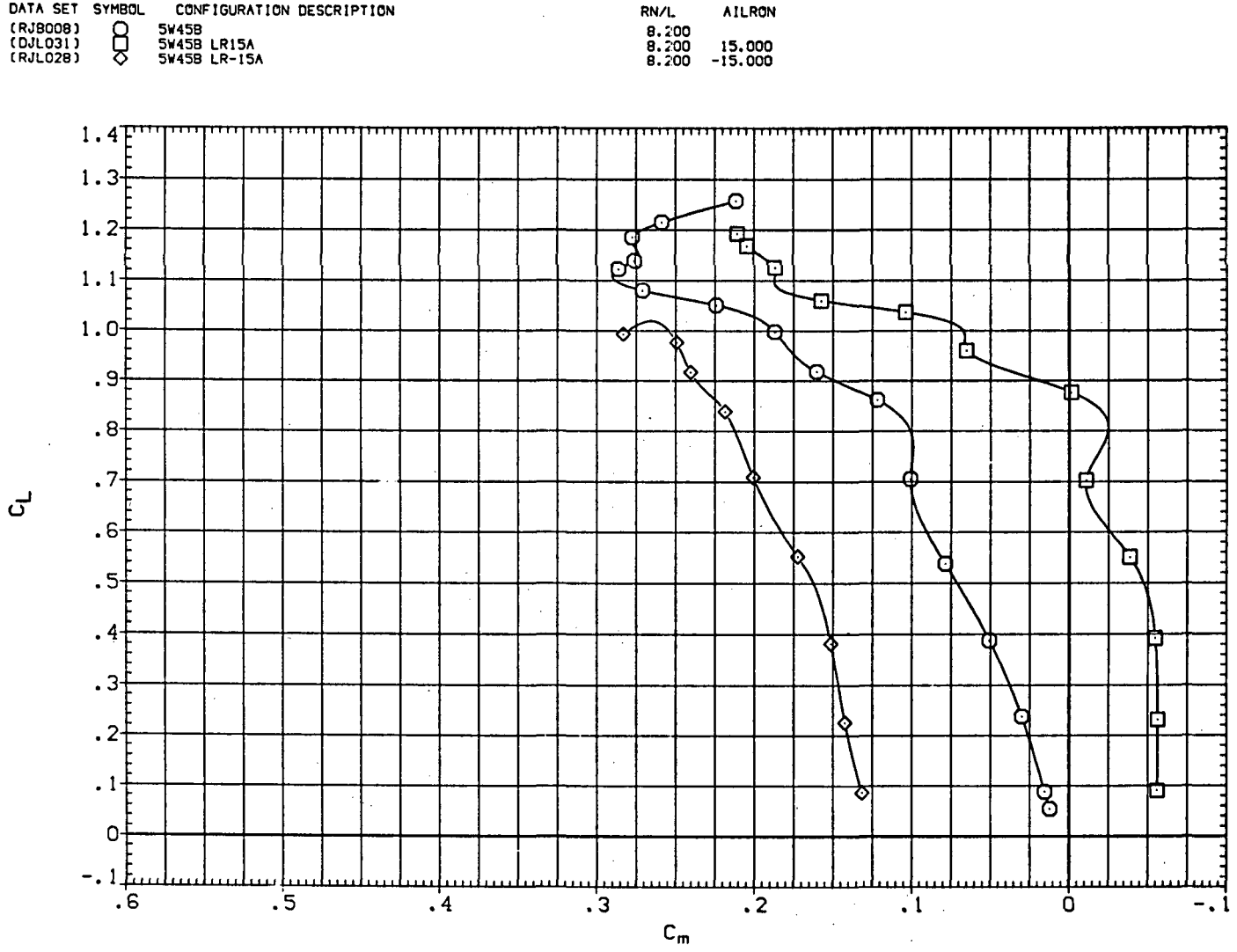

(c) C_L vs C_m

Figure 26.– Continued.

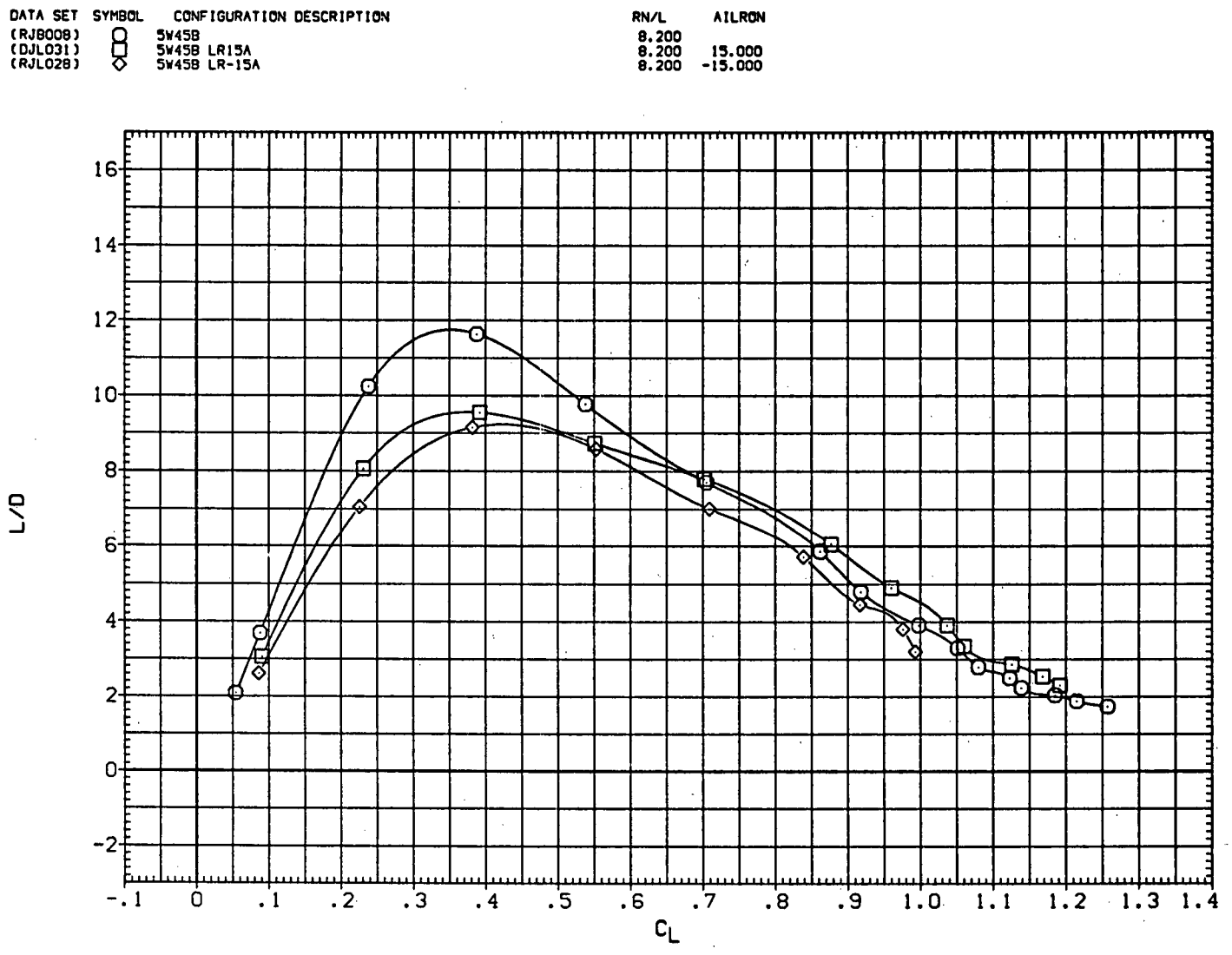

(d) L/D vs C_L

Figure 26.– Continued.

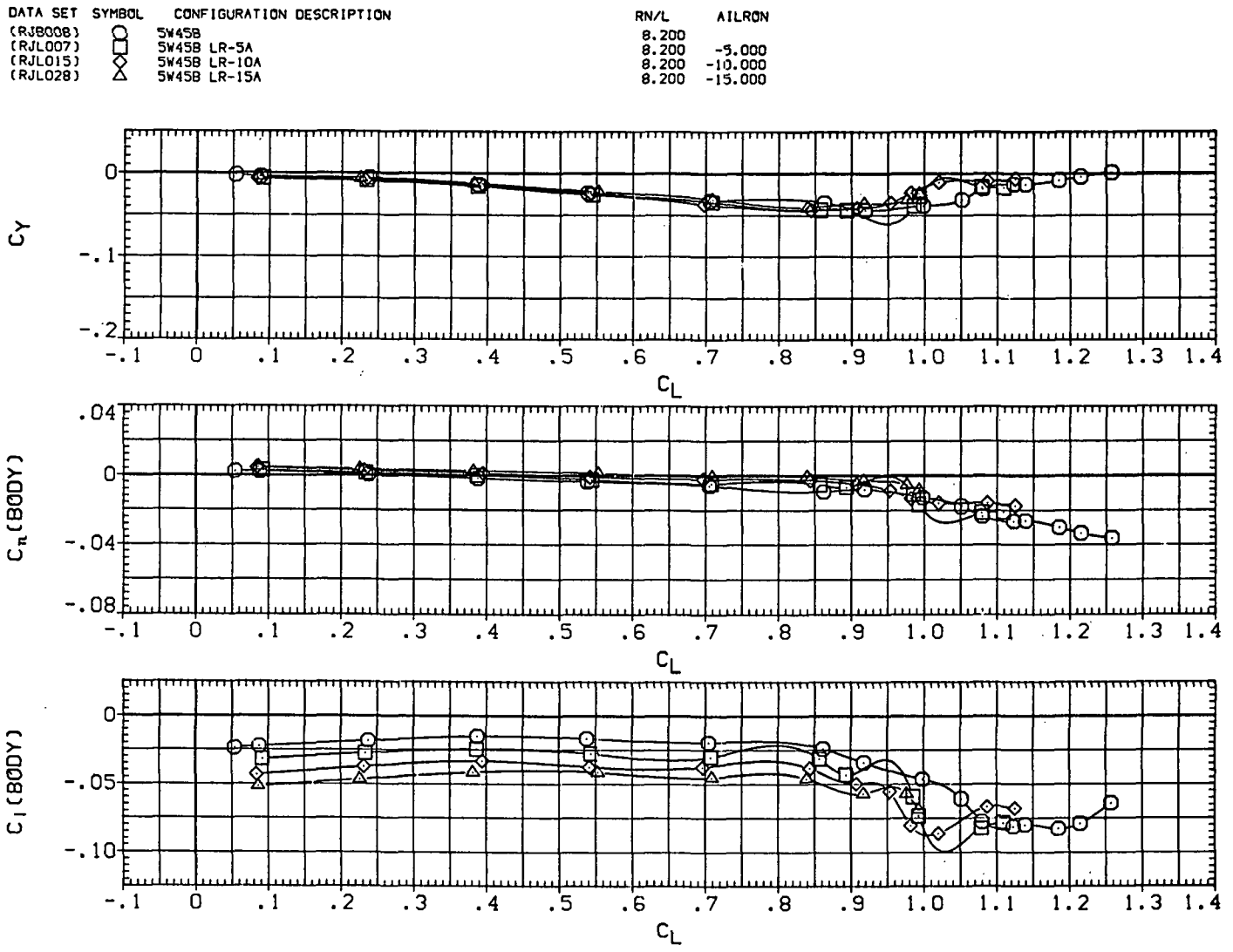

(e) C_Y, C_n, and C_l vs C_L (negative $\Delta\delta_a$'s).

Figure 26.– Continued.

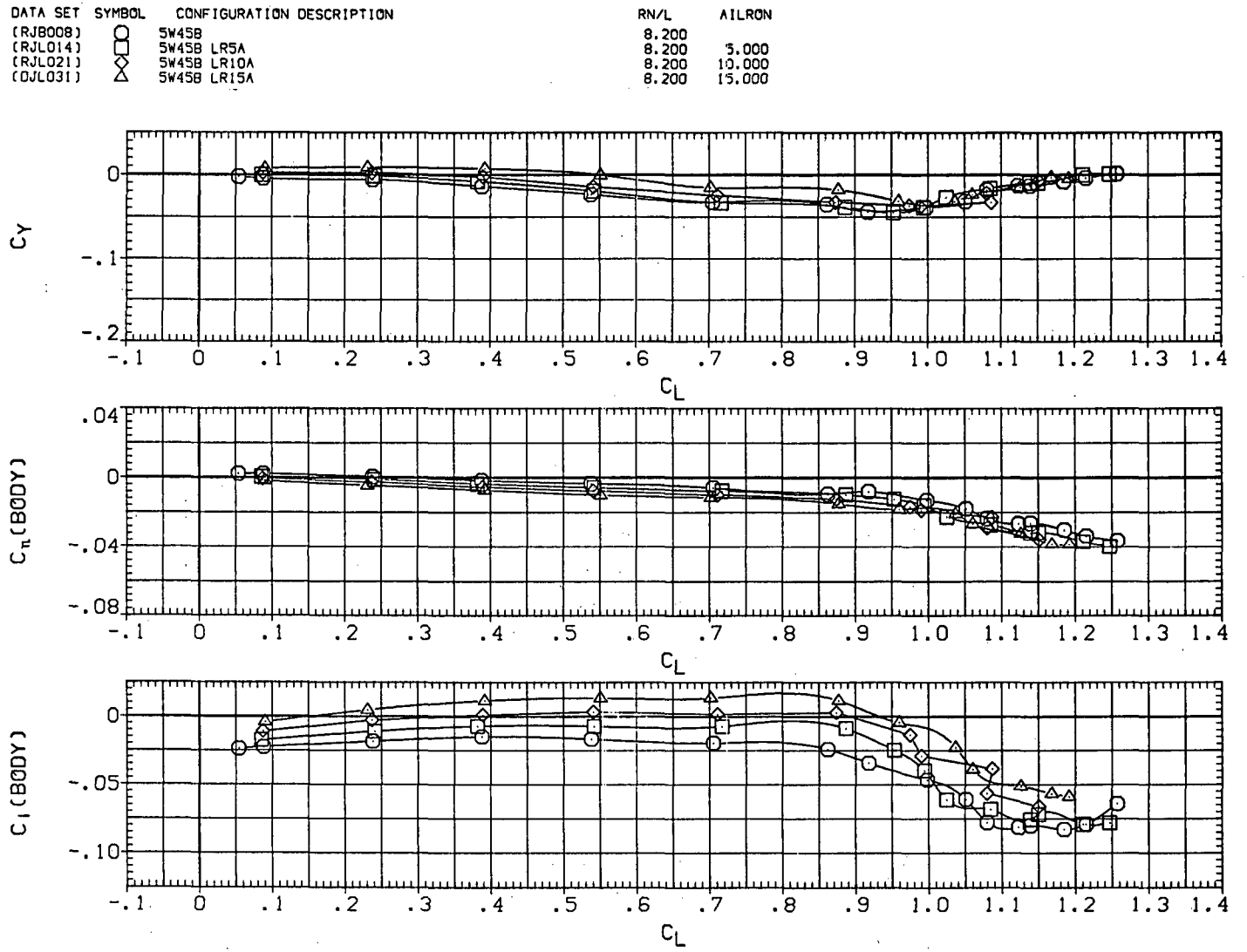

(f) C_Y, C_n, and C_l vs C_L (positive $\Delta\delta_a$'s).

Figure 26.– Concluded.

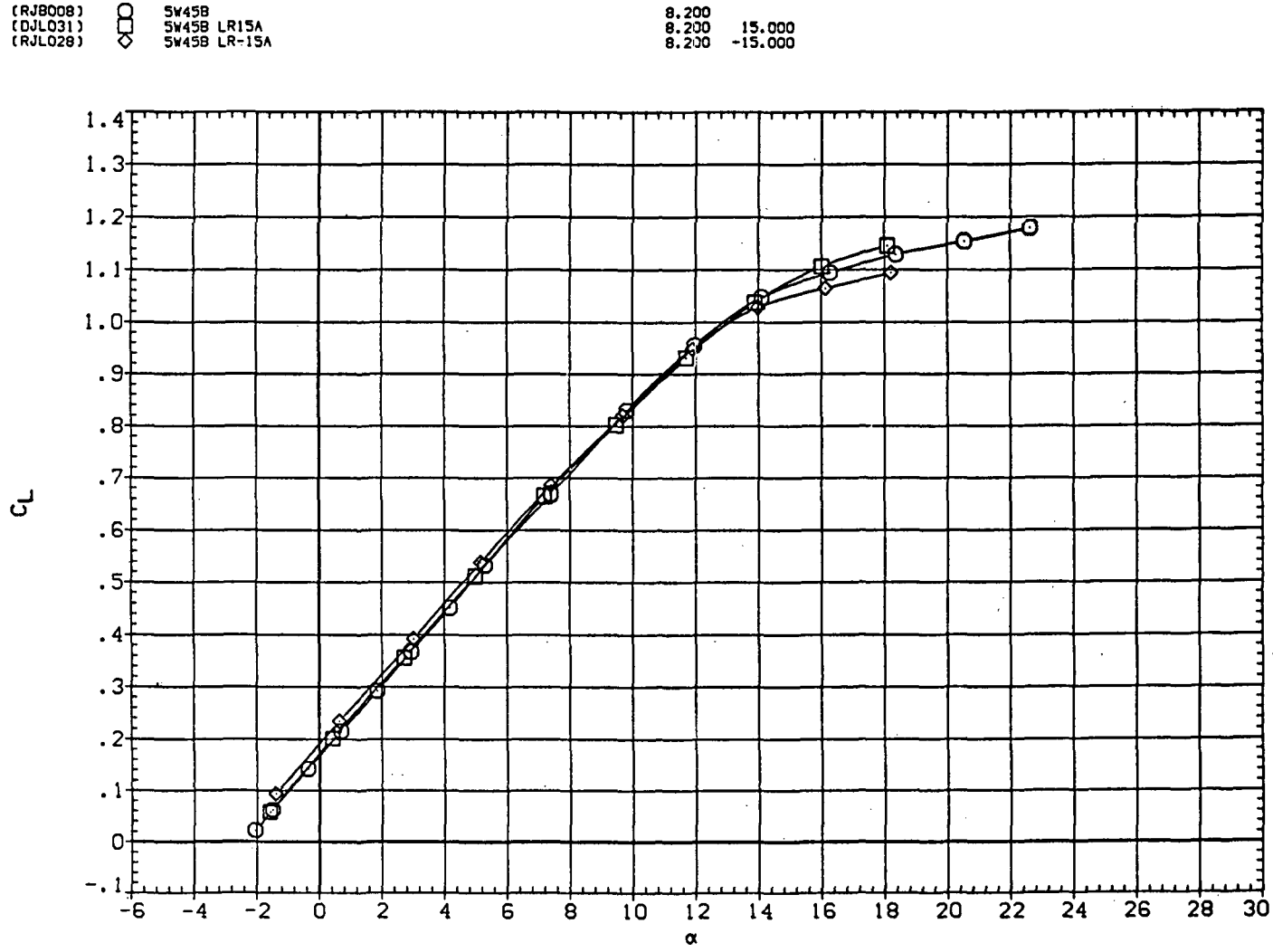

(a) C_L vs α.

Figure 27.– Aileron effectiveness on the oblique wing with intermediate bend: $\Lambda = 45°, M = 1.1$.

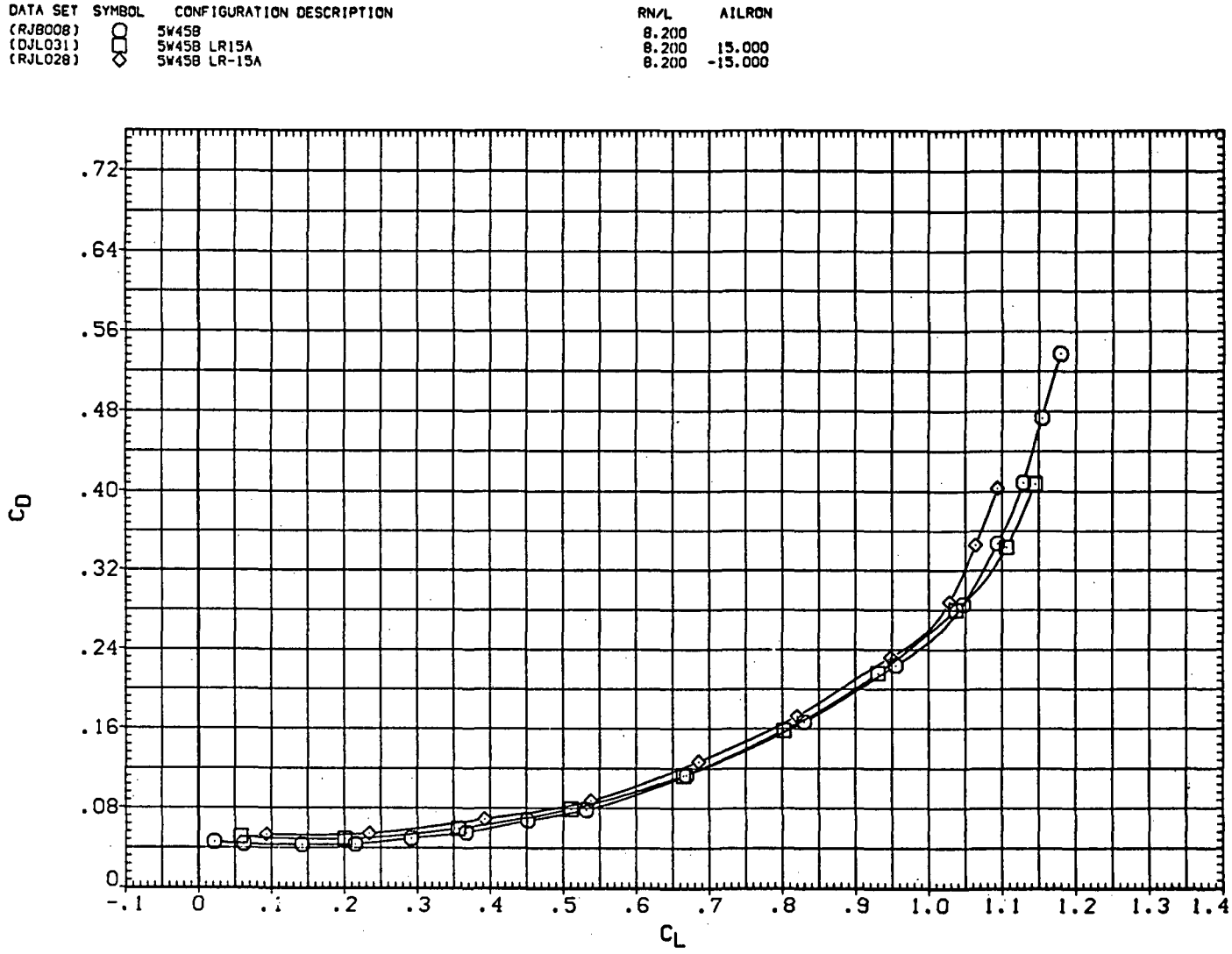

(b) C_D vs C_L

Figure 27.– Continued.

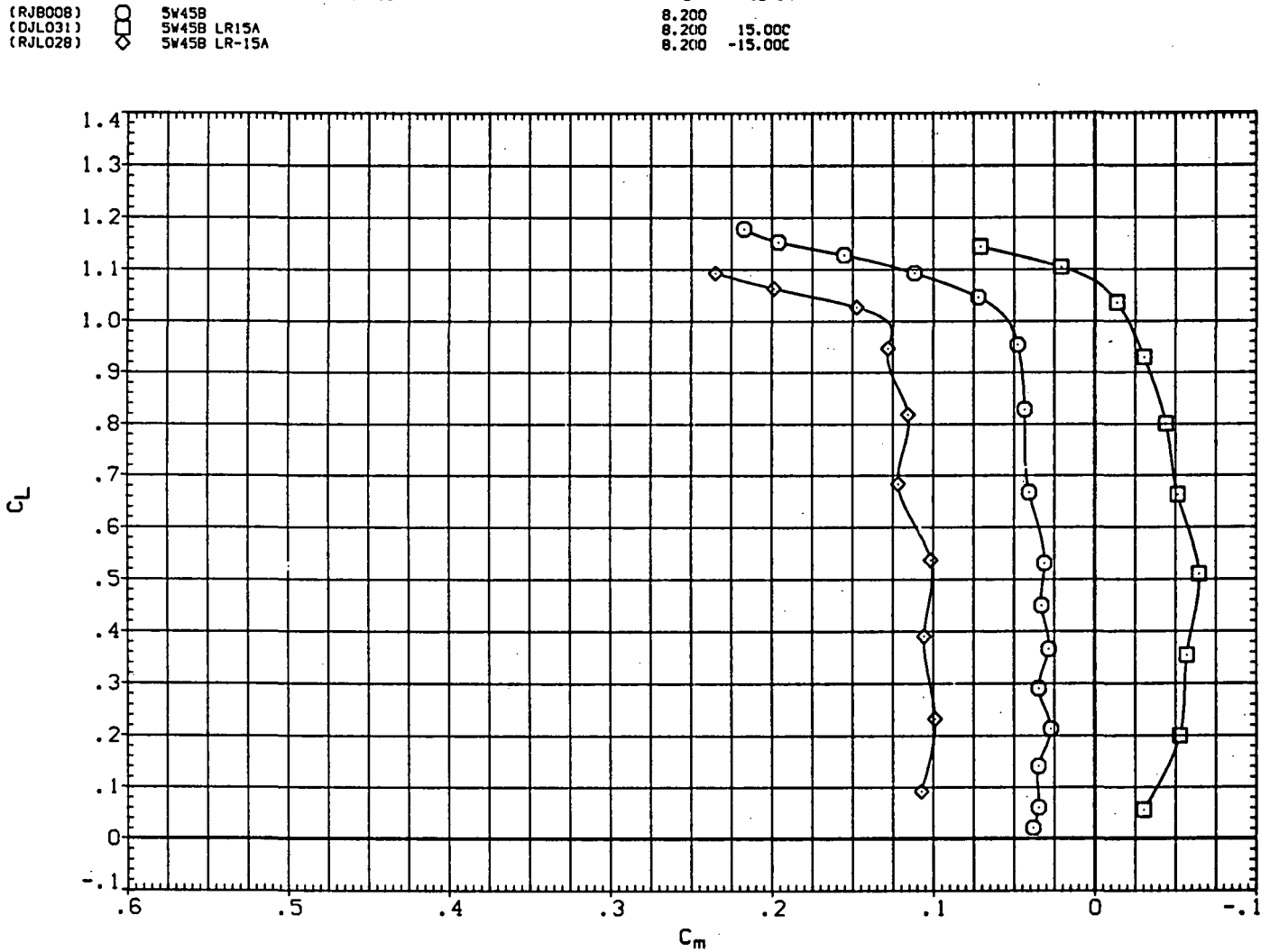

(c) C_L vs C_m

Figure 27.– Continued.

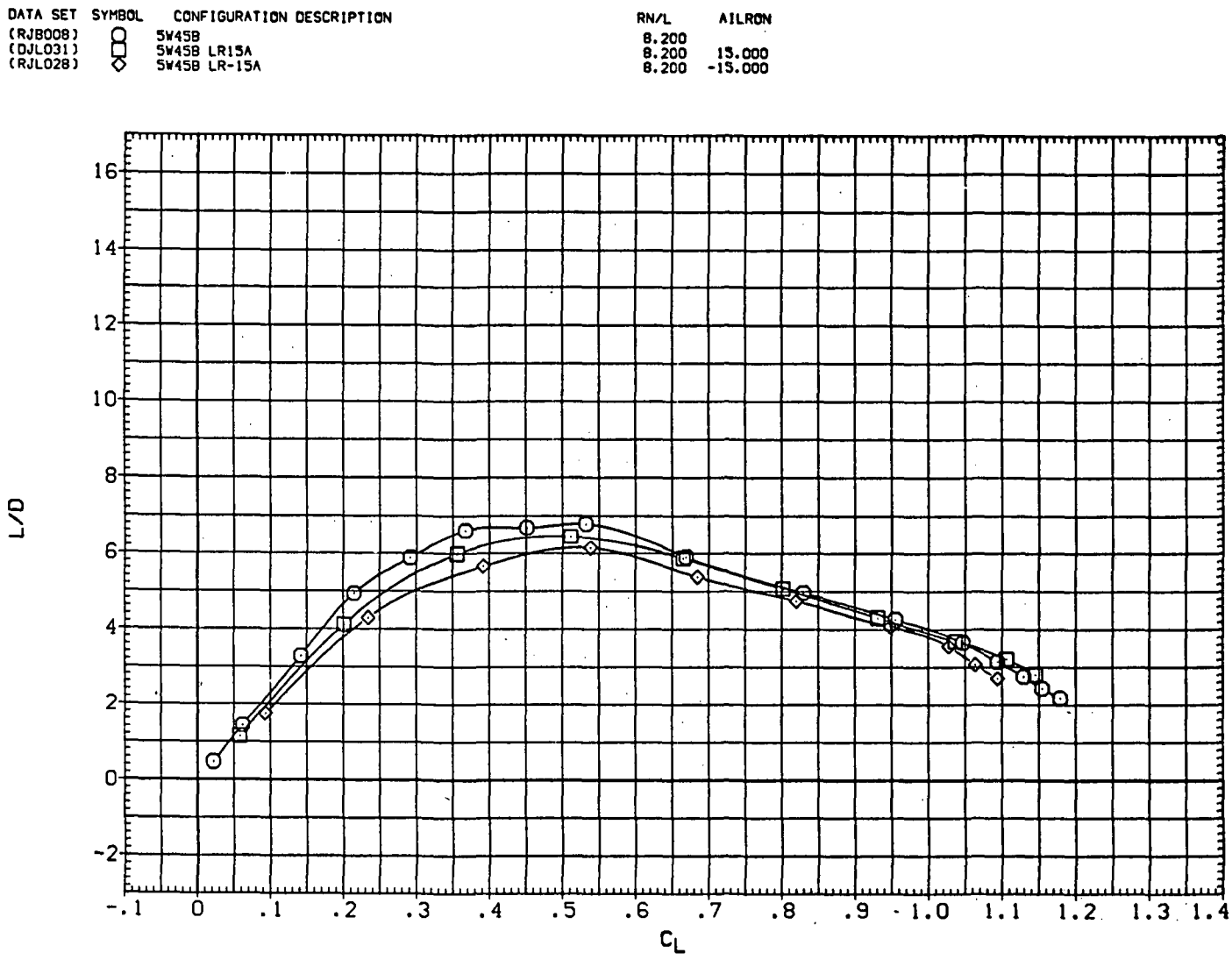

(d) L/D vs C_L

Figure 27.– Continued.

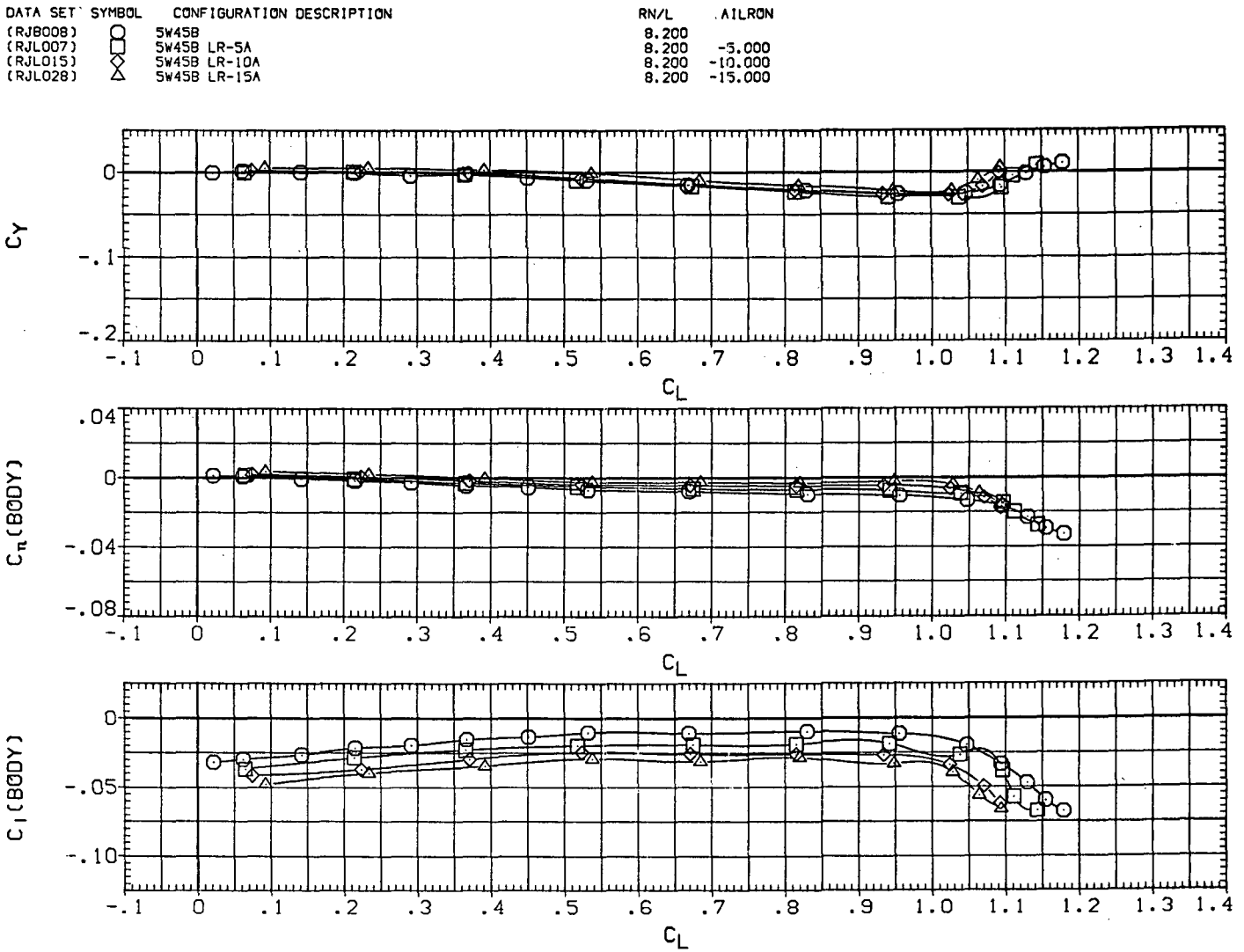

(e) C_Y, C_n, and C_l vs C_L (negative $\Delta\delta_a$'s).

Figure 27.– Continued.

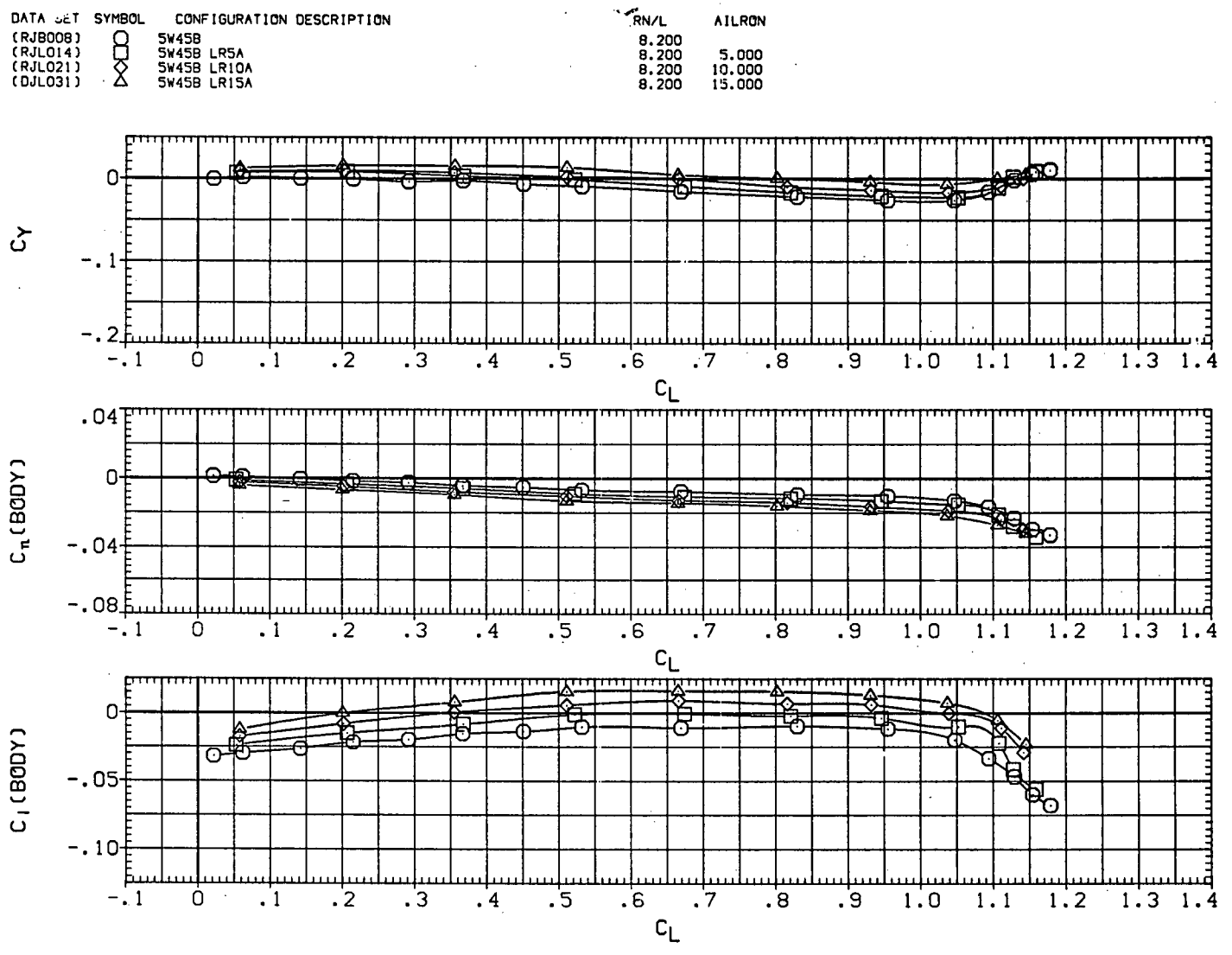

(f) C_Y, C_n, and C_l vs C_L (positive $\Delta\delta_a$'s).

Figure 27.– Concluded.

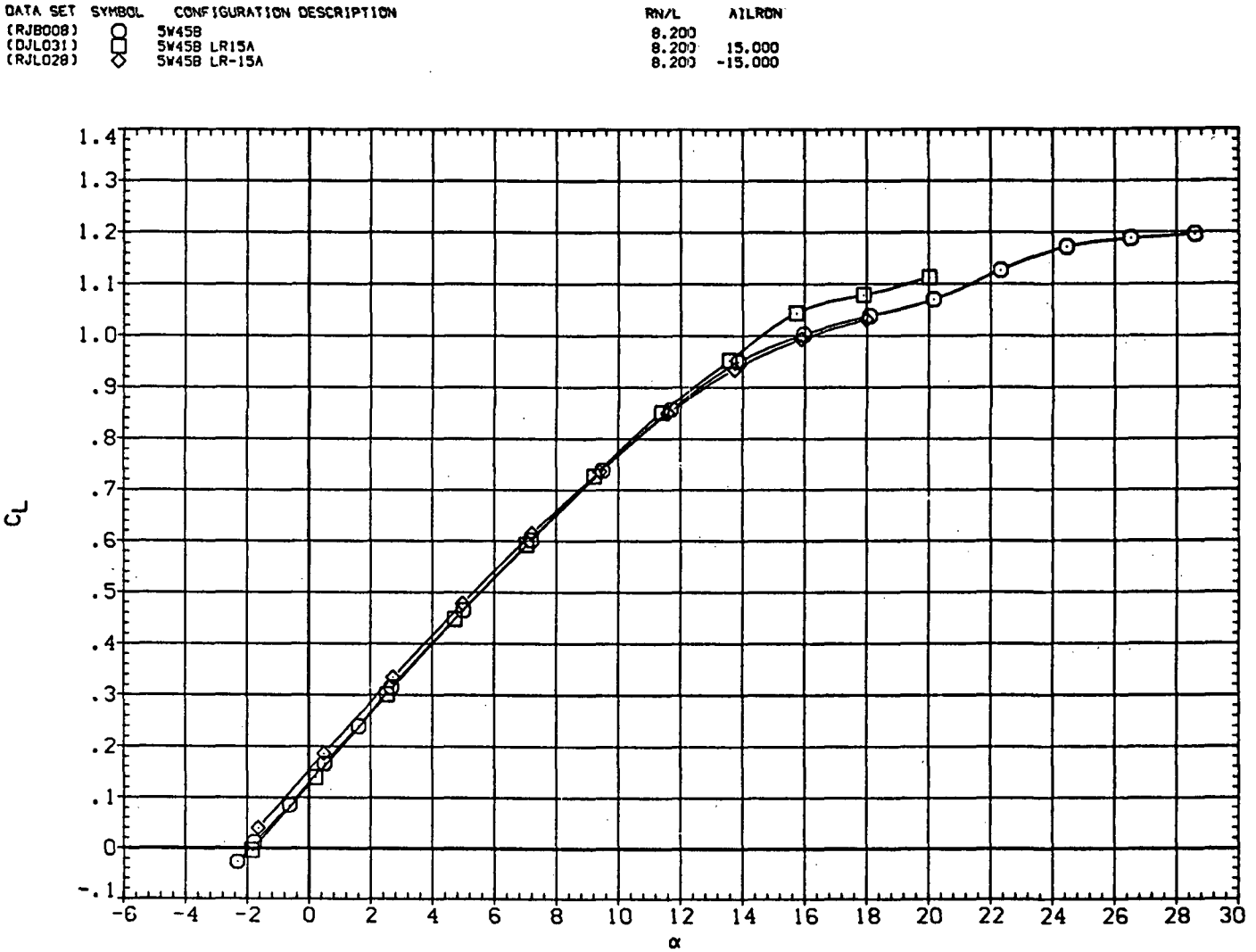

(a) C_L vs α

Figure 28.– Aileron effectiveness on the oblique wing with intermediate bend: $\Lambda = 45°, M = 1.2$.

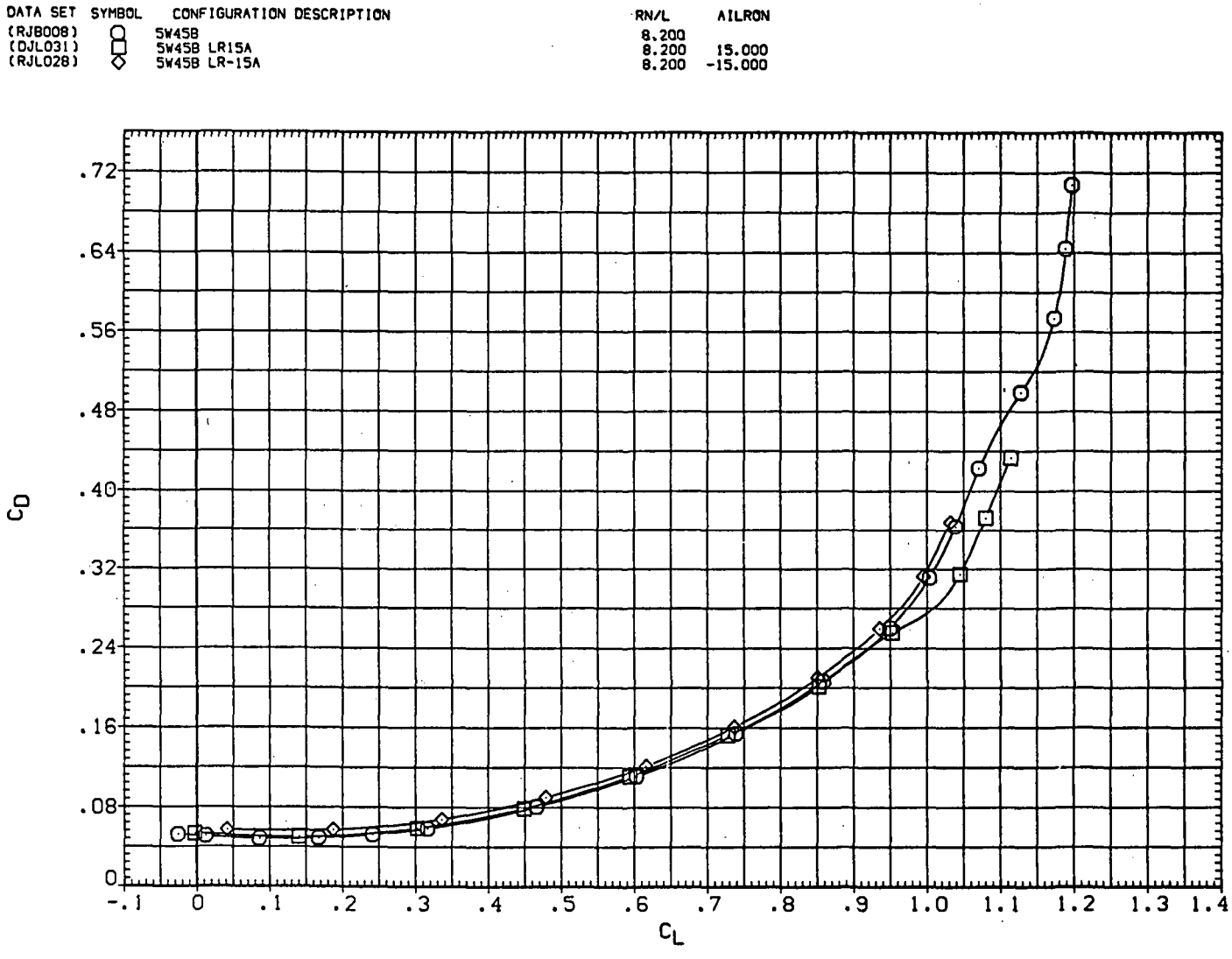

(b) C_D vs C_L

Figure 28.– Continued.

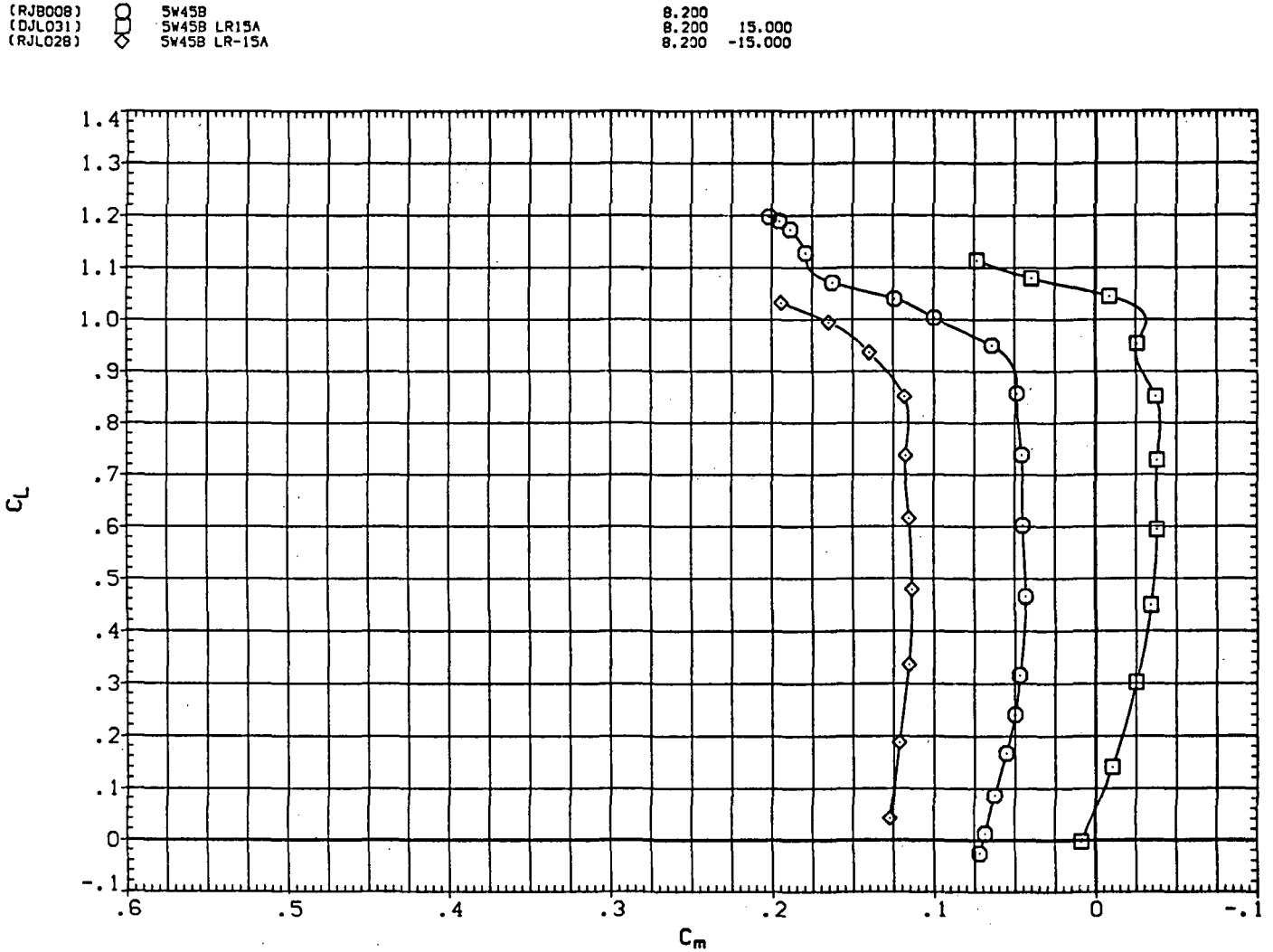

(c) C_L vs C_m

Figure 28.– Continued.

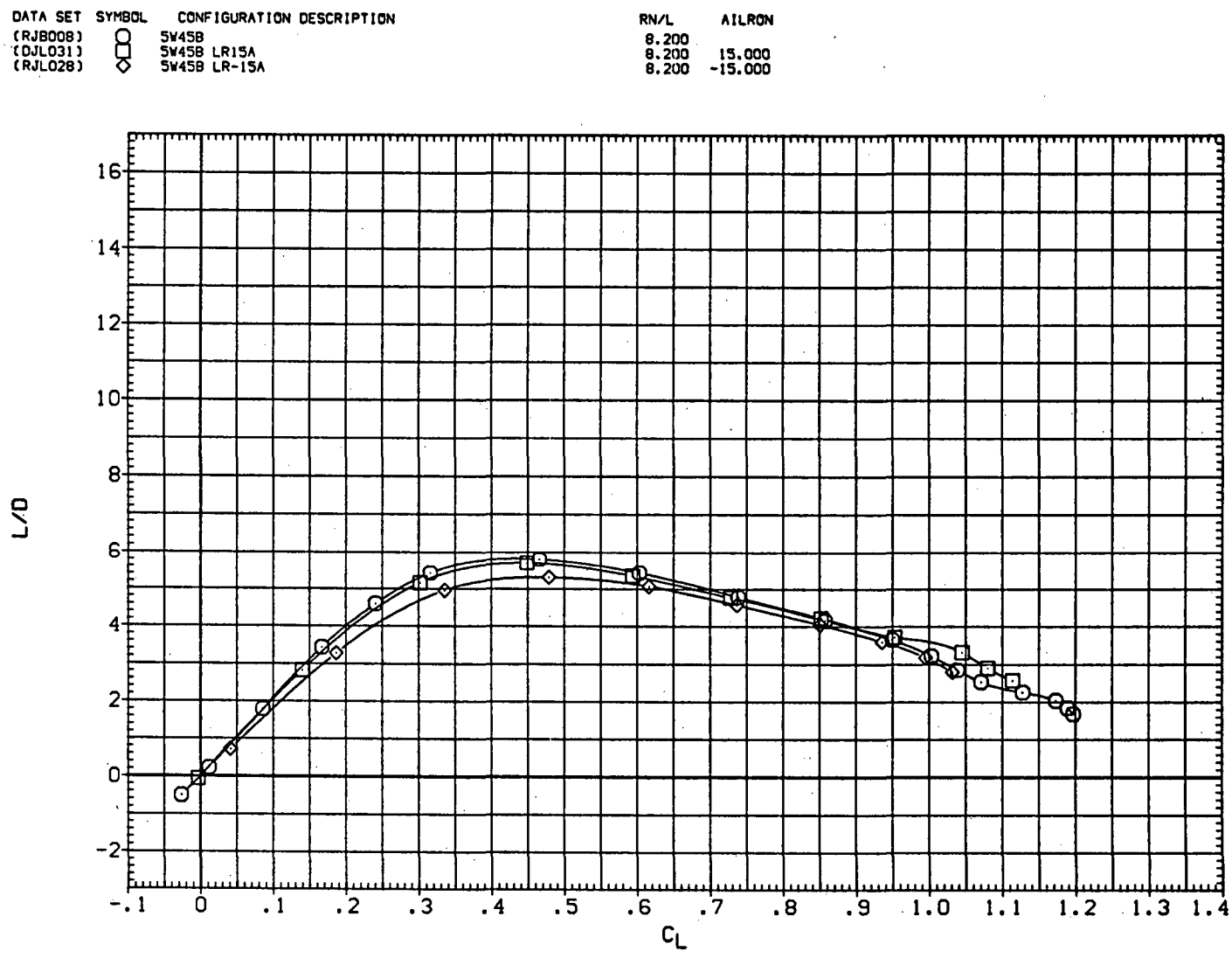

(d) L/D vs C_L

Figure 28.– Continued.

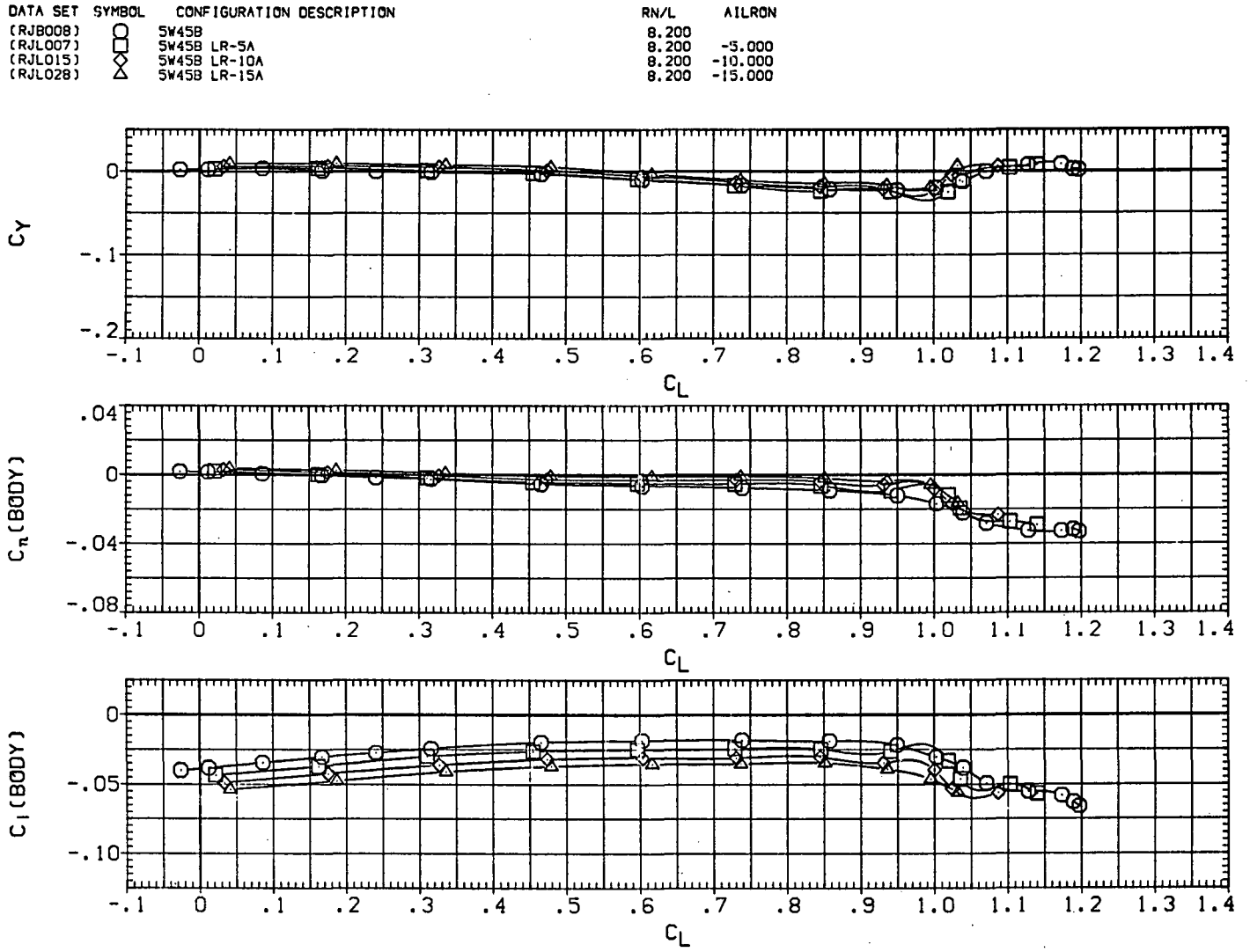

(e) C_Y, C_n, and C_l vs C_L (negative $\Delta\delta_a$'s).

Figure 28.– Continued.

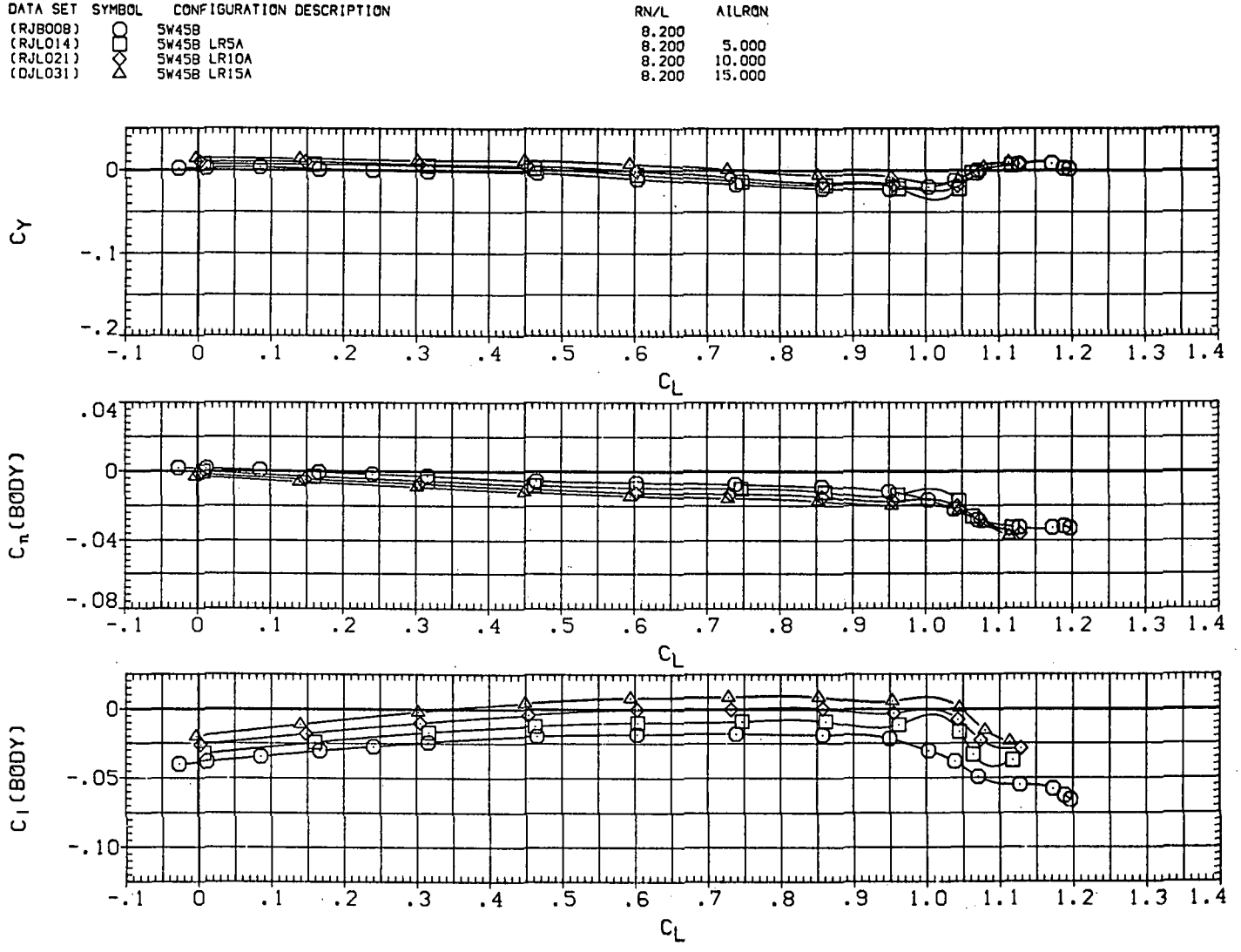

(f) C_Y, C_n, and C_l vs C_L (positive $\Delta\delta_a$'s).

Figure 28.– Concluded.

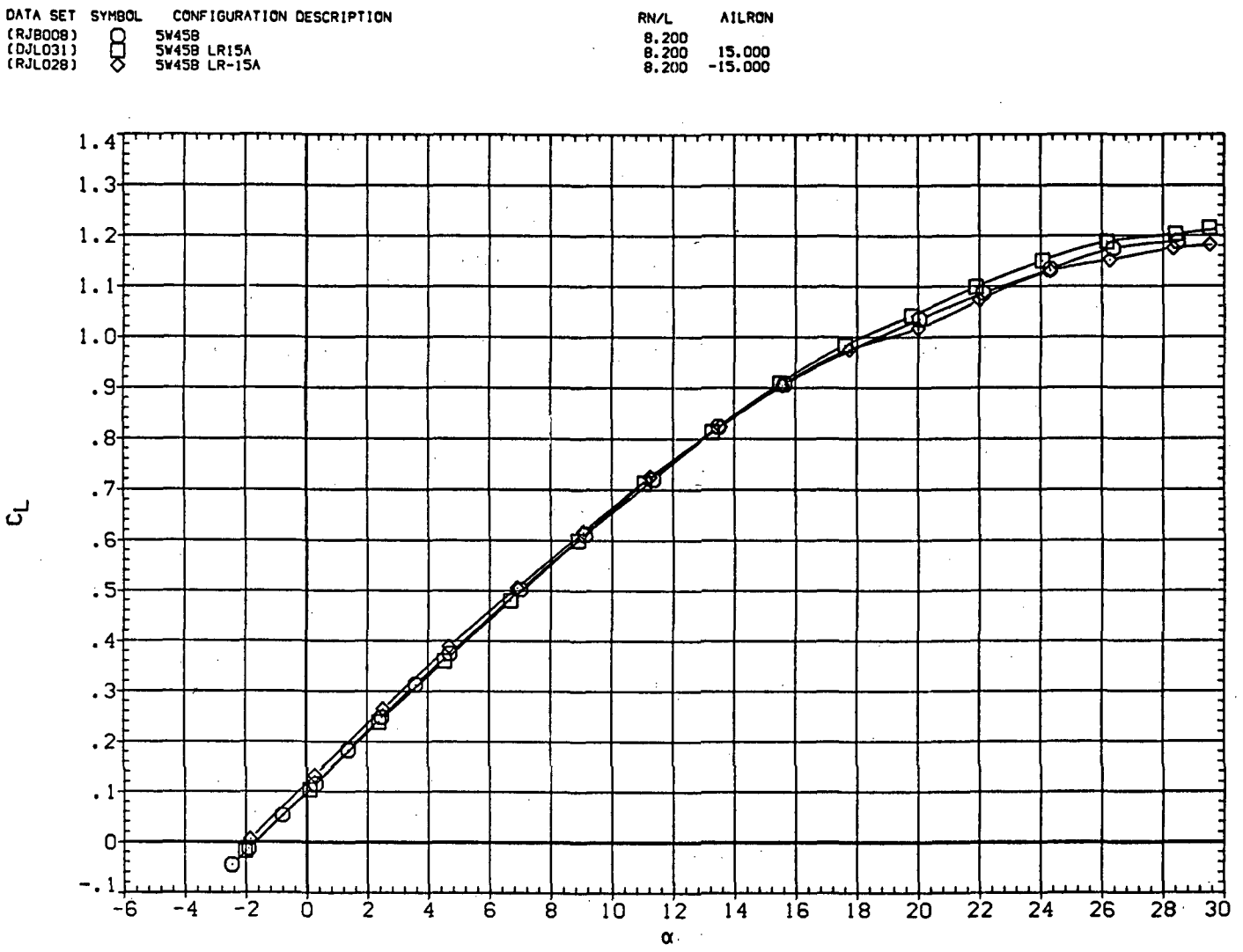

(a) C_L vs α

Figure 29.– Aileron effectiveness on the oblique wing with intermediate bend: $\Lambda = 45°, M = 1.4$.

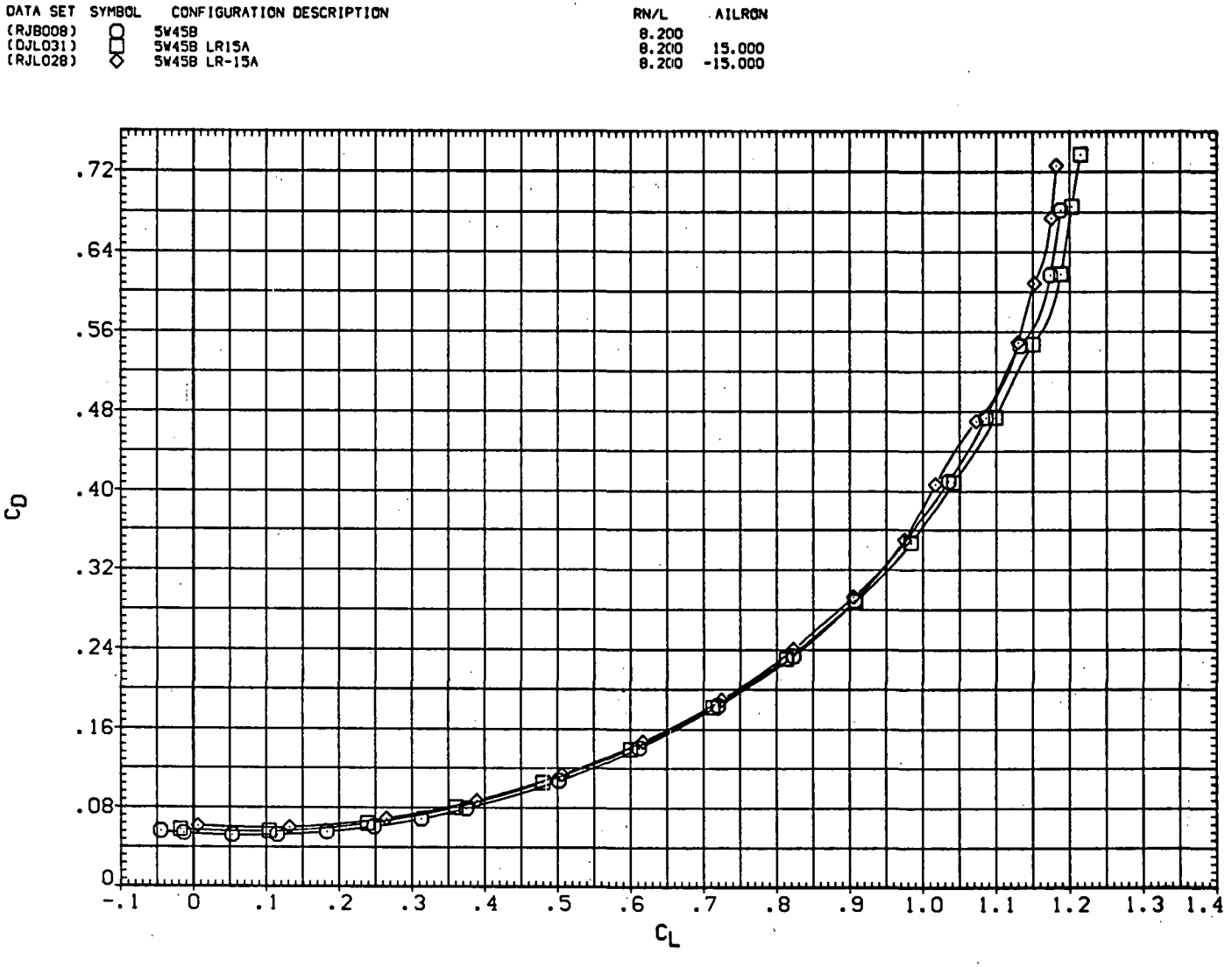

(b) C_D vs C_L

Figure 29.—Continued.

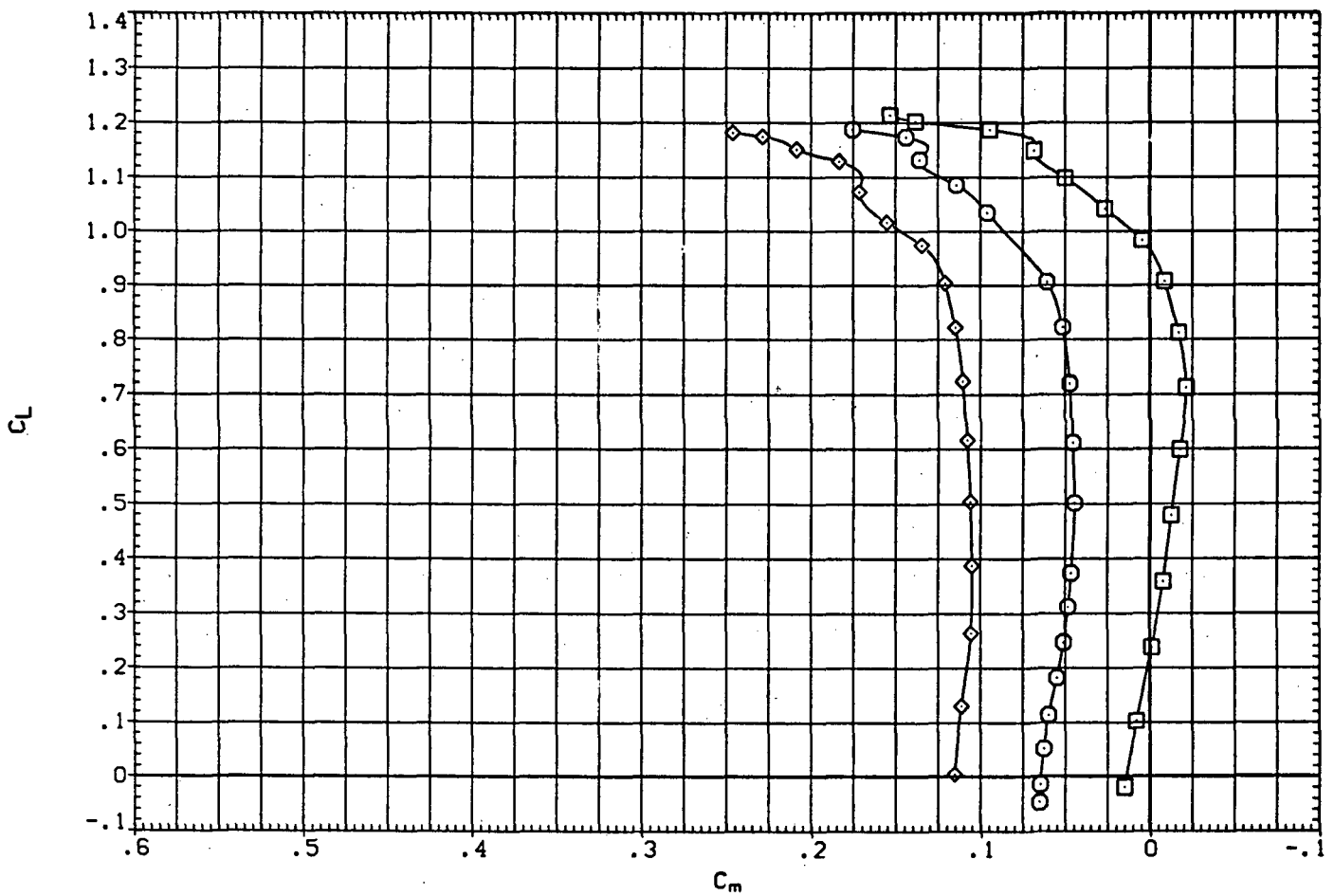

(c) C_L vs C_m

Figure 29.– Continued.

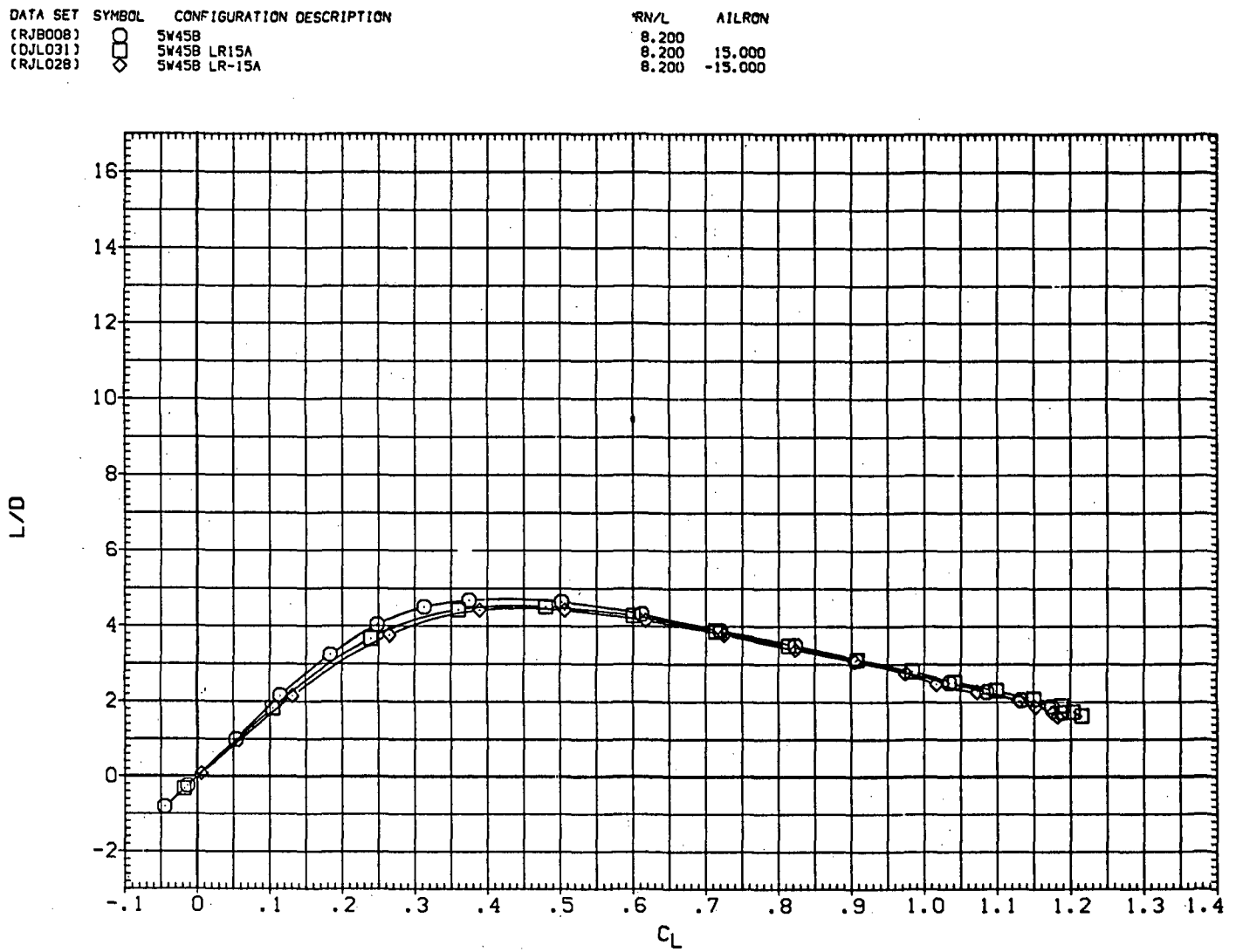

(d) L/D vs C_L

Figure 29.– Continued.

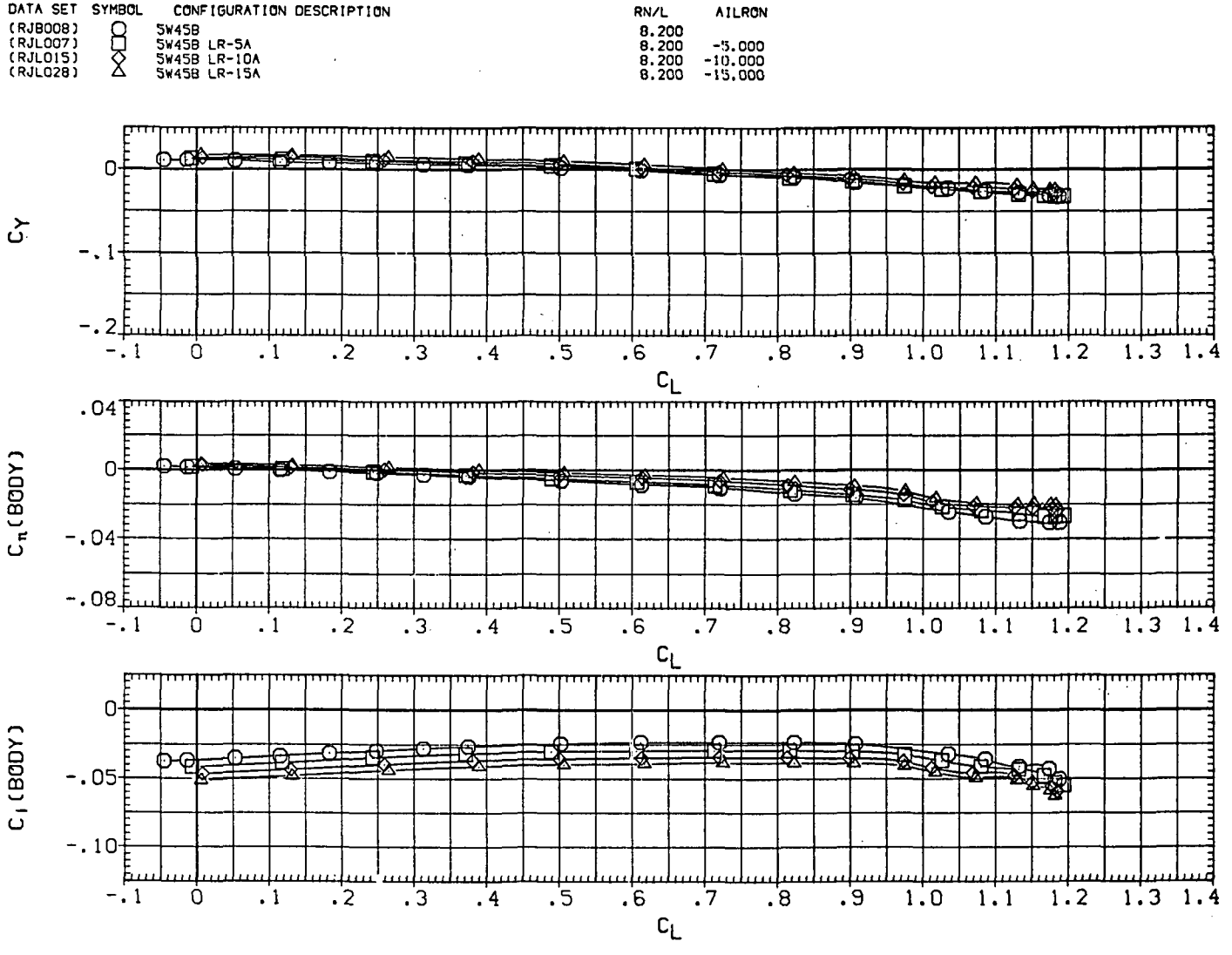

(e) C_Y, C_n, and C_l vs C_L (negative $\Delta\delta_a$'s).

Figure 29.– Continued.

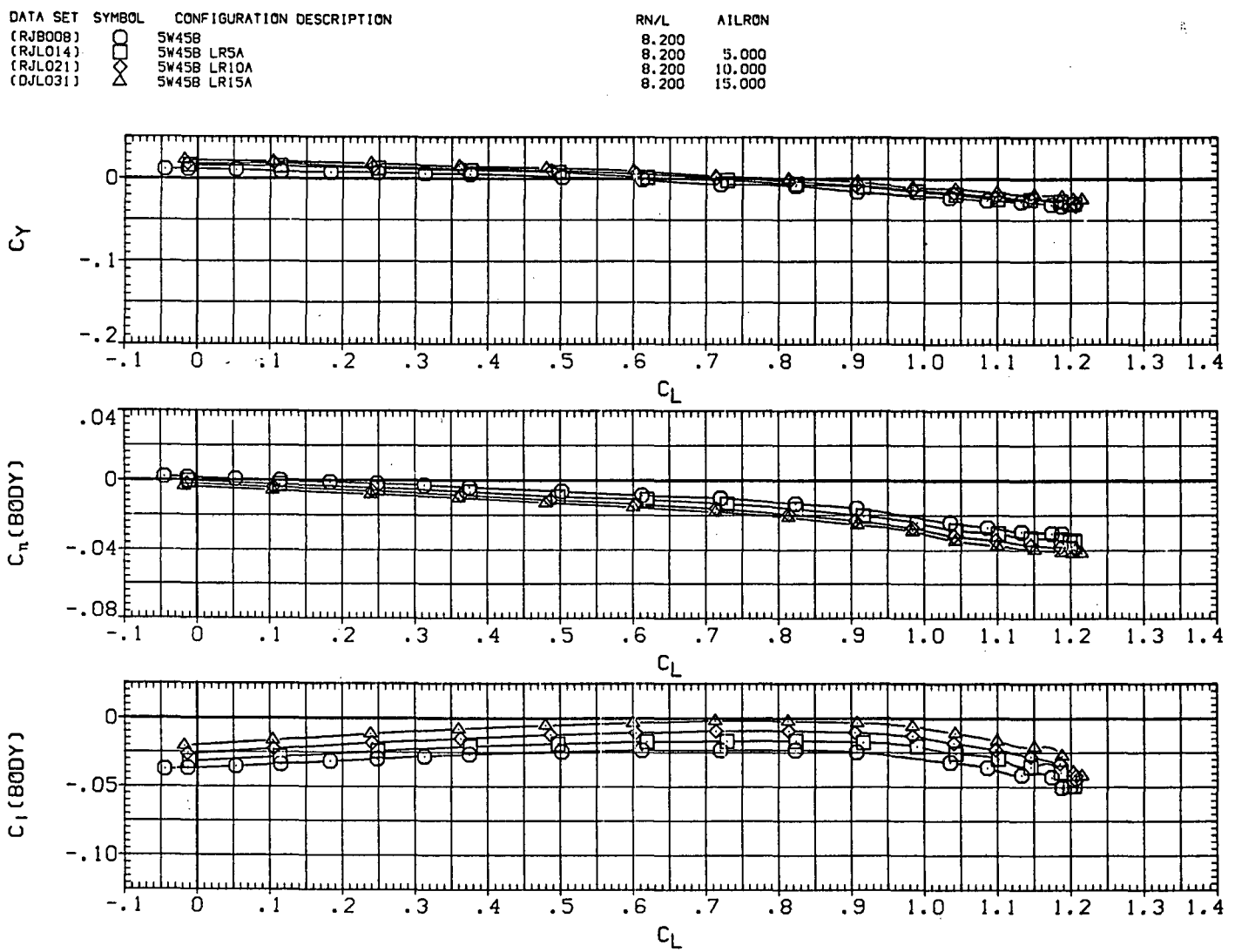

(f) C_Y, C_n, and C_l vs C_L (positive $\Delta\delta_a$'s).

Figure 29.– Concluded.

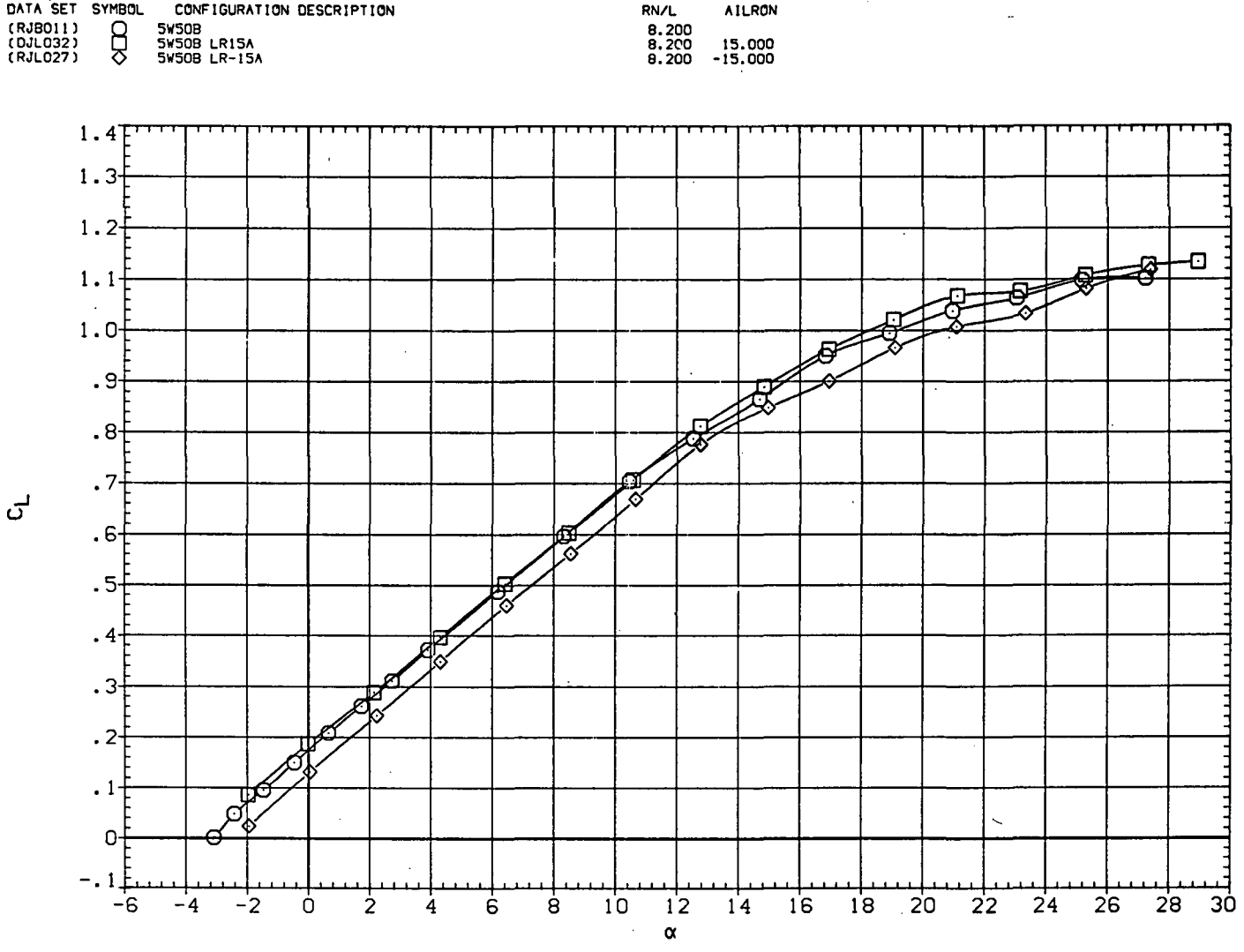

(a) C_L vs α

Figure 30.– Aileron effectiveness on the oblique wing with intermediate bend: $\Lambda = 50°, M = 0.60$.

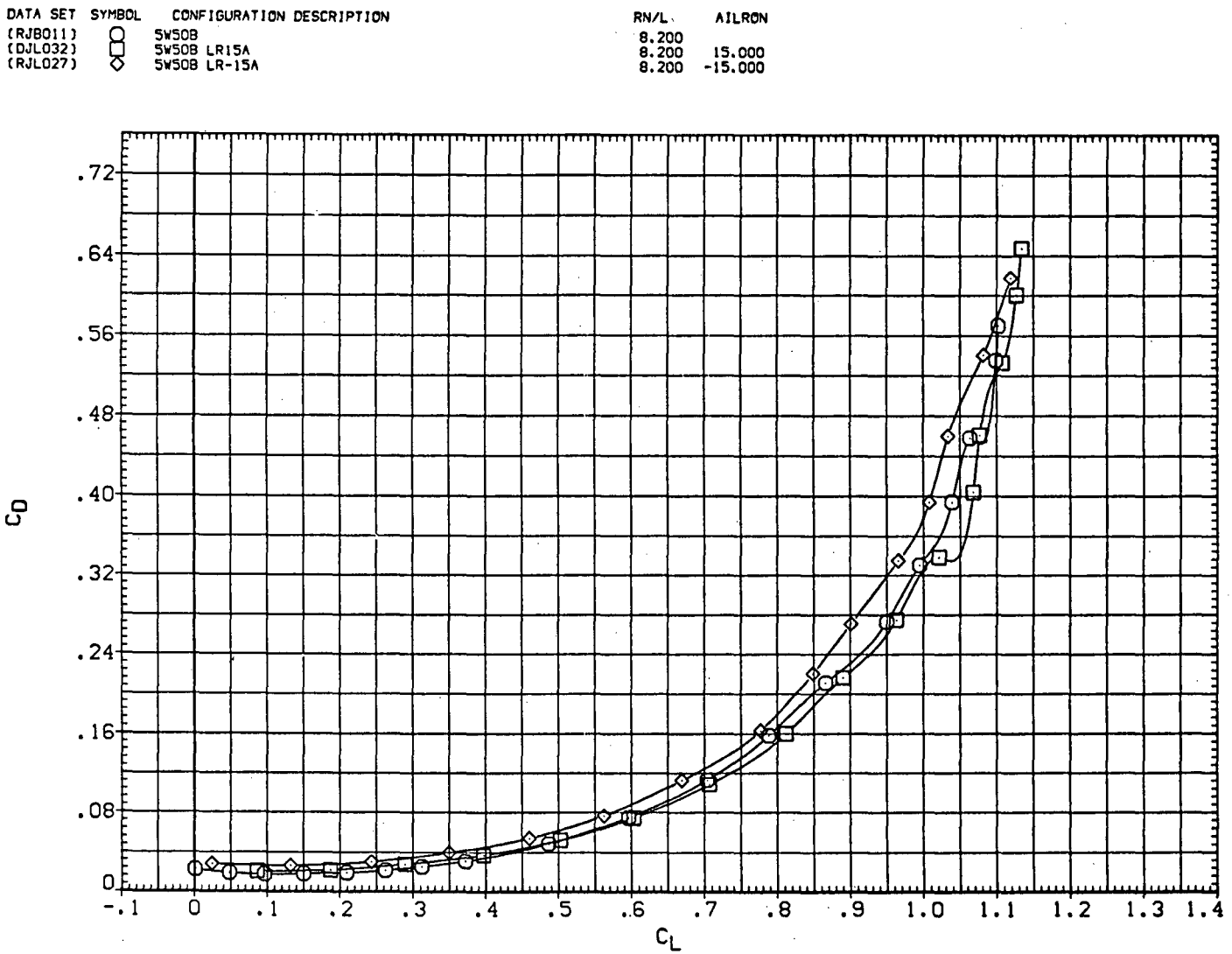

(b) C_D vs C_L

Figure 30.– Continued.

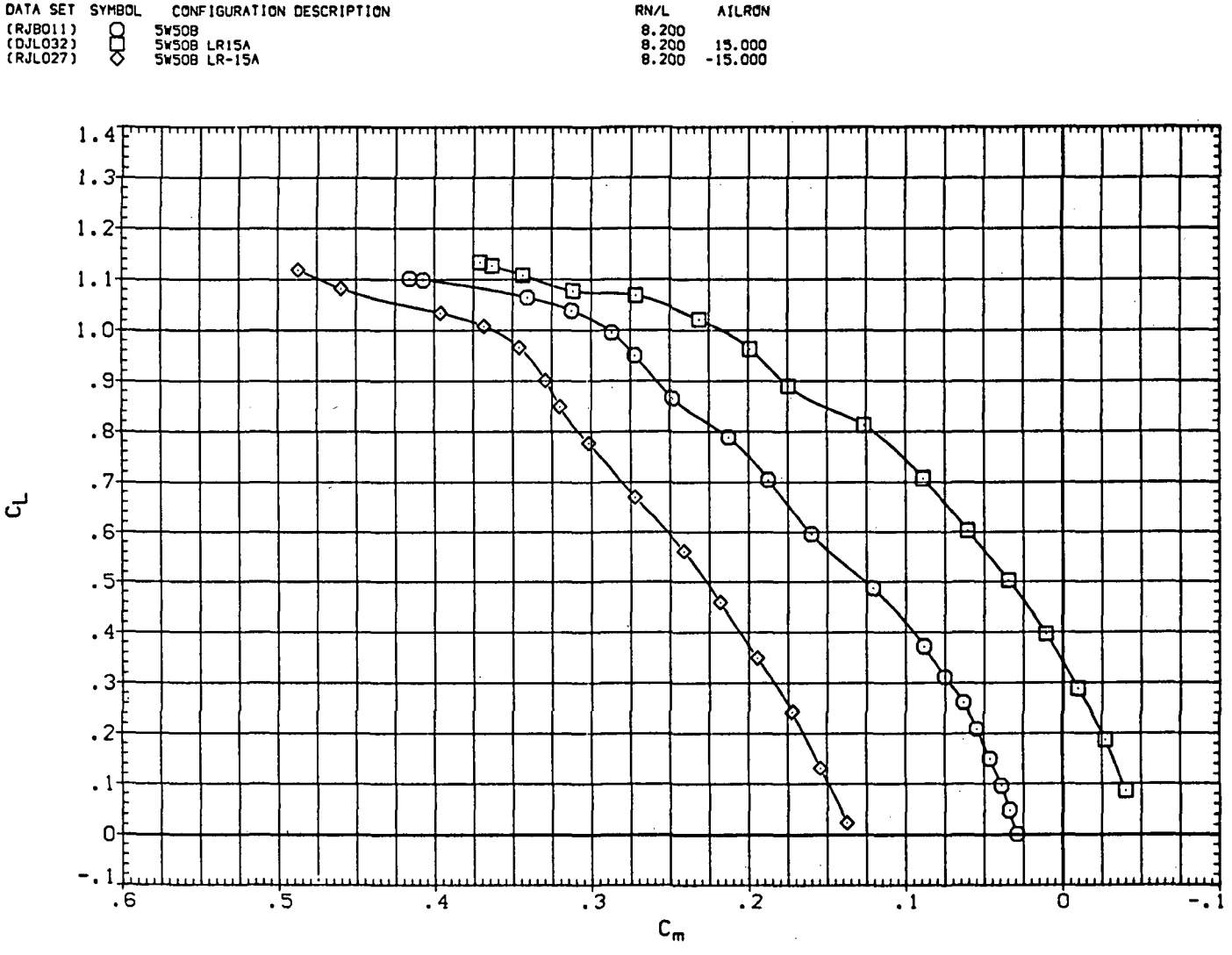

(c) C_L vs C_m

Figure 30.– Continued.

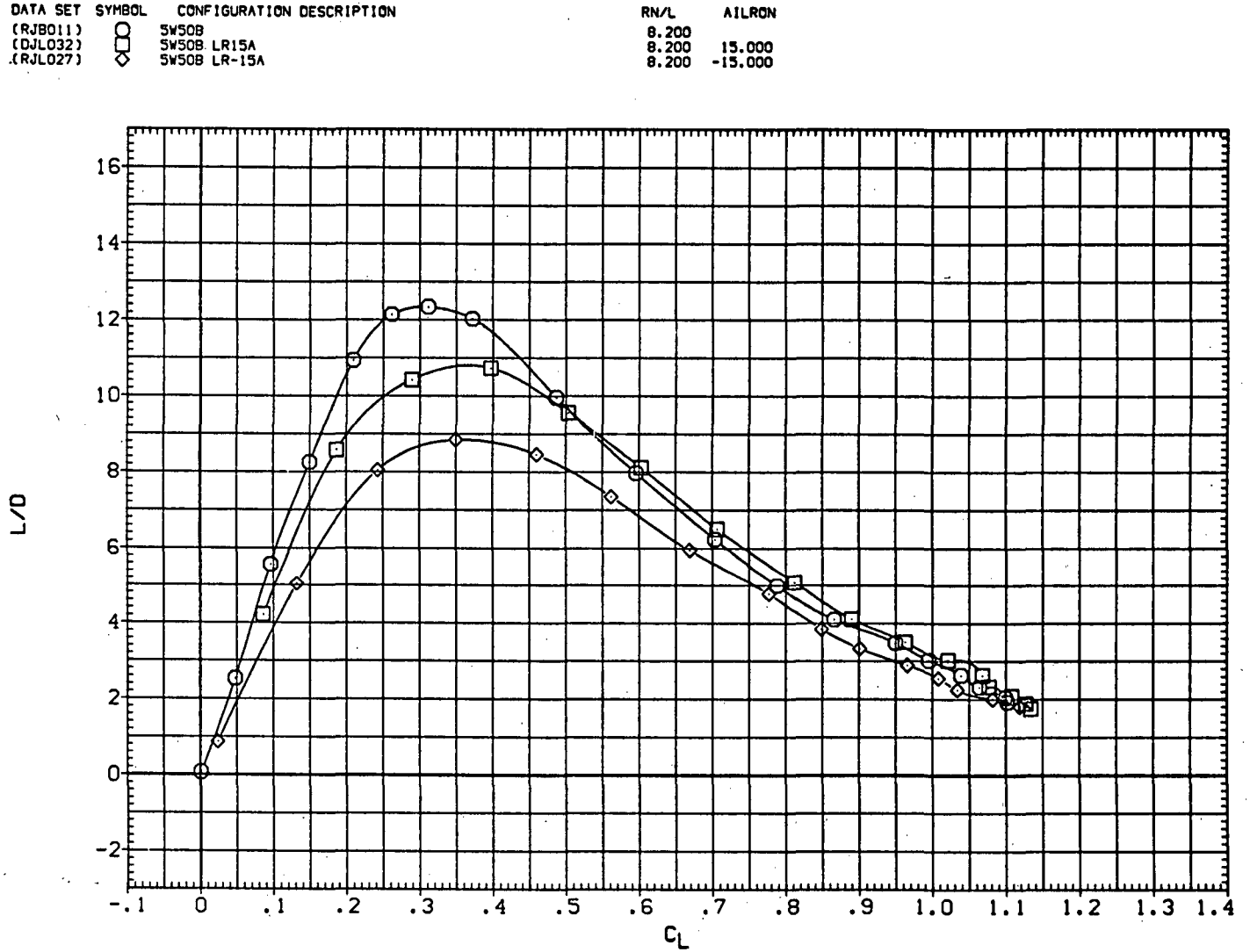

(d) L/D vs C_L

Figure 30.– Continued.

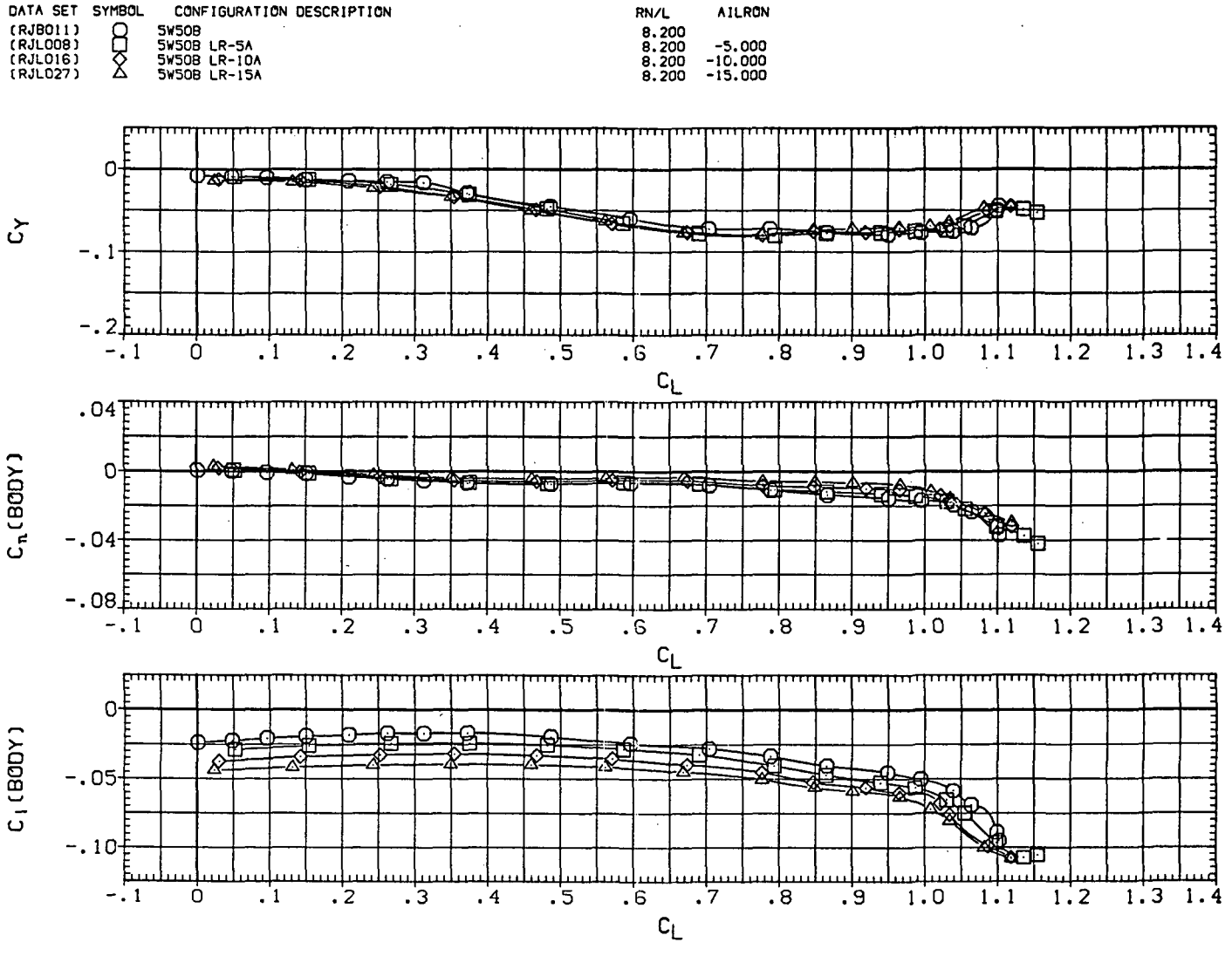

(e) C_Y, C_n, and C_l vs C_L (negative $\Delta\delta_a$'s).

Figure 30.– Continued.

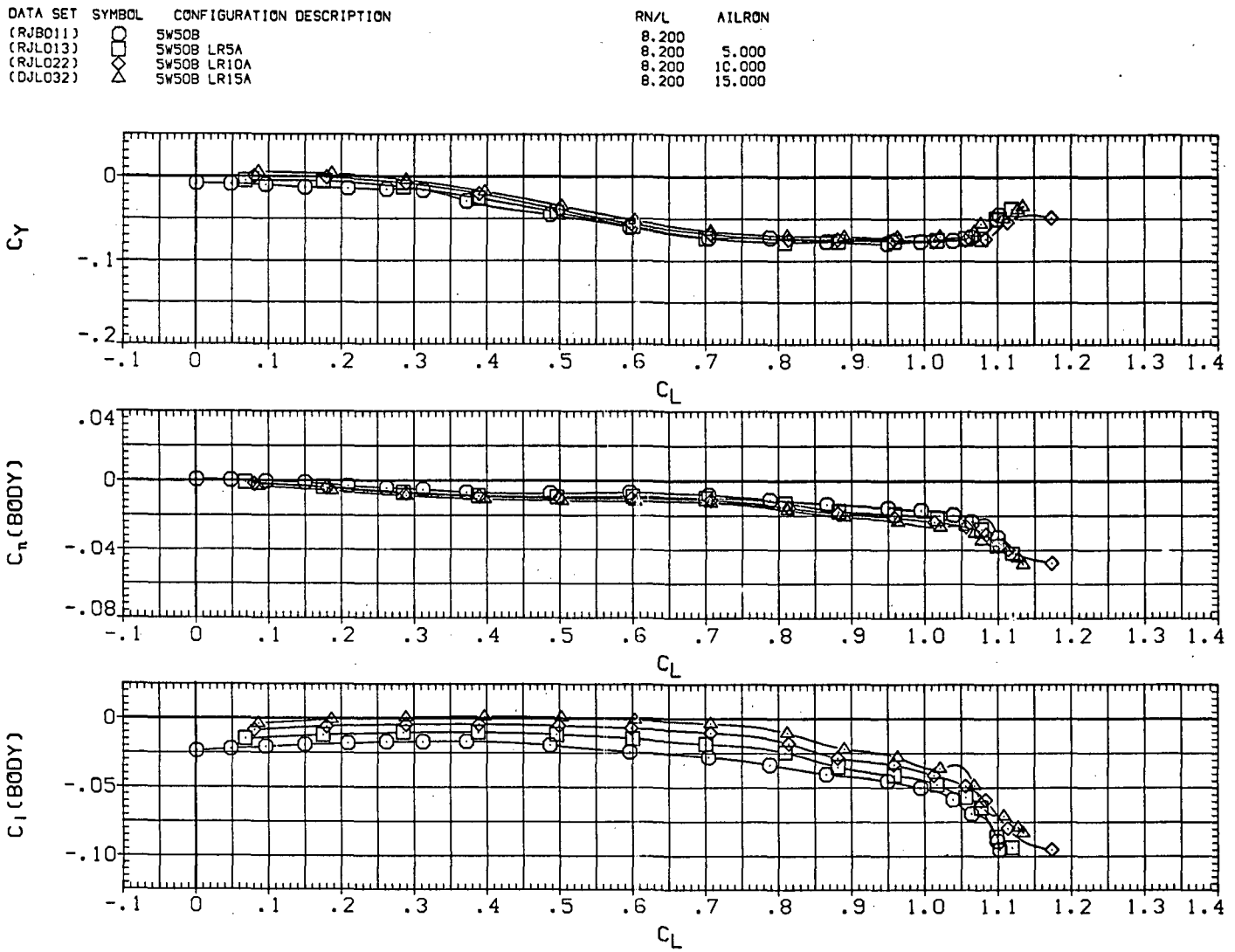

(f) C_Y, C_n, and C_l vs C_L (positive $\Delta\delta_a$'s).

Figure 30.– Concluded.

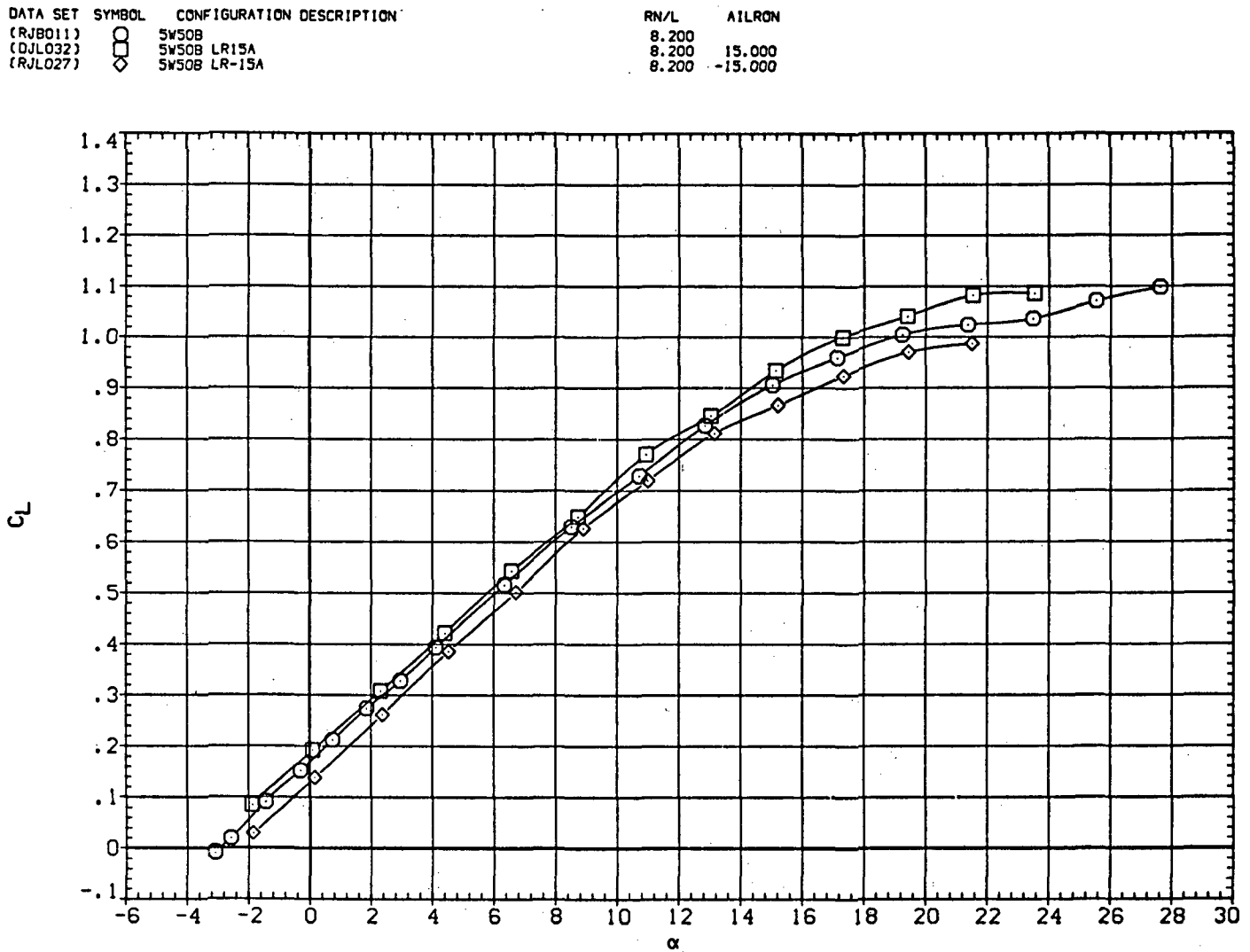

(a) C_L vs α

Figure 31.– Aileron effectiveness on the oblique wing with intermediate bend: $\Lambda = 50°, M = 0.80$.

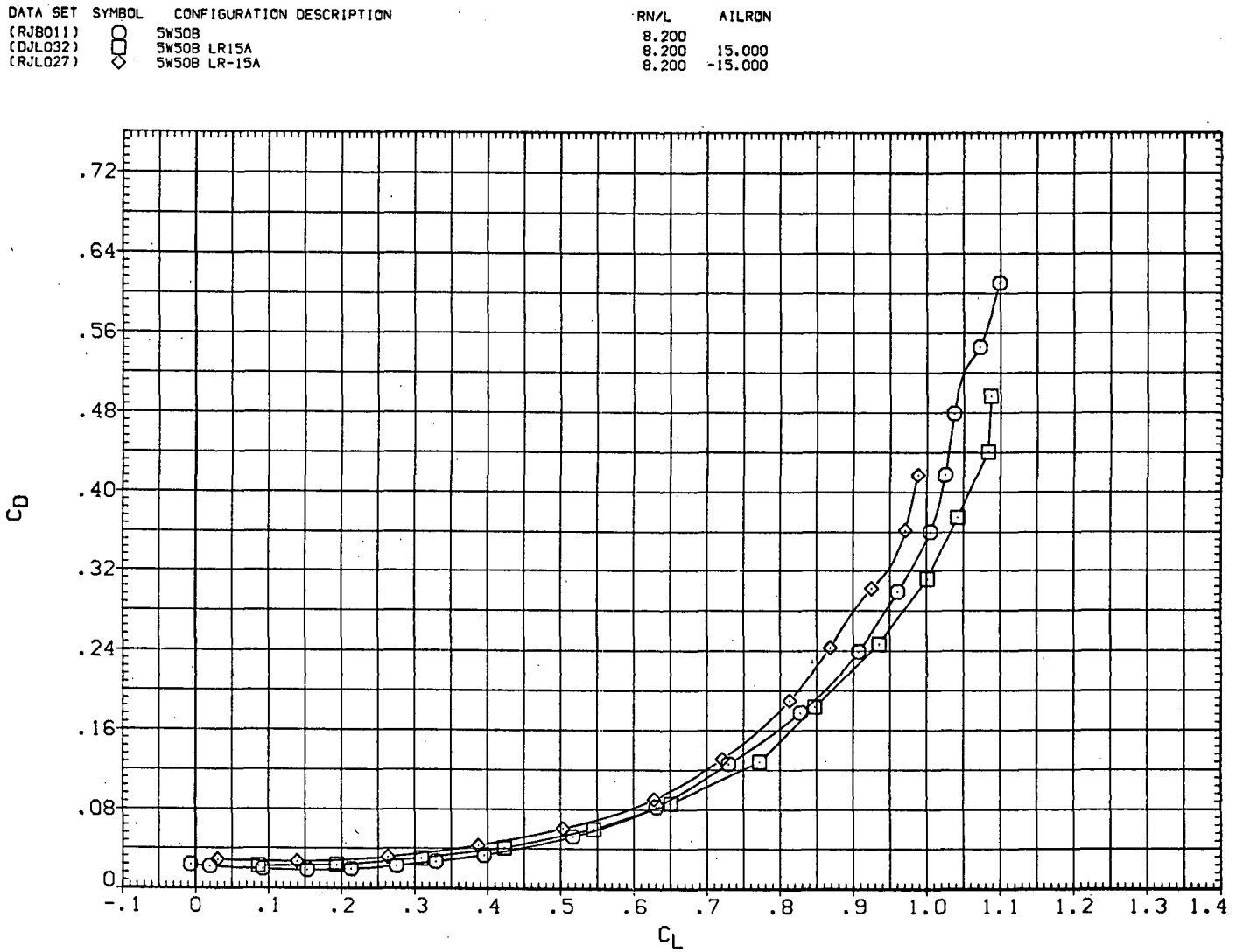

(b) C_D vs C_L

Figure 31.– Continued.

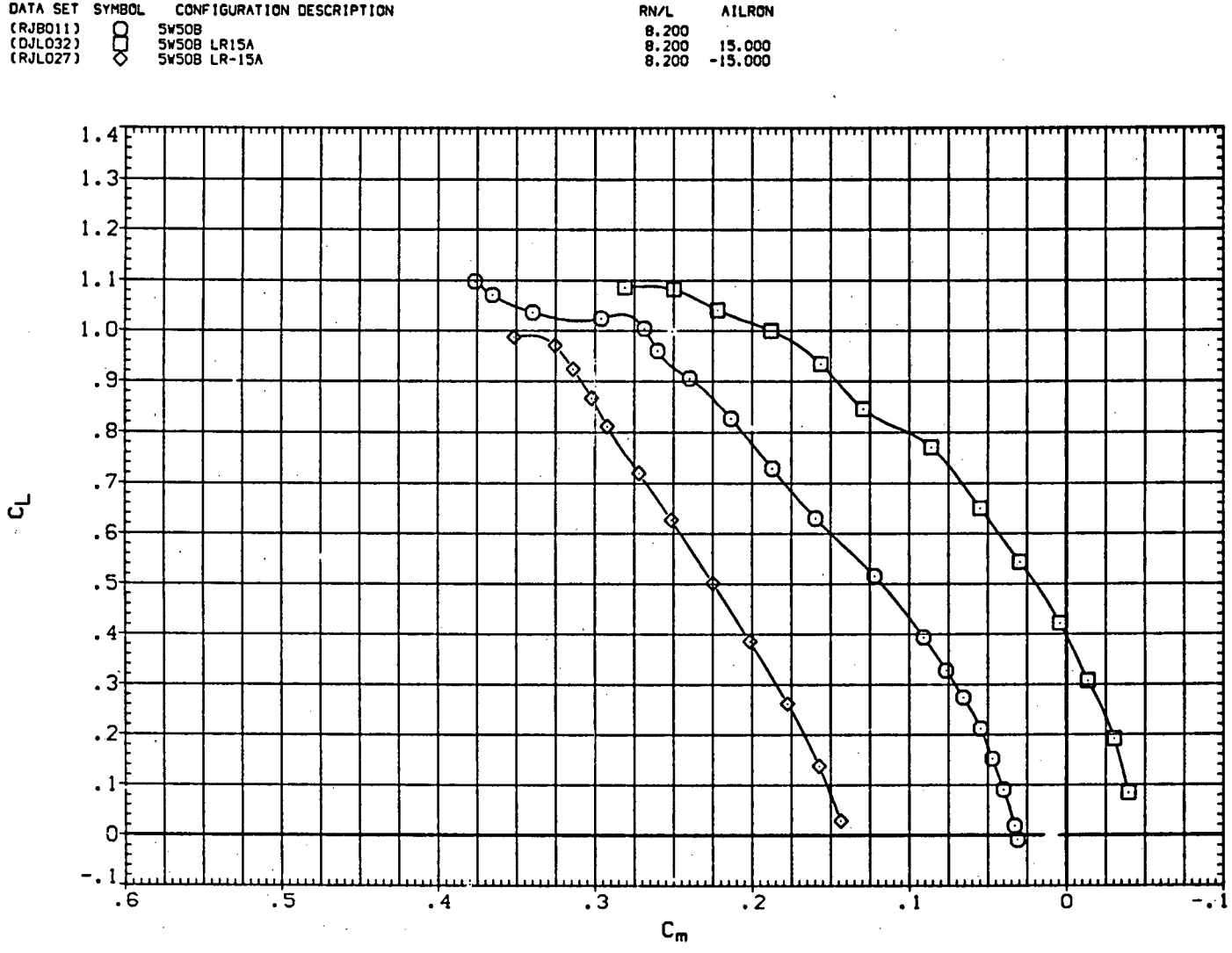

(c) C_L vs C_m

Figure 31.– Continued.

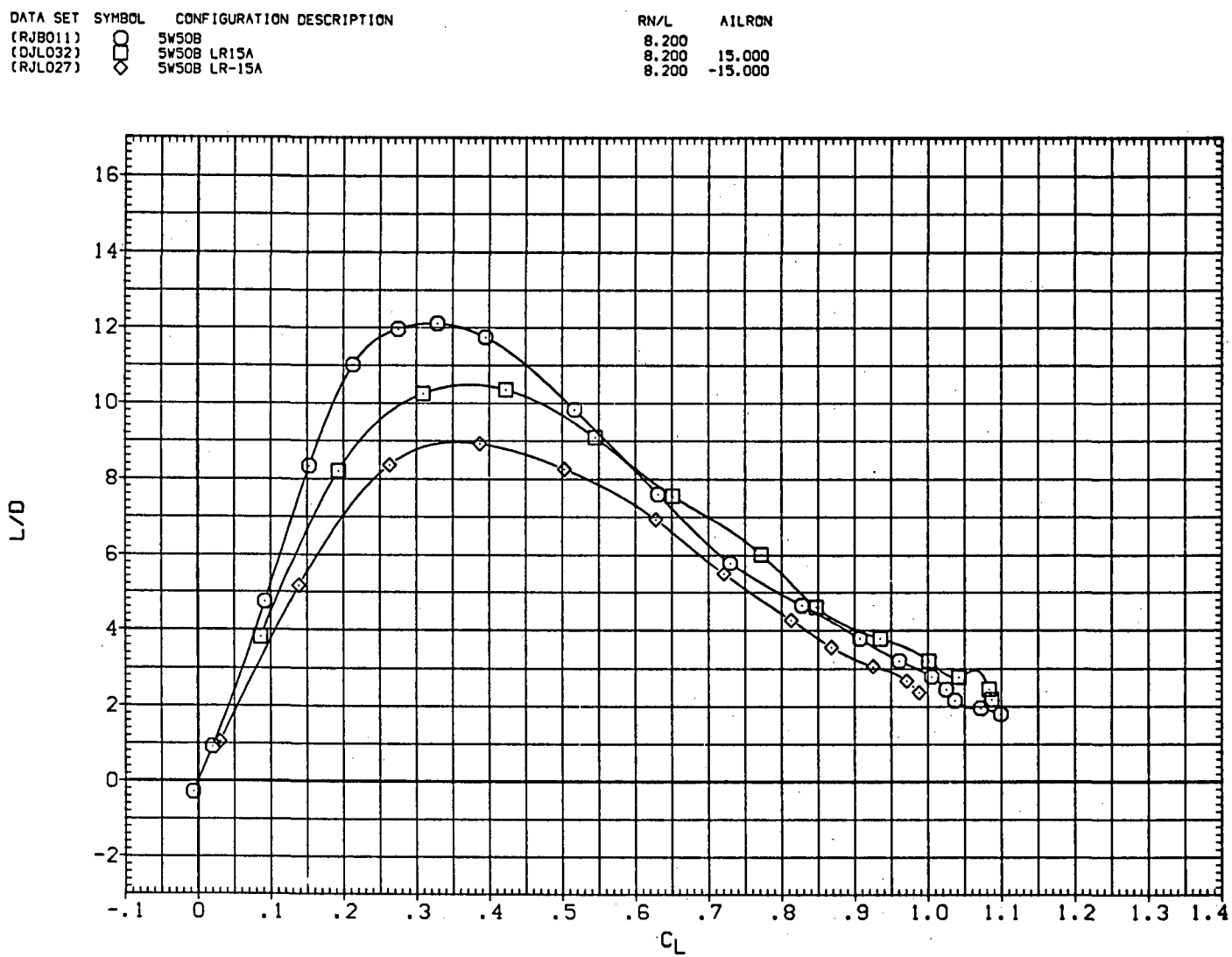

(d) L/D vs C_L

Figure 31.– Continued.

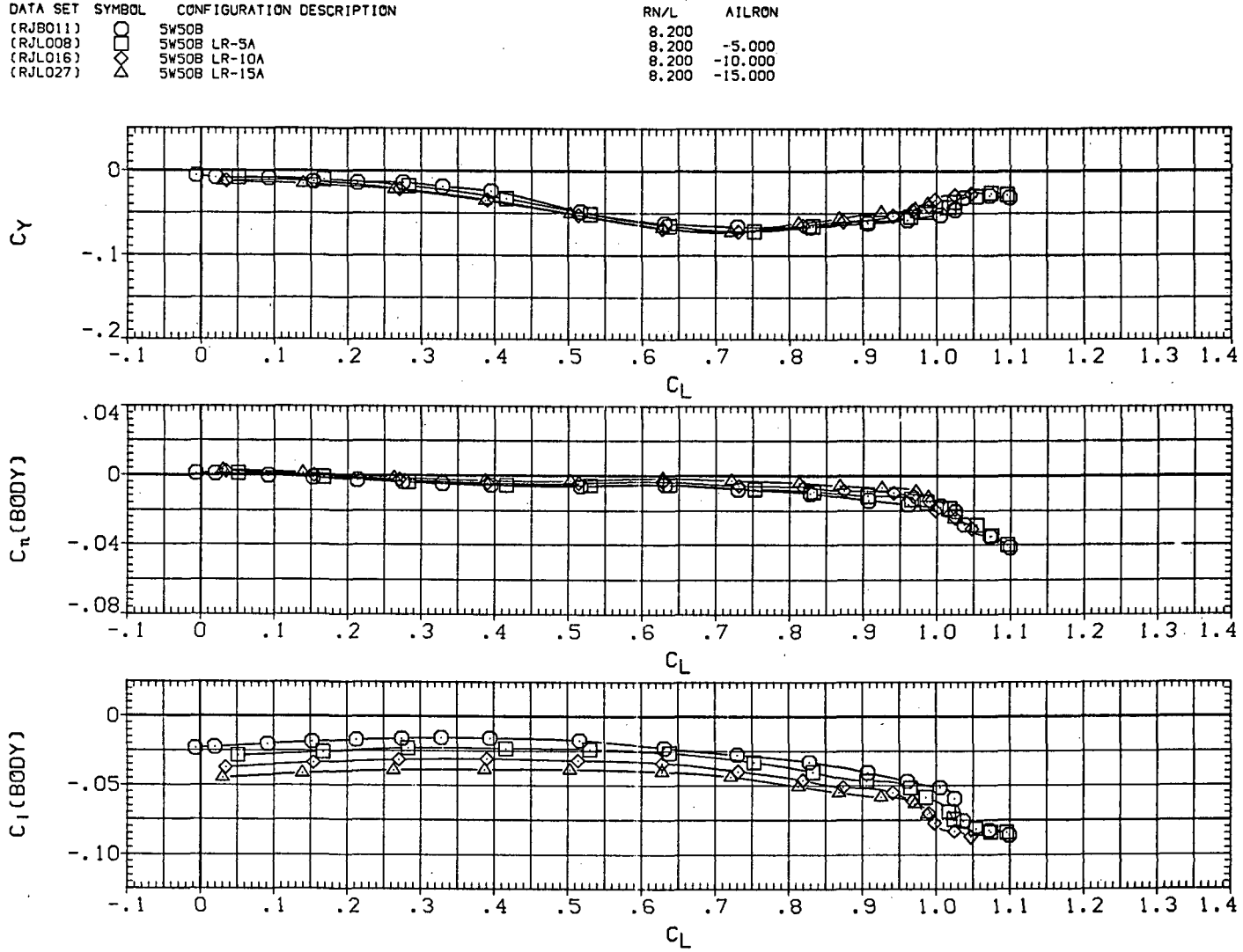

(e) C_Y, C_n, and C_l vs C_L (negative $\Delta\delta_a$'s).

Figure 31.– Continued.

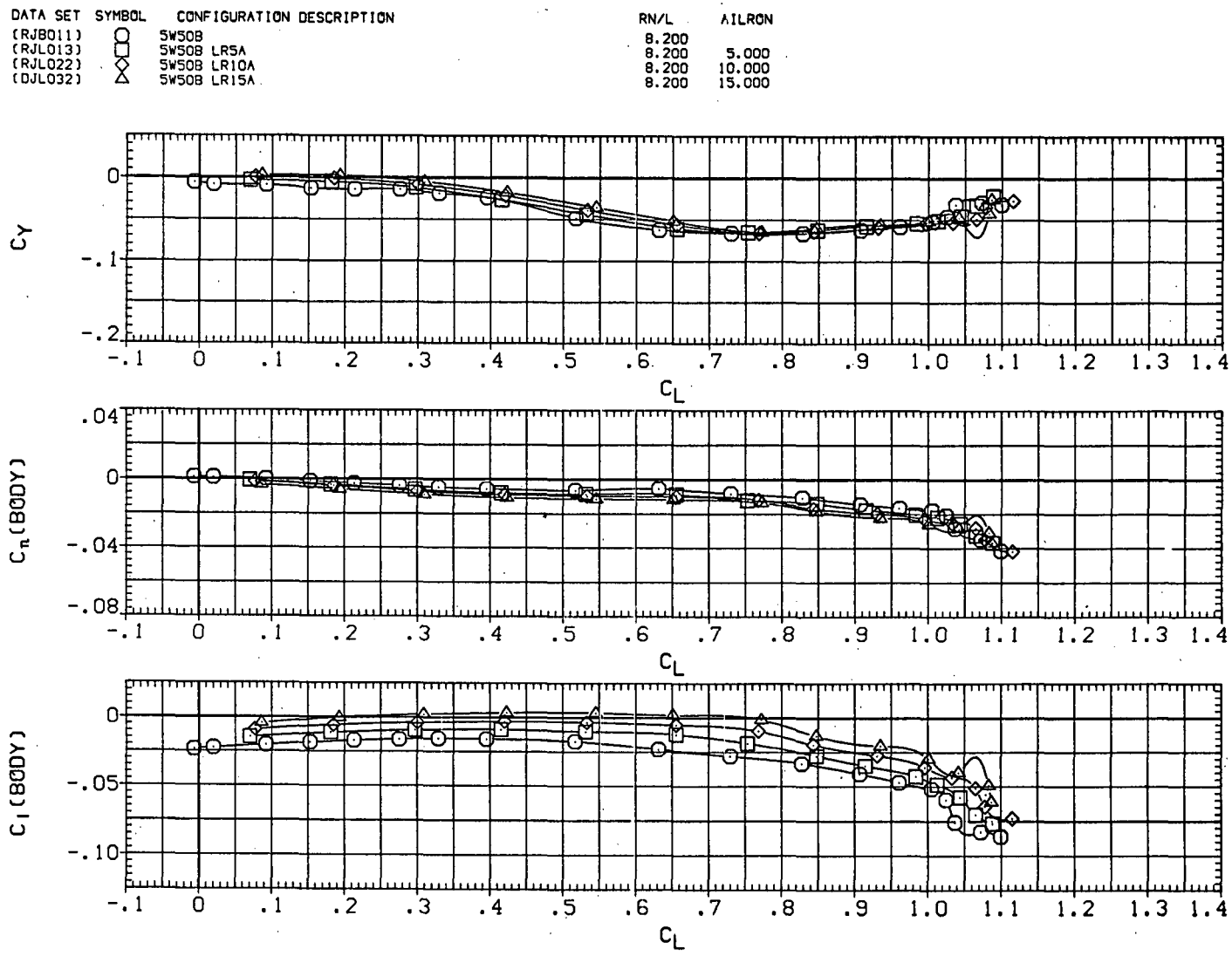

(f) C_Y, C_n, and C_l vs C_L (positive $\Delta\delta_a$'s).

Figure 31.– Concluded.

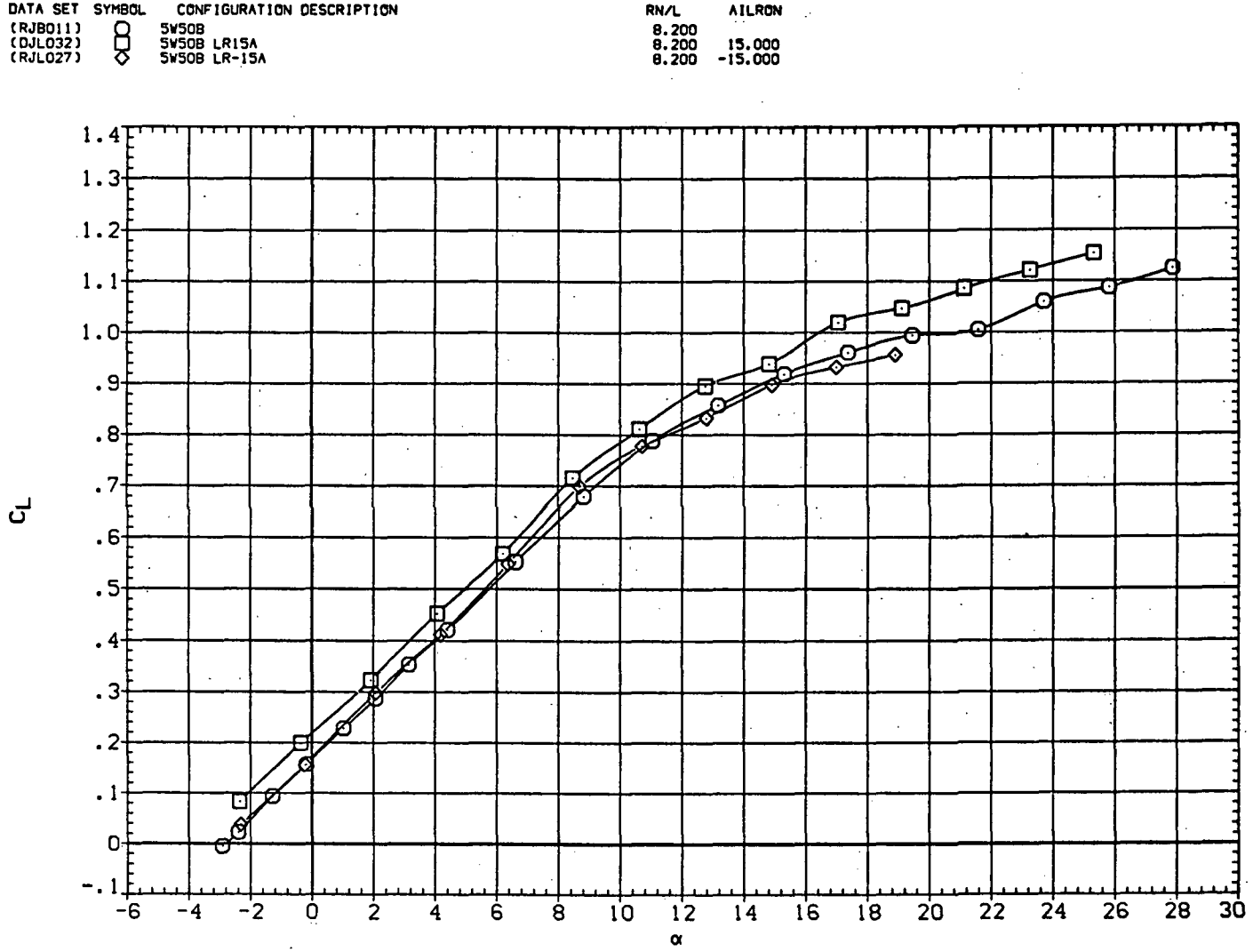

(a) C_L vs α

Figure 32.– Aileron effectiveness on the oblique wing with intermediate bend: $\Lambda = 50°, M = 0.90$.

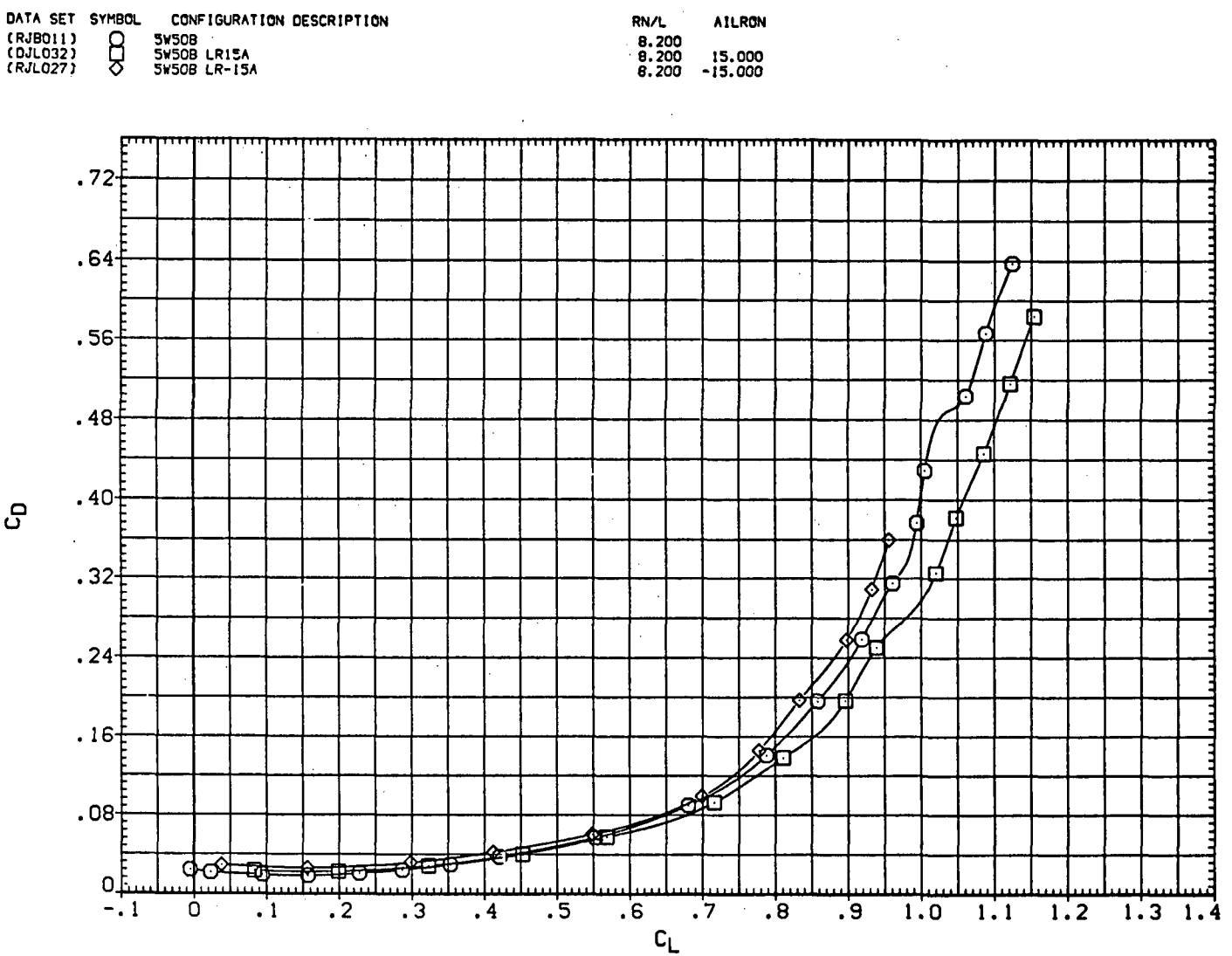

(b) C_D vs C_L

Figure 32.– Continued.

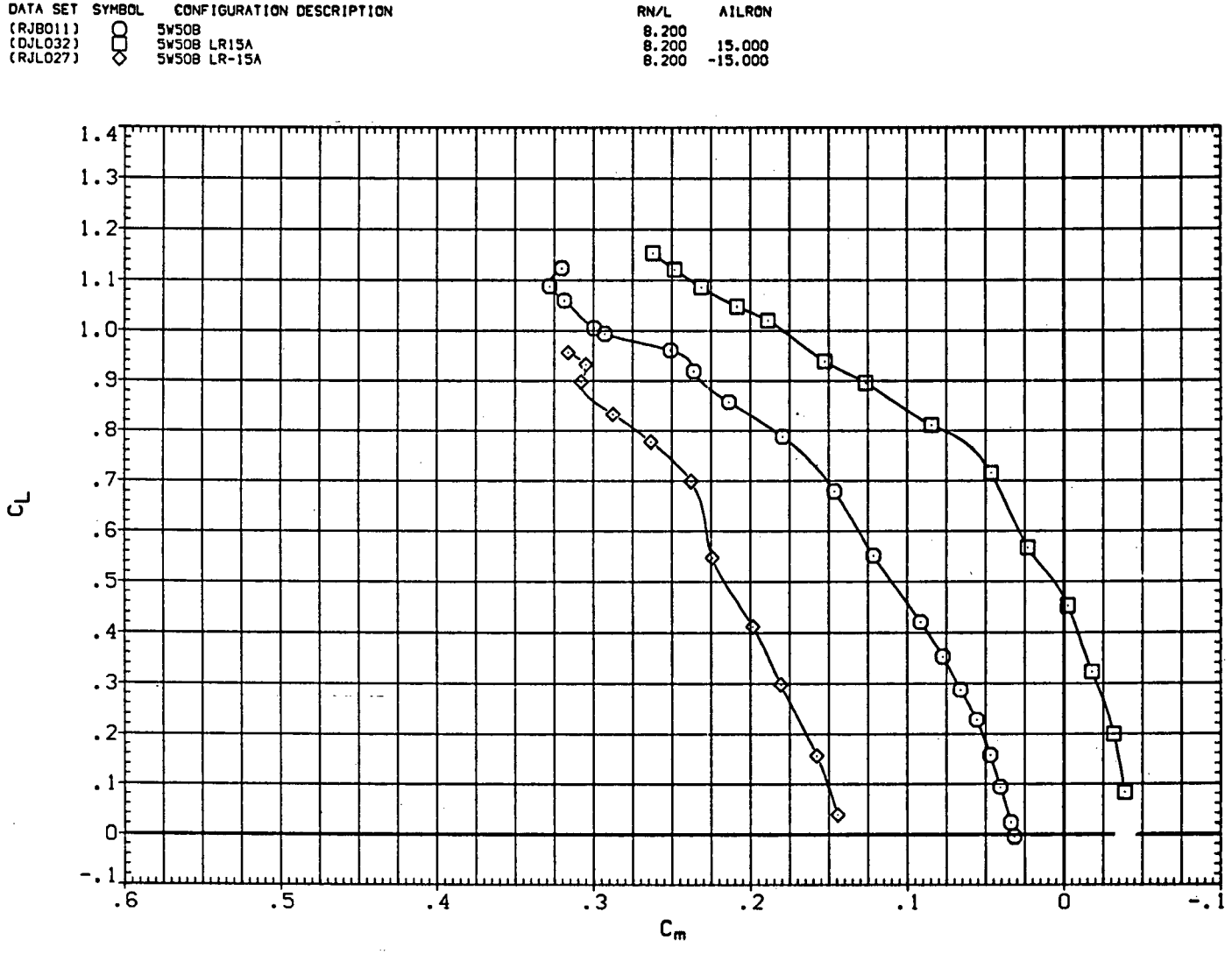

(c) C_L vs C_m

Figure 32.– Continued.

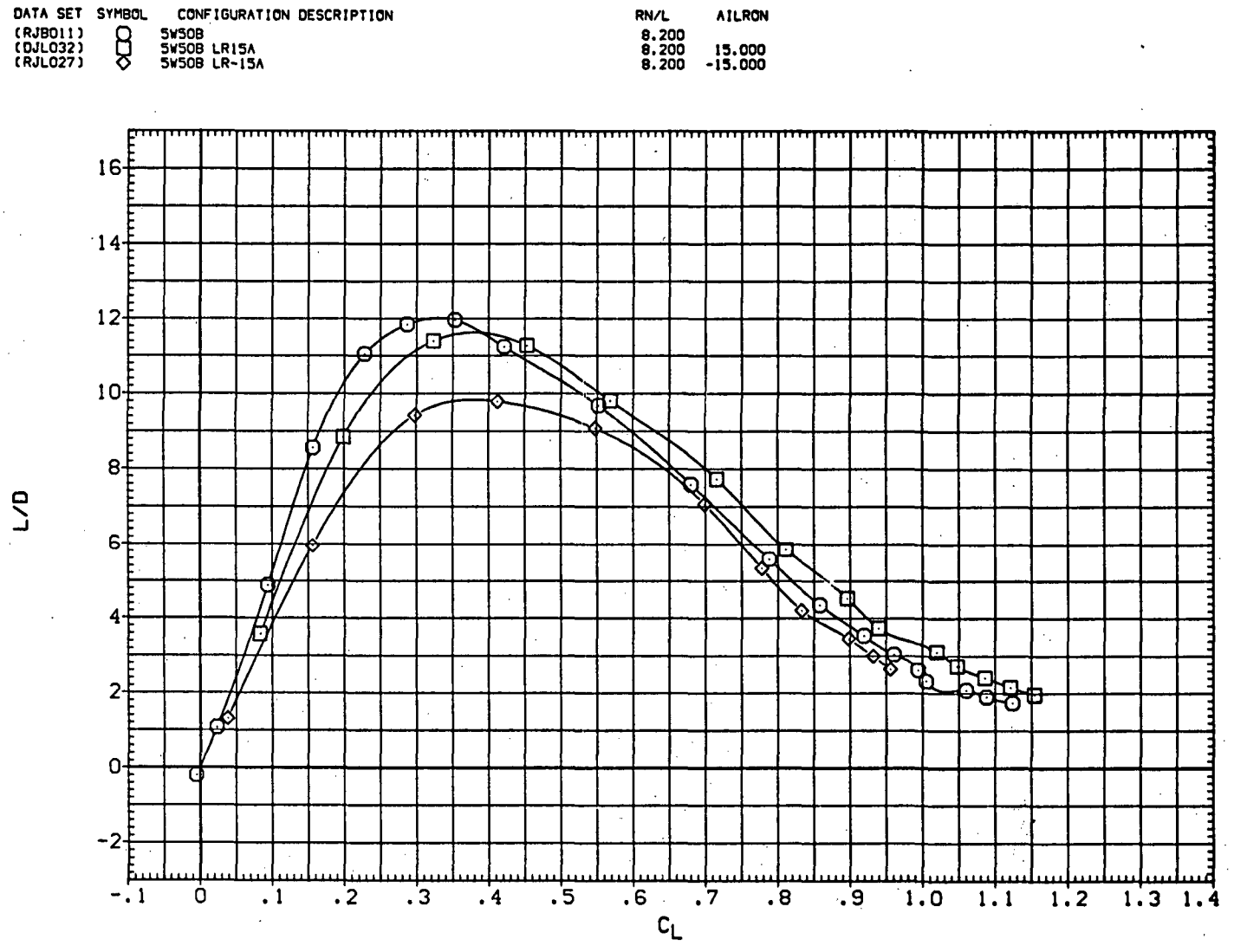

(d) L/D vs C_L

Figure 32.– Continued.

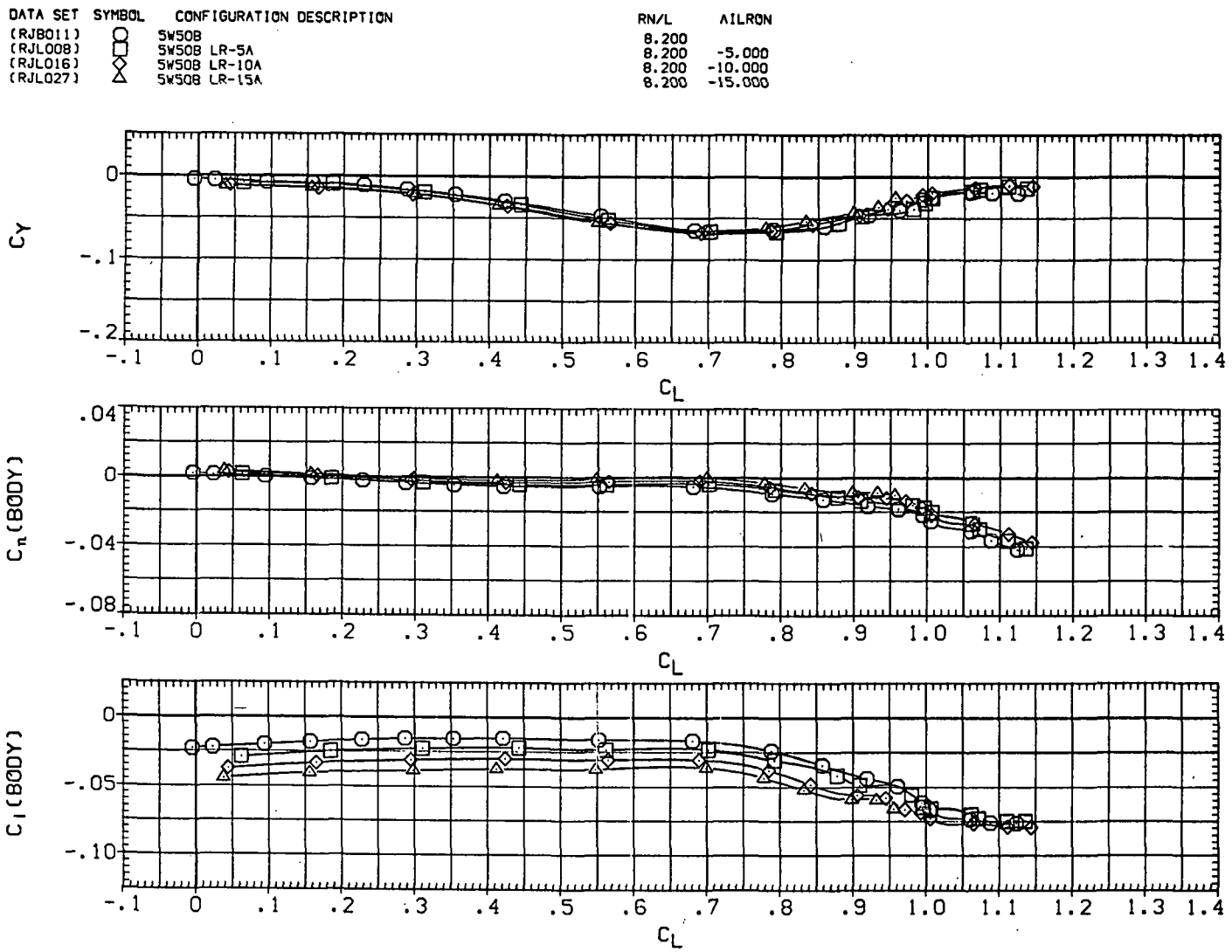

(e) C_Y, C_n, and C_l vs. C_L (negative $\Delta\delta_a$'s).

Figure 32.– Continued.

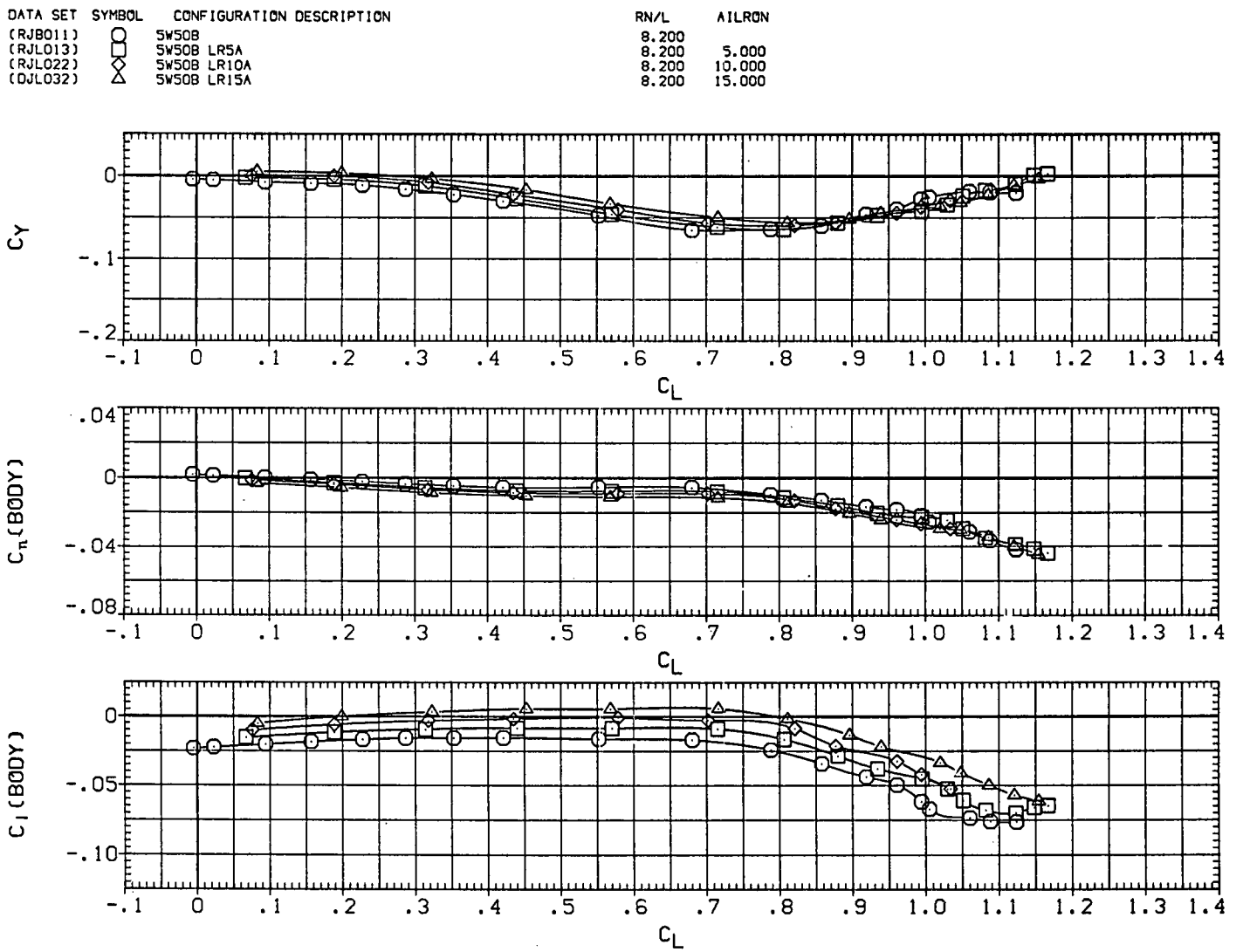

(f) C_Y, C_n, and C_l vs C_L (positive $\Delta\delta_a$'s).

Figure 32.– Concluded.

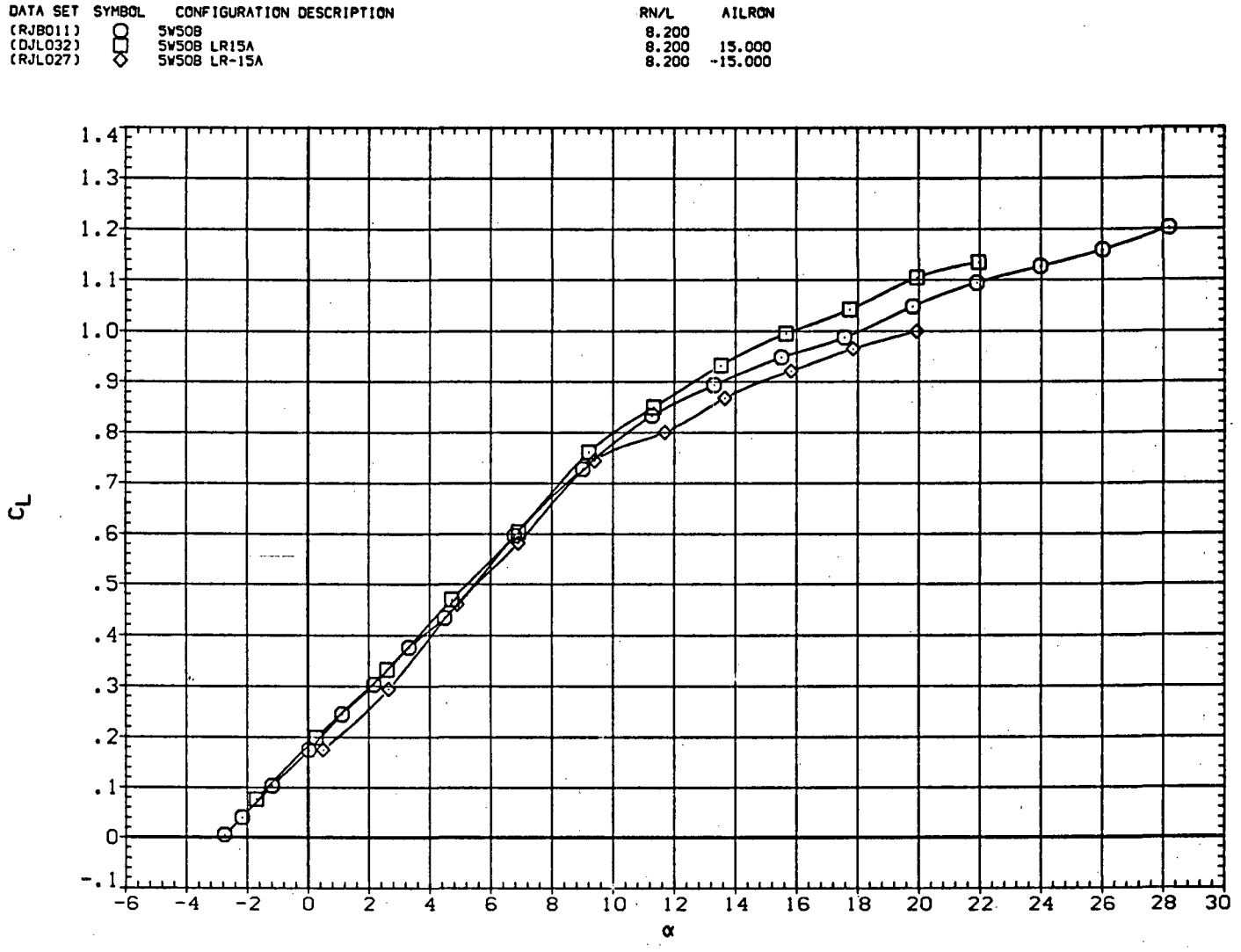

(a) C_L vs α

Figure 33.– Aileron effectiveness on the oblique wing with intermediate bend: $\Lambda = 50°, M = 0.95$.

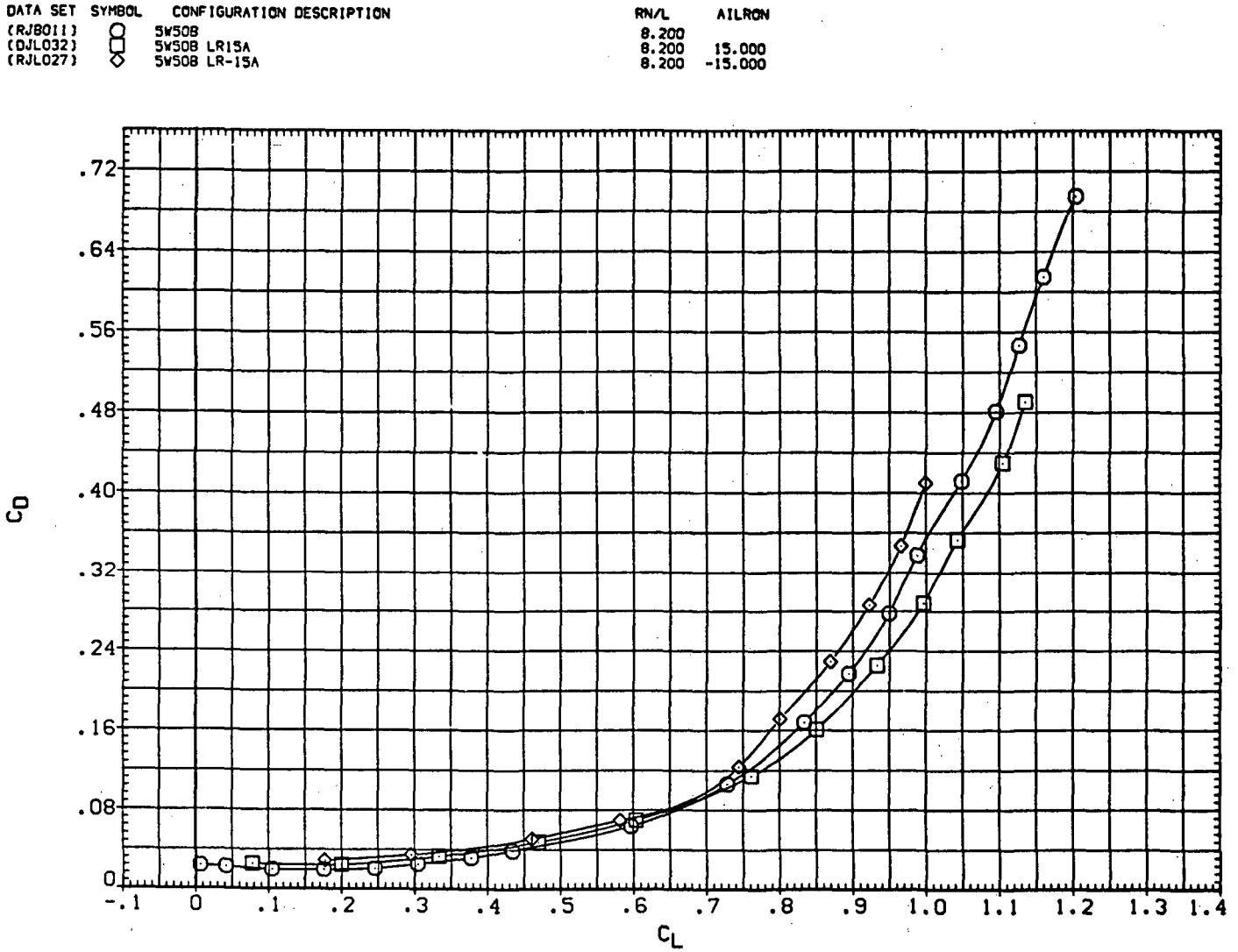

(b) C_D vs C_L

Figure 33.– Continued.

(c) C_L vs C_m

Figure 33.– Continued.

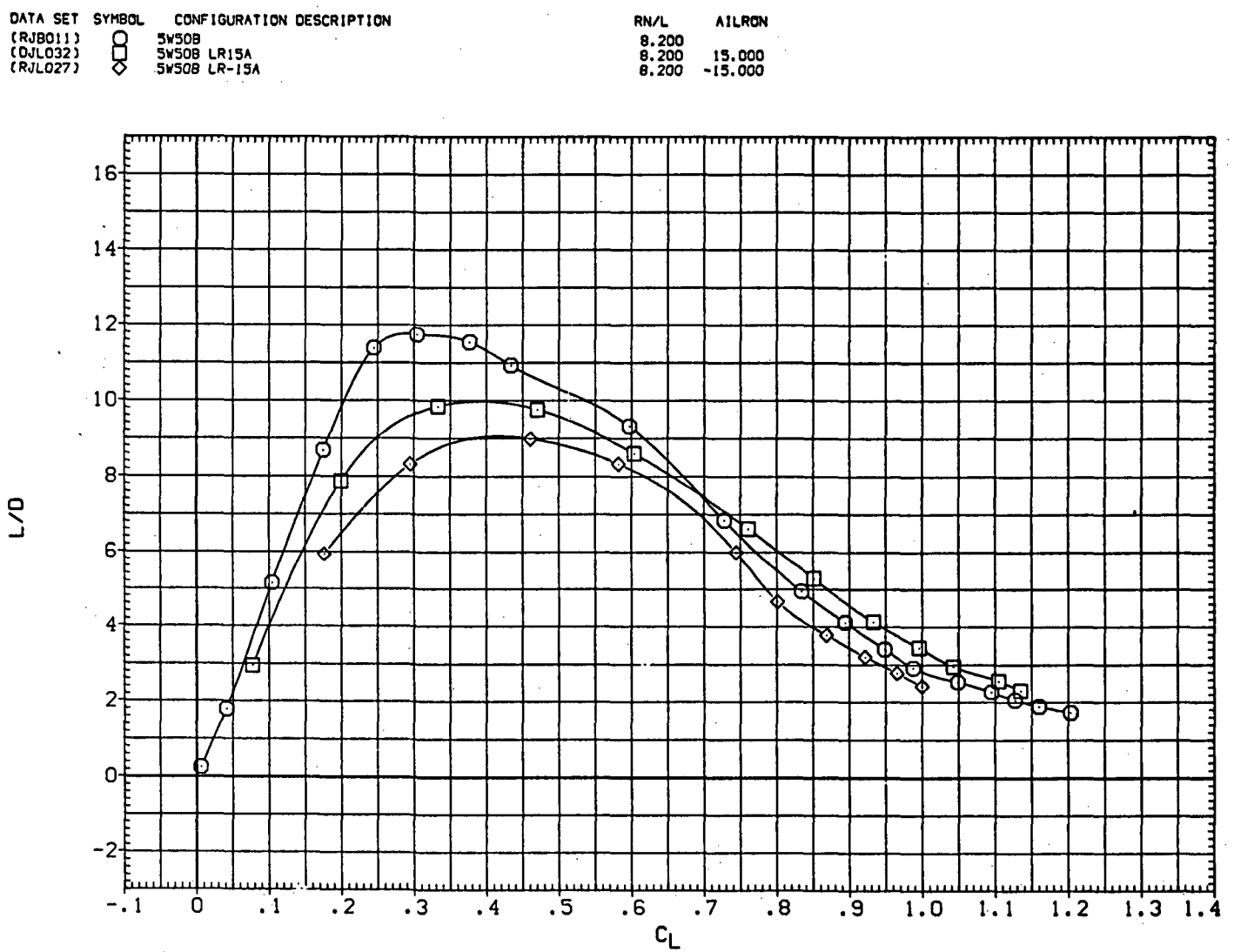

(d) L/D vs C_L

Figure 33.– Continued.

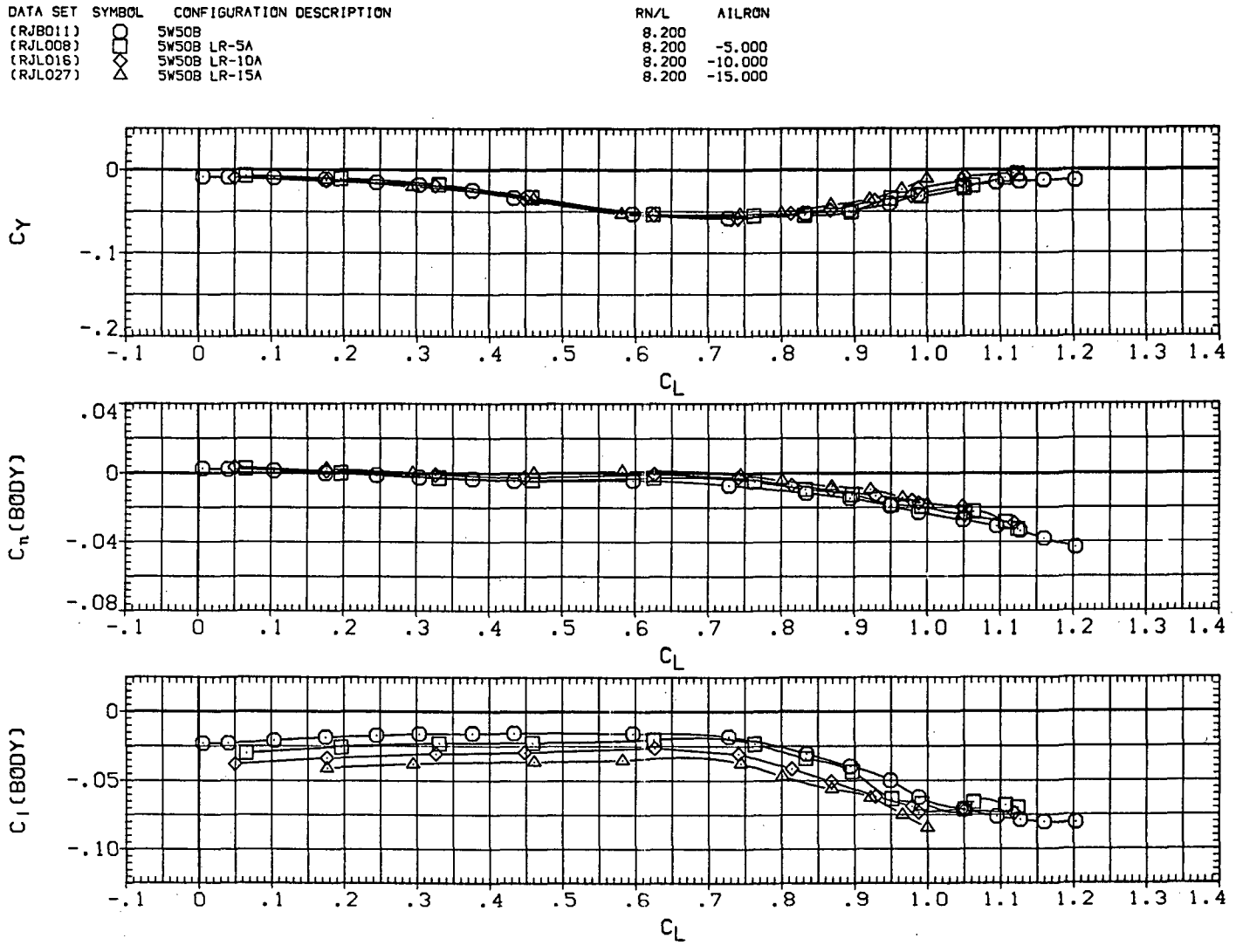

(e) C_Y, C_n, and C_l vs C_L (negative $\Delta\delta_a$'s).

Figure 33.– Continued.

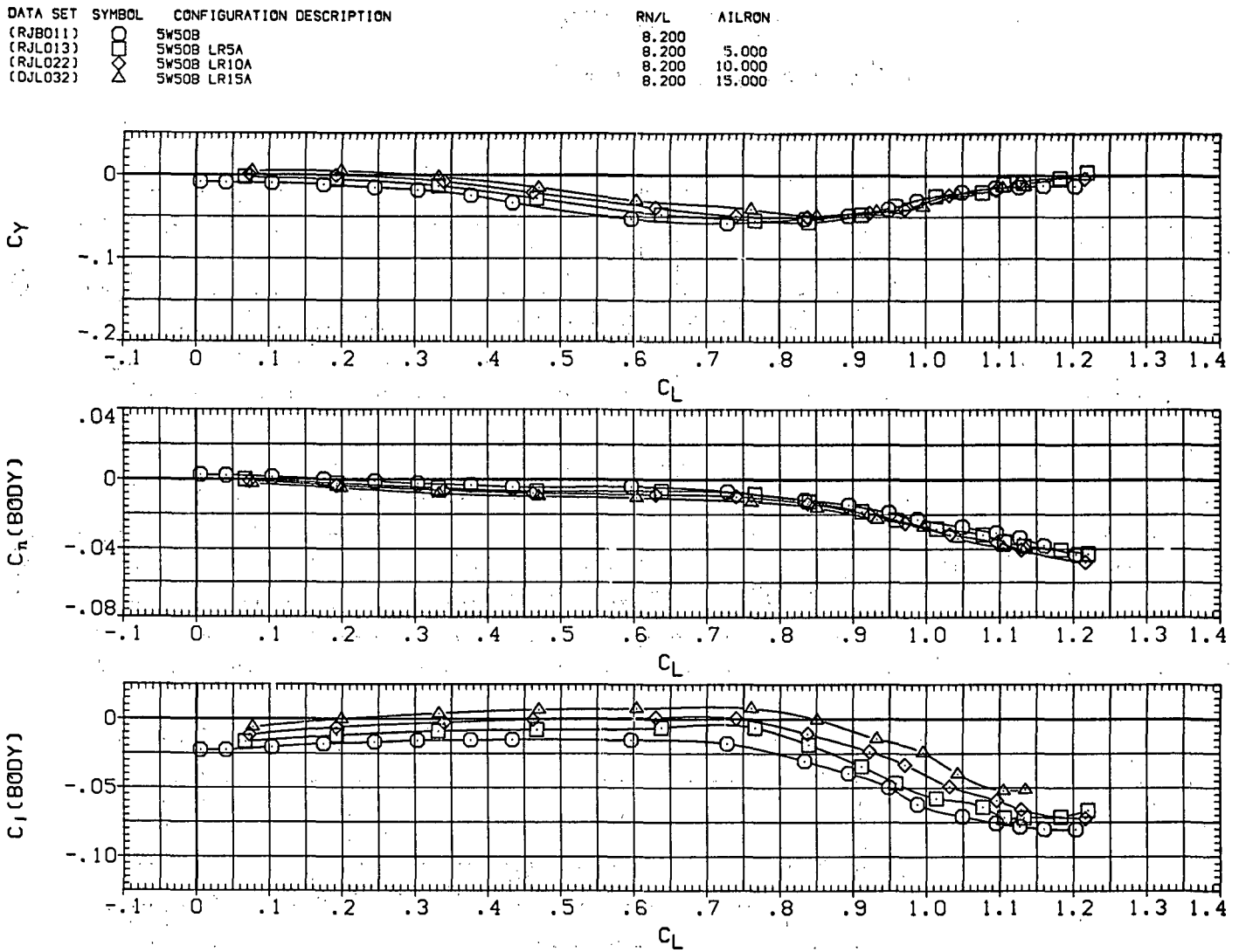

(f) C_Y, C_n, and C_l vs C_L (positive $\Delta\delta_a$'s).

Figure 33.– Concluded.

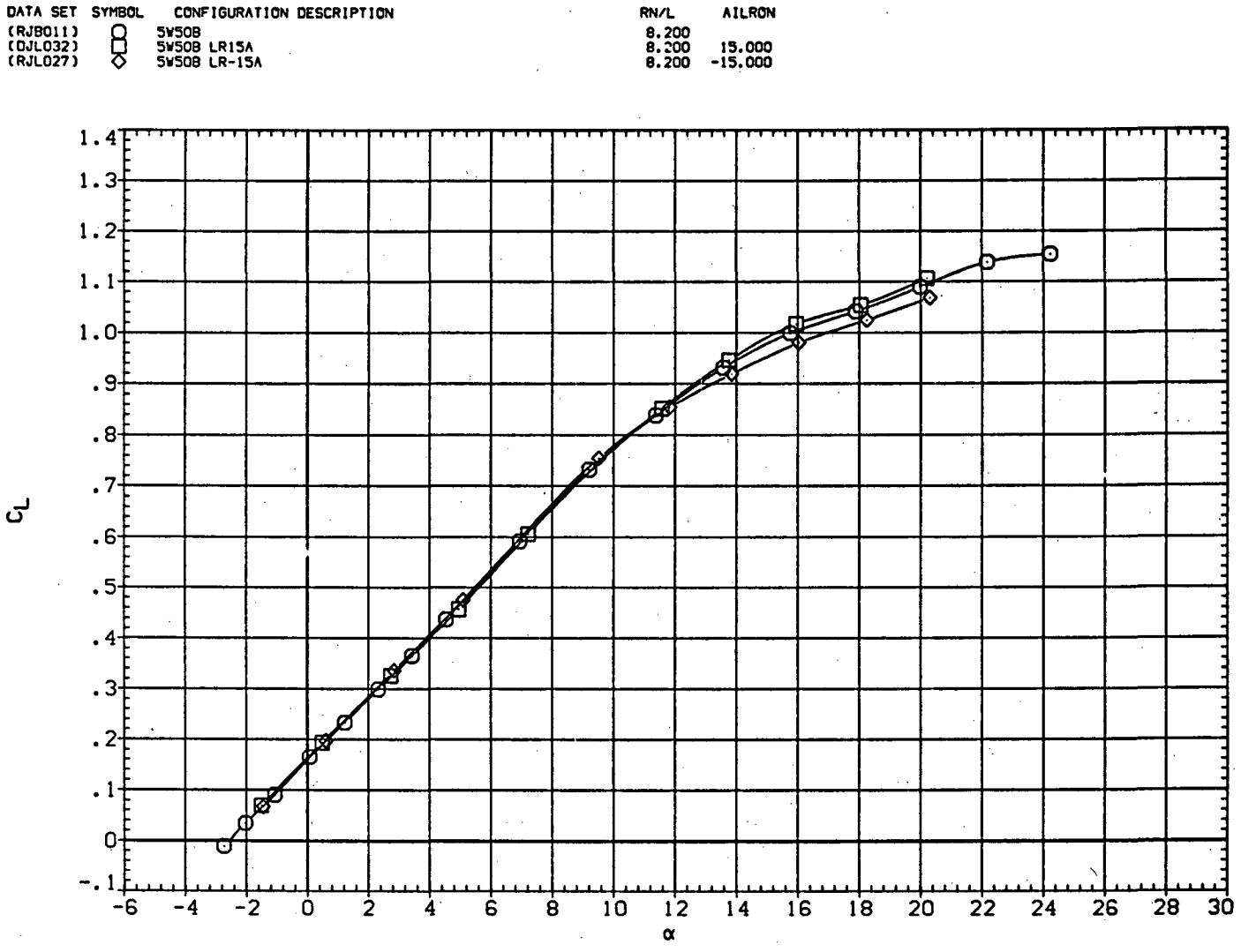

(a) C_L vs α

Figure 34.– Aileron effectiveness on the oblique wing with intermediate bend: $\Lambda = 50°, M = 1.1$.

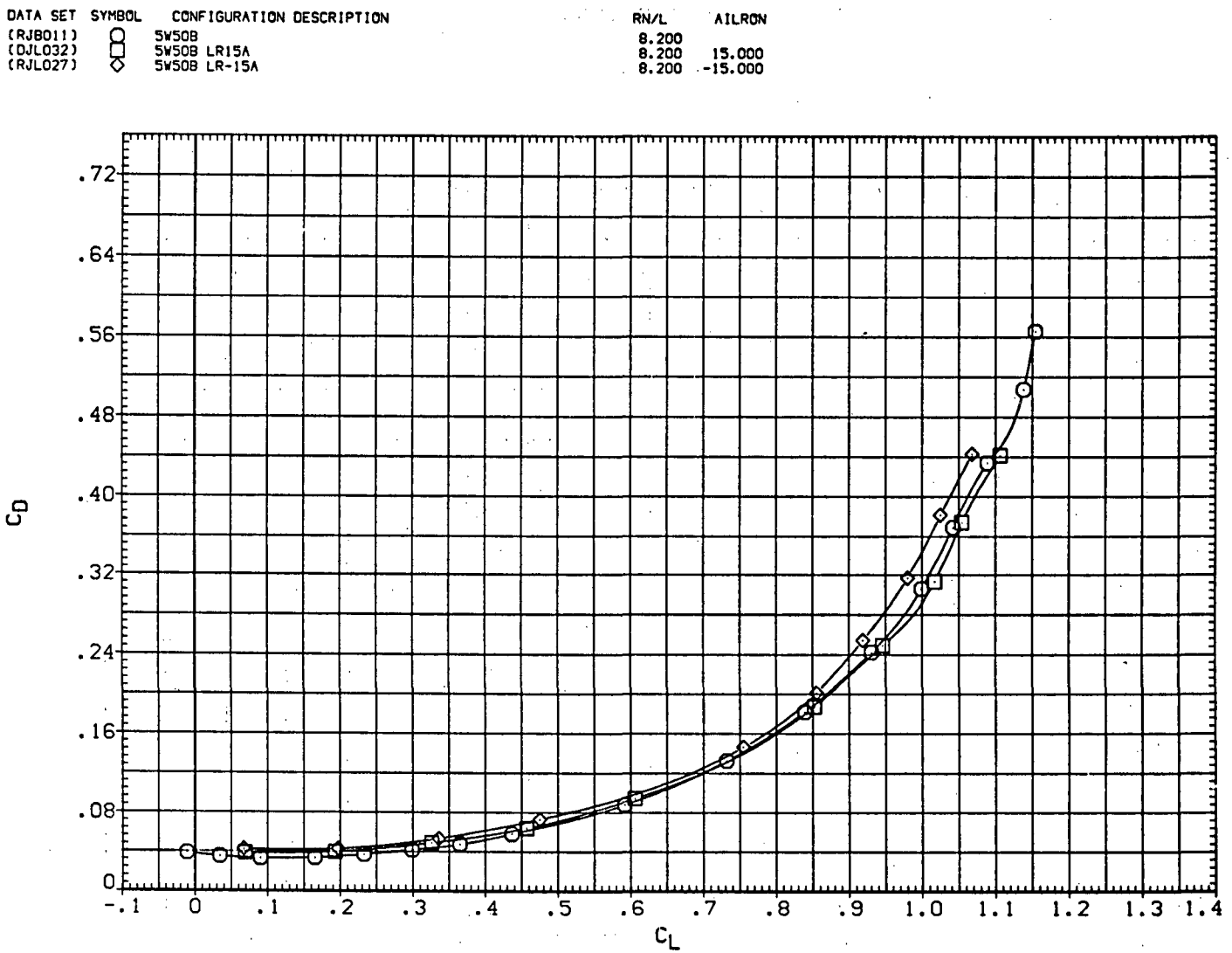

(b) C_D vs C_L

Figure 34.– Continued.

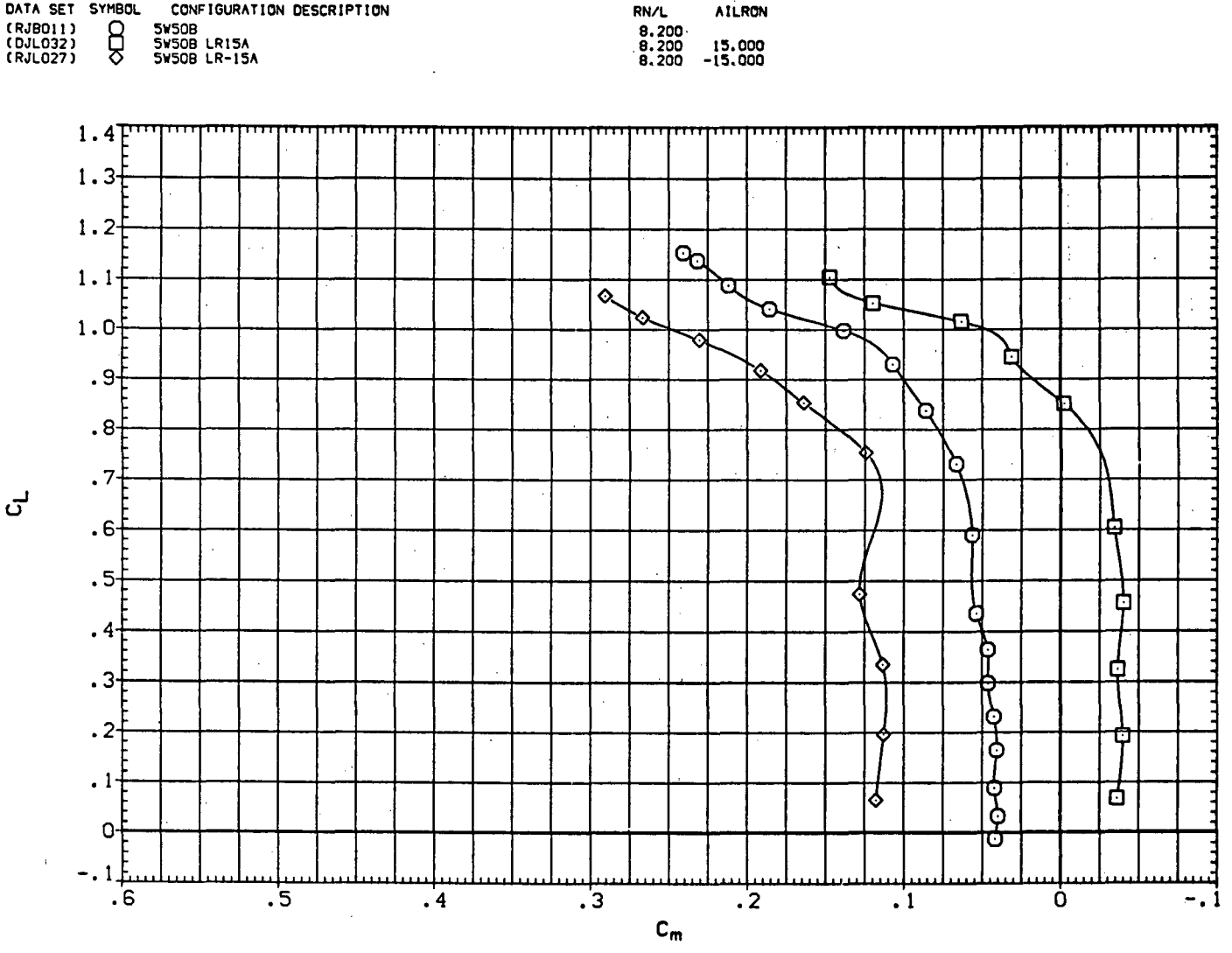

(c) C_L vs C_m

Figure 34.– Continued.

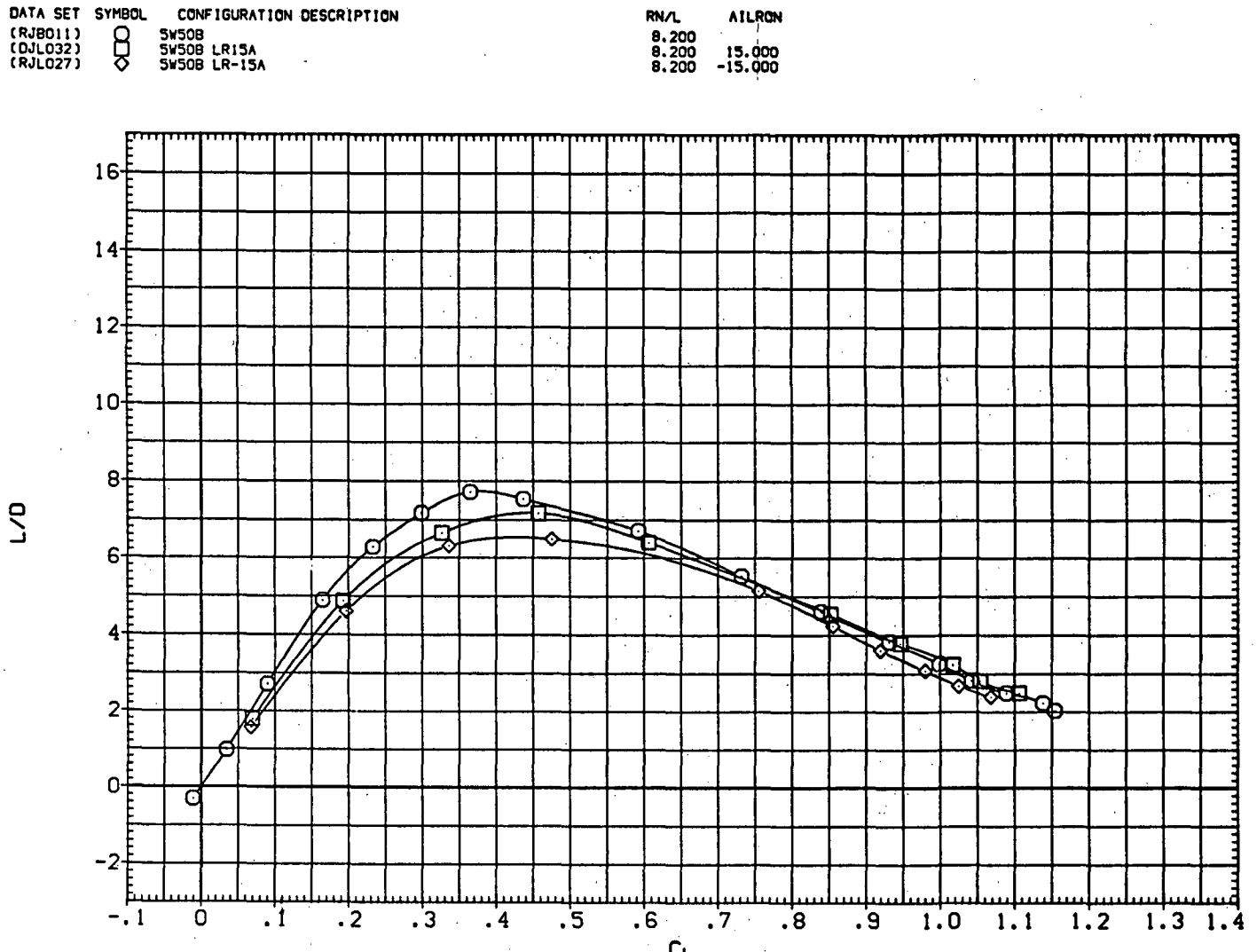

(d) L/D vs C_L

Figure 34.– Continued.

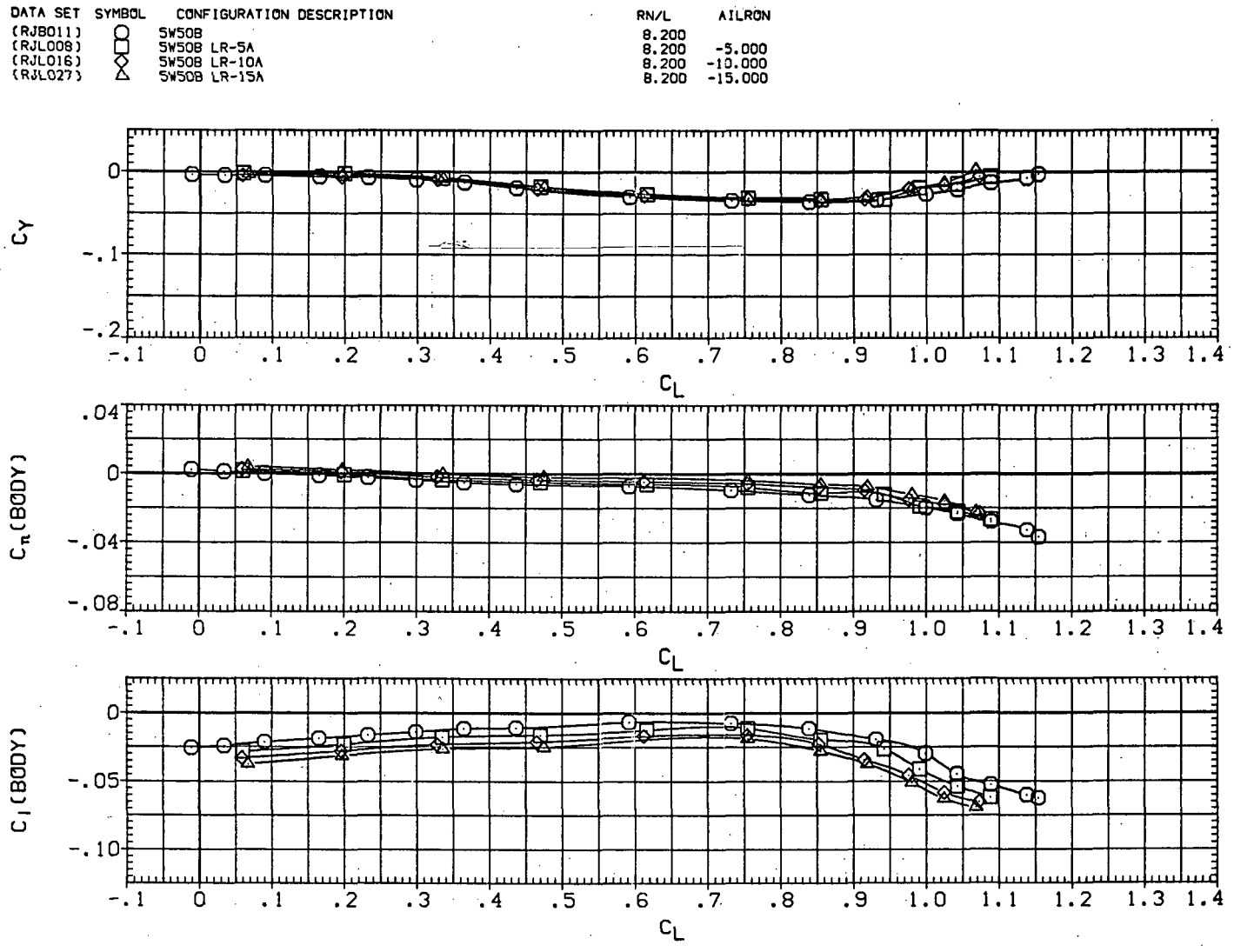

(e) C_Y, C_n, and C_l vs C_L (negative $\Delta\delta_a$'s).

Figure 34.– Continued.

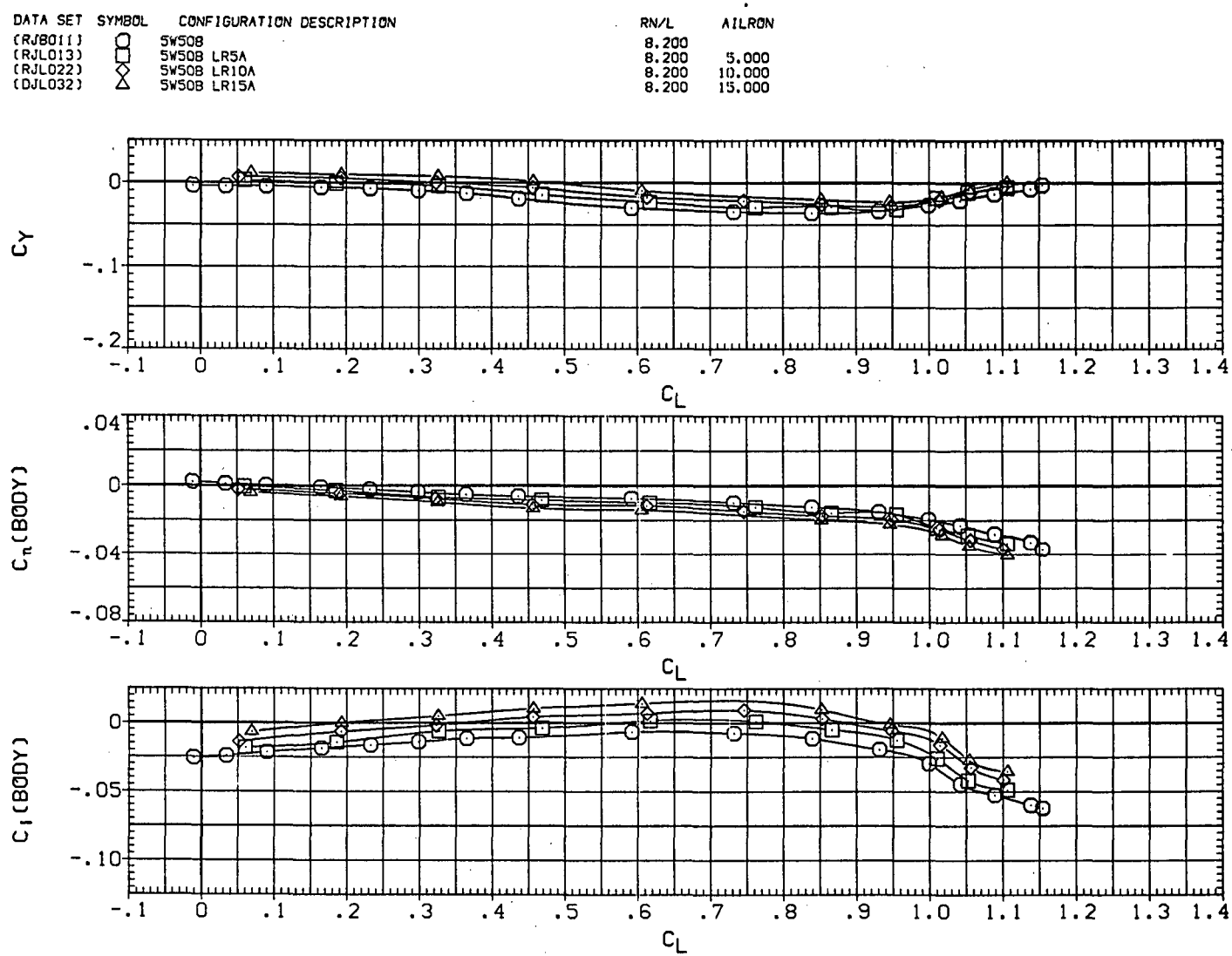

(f) C_Y, C_n, and C_l vs C_L (positive $\Delta\delta_a$'s).

Figure 34.– Concluded.

(a) C_L vs α

Figure 35.– Aileron effectiveness on the oblique wing with intermediate bend: $\Lambda = 50°, M = 1.20$.

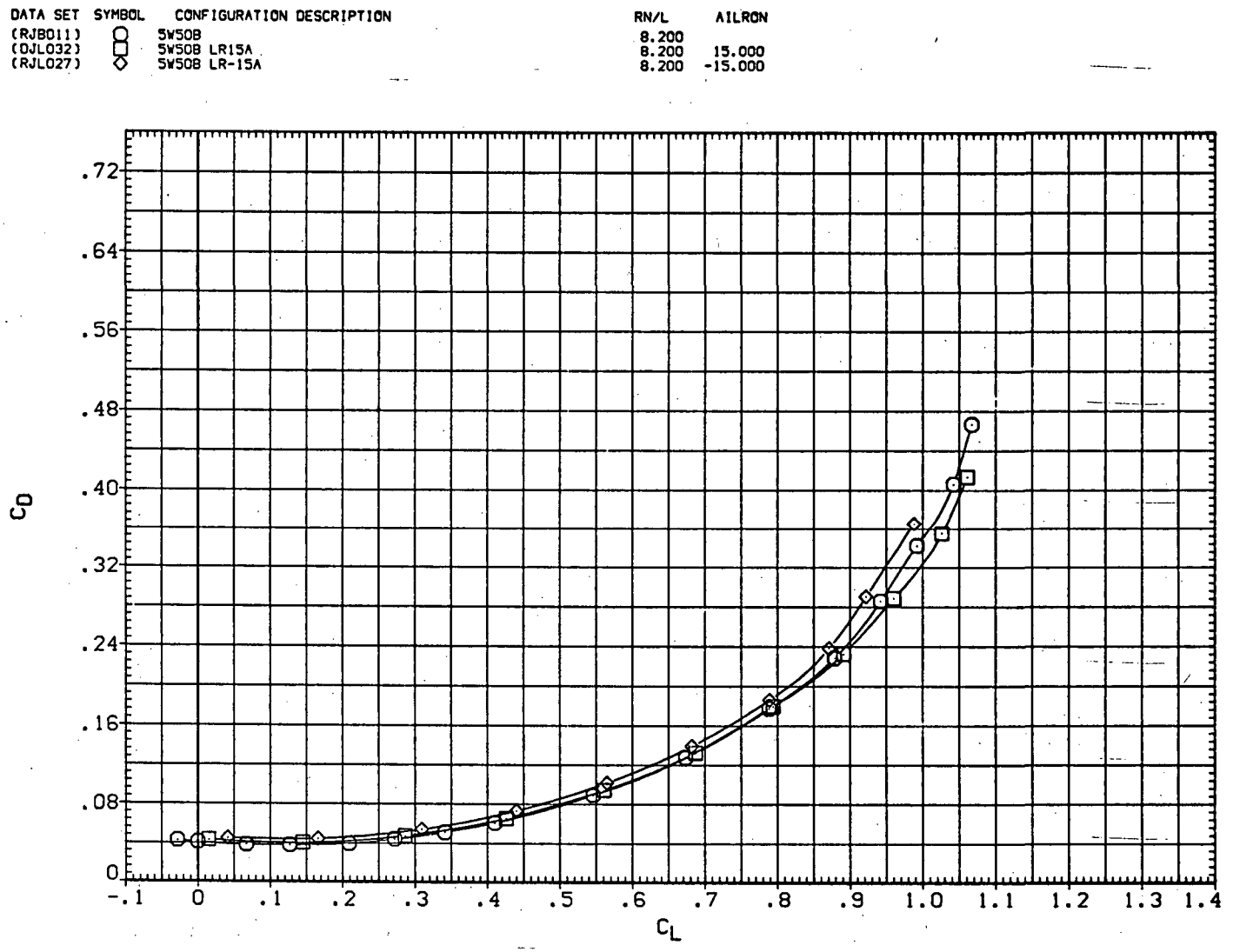

(b) C_D vs C_L

Figure 35.– Continued.

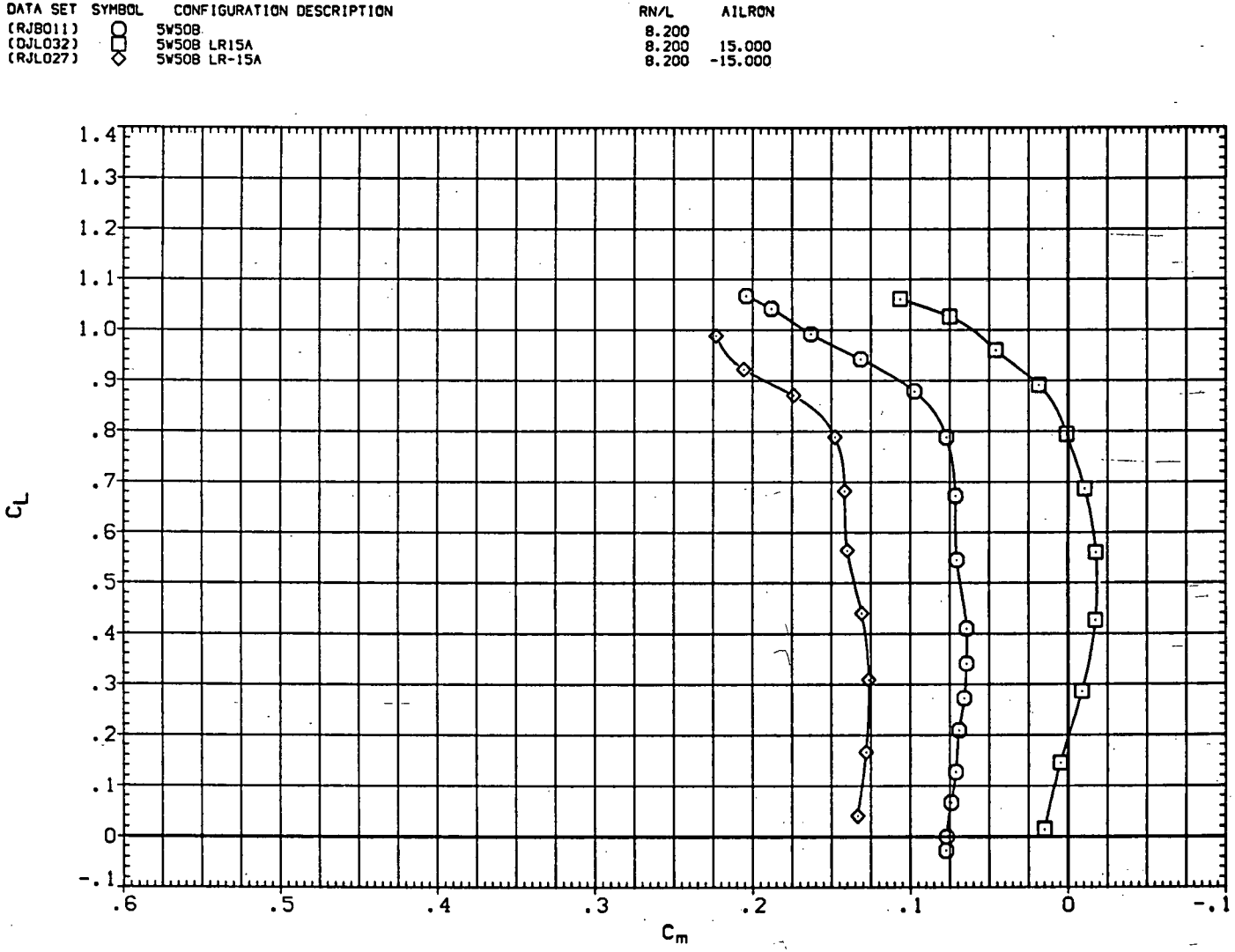

(c) C_L vs C_m

Figure 35.– Continued.

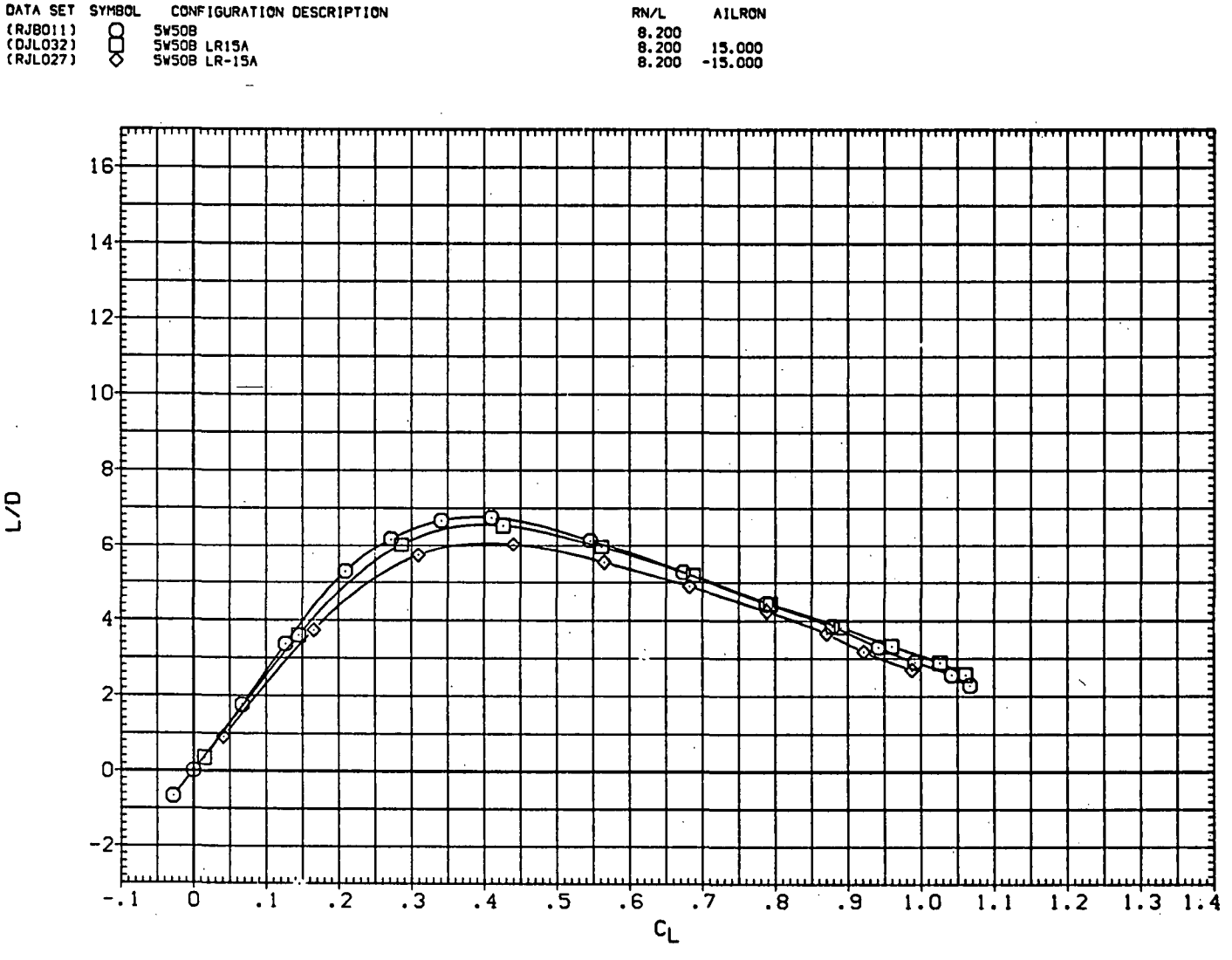

(d) L/D vs C_L

Figure 35.– Continued.

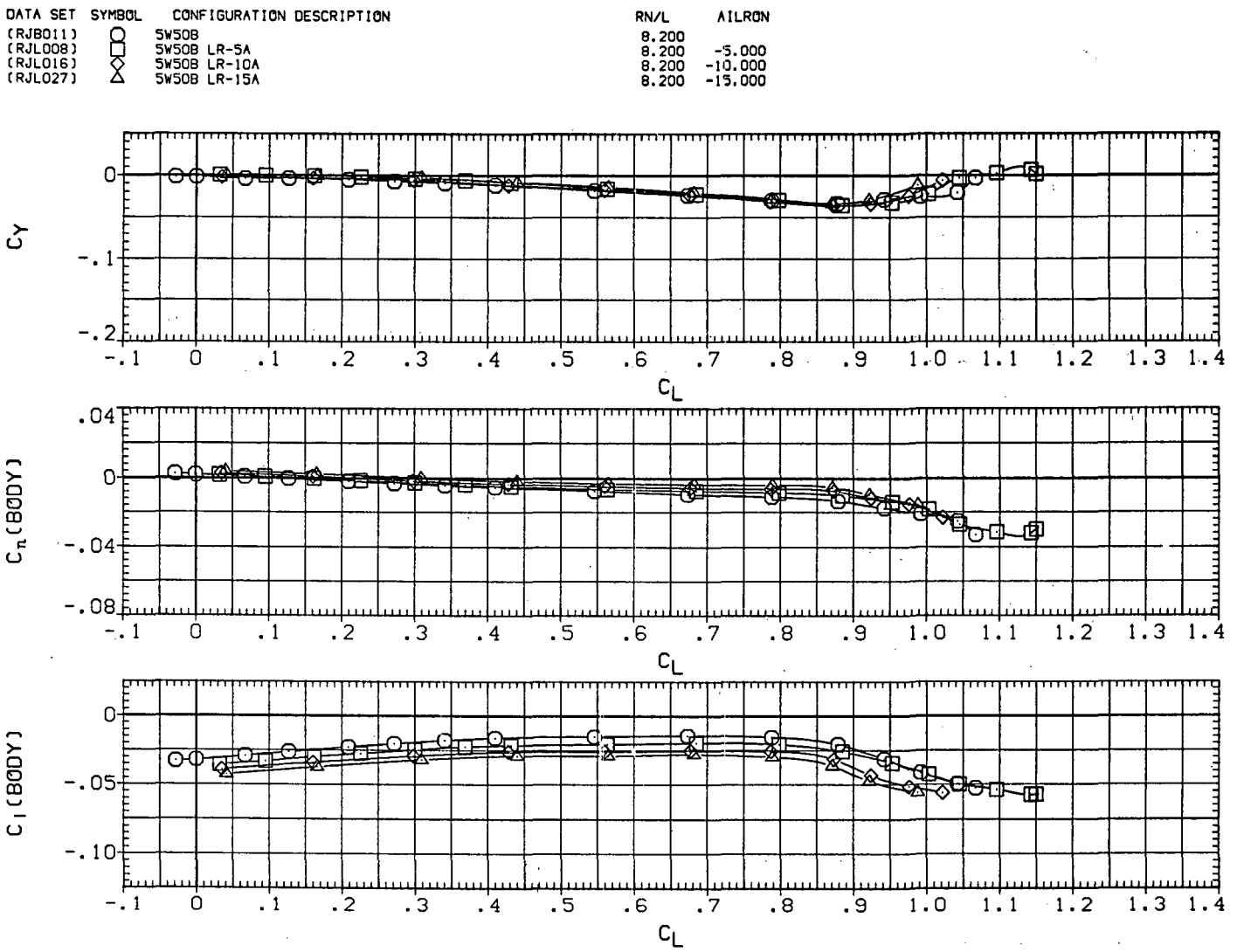

(e) C_Y, C_n, and C_l vs C_L (negative $\Delta\delta_a$'s).

Figure 35.– Continued.

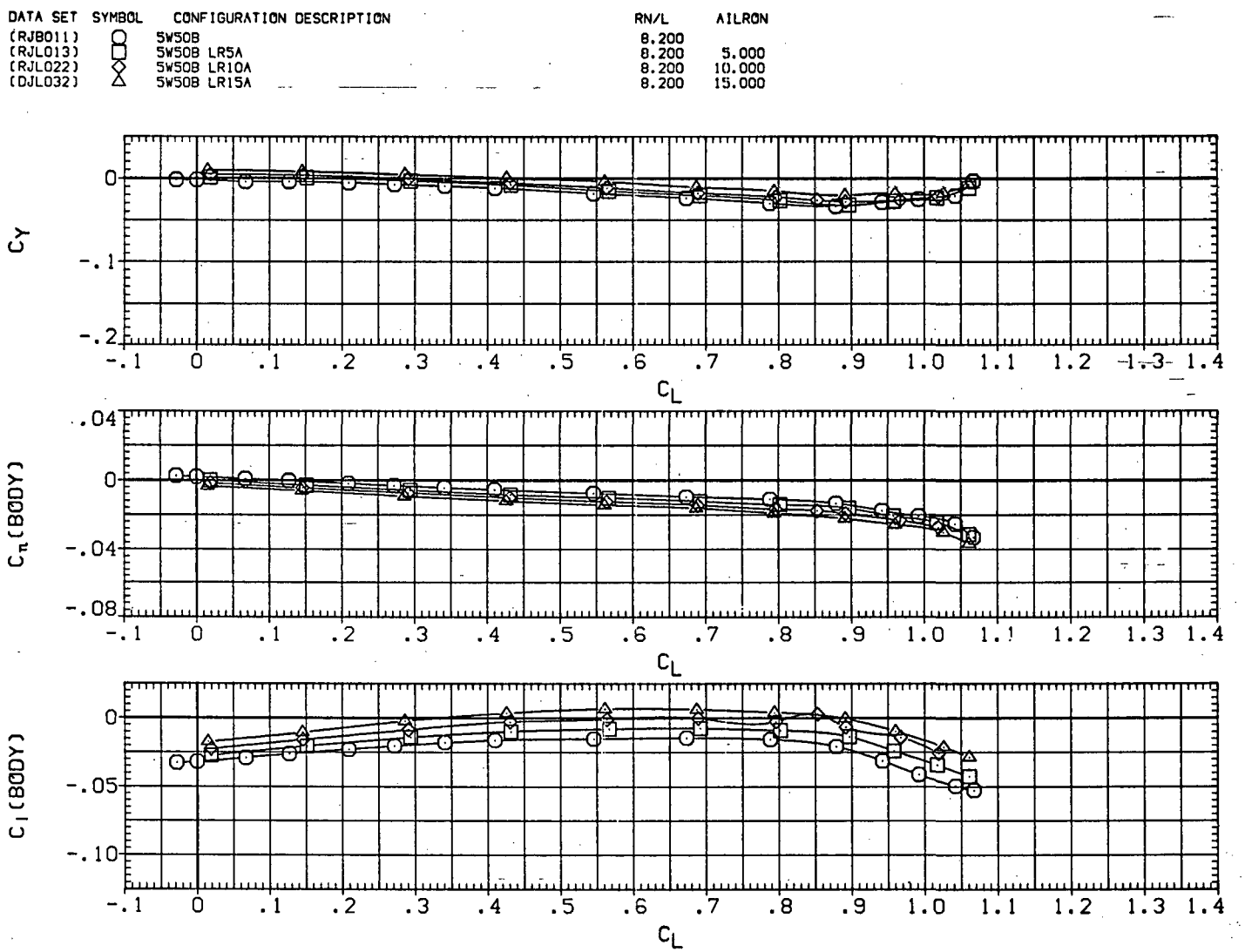

(f) C_Y, C_n, and C_l vs. C_L (positive $\Delta\delta_a$'s).

Figure 35.– Concluded.

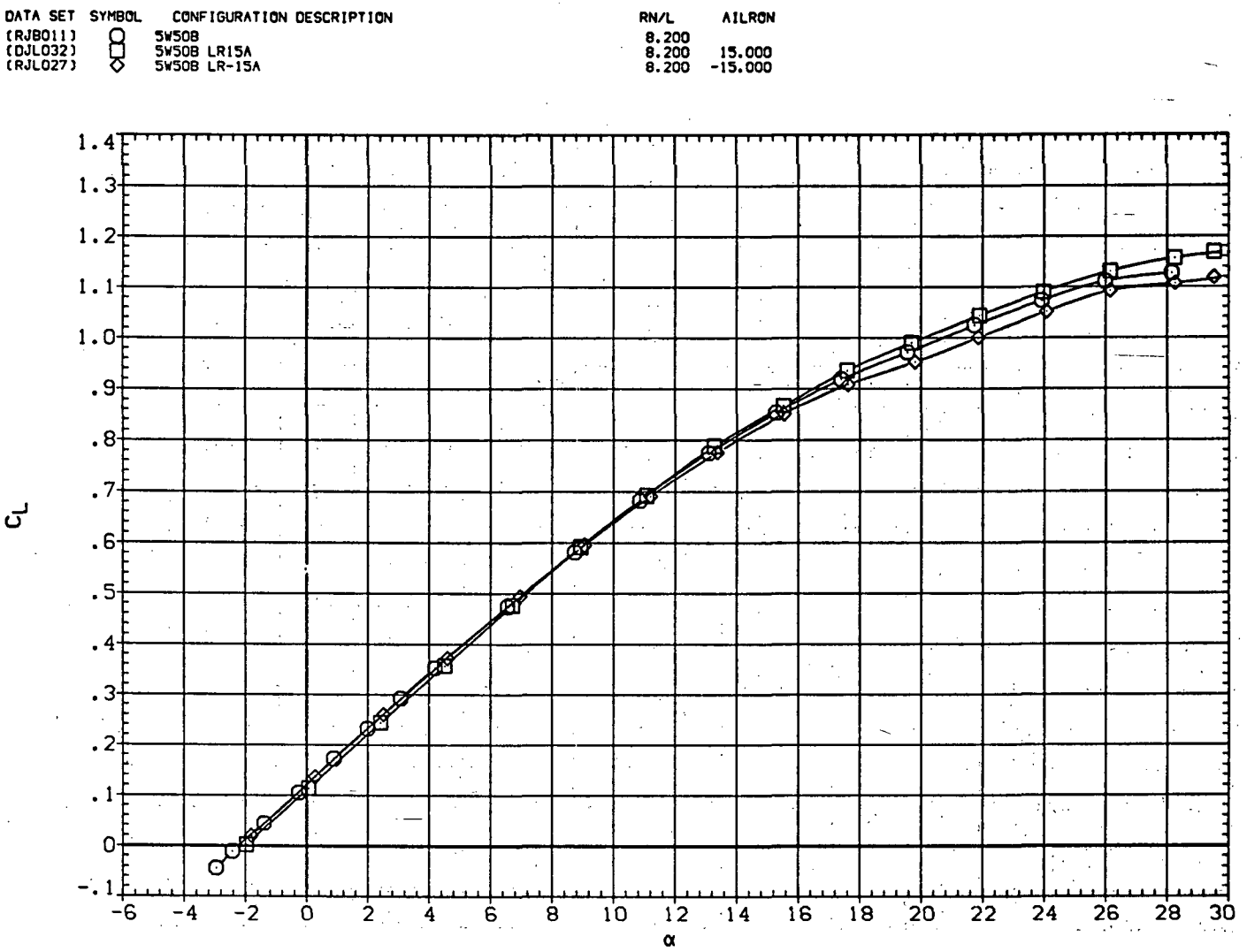

(a) C_L vs α

Figure 36.– Aileron effectiveness on the oblique wing with intermediate bend: $\Lambda = 50°, M = 1.40$.

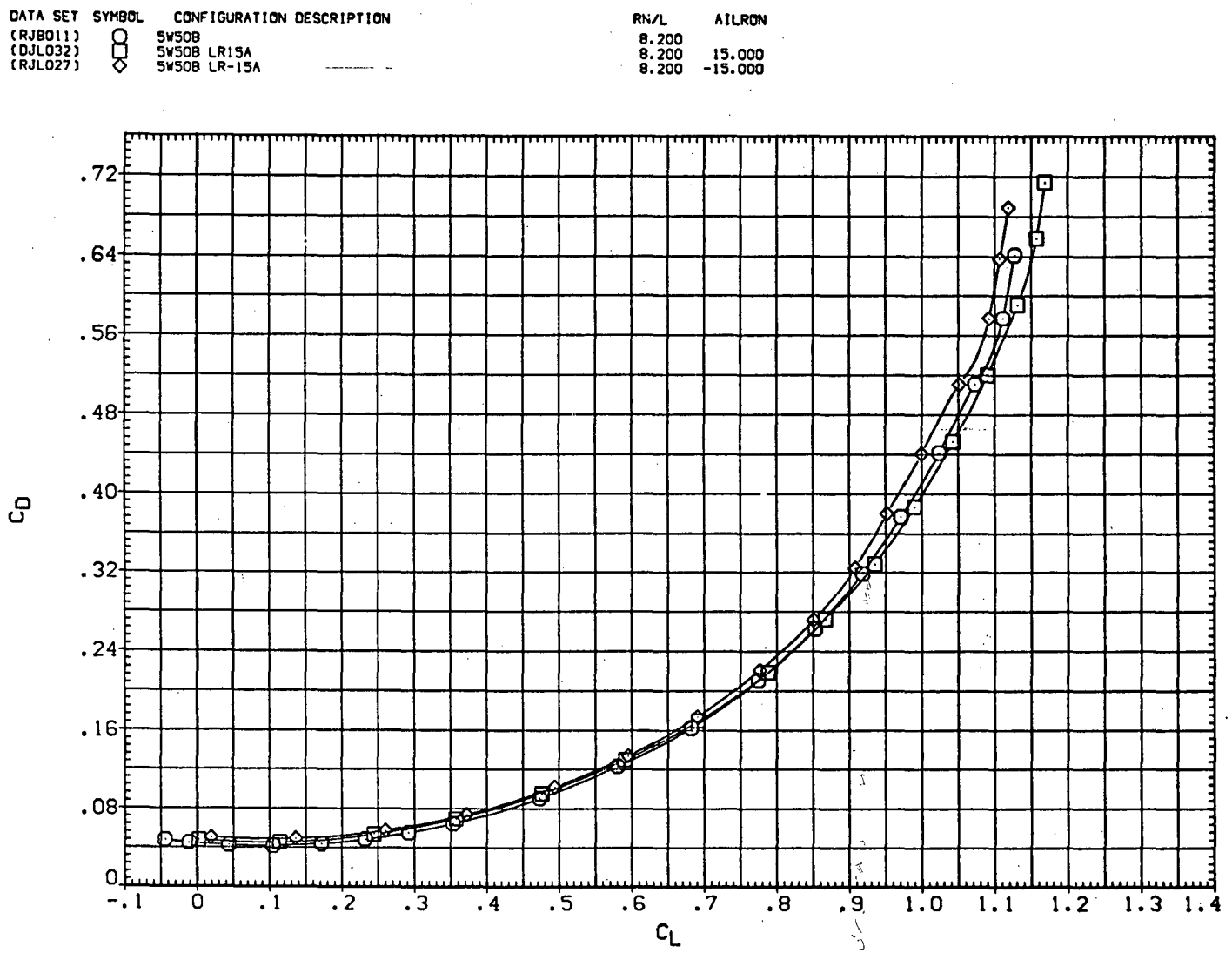

(b) C_D vs C_L

Figure 36.– Continued.

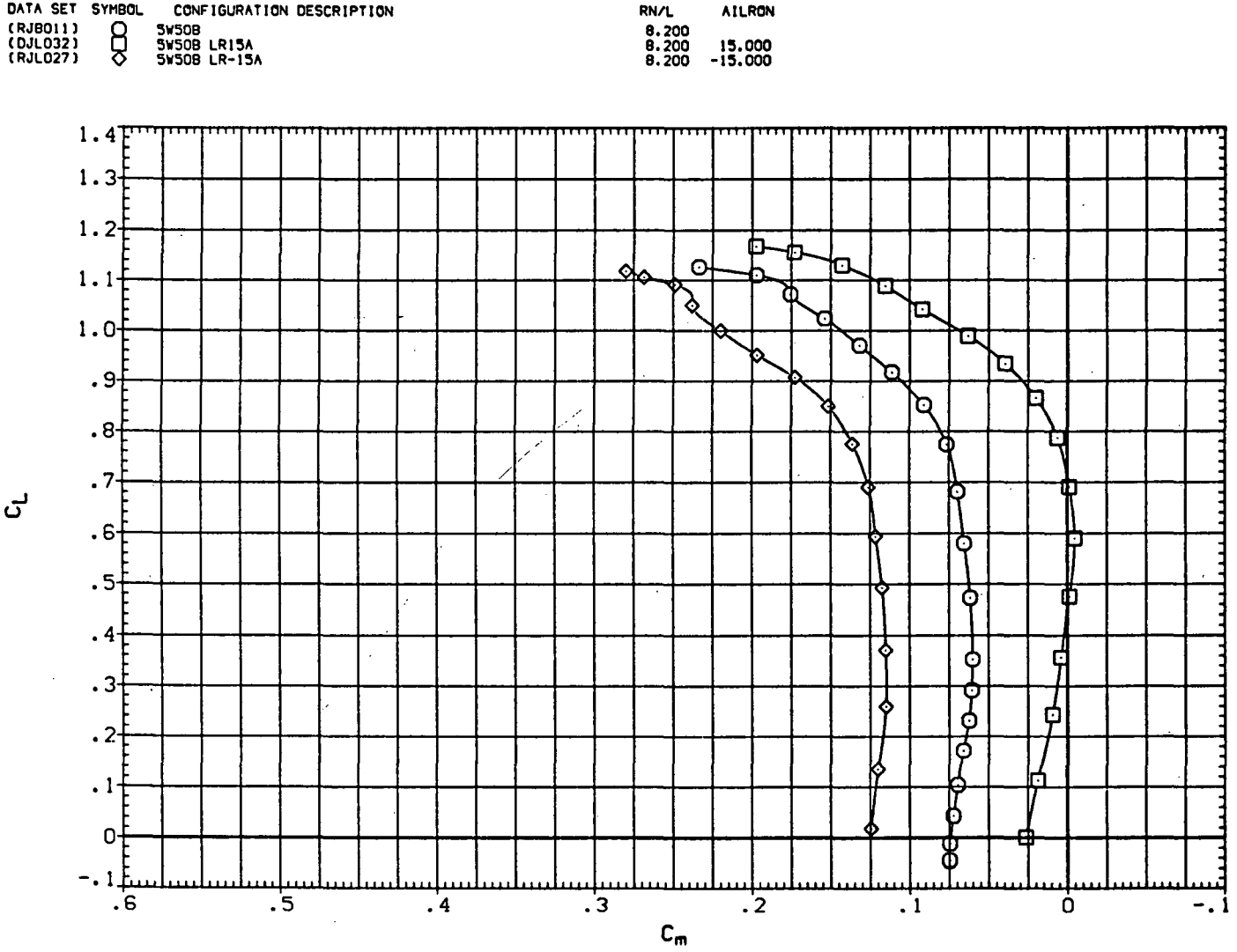

(c) C_L vs C_m

Figure 36.– Continued.

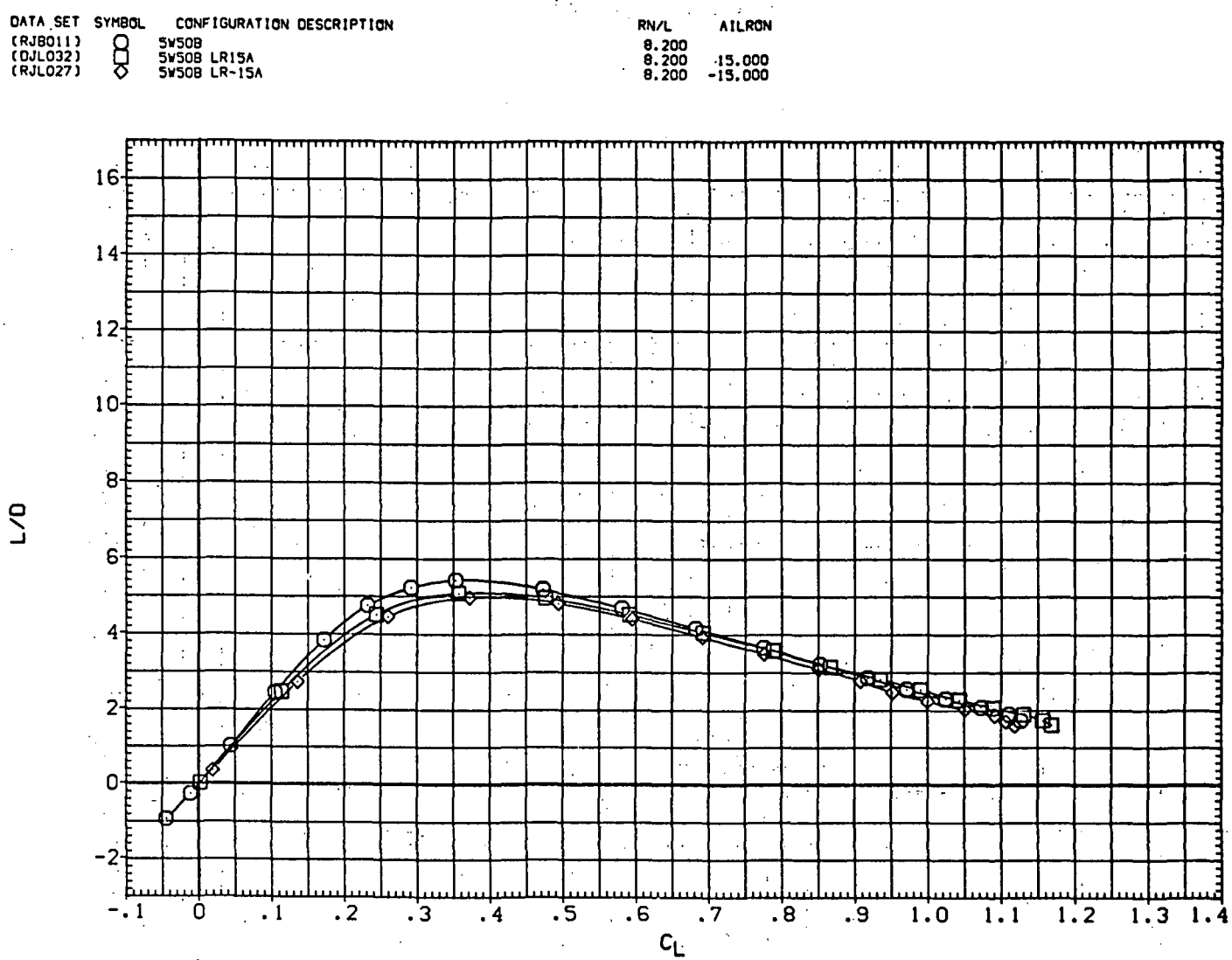

(d) L/D vs C_L

Figure 36.– Continued.

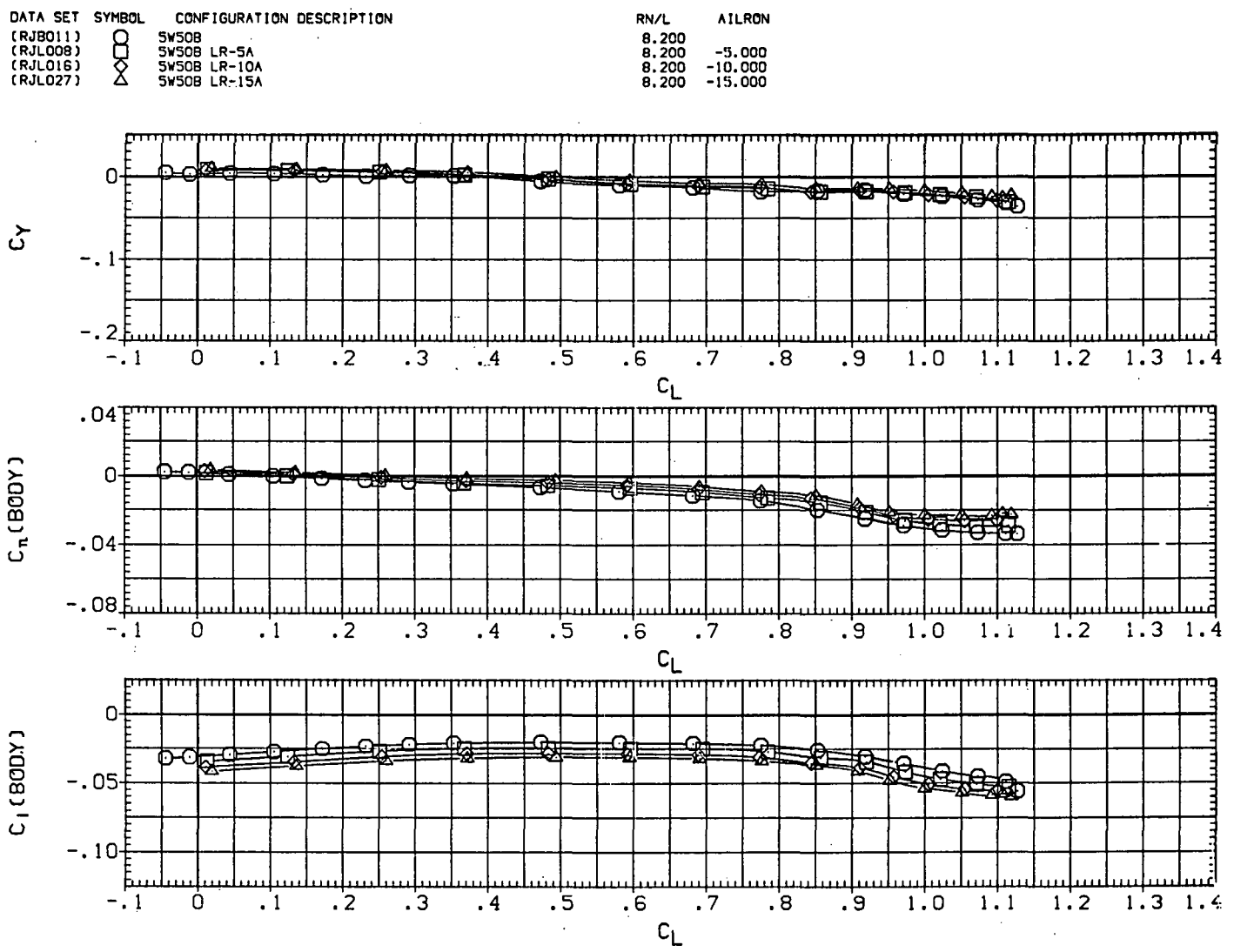

(e) C_Y, C_n, and C_l vs C_L (negative $\Delta\delta_a$'s).

Figure 36.– Continued.

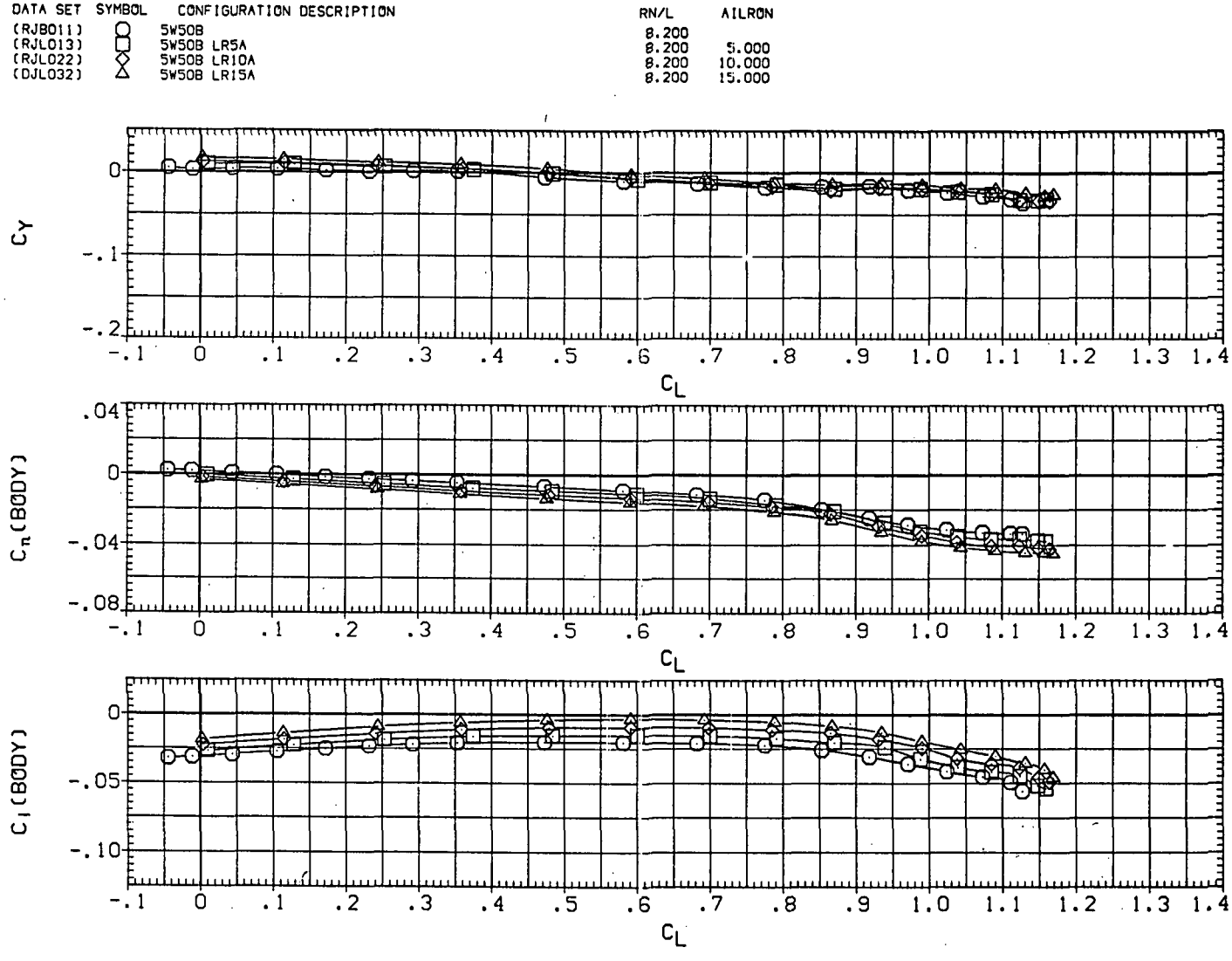

(f) C_Y, C_n, and C_l vs C_L (positive $\Delta\delta_a$'s).

Figure 36.– Concluded.

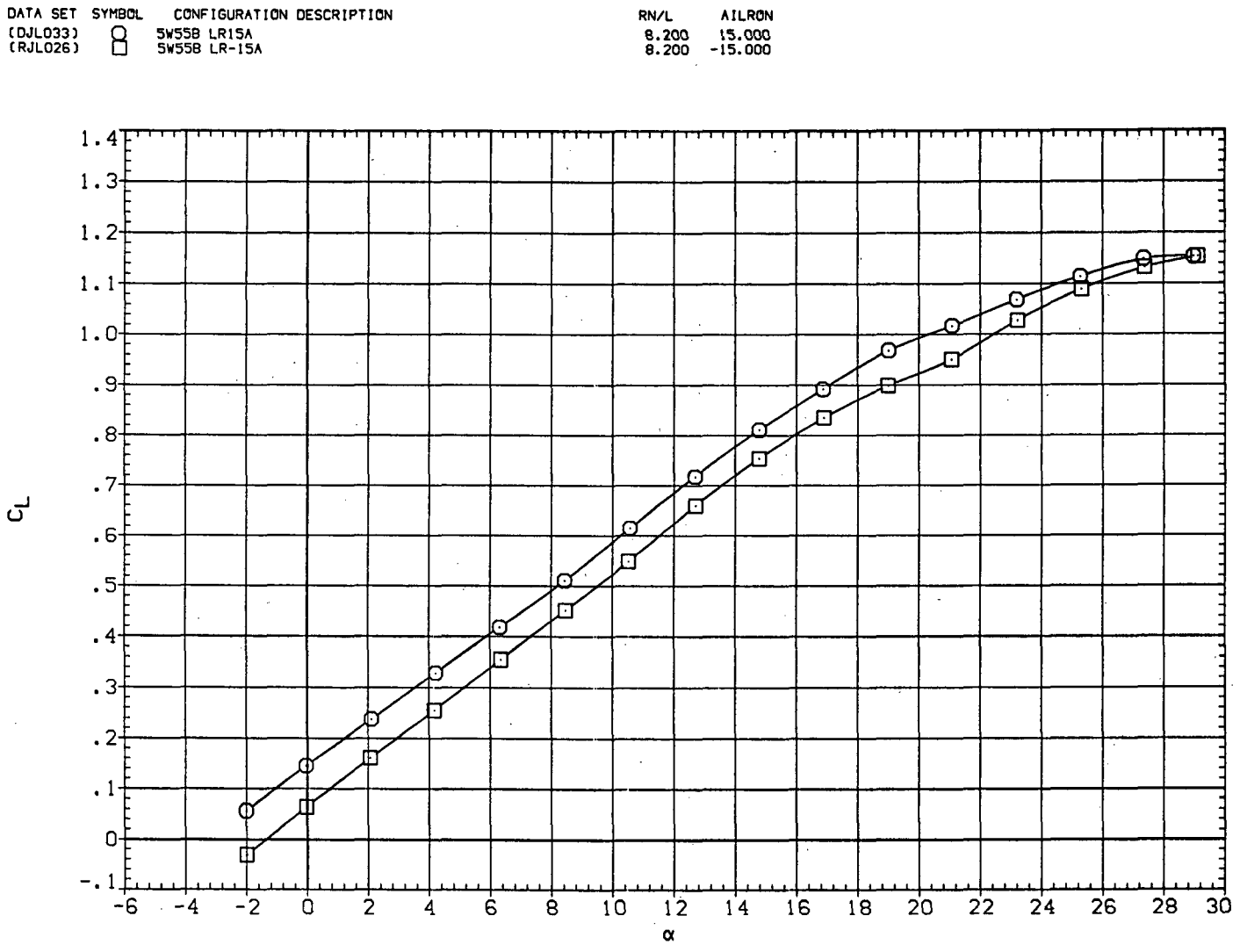

(a) C_L vs α

Figure 37.– Aileron effectiveness on the oblique wing with intermediate bend: $\Lambda = 55°, M = 0.60$.

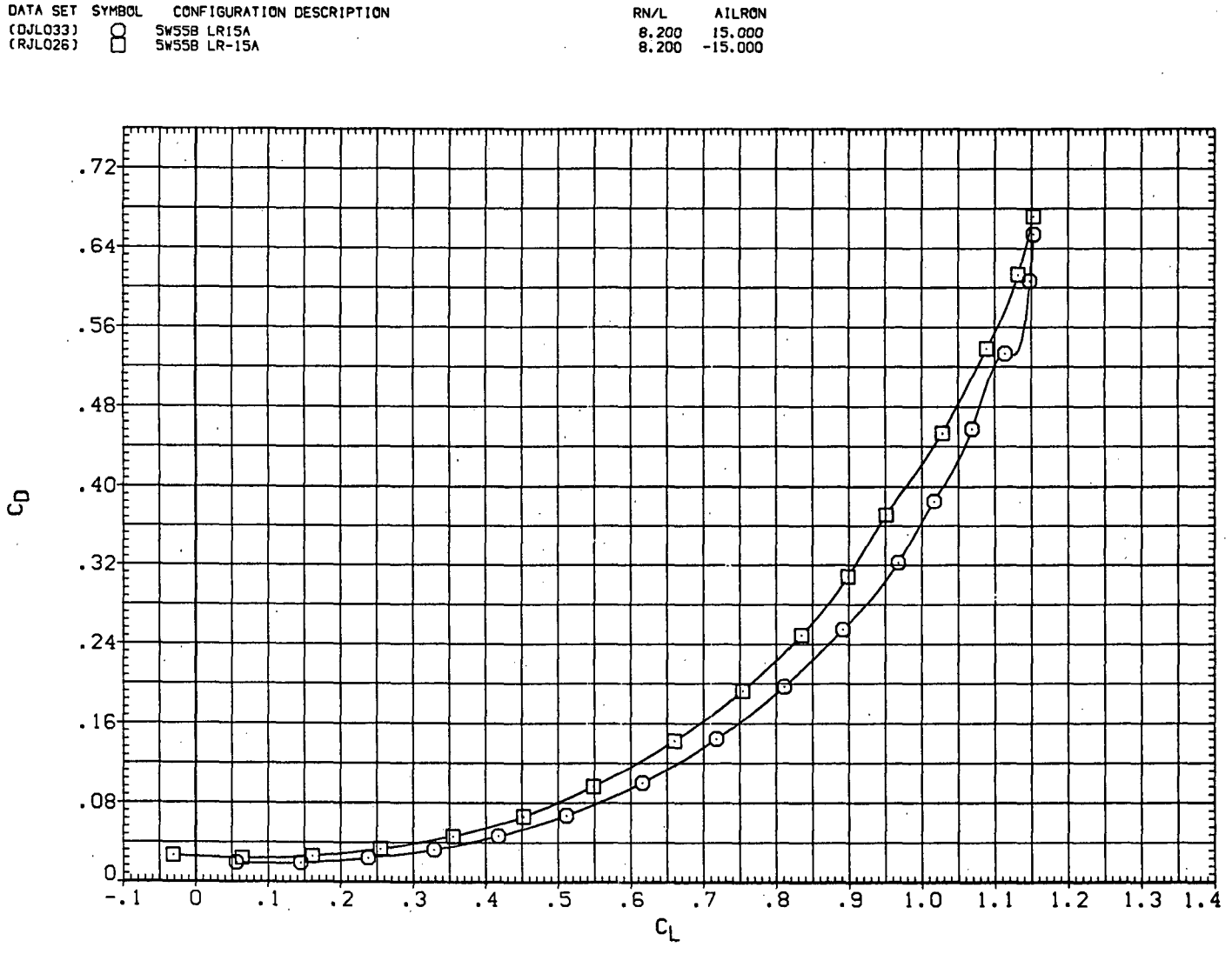

(b) C_D vs C_L

Figure 37.– Continued.

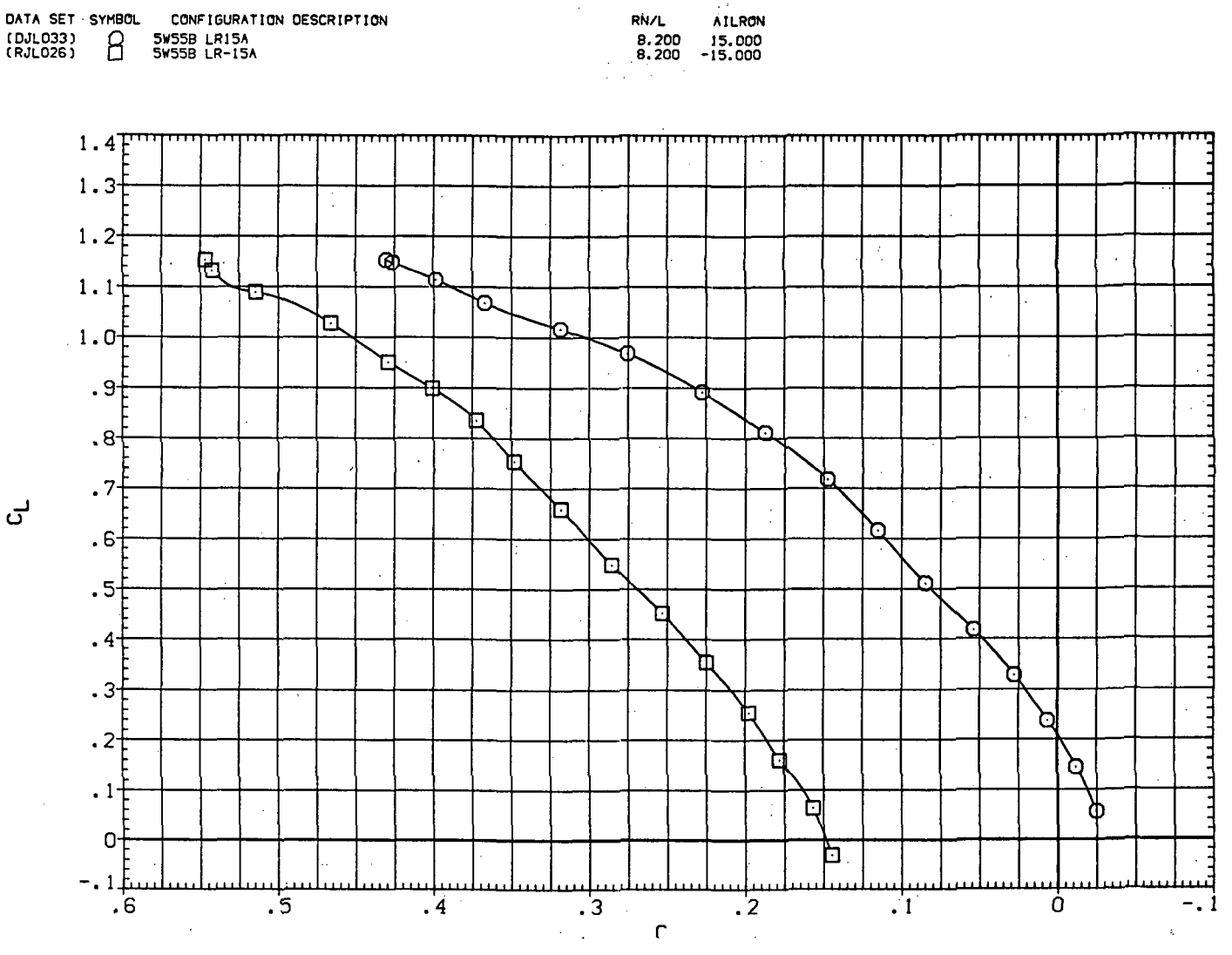

(c) C_L vs C_m

Figure 37.– Continued.

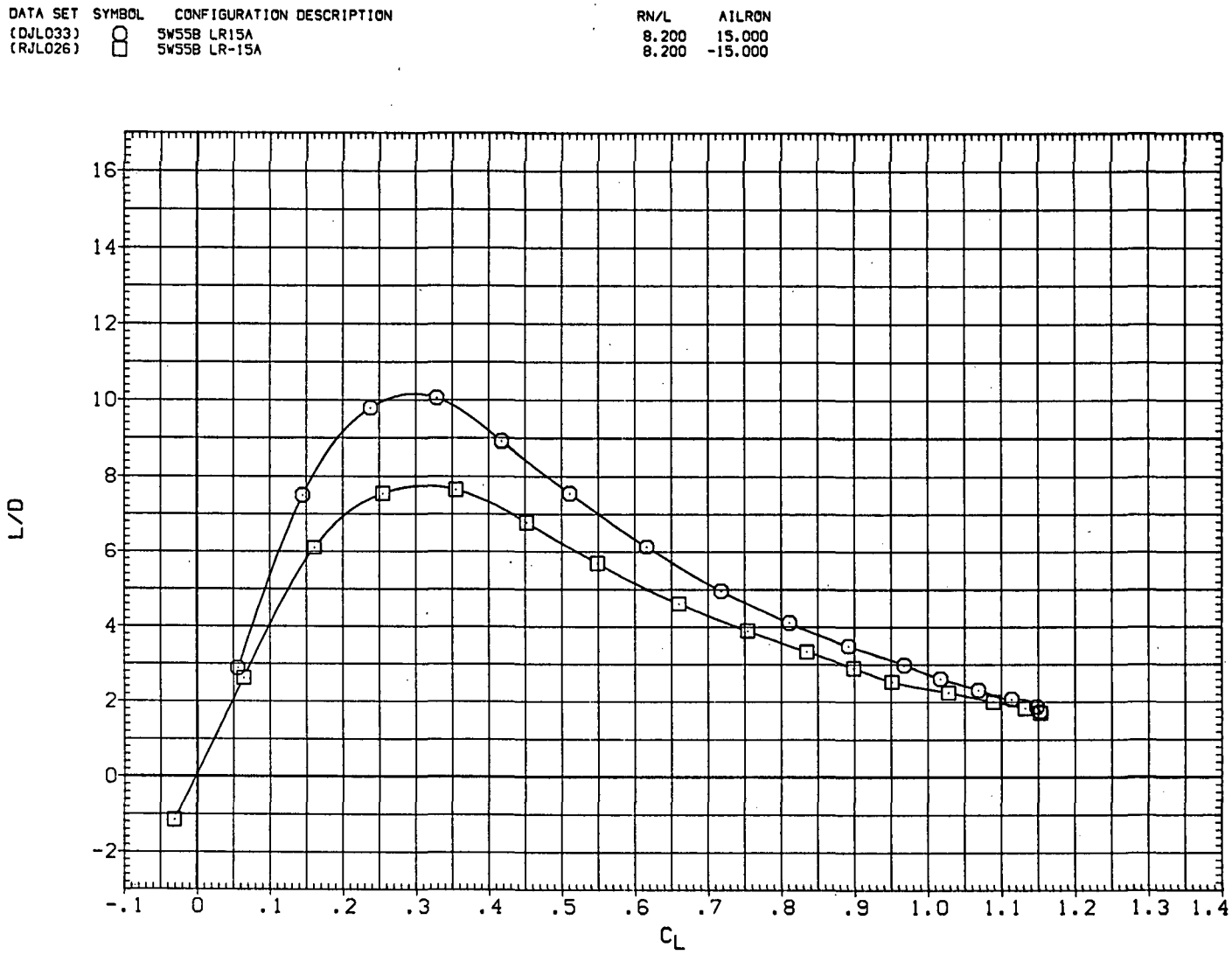

(d) L/D vs C_L

Figure 37.– Continued.

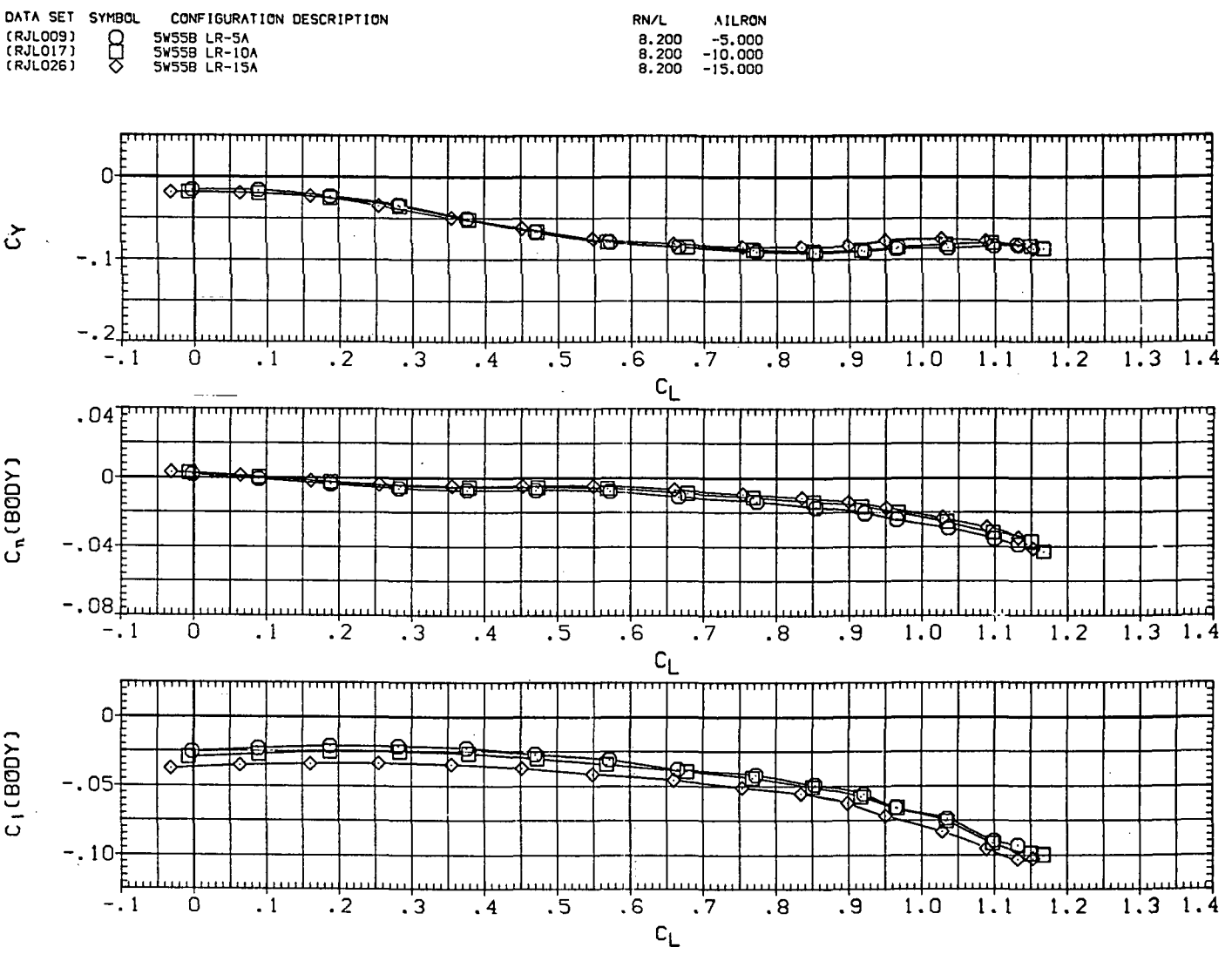

(e) C_Y, C_n, and C_l vs C_L (negative $\Delta\delta_a$'s).

Figure 37.– Continued.

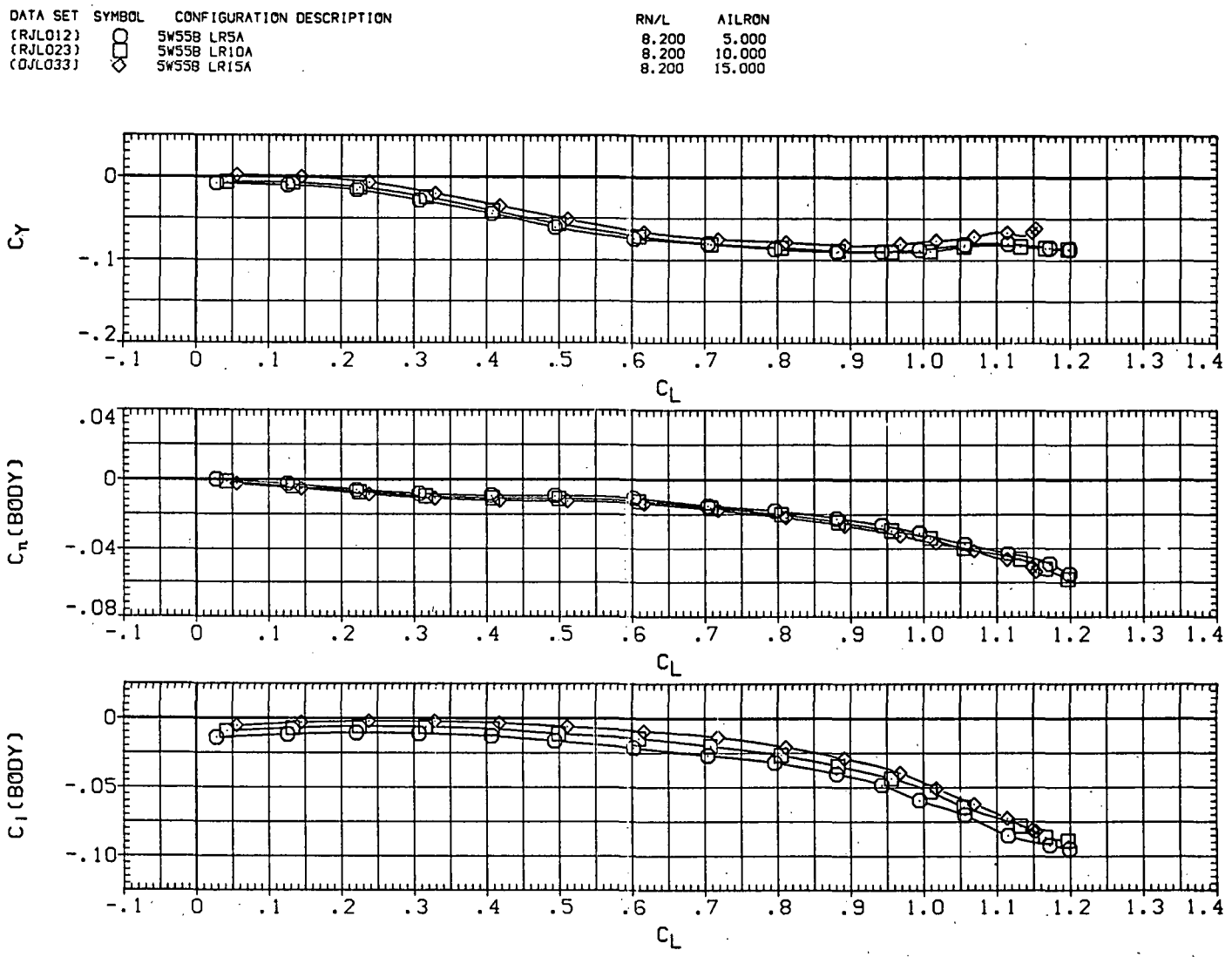

(f) C_Y, C_n, and C_l vs C_L (positive $\Delta\delta_a$'s).

Figure 37.– Concluded.

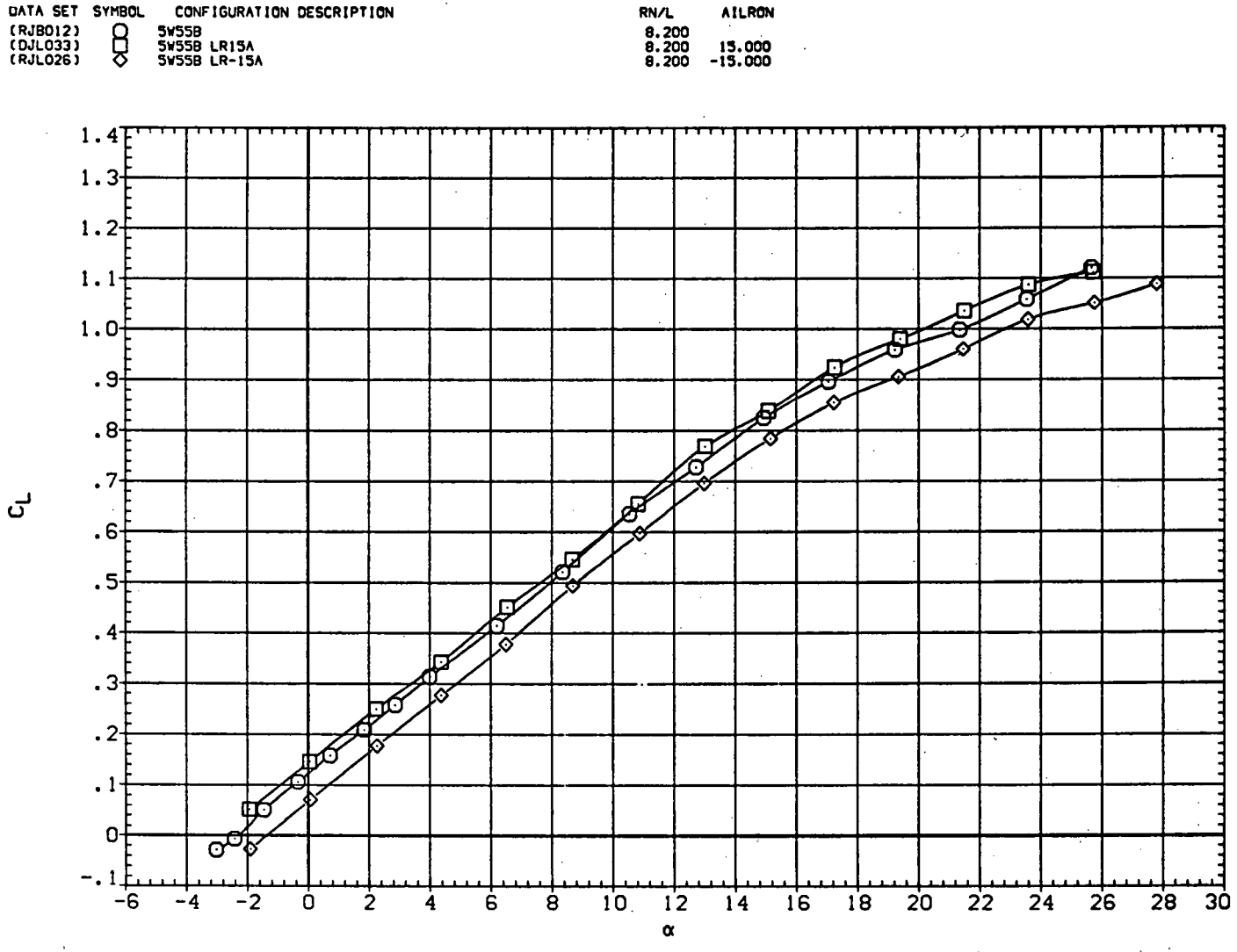

(a) C_L vs α

Figure 38.– Aileron effectiveness on the oblique wing with intermediate bend: $\Lambda = 55°, M = 0.90$.

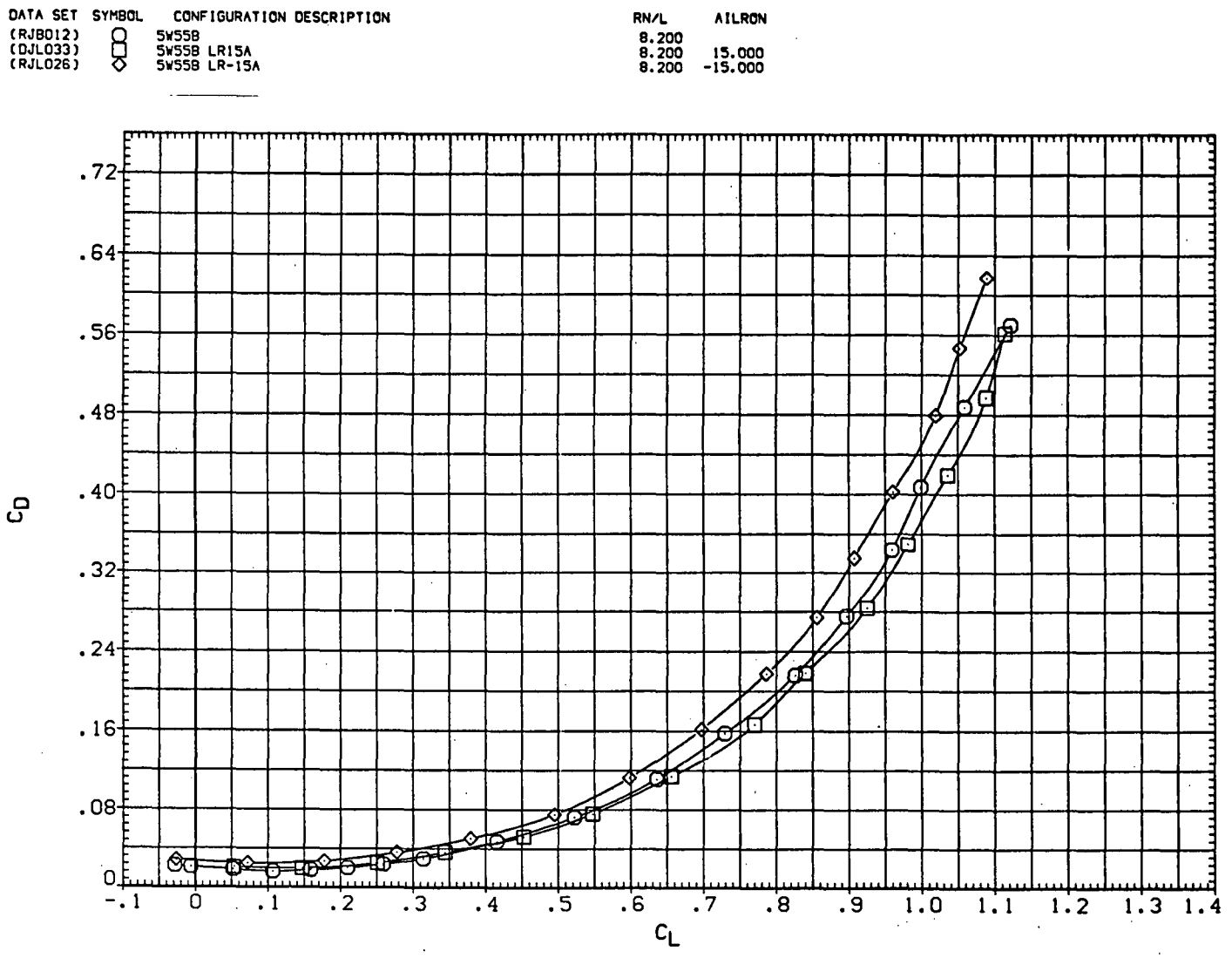

(b) C_D vs C_L

Figure 38.– Continued.

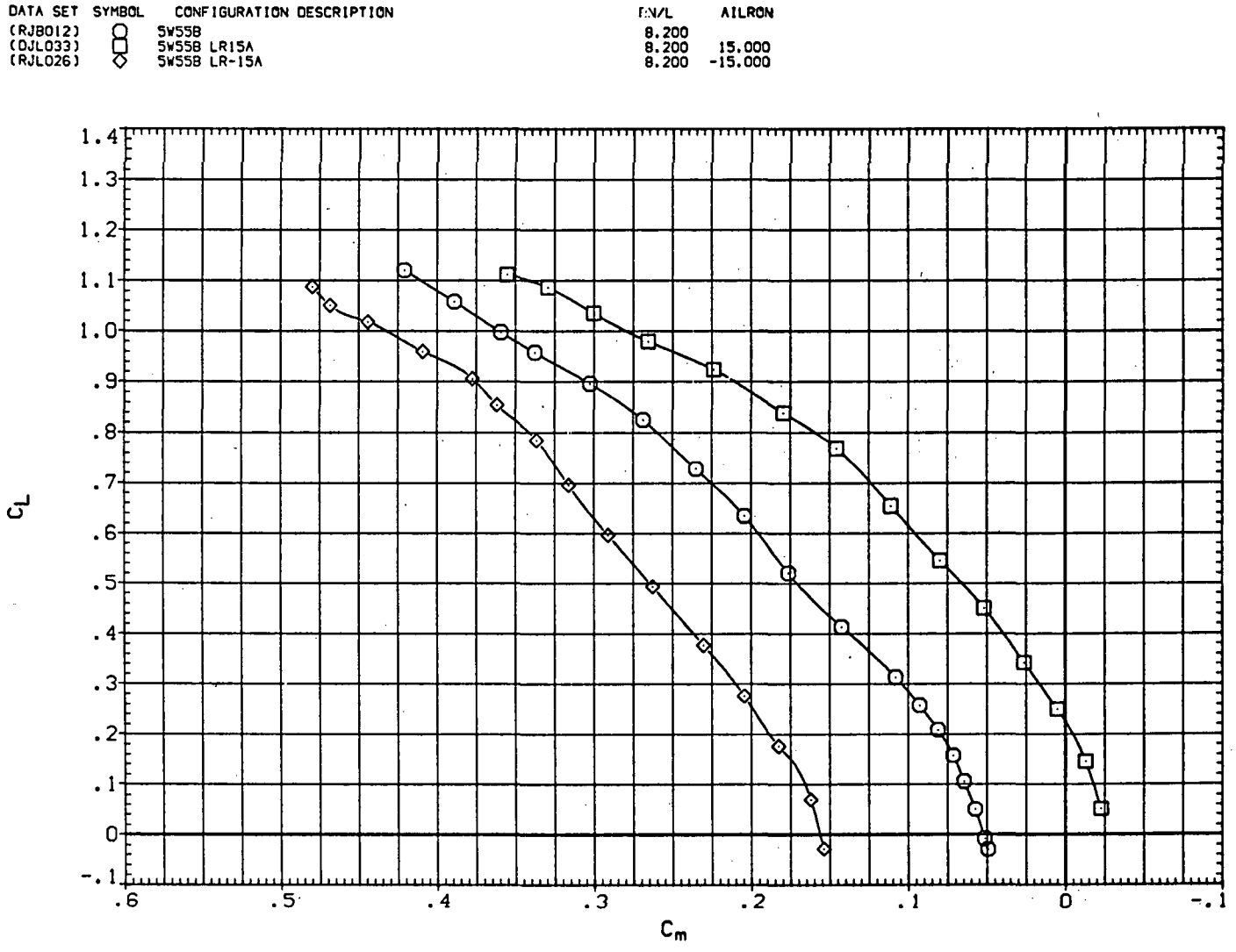

(c) C_L vs C_m

Figure 38.– Continued.

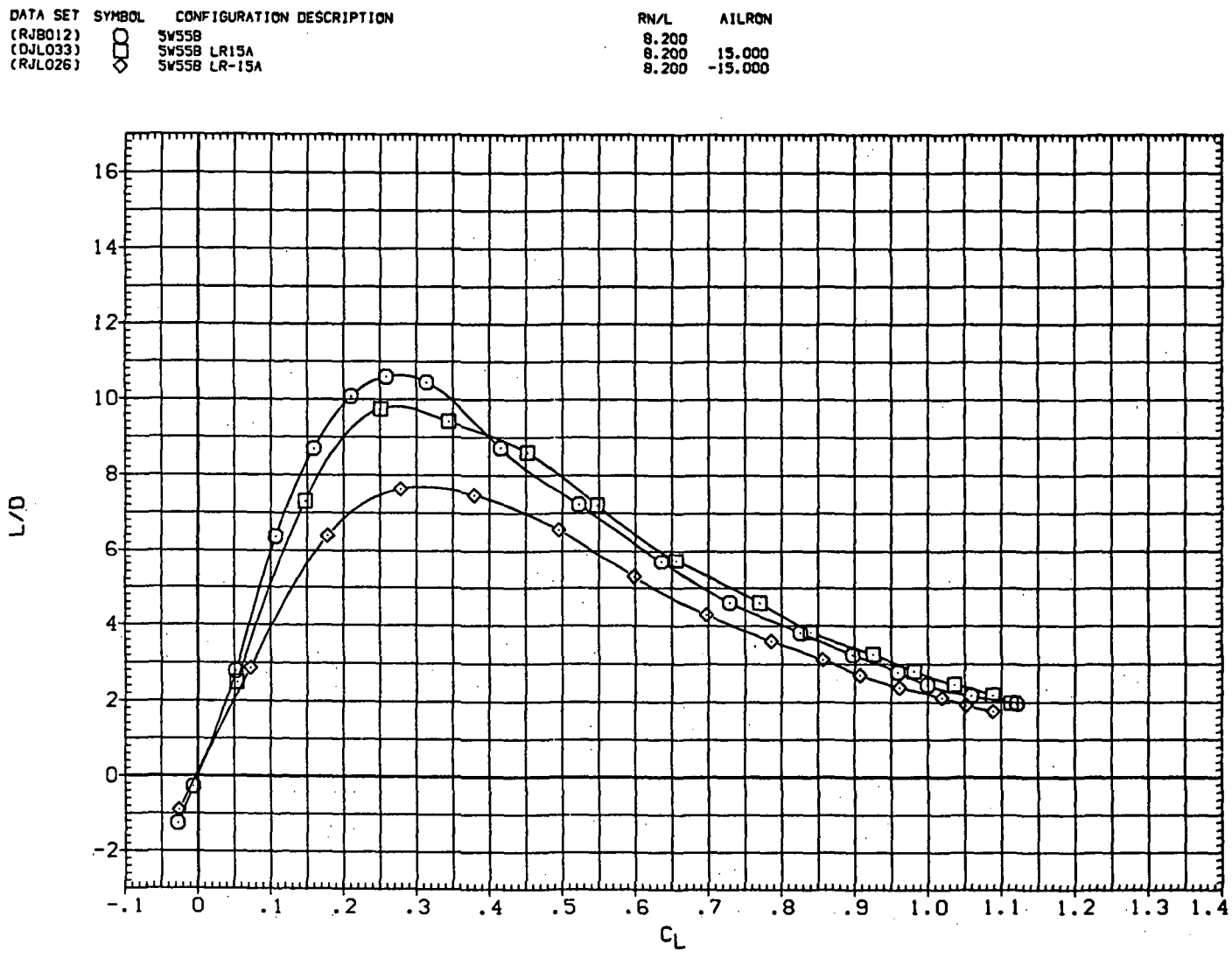

(d) L/D vs C_L

Figure 38.– Continued.

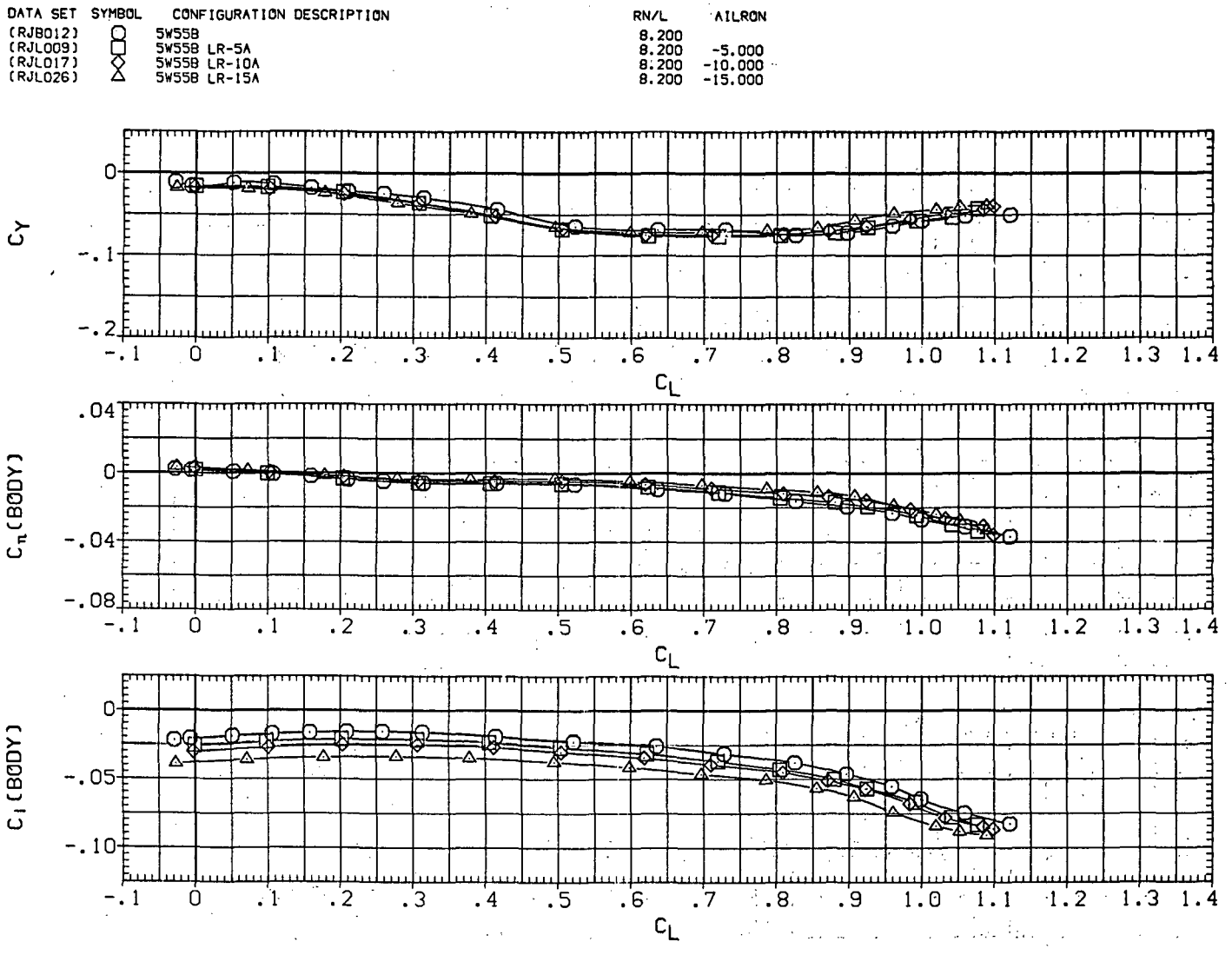

(e) C_Y, C_n, and C_l vs C_L (negative $\Delta\delta_a$'s).

Figure 38.– Continued.

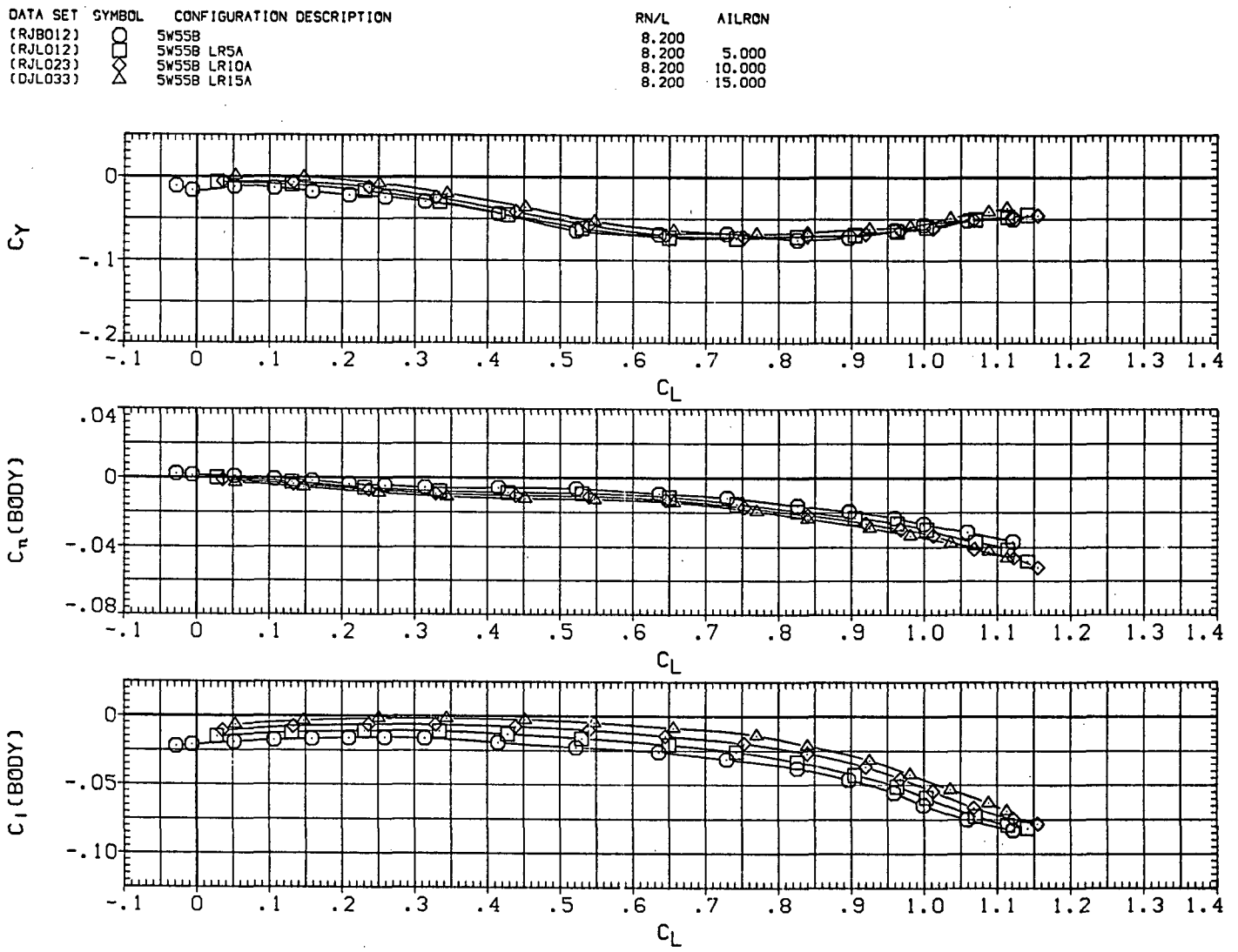

(f) C_Y, C_n, and C_l vs C_L (positive $\Delta\delta_a$'s).

Figure 38.– Concluded.

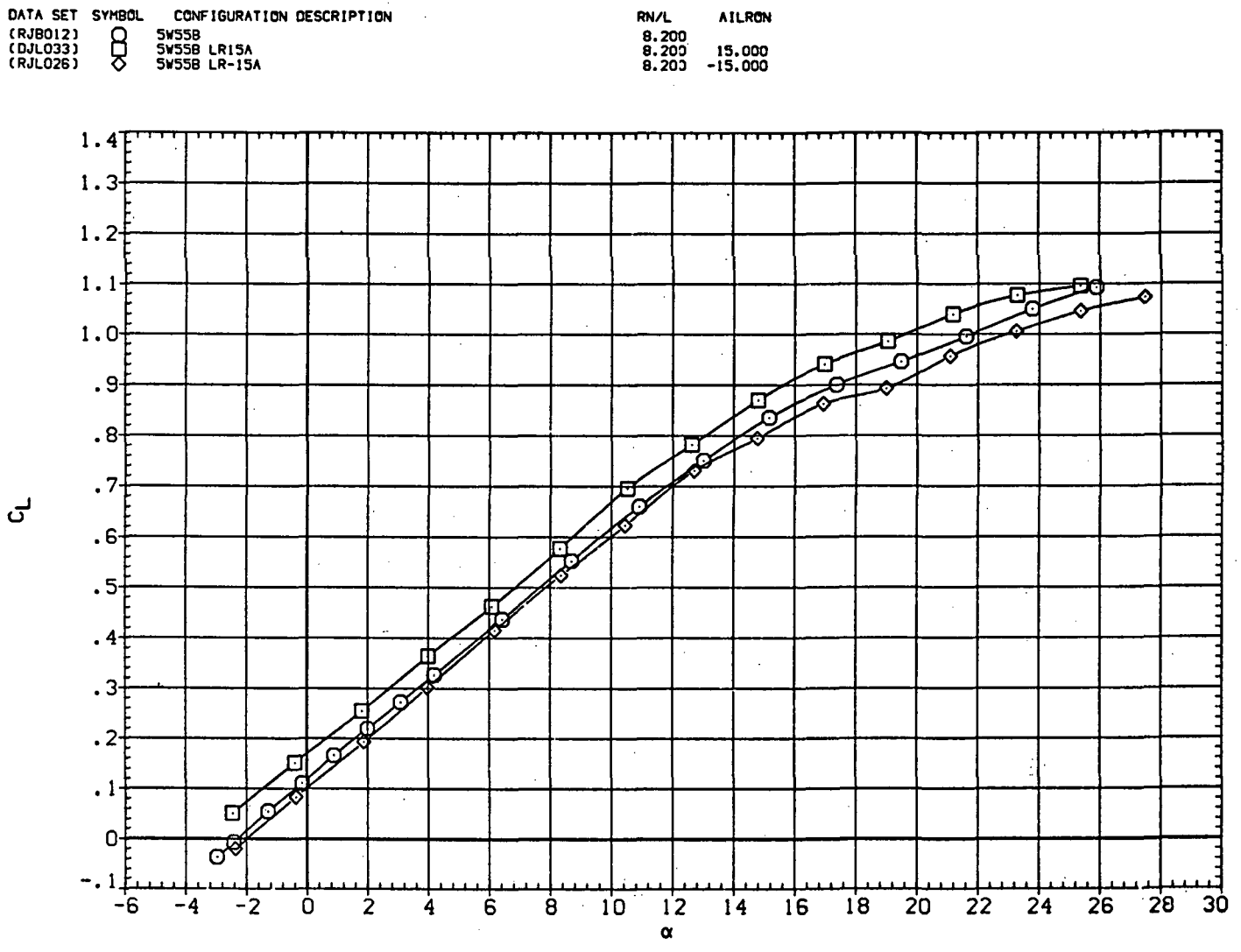

(a) C_L vs α

Figure 39.– Aileron effectiveness on the oblique wing with intermediate bend: $\Lambda = 55°, M = 0.90$.

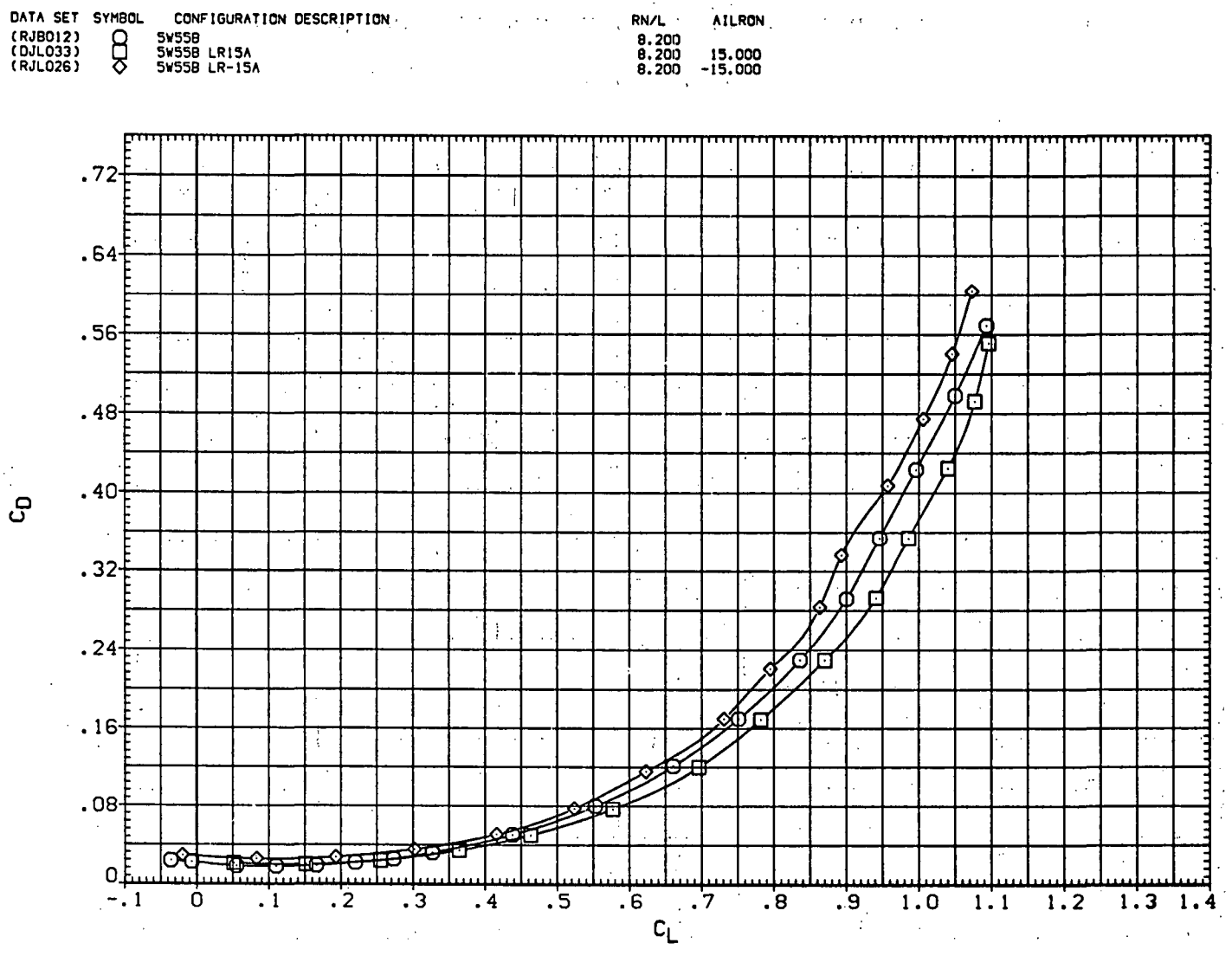

(b) C_D vs C_L

Figure 39.– Continued.

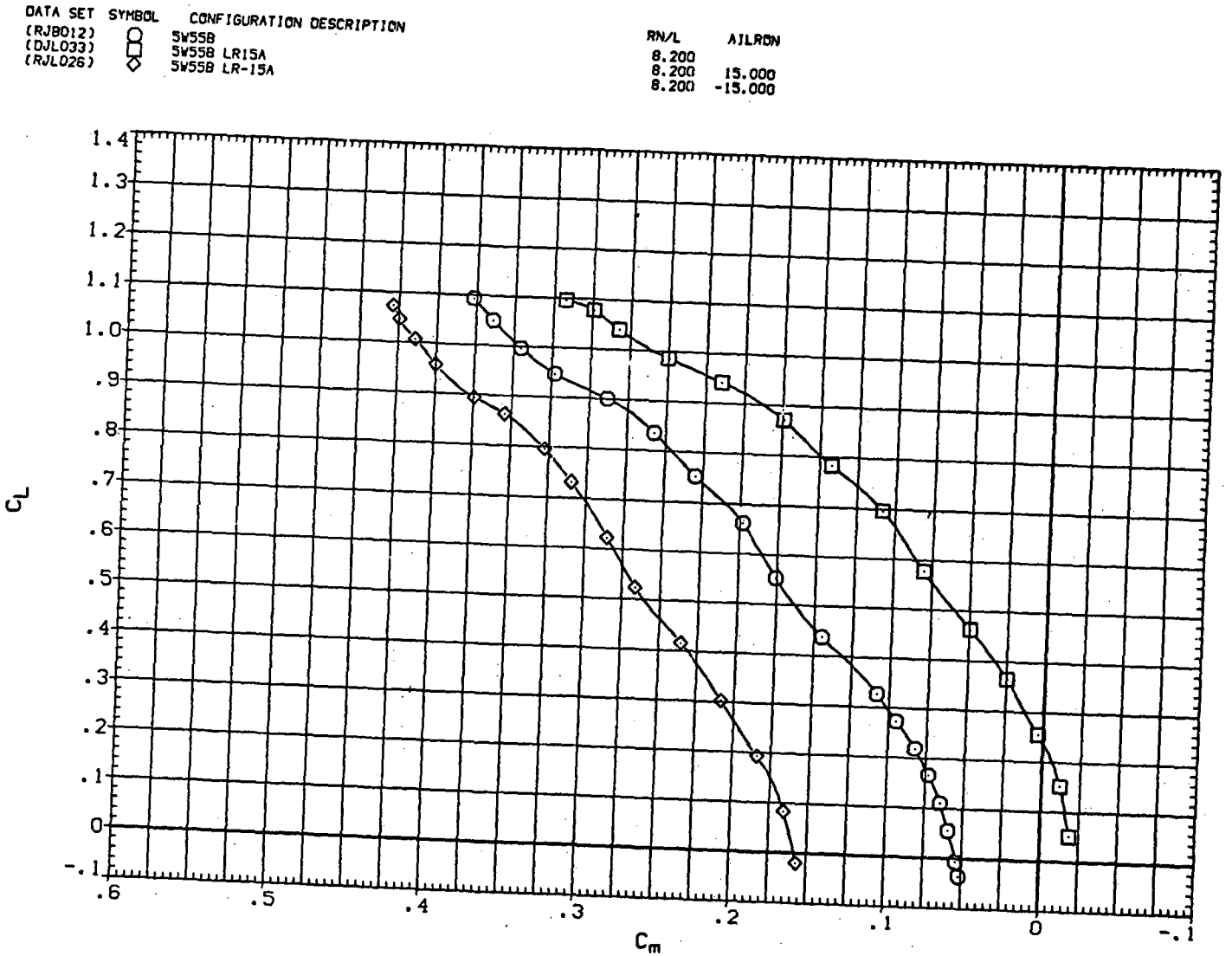

(c) C_L vs C_m

Figure 39.– Continued.

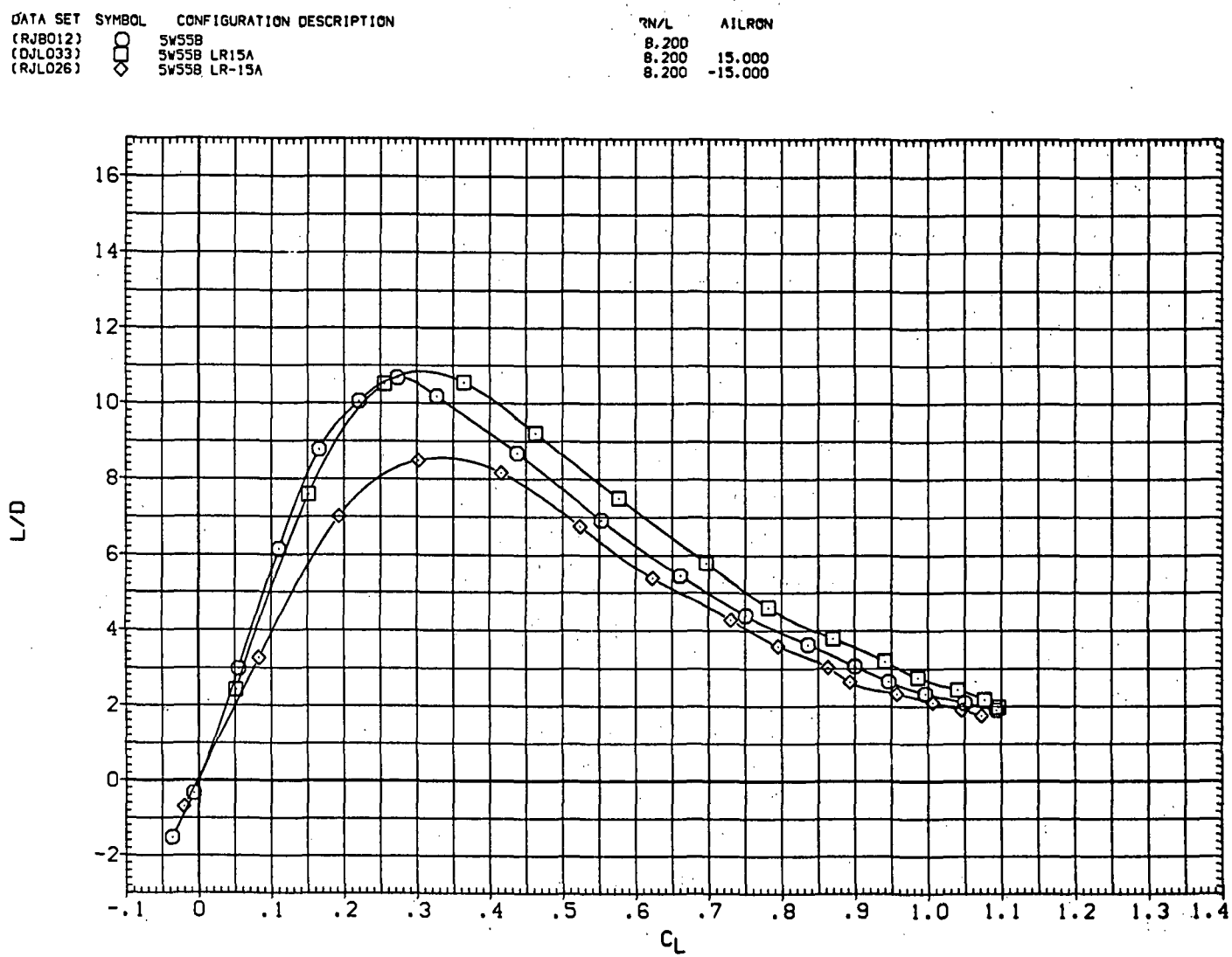

(d) L/D vs C_L

Figure 39.– Continued.

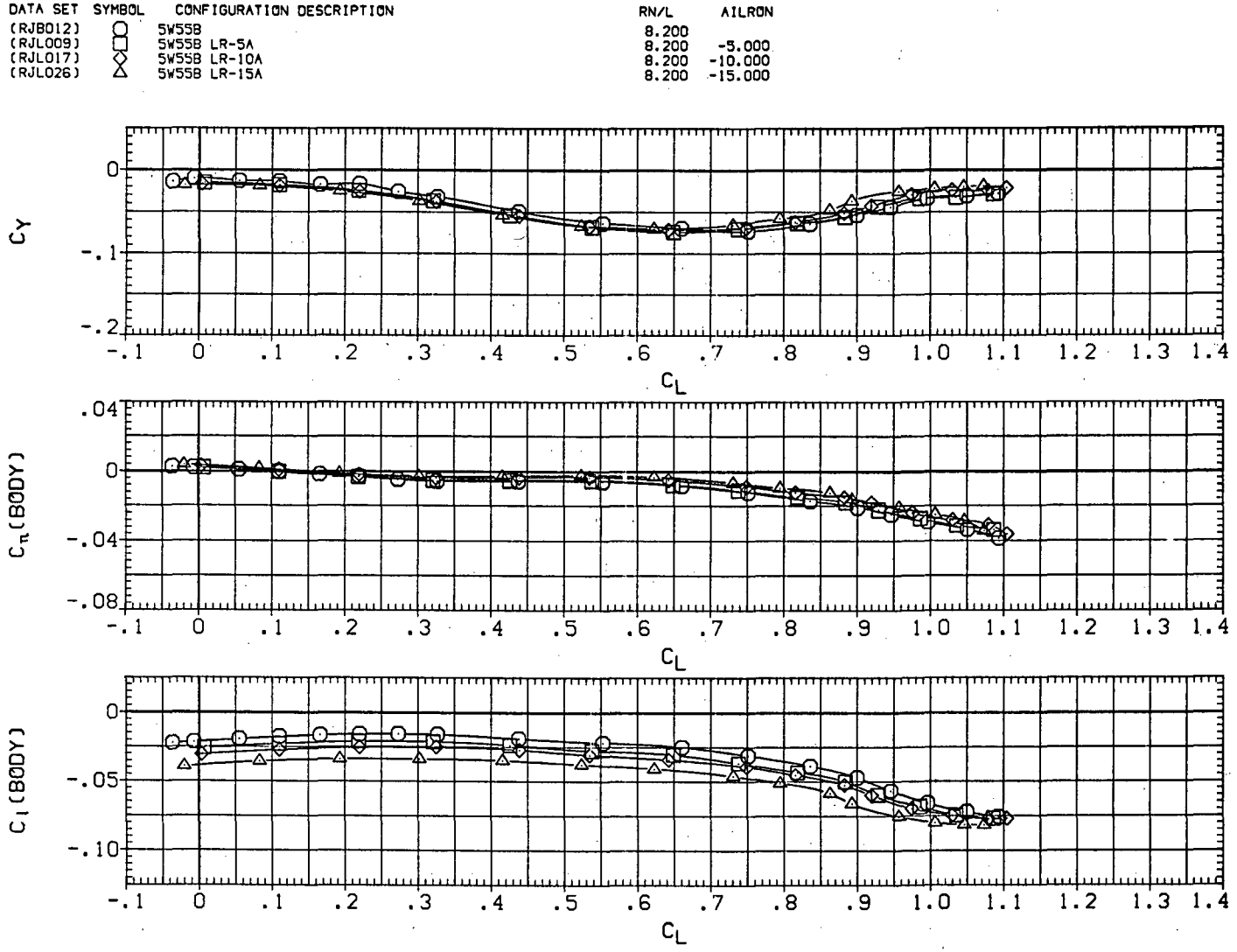

(e) C_Y, C_n, and C_l vs C_L (negative $\Delta\delta_a$'s).

Figure 39.– Continued.

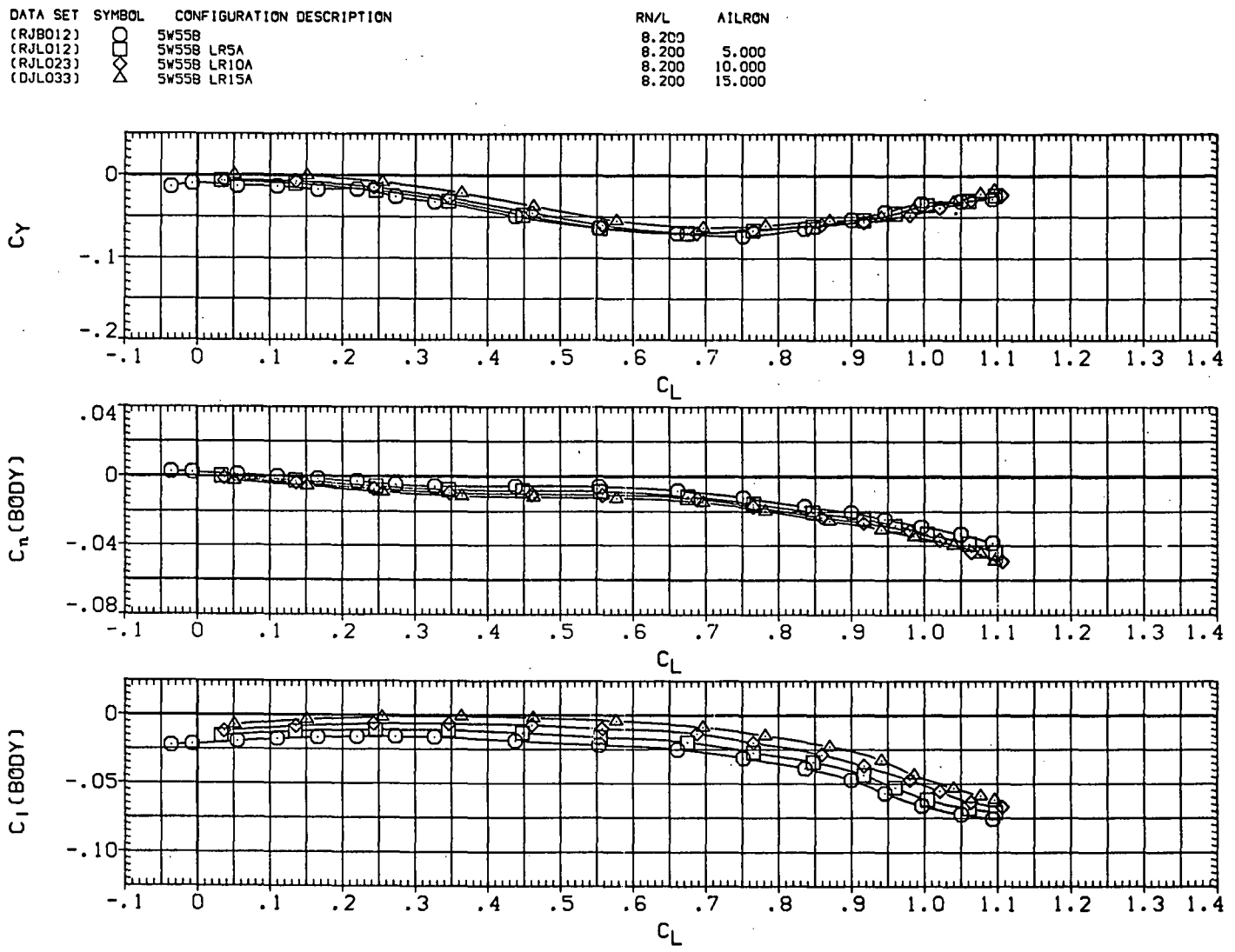

(f) C_Y, C_n, and C_l vs C_L (positive $\Delta\delta_a$'s).

Figure 39.– Concluded.

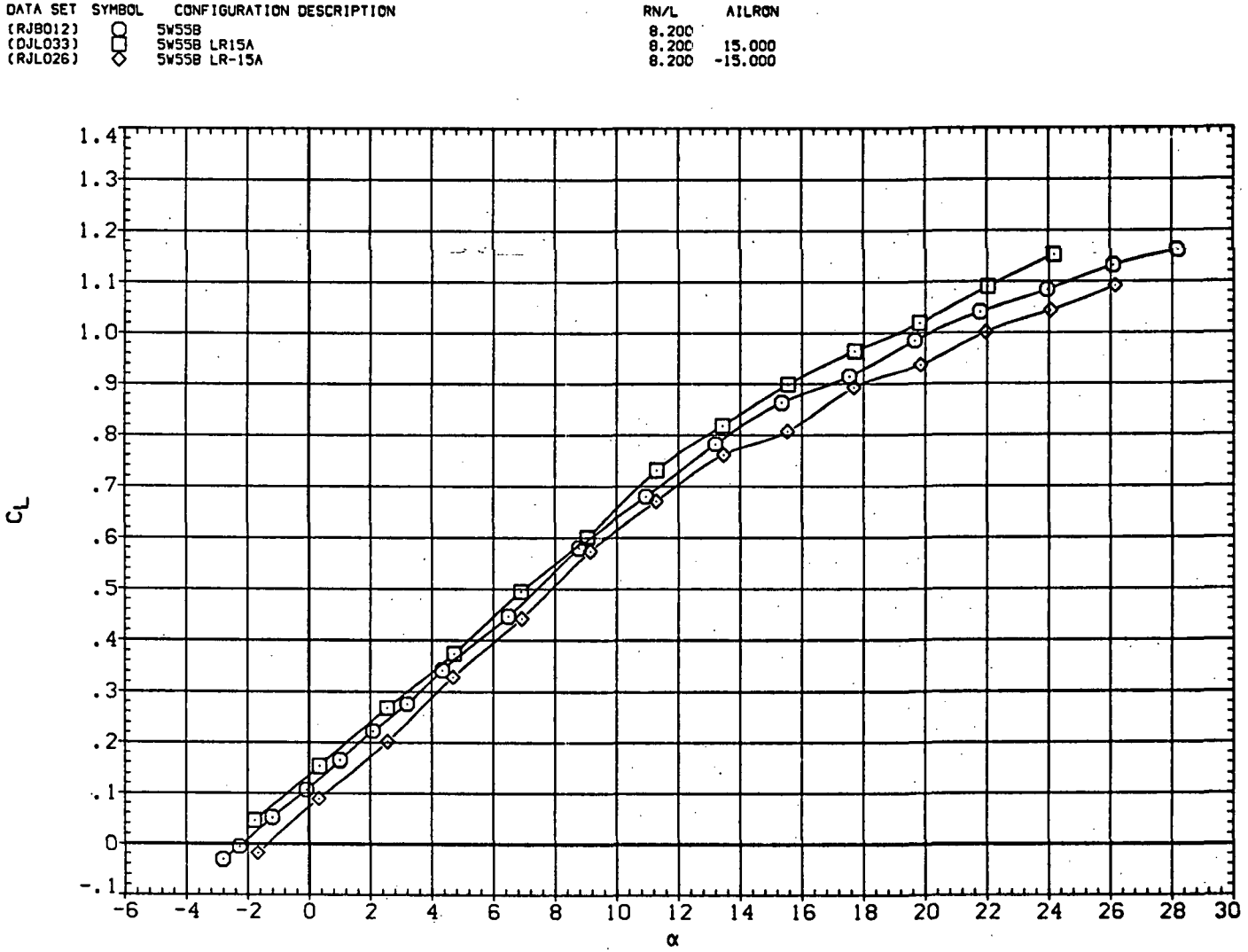

(a) C_L vs α

Figure 40.– Aileron effectiveness on the oblique wing with intermediate bend: $\Lambda = 55°, M = 0.95$.

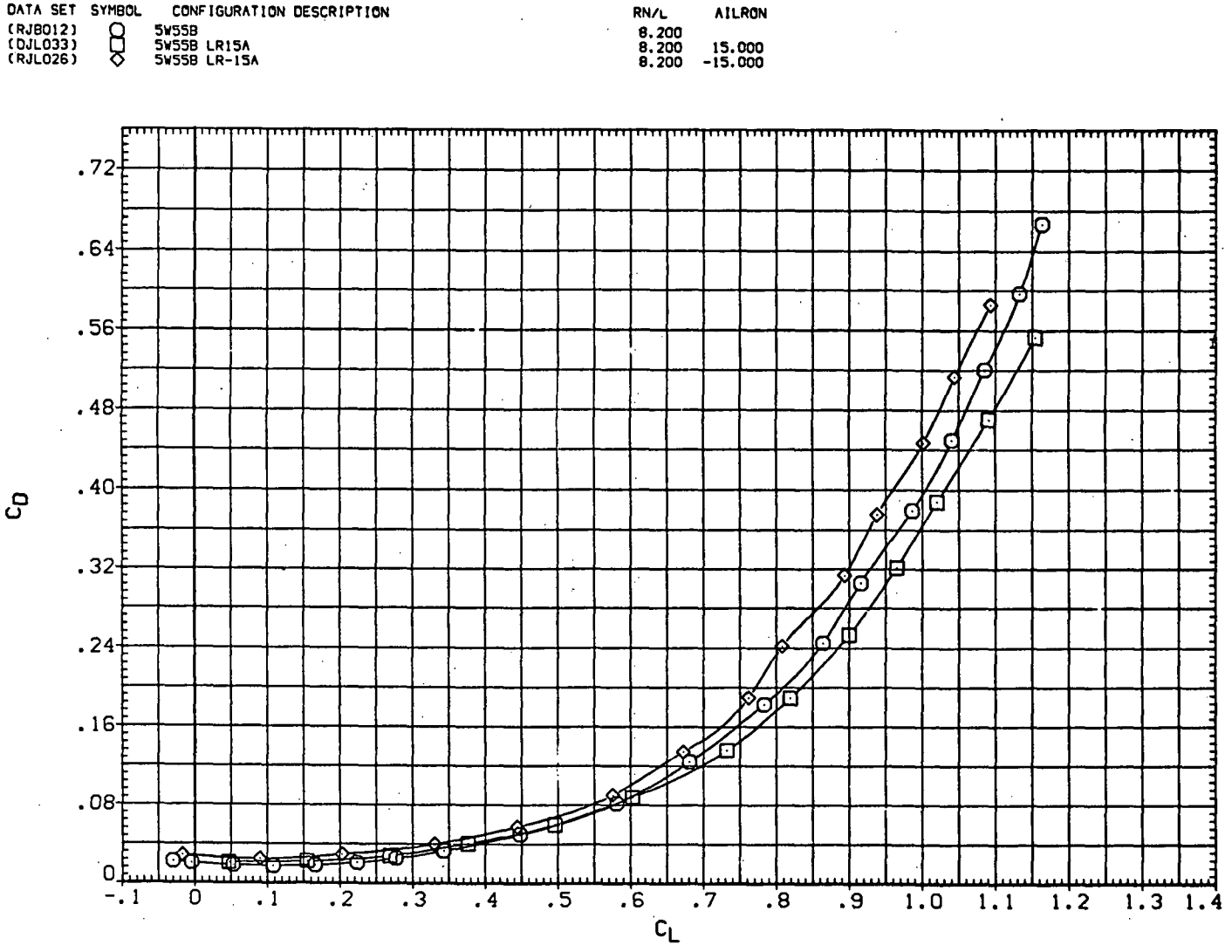

(b) C_D vs C_L

Figure 40.– Continued.

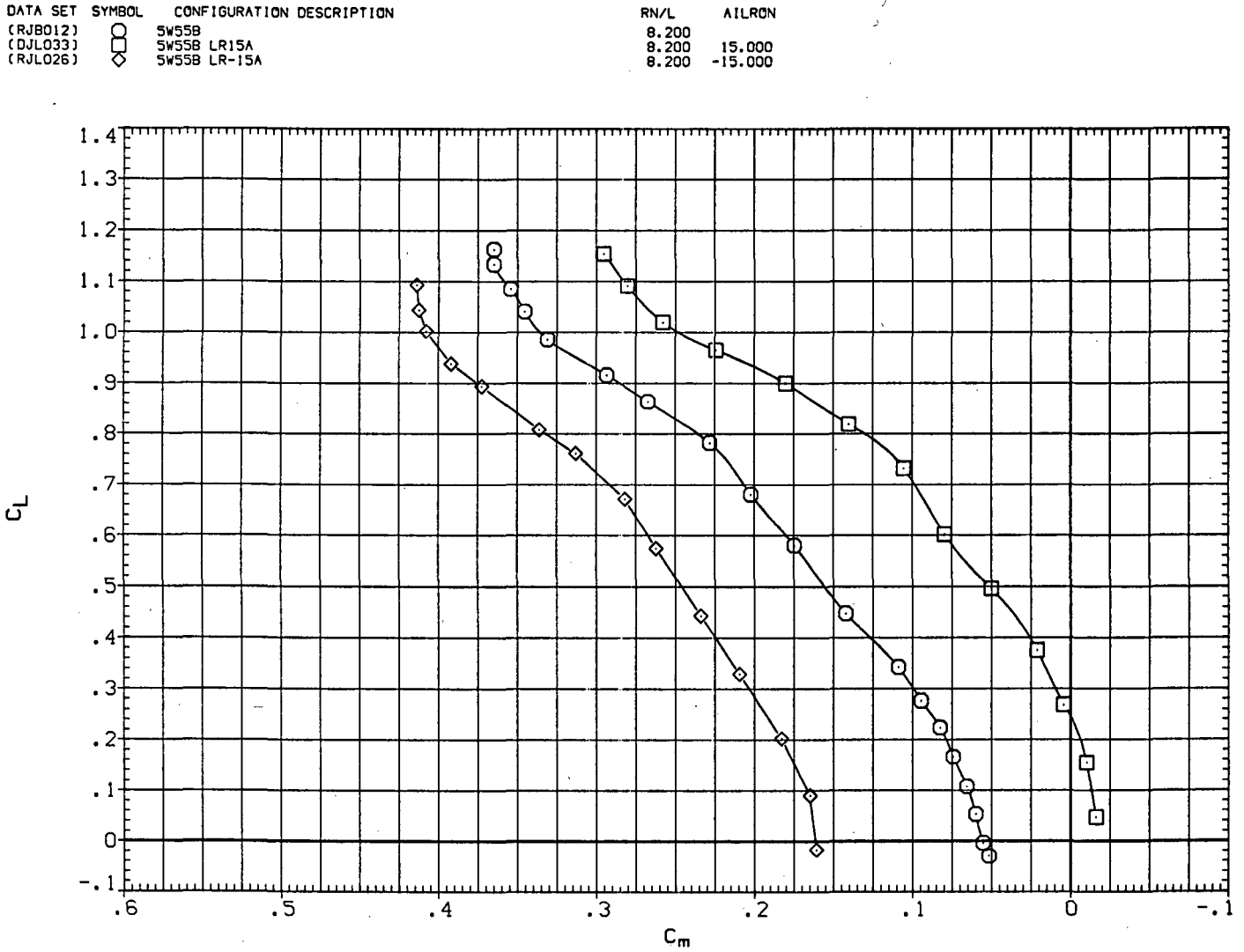

(c) C_L vs C_m

Figure 40.– Continued.

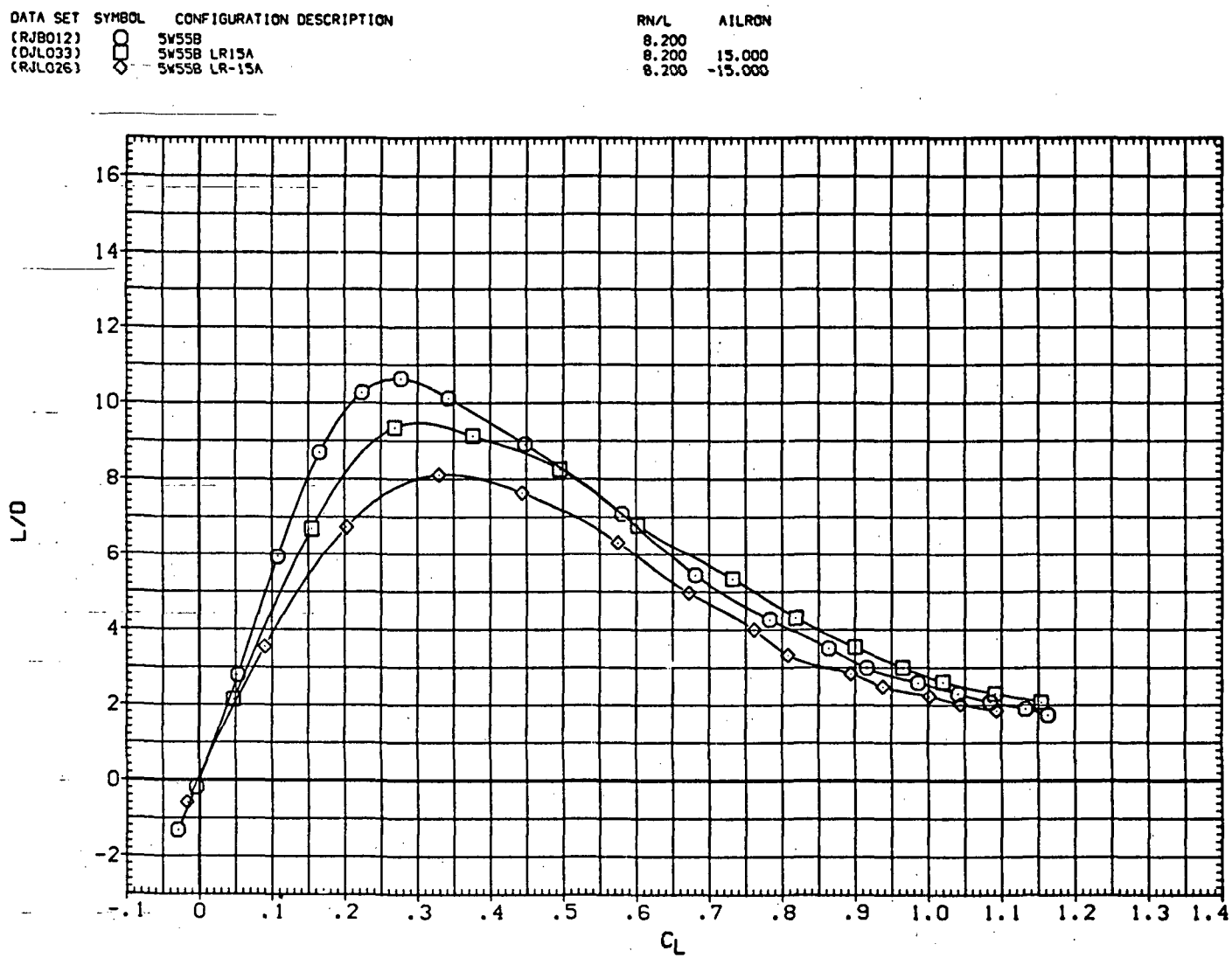

(d) L/D vs C_L

Figure 40.– Continued.

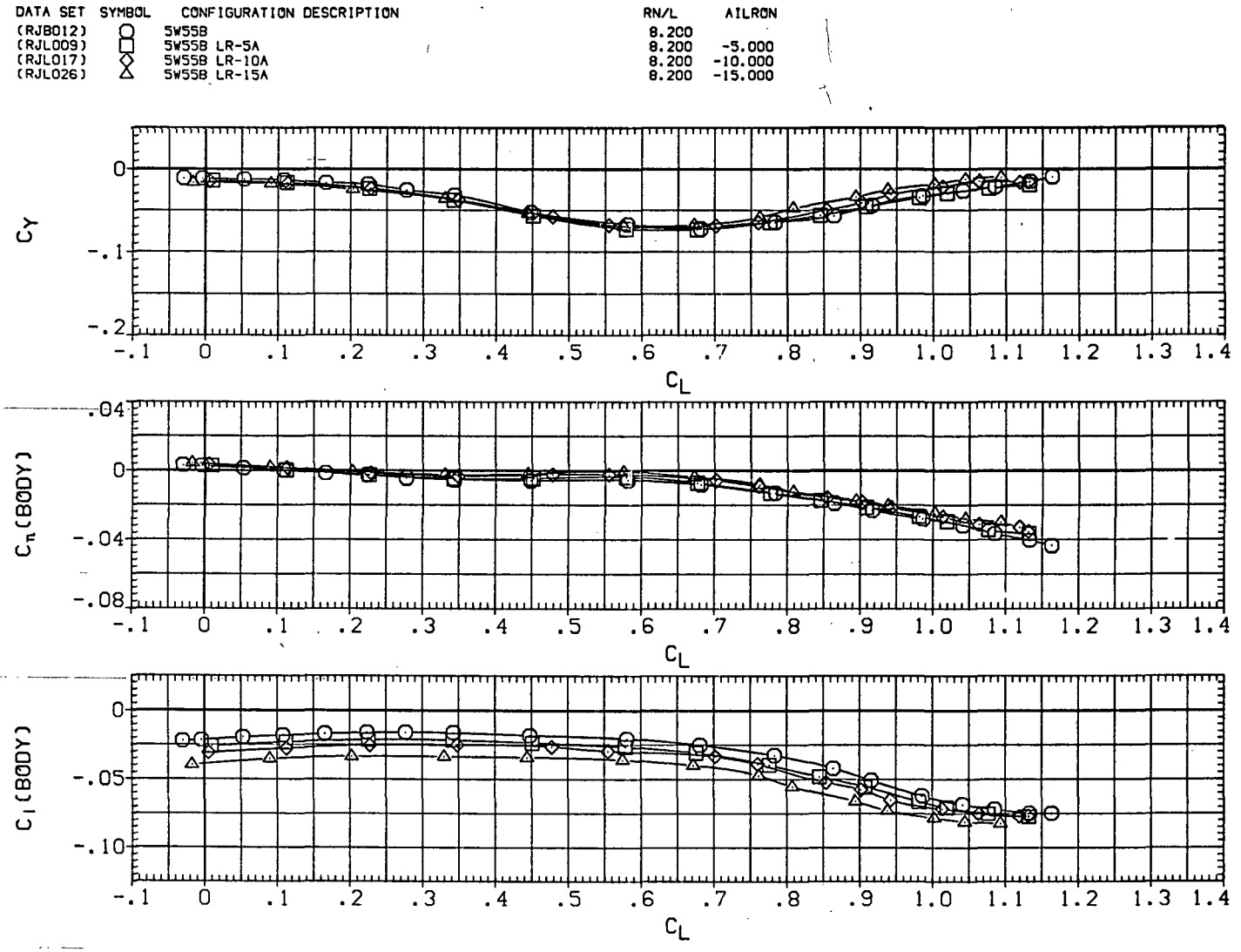

(e) C_Y, C_n, and C_l vs C_L (negative $\Delta\delta_a$'s).

Figure 40.– Continued.

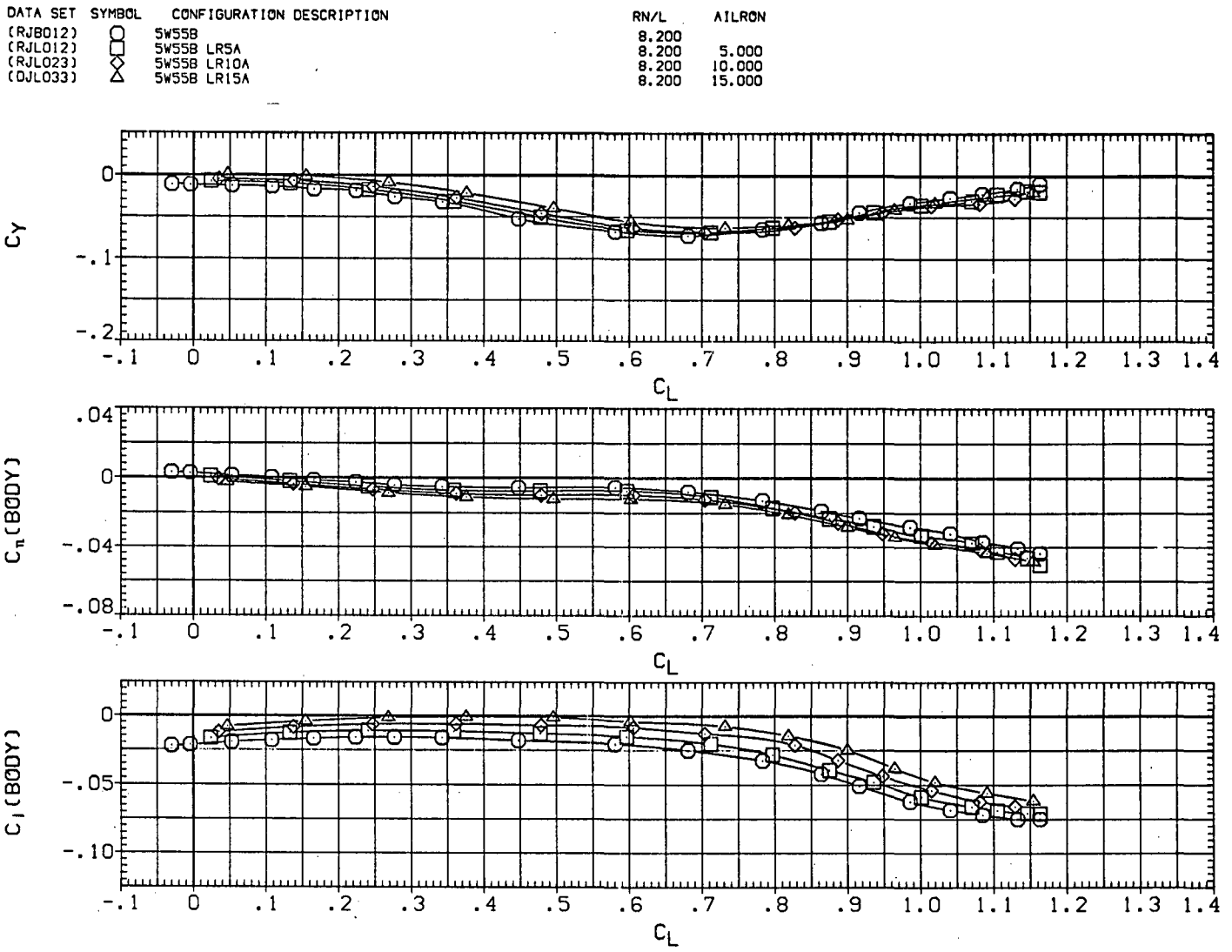

(f) C_Y, C_n, and C_l vs C_L (positive $\Delta\delta_a$'s).

Figure 40.– Concluded.

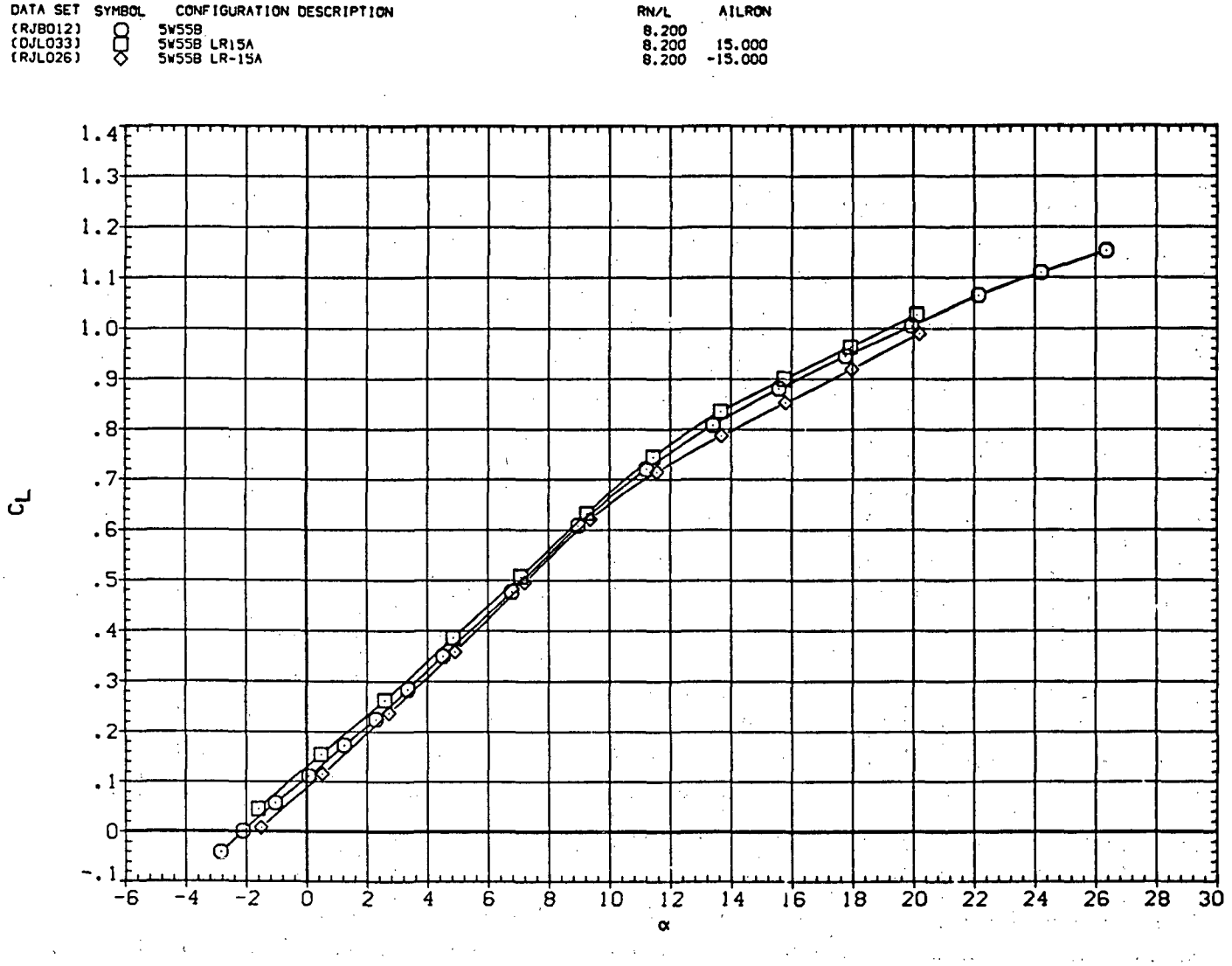

(a) C_L vs α

Figure 41.– Aileron effectiveness of the oblique wing with intermediate bend: $\Lambda = 55°, M = 1.1$.

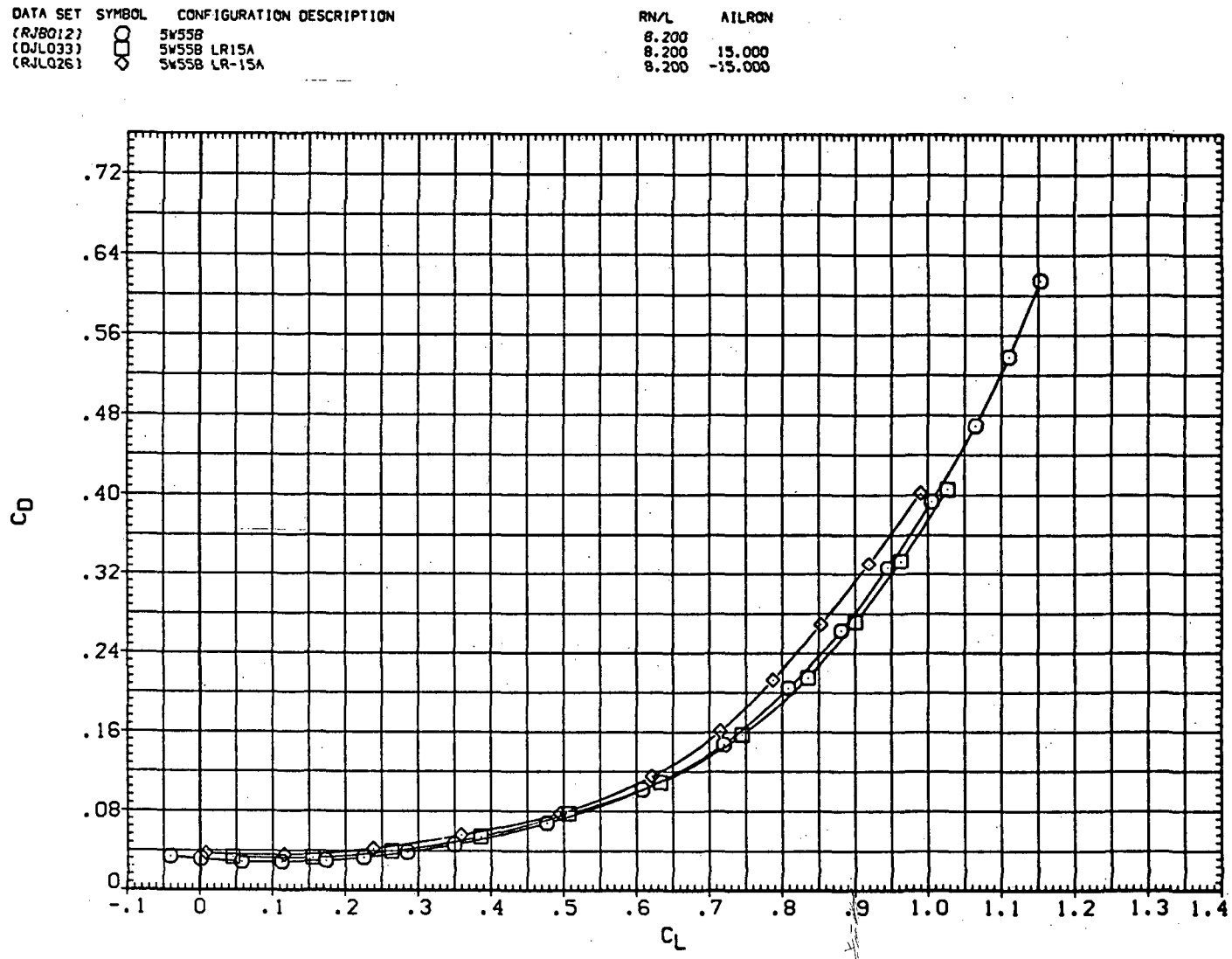

(b) C_D vs C_L

Figure 41.– Continued.

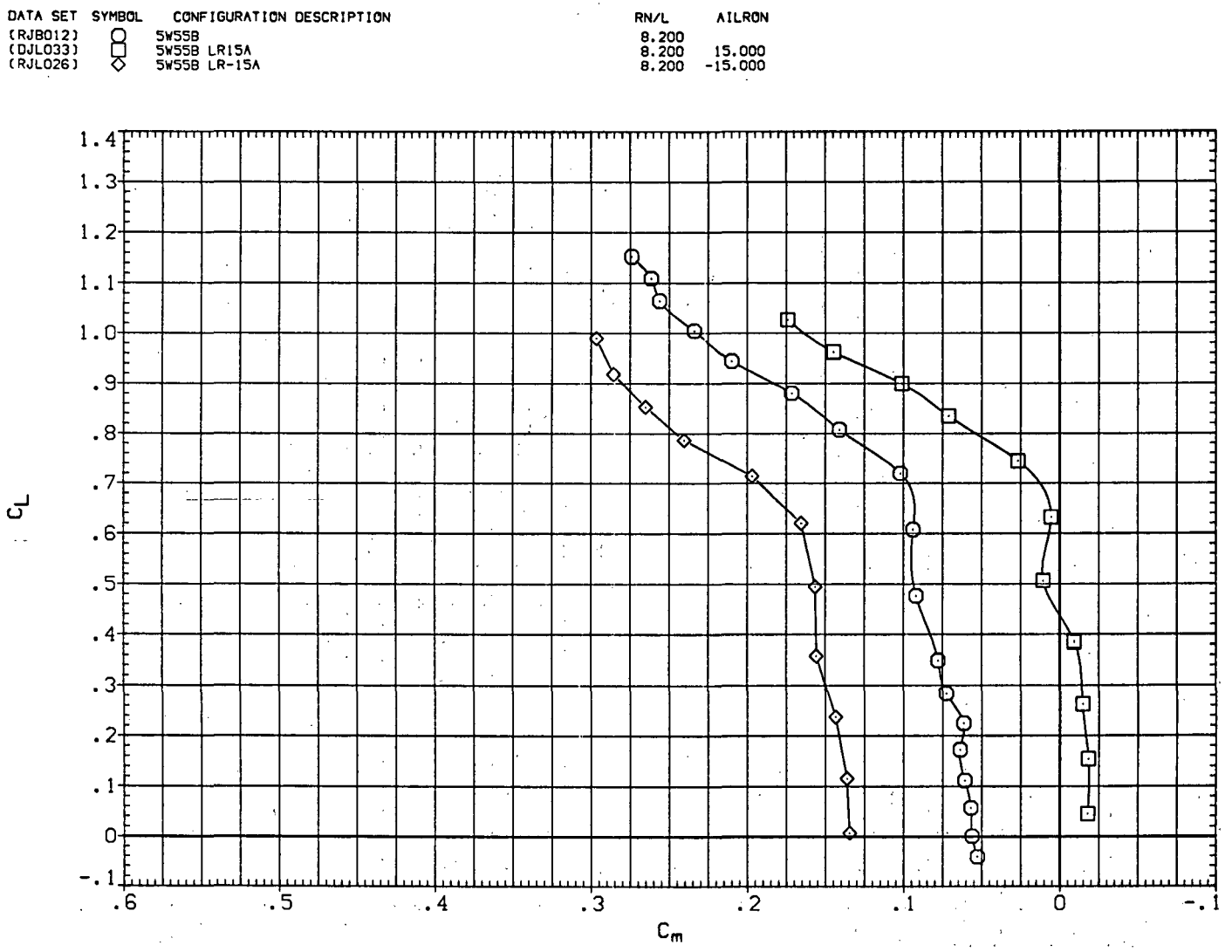

(c) C_L vs C_m

Figure 41.– Continued.

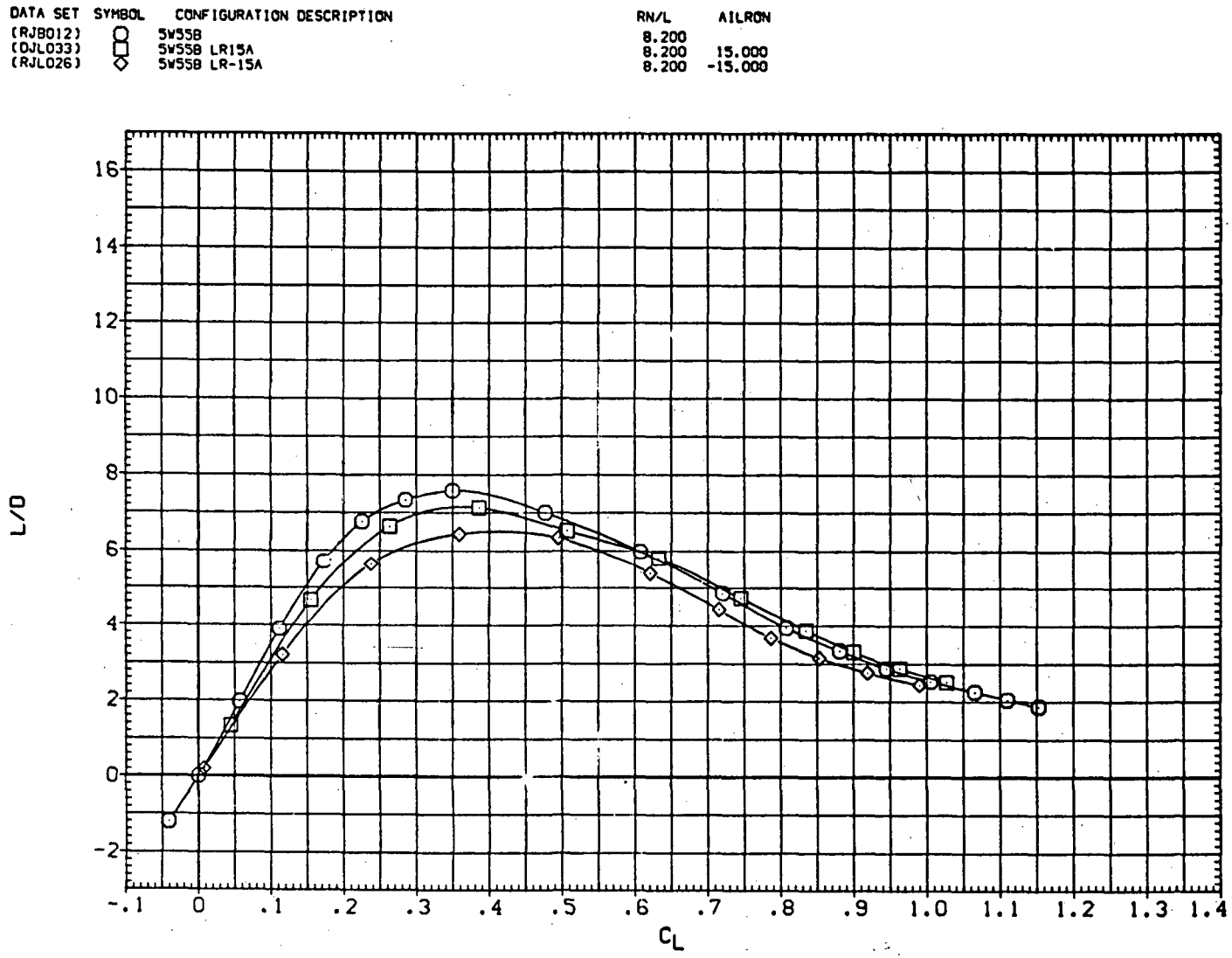

(d) L/D vs C_L

Figure 41.– Continued.

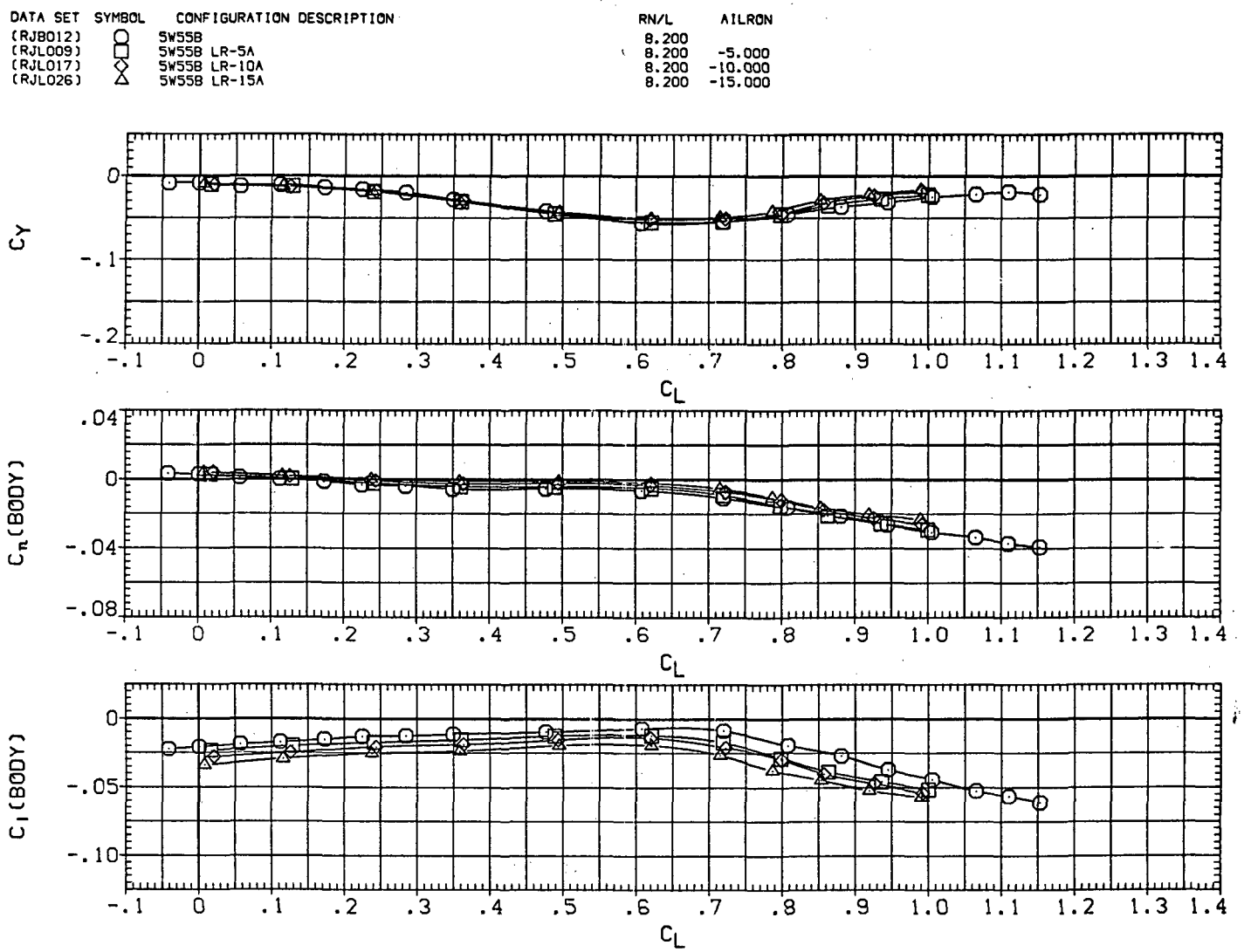

(e) C_Y, C_n, and C_l vs C_L (negative $\Delta\delta_a$'s).

Figure 41.– Continued.

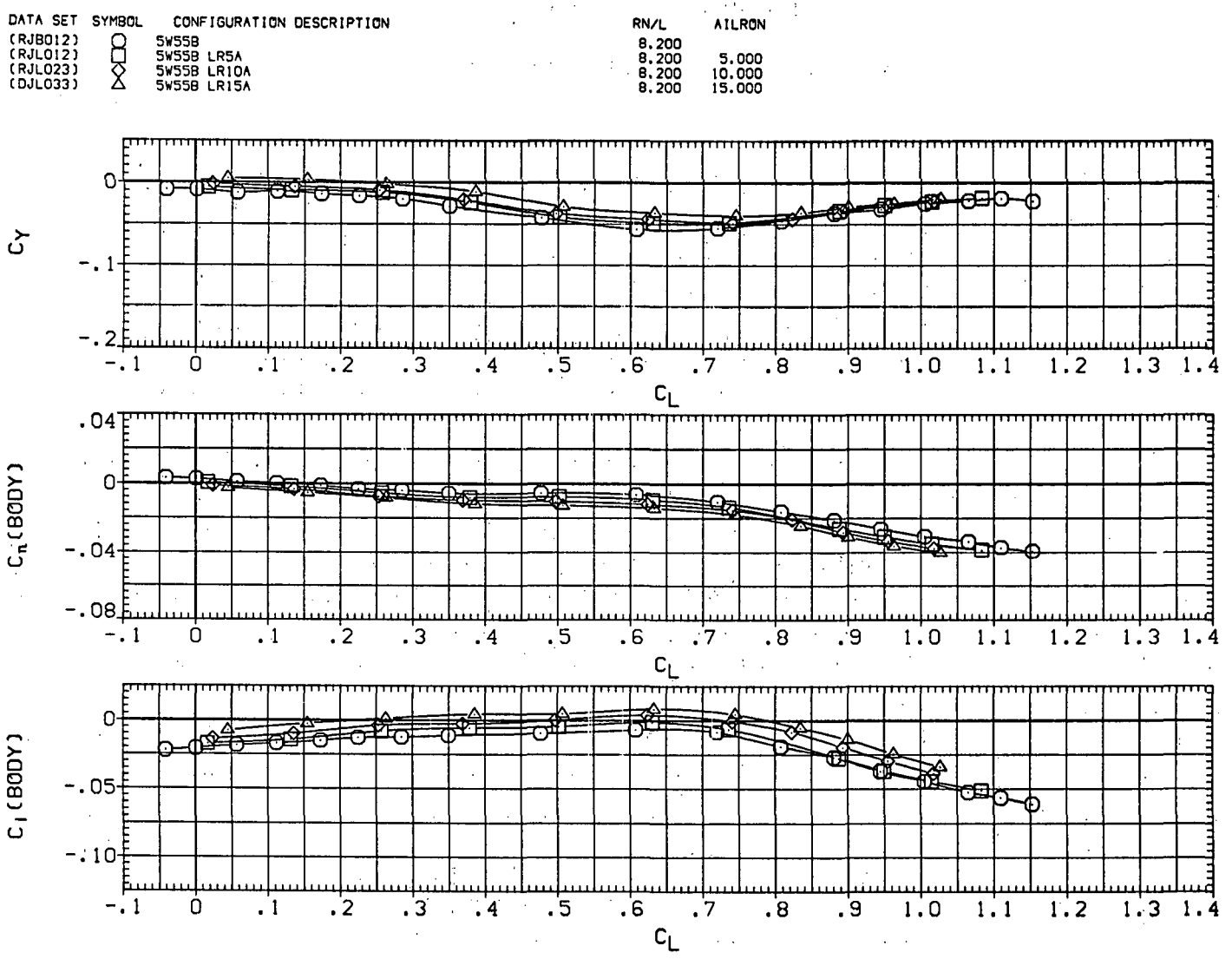

(f) C_Y, C_n, and C_l vs C_L (positive $\Delta\delta_a$'s).

Figure 41.– Concluded.

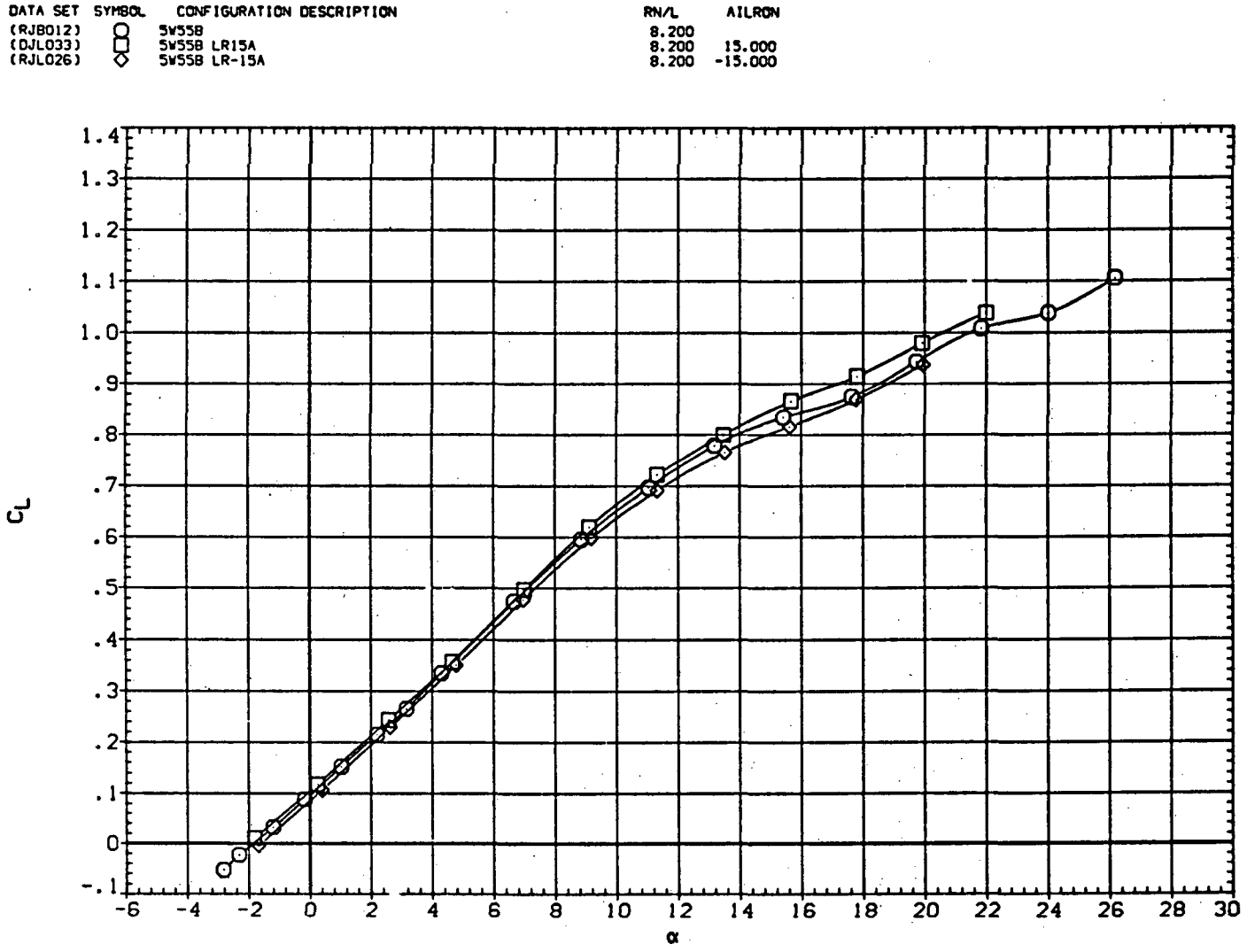

(a) C_L vs α

Figure 42.– Aileron effectiveness on the oblique wing with intermediate bend: $\Lambda = 55°, M = 1.20$.

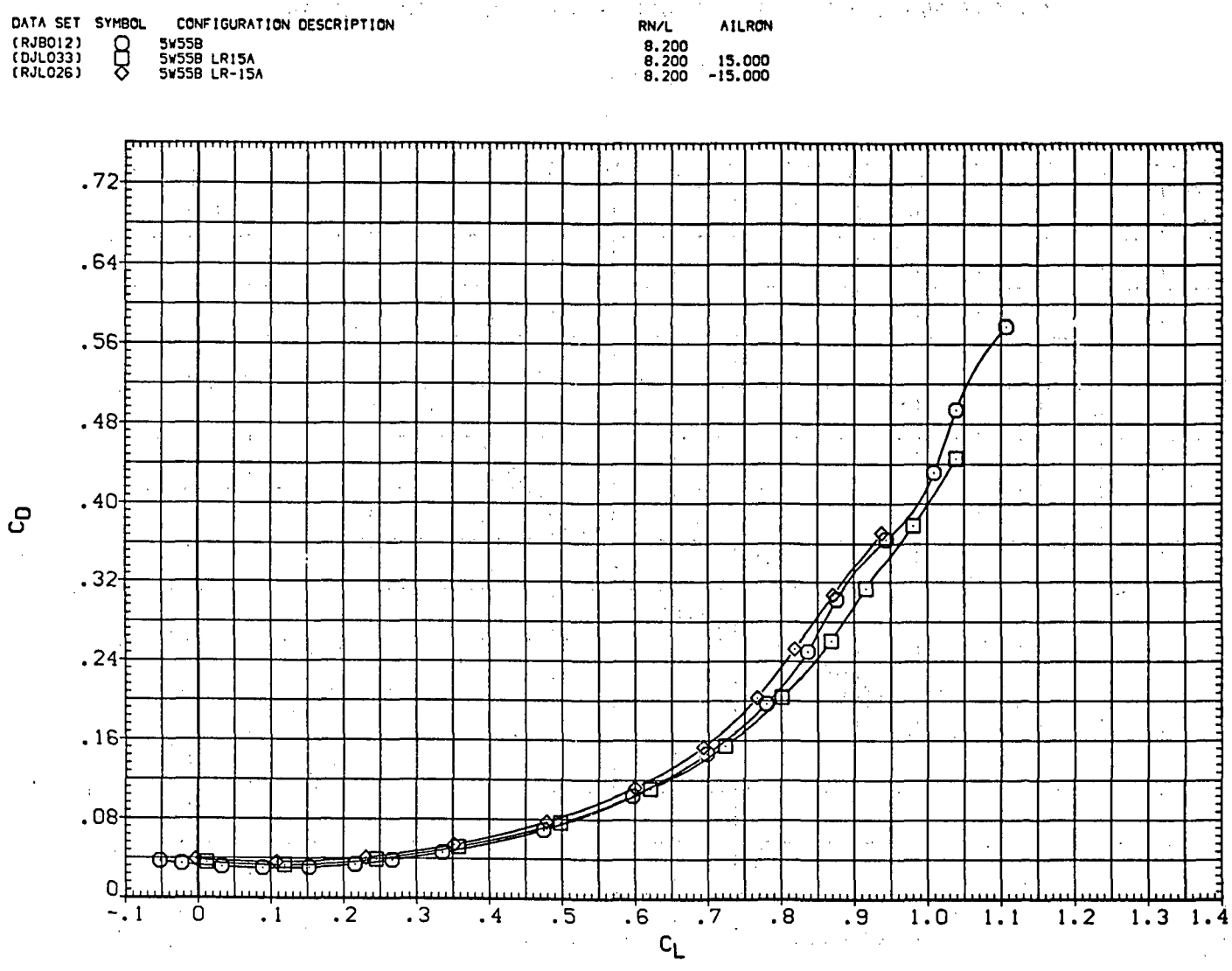

(b) C_D vs C_L

Figure 42.– Continued.

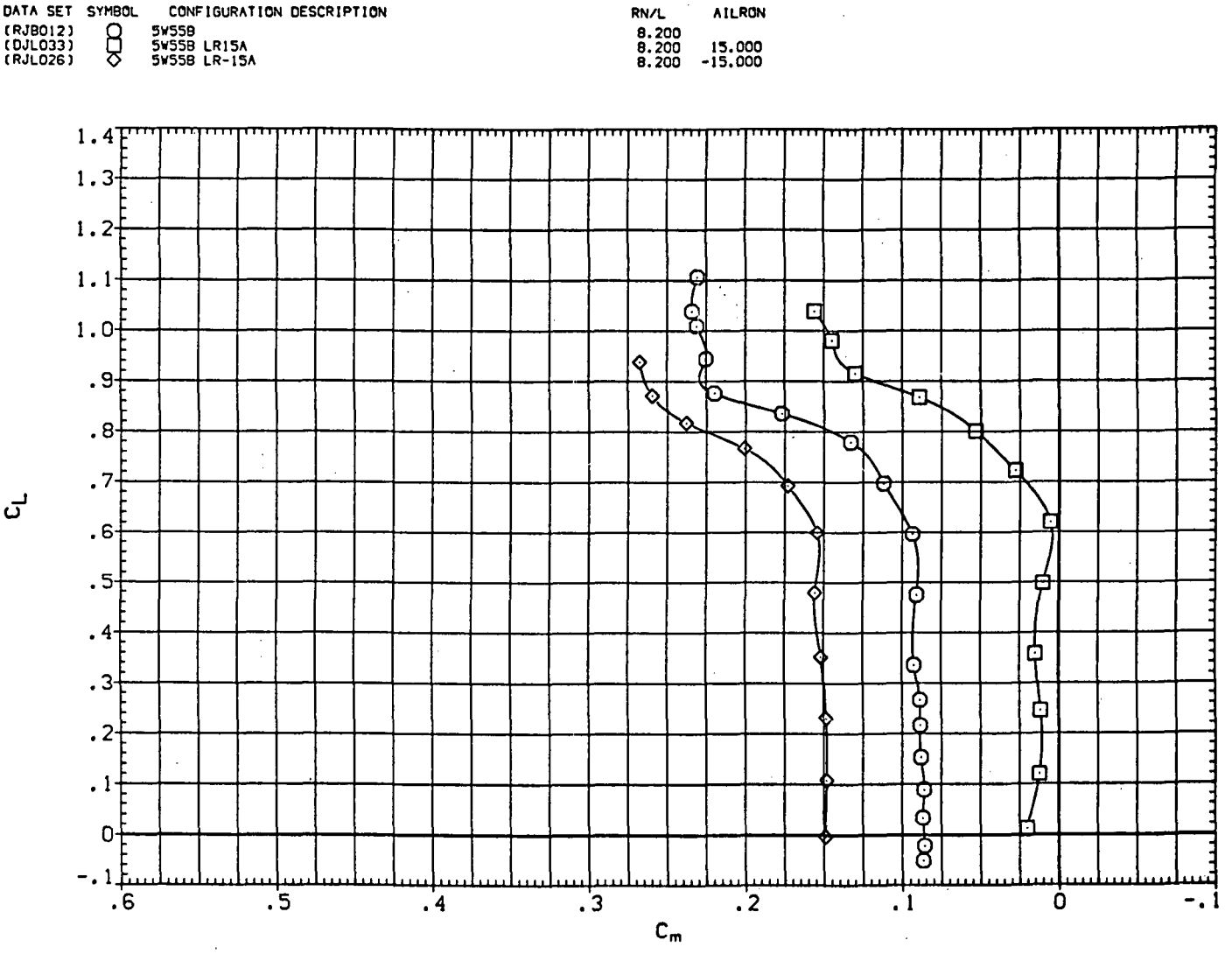

(c) C_L vs C_m

Figure 42.– Continued.

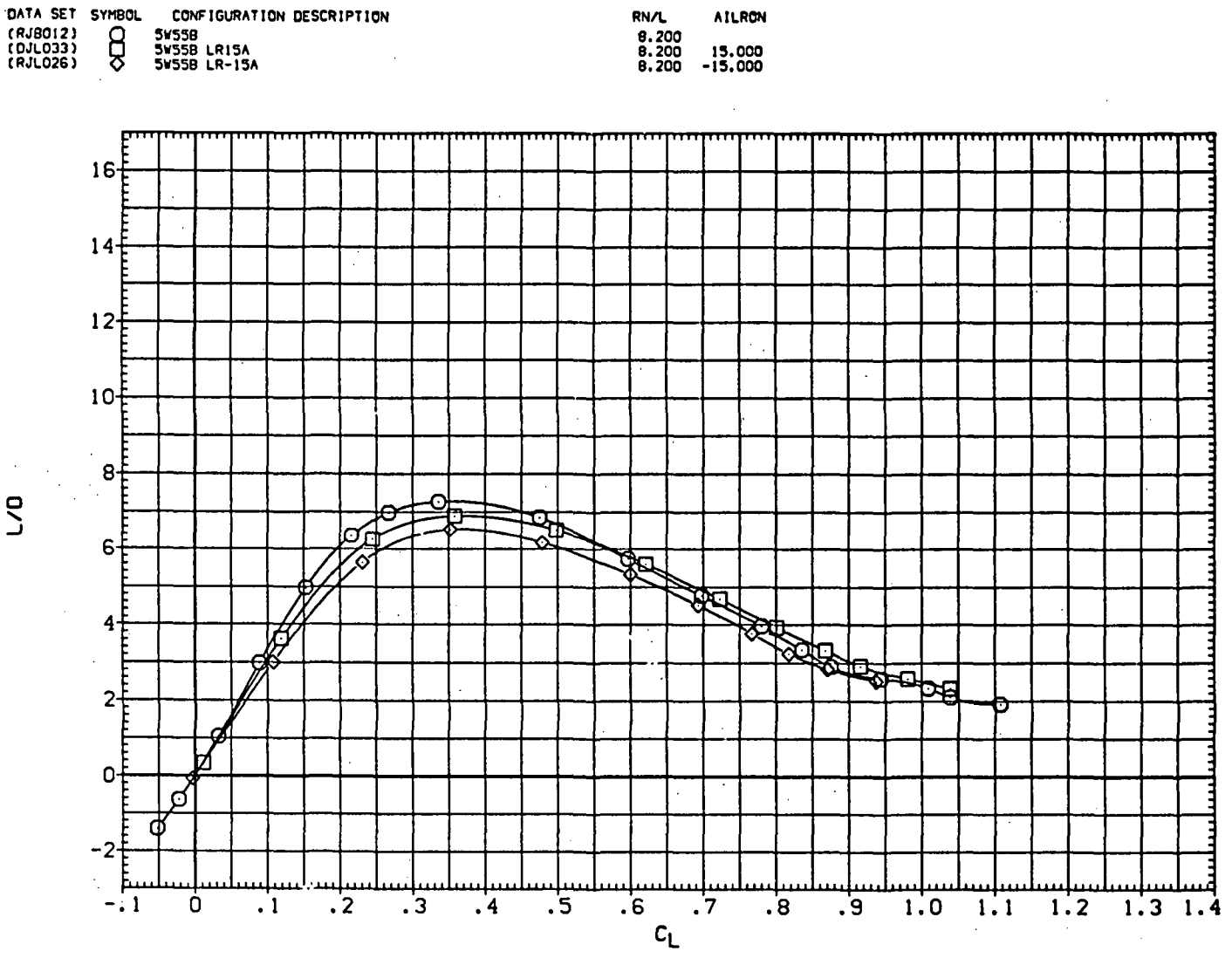

(d) L/D vs C_L

Figure 42.– Continued.

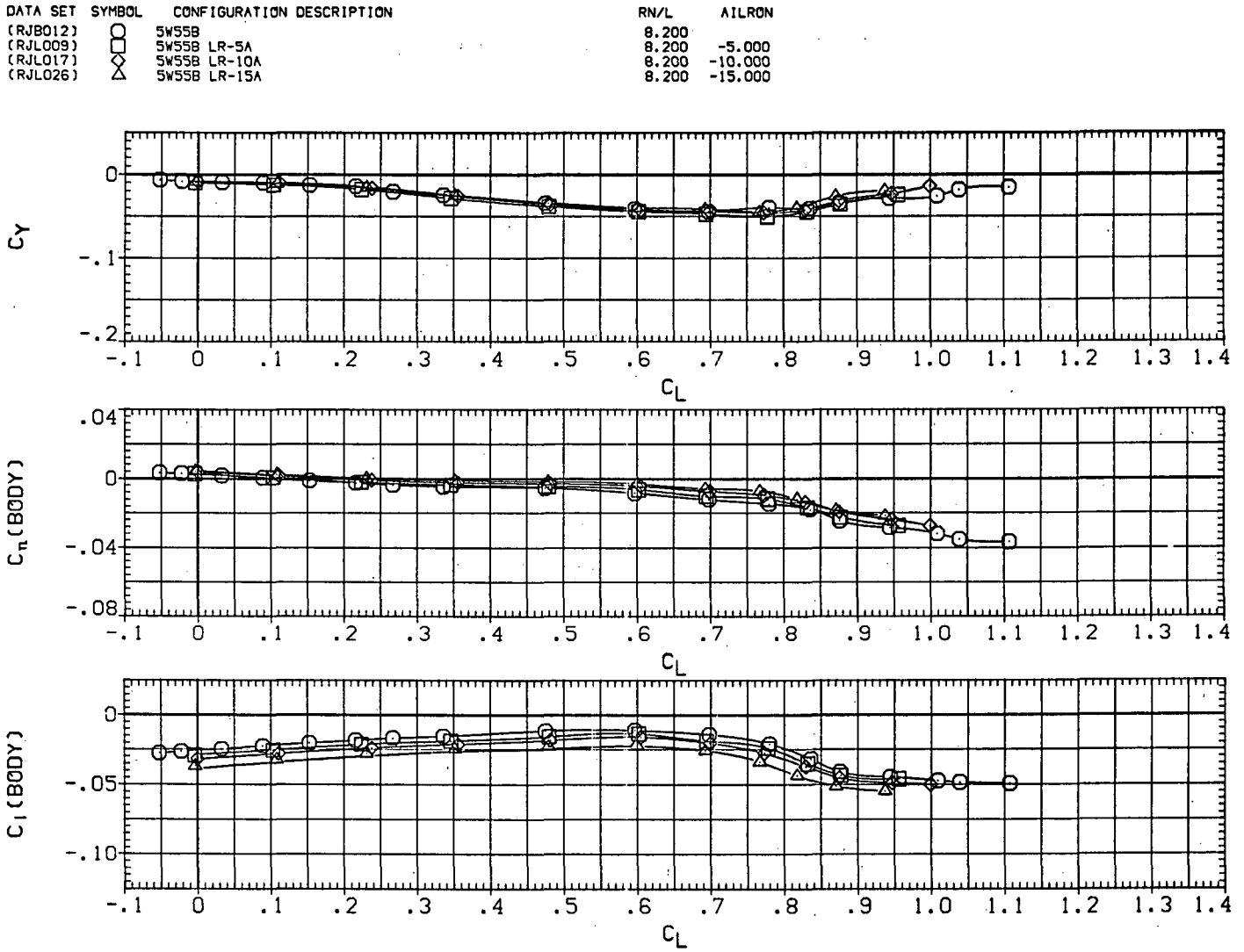

(e) C_Y, C_n, and C_l vs C_L (negative $\Delta\delta_a$'s).

Figure 42.– Continued.

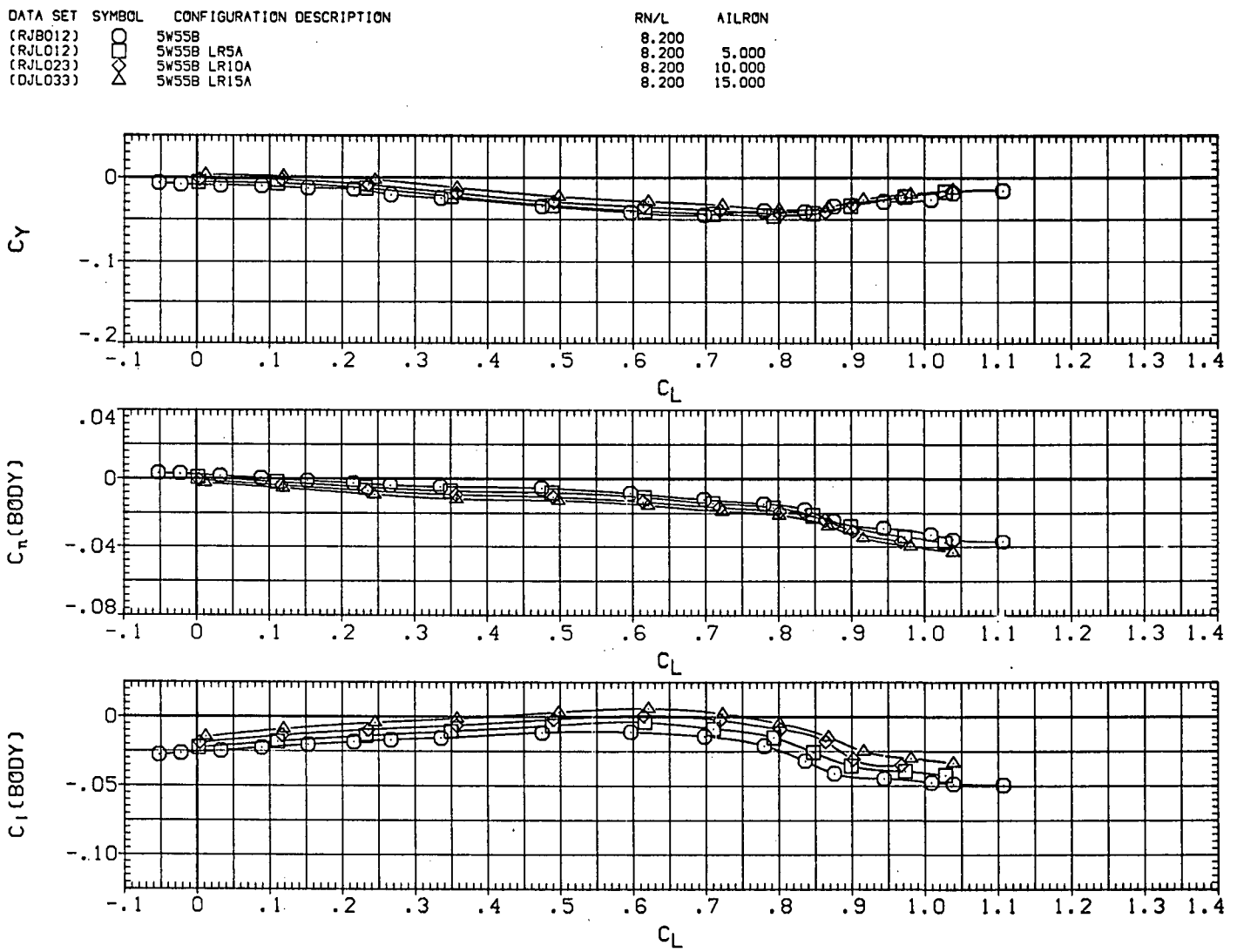

(f) C_Y, C_n, and C_l vs. C_L (positive $\Delta\delta_a$'s).

Figure 42.– Concluded.

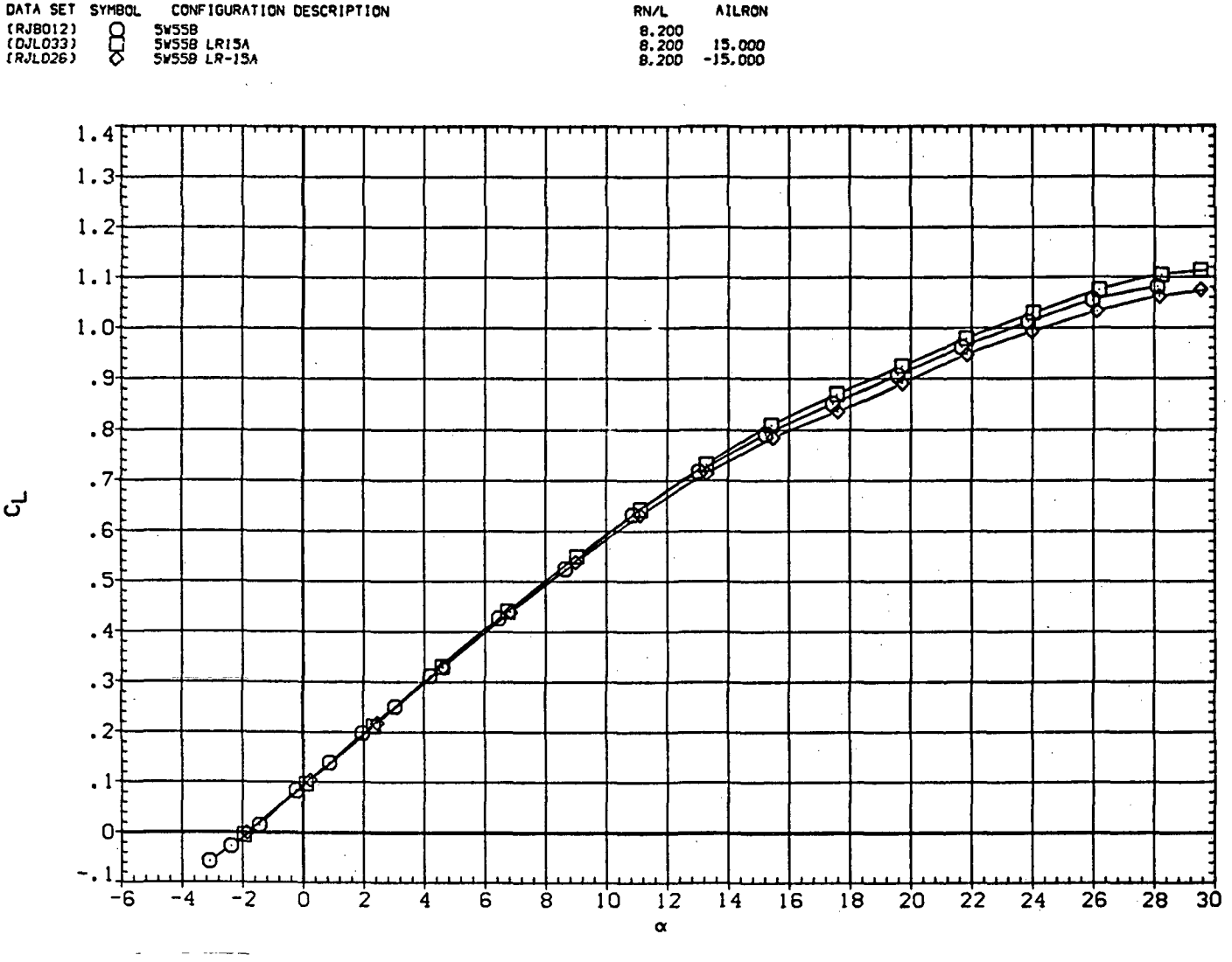

(a) C_L vs α

Figure 43.– Aileron effectiveness on the oblique wing with intermediate bend: $\Lambda = 55°, M = 1.40$.

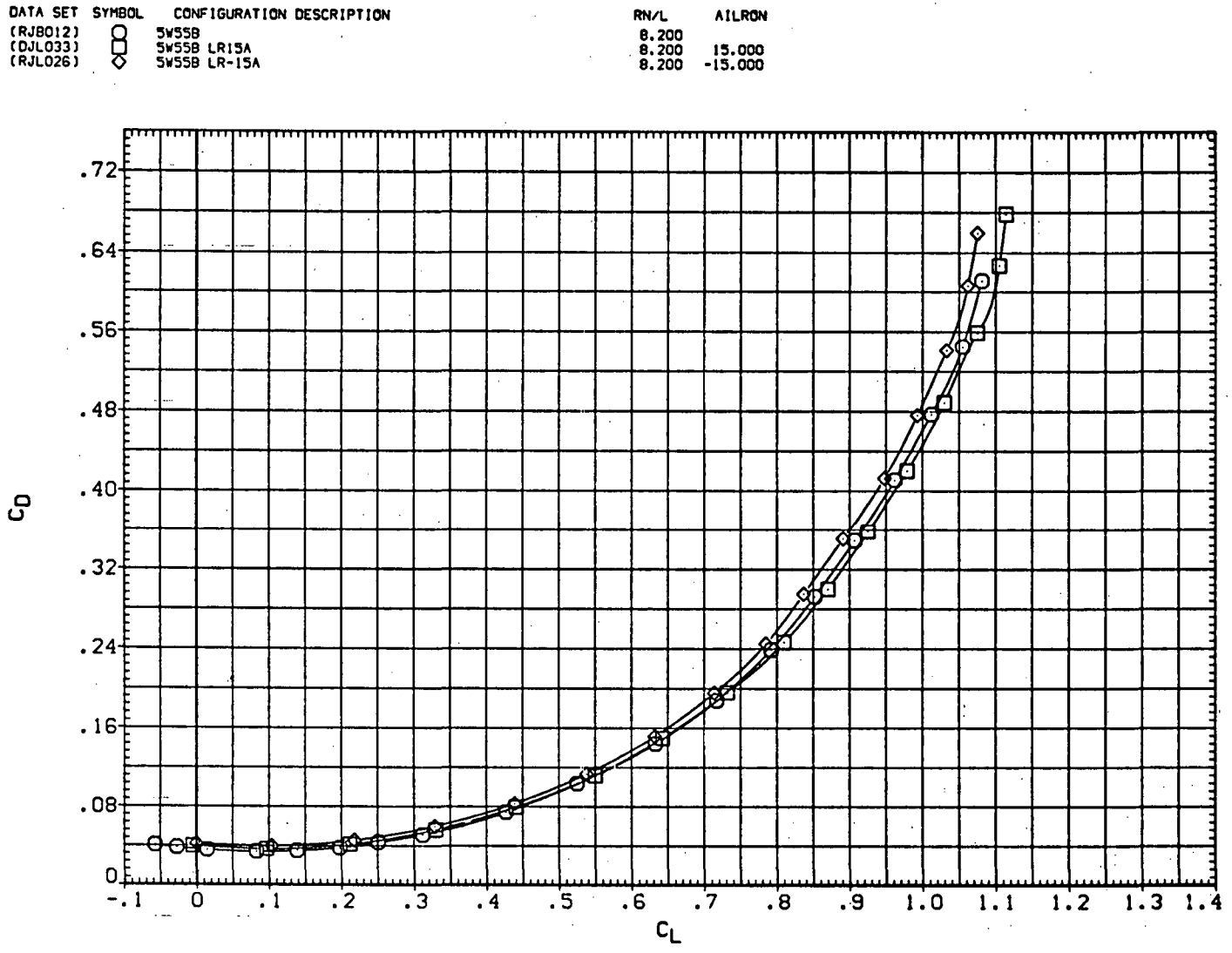

(b) C_D vs C_L

Figure 43.– Continued.

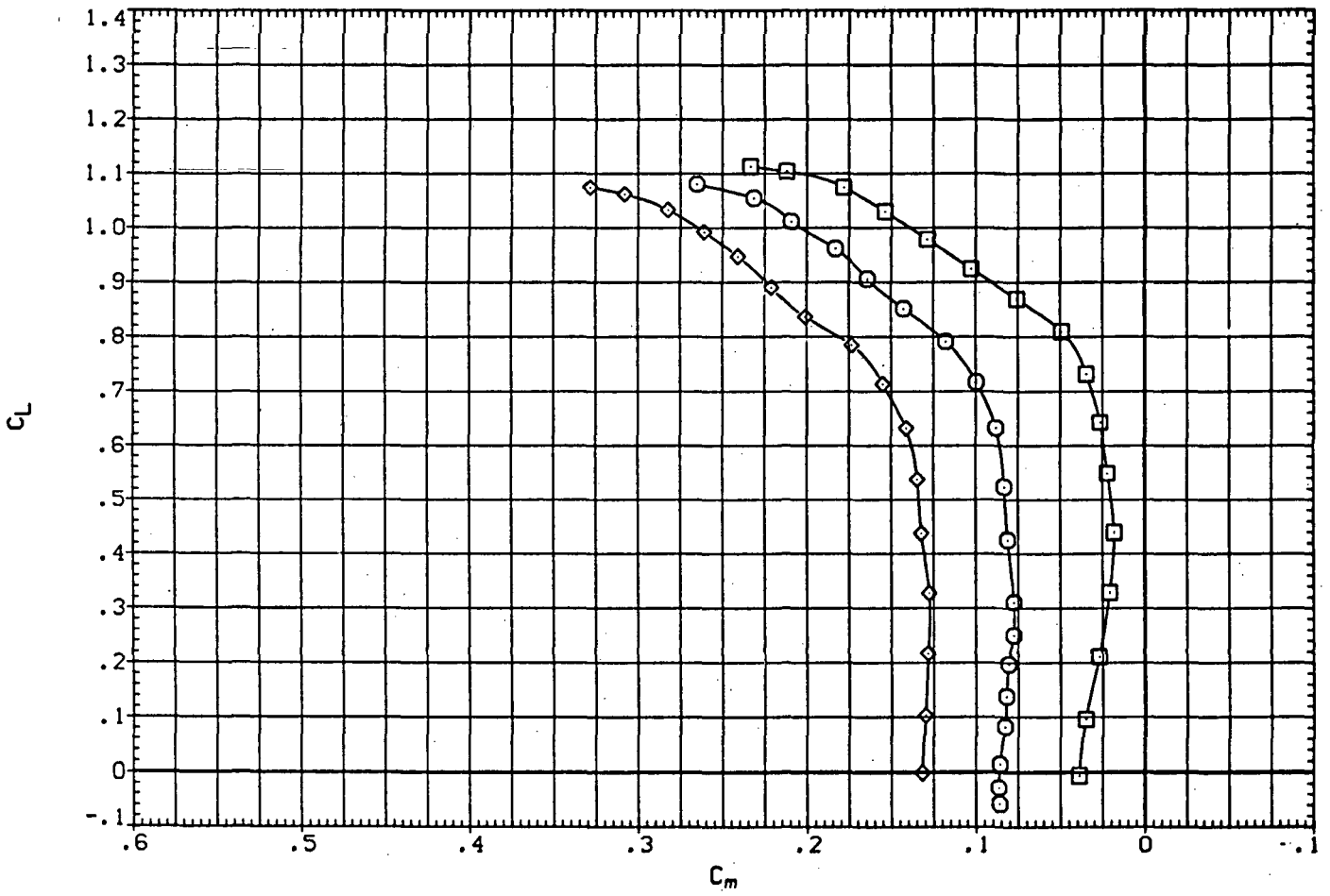

(c) C_L vs C_m

Figure 43.– Continued.

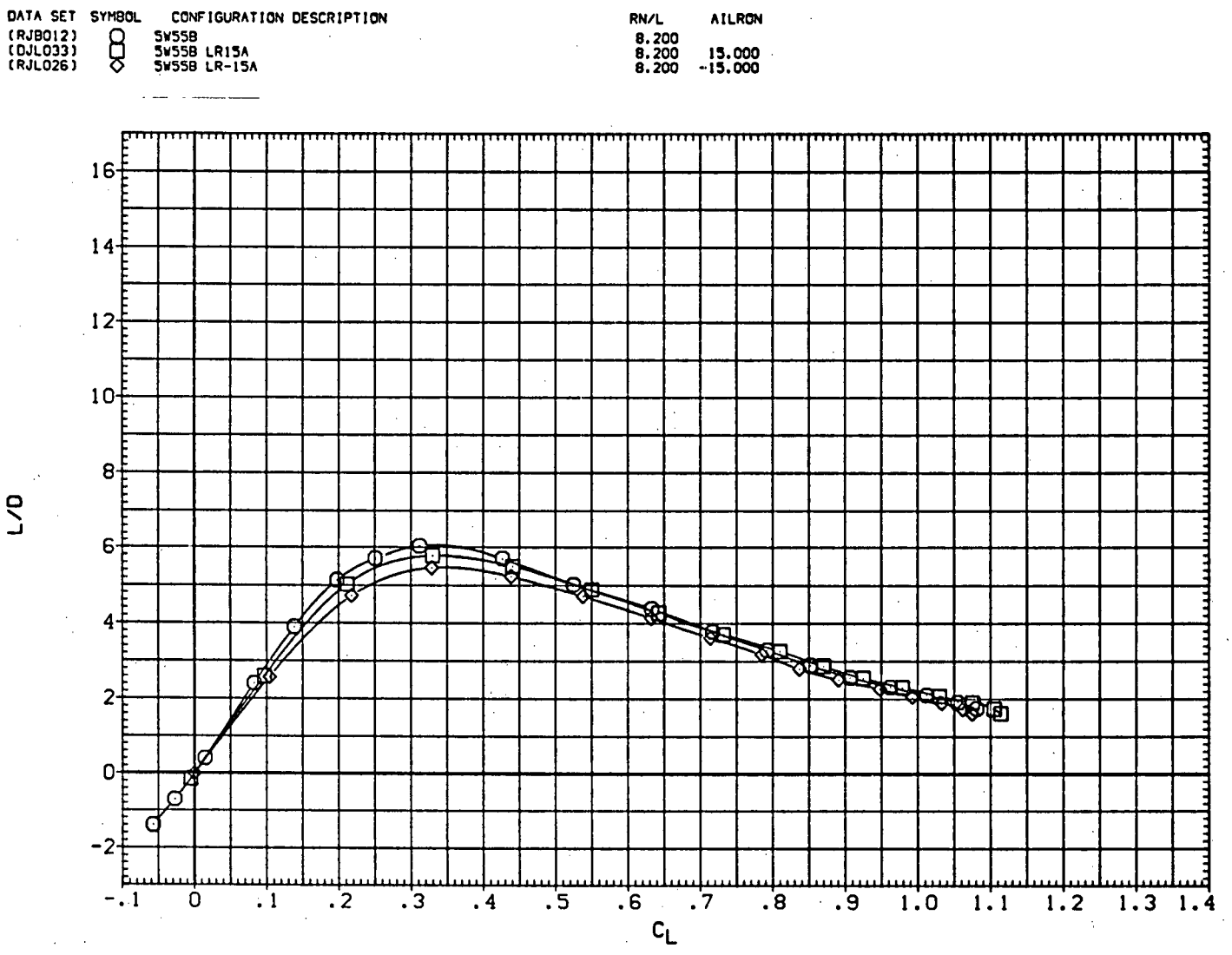

(d) L/D vs C_L

Figure 43.– Continued.

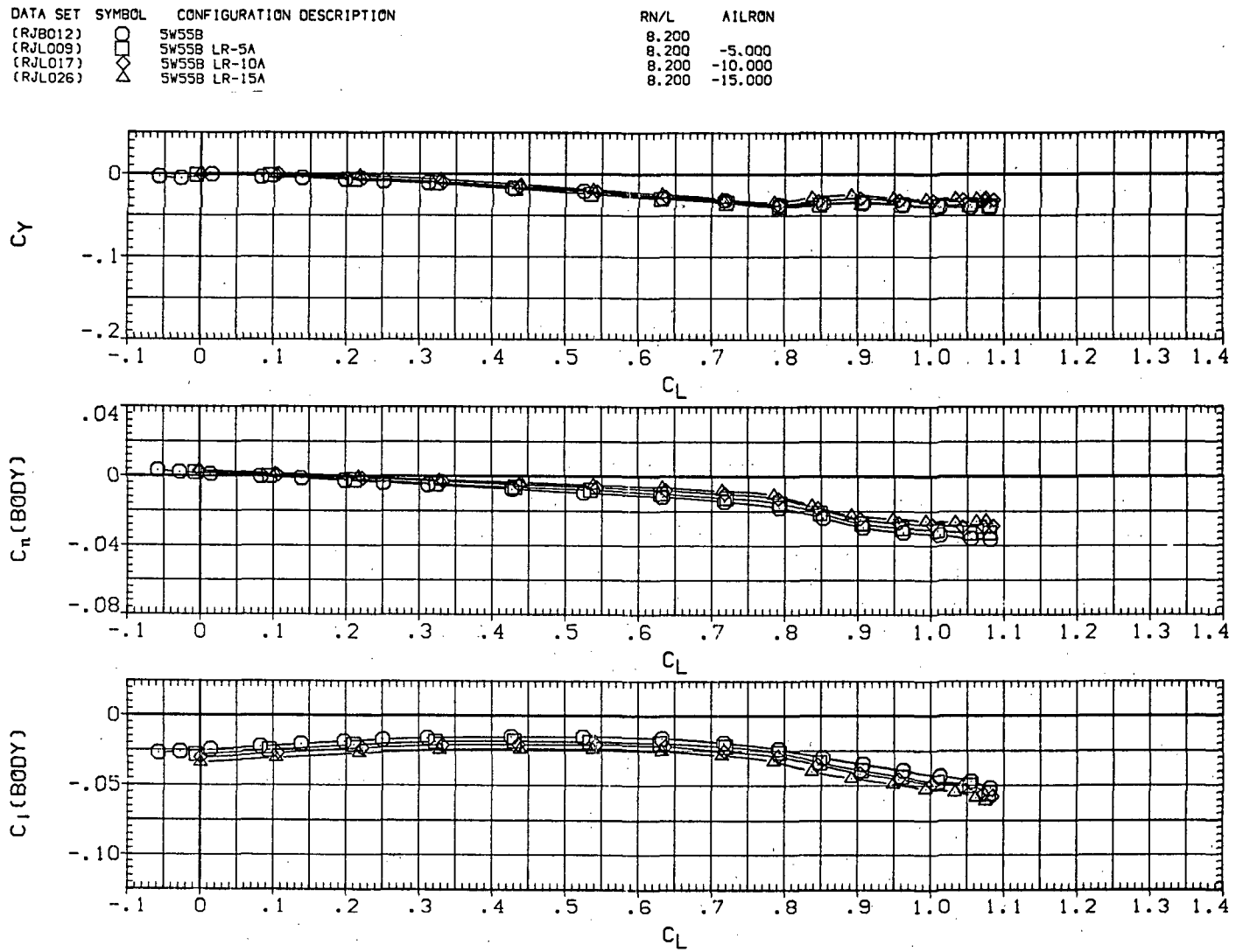

(e) C_Y, C_n, and C_l vs C_L (negative $\Delta\delta_a$'s).

Figure 43.– Continued.

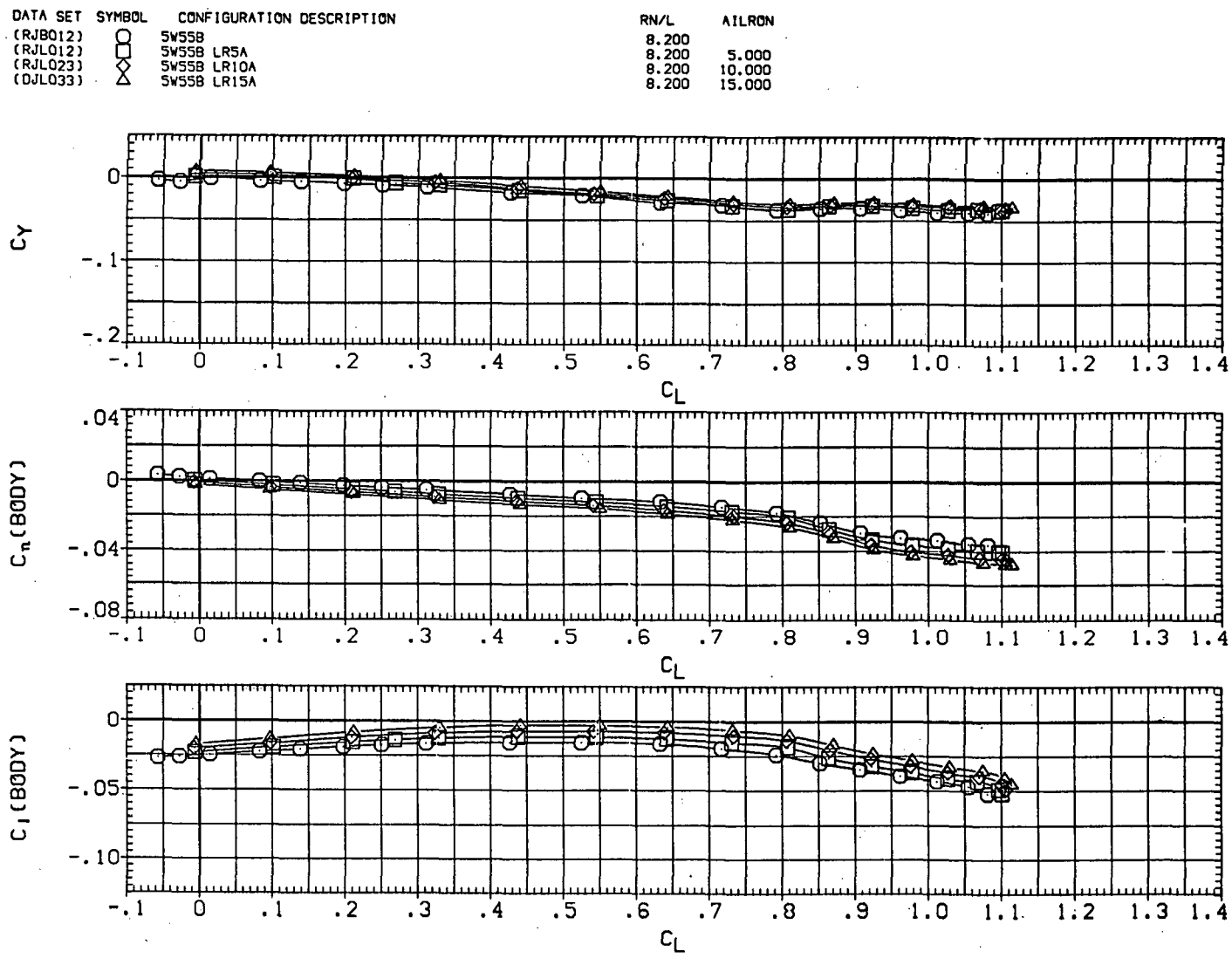

(f) C_Y, C_n, and C_l vs C_L (positive $\Delta\delta_a$'s).

Figure 43.– Concluded.

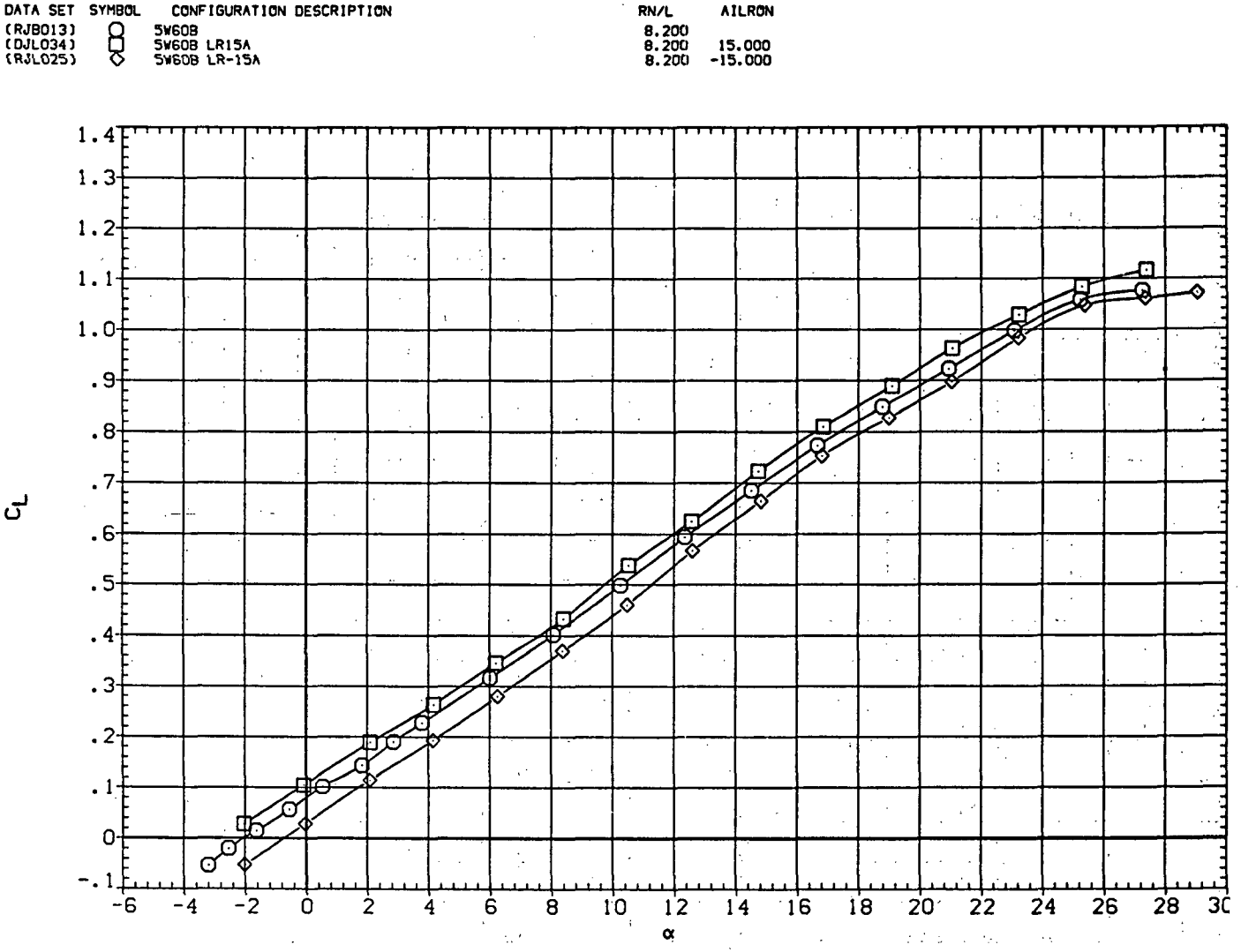

(a) C_L vs α

Figure 44.– Aileron effectiveness on the oblique wing with intermediate bend: $\Lambda = 60°, M = 0.60$.

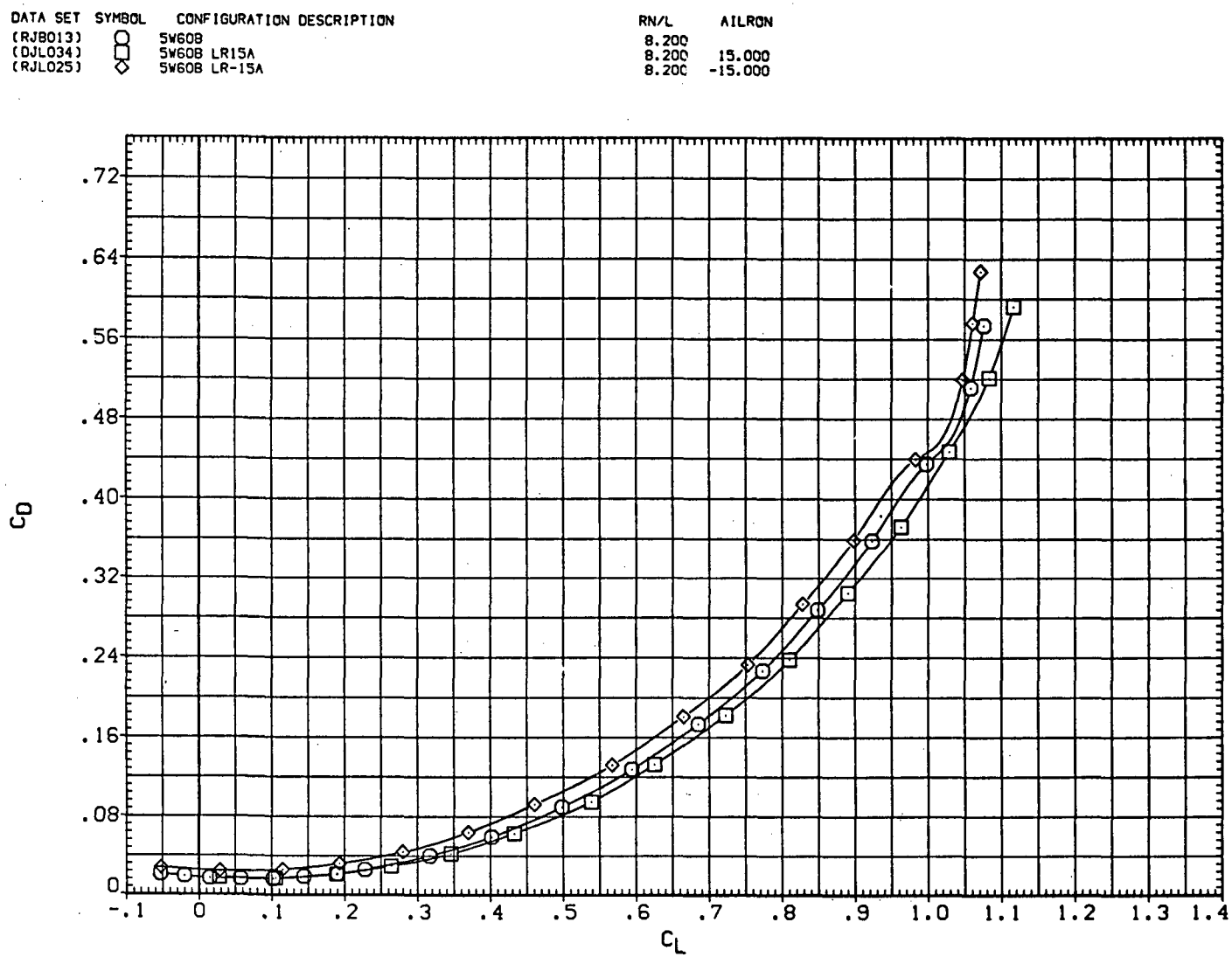

(b) C_D vs C_L

Figure 44.– Continued.

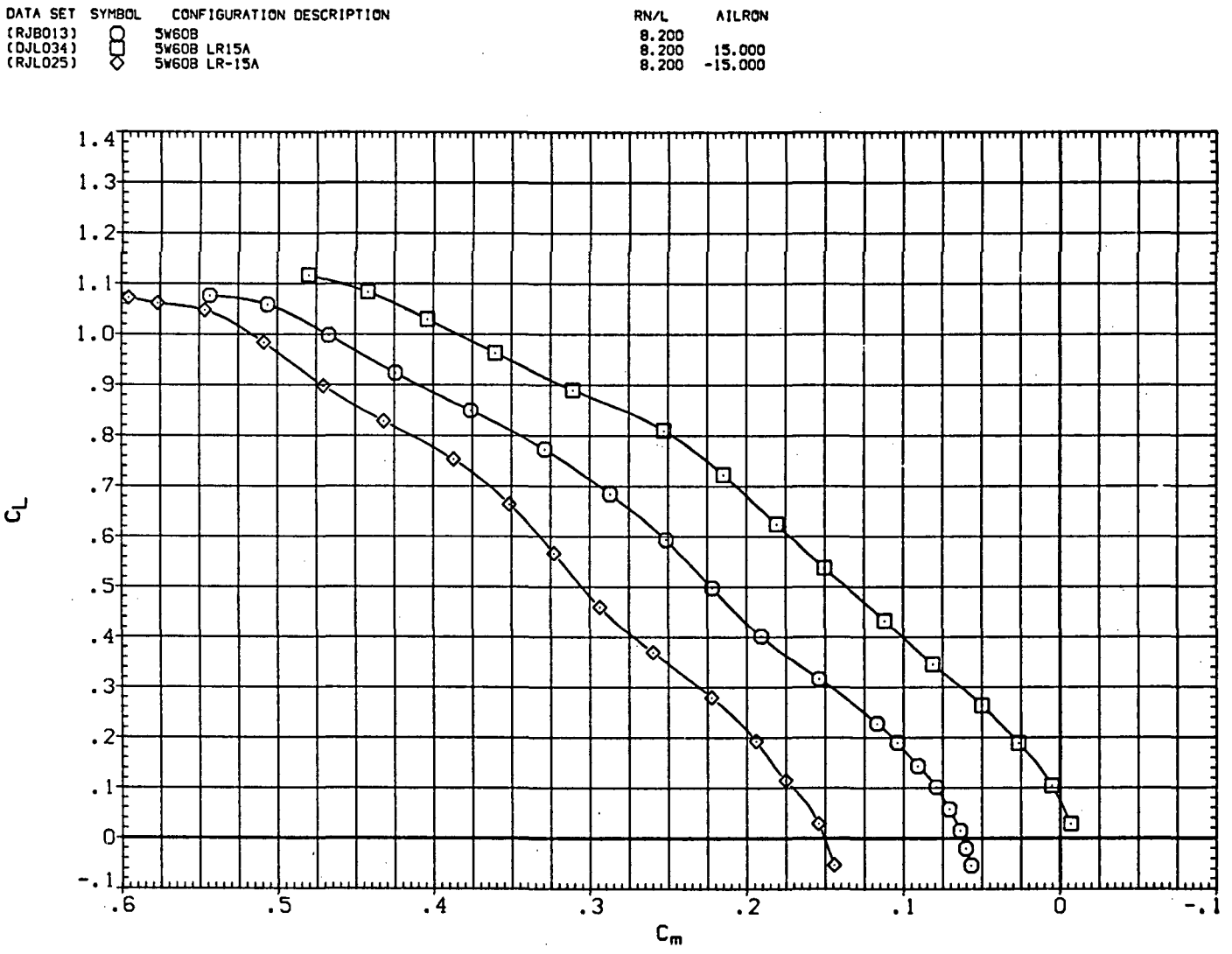

(c) C_L vs C_m

Figure 44.– Continued.

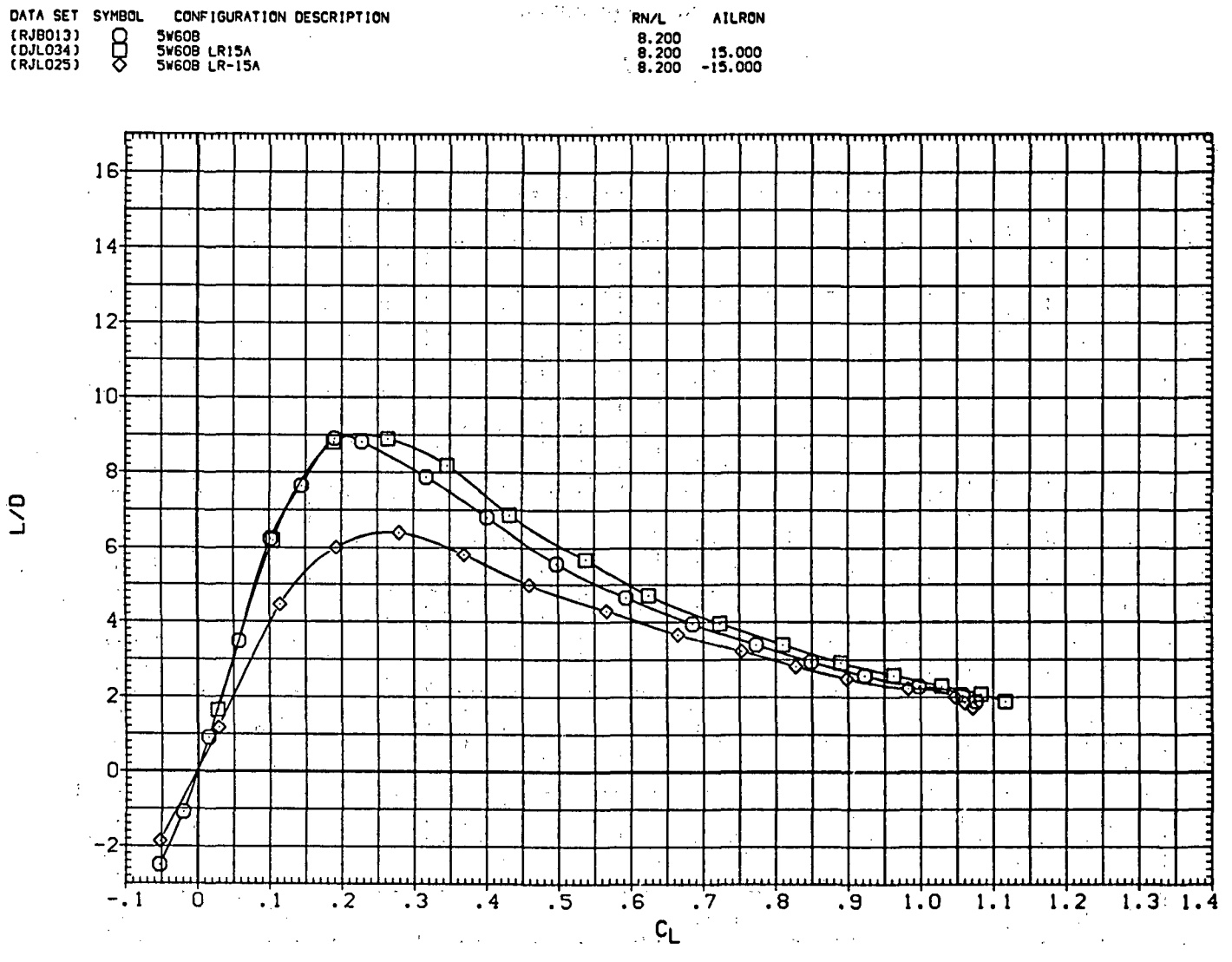

(d) L/D vs C_L

Figure 44.– Continued.

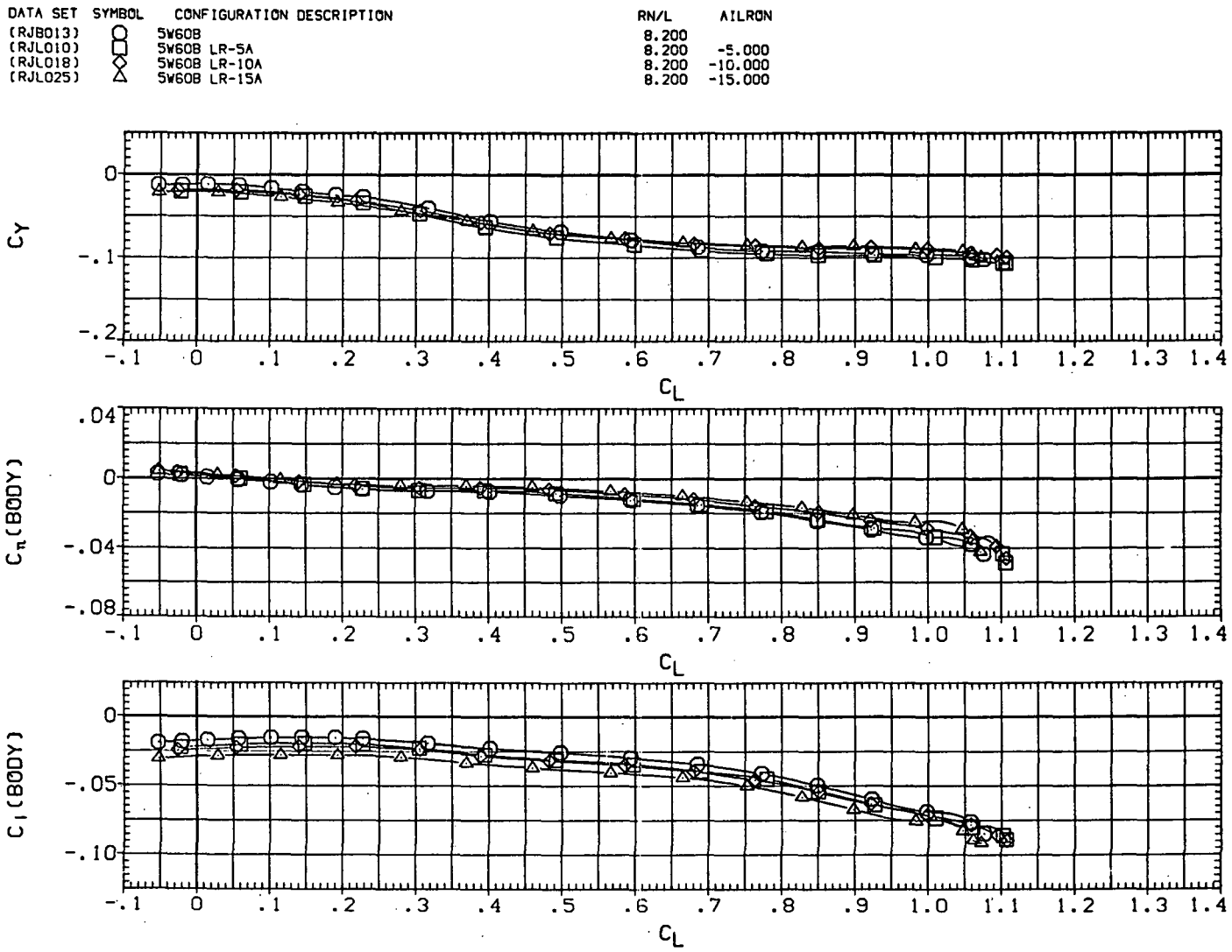

(e) C_Y, C_n, and C_l vs C_L (negative $\Delta\delta_a$'s).

Figure 44.– Continued.

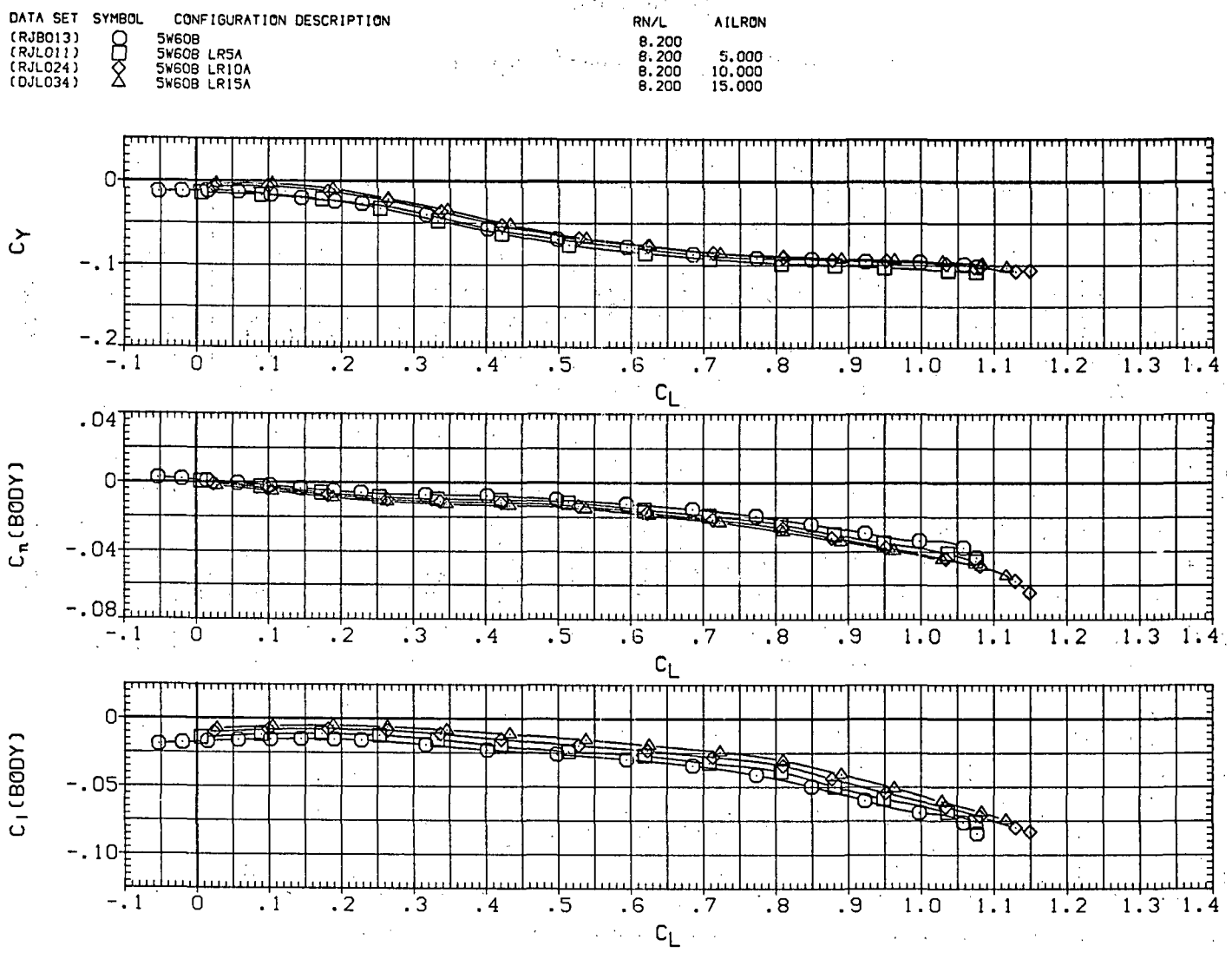

(f) C_Y, C_n, and C_l vs C_L (positive $\Delta\delta_a$'s).

Figure 44.– Concluded.

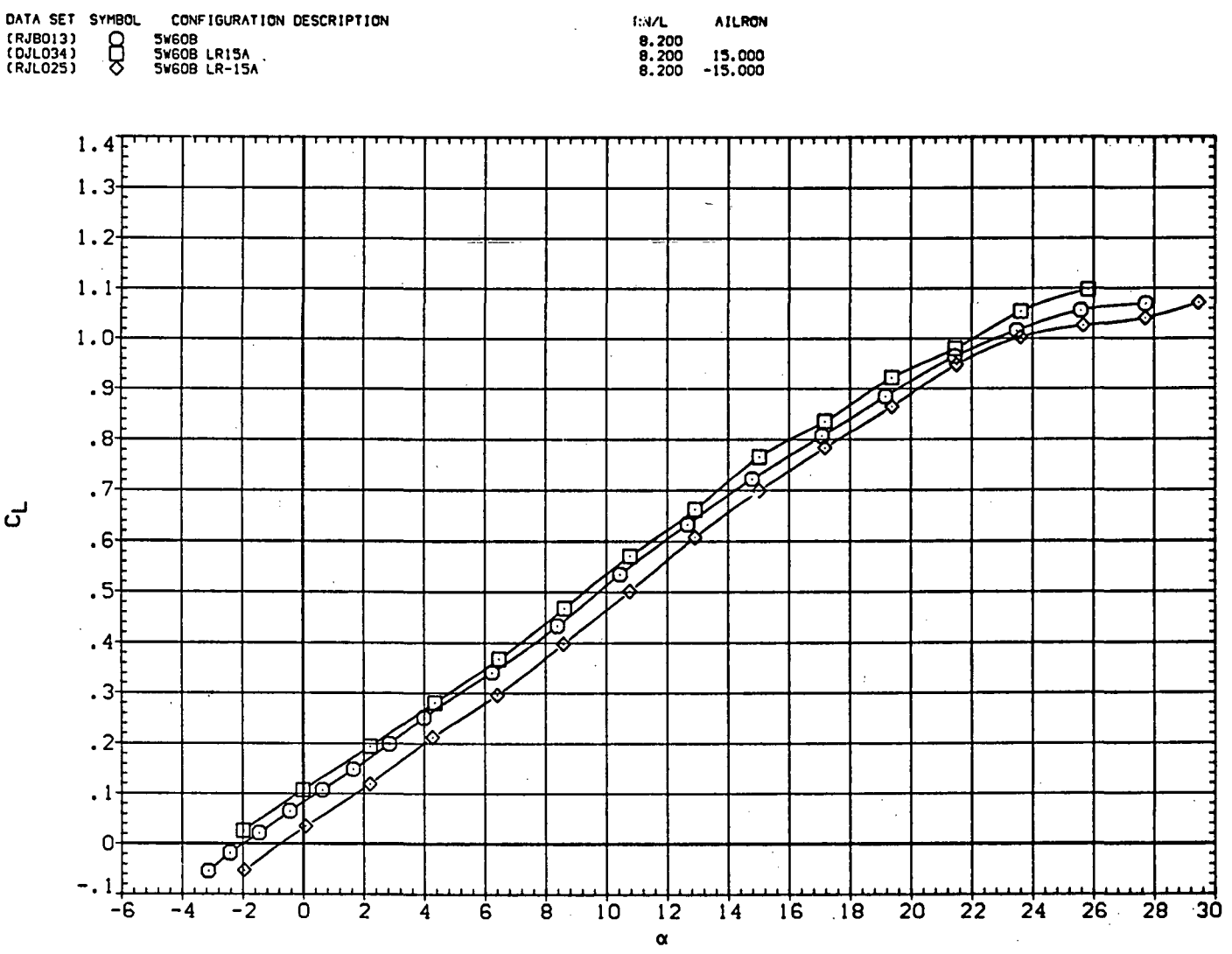

(a) C_L vs α

Figure 45.– Aileron effectiveness of the oblique wing with intermediate bend: $\Lambda = 60°, M = 0.60$.

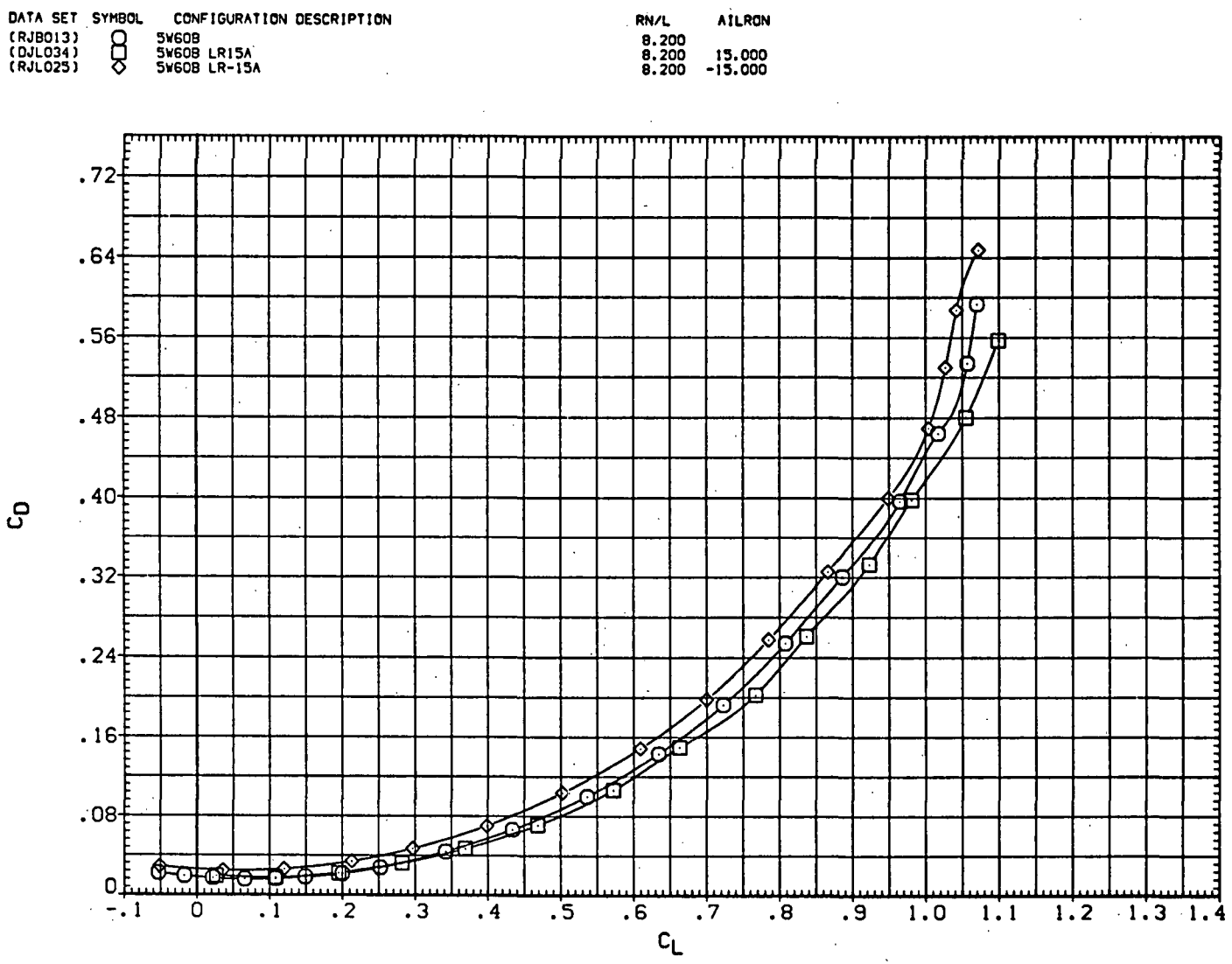

(b) C_D vs C_L

Figure 45.– Continued.

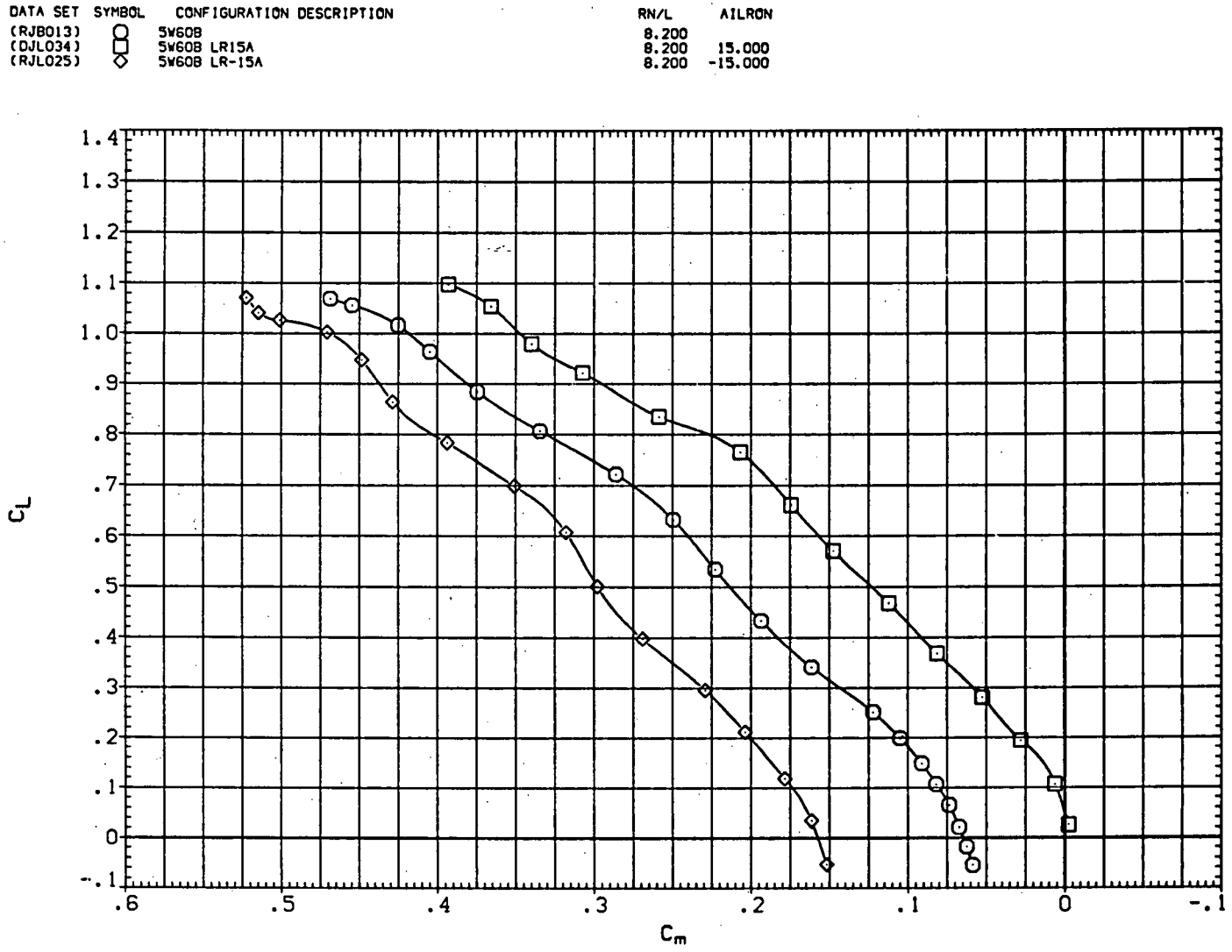

(c) C_L vs C_m

Figure 45.– Continued.

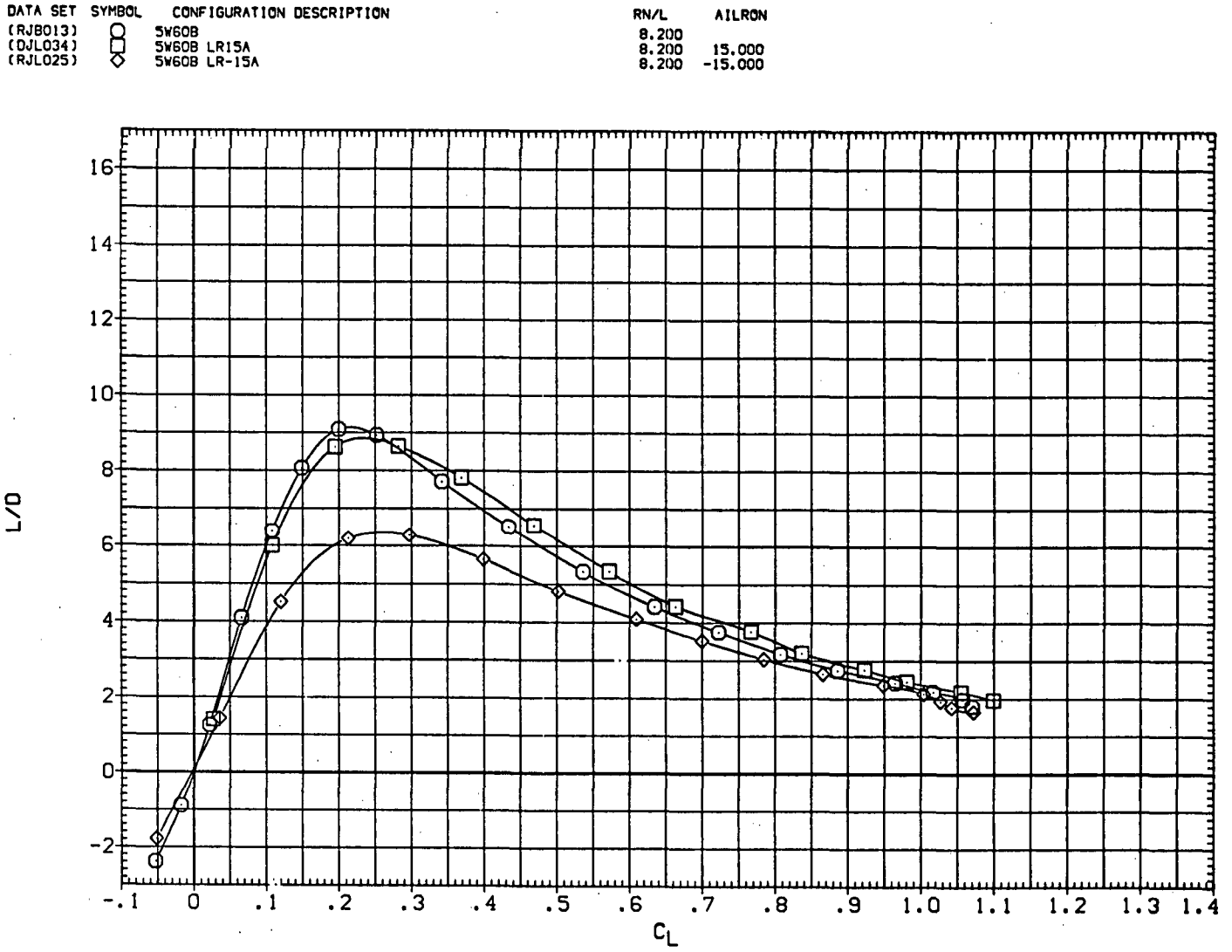

(d) L/D vs C_L

Figure 45.– Continued.

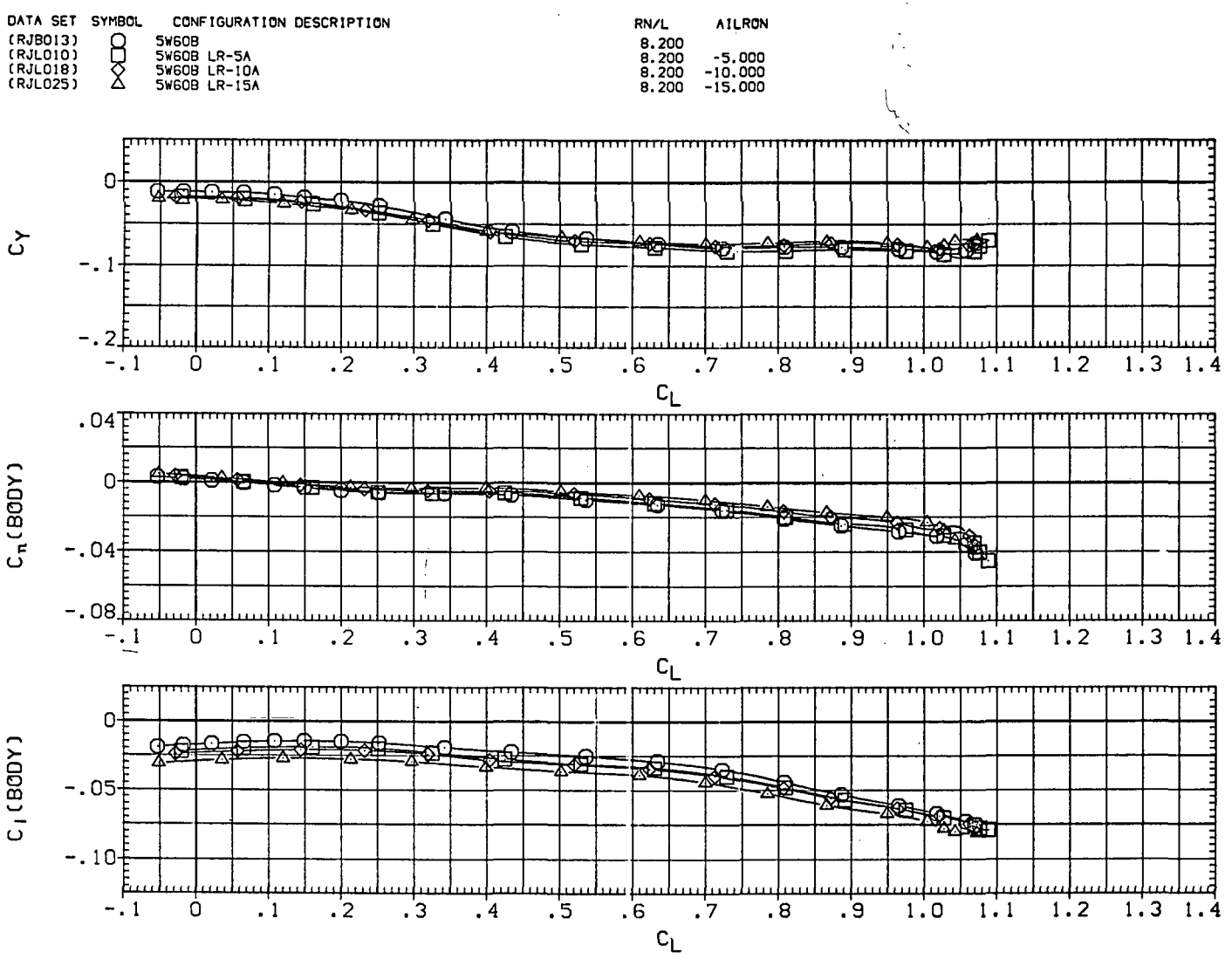

(e) C_Y, C_n, and C_l vs C_L (negative $\Delta\delta_a$'s).

Figure 45.– Continued.

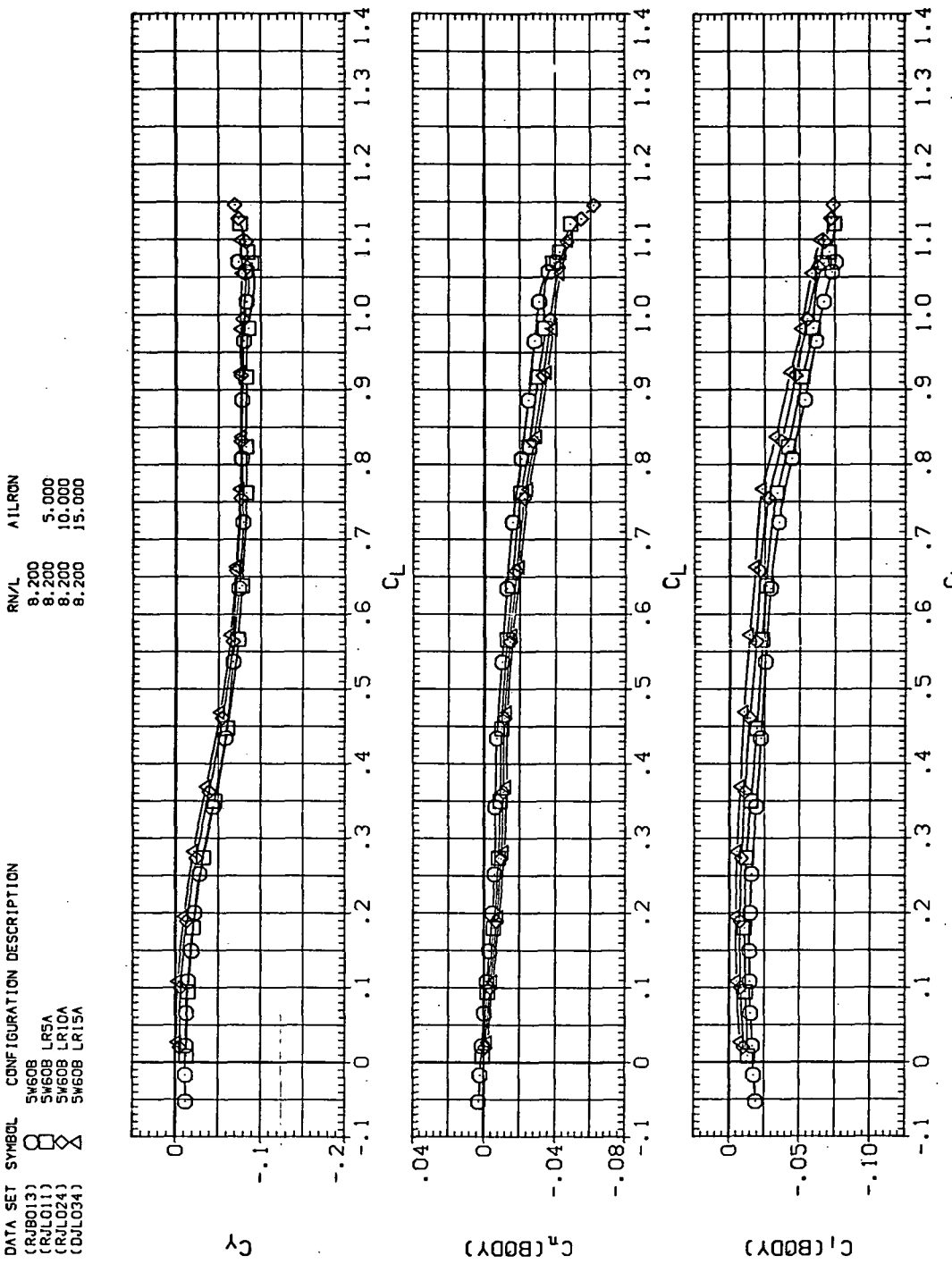

(f) Cy, C_n, and C_l vs C_L (positive $\Delta\delta_a$'s).

Figure 45.– Concluded.

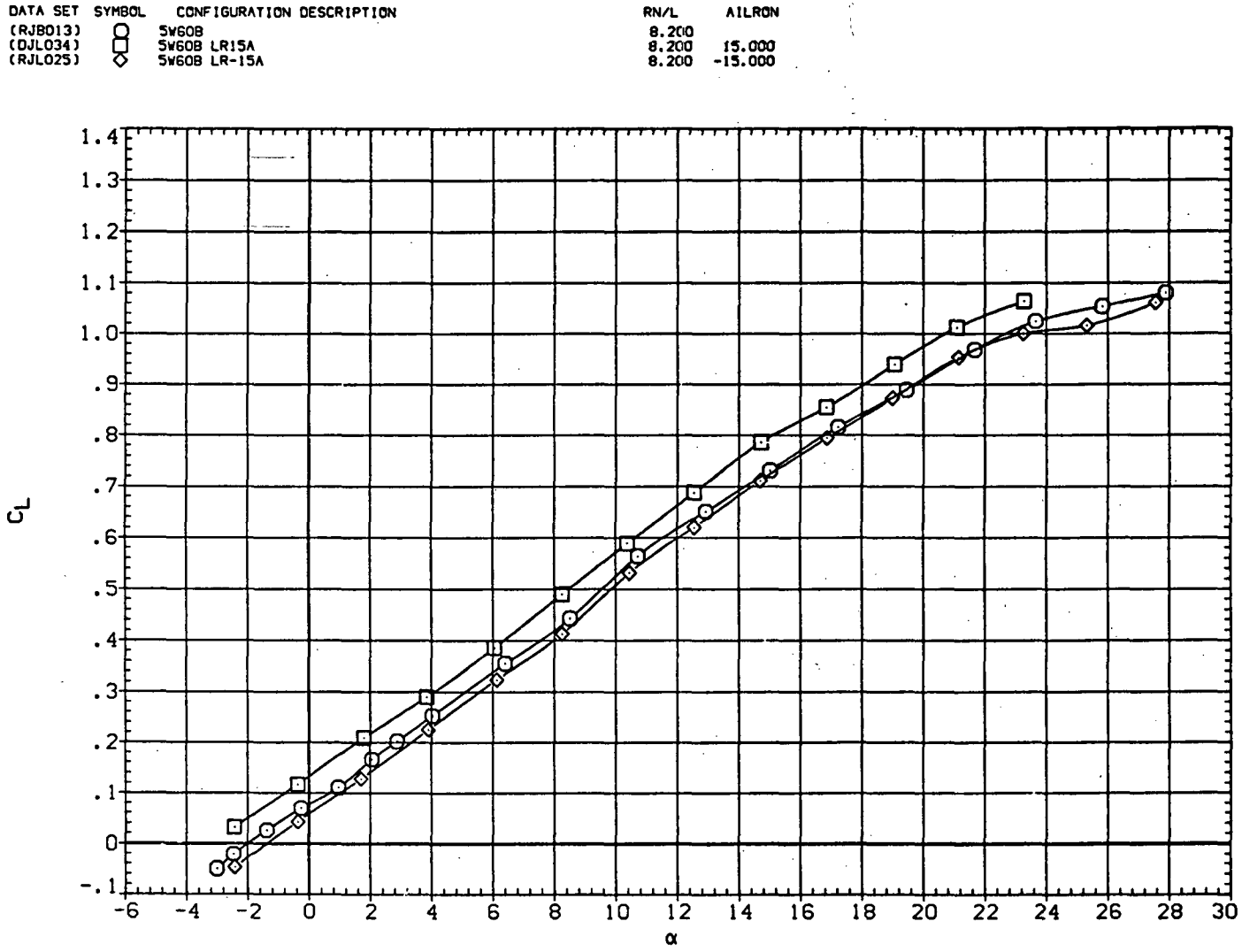

(a) C_L vs α

Figure 46.– Aileron effectiveness on the oblique wing with intermediate bend: $\Lambda = 60°, M = 0.90$.

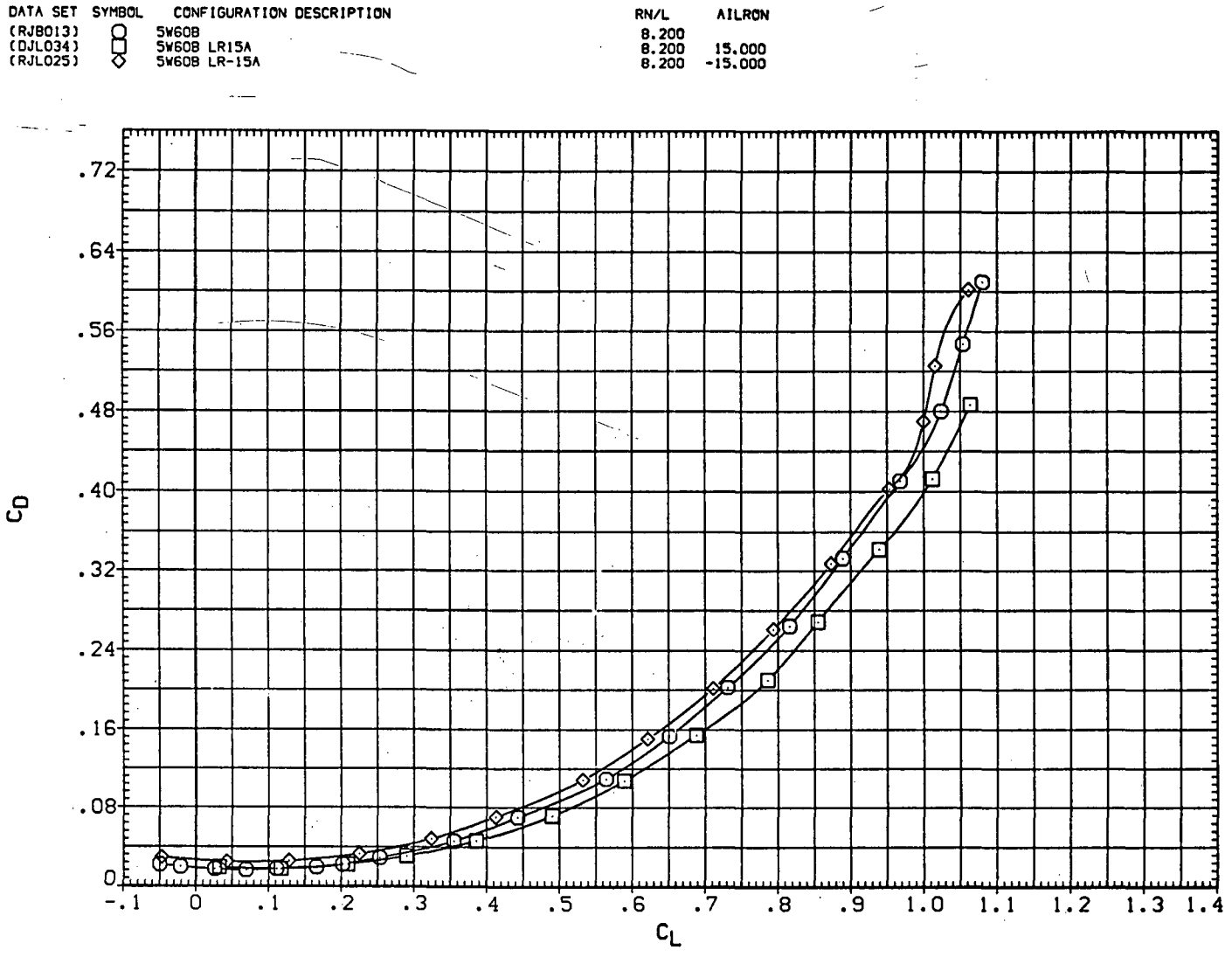

(b) C_D vs C_L

Figure 46.– Continued.

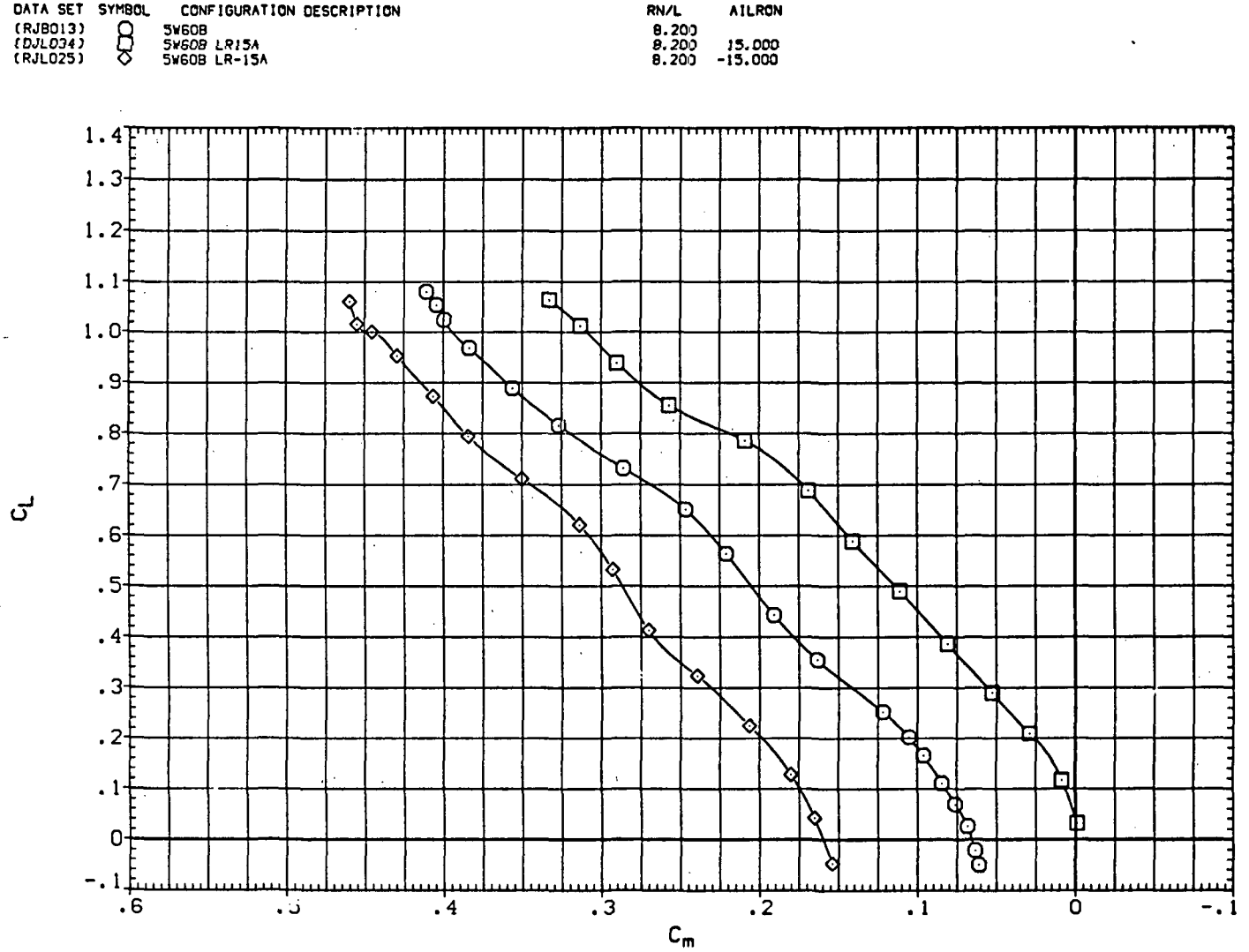

(c) C_L vs C_m

Figure 46.– Continued.

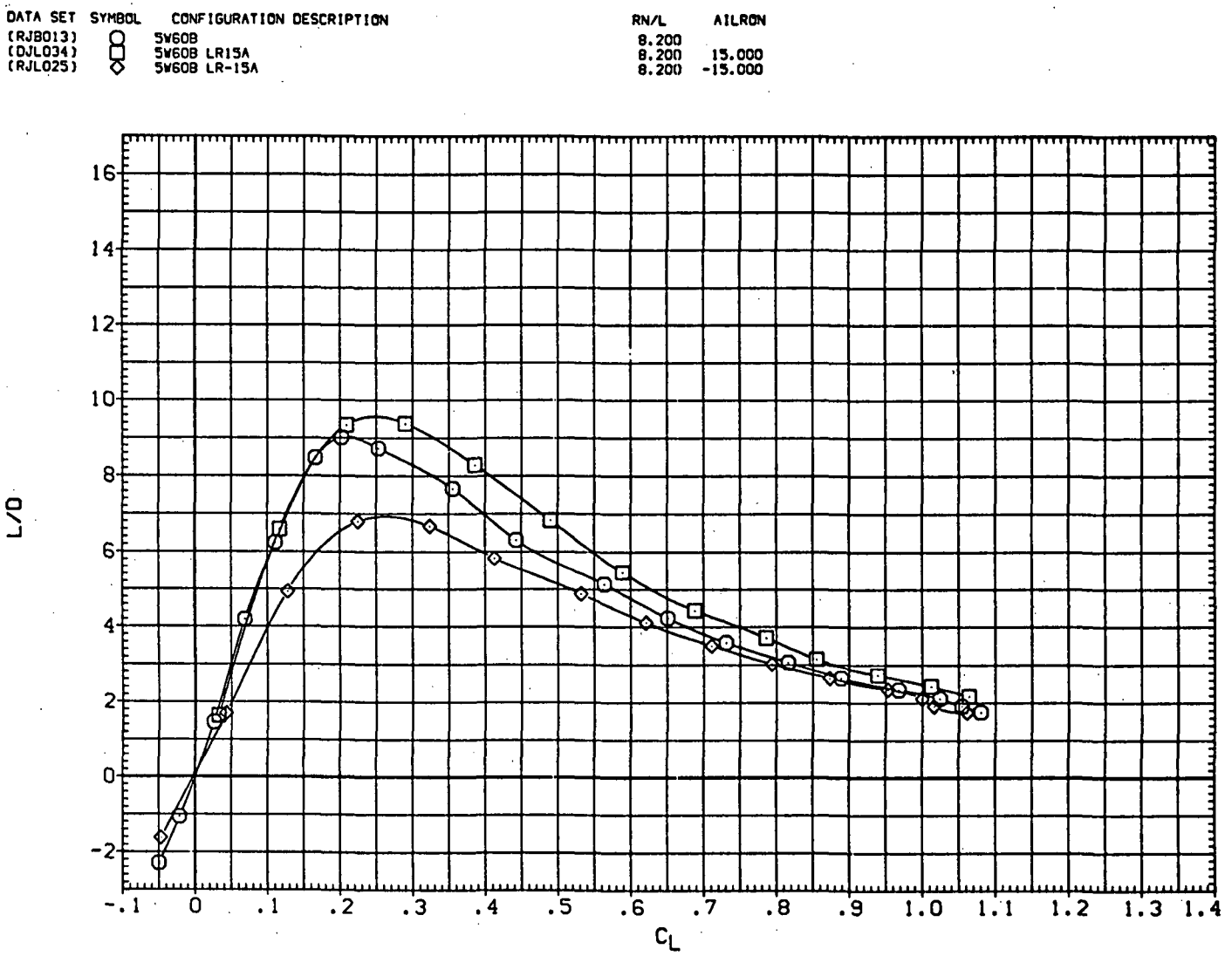

(d) L/D vs C_L

Figure 46.– Continued.

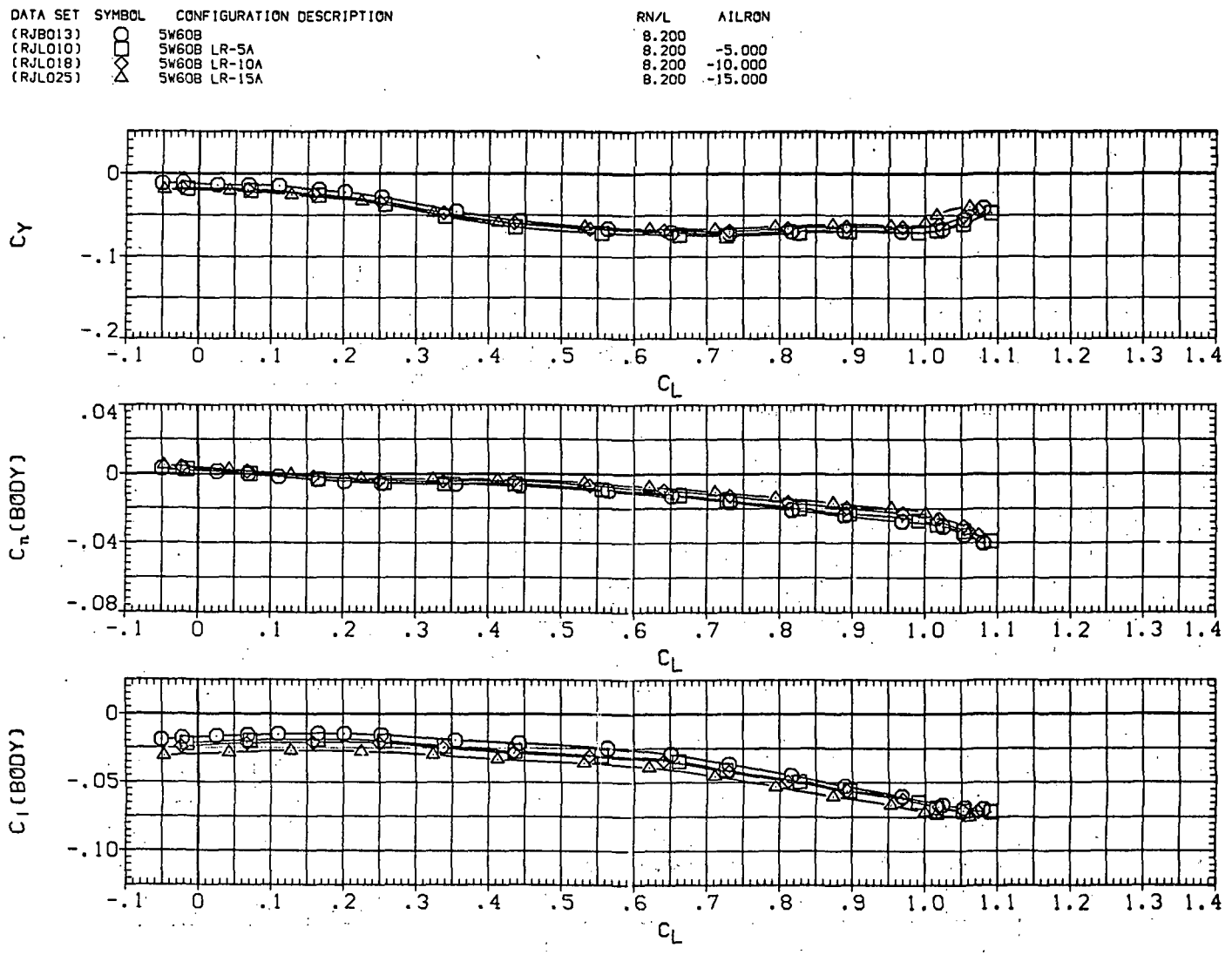

(e) C_Y, C_n, and C_l vs C_L (negative $\Delta\delta_a$'s).

Figure 46.– Continued.

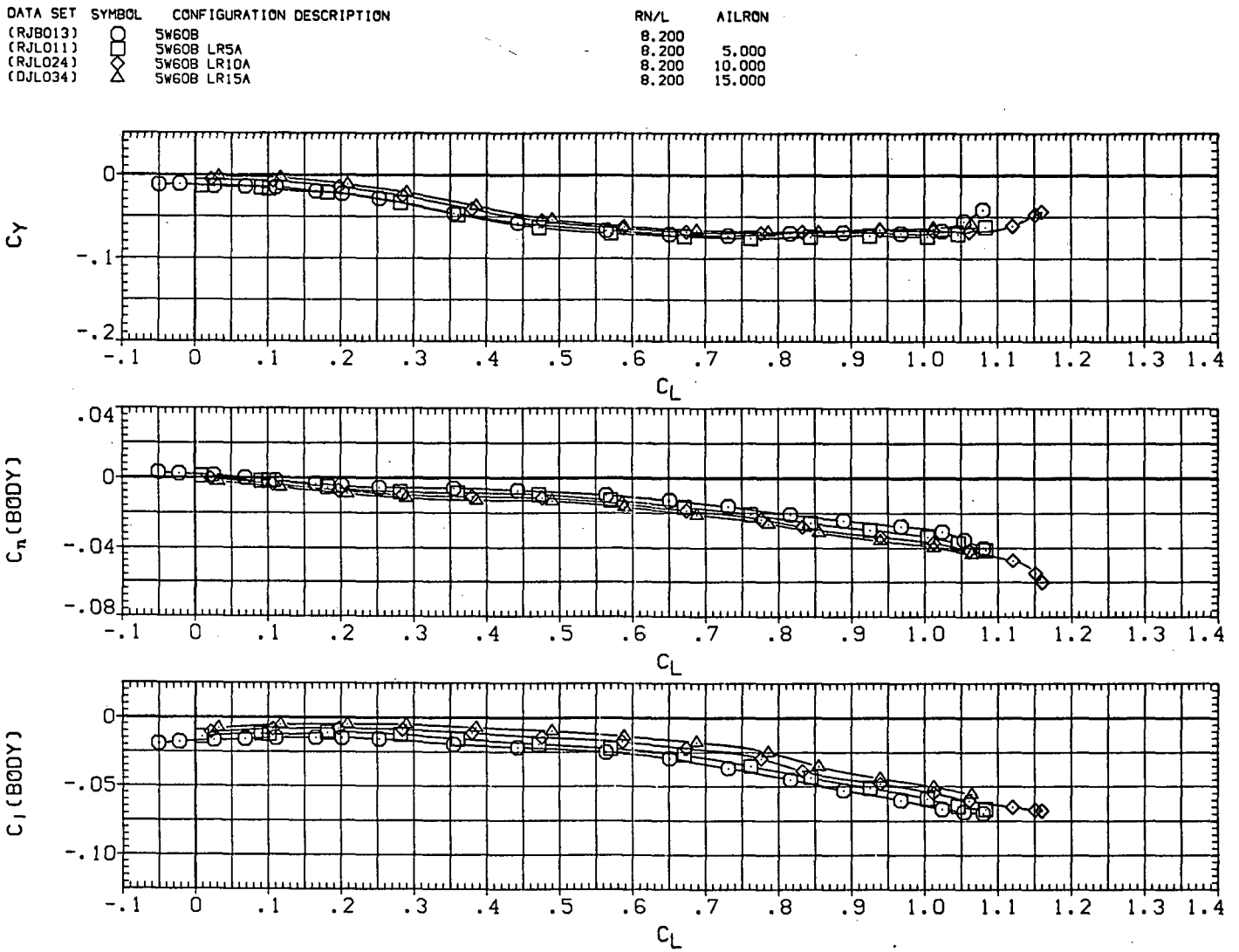

(f) C_Y, C_n, and C_l vs C_L (positive $\Delta\delta_a$'s).

Figure 46.– Concluded.

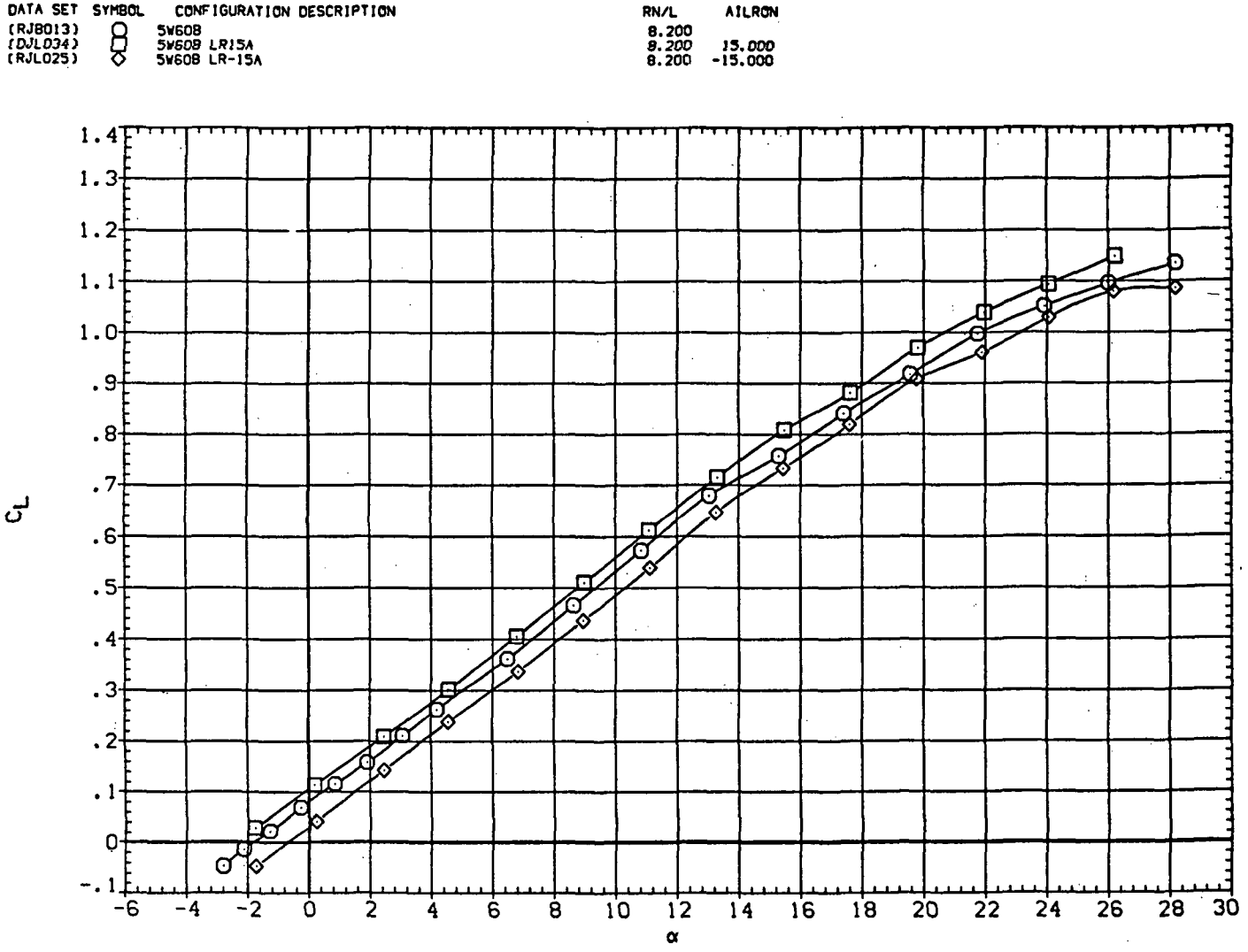

(a) C_L vs α

Figure 47.– Aileron effectiveness on the oblique wing with intermediate bend: $\Lambda = 60°, M = 0.95$.

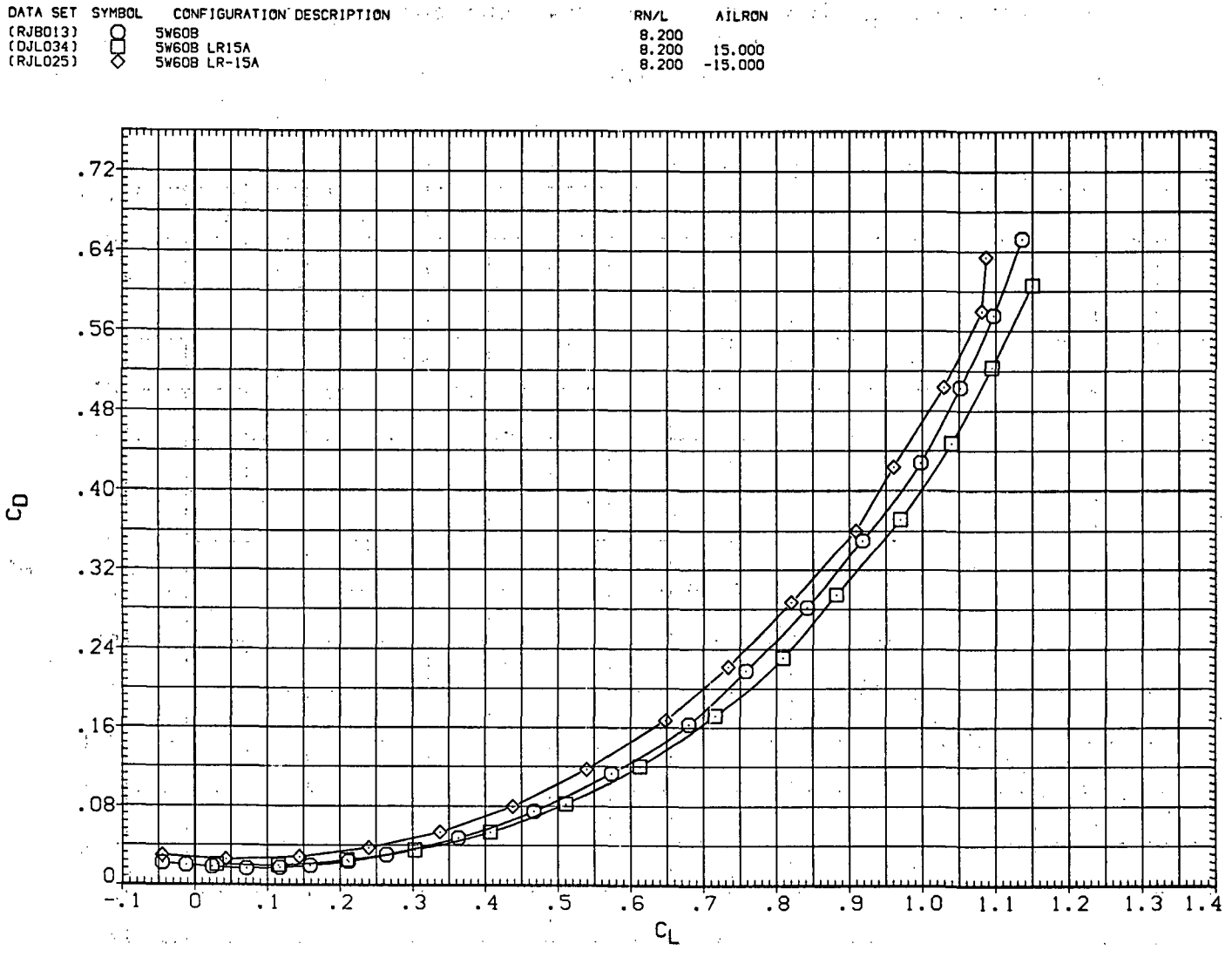

(b) C_D vs C_L

Figure 47.– Continued.

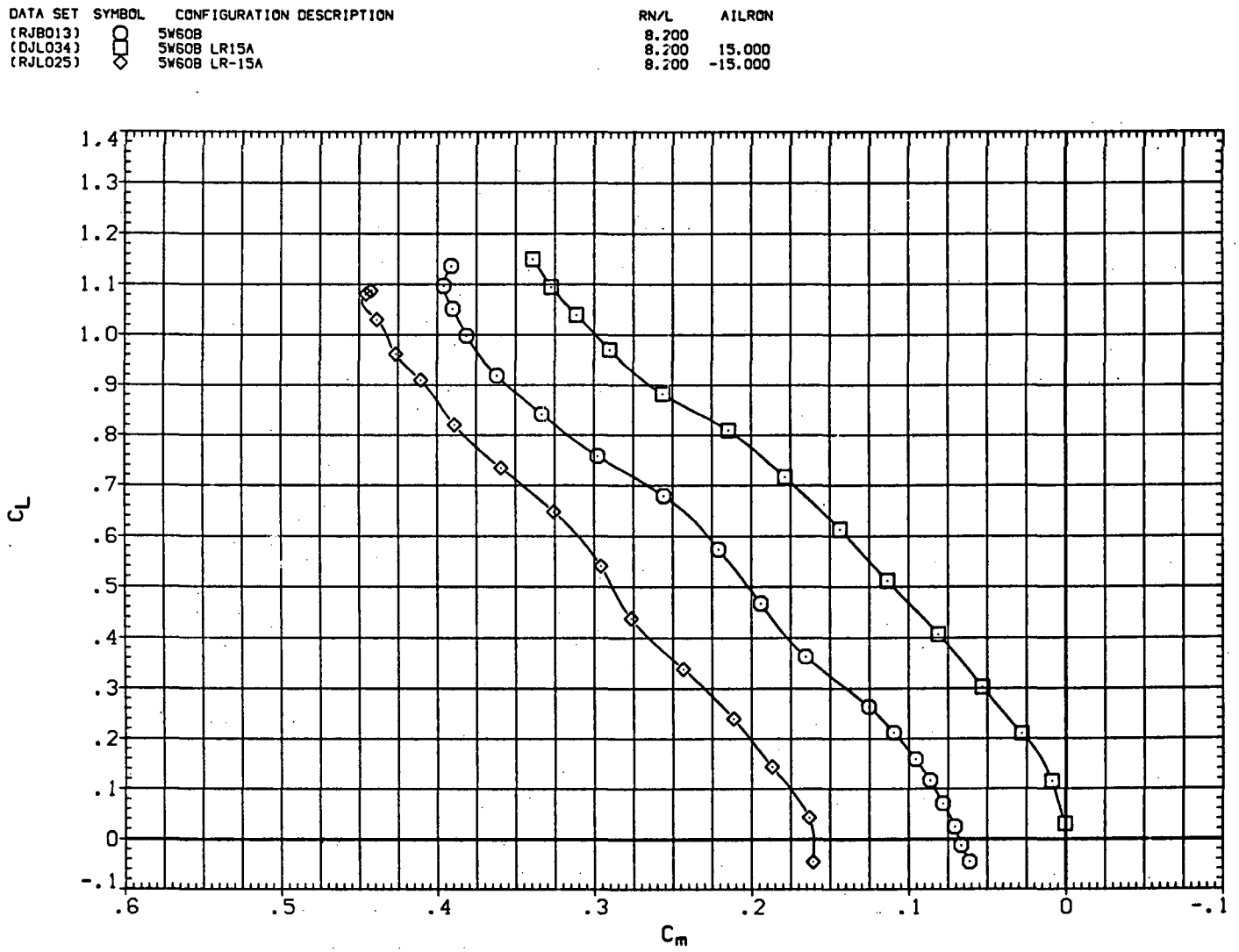

(c) C_L vs C_m

Figure 47.– Continued.

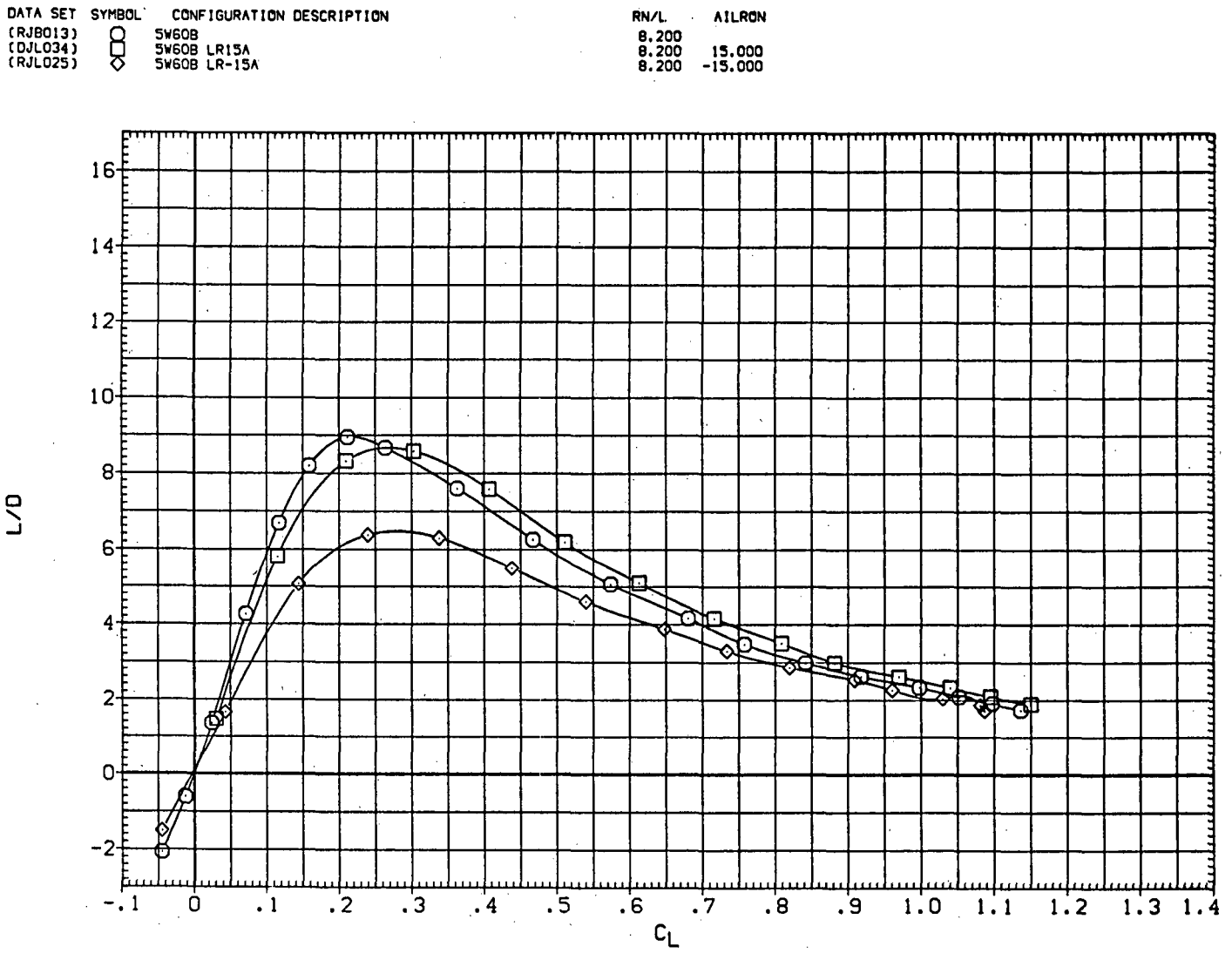

(d) L/D vs C_L

Figure 47.– Continued.

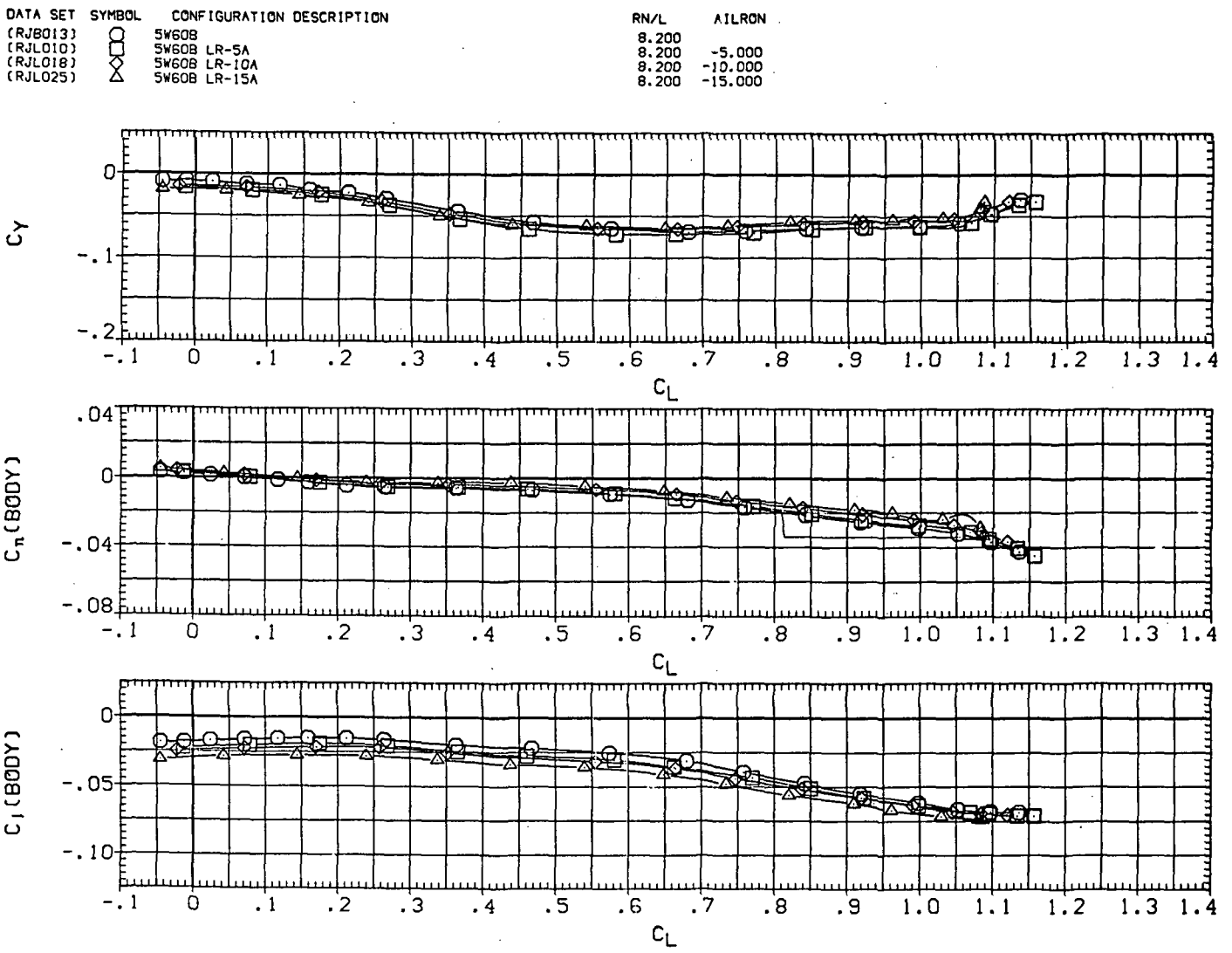

(e) C_Y, C_n, and C_l vs C_L (negative $\Delta\delta_a$'s).

Figure 47.– Continued.

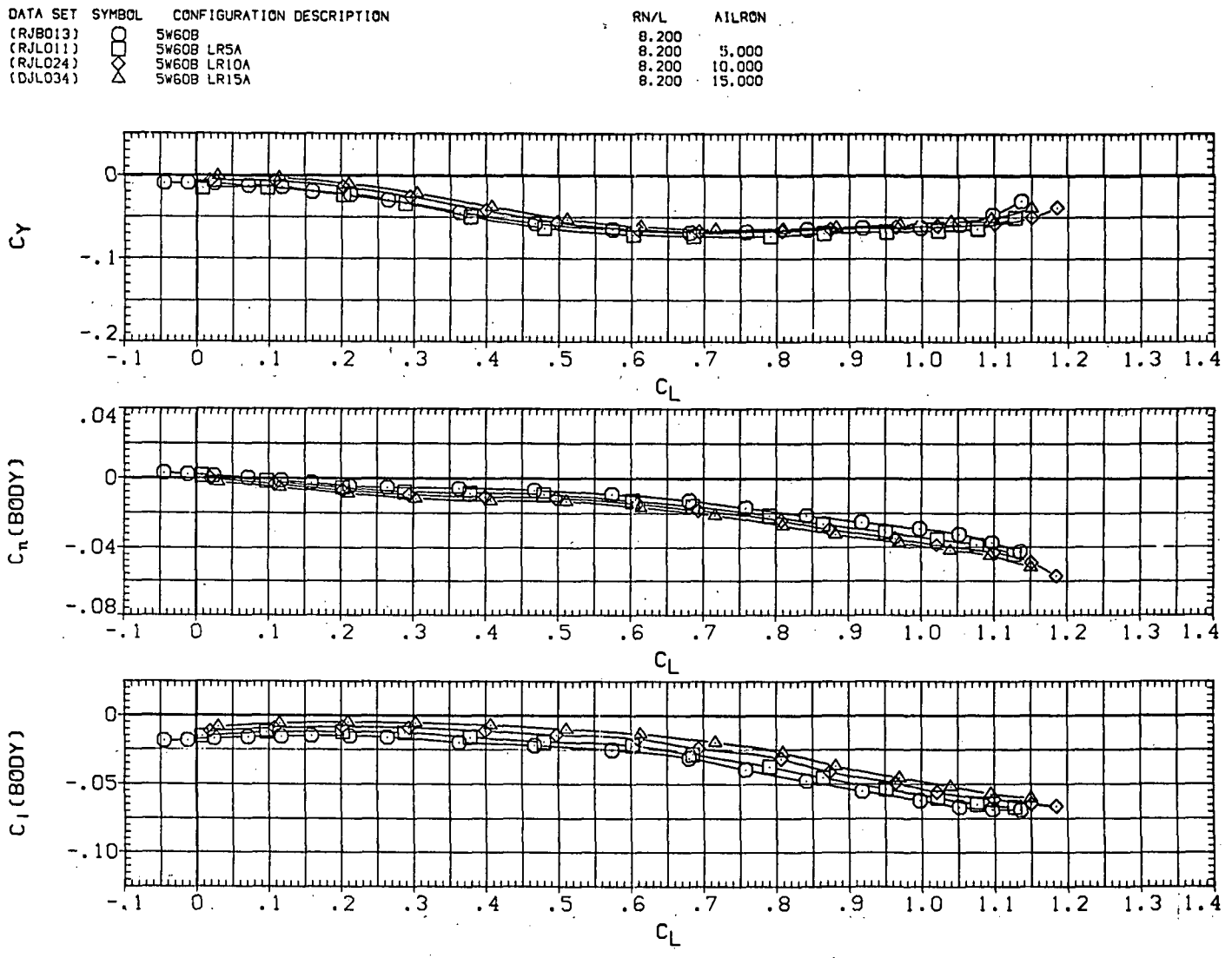

(f) C_Y, C_n, and C_l vs C_L (positive $\Delta\delta_a$'s).

Figure 47.– Concluded.

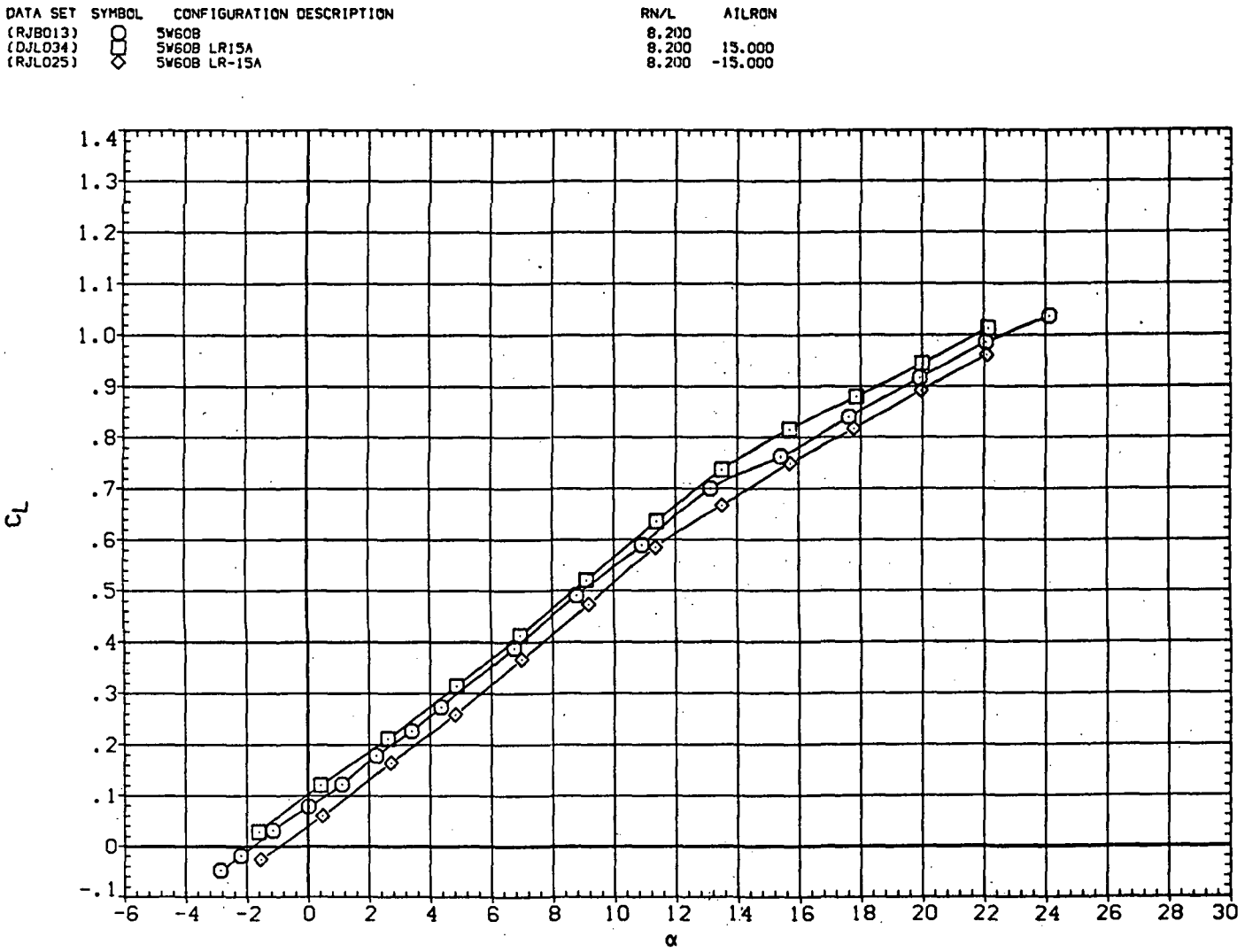

(a) C_L vs. α

Figure 48.– Aileron effectiveness on the oblique wing with intermediate bend: $\Lambda = 60°, M = 1.1$.

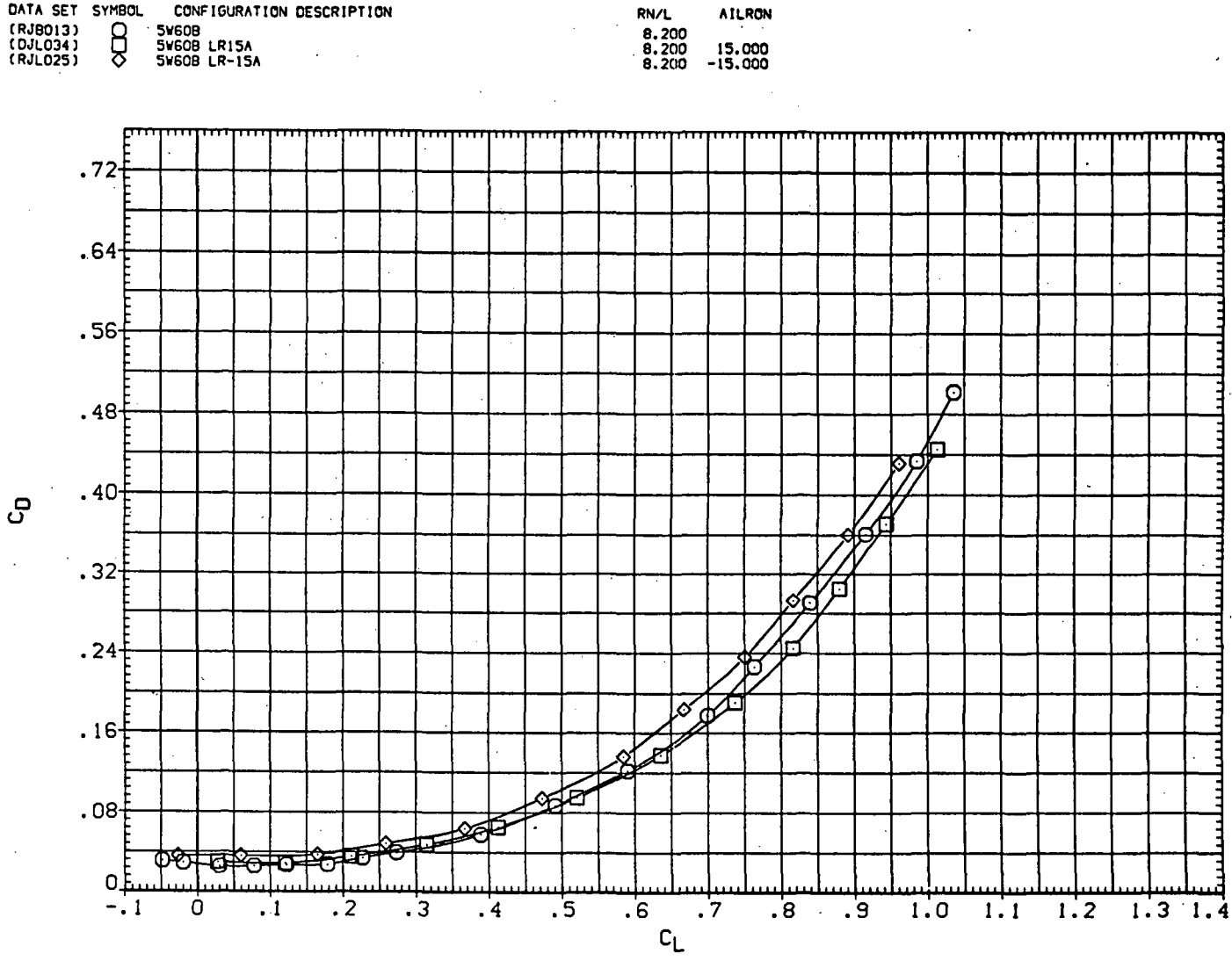

(b) C_D vs C_L

Figure 48.– Continued.

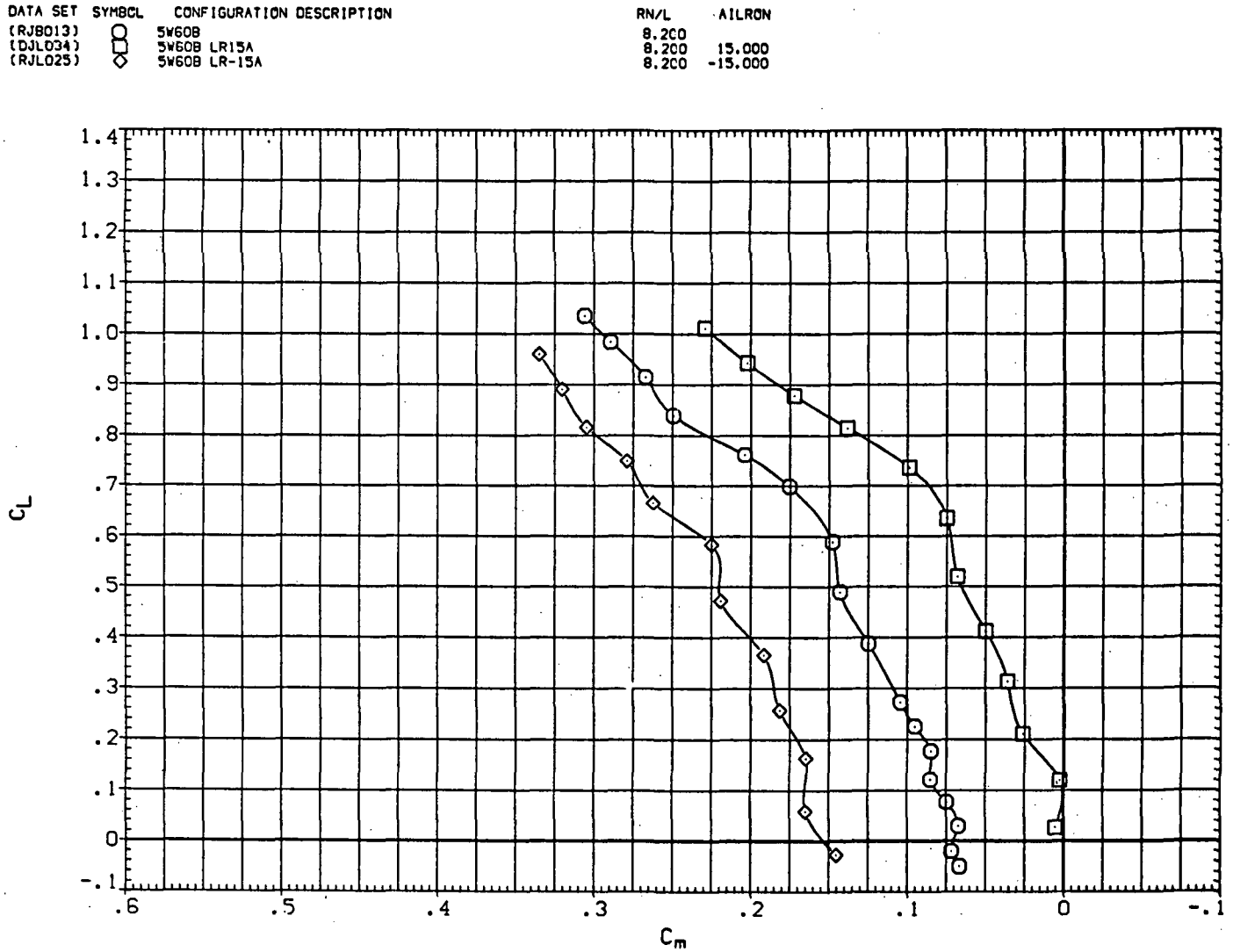

(c) C_L vs C_m

Figure 48.– Continued.

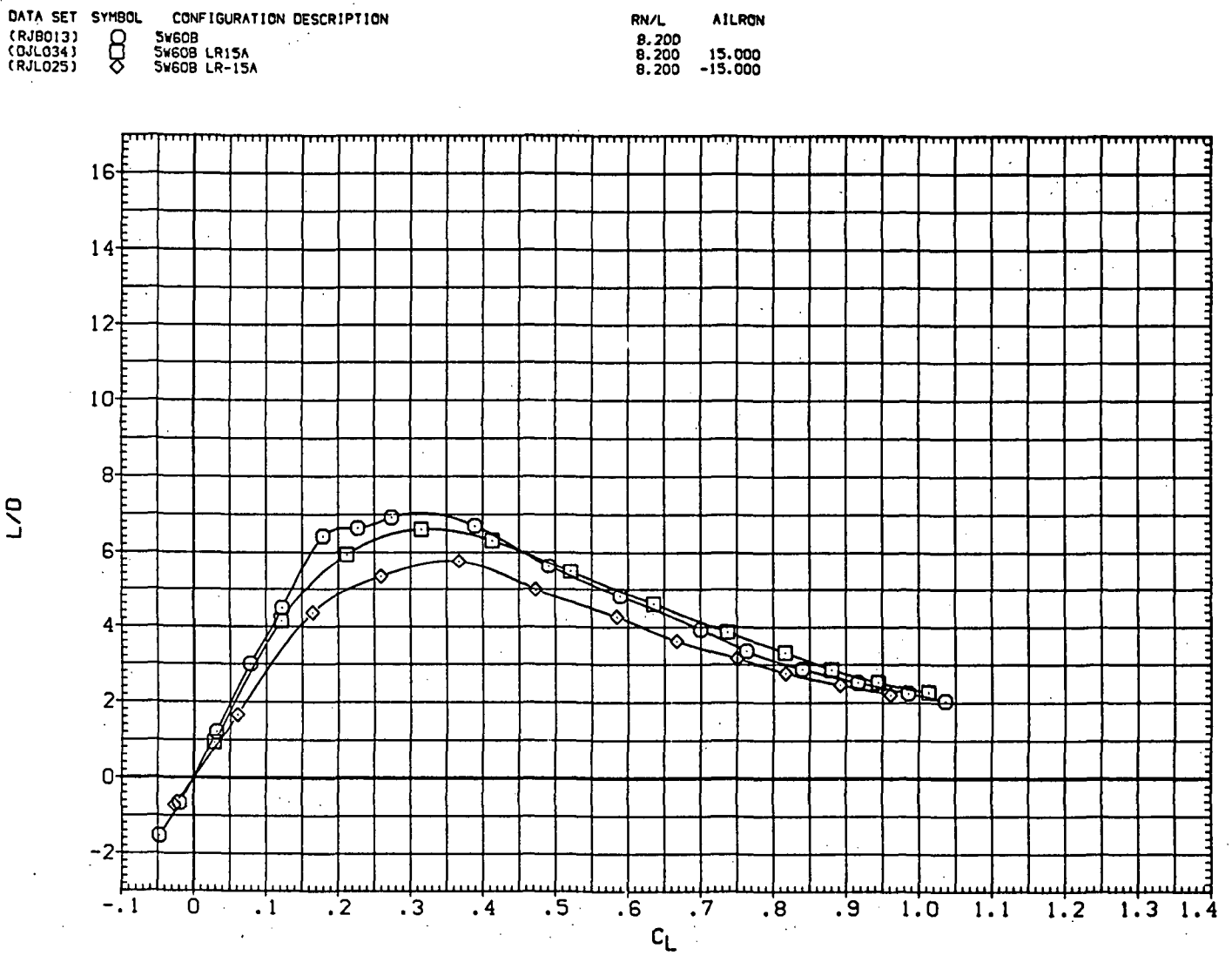

(d) L/D vs C_L

Figure 48.– Continued.

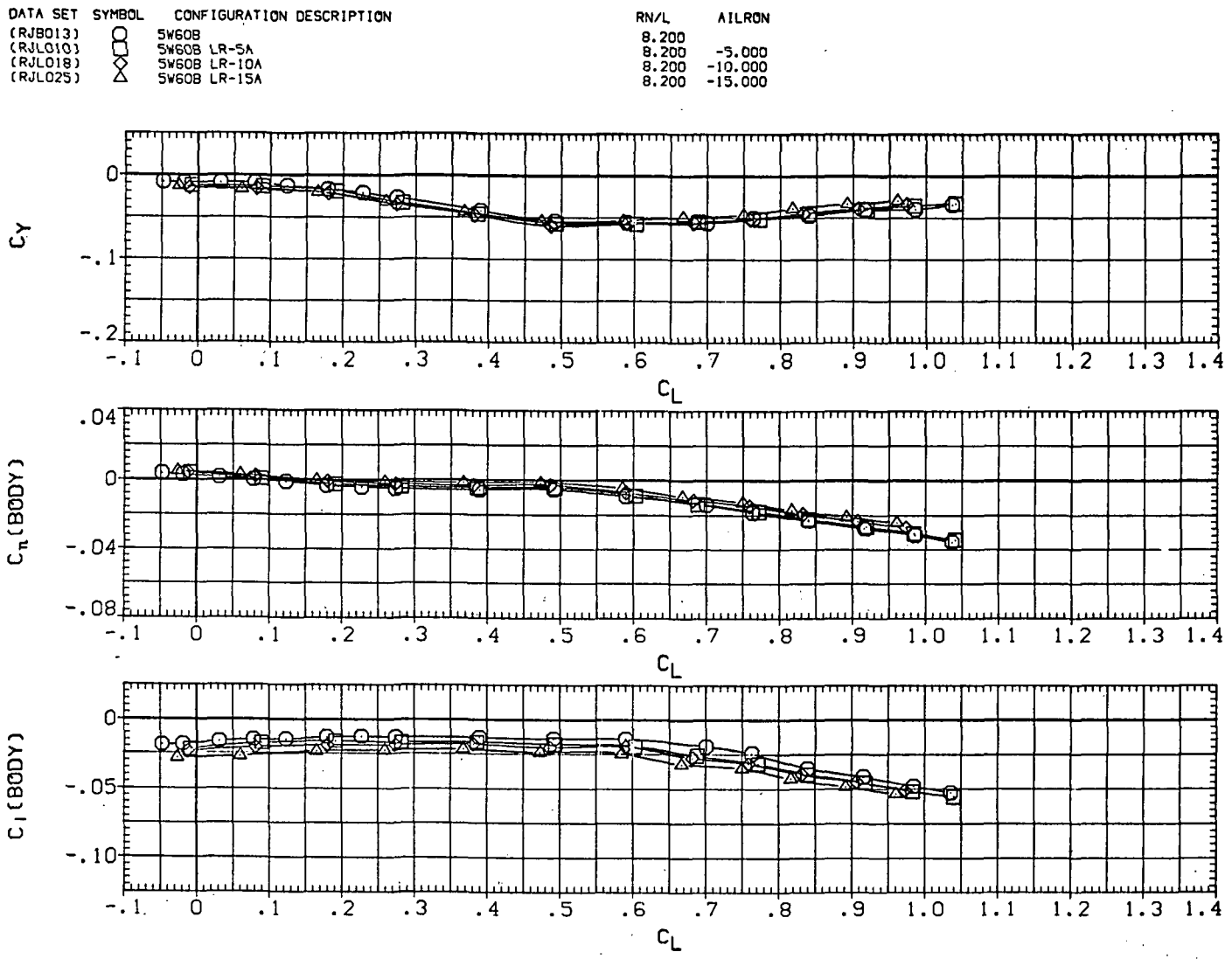

(e) C_Y, C_n, and C_l vs C_L (negative $\Delta\delta_a$'s).

Figure 48.– Continued.

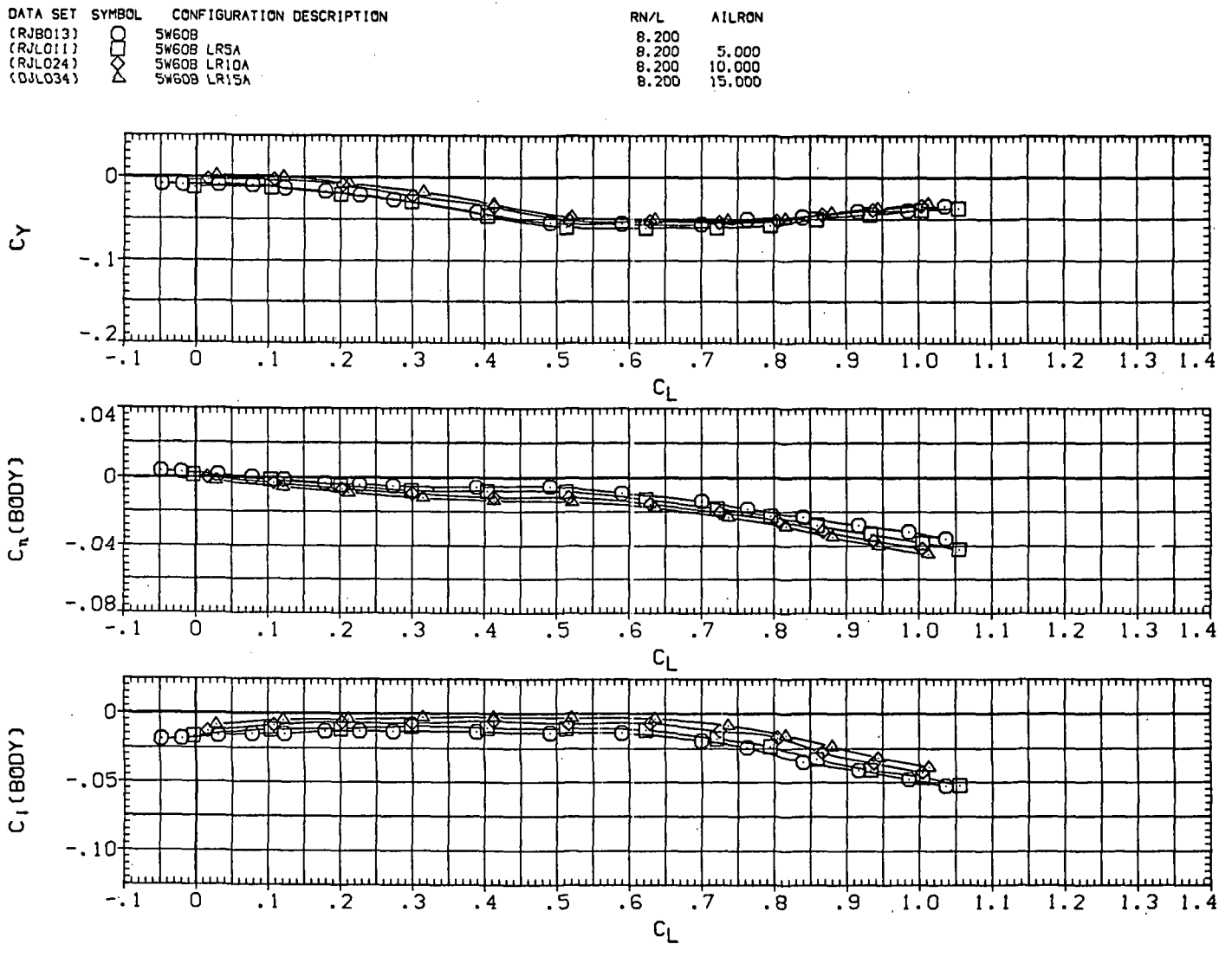

(f) C_Y, C_n, and C_l vs C_L (positive $\Delta\delta_a$'s).

Figure 48.– Concluded.

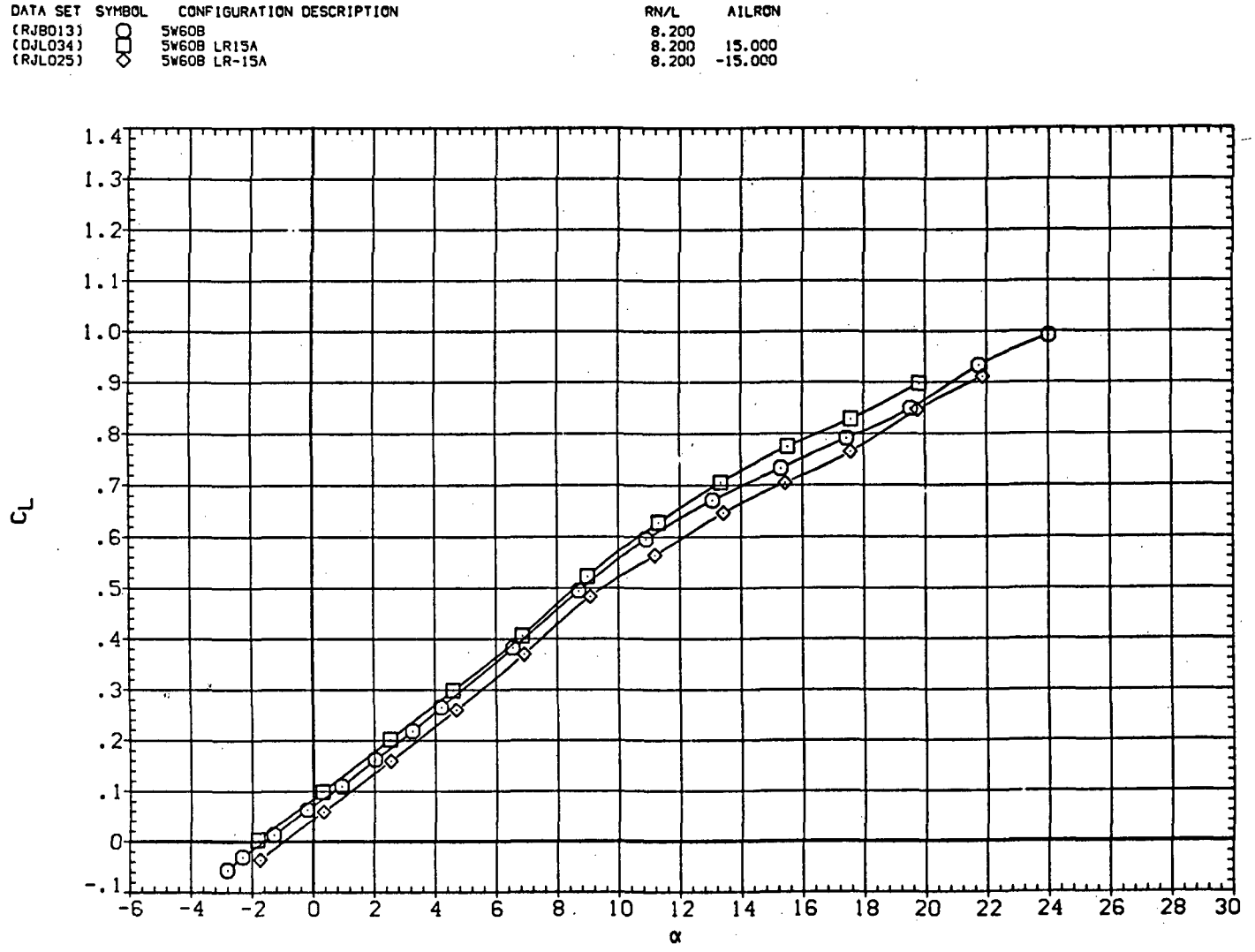

(a) C_L vs α

Figure 49.– Aileron effectiveness on the oblique wing with intermediate bend: $\Lambda = 60°, M = 1.20$.

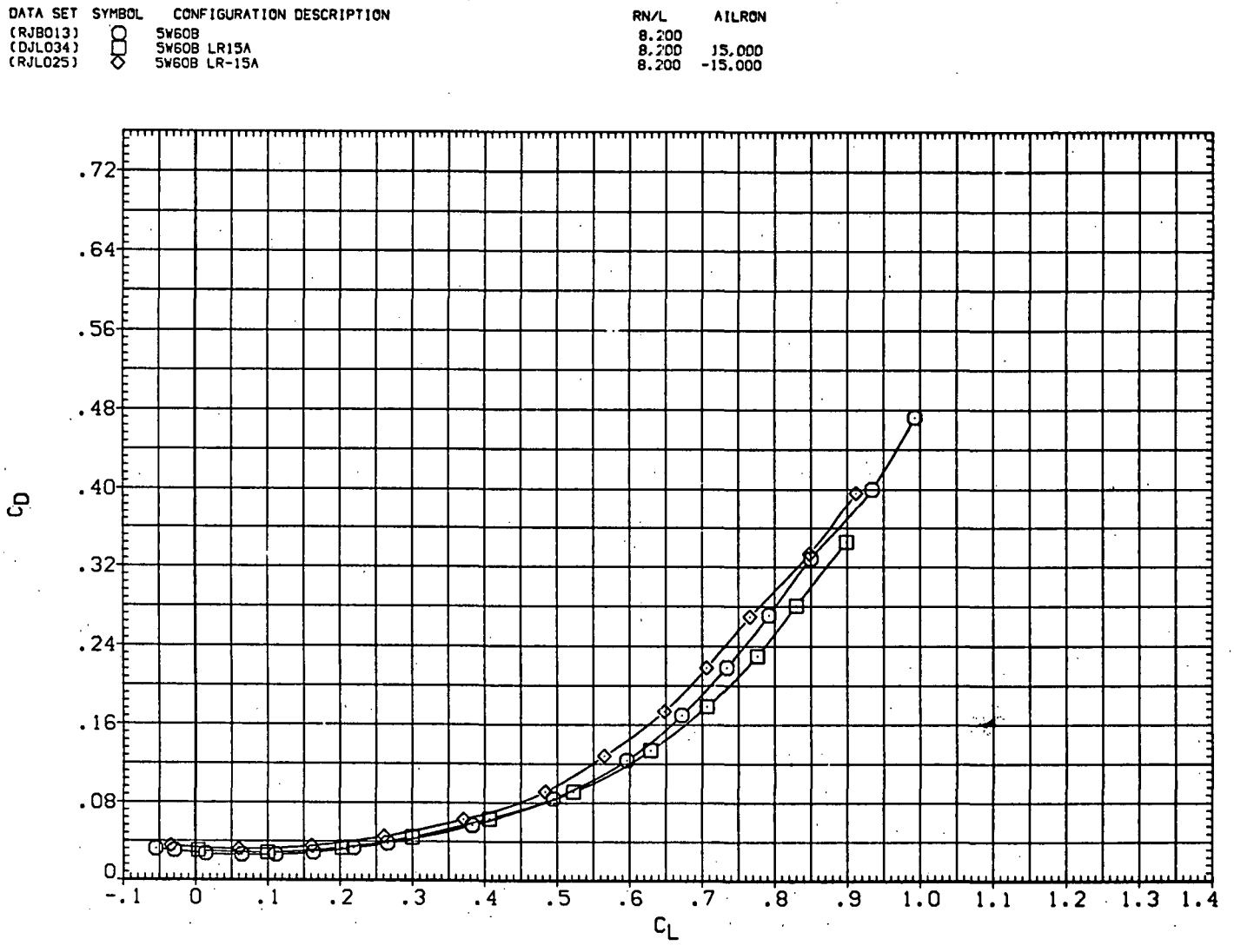

(b) C_D vs C_L

Figure 49.– Continued.

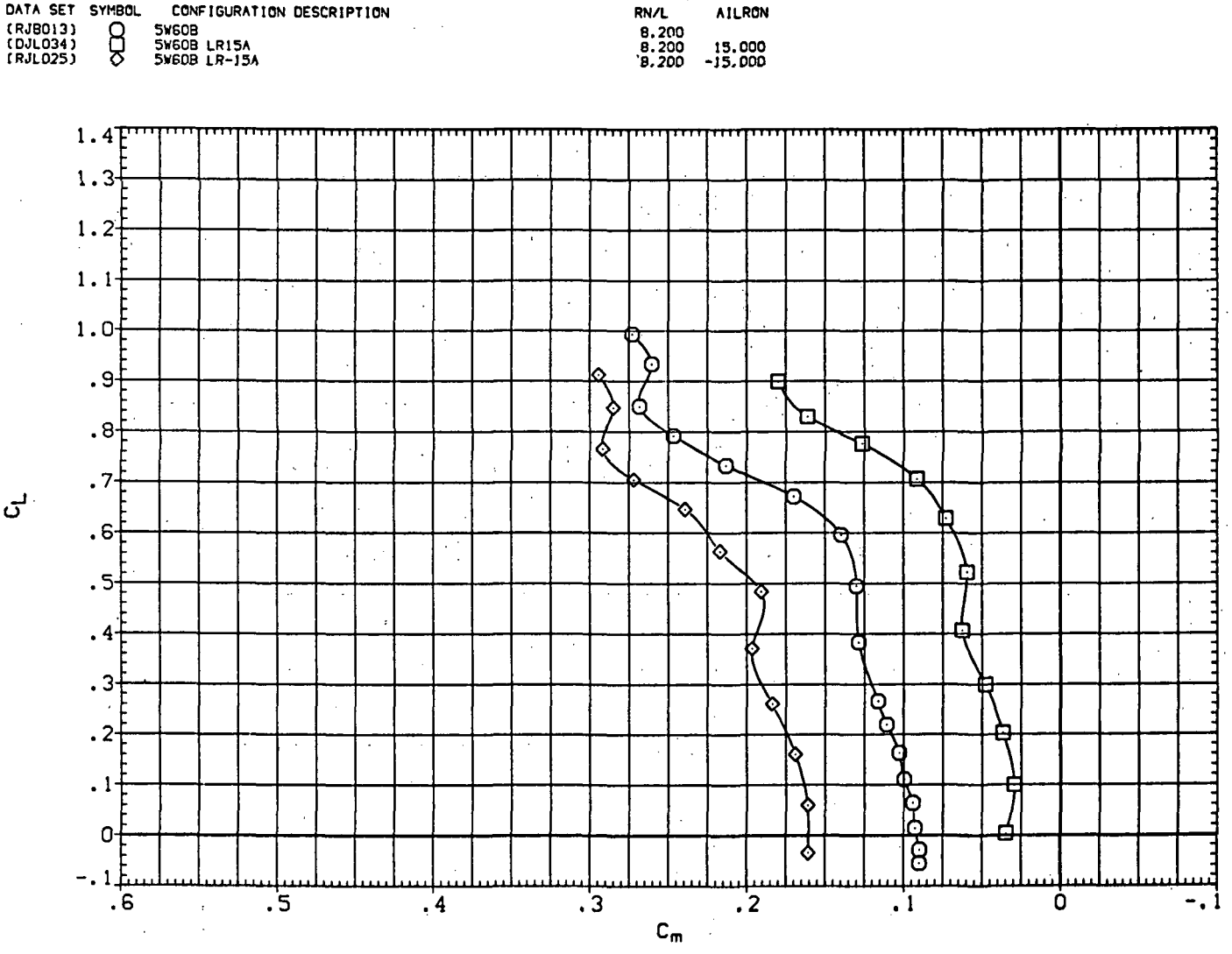

(c) C_L vs C_m

Figure 49.– Continued.

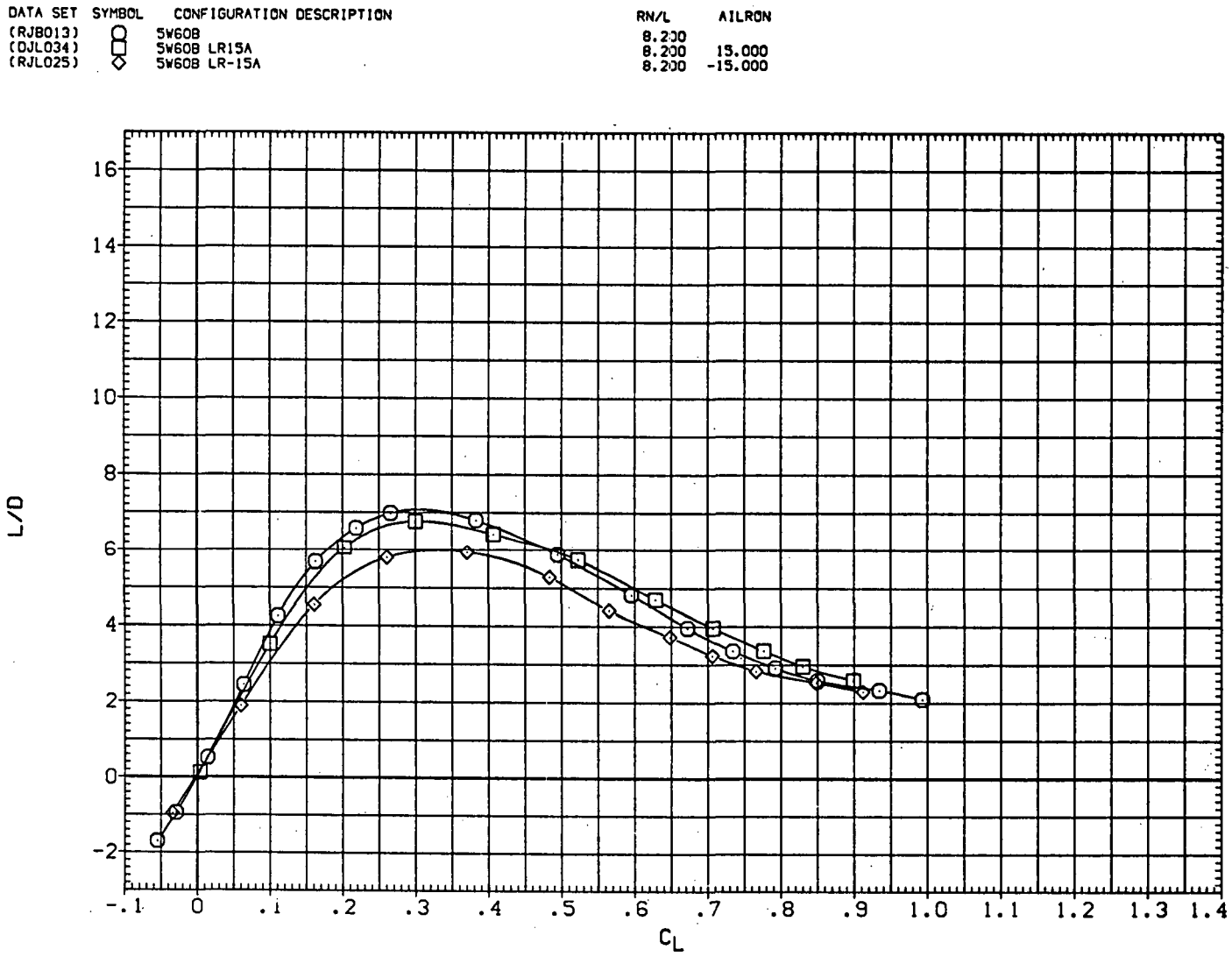

(d) L/D vs C_L

Figure 49.– Continued.

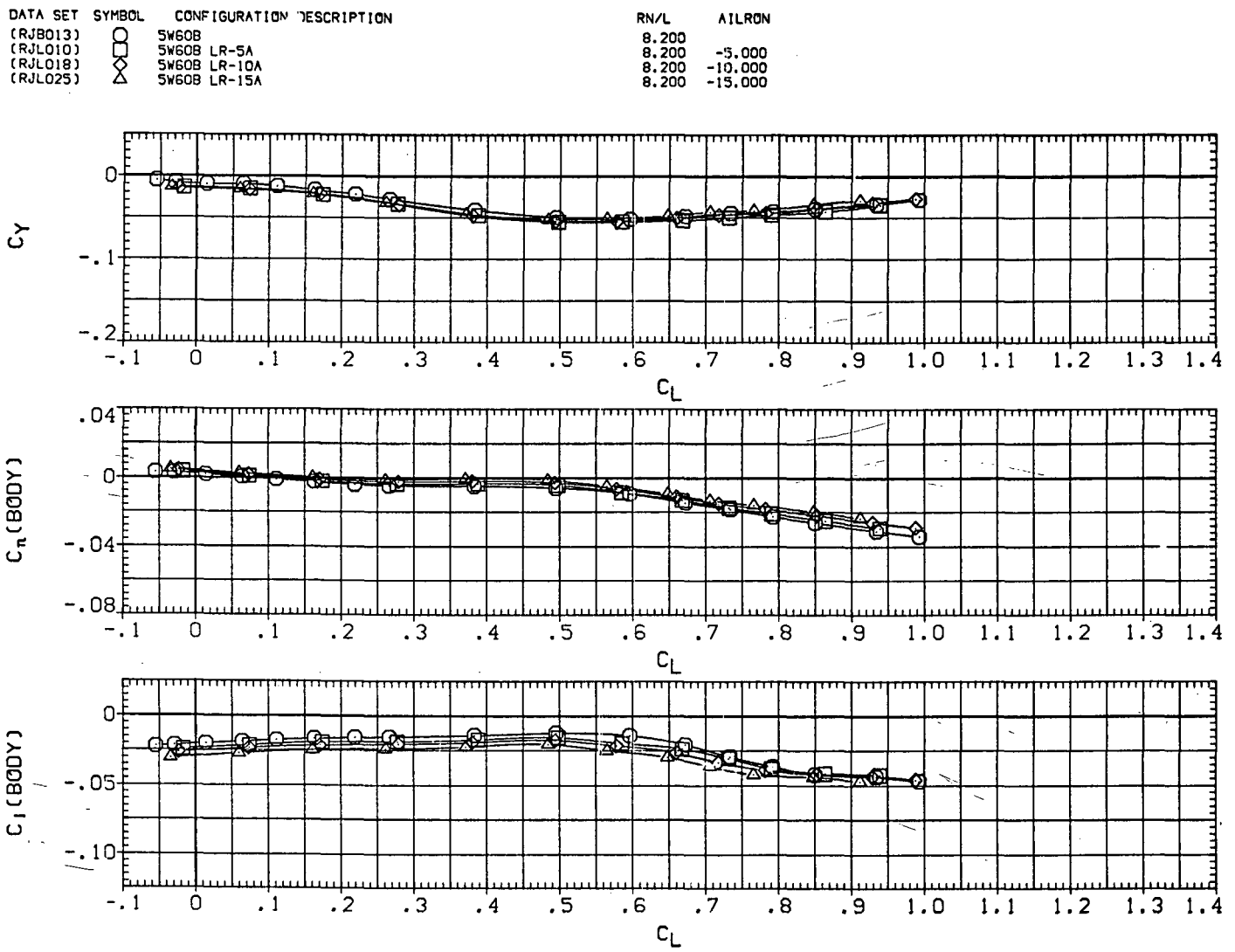

(e) C_Y, C_n, and C_l vs C_L (negative $\Delta\delta_a$'s).

Figure 49.– Continued.

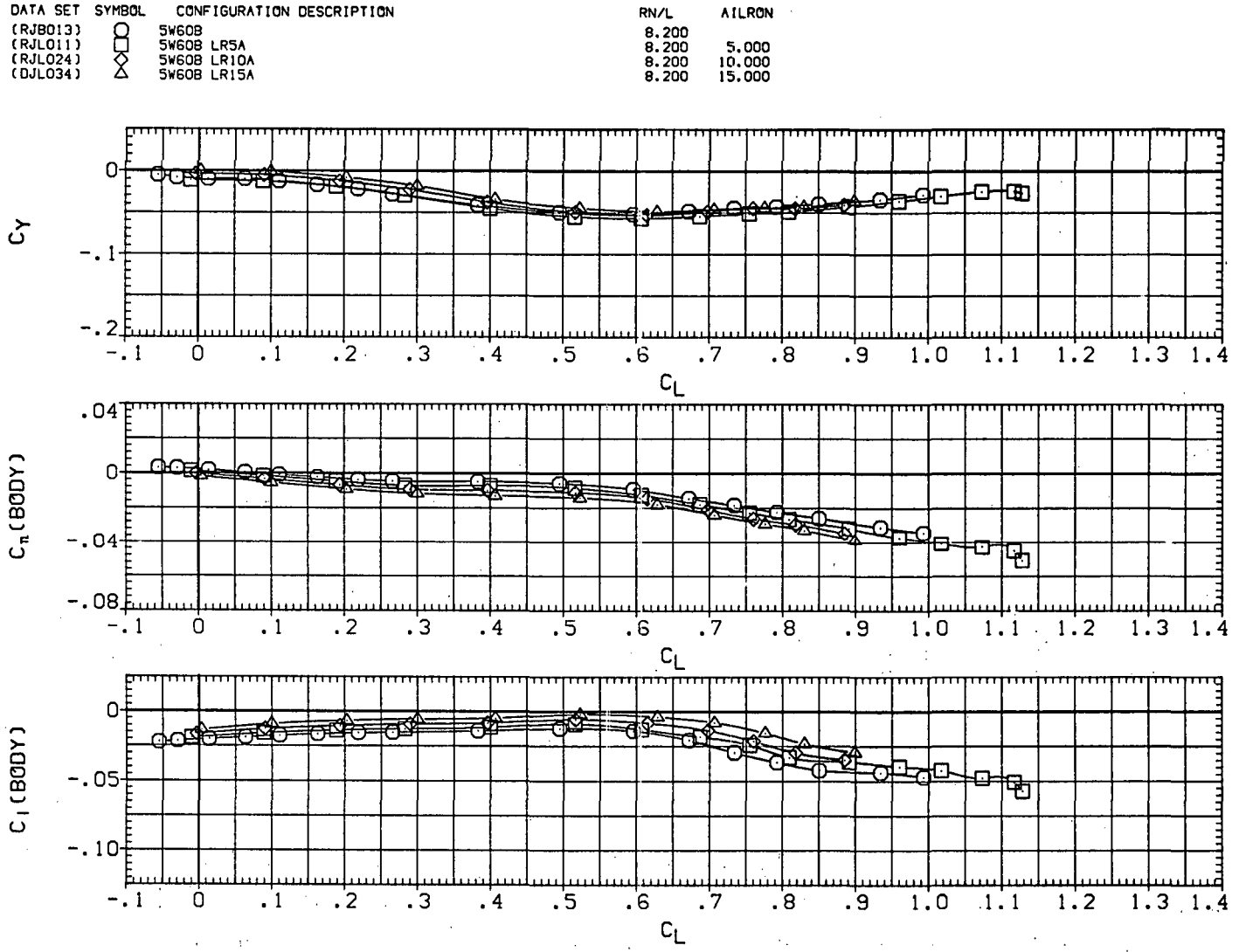

(f) C_Y, C_n, and C_l vs C_L (positive $\Delta\delta_a$'s).

Figure 49.– Concluded.

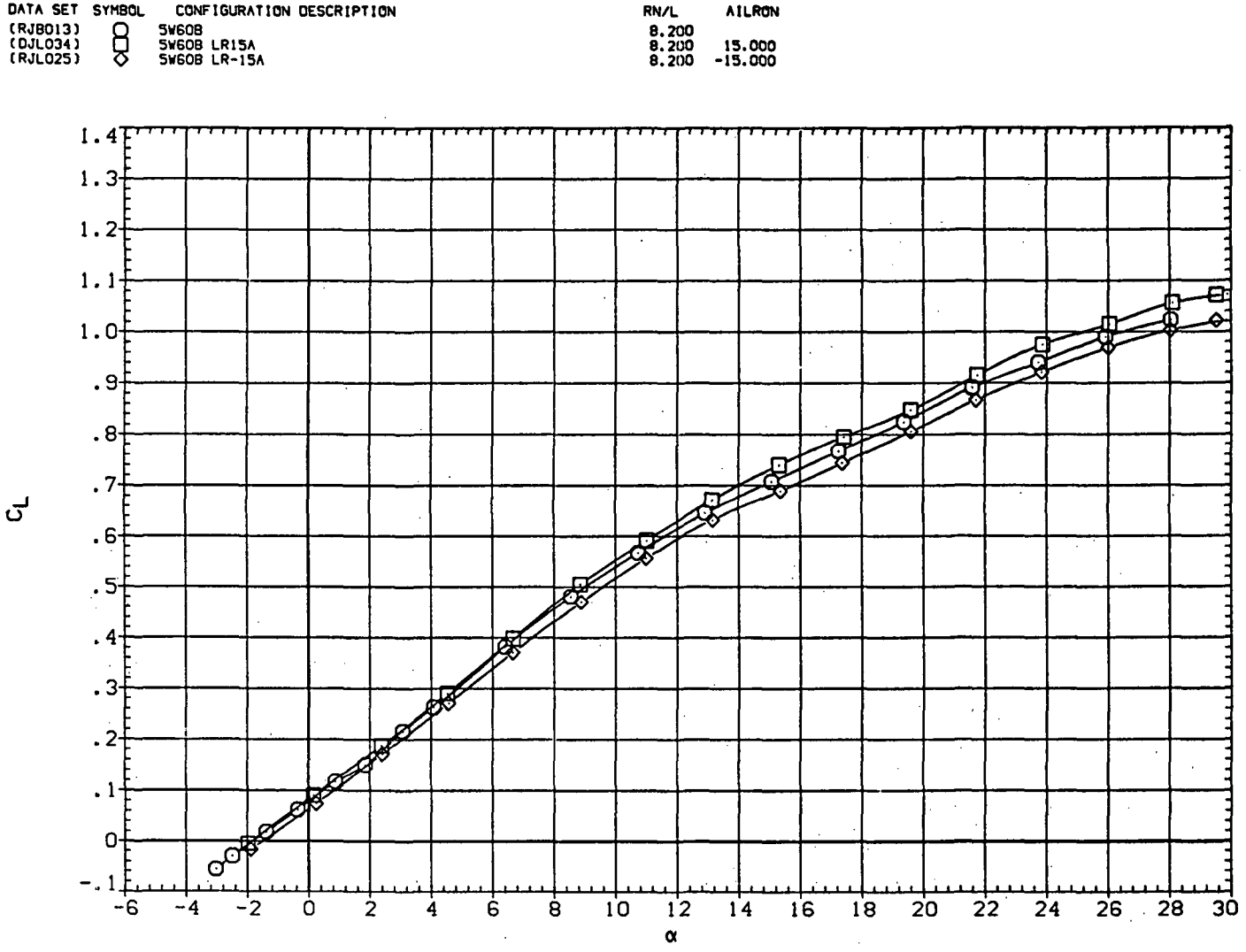

(a) C_L vs α

Figure 50.– Aileron effectiveness on the oblique wing with intermediate bend: $\Lambda = 60°, M = 1.40$.

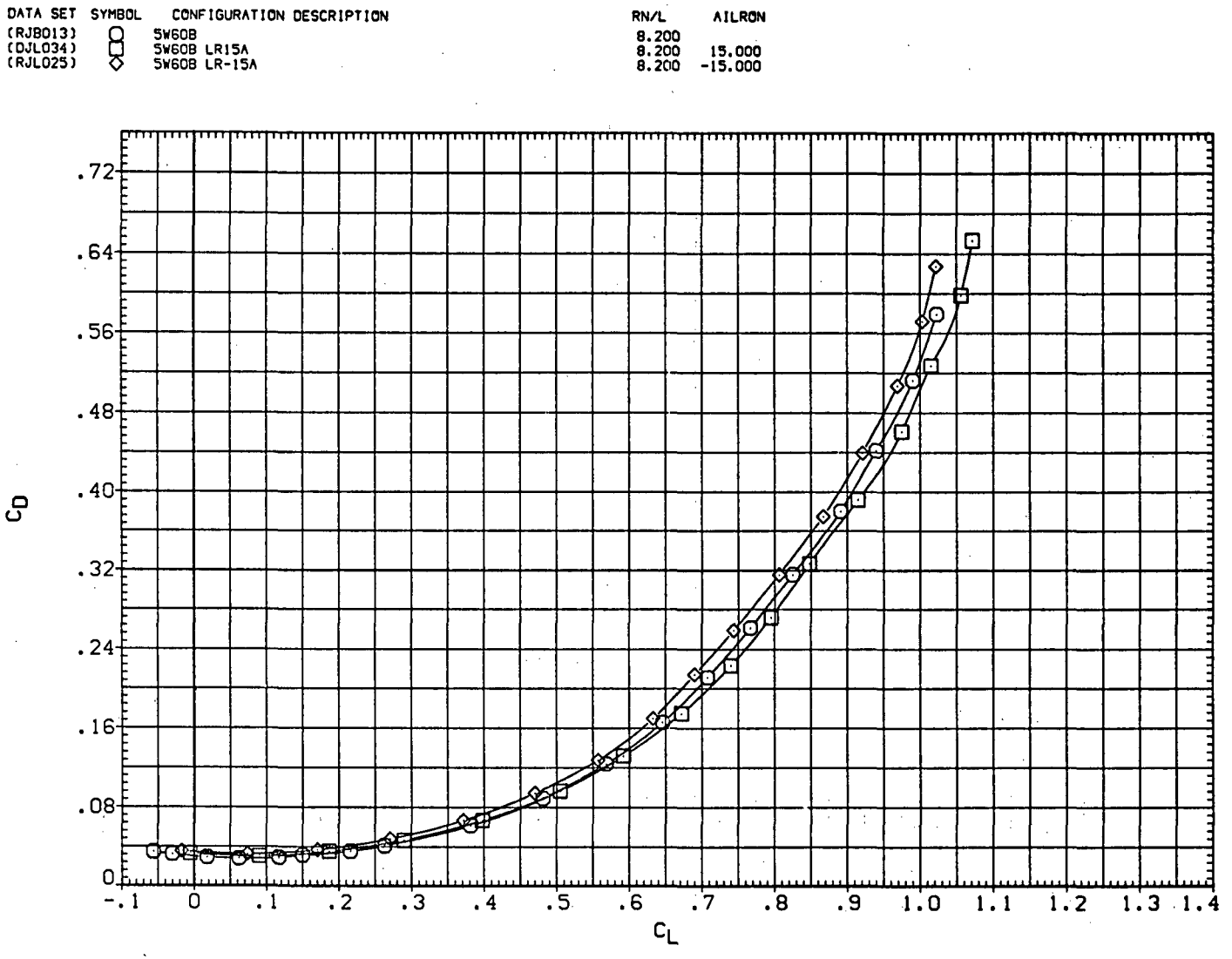

(b) C_D vs C_L

Figure 50.– Continued.

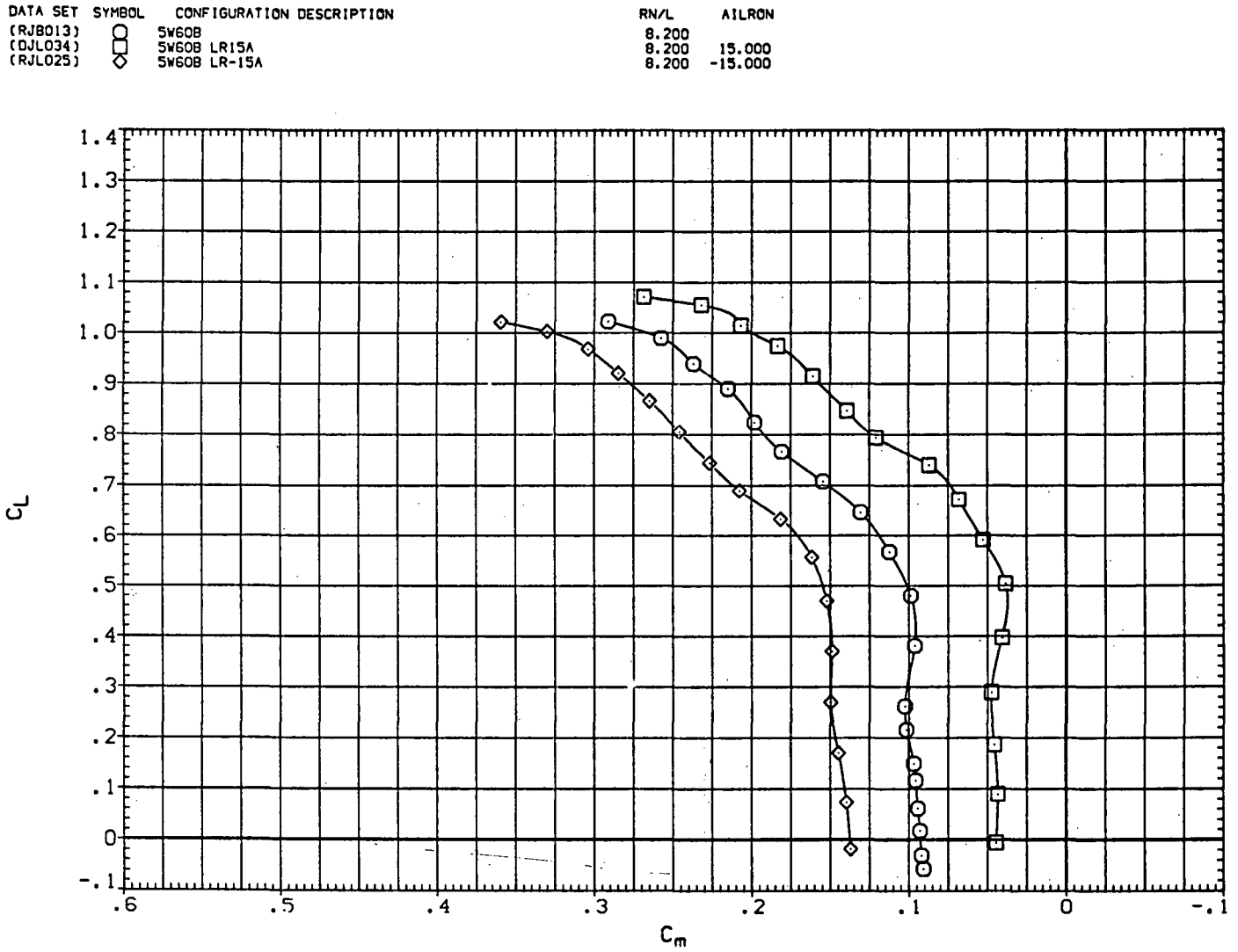

(c) C_L vs C_m

Figure 50.– Continued.

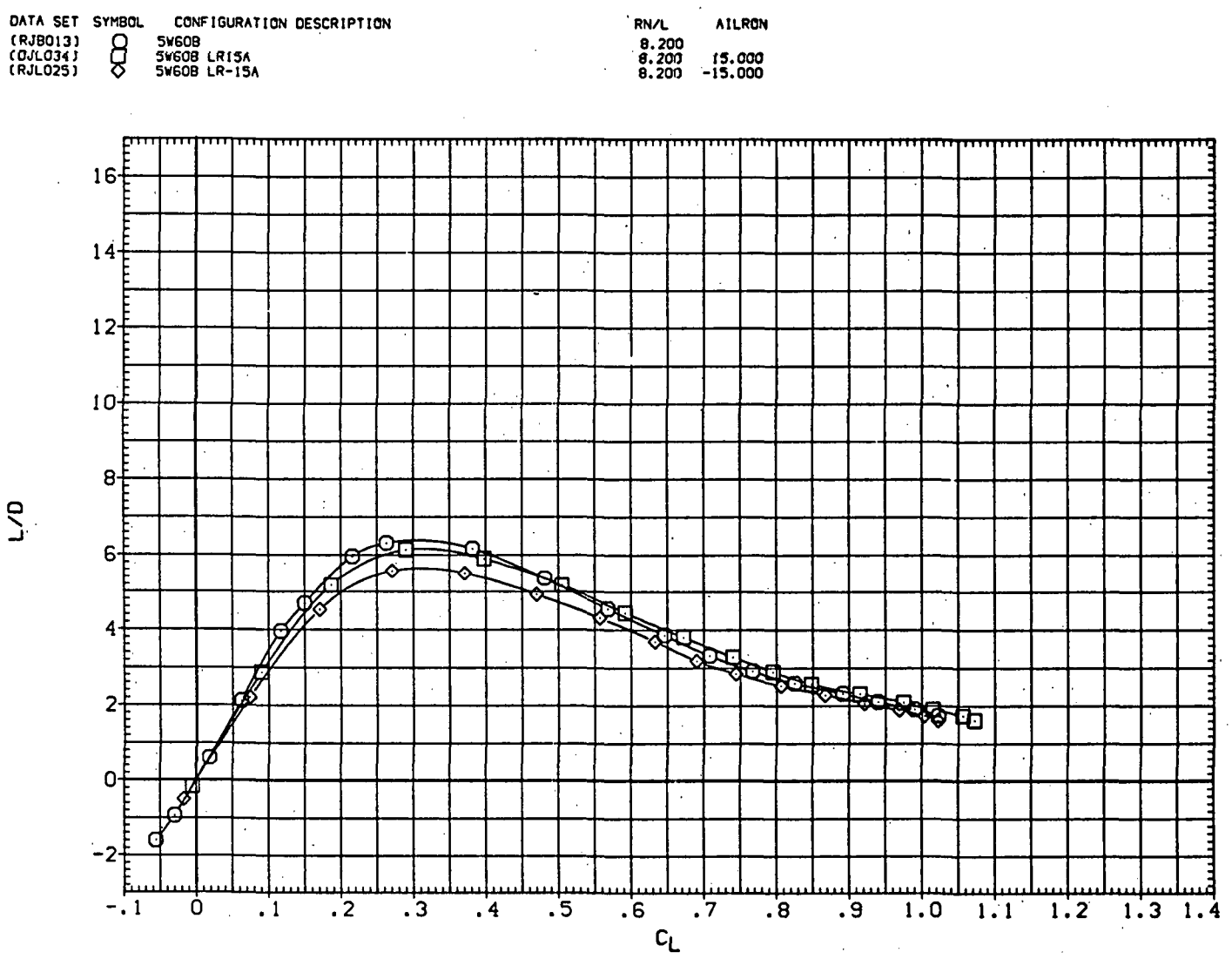

(d) L/D vs C_L

Figure 50.– Continued.

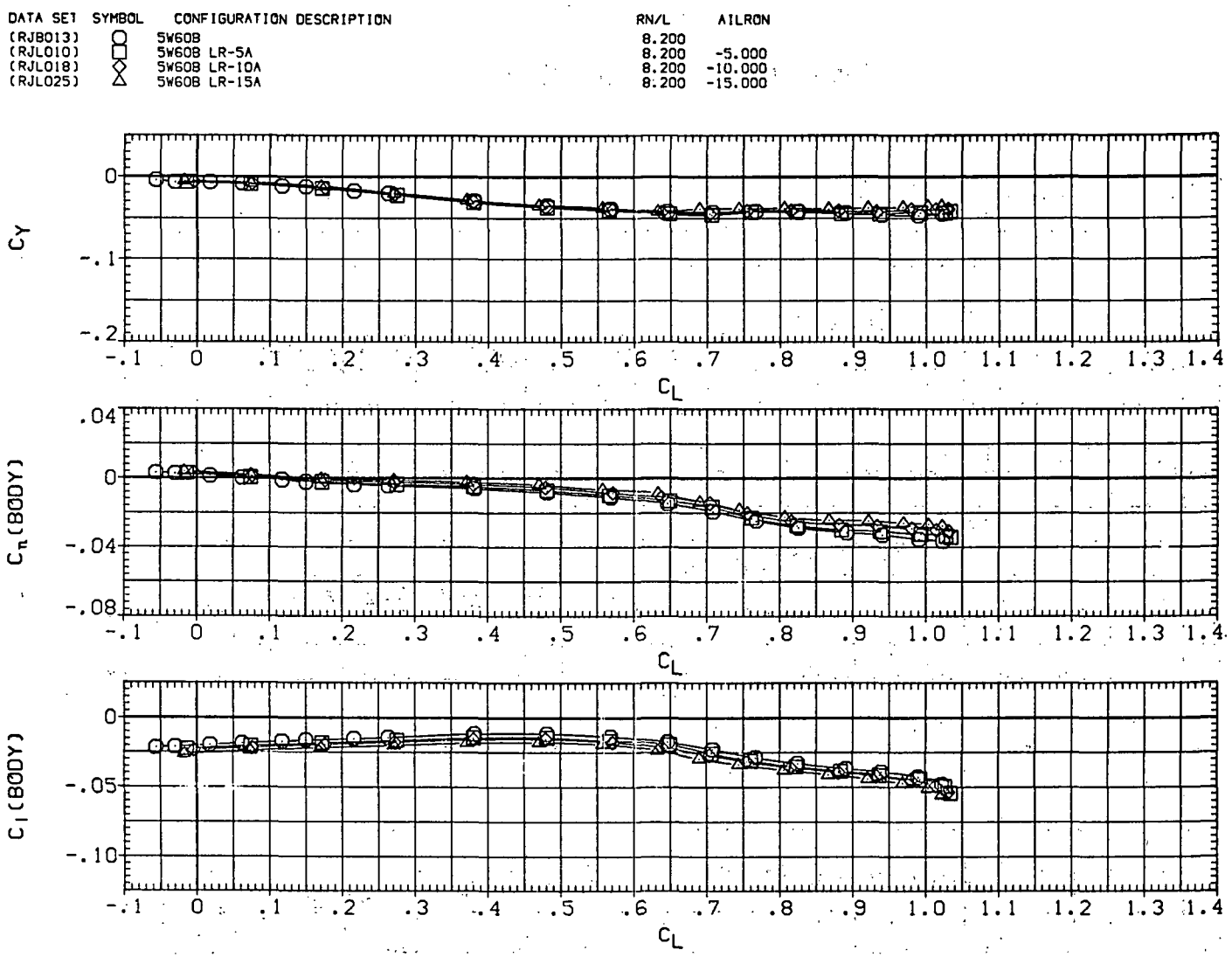

(e) C_Y, C_n, and C_l vs C_L (negative $\Delta\delta_a$'s).

Figure 50.– Continued.

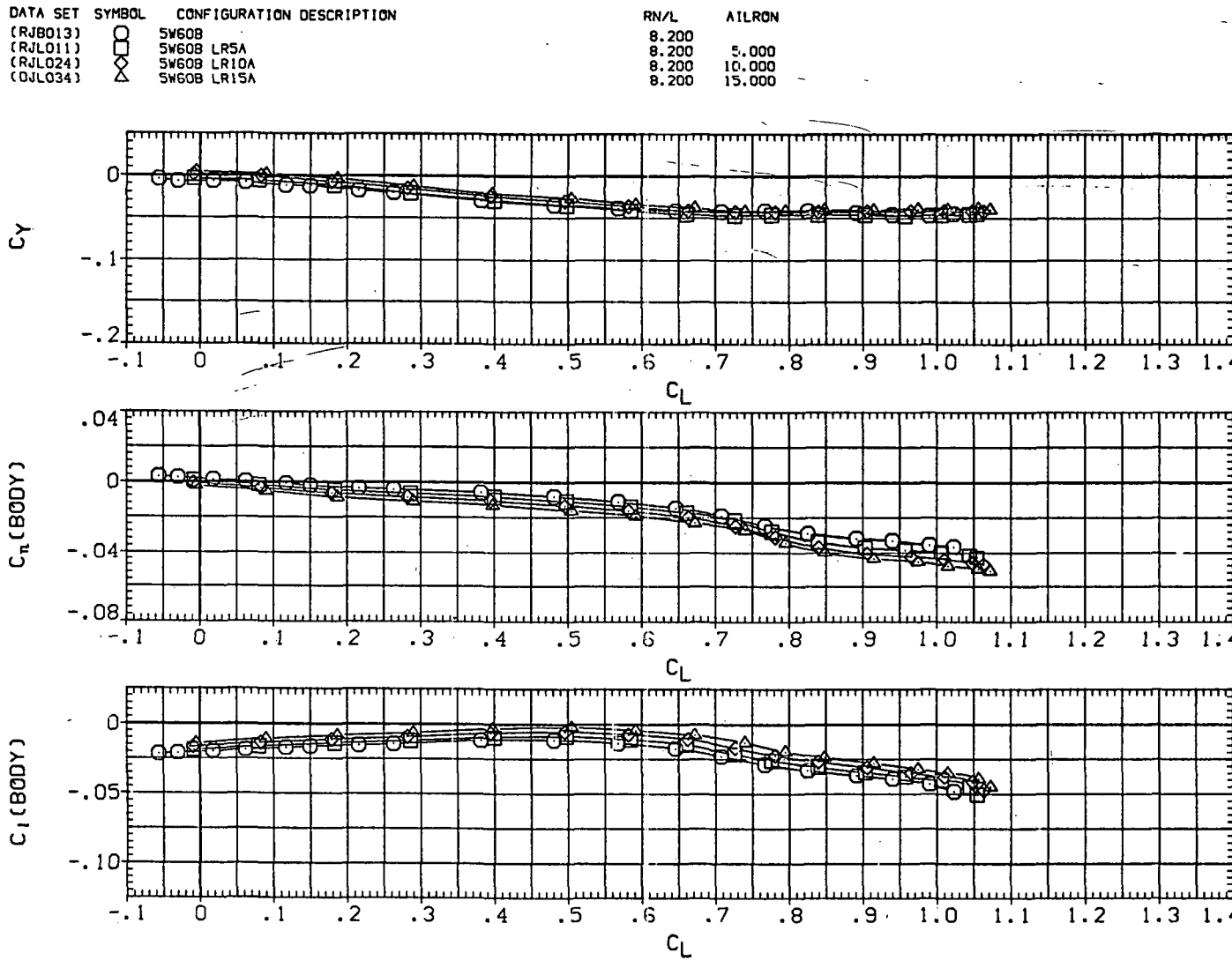

(f) C_Y, C_n, and C_l vs C_L (positive $\Delta\delta_a$'s).

Figure 50.– Concluded.

NATIONAL AERONAUTICS AND SPACE ADMINISTRATION
WASHINGTON, D.C. 20546

OFFICIAL BUSINESS
PENALTY FOR PRIVATE USE $300

SPECIAL FOURTH-CLASS RATE
BOOK

POSTAGE AND FEES PAID
NATIONAL AERONAUTICS AND
SPACE ADMINISTRATION
451

U.S.MAIL

POSTMASTER: If Undeliverable (Section 158 Postal Manual) Do Not Return

"The aeronautical and space activities of the United States shall be conducted so as to contribute . . . to the expansion of human knowledge of phenomena in the atmosphere and space. The Administration shall provide for the widest practicable and appropriate dissemination of information concerning its activities and the results thereof."

—NATIONAL AERONAUTICS AND SPACE ACT OF 1958

NASA SCIENTIFIC AND TECHNICAL PUBLICATIONS

TECHNICAL REPORTS: Scientific and technical information considered important, complete, and a lasting contribution to existing knowledge.

TECHNICAL NOTES: Information less broad in scope but nevertheless of importance as a contribution to existing knowledge.

TECHNICAL MEMORANDUMS: Information receiving limited distribution because of preliminary data, security classification, or other reasons. Also includes conference proceedings with either limited or unlimited distribution.

CONTRACTOR REPORTS: Scientific and technical information generated under a NASA contract or grant and considered an important contribution to existing knowledge.

TECHNICAL TRANSLATIONS: Information published in a foreign language considered to merit NASA distribution in English.

SPECIAL PUBLICATIONS: Information derived from or of value to NASA activities. Publications include final reports of major projects, monographs, data compilations, handbooks, sourcebooks, and special bibliographies.

TECHNOLOGY UTILIZATION PUBLICATIONS: Information on technology used by NASA that may be of particular interest in commercial and other non-aerospace applications. Publications include Tech Briefs, Technology Utilization Reports and Technology Surveys.

Details on the availability of these publications may be obtained from:

SCIENTIFIC AND TECHNICAL INFORMATION OFFICE

NATIONAL AERONAUTICS AND SPACE ADMINISTRATION

Washington, D.C. 20546